What the U.S. elections mean for science *p. 731*

Dendrite turnover in Down syndrome neurons *p. 793*

Social networks drive success in art *p. 825*

Science

$15
16 NOVEMBER 2018
sciencemag.org

AAAS

SPECIAL ISSUE

DIET AND HEALTH

Optimizing human metabolism

CONTENTS

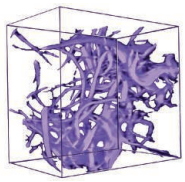

808
Superstructured biocompatible gels

16 NOVEMBER 2018 • VOLUME 362 • ISSUE 6416

SPECIAL SECTION

DIET AND HEALTH

ON THE COVER

The millennials may be onto something. Their favored avocado toast features a mixture of healthy fats, seeds, and grains recommended by nutrition experts in a consensus reading of available scientific studies. This special issue explores what we know—and what we need to learn—about defining a healthy diet that can sustain a strong body and protect against age-associated diseases. See page 762. *Photo: Scott Suchman; Styling: Nichole Bryant*

CREDITS: (TOP) R. FREEMAN *ET AL.*; (BOTTOM) PHOTO: SCOTT SUCHMAN; STYLING: NICHOLE BRYANT

NEWS

IN BRIEF

IN DEPTH

FEATURE

INSIGHTS

PERSPECTIVES

POLICY FORUM

BOOKS *ET AL.*

CONTENTS

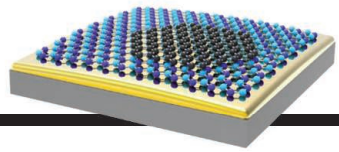

817 Single-crystal hBN films

16 NOVEMBER 2018 • VOLUME 362 • ISSUE 6416

SCIENCE (ISSN 0036-8075) is published weekly on Friday, except last week in December, by the American Association for the Advancement of Science, 1200 New York Avenue, NW, Washington, DC 20005. Periodicals mail postage (publication No. 484460) paid at Washington, DC, and additional mailing offices. Domestic individual membership, including subscription (12 months): $165 ($74 allocated to subscription). Domestic institutional subscription (51 issues): $1808; Foreign postage extra: Mexico, Caribbean (surface mail) $55; other countries (air assist delivery): $89. First class, airmail, student, and emeritus rates on request. Canadian rates with GST available upon request, GST #125488122. Publications Mail Agreement Number 1069624. **Printed in the U.S.A.**
Change of address: Allow 4 weeks, giving old and new addresses and 8-digit account number. **Postmaster:** Send change of address to AAAS, P.O. Box 96178, Washington, DC 20090–6178. **Single-copy sales:** $15 each plus shipping and handling; bulk rate on request. **Authorization to reproduce** material for internal or personal use under circumstances not falling within the fair use provisions of the Copyright Act is granted by AAAS to libraries and others who use Copyright Clearance Center (CCC) Pay-Per-Use services provided that $35.00 per article is paid directly to CCC, 222 Rosewood Drive, Danvers, MA 01923. The identification code for *Science* is 0036-8075. *Science* is indexed in the *Reader's Guide to Periodical Literature* and in several specialized indexes.

Science
AAAS
1200 New York Avenue, NW, Washington, DC 20005
Clarendon House, Clarendon Road, Cambridge, UK CB2 8FH

SUBSCRIPTION SERVICES For change of address, missing issues, new orders and renewals, and payment questions: 866-434-AAAS (2227) or 202-326-6417, FAX 202-842-1065. Mailing addresses: AAAS, P.O. Box 96178, Washington, DC 20090-6178 or AAAS Member Services, 1200 New York Avenue, NW, Washington, DC 20005

INSTITUTIONAL SITE LICENSES 202-326-6730 **REPRINTS:** Author Inquiries 800-635-7181 **COMMERCIAL INQUIRIES** 803-359-4578 **PERMISSIONS** 202-326-6765, permissions@aaas.org **AAAS Member Central Support** 866-434-2227 www.aaas.org/membercentral.

Science serves as a forum for discussion of important issues related to the advancement of science by publishing material on which a consensus has been reached as well as including the presentation of minority or conflicting points of view. Accordingly, all articles published in *Science*—including editorials, news and comment, and book reviews—are signed and reflect the individual views of the authors and not official points of view adopted by AAAS or the institutions with which the authors are affiliated.

INFORMATION FOR AUTHORS See www.sciencemag.org/authors/science-information-authors

Published by AAAS

EDITORIAL

Reform and cooperation in China

Since it was established as a science funding organization in 1986, the National Natural Science Foundation of China (NSFC) has seen its annual budget grow from CNY 80 million to 28.04 billion in 2018, as China underwent rapid transformation and became a global player in research. Now under the new leadership of President Li Jinghai, the NSFC has engaged in consultations about its future. To promote international dialogue, the NSFC convened representatives from 15 funding agencies around Europe to solicit feedback on proposed reforms. This September meeting in Paris marked a first major step by the NSFC to align its new strategies and policies with those of international partners and demonstrate its commitment to cooperation.

In the course of China's recent government reorganization, the NSFC was affiliated with the Ministry of Science and Technology, which raised concerns about the NSFC's independence. There has been speculation about possible changes since the restructuring was announced, but little detail was provided until the outline of the reform was unveiled in Paris. In that context, the message was that the NSFC will keep its due independence.

Reforms carried out by the NSFC reflect shifts in science: changing global science landscapes, the importance of transdisciplinarity, the combination of applied and basic research, and the interplay between research and innovation. To adapt to such future needs, the NSFC identifies four funding categories: (i) curiosity-driven disruptive research, (ii) burning problems at the frontiers of research, (iii) excellent science applied to economic and social demands, and (iv) transdisciplinary research dealing with grand challenges. The NSFC is considering a special division with tasks cutting across disciplinary divisions. All funding agencies pointed to the challenge of keeping "scientific excellence" as a dominant criterion.

Each of the proposed funding categories will require specific evaluation approaches. The NSFC is reviewing its evaluation mechanisms following principles of responsibility, credit, and contribution of reviewers—avoiding nonacademic biases and conflicts of interest; assessing reviewers' performance; and contributing constructive feedback to proposers. Evaluating transdisciplinary proposals and finding reviewers with the necessary skills is challenging. The NSFC plans to test artificial intelligence–assisted approaches for identifying reviewers.

International collaboration with foreign funders is a priority of the NSFC. Regularly, partners are involved in joint calls for proposals for research projects, exchange initiatives, and bilateral or multilateral workshops. For international joint peer reviews, rules are commonly agreed on and implemented successfully. But strict and differing national rules and some inflexibility of internal procedures—for example, regarding eligibility of proposers—are hindering alignment and simplification. Participants agreed that this is an area in need of future joint considerations.

"COOPERATION AND EXCHANGE BETWEEN FUNDING AGENCIES HAVE HUGE POTENTIAL TO STRENGTHEN INTERNATIONAL SCIENCE."

Following the trend from bilateral to multilateral collaboration, earlier this year the NSFC and the Joint Programming Initiative Urban Europe launched a pilot joint call on sustainable urbanization involving nine European funding agencies. Upcoming evaluation of this effort will provide guidance for future multilateral initiatives between China and Europe.

Contacted after the workshop, President Qiu Yong of Tsinghua University commended the reform as "critically important" for science in China, adding "I will give my full support to the reform as a scientist." For the European agencies, the NSFC's reform provided inspiration for their own future development as well as for their cooperation with the NSFC. Cooperation and exchange between funding agencies have huge potential to strengthen international science. Open spaces as provided by the NSFC in Paris are needed for jointly shaping funding and performing science in global settings.

–Manfred Horvat

PHOTO: FOTOSTUDIO STAUDIGL

Manfred Horvat *is honorary professor, Vienna University of Technology, Vienna, Austria; senior adviser for International Science, Technology and Innovation Cooperation, Joint Programming Initiative Urban Europe, Vienna, Austria; adjunct professor at Norwegian University of Science and Technology, Trondheim, Norway; and chairman, advisory board, URBAN EU-CHINA. manfred.horvat@gmx.net*

10.1126/science.aav9737

> “We are not anti-gun. We are anti-bullet hole. … Join us, or move over! This is our lane.”
>
> Open letter signed by more than 30,000 clinicians after the National Rifle Association tweeted that doctors should “stay in their lane” on gun violence.

IN BRIEF

Edited by **Lila Guterman**

DISASTERS

Trump’s tweet ignites clash over fires

Wildfires have struck semiurban areas of California, including this part of the San Fernando Valley.

As California struggles with some of the worst wildfires in its history, fire experts are panning U.S. President Donald Trump’s comments about the causes. At least 44 people had died, and some 200 were missing, in three fires as *Science* went to press. In a 10 November tweet, Trump blamed the state government for “gross mismanagement of the forests.” Many researchers were quick to point out that federal officials manage two-thirds of California’s forests, and that the blazes mainly struck semiurbanized areas and shrublands. “The most destructive and deadly fires in CA are NOT in forests. This is grossly irresponsible and uninformed,” tweeted wildfire scientist Crystal Kolden of the University of Idaho in Moscow. Others highlighted the role of climate change in creating the hot and dry conditions that favored fire. Ironically, Trump’s comments came just weeks after a group of prominent fire scientists, the Fire Research Consensus working group, issued a report concluding that climate change is “a strong driver of fire occurrence,” and that climate and weather are the “primary drivers of fire size.”

Europe studies hormone mimics

POLICY | The European Commission has pledged to speed up research on endocrine disruptors under its next science funding program, beginning in 2021. This pledge is part of a broader plan published on 7 November to protect human health, animals, and the environment from chemicals that alter the body’s balance of hormones. Since its previous strategy, in 1999, the commission has spent about €150 million on such research, and allocated another €52 million to studying testing methods. New research would focus on studying whether a “safe threshold” can be established, the “cocktail effect” of exposure to multiple disruptors, and the development of safer alternatives. The Endocrine Society says more research is welcome, but argues that completed research warrants stricter limits to exposure to these chemicals, found in products such as pesticides and plastics.

A reprieve for tigers and rhinos

WILDLIFE CONSERVATION | After saying last month that it would allow the use of tiger and rhinoceros bones and tissues “in medical research and healing,” the Chinese government has backpedaled. In a move cheered by conservationists, China reinstated its 1993 ban—at least temporarily.

Uganda deploys Ebola vaccine

PUBLIC HEALTH | The persistent Ebola outbreak underway in the conflict-ridden northeastern region of the Democratic Republic of the Congo (DRC) has led neighboring Uganda to start to vaccinate frontline health care workers. This is the first time the experimental Ebola vaccine is being used in a country without an outbreak. More than 2000 Ugandan health workers who live near the border will receive the vaccine, which worked well in a trial in Guinea in 2015, during the massive West African epidemic. Because the vaccine is unlicensed, Uganda’s Ministry of Health had to approve its use. The DRC has vaccinated more than 29,000 people despite an armed insurgency that has repeatedly disrupted its work. Since Ebola surfaced in the DRC in August,

PHOTO: MARCIO JOSE SANCHEZ/AP PHOTO

WILDLIFE CONSERVATION

Amazon turtles bounce back

The threatened giant South American turtle (*Podocnemis expansa*) has made a robust recovery on river beaches in the Brazilian Amazon, thanks to round-the-clock protection during its breeding season. There has been a more than ninefold increase in turtle hatchlings on beaches along a 1500-kilometer section of one of the Amazon River's tributaries since the community conservation effort began in 1977, a team led by researchers from the University of East Anglia in Norwich, U.K., reports this week in *Nature Sustainability*. The result was equivalent to adding 70,000 turtle hatchlings each year. Poachers seeking to illegally harvest meat and eggs of the turtle, which can grow to a meter, attacked just 2% of the 2000 nests on guarded beaches, compared with 99% of the 202 nests on unprotected beaches. The surveillance also provided unintended—and welcome—boosts to the populations of other species, including large-billed terns, green iguanas, and black caimans.

more than 300 people have become ill, nearly two-thirds of whom have died.

Once-wet Mars site targeted

MARS ROVER | Researchers have picked a landing site for the European-Russian ExoMars 2020 rover. Called Oxia Planum, the equatorial site contains clay-rich minerals likely formed in a large body of water, and channels that may have been cut by water some 4 billion years ago, when Mars was wetter. ExoMars, a joint project of the European Space Agency (ESA) and Russia's Roscosmos, is due to arrive in 2021. A drill, delving 2 meters below the surface, will extract samples for analysis. The mission's site selection working group spent 5 years narrowing down eight candidate sites before picking Oxia Planum. Strongly in its favor was the lack of steep slopes and large boulders, which might have endangered the landing. ESA and Roscosmos will review the site before confirming it in 2019.

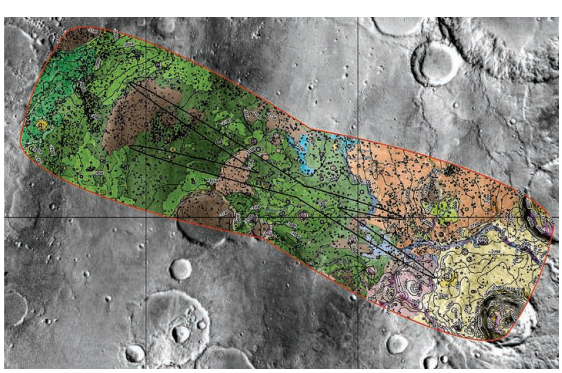

Ellipses mark the chosen landing zone for ExoMars at Oxia Planum.

IMAGES: (TOP TO BOTTOM) CAMILA FERRARA; IRSPS/TAS, NASA/JPL-CALTECH/ARIZONA STATE UNIVERSITY

Nearby star has an icy planet

EXOPLANETS | The solar system has more company in the stellar neighborhood. After the 2016 discovery of a planet orbiting Proxima Centauri, the nearest star to the sun at 4 light-years away (*Science*, 26 August 2016, p. 857), researchers have now found a strong candidate around Barnard's Star, just 6 light-years from home. The new study identified a faint wobble in the motion of Barnard's Star with a 233-day period—the signature of the tug of a planet at least 3.2 times Earth's mass. The study, published this week in *Nature*, drew on three telescopes' observations of the star's wobble as well as 20 years of archival data. The planet may be rocky, but its small, dim star may not shine brightly enough for surface water to be liquid, making the presence of life unlikely.

Keystone pipeline on hold

ENERGY | A federal judge has, at least temporarily, blocked an effort by President Donald Trump's administration to complete the Keystone XL pipeline, which would carry oil 1900 kilometers from central Canada to U.S. refineries. On 9 November, federal District Court Judge Brian Morris of Montana ruled that an environmental assessment by the U.S. Department of State "fell short" of a required "hard look" at the project's effects on climate change, Native American lands, and the broader environment. No work on the pipeline's final section, from Canada to Nebraska, can proceed until the department corrects flaws in its analysis, he ruled. It is the latest setback for Keystone XL, which had been blocked by former President Barack Obama at climate activists' urging before Trump resurrected it early in his presidency.

Farms need to fight bovine TB

WILDLIFE MANAGEMENT | A contentious debate rages in the United Kingdom over whether badgers must be killed in order to slow the spread of tuberculosis (TB) in cattle, a disease that costs farmers and taxpayers about £120 million a year. A new review of the issue, released on

12 November, finds badgers partly to blame and says culling has a reasonable chance of helping stop disease spread. But "it is wrong to put all the blame on wildlife," said population biologist Charles Godfray of the University of Oxford in the United Kingdom, an author of the review. Far more cases of TB result from transmission between cattle than from badgers, the review notes, so it urges the government and farmers to do more to control bovine TB on farms. For example, cattle already must be tested for TB before they are moved from high-risk areas, but the review suggests switching to a test with fewer false negatives.

Open-access plan draws outcry

PUBLISHING | Scientists are pushing back against Plan S, the scheme to end scholarly journals' paywalls, launched 2 months ago by 11 national research funders in Europe. In an open letter published on 5 November, more than 1000 signatories say they support open access—making papers available free to all online—but condemn Plan S as "too risky for science." The letter slams the plan's proposed crackdown on hybrid journals, saying it would restrict access to high-quality, rigorous journals published by scientific societies. Hybrid publications earn revenue from both reader subscription fees and article processing charges paid by authors who want to make their papers immediately accessible. The letter also warns that Plan S would endanger collaborations between grantees of Plan S funders and scientists still allowed to publish in paywalled journals.

Measles hits New York City

PUBLIC HEALTH | Measles-infected travelers returning from Israel have caused two outbreaks of the highly contagious disease in Orthodox Jewish communities in and near New York City. Between late September and 13 November, 92 cases were reported. Public health authorities report that suburban Rockland County has had 68 cases of measles in unvaccinated or undervaccinated children, teens, and adults. In Brooklyn, 24 people, at least 17 of them aged 7 months to 4 years old, had confirmed cases as of 13 November. Israel is experiencing a large measles outbreak, with 1401 cases this year through 6 November, 735 of them confirmed in October. The European Union recorded 13,453 cases of measles and 37 deaths in the 12 months that ended on 30 September. In 2017, there were 120 cases in the United States. This year there have been 220 cases through 3 November.

NIH's racial gap partly explained

FUNDING DISPARITIES | Publication history explains roughly one-quarter of the gap in success rates between black and white researchers who apply for National Institutes of Health (NIH) funding, according to a study published this week in *PLOS ONE*. A team led by Donna Ginther, an economist at the University of Kansas in Lawrence, added detailed publication information to data in a 2011 *Science* paper by Ginther's team, which found that black applicants' chances of winning an R01 grant were 13 percentage points lower than white applicants'. Using 2397 applications submitted to NIH between 2002 and 2006, the team now finds that the gap narrows if they account for the quality of publications, using metrics such as journal impact factor and fraction of first-authored publications. The results suggest "that the role of bias is probably smaller" than was feared after the 2011 results came out, Ginther says.

Clinical trial disappoints

RARE DISEASES | A molecule hailed as a possible treatment for Niemann-Pick type C, an extremely rare and ultimately fatal neurodegenerative disease, performed no differently from placebo in a pivotal trial in 56 children and youths, Mallinckrodt Pharmaceuticals, based in Staines-upon-Thames, U.K., announced last week. Perplexingly, the disease did not progress in either the placebo group or in patients treated with the drug, VTS-270, during the 1-year study. Some researchers say such traditional double-blind, randomized controlled trials are likely inappropriate for extremely rare conditions. VTS-270, a sugar known as a cyclodextrin, was seen as one of the most promising collaborations between industry and the National Center for Advancing Translational Sciences in Bethesda, Maryland, part of the National Institutes of Health (*Science*, 7 October 2016, p. 18).

SCIENCEMAG.ORG/NEWS
Read more news from *Science* online.

PHOTO: CAROLA RADKE/NATURAL HISTORY MUSEUM, BERLIN

MUSEUMS

Berlin museum flush with funding

Berlin's Natural History Museum received word of a windfall last week: €660 million over 10 years from local and federal governments. The money, among the largest sums ever pledged to a natural history museum, will allow it to restore buildings still damaged from World War II, preserve and digitize collections, and build a new research campus. The research campus will focus on biodiversity, environmental science, and science communication. Museum Director General Johannes Vogel had lamented the state of the Berlin buildings and collections in September, after the devastating fire at Brazil's National Museum in Rio de Janeiro. He now says he and his staff are "over the moon" at the news, announced on 6 November.

Kim Schrier, a pediatrician, played up her technical training in a winning congressional campaign.

PHOTO: AP PHOTO/ELAINE THOMPSON

IN DEPTH

U.S. ELECTIONS

Vote heralds fresh start for science panel

Democratic win of House of Representatives will bring new tone to research issues

By **Jeffrey Mervis**

The results of last week's divisive midterm elections, with Democrats reclaiming control of the U.S. House of Representatives and Republicans likely strengthening their hold on the Senate, have allowed both parties to claim victory. U.S. scientists are also experiencing mixed emotions.

Many are pleased with what they expect to be a more data-driven approach to science policy under the new Democratic chair of the House science committee. But they also face the sobering reality that, by *Science*'s count, only seven of the 49 House candidates with technical backgrounds were victorious. And environmental activists are chagrined by the defeat of a proposed tax on carbon emissions in Washington and an Arizona initiative to increase that state's reliance on renewable energy, although Nevada voters took a first step toward adopting a similar policy.

In the House, Democrats picked up nearly 40 seats. That outcome gives them control of the 435-seat body for the first time since 2010, meaning they will appoint committee chairs and decide which bills get a vote.

Representative Eddie Bernice Johnson (D–TX) is in line to replace the retiring Representative Lamar Smith (R–TX) as chair of the science committee. The two Texans represent a stark contrast. Trained as a psychiatric nurse, Johnson has promised to "restore the credibility" of a committee that for 6 years has challenged the findings of climate scientists and questioned the need for many environmental regulations.

"We were not really following our charter [under Smith]," says Johnson, who joined the panel as a new legislator in 1993 and for the past 8 years has been its top Democrat. Instead, she says, "We were trying to uncover any information that would undercut scientific findings and avoid facing what the scientific data were showing us."

Smith, a lawyer who came to Congress in 1989, regularly convened hearings designed to highlight the views of those opposed to federal action to curb greenhouse gas emissions. He also used his unilateral power to issue investigative subpoenas—an authority traditionally given to just a few committee heads—to attack climate science he found suspect. Johnson hopes to shift the debate from "ignoring what's happening" to discussing "what we should be doing to save our planet and the lives and money it takes to clean up after weather-related disasters."

That move and other changes in tone could help repair a breach between the panel and the scientific community. "Stakeholders have told me they stopped asking for meetings [with the Republican majority] because they didn't see the point," says one Democratic staffer. "That's going to change, because we will be listening."

All seven winners with technical backgrounds are Democrats, and six were first-time candidates. Two toppled Republican incumbents; the rest won open seats. Four are women—a pediatrician, a nurse, an industrial engineer, and a retired U.S. Navy commander—helping boost overall female representation in the House to nearly 25%.

The new STEM Democrats

Seven candidates with science backgrounds won seats last week in the U.S. House of Representatives.

TRAINING	NAME	STATE
Biochemical engineer	Sean Casten	Illinois
Ocean engineer	Joe Cunningham	South Carolina
Industrial engineer	Chrissy Houlahan	Pennsylvania
Nuclear engineer	Elaine Luria	Virginia
Pediatrician	Kim Schrier	Washington
Nurse	Lauren Underwood	Illinois
Dentist	Jeff Van Drew	New Jersey

Newly elected lawmakers rarely get appointed to the appropriations committee and other panels with influence over key sectors of the economy, such as tax and fiscal policy. Accordingly, they are often overrepresented on the science committee. But none of the soon-to-be House members with technical backgrounds is lobbying for a spot on the science panel.

"I don't know enough at this point about what the science committee does to have an opinion," says Representative-elect Sean Casten (D–IL), a biochemical engineer who founded a company that helps firms become more energy efficient and who defeated Representative Peter Roskam (R) in a suburban Chicago district. "While I worked in basic science for half a dozen years in my youth, I feel more confident in my ability to deploy and apply basic science than to create it. So committees that deal with infrastructure and financial services, energy, and environmental policy are closer to areas where I can apply my skills."

Representative-elect Lauren Underwood (D), who ousted Representative Randy Hultgren (R) in a north-central Illinois district, hopes to apply her background as a nurse and health care analyst to win a seat on one of two panels that oversee federal health care policy. That's also true for Representative-elect Kim Schrier (D–WA), a pediatrician who won an open seat outside of Seattle.

"Health care is where people are really hurting now," Schrier says. "I felt I could really lend my expertise to finding better ways of providing it that bring costs down and improve outcomes. … I'm also really excited to be the only woman doctor in Congress at a time when women's reproductive rights are being attacked."

Representative-elect Chrissy Houlahan (D–PA), who won an open seat in the Philadelphia suburbs, says her training as an industrial engineer is just one of many facets of her identity. "I'm a veteran, an entrepreneur, a mom, and an educator as well," says Houlahan, who helped her husband grow a sports apparel company and briefly taught high school chemistry before leading a foundation that promotes early literacy. "I feel that I am part of a wave of people elected who provide diversity on a lot of levels."

Climate change is an existential issue for two new members representing coastal districts. In South Carolina, Representative-elect Joe Cunningham (D), an ocean engineer turned environmental lawyer, hammered his opponent for voicing support of President Donald Trump's plan to lift a ban on offshore drilling along the Atlantic coast, a pivotal issue for his constituents.

Representative Eddie Bernice Johnson (D–TX) is in line to lead the House of Representatives science committee.

PHOTO: BILL CLARK/CQ ROLL CALL/NEWSCOM

Representative-elect Elaine Luria (D–VA) says her 20-year career in the Navy helps her understand both the civilian and military components of sea-level rise. And she thinks the public is already on board. "People see our roads flooding and the sea level rising," she says about her southeastern Virginia district. "I have yet to talk to anyone who doesn't think climate change is real."

Before these new members can take their seats in January 2019, the current class of legislators must finish work on a spending bill for the 2019 fiscal year that began on 1 October. An earlier agreement to increase overall spending in 2018 and 2019 allowed Congress to pass budgets for about two-thirds of the government, including the National Institutes of Health (NIH) and the Department of Energy. But budgets for the remaining agencies, including NASA, the National Science Foundation (NSF), and several science agencies within the Department of Commerce, have been frozen under a continuing resolution that expires on 7 December. Disagreement over Trump's request to build a wall between the United States and Mexico stands in the way of a final deal by the lame-duck Congress.

The annual battle over spending could intensify next year. The divided Congress will have to deal with a 2011 law aimed at reducing the federal deficit over a decade. That law imposes spending caps, and could force lawmakers to cut a combined $126 billion from civilian and military budgets unless the Democratic House and Republican-controlled Senate can broker a deal to raise the caps.

Some legislators long associated with science issues won't be around for those debates. Senator Bill Nelson (D–FL), a NASA enthusiast who once flew aboard the space shuttle, appears to have lost his bid for reelection. In the House, the losers included Representative John Culberson (R–TX), who chairs a House appropriations subcommittee that sets spending levels for several science agencies, including NASA and NSF, and has pushed for NASA to develop a mission to Jupiter's moon Europa. The science committee will lose Hultgren, a cheerleader for basic energy research, as well as Representative Barbara Comstock (R–VA), who chairs the research subcommittee, and Representative Dana Rohrabacher (R–CA), a persistent doubter of climate science.

The frontrunner to take Culberson's spending gavel is Representative José Serrano (D–NY), an advocate for science with a special interest in the Census Bureau. Representative Nita Lowey (D–NY) is poised to lead the full appropriations committee, and Representative Rosa DeLauro (D–CT) is the favorite to lead the subcommittee that oversees NIH. Both have been supportive of federal investments in research.

Meanwhile, some science candidates who didn't win last week see a silver lining. Randy Wadkins, a professor of biochemistry at the University of Mississippi in Oxford, was the only academic scientist to make it onto the general election ballot. And although he lost by a two-to-one margin to an incumbent Republican, he says his campaign "might have been the most important thing I've ever done in my life, science-wise."

Seeking a House seat gave him a platform to connect with people "who were interested in science and wanted to do something," he says. "A lot of us lost. But some of us won. And that's my take-home message: This isn't the end of scientists running for Congress; it's just the beginning." ■

CLIMATE

Eruption made 536 'the worst year to be alive'

Core from glacier reveals the Icelandic volcano that plunged Europe into darkness

By **Ann Gibbons**

Ask medieval historian Michael McCormick what year was the worst to be alive, and he's got an answer: "536." Not 1349, when the Black Death wiped out half of Europe. Not 1918, when the flu killed 50 million to 100 million people, mostly young adults. But 536. In Europe, "It was the beginning of one of the worst periods to be alive, if not the worst year," says McCormick, a historian and archaeologist who chairs the Harvard University Initiative for the Science of the Human Past.

A mysterious fog plunged Europe, the Middle East, and parts of Asia into darkness, day and night—for 18 months. "For the sun gave forth its light without brightness, like the moon, during the whole year," wrote Byzantine historian Procopius. Temperatures in the summer of 536 fell 1.5°C to 2.5°C, initiating the coldest decade in the past 2300 years. Snow fell that summer in China; crops failed; people starved. The Irish chronicles record "a failure of bread from the years 536–539." Then, in 541, bubonic plague struck the Roman port of Pelusium, in Egypt. What came to be called the Plague of Justinian spread rapidly, wiping out one-third to one-half of the population of the eastern Roman Empire and hastening its collapse, McCormick says.

Historians have long known that the middle of the sixth century was a dark hour in what used to be called the Dark Ages, but

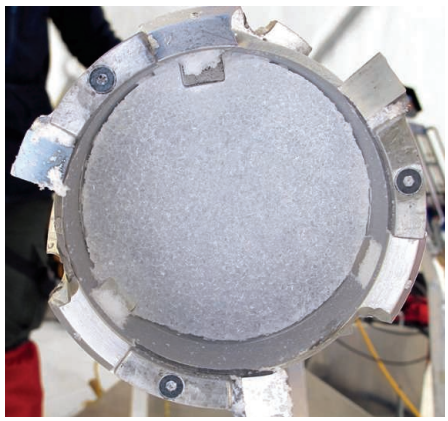

Slivers from a Swiss ice core held chemical clues to natural and humanmade events.

the source of the mysterious clouds has long been a puzzle. Now, an ultraprecise analysis of ice from a Swiss glacier by a team led by McCormick and glaciologist Paul Mayewski at the Climate Change Institute of The University of Maine (UM) in Orono has fingered a culprit. At a workshop at Harvard this week, the team reported that a cataclysmic volcanic eruption in Iceland spewed ash across the Northern Hemisphere early in 536. Two other massive eruptions followed, in 540 and 547. The repeated blows, followed by plague, plunged Europe into economic stagnation that lasted until 640, when another signal in the ice—a spike in airborne lead—marks a resurgence of silver mining, as the team reports in *Antiquity* this week.

To Kyle Harper, provost and a medieval and Roman historian at The University of Oklahoma in Norman, the detailed log of natural disasters and human pollution frozen into the ice "give us a new kind of record for understanding the concatenation of human and natural causes that led to the fall of the Roman Empire—and the earliest stirrings of this new medieval economy."

Ever since tree ring studies in the 1990s suggested the summers around the year 540 were unusually cold, researchers have hunted for the cause. Three years ago polar ice cores from Greenland and Antarctica yielded a clue. When a volcano erupts, it spews sulfur, bismuth, and other substances high into the atmosphere, where they form an aerosol veil that reflects the sun's light back into space, cooling the planet. By matching the ice record of these chemical traces with tree ring records of climate, a team led by Michael Sigl, now of the University of Bern, found that nearly every unusually cold summer over the past 2500 years was preceded by a volcanic eruption. A massive eruption—perhaps in North America, the team suggested—stood out in late 535 or early 536; another followed in 540. Sigl's team concluded that the double blow explained the prolonged dark and cold.

Mayewski and his interdisciplinary team decided to look for the same eruptions in an ice core drilled in 2013 in the Colle Gnifetti Glacier in the Swiss Alps. The 72-meter-long core entombs more than 2000 years of fallout from volcanoes, Saharan dust storms,

Darkest hours and then a dawn

A high-resolution ice core record combined with historical texts chronicles the impact of natural disasters on European society.

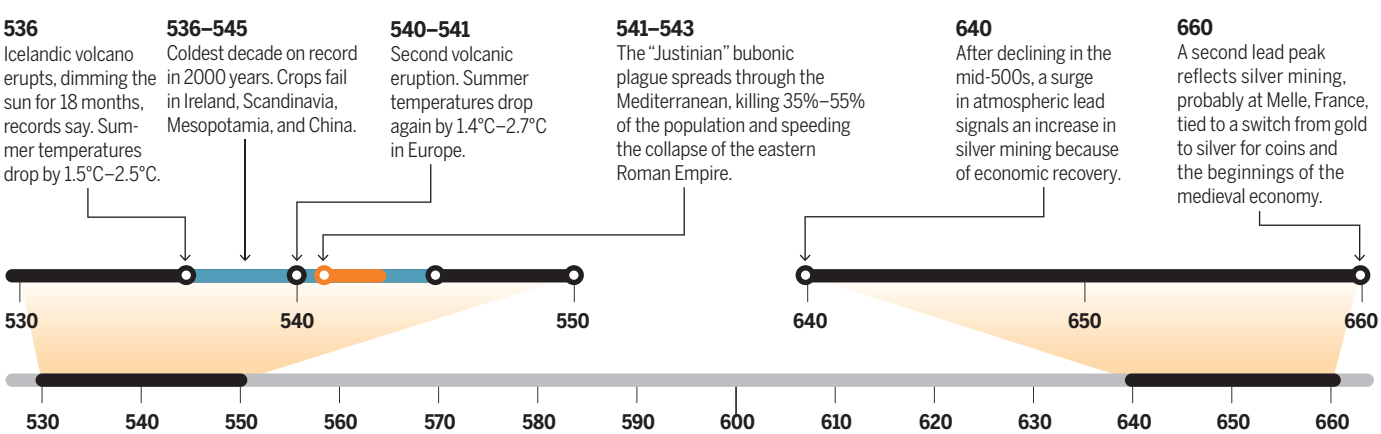

CREDITS: (PHOTO) NICOLE SPAULDING/CCI FROM C. P. LOVELUCK *ET AL.*, *ANTIQUITY* 10.15184/aq.2018.4; (GRAPHIC) A. CUADRA/*SCIENCE*; (DATA) C. P. LOVELUCK *ET AL.*, *ANTIQUITY* 2018; M. SIGL *ET AL.*, *NATURE* 2015; M. MCCORMICK

and human activities smack in the center of Europe. The team deciphered this record using a new ultra–high-resolution method, in which a laser carves 120-micron slivers of ice, representing just a few days or weeks of snowfall, along the length of the core. Each of the samples—some 50,000 from each meter of the core—is analyzed for about a dozen elements. The approach enabled the team to pinpoint storms, volcanic eruptions, and lead pollution down to the month or even less, going back 2000 years, says UM volcanologist Andrei Kurbatov.

In ice from the spring of 536, UM graduate student Laura Hartman found two microscopic particles of volcanic glass. By bombarding the shards with x-rays to determine their chemical fingerprint, she and Kurbatov found that they closely matched glass particles found earlier in lakes and peat bogs in Europe and in a Greenland ice core. Those particles in turn resembled volcanic rocks from Iceland. The chemical similarities convince geoscientist David Lowe of The University of Waikato in Hamilton, New Zealand, who says the particles in the Swiss ice core likely came from the same Icelandic volcano. But Sigl says more evidence is needed to convince him that the eruption was in Iceland rather than North America.

Either way, the winds and weather systems in 536 must have been just right to guide the eruption plume southeast across Europe and, later, into Asia, casting a chilly pall as the volcanic fog "rolled through," Kurbatov says. The next step is to try to find more particles from this volcano in lakes in Europe and Iceland, in order to confirm its location in Iceland and tease out why it was so devastating.

A century later, after several more eruptions, the ice record signals better news: the lead spike in 640. Silver was smelted from lead ore, so the lead is a sign that the precious metal was in demand in an economy rebounding from the blow a century before, says archaeologist Christopher Loveluck of the University of Nottingham in the United Kingdom. A second lead peak, in 660, marks a major infusion of silver into the emergent medieval economy. It suggests gold had become scarce as trade increased, forcing a shift to silver as the monetary standard, Loveluck and his colleagues write in *Antiquity*. "It shows the rise of the merchant class for the first time," he says.

Still later, the ice is a window into another dark period. Lead vanished from the air during the Black Death from 1349 to 1353, revealing an economy that had again ground to a halt. "We've entered a new era with this ability to integrate ultra–high-resolution environmental records with similarly high resolution historical records," Loveluck says. "It's a real game changer." ■

BIOMEDICINE

Obesity gives unexpected boost to anticancer drugs

Drugs revive immune cells exhausted by obesity hormone

By **Jocelyn Kaiser**

Second only to smoking, obesity is a top risk factor for cancer. But oncologists have noticed something surprising: Overweight patients sometimes respond better than other patients to powerful drugs that harness the immune system to fight tumors. Now, researchers tracing the complex effects of obesity on cancer are glimpsing a possible explanation: Obesity weakens the immune system and favors tumor growth by boosting the very same molecules those drugs target.

"For the most part, everybody assumes obesity is always bad. But [with these drugs], there was a net positive," says cancer immunologist William Murphy of the University of California (UC), Davis, who, with UC Davis oncologist Arta Monjazeb, led the work, reported this week in *Nature Medicine*. Murphy thinks the finding could point to ways to make the drugs more effective in all cancer patients.

> ***"... everybody assumes obesity is always bad. But [with these drugs], there was a net positive."***
>
> **William Murphy**, University of California, Davis

Called checkpoint inhibitors, the drugs block the activation of PD-1, a protein on the surface of immune sentinels called T cells. The body naturally triggers PD-1 to dampen immune responses, but tumors can also stimulate PD-1 to protect themselves. Lifting this molecular "brake" allows the T cells to attack the cancer cells. PD-1 inhibitors have caused untreatable tumors to vanish for years in people with melanoma, lung cancer, and some other cancer types.

But only a minority of patients respond to the drugs, and a study this year in *The Lancet Oncology* showed that the responders disproportionately include people who are overweight. In 330 advanced melanoma patients given a PD-1 inhibitor, researchers at MD Anderson Cancer Center in Houston, Texas, found that those who were male and overweight lived much longer on average: nearly 27 months compared with 14 months for patients with a normal body mass index.

Now, Murphy's team has firmed up this clinical observation in the lab and identified a possible basis. After confirming that tumors grow faster in obese mice, his team studied the T cells of obese mice, monkeys, and people. They found that the cells were what immunologists call "exhausted." They were slow to proliferate and had stopped making secreted proteins that stimulate other immune system helpers. They also displayed more PD-1 than average, meaning cancer cells could more easily suppress them and grow unhindered.

Leptin, a hormone made by fat cells, is one factor in the PD-1 excess, Murphy's group found. Overweight animals and people produce high levels of the hormone, which normally signals the brain that the body has had enough to eat. But leptin also affects the immune system, and the UC Davis team suspects it triggers a signaling pathway that increases PD-1 on T cells. The PD-1 excess also has a paradoxical benefit, Murphy's team found: In obese mice, it makes T cells unusually responsive to PD-1 inhibitors. Once the drugs released this brake, the T cells sprang back into action. Nourished by glucose and other nutrients abundant in an overweight animal's tissues, they worked better at curbing tumors than in normal weight animals.

The finding suggests an "unexpected" benefit of obesity for cancer patients, says Harvard University immunologist Lydia Lynch. Her group reports in *Nature Immunology* this week on a different way obesity impairs the immune system's ability to attack tumors: by hampering a type of immune cell called natural killer cells that seek out and destroy abnormal cells.

Murphy plans to explore whether briefly giving normal weight mice with cancer a high-fat diet in order to mimic some effects of obesity could boost their response to PD-1 inhibitors. But such treatments for cancer patients could have harmful effects, cautions tumor immunologist Suzanne Ostrand-Rosenberg of The University of Utah in Salt Lake City, who also studies how obesity spurs tumor growth. "It's a balance here, a very careful balance," she says. ■

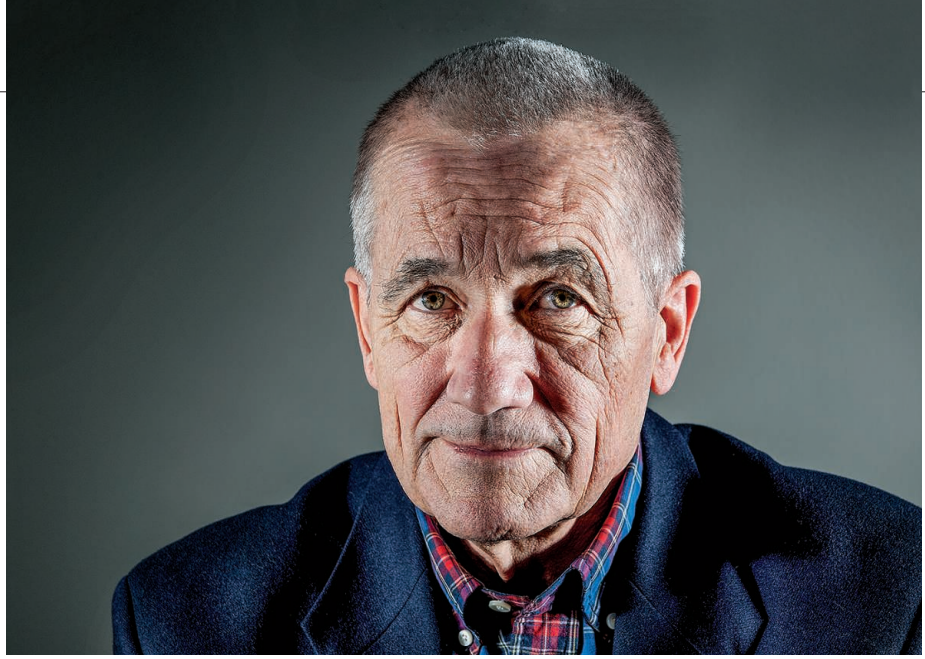

PHOTO: JOACHIM RODE

Peter Gøtzsche's clashes with Cochrane have sparked calls for policy changes.

MEDICAL SCIENCE

Fresh fights roil evidence-based medicine group

Expelled Cochrane co-founder Peter Gøtzsche is suspended as head of the Nordic Cochrane Centre

By **Gretchen Vogel**

A messy clash within Cochrane, an international network that promotes evidence-based medicine, is spiraling into what some see as a battle over the organization's character and purpose. Last week, prominent pharma critic Peter Gøtzsche failed in a bid to sever the Nordic Cochrane Centre in Copenhagen, which he led, from the wider international organization. Instead, Gøtzsche was suspended by the Rigshospitalet in Copenhagen, which hosts the center.

The move triggered protests from within the organization, which had expelled Gøtzsche 2 months ago. At stake is not just Gøtzsche's job or his center, but the extent to which Cochrane can tolerate debate and dissent, says Gerd Antes of Ludwig Maximilian University in Munich, Germany, a former head of the German Cochrane Centre in Freiburg. "It's more than a mess, it's now a whole scandal," Antes says.

Cochrane publishes systematic reviews of the evidence for the efficacy of drugs, vaccines, diagnostics, medical procedures, and other health-related interventions. The organization has centers or groups in 43 countries and a central office in London. Gøtzsche, a controversial figure who helped found Cochrane in 1993, was elected to its governing board in January 2017. Marguerite Koster, a co-chair of the board and a senior manager at Kaiser Permanente in Los Angeles, California, says there had been complaints against him for years, including several recently about his use of the Cochrane name in letters unrelated to the organization. The conflict escalated in June, when Gøtzsche and two co-authors published a scathing attack on a Cochrane review about the efficacy of human papillomavirus vaccines. (They said the review "was incomplete and ignored important evidence of bias.")

Gøtzsche's expulsion in September for what the board called "a consistent pattern of disruptive and inappropriate behaviours" led four other board members to resign in protest. Gøtzsche vowed to take his center out of the international network, but the board said he had no right to do so. With his suspension from the Rigshospitalet, it appears the board has won—at least for now. A statement by the hospital's deputy chief executive, Per Jørgensen, said it is "striving to ensure that the Nordic Cochrane Centre continues as part of the international Cochrane collaboration." "The only reason that they gave was that they no longer had confidence in my leadership," says Gøtzsche, who is working with a lawyer to challenge the suspension.

A 4 November petition triggered by rumors that Gøtzsche was about to be let go asks Danish Minister of Health Ellen Trane Nørby to "reconsider this possible dismissal." It argues that Gøtzsche's work has "played a pivotal role in favor of the transparency of clinical data, the priority of public health needs and the defense of rigorous medical research carried out independently of conflicts of interest." As *Science* went to press, more than 6000 people had signed the petition, including *The BMJ* Editor-in-Chief Fiona Godlee and Cochrane co-founder Iain Chalmers. "This shows how wrong the board is," Antes says.

Antes and 14 other Cochrane directors and editors have put together a second petition criticizing a lack of transparency at the organization and the board's statement that there will be "zero tolerance for bad behavior" in the wake of Gøtzsche's expulsion. "We fear this will easily lead to 'zero tolerance for different opinions,'" they write. Gøtzsche "has made mistakes," Antes says, but, "you need people like Peter Gøtzsche. Otherwise you get a bit too stiff."

The signatories also call for policy changes, including using revenue from Cochrane publications to support the production of reviews, rather than the group's headquarters, and moving toward an open-access publishing model. The current business model, based on selling reviews as products, is a source of tension, says David Hammerstein Mintz, a former member of the European Parliament from Spain and one of the board members who resigned. Cochrane's centers and groups raise their own funds, usually from government sources, he notes. "Many members don't see their work as products. It's a public good."

Cochrane CEO Mark Wilson says the board is preparing a response to the criticisms. He says the gist will be "We welcome members' input on issues like this." Wilson downplays the controversies and says the organization is thriving. "Cochrane is delivering on its strategy and is in a very good place."

Cochrane is holding new board elections in the coming weeks. Antes hopes candidates will support the changes he and others have proposed. But the conflict has already harmed Cochrane's credibility, says Jos Verbeek, coordinating editor of a Cochrane review group on occupational medicine. "This has had a big impact," says Verbeek, who's at the Finnish Institute of Occupational Health in Helsinki. "People are wondering, 'What is happening at Cochrane, the most trustworthy source of evidence?'" ■

With reporting by Martin Enserink.

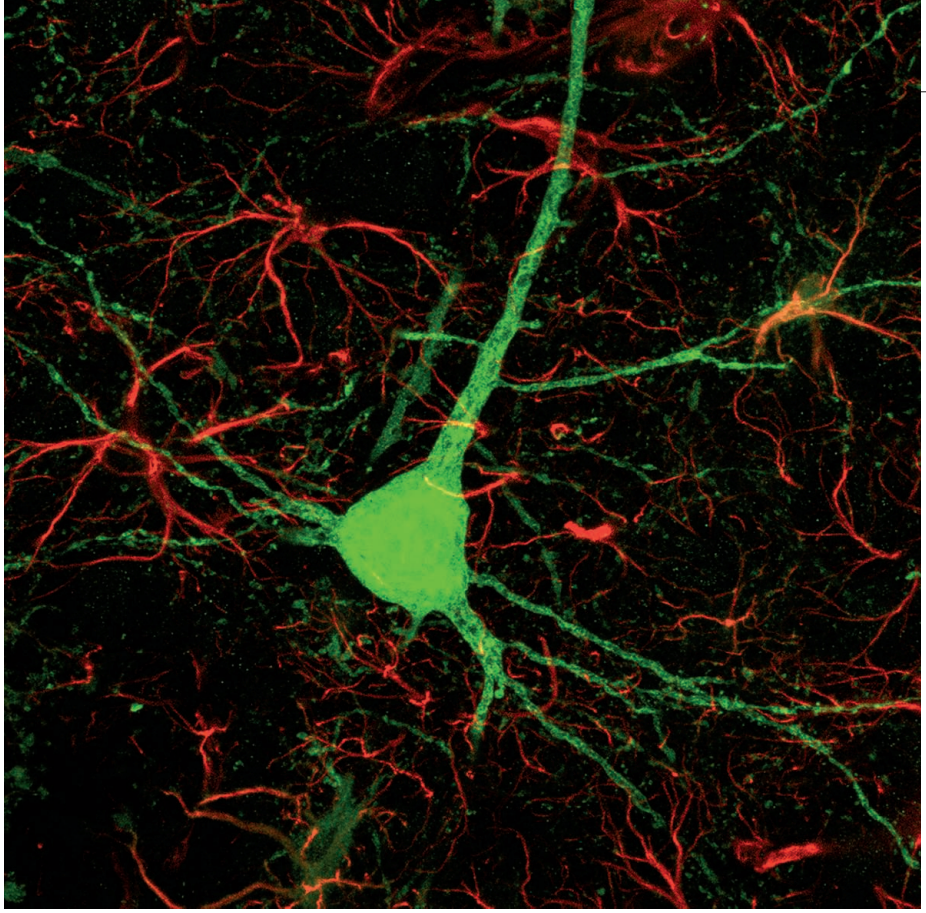

Researchers have converted astrocytes (red) into neurons (green) in a living mouse brain.

NEUROSCIENCE

Reprogrammed cells could tackle brain damage

Turning astrocytes into neurons improves symptoms in preliminary mouse studies

By **Kelly Servick**, *in San Diego, California*

If a diseased or injured brain has lost neurons, why not ask other cells to change jobs and pick up the slack? Several research teams have taken a first step by "reprogramming" abundant nonneuronal cells called astrocytes into neurons in the brains of living mice.

"Everybody is astonished, at the moment, that it works," says Nicola Mattugini, a neurobiologist at Ludwig Maximilian University in Munich, Germany, who presented the results of one such experiment here at the annual meeting of the Society for Neuroscience last week.

Now, labs are turning to the next questions: Do these neurons function like the lost ones, and does creating neurons at the expense of astrocytes do brain-damaged animals any good? Many researchers remain skeptical on both counts. But Mattugini's team, led by neuroscientist Magdalena Götz, and two other groups presented evidence at the meeting that reprogrammed astrocytes do, at least in some respects, impersonate the neurons they're meant to replace. The two other groups also shared evidence that reprogrammed astrocytes help mice recover movement lost after a stroke.

Some see the approach as a potential alternative to transplanting stem cells (or stem cell–derived neurons) into the damaged brain or spinal cord. Clinical trials of that strategy are already underway for conditions including Parkinson's disease and spinal cord injury. But Gong Chen, a neuroscientist at Pennsylvania State University in State College, says he got disillusioned with the idea after finding in his rodent experiments that transplanted cells produced relatively few neurons, and those few weren't fully functional. The recent discovery that mature cells can be nudged toward new fates pointed to a better approach, he says. His group and others took aim at the brain's most abundant cell, the star-shaped astrocyte.

Astrocytes are glial cells, named for the misconception that they're merely the brain's structure-giving "glue." In fact, they nourish and communicate with neurons and help control blood flow. After an injury, subsets of astrocytes proliferate, promote inflammation, and contribute to the formation of a scar. Many scientists think astrocytes' effects on recovery are contradictory—some helpful and some harmful.

"I cannot imagine another technology to be more efficient than using the neighboring glial cell" to repair the brain, Chen says. His group enlisted a harmless virus that, injected into the brain, infects astrocytes and introduces DNA that codes for NeuroD1, a transcription factor that activates genes typically expressed in neurons. The reprogramming apparently prompts other astrocytes to multiply, which he thinks might prevent the treatment from depleting the brain of astrocytes.

The approach, under development in several labs working with various transcription factors, is "super provocative," says Timothy Murphy, a neuroscientist at The University of British Columbia in Vancouver, Canada, who studies how brain circuits change after stroke. But, he adds: "These cells need to survive, and they need to reconnect."

No group has yet shown that the reprogrammed cells do wire up into circuits to carry out the functions of lost neurons. But several have evidence that the cells take on key neural features. In the weeks after inducing a stroke in a mouse's brain, Chen's team saw reprogrammed astrocytes retract some of their starlike tendrils and begin to produce hallmark neural proteins. Reprogrammed astrocytes also appear to fire electrical signals and extend new fibers across the brain and into the spinal cord.

Götz's team, meanwhile, documented that newly reprogrammed neurons around the site of a stab wound resemble pyramidal neurons, which send excitatory signals. (Her group, like others, is now teasing out how different combinations of transcription factors prompt astrocytes to become different types of neurons.) The researchers also found that newly reprogrammed neurons express different markers and send out different projections depending on which layer of the cortex they are in, just as native neurons do.

That's "very surprising," says Chun-Li Zhang, a neuroscientist at the University of Texas Southwestern Medical Center in Dallas. He is exploring a different reprogramming process, which turns astrocytes into

IMAGE: ZHENG WU/GONG CHEN'S LAB

primitive neural progenitor cells that then become neurons more gradually. Both approaches will have to overcome skepticism, he says. Many researchers don't expect neural newcomers, introduced abruptly into the adult brain, to mature and function normally.

"To really convince people," he says, "we need to be really careful" to document the steps in the transformation of these cells—and to prove that they begin as astrocytes and finish as mature neurons.

Researchers have also begun to look for indications that the approach helps animals heal. In a study posted in April on the preprint server bioRxiv, Chen's group reported that reprogrammed cells improved a mouse's ability to walk and use its front limbs after a stroke. At the meeting, he hinted that the same approach had restored neural tissue in the brains of stroke-injured monkeys; experiments to gauge their recoveries are ongoing at a collaborator's facility in China, he says.

Chen has founded a company to develop therapies with astrocyte reprogramming, including a cocktail of small molecules that could reprogram cells without brain surgery or the use of a virus. "I believe this is the future," he told the audience at his conference presentation. "It's the next frontier in regenerative medicine."

Stem cell biologist Cindi Morshead of the University of Toronto (U of T) in Canada is more circumspect. Scientists don't fully understand the role of astrocytes in the brain after an injury, she says, but "they're there for a purpose." As her group prepared to test the strategy, she expected it to make injured animals worse.

She's more optimistic now. At the conference, her U of T collaborator Maryam Faiz revealed that mice injected with NeuroD1 a week after a stroke recovered motor function more quickly than untreated mice, some of which were permanently disabled. By 2 months after the treatment, mice performed about as well as healthy controls on walking tests. Fully 20% of their neurons were reprogrammed cells.

The results in stroke are among the first glimmers of benefit. Last year, Swedish researchers also reported that they had restored some motor function in a mouse model of Parkinson's disease by reprogramming astrocytes into dopamine-producing neurons.

Morshead's results have encouraged her to continue experimenting. She now wants to wait longer after a stroke to inject her mice. Once stroke disability becomes chronic in humans, "we have nothing for them," she says. If long-disabled mice benefit from their new neurons, she says, "now, that would be the coolest thing." ■

ASTRONOMY

Large galaxy found lurking on the Milky Way's far side

Antlia 2 rivals the Large Magellanic Cloud in size but is strangely dim, a puzzle for theorists

By **Adam Mann**

Circling our galaxy is a stealthy giant. Astronomers have discovered a dwarf galaxy, called Antlia 2, that is one-third the size of the Milky Way itself. As big as the Large Magellanic Cloud, the galaxy's largest companion, Antlia 2 eluded detection until now because it is 10,000 times fainter. Such a strange beast challenges models of galaxy formation and dark matter, the unseen stuff that helps pull galaxies together.

"It's a very odd object and kind of exciting because we don't know yet how to interpret all of its properties," says Andrey Kravtsov of The University of Chicago in Illinois, who was not involved in the work.

> ***"It's ... kind of exciting because we don't know yet how to interpret all of its properties."***
>
> **Andrey Kravtsov**, The University of Chicago

The galaxy was discovered with data from the European Space Agency's Gaia satellite, a space telescope measuring the motions and properties of more than 1 billion stars in and around the Milky Way. Gabriel Torrealba, an astronomy postdoc at the Academia Sinica in Taipei, decided to sift the data for RR Lyrae stars. These old stars, often found in dwarf galaxies, shine with a throbbing blue light that pulses at a rate signaling their inherent brightness, allowing researchers to pin down their distance.

"RR Lyrae are so rare at these distances that even if you see two, you question why they are together," says Vasily Belokurov, an astronomer at the University of Cambridge in the United Kingdom and a collaborator on the discovery. When the team found three, some 420,000 light-years away, it was "an overwhelming signal" of a large cluster of stars in that location, Belokurov says. But because the RR Lyrae stars lie on the far side of the disk of the Milky Way and its obscuring veils of stars and gas, finding their companions was not easy.

Gaia data helped the team see past the foreground stars. Objects in the Milky Way's disk are close enough for Gaia to measure their parallax: a shift in their apparent position as Earth moves around the sun. More distant stars appear fixed in one spot. After removing the parallax-bearing stars, the researchers homed in on more than 100 red giant stars moving together in the constellation Antlia, they report in a paper posted to the preprint server arXiv this week. The giants mark out a sprawling companion galaxy 100 times less massive than anything of similar size, with far fewer stars.

To explain such a diffuse galaxy, Belokurov suggests that early in Antlia 2's history, many young stars exploded as violent supernovae. This would have blown gas and dust out of the galaxy, weakening its gravity so that it puffed up. An abundance of the heavy elements that are strewn from the guts of exploding stars adds credibility to this idea, says Shea Garrison-Kimmel, an astrophysicist at the California Institute of Technology in Pasadena. Antlia 2 could also have lost matter as stars were tugged away by gravitational tidal forces as it orbited around the larger Milky Way.

Even so, its large size is hard to explain. Galaxies are thought to have formed when the gravity of enormous clumps of dark matter drew in enough ordinary matter to fuel the birth of stars. The team speculates that Antlia 2 might have been born from a fluffier, faster-moving type of dark matter than current models hypothesize.

To Garrison-Kimmel, one example isn't enough to say the dark matter in Antlia 2 is different from that in the Milky Way and its other satellites. "There's nothing in this one galaxy that screams to me that we need to rethink dark matter," he says. "But if there are a lot of these, then we might need to take a step back and ask what's going on."

That could happen now that astronomers know how to find these big, elusive companions. "I think this object is a harbinger," Kravtsov says. "A taste of things to come." ■

Adam Mann is a journalist in Oakland, California.

ICE AGE IMPACT

A large asteroid struck Greenland in the time of humans. How did it affect the planet?

By **Paul Voosen**

On a bright July day 2 years ago, Kurt Kjær was in a helicopter flying over northwest Greenland—an expanse of ice, sheer white and sparkling. Soon, his target came into view: Hiawatha Glacier, a slow-moving sheet of ice more than a kilometer thick. It advances on the Arctic Ocean not in a straight wall, but in a conspicuous semicircle, as though spilling out of a basin. Kjær, a geologist at the Natural History Museum of Denmark in Copenhagen, suspected the glacier was hiding an explosive secret. The helicopter landed near the surging river that drains the glacier, sweeping out rocks from beneath it. Kjær had 18 hours to find the mineral crystals that would confirm his suspicions.

What he brought home clinched the case for a grand discovery. Hidden beneath Hiawatha is a 31-kilometer-wide impact crater, big enough to swallow Washington, D.C., Kjær and 21 co-authors report this week in a paper in *Science Advances*. The crater was left when an iron asteroid 1.5 kilometers across slammed into Earth, possibly within the past 100,000 years.

Though not as cataclysmic as the dinosaur-killing Chicxulub impact, which carved out a 200-kilometer-wide crater in Mexico about 66 million years ago, the Hiawatha impactor, too, may have left an imprint on the planet's history. The timing is still up for debate, but some researchers on the discovery team believe the asteroid struck at a crucial moment: roughly 13,000 years ago, just as the world was thawing from the last ice age. That would mean it crashed into Earth when mammoths and other megafauna were in decline and people were spreading across North America.

The impact would have been a spectacle for anyone within 500 kilometers. A white fireball four times larger and three times brighter than the sun would have streaked across the sky. If the object struck an ice sheet, it would have tunneled through to the bedrock, vaporizing water and stone alike in a flash. The resulting explosion packed the energy of 700 1-megaton nuclear bombs, and even an observer hundreds of kilometers away would have experienced a buffeting shock wave, a monstrous thunderclap, and hurricane-force winds. Later, rock debris might have rained down on North America and Europe, and the released steam, a greenhouse gas, could have locally warmed Greenland, melting even more ice.

The news of the impact discovery has reawakened an old debate among scientists who study ancient climate. A massive impact on the ice sheet would have sent meltwater pouring into the Atlantic Ocean—potentially disrupting the conveyor belt of ocean currents and causing temperatures to plunge, especially in the Northern Hemisphere. "What would it mean for species or life at the time? It's a huge open

IMAGE: NASA SCIENTIFIC VISUALIZATION STUDIO

A 1.5-kilometer asteroid, intact or in pieces, may have smashed into an ice sheet just 13,000 years ago.

question," says Jennifer Marlon, a paleoclimatologist at Yale University.

A decade ago, a small group of scientists proposed a similar scenario. They were trying to explain a cooling event, more than 1000 years long, called the Younger Dryas, which began 12,800 years ago, as the last ice age was ending. Their controversial solution was to invoke an extraterrestrial agent: the impact of one or more comets. The researchers proposed that besides changing the plumbing of the North Atlantic, the impact also ignited wildfires across two continents that led to the extinction of large mammals and the disappearance of the mammoth-hunting Clovis people of North America. The research group marshaled suggestive but inconclusive evidence, and few other scientists were convinced. But the idea caught the public's imagination despite an obvious limitation: No one could find an impact crater.

Proponents of a Younger Dryas impact now feel vindicated. "I'd unequivocally predict that this crater is the same age as the Younger Dryas," says James Kennett, a marine geologist at the University of California, Santa Barbara, one of the idea's original boosters.

But Jay Melosh, an impact crater expert at Purdue University in West Lafayette, Indiana, doubts the strike was so recent. Statistically, impacts the size of Hiawatha occur only every few million years, he says, and so the chance of one just 13,000 years ago is small. No matter who is right, the discovery will give ammunition to Younger Dryas impact theorists—and will turn the Hiawatha impactor into another type of projectile. "This is a hot potato," Melosh tells *Science*. "You're aware you're going to set off a firestorm?"

IT STARTED WITH a hole. In 2015, Kjær and a colleague were studying a new map of the hidden contours under Greenland's ice. Based on variations in the ice's depth and surface flow patterns, the map offered a coarse suggestion of the bedrock topography—including the hint of a hole under Hiawatha.

Kjær recalled a massive iron meteorite in his museum's courtyard, near where he parks his bicycle. Called *Agpalilik*, Inuit for "the Man," the 20-ton rock is a fragment of an even larger meteorite, the Cape York, found in pieces on northwest Greenland by Western explorers but long used by Inuit people as a source of iron for harpoon tips and tools. Kjær wondered whether the meteorite might be a remnant of an impactor that dug the circular feature under Hiawatha. But he still wasn't confident that it was an impact crater. He needed to see it more clearly with radar, which can penetrate ice and reflect off bedrock.

Kjær's team began to work with Joseph MacGregor, a glaciologist at NASA's Goddard Space Flight Center in Greenbelt, Maryland, who dug up archival radar data. MacGregor found that NASA aircraft often flew over the site on their way to survey Arctic sea ice, and the instruments were sometimes turned on, in test mode, on the way out. "That was pretty glorious," MacGregor says.

The radar pictures more clearly showed what looked like the rim of a crater, but they were still too fuzzy in the middle. Many features on Earth's surface, such as volcanic calderas, can masquerade as circles. But only impact craters contain central peaks and peak rings, which form at the center of a newborn crater when—like the splash of a stone in a pond—molten rock rebounds just after a strike. To look for those features, the researchers needed a dedicated radar mission.

Coincidentally, the Alfred Wegener Institute for Polar and Marine Research in Bremerhaven, Germany, had just purchased a next-generation ice-penetrating radar to mount across the wings and body of their Basler aircraft, a twin-propeller retrofitted DC-3 that's a workhorse of Arctic science. But they also needed financing and a base close to Hiawatha.

Kjær took care of the money. Traditional funding agencies would be too slow, or prone to leaking their idea, he thought. So he petitioned Copenhagen's Carlsberg Foundation, which uses profits from its global beer sales to finance science. MacGregor, for his part, enlisted NASA colleagues to persuade the U.S. military to let them work out of Thule Air Base, a Cold War outpost on northern Greenland, where German members of the team had been trying to get permission to work for 20 years. "I had retired, very serious German scientists sending me happy-face emojis," MacGregor says.

Three flights, in May 2016, added 1600 kilometers of fresh data from dozens of transits across the ice—and evidence that Kjær, MacGregor, and their team were onto something. The radar revealed five prominent bumps in the crater's center, indicating a central peak rising some 50 meters high. And in a sign of a recent impact, the crater bottom is exceptionally jagged. If the asteroid had struck earlier than 100,000 years ago, when the area was ice free, erosion from melting ice farther inland would have scoured the crater smooth, MacGregor says. The radar signals also showed that the deep layers of ice were jumbled up—another sign of a recent impact. The oddly disturbed patterns, MacGregor says, suggest "the ice sheet hasn't equilibrated with the presence of this impact crater."

But the team wanted direct evidence to overcome the skepticism they knew would greet a claim for a massive young crater, one that seemed to defy the odds of how often large impacts happen. And that's why Kjær found himself, on that bright July day in 2016, frenetically sampling rocks all along the crescent of terrain encircling Hiawatha's face. His most crucial stop was in the middle of the semicircle, near the river, where he collected sediments that appeared to have come from the glacier's interior. It was hectic, he says—"one of those days when you just check your samples, fall on the bed, and don't rise for some time."

The hidden crater

Under a lobe of ice on northwest Greenland, airborne radar and ground sampling have uncovered a giant and remarkably fresh impact crater. Though not as large as the dinosaur-killing Chicxulub impact, Hiawatha crater may have formed as recently as the end of the last ice age, as humans were spreading across North America. Meltwater from the impact could have triggered a thousand-year chill in the Northern Hemisphere by disrupting currents in the Atlantic Ocean.

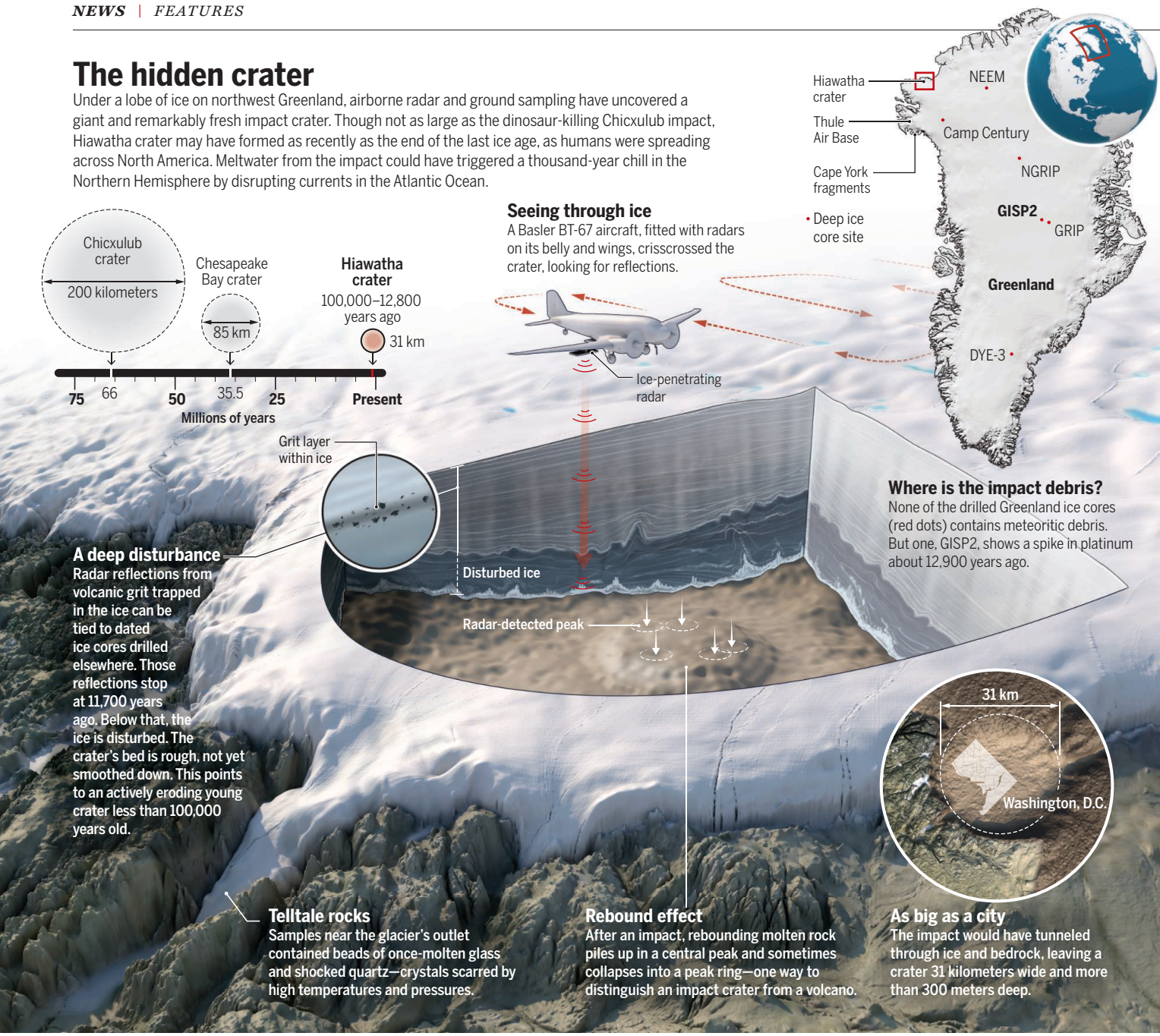

In that outwash, Kjær's team closed its case. Sifting through the sand, Adam Garde, a geologist at the Geological Survey of Denmark and Greenland in Copenhagen, found glass grains forged at temperatures higher than a volcanic eruption can generate. More important, he discovered shocked crystals of quartz. The crystals contained a distinctive banded pattern that can be formed only in the intense pressures of extraterrestrial impacts or nuclear weapons. The quartz makes the case, Melosh says. "It looks pretty good. All the evidence is pretty compelling."

Now, the team needs to figure out exactly when the collision occurred and how it affected the planet.

THE YOUNGER DRYAS, named after a small white and yellow arctic flower that flourished during the cold snap, has long fascinated scientists. Until human-driven global warming set in, that period reigned as one of the sharpest recent swings in temperature on Earth. As the last ice age waned, about 12,800 years ago, temperatures in parts of the Northern Hemisphere plunged by as much as 8°C, all the way back to ice age readings. They stayed that way for more than 1000 years, turning advancing forest back into tundra.

The trigger could have been a disruption in the conveyor belt of ocean currents, including the Gulf Stream that carries heat northward from the tropics. In a 1989 paper in *Nature*, Kennett, along with Wallace Broecker, a climate scientist at Columbia University's Lamont-Doherty Earth Observatory, and others, laid out how meltwater from retreating ice sheets could have shut down the conveyor. As warm water from the tropics travels north at the surface, it cools while evaporation makes it saltier. Both factors boost the water's density until it sinks into the abyss, helping to drive the conveyor. Adding a pulse of less-dense freshwater could hit the brakes. Paleoclimate researchers have largely endorsed the idea, although evidence for such a flood has been lacking until recently.

Then, in 2007, Kennett suggested a new trigger. He teamed up with scientists led by

CREDITS: (GRAPHIC) C. BICKEL/*SCIENCE*; (DATA) UMN POLAR GEOSPATIAL CENTER; ICEBRIDGE BEDMACHINE GREENLAND/NASA NATIONAL SNOW AND ICE DATA CENTER

Richard Firestone, a physicist at Lawrence Berkeley National Laboratory in California, who proposed a comet strike at the key moment. Exploding over the ice sheet covering North America, the comet or comets would have tossed light-blocking dust into the sky, cooling the region. Farther south, fiery projectiles would have set forests alight, producing soot that deepened the gloom and the cooling. The impact also could have destabilized ice and unleashed meltwater that would have disrupted the Atlantic circulation.

The climate chaos, the team suggested, could explain why the Clovis settlements emptied and the megafauna vanished soon afterward. But the evidence was scanty. Firestone and his colleagues flagged thin sediment layers at dozens of archaeological sites in North America. Those sediments seemed to contain geochemical traces of an extraterrestrial impact, such as a peak in iridium, the exotic element that helped cement the case for a Chicxulub impact. The layers also yielded tiny beads of glass and iron—possible meteoritic debris—and heavy loads of soot and charcoal, indicating fires.

The team met immediate criticism. The decline of mammoths, giant sloths, and other species had started well before the Younger Dryas. In addition, no sign existed of a human die-off in North America, archaeologists said. The nomadic Clovis people wouldn't have stayed long in any site. The distinctive spear points that marked their presence probably vanished not because the people died out, but rather because those weapons were no longer useful once the mammoths waned, says Vance Holliday, an archaeologist at The University of Arizona in Tucson. The impact hypothesis was trying to solve problems that didn't need solving.

The geochemical evidence also began to erode. Outside scientists could not detect the iridium spike in the group's samples. The beads were real, but they were abundant across many geological times, and soot and charcoal did not seem to spike at the time of the Younger Dryas. "They listed all these things that aren't quite sufficient," says Stein Jacobsen, a geochemist at Harvard University who studies craters.

Yet the impact hypothesis never quite died. Its proponents continued to study the putative debris layer at other sites in Europe and the Middle East. They also reported finding microscopic diamonds at different sites that, they say, could have been formed only by an impact. (Outside researchers question the claims of diamonds.)

Now, with the discovery of Hiawatha crater, "I think we have the smoking gun," says Wendy Wolbach, a geochemist at DePaul University in Chicago, Illinois, who has done work on fires during the era.

The impact would have melted 1500 gigatons of ice, the team estimates—about as much ice as Antarctica has lost because of global warming in the past decade. The local greenhouse effect from the released steam and the residual heat in the crater rock would have added more melt. Much of that freshwater could have ended up in the nearby Labrador Sea, a primary site pumping the Atlantic Ocean's overturning circulation. "That potentially could perturb the circulation," says Sophia Hines, a marine paleoclimatologist at Lamont-Doherty.

Leery of the earlier controversy, Kjær won't endorse that scenario. "I'm not putting myself in front of that bandwagon," he says. But in drafts of the paper, he admits, the team explicitly called out a possible connection between the Hiawatha impact and the Younger Dryas.

NASA and German aircraft used radar to see the contours of an impact crater beneath the ice of Hiawatha Glacier.

PHOTO: JOHN SONNTAG/NASA

THE EVIDENCE STARTS with the ice. In the radar images, grit from distant volcanic eruptions makes some of the boundaries between seasonal layers stand out as bright reflections. Those bright layers can be matched to the same layers of grit in cataloged, dated ice cores from other parts of Greenland. Using that technique, Kjær's team found that most ice in Hiawatha is perfectly layered through the past 11,700 years. But in the older, disturbed ice below, the bright reflections disappear. Tracing the deep layers, the team matched the jumble with debris-rich surface ice on Hiawatha's edge that was previously dated to 12,800 years ago. "It was pretty self-consistent that the ice flow was heavily disturbed at or prior to the Younger Dryas," MacGregor says.

Other lines of evidence also suggest Hiawatha could be the Younger Dryas impact. In 2013, Jacobsen examined an ice core from the center of Greenland, 1000 kilometers away. He was expecting to put the Younger Dryas impact theory to rest by showing that, 12,800 years ago, levels of metals that asteroid impacts tend to spread did not spike. Instead, he found a peak in platinum, similar to ones measured in samples from the crater site. "That suggests a connection to the Younger Dryas right there," Jacobsen says.

For Broecker, the coincidences add up. He had first been intrigued by the Firestone paper, but quickly joined the ranks of naysayers. Advocates of the Younger Dryas impact pinned too much on it, he says: the fires, the extinction of the megafauna, the abandonment of the Clovis sites. "They put a bad shine on it." But the platinum peak Jacobsen found, followed by the discovery of Hiawatha, has made him believe again. "It's got to be the same thing," he says.

Yet no one can be sure of the timing. The disturbed layers could reflect nothing more than normal stresses deep in the ice sheet. "We know all too well that older ice can be lost by shearing or melting at the base," says Jeff Severinghaus, a paleoclimatologist at the Scripps Institution of Ocean-

In 2016, Kurt Kjær looked for evidence of an impact in sand washed out from underneath Hiawatha Glacier. He would find glassy beads and shocked crystals of quartz.

ography in San Diego, California. Richard Alley, a glaciologist at Pennsylvania State University in University Park, believes the impact is much older than 100,000 years and that a subglacial lake can explain the odd textures near the base of the ice. "The ice flow over growing and shrinking lakes interacting with rough topography might have produced fairly complex structures," Alley says.

A recent impact should also have left its mark in the half-dozen deep ice cores drilled at other sites on Greenland, which document the 100,000 years of the current ice sheet's history. Yet none exhibits the thin layer of rubble that a Hiawatha-size strike should have kicked up. "You really ought to see something," Severinghaus says.

Brandon Johnson, a planetary scientist at Brown University, isn't so sure. After seeing a draft of the study, Johnson, who models impacts on icy moons such as Europa and Enceladus, used his code to recreate an asteroid impact on a thick ice sheet. An impact digs a crater with a central peak like the one seen at Hiawatha, he found, but the ice suppresses the spread of rocky debris. "Initial results are that it goes a lot less far," Johnson says.

EVEN IF THE ASTEROID struck at the right moment, it might not have unleashed all the disasters envisioned by proponents of the Younger Dryas impact. "It's too small and too far away to kill off the Pleistocene mammals in the continental United States," Melosh says. And how a strike could spark flames in such a cold, barren region is hard to see. "I can't imagine how something like this impact in this location could have caused massive fires in North America," Marlon says.

It might not even have triggered the Younger Dryas. Ocean sediment cores show no trace of a surge of freshwater into the Labrador Sea from Greenland, says Lloyd Keigwin, a paleoclimatologist at the Woods Hole Oceanographic Institution in Massachusetts. The best recent evidence, he adds, suggests a flood into the Arctic Ocean through western Canada instead.

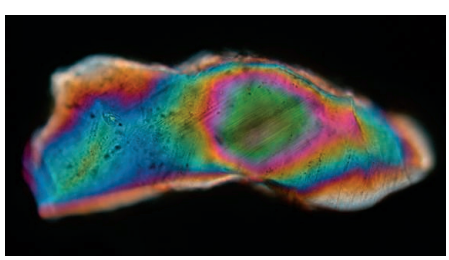

Banded patterns in the mineral quartz are diagnostic of shock waves from an extraterrestrial impact.

An external trigger may be unnecessary in any case, Alley says. During the last ice age, the North Atlantic saw 25 other cooling spells, probably triggered by disruptions to the Atlantic's overturning circulation. None of those spells, known as Dansgaard-Oeschger (D-O) events, was as severe as the Younger Dryas, but their frequency suggests an internal cycle played a role in the Younger Dryas, too. Even Broecker agrees that the impact was not the ultimate cause of the cooling. If D-O events represent abrupt transitions between two regular states of the ocean, he says, "you could say the ocean was approaching instability and somehow this event knocked it over."

Still, Hiawatha's full story will come down to its age. Even an exposed impact crater can be a challenge for dating, which requires capturing the moment when the impact altered existing rocks—not the original age of the impactor or its target. Kjær's team has been trying. They fired lasers at the glassy spherules to release argon for dating, but the samples were too contaminated. The researchers are inspecting a blue crystal of the mineral apatite for lines left by the decay of uranium, but it's a long shot. The team also found traces of carbon in other samples, which might someday yield a date, Kjær says. But the ultimate answer may require drilling through the ice to the crater floor, to rock that melted in the impact, resetting its radioactive clock. With large enough samples, researchers should be able to pin down Hiawatha's age.

Given the remote location, a drilling expedition to the hole at the top of the world would be costly. But an understanding of recent climate history—and what a giant impact can do to the planet—is at stake. "Somebody's got to go drill in there," Keigwin says. "That's all there is to it." ■

IMAGES: (TOP TO BOTTOM) SVEND FUNDER; ADAM GARDE, GEUS

CONSERVATION

Lighting up the nighttime

Artificial light at night needs to be reduced to limit negative environmental impacts

By **Kevin J. Gaston**

Among the most visually compelling images of the whole Earth have been those created using data obtained at night by astronauts or from satellites. The proliferation in use of electric lighting—including from industrial, commercial, municipal, and domestic sources—is striking. It sketches the spatial distribution of much of the human population, outlining a substantial proportion of the world's coastline, highlighting a multitude of towns and cities, and drawing the major highways that connect them. The data embodied in these nighttime images have been used to estimate and map levels of energy use, urbanization, and economic activity. They have also been key in focusing attention on the environmental impacts of the artificial light at night itself. Explicit steps need to be taken to limit these impacts, which vary according to the intensity, spectrum, spatial extent, and temporal dynamics of this lighting.

FROM DIRECT LIGHT TO SKYGLOW

Artificial light at night can usefully be thought of as having two linked components. The first component—direct emissions from outdoor lighting sources, which include streetlights, building and infrastructure lighting, and road vehicle headlamps—is spatially extremely heterogeneous. Ground-level illuminance in the immediate vicinity can vary from less than 10 lux (lx) to more than 100 lx (for context, a full moon on a clear night has an illuminance of up to 0.1 lx). It often declines rapidly over distances of a few meters. However, emissions from unshielded lights can, when unobstructed, carry horizontally over many kilometers, making artificial light at night both an urban and a rural issue.

The second component of artificial light at night is skyglow, the brightening of the nighttime sky caused mainly by upwardly emitted and reflected artificial light that is scattered in the atmosphere by water, dust, and gas molecules. Although absolute illuminance levels are at most about 0.2 to 0.5 lx, much lower than those from direct emissions, these are often sufficiently high to obscure the Milky Way, which is used for orientation by some organisms. In many urban areas, skyglow even obscures lunar light cycles, which are used by many organisms as cues for biological activity.

Environment and Sustainability Institute, University of Exeter, Penryn, Cornwall TR10 9FE, UK. Email: k.j.gaston@exeter.ac.uk

PHOTO: NASA, SCOTT KELLY

Published by AAAS

The bright lights of Tokyo and other cities in Japan, photographed from the International Space Station in 2015, show the proliferation of artificial light on our planet.

In the laboratory, organismal responses, such as suppression of melatonin levels and changes to behavioral activity patterns, generally increase with greater intensities of artificial light at night. It is challenging to establish the form of such functional relationships in the field, but experiments and observations have shown that commonplace levels of artificial light at night influence a wide range of biological phenomena across a wide diversity of taxa, including individual physiology and behavior, species abundances and distributions, community structure and dynamics, and ecosystem function and process (*1*). Exposure to even dim nighttime lighting (below 1 lx) can drastically change activity patterns of both naturally day-active and night-active species. These effects can be exacerbated by trophic interactions, such that the abundances of species whose activity is not directly altered may nonetheless be severely affected under low levels of nighttime lighting (*2*).

SHIFTING SPECTRA

Globally, the prevailing technology of outdoor lighting is undergoing a marked shift to light-emitting diodes (LEDs). Although LEDs can be used to produce a wide diversity of emission spectra, the main trend has been for narrower-spectrum street lighting with lower ("warmer") correlated color temperature (CCT) to be replaced by broader-spectrum LED lamps with higher ("cool white") CCT. This lighting provides improved color rendering, more faithfully revealing colors as seen under sunlight, but also tends to exacerbate skyglow unless accompanied by dimming and improved shielding (*3*). Biological responses to light are almost invariably spectrum-dependent, and broadening the spectrum of emissions increases the likelihood of their overlapping with these patterns of sensitivity, often increasing the biological impact.

Of particular concern is the growth in emissions of blue wavelengths, to which melatonin suppression is disproportionately sensitive. Multiple cascading processes can include stress responses, disease risk, and likelihood of obesity. Medical organizations have advised that poorly designed high-intensity and high-CCT street lighting should be avoided to minimize potential harm to human sleep patterns, sleep quality, and circadian rhythms (*4*). Studies have also raised concerns that greater exposure to artificial light at night increases some cancer risks (*5*). However, it is difficult to isolate effects of outdoor lighting from those of indoor lighting (including the trespass of outdoor lighting indoors) and to adequately control for other risk factors to human health. Concerted effort needs to be invested in assessing the existing evidence for such impacts both in principle and practice, and to find improved methods for measuring these impacts.

SPATIAL PATTERNS

The global importance of the impacts of artificial light at night rests in large part on its spatial extent. The direct footprint of light emissions is hard to estimate, being heavily dependent on the spatial resolution of available data. According to the best estimates, this extent is increasing at about 2% per year, with growth in the intensity of lighting from already lit areas occurring at a similar rate (*6*). The reduced operational costs of using LED lamps seem to have encouraged the installation of yet more lighting, rather than savings on preexisting lighting needs.

Conservatively, the overall coverage by skyglow is now nearly one-fourth of global land area, with 83% of the human population estimated to be living under light-polluted skies (*7*). Skyglow can extend hundreds of kilometers from urban sources, changing the nighttime environment in places that may be protected from many other anthropogenic pressures. Yet those persons responsible for these distant effects rarely recognize their role in creating them, nor are they held accountable.

Understanding of landscape-scale impacts of artificial light at night is in its infancy. Nonetheless, there is evidence that the attraction of nighttime-migrating birds to artificial light sources has strong negative impacts on their routes, their stopover habitat selection, and likely their energetics (*8*, *9*). Artificial light at night is also suspected to have played a role in catastrophic region-wide declines in insect populations. Although categorical evidence remains wanting, those species of moths that would seem most vulnerable, such as those attracted to lights or that are night-active, have been shown to have experienced the greatest losses (*10*).

CHANGING NIGHTTIME LIGHT PATTERNS

Artificial lighting truncates the duration of darkness attained in lit areas. Stationary and mobile (e.g., vehicle headlamp) sources tend to be switched on around the onset of dusk, decline to some degree as nighttime progresses (with some stationary lights being switched off and traffic levels declining), and continue until around the conclusion of dawn. As a consequence, the sky over urban areas often becomes somewhat darker as night progresses, whereas in nearby rural locations the sky becomes brighter as the Moon rises and darker as it sets (*11*).

Given the vital role of natural light cycles as cues for daily and seasonal timings of biological activities, it is unsurprising that these changes wrought by artificial light at night can alter those timings (*12*). This applies not only to animals. For example, artificial light at night has been found to advance the timing of budburst in temperate trees by several days (*13*). The magnitude of such changes can be similar to those caused by climate change, raising questions as to how the effects of climate change and artificial nighttime lighting interact.

REDUCING THE IMPACTS OF ARTIFICIAL LIGHT

Given the apparent pervasiveness of the negative biological impacts of artificial light at night, it is vital that these be reduced. Lag effects are common to many anthropogenic pressures on the environment. For example, even if levels of CO_2 emissions were to be dramatically reduced, Earth would continue to warm. However, such lags seem much less likely for the effects of artificial light at night. Reductions in artificial light at night would not result in instant recovery, but such recovery could be relatively swift.

Limiting the use of artificial light at night to the places, times, and forms required to ensure that people can use the nighttime appropriately would enable drastic reductions in artificial light at night in much of the world. Artificial light at night brings tangible benefits to people, most notably in extending the time available for work and social activities. However, existing regulations and requirements of lighting focusing on issues of safety and security are seldom supported by robust empirical evidence (*14*).

To reduce the negative effects of artificial light at night requires a blend of common sense and exploitation of technology. First, artificial light at night should not casually be introduced into areas in which it has not previously occurred, especially in those regions in which naturally dark spaces are now scarce (e.g., Western Europe, the eastern United States, East Asia).

Second, lighting should be at the lowest realistic intensity. The environmental impacts and energy costs of artificial light at night could be much reduced if emissions were cut to the low levels already used in some cities (e.g., Berlin).

Third, outdoor sources should be designed to ensure that lighting is limited to the places where it is actually required; many of the problems caused by artificial light at night result from poor lighting design, especially inadequate shielding. To date, attention here has fallen foremost on improved shielding of streetlights, which are often funded from the public purse. However, attention also needs

to be paid to the impacts of other major local contributors to artificial light at night, including gas stations, parking lots, transport hubs, sports stadiums, and billboards.

Fourth, lighting should only be used at times when it is required; most outdoor lighting should routinely be dimmed or switched off during periods of low demand. Although, despite energy savings, the costs of smart technologies remain limiting, these can assist in assessing needs and modifying lighting levels accordingly.

Finally, a more nuanced approach needs to be taken with regard to the spectrum of lighting, with preferential use of lower-CCT (<2400 K) and thus environmentally less disruptive lamps. Near environmentally sensitive zones (e.g., around protected areas, around otherwise dark habitat corridors), only narrow-spectrum lighting should be used, if lighting is needed at all. Use of dimmer and warm white or amber lighting along rural roads and in residential areas would help to reduce impacts, even if brighter and higher-CCT lighting is used in areas with heavier nighttime use by people and at busy road junctions. The present trend toward widespread introduction of high-CCT lighting (4000 K) brings major negative environmental impacts, relative to lower-CCT lighting, for no obvious benefit.

The ongoing and planned modernization of public lighting systems in many regions of the world provides a vital and ready opportunity to reduce the environmental impacts of artificial light at night. It could also facilitate the establishment of new norms that can help to shape future developments (including in regions that currently have no or little urbanization) that otherwise have enormous potential to further erode the nighttime, such as the inevitable growth in off-grid lighting schemes. Future nighttime images of Earth need not be records of further progression toward loss of the nighttime and its benefits. ■

REFERENCES

1. K. J. Gaston *et al.*, *Biol. Rev.* **88**, 912 (2013).
2. D. Sanders *et al.*, *Curr. Biol.* **28**, 2474 (2018).
3. M. Aubé, *Philos. Trans. R. Soc. B* **370**, 20140117 (2015).
4. American Medical Association, "AMA Adopts Guidance to Reduce Harm from High Intensity Street Lights" (2016); www.ama-assn.org/ama-adopts-guidance-reduce-harm-high-intensity-street-lights.
5. A. Garcia-Saenz *et al.*, *Environ. Health Persp.* **126**, 047011 (2018).
6. C. C. M. Kyba *et al.*, *Sci. Adv.* **3**, e1701528 (2017).
7. F. Falchi *et al.*, *Sci. Adv.* **2**, e1600377 (2016).
8. F. A. La Sorte *et al.*, *Glob. Change Biol.* **23**, 4609 (2017).
9. B. M. Van Doren *et al.*, *Proc. Natl. Acad. Sci. U.S.A.* **114**, 11175 (2017).
10. F. van Langevelde *et al.*, *Glob. Change Biol.* **24**, 925 (2018).
11. C. C. M. Kyba *et al.*, *Sci. Rep.* **5**, 8409 (2015).
12. K. J. Gaston *et al.*, *Annu. Rev. Ecol. Evol. Syst.* **48**, 49 (2017).
13. R. H. ffrench-Constant *et al.*, *Proc. R. Soc. B* **283**, 20160813 (2016).
14. S. Fotios, R. Gibbons, *Lighting Res. Technol.* **50**, 154 (2018).

10.1126/science.aau8226

CELL BIOLOGY

Endothelial cell transitions

Are endothelial-to-mesenchymal transitions in various vascular pathologies a consequence, cause, or defense?

By **Elisabetta Dejana**[1,2,3] *and* **Maria Grazia Lampugnani**[1,4]

Endothelial cells cover the internal surface of all types of vessels in the body and play a highly specialized role in protecting the vessel wall and the underlying tissues from noxious stimuli. These cells show organ-directed specialization and adapt to the requirements of different organs. However, in pathological conditions—such as inflammation, fibrosis, and atherosclerosis—endothelial cells can change their morphological and functional characteristics and acquire properties of other cell lineages such as fibroblasts, myofibroblasts, smooth muscle cells, and pericytes (which wrap around vessels) in a process called endothelial-to-mesenchymal transition (EndMT). This change of endothelial phenotype may increase the vascular responses to thrombosis (blood clot), decrease permeability control, and increase fibrotic reactions. In addition, when endothelial cells undergo EndMT, they release abnormal amounts and types of growth factors and extracellular matrix proteins that constitute important mediators in a dysfunctional cross-talk with the surrounding cells. Given the relevance of EndMT in several pathologies, understanding the molecular basis of EndMT could be instrumental for the development of new therapeutic interventions.

The switch to a mesenchymal phenotype is not a simple binary event. Instead, it occurs as a continuum with temporal changes in endothelial and mesenchymal marker expression. Cells that express at the same time both endothelial and mesenchymal markers are frequently observed in vivo in samples from both mice and humans, and detection of such coexpression has been crucial for the documentation of EndMT (*1*). It is therefore tempting to hypothesize that in a manner similar to the better characterized epithelial-to-mesenchymal transition (EMT), endothelial cells undergo a set of multiple and dynamic transitional states characterized by the fine-tuning of different transcription factors, sequential expression of mesenchymal markers, and modification of cellular functions (*2*–*5*). EndMT can be reverted pharmacologically in cultured cells (*2*), although the persistence of such reversion upon drug withdrawal is not known. Currently, we do not know whether EndMT is a reversible phenomenon in vivo (to which extent it is reversible and in response to which stimuli) or whether some cells can reach and maintain an intermediate phenotype without progression to a clearly defined mesenchymal cell phenotype. These considerations are important because the progressive acquisition of mesenchymal features corresponds to different functional responses of the cell. These questions require further experimental investigation.

The process of EndMT has been documented to occur in many pathological model systems and also in humans, although the actual contribution of this phenomenon to pathological dysfunctions remains a matter of debate (*6*–*9*). Skepticism about the biological relevance of EndMT appears mainly because of technical limitations, including that individual mesenchymal cells derived from samples with evidence of EndMT are not always easily distinguishable from fibroblasts of other origins, such as mesenchymal stem cells or stromal cells that are normally within tissues; it is also difficult to track EndMT in vivo. We envisage that EndMT is the result of a multistep phenomenon that follows specific kinetics. Consistently, endothelial cells express different mesenchymal markers at different time points after EndMT-triggering events (*2*). Moreover, endothelial cells cannot be synchronized in vivo, and this leads to variability in the type of markers expressed. Additionally, the costaining of cells with specific endothelial and mesenchymal markers can be difficult to interpret if the antibodies are not strictly specific and the signals sufficiently bright; cell-tracking experiments in mice are valuable, although the promoters that drive gene activation for those that encode endothelial cell markers can be leaky and can also be expressed at low levels by nonendothelial cell types, thus making the interpretation of data difficult.

These technical problems, however, can be solved to a large extent through the combination of different approaches, such as in vivo cell-lineage tracing in mice and in vitro cell

[1]*FIRC Institute of Molecular Oncology, University of Milan, Milan, Italy.* [2]*Department of Oncology and Haemato-Oncology, University of Milan, Milan, Italy.* [3]*Department of Immunology, Genetics and Pathology, Uppsala University, Uppsala, Sweden.* [4]*Mario Negri Institute for Pharmacological Research Milan, Italy. Email: elisabetta.dejana@ifom.eu*

characterization for the expression of multiple markers. Most importantly, cell tracking studies will become possible in vivo in humans by use of highly advanced imaging techniques (*10*). These approaches could be used to track endothelial cell dynamics and phenotype in vivo in various disease settings.

In the embryo, EndMT is a physiological process that is necessary for correct heart development (*2, 10*). The cells of the endocardium undergo the EndMT switch to be able to easily migrate into the cardiac jelly and to participate in valve formation. This process is strictly controlled in time and space during development. In the adult, EndMT has been associated mainly with pathological conditions characterized by vascular degeneration and fibrosis. For example, in atherosclerosis, endothelial cells lose their vascular cell fate and acquire perivascular smooth muscle and mesenchymal characteristics and thus participate in the thickening of the muscular layer of arteries (media) that is typical of this condition (*2, 7, 11*). EndMT is also implicated in other pathological reactions, including vascular calcification; pulmonary arterial hypertension; vein graft rejections; heart, kidney, and lung fibrosis; cancer-associated fibrosis; fibrodysplasia ossificans progressive (a condition in which muscle and connective tissue is replaced with bone); and brain vascular cavernomas (clusters of abnormal blood vessels) (*2, 4, 7, 8, 11–13*). In these conditions, endothelial cells react to a pathological environment by acquiring mesenchymal characteristics and thereby potentially contribute to the evolution of the disease. It is striking how the same environmental stimuli—for example, transforming growth factor–β (TGF-β), Notch ligands, and Wnt ligands—that finely orchestrate EndMT in embryonic heart development might induce pathological reactions of endothelial cells in the adult (see the figure).

An interesting hypothesis is that EndMT is the result of unresolved vascular remodeling (*3*). If endothelial cells are exposed for prolonged times to disturbed shear stress (as in atherosclerosis) or to other noxious stimuli in the blood and lymph or in the organ environment, they can undergo EndMT. This in turn will act as a feedback mechanism that maintains the vasculature in an unstable condition through induction of matrix metalloproteases (MMPs) and liberation of extracellular matrix–bound and extracellular matrix–contained ligands, formation of provisional extracellular matrix, and expression of leukocyte-adhesion molecules and inflammatory cell recruitment, all of which will contribute to chronic pathological conditioning of the vasculature (*2*). Thus, the same stimuli necessary for the correct development of the embryo vasculature might induce pathological reactions in the adult if they are expressed for prolonged amounts of time and at high levels. It is also possible that EndMT represents an inadequate attempt to restore functionality after vascular damage. Further research is needed to solve these issues.

EndMT has a number of similarities with EMT, which is observed during tissue embryogenesis and under pathological conditions, such as invading carcinomas (*5, 10, 14, 15*). EMT and EndMT are triggered by activation of transcription factors—such as SNAIL1, SNAIL2, zinc finger E-box binding homeobox 1 (ZEB1), Kruppel-like factor 2 (KLF2), and KLF4—and up-regulated expression of a set of mesenchymal and stem cell markers, which includes CD44, fibroblast-specific protein 1 (FSP1), stem cell antigen 1 (SCA1), vimentin, MMP2, and MMP9. The coexpression of stem and mesenchymal markers in EndMT and EMT suggests that in the course of transition to a mesenchymal phenotype, endothelial cells (such as epithelial cells) can also acquire stem cell–like properties. This introduces the concept that in specific contexts, mesenchymal status may favor a condition of pluripotency. However, although extensively studied in cancer, the precise relationship between the EMT program and the stem cell state is not yet clarified and remains to be demonstrated in endothelial cells (*4, 15*).

Stimuli, phenotype, and cell fate in EndMT

Endothelial cells may undergo EndMT in response to various stimuli. EndMT can occur gradually with multiple and dynamic intermediate stages (characterized by various phenotypes) and can result in the acquisition of distinct cell fates.

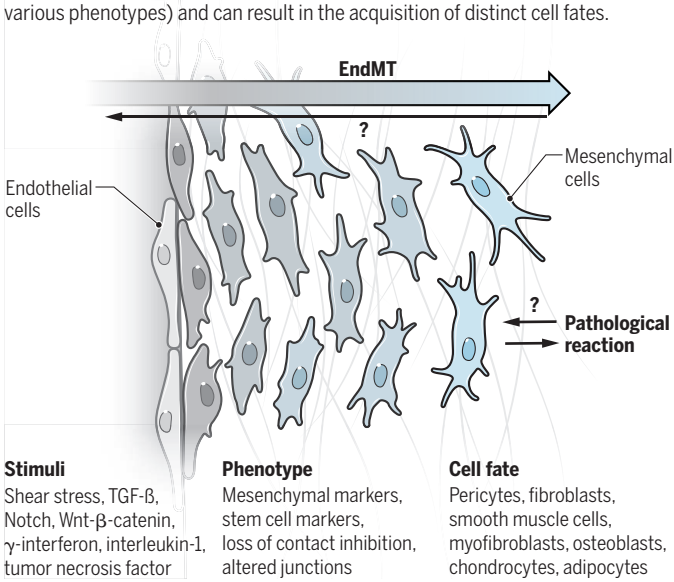

GRAPHIC: JOSHUA BIRD/*SCIENCE*

Agents that prevent or revert EndMT could be beneficial to treat several vascular diseases that accompany EndMT (*2, 11*). While the molecular mechanisms that drive EndMT start to be unraveled, inhibitors for selective EndMT targeting have still to be identified (*2, 11*). Currently, inhibitors of EndMT-driving stimuli—such as TGF-β, bone morphogenetic proteins, inflammatory cytokines or their receptors, and Wnt–β-catenin signaling—can prevent EndMT in vivo and revert several EndMT traits in cultured cells (*2, 4, 8*). However, although prevention of EndMT can be achieved, the full restoration of endothelial cell functional identity might be more difficult once this is lost through EndMT.

Endothelial cells have a high degree of diversity and specialization that are dictated by the surrounding cells, nutrients, and blood and lymph flow. Thus, the endothelial cells that undergo EndMT might not follow identical pathways or respond to identical inhibitors or activators. The restoration and maintenance of their original functional state might therefore be a particularly difficult task. Several stimulating questions on the process of EndMT still wait to be answered. Increasing our knowledge of EndMT should help to design more specific inhibitors to interfere with the pathological occurrence of such endothelial cell fate transitions in different conditions such as atherosclerosis, fibrosis in cancer, kidney disease, heart disease, and others. ■

REFERENCES AND NOTES

1. E. M. Zeisberg *et al.*, *J. Am. Soc. Nephrol.* **19**, 2282 (2008).
2. E. Dejana *et al.*, *Nat. Commun.* **8**, 14361 (2017).
3. M. A. Schwartz *et al.*, *Science* **360**, 270 (2018).
4. D. Medici, R. Kalluri, *Semin. Cancer Biol.* **22**, 379 (2012).
5. T. Brabletz *et al.*, *Nat. Rev. Cancer* **18**, 128 (2018).
6. Y. Li, K. O. Lui, B. Zhou, *Nat. Rev. Cardiol.* **15**, 445 (2018).
7. S. M. Evrard *et al.*, *Nat. Commun.* **7**, 11853 (2016).
8. L. Maddaluno *et al.*, *Nature* **498**, 492 (2013).
9. L. Hong *et al.*, *Eur. J. Cell Biol.* 10.1016/j.ejcb.2018.07.005 (2018).
10. J. C. Kovacic *et al.*, *Circulation* **125**, 1795 (2012).
11. P. Y. Chen *et al.*, *J. Clin. Invest.* **125**, 4514 (2015).
12. D. James, S. Rafii, *Sci. Transl. Med.* **6**, 227fs12 (2014).
13. G. Sánchez-Duffhues *et al.*, *Dev. Dyn.* **247**, 492 (2018).
14. M. A. Nieto *et al.*, *Cell* **166**, 21 (2016).
15. Y. Zhang, R. A. Weinberg, *Front. Med.* **12**, 361 (2018).

ACKNOWLEDGMENTS

The authors acknowledge support from the Italian Association for Cancer Research (IG16683) and Mynerva 5xMille Project (21267), European Research Council (ERC 742922), Swedish Research Council, and Knut and Alice Wallenberg Foundation. They thank F. Orsenigo for the construction of the figure and C. Berrie for proofreading. E. D. and M. G. L. contributed equally to this work.

10.1126/science.aas9432

IMMUNOLOGY

A target to suppress inflammation

A small-molecule inhibitor of the OGG1 DNA glycosylase has anti-inflammatory effects

By **Leona D. Samson**

Tissues that are stressed by injury or by invading pathogens elicit signals for the recruitment of inflammatory immune cells such as macrophages and neutrophils, which consequently release reactive oxygen and nitrogen species (RONS) as part of the innate immune response (*1*). This flood of RONS is important for directly attacking invading pathogens and for warding off infection of damaged tissue. But the efficiency of RONS in inactivating invading cells and viruses creates an Achilles heel of the innate immune response, namely that RONS are also able to kill and mutate cells in healthy tissues. Although inflammatory responses are usually counterbalanced over time by an opposing anti-inflammatory response, achieving the optimal balance with minimal collateral tissue damage is difficult even in healthy individuals, and virtually impossible in individuals with certain disease conditions such as ulcerative colitis and rheumatoid arthritis (*2*). Therefore, the development of anti-inflammatory drugs, targeting inflammation from a variety of different angles, has flourished in recent decades. On page 834 of this issue, Visnes *et al.* (*3*) present an entirely new approach to suppressing the inflammatory response. Counterintuitively, this approach involves the inhibition of the 8-oxoguanine DNA glycosylase 1 (OGG1) DNA repair enzyme that recognizes and initiates the base excision repair of 7,8-dihydro-8-oxoguanine (8-oxoG), one of the major types of DNA base damage induced by RONS.

The recognition and binding of 8-oxoG by OGG1, which frequently occurs in the G-rich promoters of proinflammatory genes, facilitates the loading of the nuclear factor κB (NF-κB) transcription factor that stimulates transcription of proinflammatory chemokine and cytokine genes, thus promoting an inflammatory response (*4*). Visnes *et al.* identified a small-molecule inhibitor that neatly binds the active site of OGG1 and prevents its search for 8-oxoG in DNA. Therefore, inhibited OGG1 cannot bind to the G-rich regions adjacent to NF-κB binding sites in promoters of proinflammatory genes. This inhibitor (called TH5487) robustly inhibits the tumor necrosis factor (TNF)–induced inflammatory response in cultured mouse and human lung epithelial cells and, most notably, inhibits TNF-induced neutrophilic inflammation in an in vivo mouse model. Additionally, small-molecule OGG1 inhibitors have also recently been reported, demonstrating the potential importance of this target (*5*, *6*).

Central to this study is the hitherto underappreciated role that OGG1 plays in regulating a vigorous transcriptional response to oxidative DNA damage (*4*) (see the figure). Hints at the role of OGG1 in innate immunity were gleaned from the phenotype of mice in which the *Ogg1* gene is inactivated (*7*). We now know that evolution has exploited the specificity of OGG1 for finding and binding to 8-oxoG lesions in the genome and deployed it as a signal for the coordinated up-regulation of NF-κB–regulated proinflammatory genes; OGG1 thus appears to be a major player in launching inflammatory responses.

That the presence of DNA damage should signal the activation of cellular responses seems like a tale as old as time. Indeed, it is more than 60 years since Weigle and Bertani showed that bacteriophages exposed to ionizing radiation (which induces DNA damage) survive better in irradiated versus unirradiated bacterial hosts (*8*). This improved survival occurred because preirradiated bacteria launch the SOS DNA damage response, which enables survival of damaged phage DNA. The DNA damage response proteins RecA in *Escherichia coli* and the mammalian ataxia-telangiectasia mutated (ATM) and taxia telangiectasia and Rad3 related (ATR) recognize single-stranded DNA and broken DNA ends, abnormal DNA structures that are generated by attempted DNA replication and transcription of damaged DNA, and intermediates of DNA repair. These proteins may be thought of as detecting common kinds of damage that arise as a result of a myriad of initial lesions that affect many sites on each of the four DNA bases, the deoxyribose sugar, and the sugar-phosphate backbone of DNA. However, OGG1 stimulates a cellular response to a specific DNA base lesion (8-oxoG) that has not yet been pro-

Inhibition of inflammation

Inflammation is associated with the generation of RONS, which damage G-rich promoters, including those adjacent to NF-κB binding sites. OGG1 binding to oxidized guanines facilitates the recruitment of transcription factors that drive proinflammatory gene expression and a cellular inflammatory response. TH5487 prevents OGG1 from interacting with DNA substrates in promoters, inhibiting inflammatory gene expression.

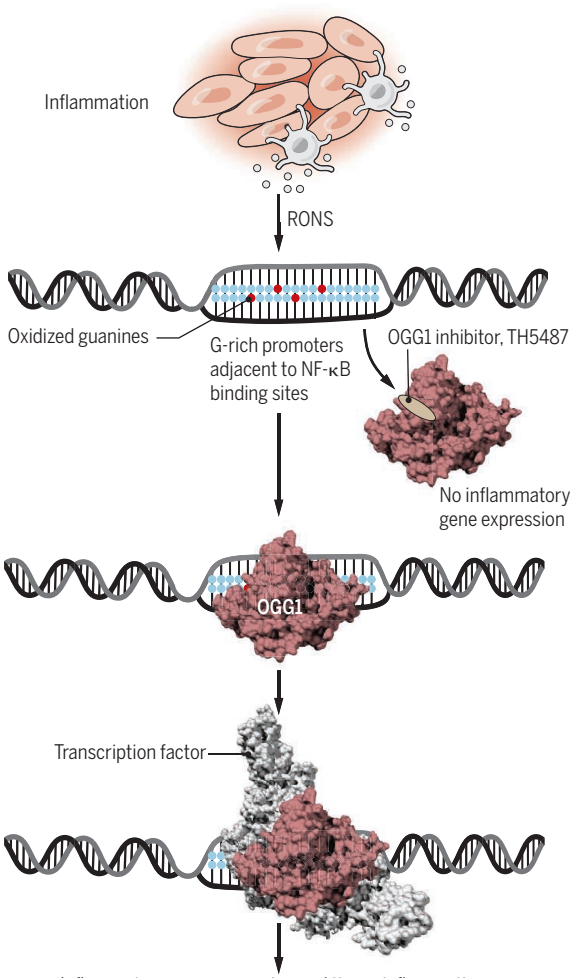

GRAPHIC: N. DESAI/*SCIENCE*

Departments of Biology and Biological Engineering, Massachusetts Institute of Technology, Cambridge, MA, USA. Email: lsamson@mit.edu

cessed by the DNA replication, transcription, and repair machineries, and the transcriptional response is stimulated directly by the interaction of OGG1 with NF-κB, as opposed to the signal transduction cascade of events that follow recognition of damaged DNA by RecA, ATM, and ATR (*9*). Perhaps the closest analog to OGG1 acting as both a DNA repair enzyme and as a transcription regulator is the *E. coli* Ada DNA repair methyltransferase that, having transferred a methyl group from the DNA sugar-phosphate backbone to a cysteine in one of its active sites, acts as a transcriptional regulator for a number of other genes that promote resistance to methylating agents (*10*, *11*).

In 2004, inflammation was dubbed the "secret killer" (*12*), owing to established links between inflammation and heart disease, cancer, Alzheimer's disease, and many other diseases. By exploiting this newly recognized role of OGG1 and identifying the potent TH5487 inhibitor, Visnes *et al.* have developed a new approach to combating the ravages of uncontrolled inflammation. Adding an OGG1 inhibitor to the panoply of steroidal and nonsteroidal drugs, plus the more recently developed biologics that target TNF and other potent mediators of inflammation, can only help the cause. The obvious downside to systemically inhibiting the DNA repair function of OGG1 is that potentially mutagenic DNA lesions may accumulate in the genome, which might accelerate the very diseases inflammation has been linked to, particularly, cancer. Other enzymes that repair 8-oxoG may compensate for inhibited OGG1 and thereby alleviate this potential for collateral damage. It is possible that transiently inhibiting OGG1 in conditions of severe inflammation, such as sepsis or severe flare-ups in rheumatoid arthritis and other autoimmune diseases, may prove beneficial, whereas chronic administration of an OGG1 inhibitor to prevent inflammation may not pass the health risk-benefit analysis. Visnes *et al.* have revealed fascinating new depths to plumb in the long search for alternative anti-inflammatory drugs to alleviate pain and reduce the effects of inflammatory diseases. ■

REFERENCES

1. P. Lonkar, P. C. Dedon, *Int. J. Cancer* **128**, 1999 (2011).
2. P. Li, Y. Zheng, X. Chen, *Front. Pharmacol.* **8**, 460 (2017).
3. T. Visnes *et al.*, *Science* **362**, 834 (2018).
4. L. Pan *et al.*, *J. Biol. Chem.* **291**, 25553 (2016).
5. N. Donley *et al.*, *ACS Chem. Biol.* **10**, 2334 (2015).
6. Y. Tahara *et al.*, *J. Am. Chem. Soc.* **140**, 2105 (2018).
7. E. Touati *et al.*, *Helicobacter* **11**, 494 (2006).
8. J. J. Weigle, G. Bertani, *Virology* **2**, 344 (1956).
9. A. Ciccia, S. J. Elledge, *Mol. Cell.* **40**, 179 (2010).
10. L. Samson, J. Cairns, *Nature* **267**, 281 (1977).
11. T. Lindahl, B. Sedgwick, M. Sekiguchi, Y. Nakabeppu, *Annu. Rev. Biochem.* **57**, 133 (1988).
12. C. Gorman *et al.*, "Health: The fires within," *Time*, 23 February 2004; http://content.time.com/time/magazine/article/0,9171,993419,00.html.

10.1126/science.aav4744

CELL BIOLOGY

Cell types behaving in their natural habitat

Defining cell types in situ connects gene expression, anatomy, and function during certain behaviors

By **Bosiljka Tasic** *and* **Philip R. Nicovich**

A full understanding of a complex system is difficult, perhaps impossible, to accomplish without an inventory of the components involved. When that system is an organ in an organism, the parts list becomes a census of cell types, including their identity, number, location, and function. On page 792 of this issue, Moffitt *et al.* (*1*) demonstrate an advanced method for in situ profiling of gene expression within the preoptic region of the intact mouse hypothalamus. Their approach not only yields a census of cell types in this region of the brain, but also assesses which cell types are activated during certain behaviors. This region of the brain is involved in the regulation of homeostasis and social behaviors such as aggression, sex, and parenting.

"Which cell types are responsible for which behaviors, and how do their functions change upon experience?"

Recently, comprehensive (genome-wide) analysis of gene expression in single cells for the purposes of cell classification has grown rapidly, but it is most frequently performed on dissociated cells (*2*). The current technique of choice is single-cell RNA sequencing (scRNA-seq), which can detect thousands of different messenger RNA (mRNA) species per cell in a relatively unbiased fashion. In this process, thousands of mRNA species are isolated from individual cells and then quantified. Cell classes and types are defined on the basis of similar gene expression, but the spatial context is lost. By contrast, profiling cells in intact tissue involves techniques that, to be informative, detect only a subset of genes, selected by researchers (*3*). The main reason for relying on gene selection is that many RNAs in cells are "packed" in a very small volume; for example, the volume of a mouse neuron is ~1 to 5 picoliters (*4*), and it contains ~200,000 RNA molecules (*5*). It is hard to detect all mRNA molecules in such a tiny volume. In addition, expression levels of different mRNA species vary by several orders of magnitude, meaning that the most abundant mRNAs will be preferentially detected (*6*). However, many less-abundant transcripts define cell identity and confer specific properties to a cell.

The common principle of techniques to spatially map gene expression is based on RNA fluorescence in situ hybridization (FISH), whereby single-stranded DNA or DNA nanostructures that complementarily hybridize with target mRNAs are conjugated to fluorophores and are detected in tissue samples using fluorescence microscopy. These assays are not "omic"—genome-wide and unbiased—but with thoughtful gene selection they can distinguish all cell types within a tissue.

Moffitt *et al.* use the now relatively standard scRNA-seq combined with their latest version of multiplexed error-robust FISH (MERFISH) (*7*, *8*) to define cell types in the preoptic area of the mouse brain. First, they perform scRNA-seq to find mRNAs that would be most informative for distinguishing cell types. Then, they design MERFISH experiments to detect these select mRNAs and define cell types in situ. MERFISH can detect hundreds of genes rapidly, owing to efficient and robust tissue and probe chemistry (*7*, *8*). Because of its high sensitivity (six to eight times higher than scRNA-seq), MERFISH can focus on low-abundance mRNAs and detect many at the same time in the crowded space of a single cell.

Moffitt *et al.* find that the mouse preoptic area has ~70 neuronal cell types, and that MERFISH provides better cell-type resolution than scRNA-seq. This is the first time this brain area has been characterized at this level of detail; therefore, many of the cell types have not previously been defined. The MERFISH results also provided high-resolution information on cell-type distribution and some generalizations: In the preoptic area, many excitatory cell types are spatially clustered, whereas the inhibitory ones are frequently dispersed throughout the area.

Allen Institute for Brain Science, 615 Westlake Avenue North, Seattle, WA, USA. Email: bosiljkat@alleninstitute.org

Some newly defined cell types differ in their abundance and distribution between males and females (referred to as sexual dimorphism in brain structure) (*9*).

The authors were interested in specific functions of these newly discovered cell types in homeostasis and social behaviors. To address these questions, they repeated the same cell-type detection experiments by MERFISH, but in animals that had undergone specific treatments or engaged in specific behaviors. By detecting gene expression that indicates neuronal activity, they found cell types that were activated in these specific contexts. They found clear differences in cell types that were active in different behaviors (for example, aggression versus parenting) and different organismal states (virginity versus postsexual experience), suggesting specific functions. The study provides avenues for addressing many intriguing biological questions. The most pressing are: Which cell types are responsible for which behaviors, and how do their functions change upon experience? For example, which cell types and what types of changes cause a switch from aggression to parenting in males after sexual experience? To address these questions, carefully designed cell type–specific perturbation experiments are necessary (see the figure).

In a broader context, the study of Moffitt *et al.* is a shining example for defining cell types in their "natural habitat" that should be emulated to create the next generation of brain atlases (*10, 11*). To transform the quagmire of unrecognizable neurons, we first need to define genes that are expressed in them by scRNA-seq. Once the cells are defined by genes they express (like linking a face to a person), we can define their spatial patterns and frequencies by MERFISH or similar methods. Then, we can repeatedly go back to these cells in different animals and assign them other cellular properties, such as morphology or connectivity, or putative biological function by assaying their activity. Finally, to establish their function, we need to be able to perturb these cell types. Although not utilized in the current study, the identifying genes can be used to generate genetic tools to perturb corresponding cell types in specific behaviors and states. These types of experiments define cells that are necessary and/or sufficient to produce certain behaviors. In the future, step by step, marching through the brain, the approach outlined here will lead to unprecedented descriptions of nervous systems and an abundance of salient hypotheses to be tested toward understanding nervous system function. ■

REFERENCES

1. J. R. Moffitt *et al.*, *Science* **362**, eaau5324 (2018).
2. B. Tasic, *Curr. Opin. Neurobiol.* **50**, 242 (2018).
3. E. Lein, L. E. Borm, S. Linnarsson, *Science* **358**, 64 (2017).
4. J. P. Gilman, M. Medalla, J. I. Luebke, *Cereb. Cortex* **27**, 2078 (2017).
5. E. Shapiro, T. Biezuner, S. Linnarsson, *Nat. Rev. Genet.* **14**, 618 (2013).
6. J. H. Lee *et al.*, *Science* **343**, 1360 (2014).
7. J. R. Moffitt *et al.*, *Proc. Natl. Acad. Sci. U.S.A.* **113**, 14456 (2016).
8. J. R. Moffitt *et al.*, *Proc. Natl. Acad. Sci. U.S.A.* **113**, 11046 (2016).
9. T. Yang, N. M. Shah, *Curr. Opin. Neurobiol.* **38**, 89 (2016).
10. A. Regev *et al.*, *eLife* **6**, e27041 (2017).
11. J. R. Ecker *et al.*, *Neuron* **96**, 542 (2017).

10.1126/science.aav4841

Defining behaviorally relevant cell types in the brain

Once cell types are defined by sets of genes identified by scRNA-seq, their activity in different contexts and during various behaviors can be characterized in situ by MERFISH. To define whether the cells are necessary or sufficient for specific behavior, additional experiments, such as genetic perturbations, are necessary.

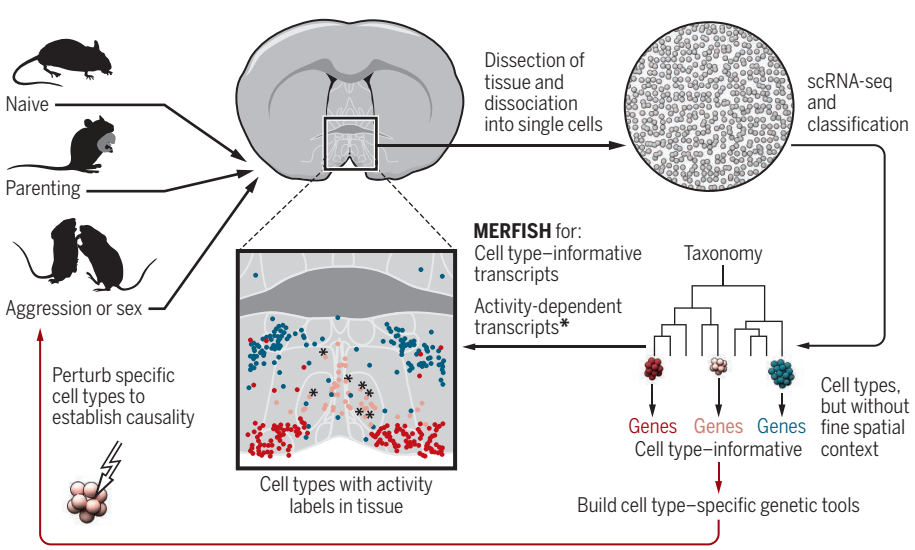

OPTICS

Polarimetry enabled by nanophotonics

Nanoantenna and plasmonic structures can be used to measure light polarization

By **Alejandro Martínez**

Light beams consist of oscillatory electric (and magnetic) fields having a certain amplitude, phase, and frequency. In transverse waves, the state of polarization (SoP) characterizes how the electric field oscillates in the plane perpendicular to the propagation direction. Light-matter interactions strongly depend on the SoP, so its complete measurement is of paramount importance in a wide array of disciplines including chemistry, imaging, optical communications, and astronomy. However, measuring the SoP of a light beam, the main goal of polarimetry, is much trickier than knowing its intensity or frequency, because it involves the simultaneous measurement of the four Stokes parameters, which even account for the case of unpolarized light.

For decades, polarimeters have consisted of a combination of linear retarders, polarizers, and quarter-wave plates, which were able to obtain the four required measurements by spatial or temporal splitting of the incoming light beam (*1*). Such macroscopic polarimeters, widely used in many applications, are complex, bulky, and expensive; there have been few attempts to miniaturize them, with the notable exception of the fiber-grating polarimeter, highly useful in fiber optics (*2*). Recent advances in nanoscience and nanotechnology have unveiled new ways to shrink polarimeters, with all of the subsequent advantages that miniaturization and on-chip integration may bring (*3*).

Because the optical response of nanostructures depends on the polarization of the incident light beam, it should be possible to retrieve the SoP from outgoing signals. Possible polarization states are linearly polarized light along the horizontal

Nanophotonics Technology Center, Universitat Politècnica de València, Camino de Vera s/n, Valencia, Spain. Email: amartinez@ntc.upv.es

(I_0) or vertical (I_{90}), and right-handed (σ^+) and left-handed (σ^-) circularly polarized light. Then, a metasurface (an array of nanostructures) can be designed to scatter such polarization states into different directions (see the figure, left), which enables the retrieval of the Stokes parameters at a certain wavelength (*4*–*8*). The scattering paths could even be parallel to the metasurface and guided on the chip substrate to facilitate on-chip processing and detection (*5*).

However, the light-matter interaction enabling the polarization-dependent response in these implementations is distributed among all of the elements of the array, so the device footprint is much larger than one square wavelength. Local nanoscale measurement of the SoP requires polarization-dependent photonic responses in individual metallic or dielectric nanostructures. For instance, plasmonic nanostructures could be engineered in certain in-plane shapes that produce optical hot spots depending on the SoP of the illumination (see the figure, middle). An absorbing semiconductor placed in the hot-spot regions can generate output photocurrents proportional to the SoP (*9*). Although the device footprint is much smaller than in the case of metasurface polarimeters, this approach still requires at least four nanostructures to fully retrieve the SoP. Thus, this polarimeter would efficiently work for transverse light beams but would fail when measuring the SoP of complex, structured beams that have variations of the local polarization in the transverse plane (*10*).

The SoP at a single spatial point and in a single-incident light pulse can be determined by mixing both previous approaches—that is, by measuring the polarization-dependent scattering from individual nanostructures. As a result of spin-orbit interaction (*11*), the direction of the scattered light paths depends on the incident polarization. Moreover, the scattering paths can be defined with lithographically etched waveguides that support different guided modes that will carry all the information needed to retrieve the SoP (see the figure, right) (*12*). In principle, there is no limit for downscaling the size of the scatterer as long as it partly scatters the incoming beam. Remarkably, spin-orbit interactions would also enable a full-vector description of the incident light, beyond the transverse picture (*13*).

By a suitable design (materials, shape, and size) of the underlying nanostructures, the previous approaches can be used to build ultracompact polarimeters across the entire electromagnetic spectrum, even into the terahertz regime. Such polarimeters would be extremely broadband; by calibrating the polarization scattering paths or absorption at each working wavelength, they could be used for spectropolarimetry (*6*, *12*). Notably, they may also be implemented with resonant dielectric nanostructures (*14*), which would avoid the ohmic losses inherent in metals and also facilitate mass manufacturing in silicon chips. Although the absorptive approach is highly appropriate to build a device for SoP measurement that blocks beam propagation, the approaches based on scattering may operate in a nondestructive way with low insertion losses and are highly suitable for an in-line configuration.

On-chip polarimeters should easily displace their bulk free-space counterparts because of the inherent advantages of integration, such as low cost, reliability, repeatability, and integration with electronics (*8*). Several applications of on-chip polarimeters could immediately open up. Low-cost in-line polarimeters with low insertion losses operating at telecommunication wavelengths could monitor SoP in real time in present and future optical communication networks that use polarization multiplexing schemes. Spin-orbit polarimeters with near-atomic dimensions may locally test the polarization of single photons in quantum systems and networks. Now that the fundamentals for on-chip nanoscale polarimeters have been settled, it is time to make them a practical reality. ■

"On-chip polarimeters should easily displace their bulk free-space counterparts because of the inherent advantages of integration..."

Nanoscale polarimeters

Transverse light, with an electric field **E**, wave vector **k**, and wavelength λ, illuminates a set of nanostructures. In all cases, measuring at least four outputs enables the retrieval of the state of polarization. Dielectric and metallic nanostructures are depicted in blue and yellow, respectively.

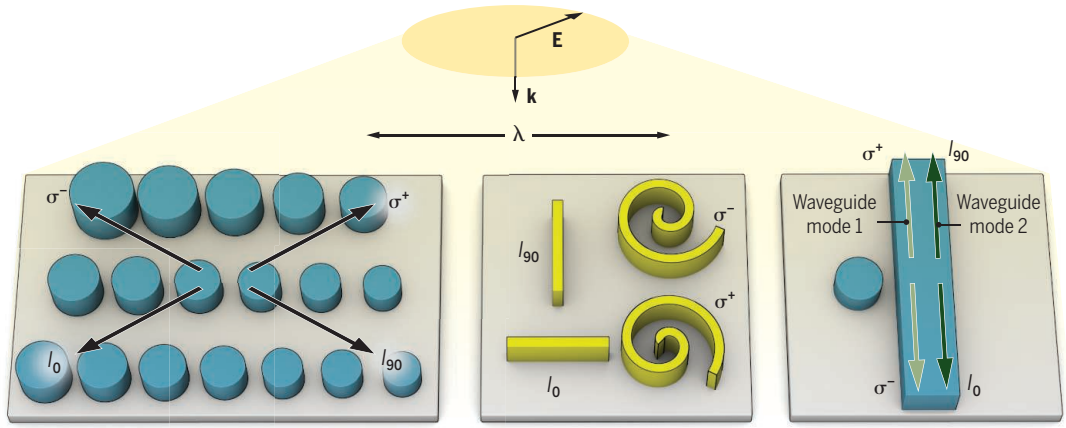

Scattered output
A metasurface consisting of a set of nanoantennas scatters different polarization states into well-defined spatial pathways.

Absorbed output
Plasmonic nanoantennas can be fabricated in shapes designed to absorb light of a certain polarization.

Guided radiation
Spin-orbit interactions help scatter different input polarizations into different directions and modes of a waveguide.

GRAPHIC: V. ALTOUNIAN/*SCIENCE*

REFERENCES

1. R. M. A. Azzam, *J. Opt. Soc. Am. A* **33**, 1396 (2016).
2. P. S. Westbrook, T. A. Strasser, T. Erdogan, *IEEE Photon. Technol. Lett.* **12**, 1352 (2000).
3. A. F. Koenderink, A. Alù, A. Polman, *Science* **348**, 516 (2015).
4. A. Pors, M. G. Nielsen, S. I. Bozhevolnyi, *Optica* **2**, 716 (2015).
5. J. P. Balthasar Mueller, K. Leosson, F. Capasso, *Optica* **3**, 42 (2016).
6. E. Maguid *et al.*, *Science* **352**, 1202 (2016).
7. P. C. Wu *et al.*, *ACS Photonics* **5**, 2568 (2018).
8. N. A. Rubin *et al.*, *Opt. Express* **26**, 21455 (2018).
9. F. Afshinmanesh, J. S. White, W. Cai, M. L. Brongersma, *Nanophotonics* **1**, 125 (2012).
10. T. Bauer *et al.*, *Science* **347**, 964 (2015).
11. K. Y. Bliokh, F. J. Rodríguez-Fortuño, F. Nori, A. V. Zayats, *Nat. Photonics* **9**, 796 (2015).
12. A. Espinosa-Soria, F. J. Rodríguez-Fortuño, A. Griol, A. Martínez, *Nano Lett.* **17**, 3139 (2017).
13. T. Bauer, S. Orlov, U. Peschel, P. Banzer, G. Leuchs, *Nat. Photonics* **8**, 23 (2014).
14. A. I. Kuznetsov *et al.*, *Science* **354**, aag2472 (2016).

10.1126/science.aau7494

RETROSPECTIVE

Paul G. Allen (1953–2018)

Cofounder of Microsoft, visionary, and philanthropist

By **Rick Horwitz[1], Allan Jones[2], Tom Daniel[3]**

On 15 October, Paul G. Allen died after a 9-year battle with non-Hodgkin's lymphoma. He was 65. Often dressed in a timeless blue shirt and dark pants, the cofounder of Microsoft and investor in myriad domains didn't stand out by appearance; in conversation, he was soft-spoken and reserved. What stood out about Paul was his insatiable curiosity, vision, breadth of knowledge, and generosity. Throughout his life, he focused on identifying big problems and making a difference. His push to move us out of our comfort zone and focus on scientific horizons appearing just beyond reach will be greatly missed.

Paul was born in 1953, in Seattle, Washington. His father was associate director of the University of Washington Libraries. He attended Lakeside School where he met Bill Gates, who was 2 years younger. The two became passionate about computing, which was done on the large mainframes that were seen as the future of the field. Paul took his perfect SAT score to Washington State University for college but dropped out after 2 years and moved to Boston to work near Bill, who was attending Harvard. In 1974, the cover of an upcoming issue of *Popular Electronics* showed the Altair 8800, touted as the world's first microcomputer. Paul rushed over to show it to Bill and quickly envisioned that this could lead to a computer on every desk. Struck by the potential opportunities, Bill dropped out of school as well. Whereas most of the interest at the time was in improving the hardware, Paul and Bill saw the need for software that would democratize computing, making the computer accessible to everyone and allowing it to play a pervasive role in writing, communication, and accounting. They launched Microsoft in 1975, and in 1981 their operating system was adapted by IBM for its new personal computer.

In 1983, Paul was diagnosed with Hodgkin's lymphoma and retired from Microsoft. He formed Vulcan, Inc., in 1986. The privately held company oversaw his wide swath of business and philanthropic activities, which reflected his passions. These included pop culture (Museum of Pop Culture, or MoPOP), music (Upstream Music Fest), art (Seattle Art Fair), sports (Seattle Seahawks, Portland Trail Blazers, and Seattle Sounders FC), movies (Cinerama), film (Vulcan Productions), airplanes (Stratolaunch and Flying Heritage Collection), the environment, and climate and conservation. All of these endeavors were marked by Paul's desire to do it differently and make a big impact.

Paul also funded a multitude of scientific initiatives, including the Allen Institute for Brain Science, Allen Institute for Cell Science, the Allen Distinguished Investigators, the Allen Institute for Artificial Intelligence, and the Paul G. Allen Frontiers Group, along with diverse workshops. All such ventures focused on fundamental questions about the nature of computations and the inherent complexity of living systems. The guiding principles of his initiatives included team science and open science. The Allen institutes diverged from the typical academic university or institute, practicing industrial-scale science with clearly specified objectives and time lines. In the early 2000s, for example, the Allen Institute for Brain Science introduced large-scale team science to create an atlas of gene expression in the mouse brain. The atlas was presented in an easily accessible and useful format, providing a unique resource for the neuroscience community.

PHOTO: COURTESY OF VULCAN, PHOTO BY KEVIN CRUFF

Paul had a passion for science; had life played out differently, he might have been a professor at a university. He was always pushing for "big ideas" and "ways in." He was deeply interested in unlocking the mysteries of wildly complex processes, pressing us to address the "unsolved mysteries" and find the "codes" in biological sciences. His interests spanned from brains to cells, evolution to artificial intelligence, and elephants to oceans, areas in which he took both an intellectual and personal interest.

Paul was most animated when a small group of colleagues was circling around a new idea, something he had spurred as part of his uncanny ability to question dogma. A visit to his office often ended up at the whiteboard, which we would fill with diagrams of cellular processes. He was right there at the board with us, drawing ideas and pacing. And there on the windowsill sat elephant statues and awards for discoveries and films, reminding us all of the vast range of concerns he had for living things and for science.

His style was to engage small groups of experts in charrettes (multiday planning meetings), listening intently to the arguments for and against various ideas and approaches. Once a topic was chosen and a plan developed, it would be presented to Paul, who then asked the hard questions about feasibility, strategic advantage, risks, and alternative approaches. He entered these meetings well prepared: Rather than have us simply recapitulate the plan, he went right to the few key ideas, asking for embellishment and clarity. He would ask "How will we know if we're successful?" and "Is this the right time?" His approach drove a discipline of thought and focus that spurred the success of his many endeavors. In these meetings, Paul showed his enormous intellectual breadth and creativity as he looked for new ways to think about the problem, conjoin disciplines, and penetrate deeply into the topic.

Although we only saw Paul occasionally, he emailed often, at nearly any time of the day or night. He sent articles he had read or asked about talks he had heard. The emails came with questions about our thoughts, how we could make a difference, what the roadblocks would be, or how much it would cost.

It is comforting to know that what Paul started will live on through the research and discovery enterprises he fostered and through the people in whom he invested. We wish we had had more time with him; he never shied away from pushing us to think big and tackle unsolved mysteries in science. Paul always reminded us, as he wrote in his 1 April 2016 Editorial in *Science*, that "all of us—philanthropists, governments, universities, and private companies alike—must invest much more in basic, fundamental science and in the intrepid scientists who are willing to pursue out-of-the-box approaches at the very edges of knowledge." ■

[1]*Allen Institute for Cell Science, Seattle, WA, USA.* [2]*Allen Institute, Seattle, WA, USA.* [3]*University of Washington and Board of Directors, Allen Institute, Seattle, WA, USA.*
Email: rickh@alleninstitute.org

10.1126/science.aav8254

POLICY FORUM

SCIENCE AND SECURITY

Preventing chemical weapons as sciences converge

Focus must extend beyond 20th-century technologies

By **Michael Crowley, Lijun Shang,** *and* **Malcolm Dando**

Stark illustrations of the dangers from chemical weapons can be seen in attacks using toxic industrial chemicals and sarin against civilians and combatants in Syria and toxic industrial chemicals in Iraq, as well as more targeted assassination operations in Malaysia and the United Kingdom, employing VX and novichok nerve agents, respectively. Concerns about such malign applications of chemical technology are exacerbated by the unstable international security environment and the changing nature of armed conflict, "where borderlines between war, civil war, large-scale violations of human rights, revolutions and uprisings, insurgencies and terrorism as well as organized crime are blurred" (*1*). It is thus essential that the global community regularly review the nature and implications of developments in chemistry, and its convergence with the life and associated sciences, and establish appropriate measures to prevent their misuse. With the parties to the Chemical Weapons Convention (CWC) convening a Review Conference to address such issues beginning 21 November 2018, we highlight important scientific aspects (*2*).

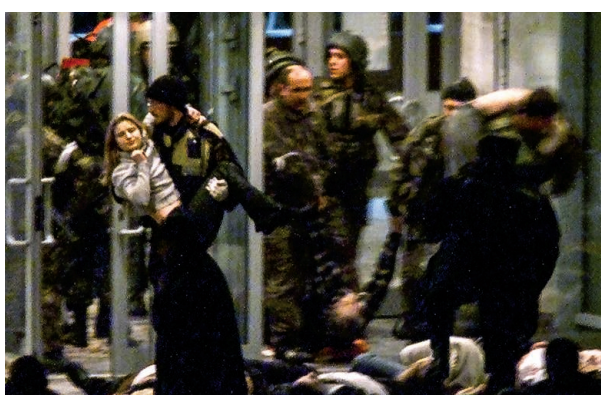

Russian special forces remove hostages from a Moscow theatre following use of aerosolized anaesthetics to end an armed siege in October 2002; 125 of the 900 hostages died as a result of the chemicals employed.

PHOTO: SERGEI KARPUKHIN/REUTERS PICTURES

COMPREHENSIVE PROHIBITION

The CWC is a multilateral treaty in effect since 1997 that proscribes the development, production, stockpiling, transfer, and use of chemical weapons "under any circumstances" and requires their destruction within a specified time period. The CWC allows the use of toxic chemicals for a range of industrial, agricultural, research, medical, pharmaceutical, or other peaceful purposes, including law enforcement, as long as the "types and quantities" of chemicals employed are "consistent with such purposes." The CWC has declaration requirements (obliging States to detail facilities that produce or use certain chemicals of concern, grouped into three "schedules," based on the risk they pose to the CWC), industry inspections, and other verification measures to ensure that toxic chemicals and related technologies are not misused in weapons production and to investigate alleged chemical weapons use.

The Organisation for the Prohibition of Chemical Weapons (OPCW), which is the implementing body of the CWC, comprises the 193 State Parties and a Technical Secretariat that provides technical assistance to States, routinely inspects relevant State and commercial industrial facilities, and monitors activities to ensure compliance. It was awarded the Nobel Peace Prize in 2013 for overseeing and facilitating the verified destruction of most of the declared chemical weapons stocks produced in the last century—to date totaling more than 96% (69,750 metric tons) of the declared stockpiles of chemical agents.

Now that this first phase of the CWC's implementation is nearing completion, the OPCW has to increasingly focus on preventing the reemergence of chemical weapons. Thus, in addition to combatting possession and employment of 20th-century chemical weapons types, the OPCW must also address a changing external environment where the risks associated with toxic chemicals and their potential misuse as weapons are becoming more diffuse and less well defined in terms of chemical compounds or dissemination methods. To respond effectively to such shifts and maintain the comprehensive nature of the chemical weapons prohibition, the OPCW should prioritize key issues below.

Ensure effective implementation of the General Purpose Criterion

Although the CWC includes three schedules of toxic chemicals for the application of verification measures, the scope of the CWC is not constrained to these schedules but by its General Purpose Criterion (GPC), which prohibits misuse of toxic chemicals based on intent rather than on this limited list of chemicals (*3*). The CWC negotiators sought to ensure that the CWC could accommodate, and the States Parties be able to respond to, future developments in chemistry, biology, and associated sciences and technologies. Consequently, "even toxic chemicals whose existence is not yet known are covered," while "legitimate uses of all toxic chemicals and chemicals from which they can be made" are protected (*4*).

But there is contested interpretation of the GPC as to the range of chemicals and delivery mechanisms that could be employed for law enforcement, and the nature of what constitutes legitimate use. The upcoming Review Conference should thus establish an Open-Ended Working Group (OEWG) involving scientific experts to design guidelines to prevent research, development, production, and employment activities that, while purportedly intended to support law enforcement, would undermine the prohibitions of the CWC. The OEWG should consider existing obligations under international law, notably, international human rights law (IHRL), and their bearing on the CWC. The OEWG should specifically address the following:

1) Riot control agents (RCAs). The CWC defines RCAs—such as tear gas and pepper spray—as "any chemical not listed" in one of its three schedules that can produce "rapidly in humans sensory irritation or disabling physical effects which disappear within a short time following termination of exposure." Thus, chemicals should only be employed as RCAs if there is solid scientific evidence to show that such agents are not dangerous to humans when used in an appropriate manner. The CWC permits their use for "law enforcement including domestic riot control" (*5*), as long as the "types and quantities" (*6*) are consistent with such purposes. However, a recurring concern documented by the med-

University of Bradford, Bradford, UK.
Email: m.r.dando@bradford.ac.uk

ical community and human rights monitors has been the widespread misuse of RCAs by police and security forces in excessive quantities, including in hospitals, prisons, homes, and automobiles, where targeted individuals cannot disperse. In such situations, serious injury or death can result from toxic properties of chemicals or from asphyxiation.

Although a variety of chemicals were developed, considered, or used as RCAs in the past century, the OPCW Scientific Advisory Board (SAB, comprised of independent experts) clarified that only 17 chemicals from the 60 it examined were consistent with the RCA definition under the CWC (*7*). For example, certain States designated Adamsite (DM) as an RCA, but it has been removed from this category because of its danger to human health [(*7*), appendix 3]. The OEWG should now clarify the nature and scope of "law enforcement" activities and develop guidance as to "types and quantities" of RCAs that can legitimately be used in such circumstances, highlighting obligations under IHRL.

2) Delivery systems. If the OPCW does not take appropriate action on RCAs, the situation could dramatically worsen as a result of ongoing development and marketing of systems capable of delivering far greater amounts of RCAs (and potentially other toxic chemicals) over wider areas or more extended distances than current standard law enforcement delivery mechanisms, such as handheld sprays, grenades, and single launched projectiles. Such new systems include large-capacity spraying devices, automatic grenade launchers, multibarrel projectile launchers, large-caliber RCA projectiles, and unmanned ground or aerial vehicles capable of carrying spraying devices or projectile launchers (*8*). The OEWG should develop criteria for determining which means of delivering and dispersing RCA are inconsistent with the purpose of law enforcement and should thus be prohibited. Such prohibited means of delivery should, at a minimum, include artillery shells, aerial bombs, mortar shells, and cluster munitions.

3) Incapacitating chemical agent (ICA) weapons. Although the CWC permits use of appropriate types and quantities of RCAs for law enforcement, certain countries have conducted research into weapons employing other distinct toxic chemicals, so-called ICAs. Not separately defined under the CWC, ICAs can be considered as a range of toxic chemicals—only one of which [3-quinuclidinyl benzilate (BZ) and two of its immediate precursors] is currently scheduled—including anesthetics and other pharmaceutical chemicals that are purportedly intended to act on the body's core biochemical and physiological systems, notably the central nervous system (CNS), to cause prolonged but non-permanent disability. Such CNS-acting chemicals can produce unconsciousness, sedation, hallucination, incoherence, disorientation, or paralysis. With inappropriate doses, however, death can result. Leading medical and scientific organizations have highlighted grave dangers to health and well-being of such weapons (*9*); in the only confirmed example of their large-scale use, an aerosolized mixture of two anesthetics—carfentanil and remifentanil—employed by Russian security forces to end the Moscow theatre siege of October 2002 caused the deaths of 125 of the 900 hostages (*10*).

As the U.S. Ambassador to the OPCW noted in October of this year, "The United States and many other States Parties are seriously concerned that some States may be developing these chemicals for warfare…while cloaking their efforts as legitimate activities such as law enforcement" (*11*). The U.S. concern is reflected in a recent Department of Defense solicitation that "seeks to develop field diagnostic capabilities for detection of exposure to the ever-growing opioid class of chemical threat agents."

The chemical threat spectrum includes bioregulators and toxins, and our increasing understanding of the CNS is likely to uncover many more potential targets and agent classes that might be weaponized. Scientists should be aware of such possibilities and be able to alert their CWC National Authority and the OPCW Technical Secretariat to potential dangers. The OEWG could determine either that development, stockpiling, transfer, and use of ICA weapons for law enforcement are prohibited under the CWC or that such actions are permitted but should be severely restricted.

Improve OPCW monitoring and risk assessment of science and technology

In 2011, an expert panel recommended that the OPCW should "improve and widen the scope of monitoring and evaluating developments in chemical science and technology" (*12*). In 2013, in response to such concerns, the OPCW appointed a Science Policy Adviser at the Technical Secretariat. In addition, over the past 5 years, the SAB has regularly provided technical reports and briefings on key scientific and technological (S&T) developments. Building upon these advances, and informed by SAB recommendations (*13*), the OPCW should consider further measures to strengthen the Technical Secretariat's capability to monitor and forecast S&T developments and their implications, and to strengthen its ability and mandate to proactively bring specific cases of concern to the attention of the States Parties. However, this is not something that the OPCW can do alone, given the range of scientific disciplines and

A Syrian man mourns children killed in a chemical attack on the town of Douma, Syria, in April 2018. Advances in science and technology could aid OPCW investigations into such attacks and help uncover those responsible.

PHOTO: MOHAMMED HASSAN/UPI/NEWSCOM

technologies that need to be monitored, their complexity, their rapidity of advance, and the geographical scope of research and development. Thus the nongovernmental chemical and life scientific community, in particular, has an important role to play by undertaking technology tracking of generic trends in technologies of relevance to the CWC (as has been undertaken previously by the International Union of Pure and Applied Chemistry in preparation for previous CWC Review Conferences), and by undertaking targeted research into S&T developments of particular concern, for example, in the fields of medicinal chemistry, pharmacology, synthetic biology, nanotechnology, and, as undertaken by the Royal Society, neuroscience (*9*).

IMPLEMENTATION AND VERIFICATION

Advances in S&T may have several effects on national implementation of the CWC by its States Parties and on how the OPCW verification mechanisms function, which the Review Conference should address.

Update industry verification measures

OPCW verification measures currently focus on the list of scheduled chemicals, which were previously identified from past State chemical weapons programs. But new production pathways to old chemical warfare agents may become feasible as a result of technological advances; alternatively, new potential chemical warfare agent types may become relevant involving toxic chemicals not listed on any of the schedules. Consequently, the routine industry verification regime (as well as the analytical methods and databases available for challenge inspection and for investigation of alleged chemical weapons use) need to be adapted to these new technological and chemical realities. The SAB has suggested that "efforts to ensure that the verification regime remains effective would benefit from more extensive engagement with technical experts from industry, and review of industry-focused research and development, including the driving forces for adoption of new technologies into industrial processes" (*13*). Favorable consideration should also be given to updating the schedules themselves (*13*), at least to provide indicators of the new or additional types of potential chemical agents (and their precursors) of concern, such as the novichock agent (and its associated families).

Other chemical production facilities

Other chemical production facilities (OCPFs) are chemical plants that do not currently produce, but are capable of manufacturing, chemical warfare agents or precursors. At present, a small fraction of declared OCPFs are selected for verification by the OPCW; the Review Conference should consider authorizing a substantial increase in OCPF inspections per year. The OPCW should also be directed to refine the process of site selection so as to target inspections on multipurpose chemical plants that pose the greatest risk of being utilized for prohibited purposes.

Biological and biologically mediated processes for production of discrete organic chemicals

Some products and processes used by the biomanufacturing industry are as relevant to the CWC as those used by other OCPF facilities, including those the Technical Secretariat considers pose notable risks. Thus, the SAB has consistently recommended that biomanufacturing of chemical products should be covered under the scope of the CWC. However, States Parties have yet to agree on how to treat these types of production processes and facilities. The Review Conference should follow SAB advice and establish measures to determine the relevance of various types of biomanufacturing processes and facilities for CWC verification purposes.

PREVENTING AND RESPONDING

The OPCW should continue improvements in the operational and technical capacity of the Technical Secretariat to conduct challenge inspections and investigations of alleged use of chemical weapons, with an increased focus on chemical forensics. An important development in this regard was the June 2018 decision to empower the OPCW to develop an attribution mechanism to determine who conducted a chemical attack (*14*). Ongoing work by the SAB into opportunities and difficulties associated with chemical forensics will enable the OPCW to most effectively utilize new tools and methods. Such work, which would benefit from wide consultation with scientific experts, must be complemented by efforts to compile, expand, and properly curate the databases of reference spectra and collections of reference materials that will be needed for such forensic analysis.

The SAB highlighted the critical role of biomedical samples in investigations of alleged use of toxic chemicals and recommended that the Technical Secretariat should "actively encourage further research on potential markers of exposure to such chemicals." The OPCW should also build on the considerable progress made toward developing a network of designated laboratories for the analysis of biomedical and biological samples (*15*). Advances in other fields could also facilitate more effective evidence collection, for example, exploring the potential of unmanned aerial vehicles to support reconnaissance, detection, and chain of custody.

The OPCW should also consider how best to strengthen the resilience of States against hostile use of toxic chemicals. This could include expanding the number of viable national protective programs supported by OPCW training and capacity building, and the establishment of well-equipped regional capacities for effective response to the use of chemical weapons or the accidental release of toxic chemicals.

SCIENTISTS AND AN EVOLVING OPCW

The OPCW faces the task of deciding how best to evolve to prevent the reemergence of chemical weapons in a period of rapid scientific change and unstable international security. There is growing recognition within the OPCW of the vital importance of engaging with and ensuring the support of the worldwide scientific community, in particular via relationships with professional societies (*13*). Chemical and life scientists could play their part by being better informed of the issues at stake, and by ensuring that their colleagues and students are alerted to the dangers of the misuse of dual-use technologies and are implementing relevant ethical codes, codes of conduct, and the Hague Ethical Guidelines recently developed by the OPCW to promote a culture of responsible conduct in the chemical sciences and to guard against the misuse of chemistry for malign intent. ■

REFERENCES

1. OPCW, "Report of the advisory panel on future priorities of the OPCW" (S/951/2011, OPCW, 2011), paragraph 11.
2. M. Crowley, M. Dando, L. Shang, Eds., *Preventing Chemical Weapons: Arms Control and Disarmament as the Sciences Converge* (Royal Society of Chemistry, 2018).
3. OPCW, *Chemical Weapons Convention*, Article II.1.
4. M. Meselson, J. P. Robinson, *Chem. Weapons Conv. Bull.* **23**, 1 (1994).
5. OPCW, Chemical Weapons Convention, Article II.9 (d).
6. OPCW, Chemical Weapons Convention, Article II.1 (a).
7. OPCW, "Response to the Director-General's request to the Scientific Advisory Board to consider which riot control agents are subject to declaration under the Chemical Weapons Convention" (SAB-25/WP.1, OPCW, 2017).
8. M. Crowley, *Chemical Control: Regulation of Incapacitating Chemical Agent Weapons, Riot Control Agents and their Means of Delivery* (Palgrave Macmillan, 2016).
9. The Royal Society, *Brain Waves Module 3: Neuroscience, Conflict and Security* (RS Policy Document 06/11, The Royal Society, 2012).
10. J. Riches *et al.*, *J. Anal. Toxicol.* **36**, 647 (2012).
11. OPCW, "Statement by H.E. Ambassador Kenneth D. Ward permanent representative of the United States of America to the OPCW at the eighty-ninth session of the Executive Council" (EC-89/NAT.10, OPCW, 2018).
12. OPCW, Technical Secretariat, "Report of the Advisory Panel on future priorities of the OPCW" (S/951/2011, OPCW, 2011).
13. OPCW, "Report of the Scientific Advisory Board on developments in science and technology for the fourth special session of the Conference of the States Parties to review the operation of the Chemical Weapons Convention" (RC-4/DG.1, OPCW, 2018).
14. OPCW, "Decision: Addressing the threat from chemical weapons use, Conference of the States Parties, Fourth Special Session" (C-SS-4/DEC.3, OPCW, 2018).
15. OPCW, "SAB Report of the Scientific Advisory Board on developments in science and technology for the fourth special session of the Conference of the States Parties to review the operation of the Chemical Weapons Convention" (RC-4/DG.1, OPCW, 2018).

10.1126/science.aav5129

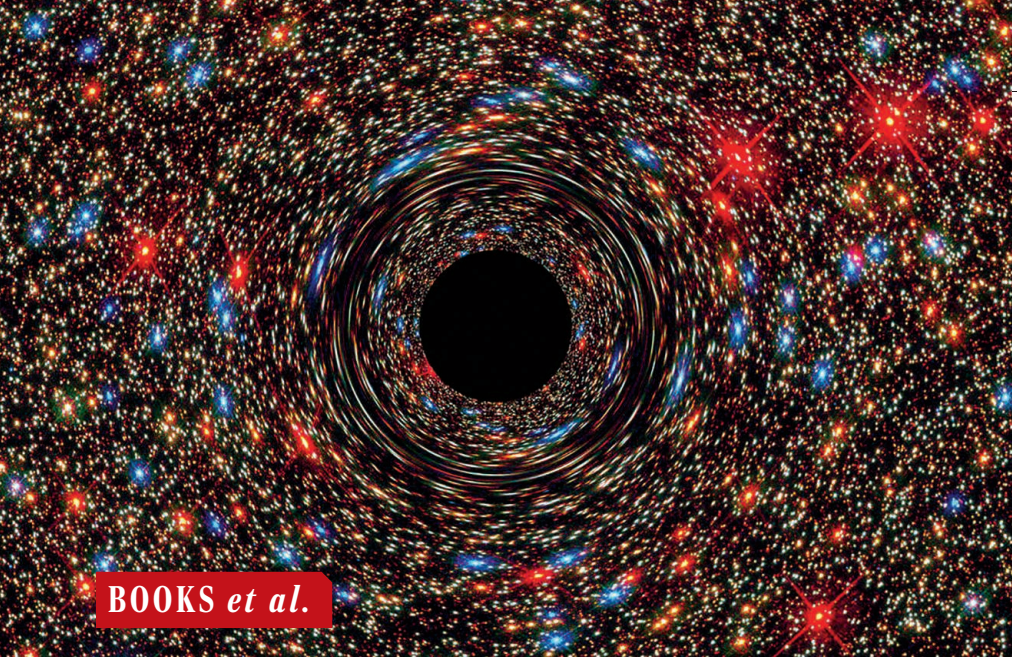

BOOKS *et al.*

A computer-simulated image depicts a supermassive black hole at the center of a galaxy.

ASTROPHYSICS

Approaching the singularity

New data, old rivalries, and enduring questions fill a welcome overview of black hole research

By **Jeremy Schnittman**

What happens at the black hole event horizon, where time stands still and intuition breaks down? In the opening chapter of his new book, *Einstein's Monsters*, astronomer and popular science writer Chris Impey puts the problem succinctly: "It made no sense for a physical object to have zero size and infinite mass density. Einstein's theory had created something monstrous."

Impey does an admirable job describing multiple facets of the often contradictory field of black hole astrophysics, including its history, science, and colorful human interactions. For example, we now know that most astrophysical black holes are notoriously difficult to detect and observe, and yet some are the brightest x-ray sources in the sky and can be seen from across the entire universe. They seem to come in two sizes: small and extra-extra-extra-large. The small ones have huge densities, whereas the largest ones are lighter than air.

Even the (seemingly) most fundamental fact about black holes—that not even light can escape one—is not entirely true. In the 1970s, Stephen Hawking proved that black holes of all sizes give off a faint glow of extremely low-temperature blackbody radiation.

In the far distant future, every black hole in the Universe will eventually evaporate, leaving nothing behind but a dilute, near-uniform bath of radio waves. A related paradox: An astronaut plunging into a black hole would feel nothing as she slips quietly past the event horizon and reaches the singularity only a few moments later, yet to her crew mates watching from the safety of the nearby mothership, it would take an eternity for her to even reach the horizon. Like Zeno's tortoise, she would seem to get closer and closer, fainter and fainter, but never quite disappear.

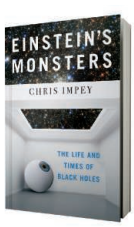

Einstein's Monsters
The Life and Times of Black Holes
Chris Impey
Norton, 2018. 315 pp.

In addition to these physical contradictions, the book also covers many of the field's more interesting human conflicts and competitions throughout the past century: Eddington versus Chandrasekhar, Zwicky versus Sandage, Thorne versus Hawking, even Einstein versus Einstein. Impey paints a colorful picture of the personalities involved, including personal anecdotes from his own firsthand interactions with many of the leading actors of the story.

One may reasonably ask, "Does the world really need another popular science book about black holes?" Anyone who has read and enjoyed Kip Thorne's gold standard, *Black Holes and Time Warps*, will learn relatively little from *Einstein's Monsters*. Yet the intended target audience is more likely to have read Hawking's *A Brief History of Time* (if they have read anything on the topic) and thus may not be familiar with many of the critical observational discoveries over the past half-century.

For the next generation of popular astronomy buffs, *Einstein's Monsters* is a reasonable entry point, covering a broad—if not particularly deep—range of theoretical and observational topics in black hole research. Particularly welcome, even for more experienced black hole aficionados, are the excellent chapters about the Laser Interferometer Gravitational-Wave Observatory's recent discovery of gravitational waves and the Event Horizon Telescope's imminent discovery of black hole shadows.

Impey's broad and relatively cursory approach to black holes mirrors his earlier works in popular astronomy, this being his seventh book in about as many years. Unfortunately, this prolific productivity is occasionally betrayed by factual errors in the text, especially in the more theoretical passages. In chapter 8, for example, Impey claims that fermions and bosons cannot interact with each other, when in fact that is exactly how photons and gluons convey the fundamental forces of nature. Elsewhere, he asserts that Mercury's precession is 5600 arc sec per century, which is off by an order of magnitude. A number of theoretical results—for example, using x-ray oscillations to measure black hole mass and spin—are also quoted as established fact despite widespread skepticism in the research community.

Certain passages, and even chapters, of *Einstein's Monsters* have a distinctly haphazard feel to them, throwing together a collection of topics without an obvious theme. Chapter five jumps from γ-ray bursts to intermediate-mass black holes to microquasars to numerical relativity and then cosmological N-body simulations. Perhaps the goal here is to impress the reader with how important black holes are in modern astronomy, but it gives the impression of disorganization.

Despite these few shortcomings, *Einstein's Monsters* will be sure to capture the imagination of most who pick it up, simultaneously convincing the reader that these monsters, while in fact quite certainly real, should be loved and not feared. ■

The reviewer is at the Sciences and Exploration Directorate, NASA Goddard Space Flight Center, Greenbelt, MD 20771, USA. Email: jeremy.d.schnittman@nasa.gov

10.1126/science.aav2003

PHOTO: NASA, ESA, AND D. COE, J. ANDERSON, AND R. VAN DER MAREL (STSCI)

COSMOLOGY

A physicist's final reflections

An unfinished tome reveals the late Stephen Hawking's musings on life's biggest mysteries

By **Andrew Robinson**

The death of cosmologist Stephen Hawking earlier this year happened to fall on the birthday of Albert Einstein. This felt like an appropriate coincidence, given the centrality of Einstein's general theory of relativity in Hawking's much-celebrated life as a scientist.

Einstein is mentioned in Hawking's posthumously published book—*Brief Answers to the Big Questions*, which he left unfinished—far more frequently than any other scientist, past or present, including Isaac Newton, Hawking's illustrious predecessor as Lucasian professor of mathematics at the University of Cambridge. Indeed, the concluding "big question" of the 10 explored in 10 chapters, "How do we shape the future?" begins with Einstein. "Where did his ingenious ideas come from?" asks Hawking. He answers, "A blend of qualities, perhaps: intuition, originality, brilliance. Einstein had the ability to look beyond the surface to reveal the underlying structure. He was undaunted by common sense, the idea that things must be the way they seemed. He had the courage to pursue ideas that seemed absurd to others. And this set him free to be ingenious, a genius of his time and every other."

Hawking enjoys a moment of weightlessness in zero gravity in 2007.

Was Hawking a genius, too? He never won a Nobel Prize, and the book gives no indication that Hawking regarded himself as a genius. On the other hand, he was one of the very few scientists since Einstein to become a household name. As his close collaborator, Nobel laureate Kip Thorne, remarked in his eulogy: "Newton gave us answers. Hawking gave us questions. And Hawking's questions themselves keep on giving, generating breakthroughs decades later. When ultimately we master the quantum gravity laws, and comprehend fully the birth of our universe, it may largely be by standing on the shoulders of Hawking."

Hawking was well known for two additional reasons unrelated to his mind-boggling cosmological theories. The first was his 1988 book, *A Brief History of Time*, an international bestseller that sought to explain the physics of time to the general reader without using mathematical equations. The second was his courageous struggle with motor neuron disease, which rendered him wheelchair-bound and dependent on a computer screen and speech synthesizer to communicate. "[A]s someone who at the age of twenty-one was told by their doctors that they had only five years to live, and who turned seventy-six in 2018, I am an expert on time in another sense, a much more personal one," he writes. "I am uncomfortably, acutely aware of the passage of time, and have lived much of my life with a sense that the time that I have been granted is, as they say, borrowed."

Some of Hawking's "big questions" and answers are firmly rooted in science—for example, "What is inside a black hole?" and "Is time travel possible?"—whereas others inherently cannot be, such as "Will we survive on Earth?" "Should we colonise space?" "Will artificial intelligence outsmart us?" and "Is there a God?" To the last question, he answers, "If you like, you can call the laws of science 'God,' but it wouldn't be a personal God that you would meet and put questions to. Although, if there were such a God, I would like to ask however did he think of anything as complicated as M-theory in eleven dimensions."

Brief Answers to the Big Questions
Stephen Hawking
Bantam Press, 2018. 255 pp.

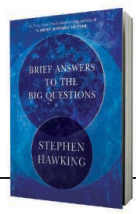

Certain of Hawking's assertions may be considered questionable and at times myopic. As an ardent advocate of space travel, he believes, "Not to leave planet Earth would be like castaways on a desert island not trying to escape." Indeed, he goes much further and claims that space colonization is the only hope for the survival of the human race after the "almost inevitable" destruction of Earth, which he predicts will happen within the next 1000 years.

Regarding artificial intelligence (AI), he anticipates, "AI may automate our jobs, to bring both great prosperity and equality" in the medium term. Looking further ahead, he writes, "the future of communication is brain–computer interfaces. ... If we can connect a human brain to the internet it will have all of Wikipedia as its resource." Perhaps it is not surprising that someone who was intimately dependent on information technology should have held such an opinion about its future. Although Hawking acknowledges potential negative scenarios, referring to HAL, the highly intelligent computer in the film *2001: A Space Odyssey* that unsuccessfully attempts to destroy its human masters, he remarks merely, "but that was fiction. We deal with fact."

Nonetheless, the final testament of this unique scientist is well worth reading. One cannot help but be moved by Hawking's lifelong struggle to lead a creative life. "[R]emember to look up at the stars and not down at your feet," he sums up. ■

The reviewer is the author of Einstein: A Hundred Years of Relativity *(Princeton Univ. Press, 2015) and* Genius: A Very Short Introduction *(Oxford Univ. Press, 2011). Email: andrew@andrew-robinson.org*

10.1126/science.aav7499

PHOTO: NASA

PHOTO: ALL CANADA PHOTOS/ALAMY STOCK PHOTO

Edited by **Jennifer Sills**

Climate change drives tree mortality

In their Report "Classifying drivers of global forest loss" (14 September, p. 1108), P. G. Curtis *et al.* reported a global assessment of forest loss from 2001 to 2015. They attributed 99% of the loss to land-use change and wildfire, and they urge companies to eliminate 5 million hectares of land-use change per year to prevent further deforestation. Their analysis underestimates climate change–driven drought, storms, and insect epidemics, which also contribute to substantial tree mortality each year.

During the period Curtis *et al.* investigated (2001 to 2015), climate change–driven forest loss increased, affecting large forest areas across the globe (*1*). Growing evidence shows that increasingly hot droughts killed most of the trees in an area of 1.2 million hectares in southwest North America (*2*), and warming-driven mountain pine beetle outbreaks affected forests in northwest North America at a rate of 6 to 7 million hectares per year between 2005 and 2008 (*3*). Additional forest losses of large magnitude due to drought, ice, snow, and wind storms occurred in China, Spain, Chile, and other countries (*1*). The order of magnitude of these forest loss events is similar to the estimated deforestation rate of 5 million hectares a year reported by Curtis *et al.*

One potential cause of the substantial underestimation of climate change–driven forest loss is our limited ability to detect it with remote sensing tools (*4*), which Curtis *et al.* used for their analysis. Unlike most land-use change forest losses and wildfire, climate change–driven tree mortality is often diffuse and gradual. Although measurements on the ground are sufficient to infer that climate change has caused tree loss [e.g., (*1*–*3*)], algorithms and analysis tools that rely on remote sensing data are still under development. In some cases, Curtis *et al.*'s analysis places climate change–induced changes in other categories. For example, they attributed both mountain pine beetle damage in Canada (*3*) and drought-induced tree mortality near Los Alamos, New Mexico (*2*), and Beetle Rock, California (*1*), to forestry.

The analysis presented by Curtis *et al.* provides only a partial view of the magnitude and causality of global forest loss. Ground-based data from national forest inventories and research plot networks, combined with improved remote sensing image analysis, are essential to identify diffuse forest losses due to climate change. Given that global temperatures continue to rise and droughts are expected to occur more frequently and with higher severity (*5*), quantifying and monitoring these forest losses could potentially become even more important than controlling man-made deforestation.

Tamir Klein[1]* and Henrik Hartmann[2]
[1]Department of Plant and Environmental Sciences, Weizmann Institute of Science, Rehovot, Israel.
[2]Department of Biogeochemical Processes, Max Planck Institute for Biogeochemistry, Jena, Germany.
*Corresponding author. Email: tamir.klein@weizmann.ac.il

REFERENCES

1. C. D. Allen *et al.*, *For. Ecol. Manage.* **259**, 660 (2010).
2. D. D. Breshears *et al.*, *Proc. Natl. Acad. Sci. U.S.A.* **102**, 15144 (2005).
3. W. A. Kurz, *Nature* **452**, 987 (2008).
4. H. Hartmann *et al.*, *New Phytol.* **217**, 984 (2018).
5. IPCC, *Climate Change 2014: Synthesis Report; Contribution of Working Groups I, II and III to the Fifth Assessment Report of the Intergovernmental Panel on Climate Change*, Core Writing Team, R. K. Pachauri, L. A. Meyer, Eds. (IPCC, Geneva, Switzerland, 2014).

10.1126/science.aav6508

Halt speculation on U.S. embassy in Cuba

Since 2016, the U.S. State Department has reported that 25 staff at the U.S. embassy in Havana have complained of symptoms such as hearing loss and vertigo (*1*). Embassy staff have reported hearing unusual and unsettling sounds at home or at hotel rooms in addition to their workplaces at the embassy (*2*). In the ensuing 2 years,

Pine beetle infestations driven by climate change can lead to deforestation.

scientists have allowed speculation about the causes of these health issues to outpace the evidence.

Neuroscientists at the University of Pennsylvania (the affiliation of K.R.F., who was not involved in the study) reported evidence for brain injury related to perceived sound in some of the affected individuals (*2*), but this work has been firmly contested by other scientists, some of whom advance other, more mundane explanations for the symptoms (*3*–*5*). An editorial in the neuroscience journal *Cortex* notes internal inconsistencies in the neuroscience evidence published so far (*6*). After nearly 2 years of investigation, neither Cuban nor U.S. officials have identified the cause of the health problems or even provided convincing evidence that the diverse health problems reported by the staff have a common cause (*7*). While acoustic or electromagnetic fields might conceivably have produced audible sounds at the embassy, no physical agents have been reported at levels that might plausibly have injured the employees. Evidence available to the public remains largely anecdotal.

Nevertheless, discussion by scientists and the media about the cause of the reported health problems has been characterized by speculation and unwarranted inferences about possible effects of physical agents supposedly directed at the employees [e.g., (*8*, *9*)]. Such speculation is unhelpful in treating the affected individuals and hinders relations between the two countries. The affected members of the embassy staff need careful medical follow-up without presumptions about the etiology of their problems, and the U.S. embassy needs a careful occupational health assessment to identify any potential health risks. Alternative explanations (including preexisting diseases or stress-induced exacerbation of functional disorders) must not be discarded because they do not fit in preconceived theories. There is insufficient evidence to guess about the cause of the sounds, let alone assess their potential health relevance. We need to halt the speculation and instead encourage more science and careful medicine.

Mitchell Joseph Valdés-Sosa[1] and Kenneth R. Foster[2]*
[1]Cuban Center for Neuroscience, Havana, Cuba.
[2]Department of Bioengineering, University of Pennsylvania, Philadelphia, PA 19106, USA.
*Corresponding author.
Email: kfoster@seas.upenn.edu

REFERENCES

1. R. Rubin, *JAMA* **319**, 1079 (2018).
2. R. L. Swanson *et al.*, *JAMA* **319**, 1125 (2018).
3. S. Della Sala, R. Cubelli, *Cortex* **103**, 387 (2018).
4. S. Della Sala *et al.*, *Cortex*, 10.1016/j.cortex.2018.10.002 (2018).
5. R. E. Bartholomew, *J. R. Soc. Med.* **110**, 474 (2017).
6. Cortex Editorial Board, *Cortex*, 10.1016/j.cortex.2018.10.001 (2018).
7. C. C. Muth, S. L. Lewis, *JAMA* **319**, 1098 (2018).
8. O. Dyer, *BMJ* **362**, k3848 (2018).
9. B. A. Golomb, *Neur. Comput.* **Sep 5**, 1 (2018).

10.1126/science.aav5485

Standardizing return of participant results

As members of the National Academies of Sciences, Engineering, and Medicine committee that wrote the report on the return of individual research results (*1*), we reject the allegations in the Policy Forum "Return of results and data to study participants" (S. M. Wolf and B. J. Evans, 12 October, p. 159) that the report is paternalistic, misunderstands the law, burdens Institutional Review Boards (IRBs), and creates barriers to the return of results.

In the National Academies report, we advocate regulatory changes to expand the opportunities to give research participants access to their individual results. The Centers for Medicare and Medicaid Services (CMS) interprets the law governing laboratory standards as prohibiting any communication about research results to participants unless the laboratory is certified according to the Clinical Laboratory Improvement Amendments of 1988 (CLIA). Wolf and Evans contend that CMS does not have the statutory authority for this restriction. However, there is no consensus regarding this position (*2*, *3*) and CMS's interpretation has not been overruled by the courts. Given substantial penalties for noncompliance, many research institutions abide by CMS's interpretation. Our report recommends an explicit change to the regulations to bring clarity to the field that will not be achieved by assuming that CMS's position can be ignored, as Wolf and Evans suggest.

We recommend that the Office of Civil Rights (OCR) clarify what research results participants have a right to under the Health Insurance Portability and Accountability Act (HIPAA) rule by clearly defining the Designated Record Set (DRS) to include all research results generated in laboratories that meet an accepted quality standard. Although the DRS includes information maintained by a covered entity that could be used for individual decision-making (*4*), there is no consensus about what research data should be included. In the absence of guidance from OCR, some institutions are excluding some research data from the

DRS (*5*). Our recommendation supports broadening participant access to high-quality research results while adhering to the principle that results lacking demonstrated quality should not be used by participants or their health care providers for individual decision-making.

We disagree with the notion that our recommendations are paternalistic. During our study, we consulted a diverse group of community members, study participants, and advocacy groups to fully understand how individuals might use results, as well as barriers to using and understanding results. The committee sought a balance that promotes broad access to results while addressing public expectations that results are accurate. Disclosing poor-quality results reflects bad science and does not respect participant autonomy or welfare. We maintain that quality standards for research laboratories will better ensure accurate results that meet the expectations of participants and will enhance the overall validity and reproducibility of the research enterprise.

We believe that IRBs are up to the challenge of addressing the new responsibilities recommended by our report, although we acknowledge that these demands cannot be addressed overnight. The report recommends that investigators work with stakeholders to develop plans on whether and how to disclose results as protocols are developed. The informed consent process is key to fostering participant understanding of their options for return of results and to documenting expression of their preferences. IRBs must be involved in evaluating the return of results plan and consent process and, over time, will need to develop expertise and policies for this purpose.

We are confident that our recommendations break down many of the existing barriers to the return of individual research results and, if followed, will enhance the collaboration among all stakeholders. Return of individual results is not a common practice (*6*) despite existing guidelines, and research participants rarely request results under their HIPAA access rights. Our report promotes the routine consideration of return of results by funders, researchers, and participants; the development of standards and policies to foster return, greater transparency, and engagement with participants; and an informed consent process that informs participants of their opportunities and rights.

Jeffrey R. Botkin[1]*, Paul S. Appelbaum[2], Suzanne Bakken[3], Chester Brown[4], Wylie Burke[5], Richard Fabsitz[6], Vanessa Northington Gamble[7], Gregg Gonsalves[8], Rhonda Kost[9], Debra G. B. Leonard[10], Amy McGuire[11], James H. Nichols[12], Bray Patrick-Lake[13], Consuelo H. Wilkins[14], Brian J. Zikmund-Fisher[15]

[1]Department of Pediatrics, University of Utah, Salt Lake City, UT 84112, USA. [2]Department of Psychiatry, Columbia University Medical Center, New York, NY 10032, USA. [3]School of Nursing and Department of Biomedical Informatics, Columbia University, New York, NY 10032, USA. [4]Department of Pediatrics, University of Tennessee Health Science Center, Memphis, TN 38105, USA. [5]Department of Bioethics and Humanities, University of Washington, Seattle, WA 98195, USA. [6]Department of Global and Community Health, George Mason University, Fairfax, VA 22030, USA. [7]The George Washington University, Washington, DC 20052, USA. [8]Department of Epidemiology of Microbial Diseases, Yale School of Public Health, New Haven, CT 06511, USA. [9]Center for Clinical and Translational Science, The Rockefeller University, New York, NY 10065, USA. [10]Department of Pathology, University of Vermont Medical Center, Burlington, VT 05401, USA. [11]Center for Medical Ethics and Health Policy, Baylor College of Medicine, Houston, TX 77401, USA. [12]Department of Pathology, Microbiology, and Immunology, Vanderbilt University School of Medicine, Nashville, TN 37232, USA. [13]Duke Clinical Research Institute, Duke University, Durham, NC 27705, USA. [14]Department of Medicine, Vanderbilt University Medical Center and Meharry Medical College, Nashville, TN 37208, USA. [15]Department of Health Behavior and Health Education, University of Michigan School of Public Health, Ann Arbor, MI 48109, USA.
*Corresponding author.
Email: jeffrey.botkin@hsc.utah.edu

REFERENCES

1. The National Academies of Sciences, Engineering, and Medicine, "Returning individual research results to participants: Guidance for a new research paradigm" (Consensus Study Report, 2018); http://nationalacademies.org/hmd/Reports/2018/returning-individual-research-results-to-participants.aspx.
2. M. Barnes *et al.*, "The CLIA/HIPPA conundrum of returning test results to research participants," *Medical Research Law & Policy Report* (2015); www.ropesgray.com/~/media/Files/articles/2015/July/2015-07-15-Bloomberg-BNA.ashx.
3. U.S. Department of Health and Human Services, Office for Human Research Protections, "Attachment C: Return of individual results and special consideration of issues arising from amendments of HIPAA and CLIA," Office for Human Research Protections (2015); www.hhs.gov/ohrp/sachrp-committee/recommendations/2015-september-28-attachment-c/index.html.
4. U.S. Department of Health and Human Services, § 164.501 Definitions (2004); www.gpo.gov/fdsys/pkg/CFR-2004-title45-vol1/pdf/CFR-2004-title45-vol1-sec164-501.pdf.
5. Johns Hopkins Medicine, Office of Human Subjects Research—Institutional Review Board, HIPAA Questions and Answers Relating to Research, VI: Subject Requests for Access to Research Data or Test Results (www.hopkinsmedicine.org/institutional_review_board/hipaa_research/faq_research.html#access).
6. P. S. Appelbaum *et al.*, *Gen. Med.* **17**, 644 (2015).

10.1126/science.aav8095

TECHNICAL COMMENT ABSTRACTS

Comment on "Predicting reaction performance in C–N cross-coupling using machine learning"

Kangway V. Chuang and Michael J. Keiser

Ahneman *et al.* (Reports, 13 April 2018) applied machine learning models to predict C–N cross-coupling reaction yields. The models use atomic, electronic, and vibrational descriptors as input features. However, the experimental design is insufficient to distinguish models trained on chemical features from those trained solely on random-valued features in retrospective and prospective test scenarios, thus failing classical controls in machine learning.

Full text: dx.doi.org/10.1126/science.aat8603

Response to Comment on "Predicting reaction performance in C–N cross-coupling using machine learning"

Jesús G. Estrada, Derek T. Ahneman, Robert P. Sheridan, Spencer D. Dreher, Abigail G. Doyle

We demonstrate that the chemical-feature model described in our original paper is distinguishable from the nongeneralizable models introduced by Chuang and Keiser. Furthermore, the chemical-feature model significantly outperforms these models in out-of-sample predictions, justifying the use of chemical featurization from which machine learning models can extract meaningful patterns in the dataset, as originally described.

Full text: dx.doi.org/10.1126/science.aat8763

TECHNICAL COMMENT

ORGANIC CHEMISTRY

Comment on "Predicting reaction performance in C–N cross-coupling using machine learning"

Kangway V. Chuang and Michael J. Keiser*

Ahneman *et al*. (Reports, 13 April 2018) applied machine learning models to predict C–N cross-coupling reaction yields. The models use atomic, electronic, and vibrational descriptors as input features. However, the experimental design is insufficient to distinguish models trained on chemical features from those trained solely on random-valued features in retrospective and prospective test scenarios, thus failing classical controls in machine learning.

A recent report by Ahneman *et al.* (*1*) describes a machine learning approach for modeling chemical reactions with data collected through ultrahigh-throughput experimentation. The Buchwald-Hartwig coupling (*2*) is used as a model reaction, with a Glorius interference approach (*3*) to study reaction poisoning by isoxazole additives. Reactions are represented by atomic, electronic, and vibrational descriptors that are automatically calculated through a new computational pipeline. The authors find that random forest models outperform linear models in predicting yields on a 70/30 train-test random split, and claim strong performance on an out-of-sample test set of unseen isoxazoles.

We applied the classical method of multiple hypotheses (*4*, *5*) to investigate alternative explanations for the observed machine learning model performance. The experiments in this study explore the effect of four reaction parameters—aryl halide, catalyst, base, and additive—with all combinations exhaustively generated through 4608 different reactions. This complete combinatorial layout provides an underlying structure to the data irrespective of any chemical knowledge. Correspondingly, we posited the alternative hypothesis that the machine learning algorithms exploit patterns within the underlying experimental design, instead of learning solely from meaningful chemical features. A model that learns patterns particular to an experimental layout, rather than from meaningful input features, cannot be relied upon to generalize to new examples (i.e., reaction components).

Following the logic of exclusions (*4*), we performed two experiments intended to disprove the alternative hypothesis, wherein we ablated all chemical information from the Ahneman *et al.* dataset and evaluated the same machine learning methods. All computational analyses were performed in the Python package Scikit-learn (*6*). In the first experiment, we replaced the extracted chemical features of each molecule with random numbers, which effectively creates a unique, random "barcode" mimicking the reaction fingerprints used in the paper (Fig. 1A). For example, the 27 chemical descriptors (^{1}H and ^{13}C nuclear magnetic resonance shifts, dipole moment, etc.) that had been used to represent 4-bromotoluene were replaced with 27 random numbers drawn from a standard normal distribution. Applying these random barcodes to the exact train-test split of the dataset used by Ahneman *et al.* resulted in "straw" models (*7*) that achieved predictive performance nearly identical to those trained on actual chemical features (Fig. 1B). In a related second experiment, we encoded each reaction component as a "one-hot" vector (i.e., a "dummy" encoding) that denotes only the presence or absence of each component (e.g., additive-1, additive-2, etc.; see Fig. 1A). (*8*) One-hot encoding likewise provided near-identical performance for each model (Fig. 1C). Critically, both of these approaches encode no notion of chemistry, and by definition cannot generalize to new chemical entities. We note that these results do not indicate that chemical features are unimportant,

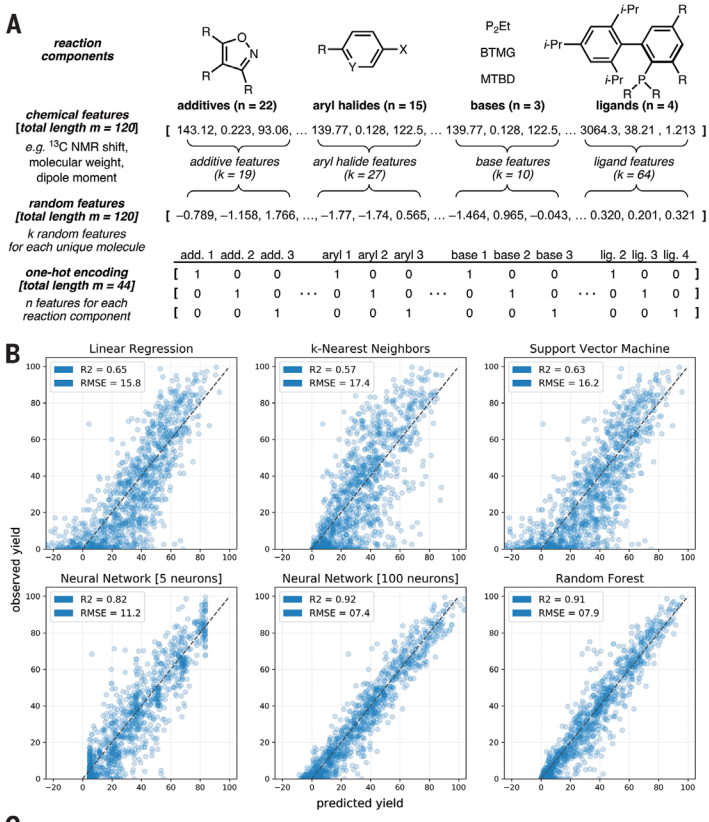

C

		Lin. Reg.	*k*-NN	SVM	NN	RF
Ahneman et al.	R^2	0.66	0.64	0.64	0.93	0.92
	RMSE	15.6	16.1	16.1	7.0	7.5
Random Features	R^2	0.65	0.57	0.63	0.92	0.91
	RMSE	15.8	17.4	16.2	7.4	7.9
One-Hot Encoded	R^2	0.65	0.45	0.66	0.93	0.90
	RMSE	15.8	19.8	15.5	7.1	8.6

Fig. 1. Comparison of input representation control experiments. (**A**) Schematic of Ahneman's featurization versus random features and one-hot encoded categorical features. (**B**) Machine learning models trained using random feature barcodes provide near-identical performance on the exact 70/30 train-test split reported. Note: Bayes' generalized linear model was not assessed; five-neuron versus 100-neuron networks are shown instead. (**C**) Comparison of coefficient of determination (R^2) and RMSE values between input representations.

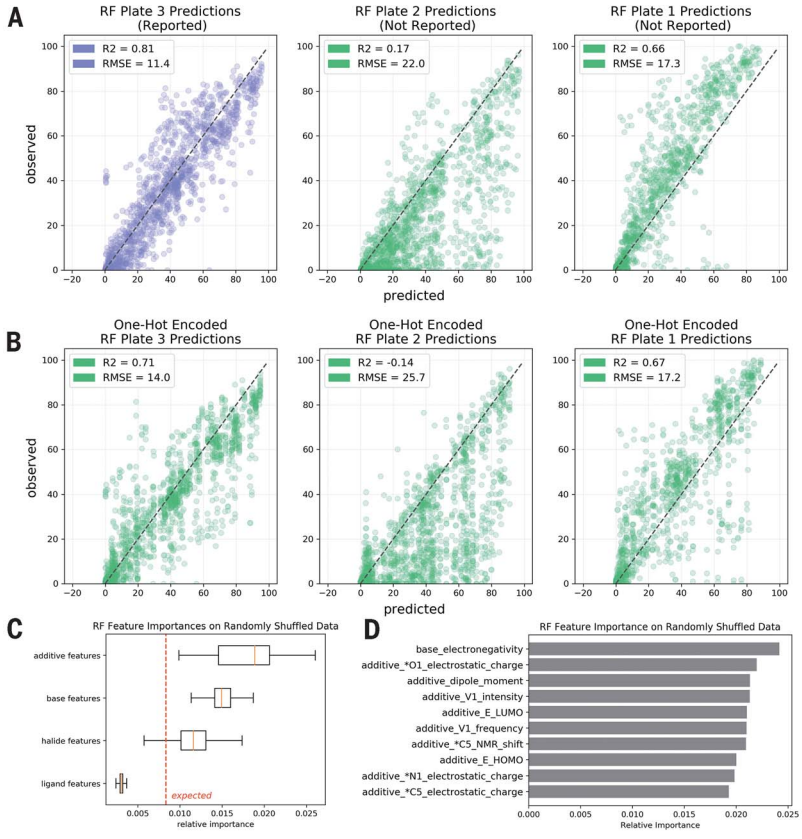

Fig. 2. Out-of-sample performance on individual plate predictions and analysis of feature importance bias. (**A**) Platewise predictions on additives using Ahneman *et al.*'s chemical featurization. (**B**) Analogous platewise predictions on additives using one-hot encoding. (**C**) Box plot of average feature importances extracted from 100 trials of shuffled data, showing median values with first and third quartiles. Plot whiskers represent minimum and maximum importance values across random trials. (**D**) Top 10 feature importances from a single representative trial.

but instead suggest that the retrospective study performed in the paper is incapable of distinguishing between meaningful featurization and random featurization.

Prospective out-of-sample test sets provide a more rigorous measure of model generalization. Ahneman *et al.* reported that an out-of-sample set of eight isoxazole additives, representing one of the three 1536-well plates used in their study, shows good generalization [root mean square error (RMSE) = 11.3%]. To account for variance in sampling and to establish a comprehensive picture, we completed analyses that, in turn, independently hold out each of the remaining two experimental plates (Fig. 2A). We found that performance dropped starkly (RMSE = 22.0 and 17.3%, respectively), indicating that the models' generalizability was more limited than expected. Similarly, we repeated the analysis using one-hot encoded representations in place of chemical features, as in Fig. 1A. Machine learning algorithms trained on one-hot representations learn only from the presence or absence of additives in the training set, and by definition cannot generalize to unseen additives. We thus anticipated highly diminished straw model performance in this sanity check. Surprisingly, platewise performance (Fig. 2B) using one-hot encoding tracked closely with that obtained using chemical features (Fig. 2A, as did random barcode results, not shown). These results failed to strongly distinguish meaningful from random featurization, despite the prospective context.

Looking beyond prediction performance, Ahneman *et al.* thoughtfully analyzed the relative importance of the chemical features used by their top-performing random forest model. They found that isoxazole additive–based descriptors most significantly affect yield prediction mean square error under permutation analysis (*9*). By contrast, the random-feature and one-hot encoding straw experiments we performed above suggest that isoxazole additives play only a limited role in predicting reaction outcome, and we looked to understand this discrepancy. Traditional random forest implementations can exhibit feature-importance bias when inputs vary in scale or when categories vary in number of classes (*10*, *11*). We suspected that additive feature importance may be enriched as the result of a similar effect. Consequently, we shuffled all training data to decorrelate the predictive variables (features) from the output (yields) and trained a random forest regressor on the shuffled data. In 100 trials of this randomized-data test, additive features were nonetheless consistently identified as most important, and consistently occupied 9 of the top 10 by rank (Fig. 2, C and D). These results indicate that apparently high additive feature importances cannot be distinguished from hidden structure within the dataset itself.

We believe that these results, taken together, illustrate the need to incorporate random-control procedures (*7*) when applying machine learning to new scientific domains. We find that the experimental design is insufficient to establish that models built on the proposed chemical featurization can generalize to new chemical entities, or meaningfully outperform straw models trained on randomly assigned features. However, we do not conclude that chemical features are unimportant, nor that the ones used here are necessarily incorrect. Nor do we believe that careful design of chemical features is futile. Rather, further studies that more expansively explore each reaction dimension (additional bases, ligands, substrates, and additives) may be a means to demonstrate that these models can be usefully adopted for reaction prediction. Flexible and powerful machine learning models have become widespread and readily available. As these tools permeate the physical and life sciences, so too must accompanying methods to distinguish models that learn peculiarities of an experiment's layout from those that extract meaningful and actionable patterns beyond it. With randomized controls to guide experimental design, Ahneman *et al.*'s novel machine learning approach to reaction prediction may best prove its merit.

Department of Pharmaceutical Chemistry, Department of Bioengineering and Therapeutic Sciences, Institute for Neurodegenerative Diseases, and Bakar Computational Health Sciences Institute, University of California, San Francisco, CA 94143, USA.
***Corresponding author. Email: keiser@keiserlab.org**

REFERENCES AND NOTES

1. D. T. Ahneman, J. G. Estrada, S. Lin, S. D. Dreher, A. G. Doyle, *Science* **360**, 186–190 (2018).
2. P. Ruiz-Castillo, S. L. Buchwald, *Chem. Rev.* **116**, 12564–12649 (2016).
3. K. D. Collins, F. Glorius, *Acc. Chem. Res.* **48**, 619–627 (2015).
4. J. R. Platt, *Science* **146**, 347–353 (1964).
5. T. C. Chamberlin, *Science* **148**, 754–759 (1965).
6. F. Pedregosa *et al.*, *J. Mach. Learn. Res.* **12**, 2825–2830 (2011).
7. P. Langley, *Mach. Learn.* **3**, 5–8 (1988).
8. N. R. Draper, H. Smith, in *Applied Regression Analysis*, N. R. Draper, H. Smith, Eds. (Wiley, 1998), pp. 299–325.
9. L. Breiman, *Mach. Learn.* **45**, 5–32 (2001).
10. C. Strobl, A.-L. Boulesteix, A. Zeileis, T. Hothorn, *BMC Bioinformatics* **8**, 25 (2007).
11. H. Kim, W.-Y. Loh, *J. Am. Stat. Assoc.* **96**, 589–604 (2001).

ACKNOWLEDGMENTS

We thank D. T. Ahneman, J. G. Estrada, and A. G. Doyle for their collegiality and discussions of one-hot results. **Funding:** Supported by a Paul G. Allen Family Foundation Distinguished Investigator Award (M.J.K.). **Competing interests:** The authors declare no competing interests. **Data and materials availability:** All code and data used in these analyses are available at www.github.com/keiserlab/comments/.

11 April 2018; accepted 18 September 2018
10.1126/science.aat8603

TECHNICAL RESPONSE

ORGANIC CHEMISTRY

Response to Comment on "Predicting reaction performance in C–N cross-coupling using machine learning"

Jesús G. Estrada[1], Derek T. Ahneman[1], Robert P. Sheridan[2], Spencer D. Dreher[3]*, Abigail G. Doyle[1]*

We demonstrate that the chemical-feature model described in our original paper is distinguishable from the nongeneralizable models introduced by Chuang and Keiser. Furthermore, the chemical-feature model significantly outperforms these models in out-of-sample predictions, justifying the use of chemical featurization from which machine learning models can extract meaningful patterns in the dataset, as originally described.

In Ahneman *et al.* (*1*), we showed that a random forest (RF) algorithm built using computationally derived chemical descriptors for the components of a Pd-catalyzed C–N cross-coupling reaction (aryl halide, ligand, base, and potentially inhibitory isoxazole additive) could identify predictive and meaningful relationships in a multidimensional chemical dataset comprising 4608 reactions. Chuang and Keiser (*2*) built alternative models using random barcode features ("straw" models), wherein the chemical descriptors are replaced with random numbers selected from a standard normal distribution. One-hot encoded features, wherein each reagent acts as a categorical descriptor and is marked as absent or present, were also evaluated. Models built with either set of label features are not generalizable, meaning that they cannot make distinct predictions for new chemical entities not found in the training set. Using these alternative models, Chuang and Keiser conclude that the dataset described in our paper is insufficient to establish that models built with chemical features can generalize to new chemical entities or outperform models built with reagent-label features. However, the authors disregard the chemistry underlying the dataset, and in so doing, they base their conclusions on test sets that are poor indicators of model similarity (Plate 1 or 3) and performance (Plate 2). Here, we show that our original out-of-sample test set (Plate 3), although representative of the generalizability of the chemical descriptor model, was suboptimal in distinguishing nongeneralizable models because it was composed of primarily average-yielding additives. However, using rigorous tests of generalizability, we demonstrate that the chemical descriptor model presented in our original study is statistically distinct from and significantly outperforms models built on reagent-label features.

In our original paper, we demonstrated that a RF model delivered high predictive performance among a panel of machine learning (ML) algorithms in a 70/30 train-test split of the dataset. Chuang and Keiser show that models built with barcodes and one-hot encoding achieved near-identical predictive performances. Because a 70/30 random split of the entire data results in a test set composed of reactions with components that the model has seen in the training set at least once, a ML algorithm is capable of learning the reactivity of each reaction component. Thus, ML algorithms can perform well using a variety of representations for the reaction components, whether the representations are continuous chemical descriptors or reagent labels. For this reason, retrospective tests like those in our manuscript and Chuang and Keiser's comment can only be used to conclude that the RF algorithm outperforms other ML algorithms.

That a ML algorithm can be built with random barcodes or reagent labels does not mean that these or the chemical descriptors are meaningless, nor does it invalidate any structure-activity relationship present in a chemical descriptor model. Performing a Y-randomization test—a well-accepted control for interrogating the null hypothesis that there is no structure-activity relationship in the data—on the chemical descriptor model results in an average cross-validated R^2 value of −0.01, demonstrating that the model encodes meaningful information (*3*, *4*). Nonetheless, a model built on reagent labels as descriptors cannot be extrapolated to chemical entities not in the original set. For that, one needs some flavor of chemical descriptors. Thus, out-of-sample prediction is the appropriate test of generalizability and is the overall justification for using chemical features.

In our manuscript, we investigated the generalizability of the chemical descriptor model by using isoxazole additives on Plates 1 and 2 for training and additives on Plate 3 for out-of-sample predictions. Chuang and Keiser also investigated two alternative splits along plate lines. In so doing, they found that prediction of Plate 2 additives is poor [R^2 = 0.19, root mean square error (RMSE) = 21.7%] and conclude that the generalizability of the chemical descriptor model is more limited than we reported. However, to use the large variation in model performance across the different plate test sets to assess model generalizability, one must assume that the training sets of all three models cover a similar spread in chemical space. Figure 1A illustrates the effect of additives on yield across plate lines. Among the 23 additives examined, four additives (**10**, **11**, **13**, and **14**) serve as severe reaction poisons, resulting in substantially lower average yields than the rest. All four of these additives are located in Plate 2. Thus, a test set comprising Plate 2 additives involves a training set without any of the reaction poisons. Such a training set would be expected to result in a poorly predictive model whose performance would also be a poor indicator of generalizability (*5*). Investigating the Plate 2 predictions further, we replaced one of the reaction poisons (**13**) in Plate 2 with an average-yielding isoxazole (**2**) to afford a Plate 2′ test set, thus guaranteeing that the training set includes at least one example of a reaction poison. The model performance increased from R^2 = 0.19 to R^2 = 0.64 (Fig. 1B) (*6*).

For a more systematic evaluation of model generalizability, we turned to activity ranking for out-of-sample test set design (Fig. 1C), which is considered a better indicator of generalization than random splitting, as used in our original study (*7*). Using this method of training/test set design, we split the data into four additive out-of-sample test sets, resulting in models with an R^2 range of 0.69 ± 0.12. Whereas the observed mean performance is slightly lower than we reported based solely on Plate 3 (R^2 = 0.81), Plate 3 predictions are well within the observed range, as are Plate 1 and Plate 2′ predictions (R^2 = 0.66 and 0.64, respectively). By comparison, Plate 2 predictions (R^2 = 0.19) are significantly out of the observed range of performance. These results confirm that the chemical descriptor model has good generalizability along the additive dimension.

We next turned to the question of whether the chemical descriptor model was distinguishable from the nongeneralizable models. Chuang and Keiser show that the three models have similar aggregate test set performances for Plate 3 predictions. However, evaluating the predictions of the models for individual additives on Plate 3 reveals that the models make distinct predictions. For example, a plot of predicted yields for the chemical descriptor versus one-hot encoded models, as shown in Fig. 2A, illustrates that the chemical descriptor model makes different predictions for different out-of-sample additives, something that the one-hot and random barcode models cannot do. Furthermore, for the

[1]Department of Chemistry, Princeton University, Princeton, NJ 08544, USA. [2]Modeling and Informatics, Merck & Co., Inc., Kenilworth, NJ 07033, USA. [3]Chemistry Capabilities and Screening, Merck & Co., Inc., Kenilworth, NJ 07033, USA.
*Corresponding author. Email: spencer_dreher@merck.com (S.D.D.); agdoyle@princeton.edu (A.G.D.)

poorer-performing additives in the test set (**16** and **18**), the one-hot encoded model overpredicts yields (e.g., R^2 = 0.31 for **16**), consistent with the model's inability to predict these additives as mild reaction poisons (Fig. 2B). By contrast, the chemical descriptor model predicts that these additives will lead to diminished yields relative to the average (e.g., R^2 = 0.90 for **16**), thereby capturing chemically meaningful information in the additive dimension.

Given these findings, why are the aggregate test set performances between the various models for Plate 3 predictions similar? Using principal components analysis, we found that six of the eight additives in the test set have highly correlated outputs and are average-yielding. As such, the nongeneralizable models perform competitively with the chemical descriptor model because these models make a single prediction that is an average of all of the additives in the training set. A chemical descriptor model is expected to statistically outperform a one-hot model in test sets with a greater number of extreme outcomes. Indeed, the Plate 2′ test set described in this response exhibited a large difference between the two models, with R^2 values of 0.64 versus 0.19 (Fig. 1B). Thus, we proceeded to use Plate 2 as a template to evaluate Chuang and Keiser's null hypothesis that the two models are indistinguishable (*8*).

A total of 14 test sets were created by replacing one (four test sets), two (six test sets), or three reaction poisons (four test sets). Not surprisingly, we found the greatest difference in performance between the chemical descriptor and one-hot model for the test sets incorporating three reaction poisons (Fig. 2C). Across the 14 test sets, we observed R^2 values of 0.63 ± 0.12 for the chemical descriptor model and 0.36 ± 0.20 for the one-hot model; these values indicate that the one-hot model affords an overall worse and more variable predictive performance and that the models are distinguishable at a statistically significant level ($P < 0.01$). To evaluate the predictive value of the additive features for these 14 test sets, we also compared the chemical-feature model to a RF model built using no chemical features for the additives (R^2 = 0.54 ± 0.15) and a model built using one-hot features for the additives but chemical features for the aryl halides, bases, and ligands (R^2 = 0.36 ± 0.19) (Fig. 2D). These experiments clearly show the benefit of using chemical descriptors for out-of-sample prediction and demonstrate that the chemical descriptors used in our original study are not solely acting as reagent identifiers (*9*).

Having confirmed that the chemical descriptor model is generalizable and that the features used have chemical meaning, variable-importance analysis provides a useful tool to obtain chemical insights and guide mechanistic inquiry, as highlighted in our original study. Nonetheless, Chuang and Keiser show that RF algorithms can exhibit descriptor bias, which can skew the analysis of important features. To evaluate the impact that this might have had on our analysis, we investigated an alternative to the randomforest function: the cforest function, which has been shown to avoid descriptor selection bias (*10*). Use of the cforest algorithm resulted in cross-validation test set statistics (R^2 = 0.84) similar to those of the randomforest function. As in our original study, aryl halide and additive *C3 nuclear magnetic resonance (NMR) shifts appeared in the top five chemical descriptors, reinforcing the inference that led to the experiments designed to test whether competitive oxidative addition of the isoxazole could be a source of deleterious side reactivity. Evaluation of a decision tree (DT) model further supplemented our analysis of important descriptors. The aryl halide and additive *C3 NMR shifts appear in the first two discriminating nodes, consistent with the variable importances from the RF model discussed above. Analysis of how chemical descriptors bin reaction components in the DT model (i.e., along aryl halide electronic properties) suggests that the chemical descriptors supply the RF model with the ability to recognize chemical phenomena along the aryl halide and additive dimensions (*11*).

In summary, Chuang and Keiser's reagent-label models are valuable representations of a closed dataset and useful comparator models in tests of generalizability. Incorporation of these models into our workflow has revealed that the out-of-sample validation test in our study was not an optimal test for generalization; however, it delivered a performance representative of the

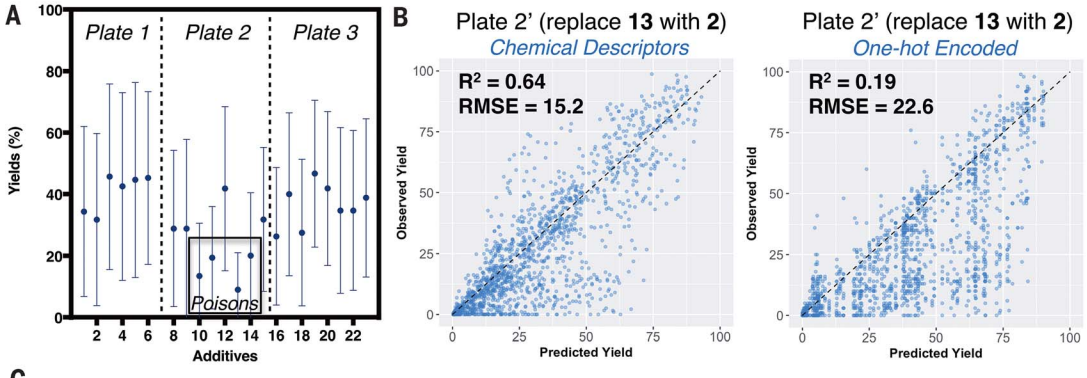

C

decreasing effect as a reaction poison →

Additives	13, 10, 11, 14, 16, 18, 9, 8, 2, 15, 1, 21, 22, 23, 17, 12, 20, 4, 5, 6, 3, 19	R^2	RMSE
Test Set 1	16 2 22 20 3	0.80	12.1
Test Set 2	14 8 21 12 6	0.77	12.9
Test Set 3	11 9 1 17 5	0.64	16.8
Test Set 4	10 18 15 23 4	0.54	17.9
	average	0.69	14.9
	std. dev.	0.12	2.9

Fig. 1. Identifying reaction poisons and their effect on prediction. (**A**) Average yields (dots) and standard deviations (error bars) of the 180 reactions involving all combinations of aryl halides (15), catalysts (4), and bases (3) of each of the 23 additives except additive **7** (control). Box highlights four additives (**10**, **11**, **13**, and **14**) with substantially lower reaction yields than the rest, indicating their characteristic as reaction poisons. (**B**) The Plate 2 out-of-sample test set was altered by replacing additive **13**, a reaction poison, with average-yielding isoxazole **2**, thereby ensuring that the training set contained one additive that served as a reaction poison. RF models were built using chemical descriptors and one-hot encoded labels for comparison. (**C**) To guarantee that the training set and test set would cover chemical space similar to that covered by the entire dataset, we designed test sets according to activity ranking. Isoxazole additives were ranked according to increasing average yields. The lowest- and highest-yielding additives were kept in all training sets to maximize chemical space. The middle 20 isoxazole additives were used to form four out-of-sample test sets by taking every fourth additive as shown; the remaining additives were used for training. Coefficient of determination (R^2) and RMSE were used to analyze model performance.

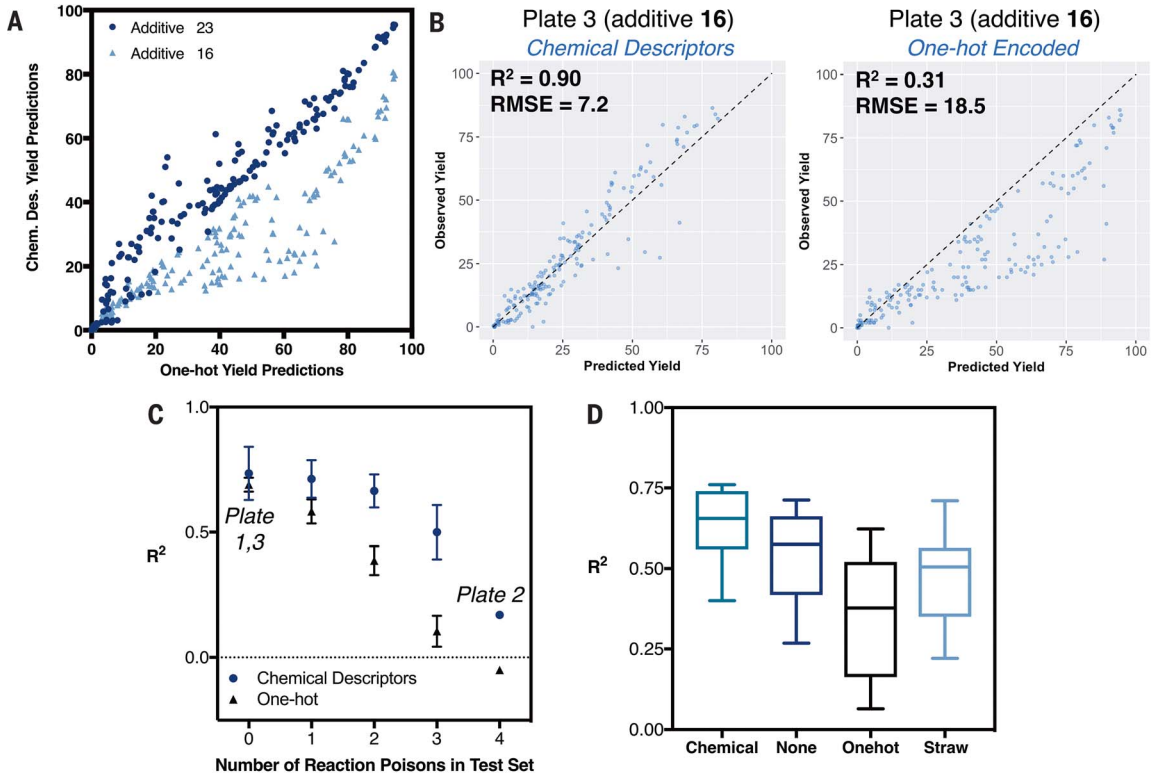

Fig. 2. Distinguishing chemical featurization from one-hot encoding. (**A**) Comparison of chemical descriptor model yield predictions versus one-hot model yield predictions for additives **16** (triangles, light blue) and **23** (circles, dark blue). A nongeneralizable model cannot make distinct predictions for out-of-sample additives. Shown are two distinct predictions made by the chemical descriptor model. (**B**) Calibration plots of observed versus predicted yields for additive **16**, a mild reaction poison. The chemical descriptor model (left) captures the effect of additive **16** causing lower reaction yields, whereas the one-hot model (right) overpredicts. (**C**) Analysis of various prospective predictions according to R^2 values. Plates 1 and 3, which contain no significant reaction poisons in the test set, show minimal differences between the chemical descriptor and one-hot models. Plate 2 contains all four reaction poisons, resulting in a poorly designed training set. Fourteen test sets were designed to incorporate various numbers of reaction poisons and were used to assess the robustness of the chemical descriptor RF model relative to a one-hot encoded RF model. Shown are R^2 averages (dots, triangles) with standard deviations. (**D**) Comparison of the 14 additive out-of-sample test performances of RF models in which the additives are described by chemical descriptors (Chemical), no features (None), one-hot features (Onehot), and straw features (Straw). Relative to absence of additive features, the use of chemical descriptors boosts model performance, whereas the use of reagent label features diminishes model performance. Shown is a box-and-whisker plot.

model's generalizability. On the other hand, our evaluation of Chuang and Keiser's conclusions highlights that an understanding of the chemical reactivity underlying a dataset is necessary in order to use the dataset and reagent-label models to assess the scope and limitations of chemical featurization for reaction prediction. Ultimately, our original conclusion that the RF model is based on meaningful and generalizable chemical features has been strengthened by this additional analysis.

Machine learning offers numerous opportunities to augment how synthetic chemists generate and use data for discovery, optimization, and adoption of synthetic methods (*12*). Its advancement and proliferation will require continued progress in the collection, analysis, and reporting of data, in the description of chemical space, and in predictive modeling. Constructive discussions among chemists, computer and data scientists, and chemical engineers will be important in making this happen.

REFERENCES AND NOTES

1. D. T. Ahneman, J. G. Estrada, S. Lin, S. D. Dreher, A. G. Doyle, *Science* **360**, 186–190 (2018).
2. K. V. Chuang, M. J. Keiser, *Science* **362**, eaat8603 (2018).
3. A. Tropsha, P. Gramatica, V. K. Gombar, *QSAR Comb. Sci.* **22**, 69–76 (2003).
4. All model analyses were performed in R-Studio.
5. We describe exactly in (*1*) this limitation for a model trained on aryl bromides and tested on aryl chlorides.
6. No change in performance was observed for the chemical descriptor model on the resulting Plate 1′ test set (R^2 = 0.66, RMSE = 17.6%), whereas the one-hot model exhibited a lower performance (R^2 = 0.54, RMSE = 20.6%).
7. A. Golbraikh, A. Tropsha, *Mol. Divers.* **5**, 231–243 (2002).
8. One-hot model performance according to activity ranking is R^2 = 0.61 ± 0.11.
9. Similar studies were performed using Chuang and Keiser's straw additive features (R^2 = 0.47 ± 0.15).
10. C. Strobl, A. L. Boulesteix, A. Zeileis, T. Hothorn, *BMC Bioinformatics* **8**, 25–46 (2007).
11. For the smaller base and catalyst dimensions, it is difficult to distinguish whether the RF model uses chemical features to describe meaningful chemical patterns (i.e., Base N1 electrostatic charge) or simply to label reagents.
12. For another study using a RF algorithm to predict reaction performance wherein we constructed one-hot models as comparator models and found that they delivered significantly inferior predictive ability for out-of-sample test sets relative to a chemical descriptor model; see (*13*).
13. M. K. Nielsen, D. T. Ahneman, O. Riera, A. G. Doyle, *J. Am. Chem. Soc.* **140**, 5004–5008 (2018).

ACKNOWLEDGMENTS

We thank M. K. Nielsen for initial design of the one-hot encoded dataset and helpful discussions. **Funding:** Supported by Princeton University and a Camille Dreyfus Teacher-Scholar Award. **Competing interests:** The authors declare no competing interests. **Data and materials availability:** All data used to produce the reported results and additional analyses can be found online at https://github.com/doylelab/rxnpredict.

26 June 2018; accepted 18 September 2018
10.1126/science.aat8763

SPECIAL SECTION

REVIEWS

RELATED ITEM

► PODCAST

OPTIMIZING THE DIET

By **L. Bryan Ray**

In every stage race, competitive cyclists perform an experiment of sorts to discover who can most efficiently turn dietary energy sources into maximal power output on the bike. More broadly, we're all interested in diet because abundant evidence shows that diet has major effects on human health and resistance to rampant diseases associated with aging, such as obesity, cardiovascular disease, and diabetes. Advice on what constitutes a healthy diet is more prevalent and more inconsistent than ever. For this special issue, we checked in with the experts. On the question of how much fat we should eat, recommendations have swung from one extreme to the other. We consulted with a group of scientists representing different sides in the debate over the proportion of fat in a healthy diet and, importantly, which particular fats are most healthful. We share our meals with trillions of bacteria in the digestive system, so a promising and emerging area of investigation explores how diet influences our give-and-take interaction with gut symbionts. It's not just what you eat but when you eat it, and periods of fasting have some remarkable benefits.

A pervasive theme is that much of the disagreement and confusion reflects a lack of solid scientific studies on humans. Clearly, many more well-designed studies are needed to determine the best diet for people, and how that varies with activity, at different life stages and for different individuals. And individual needs can be extreme—a cyclist at the top of the sport recorded massive carbohydrate loading before an intense stage, eating the equivalent of 85 slices of bread!

Maximum performance or maximized health benefits require a nutritious mix of foods in the diet.

PHOTO: SCOTT SUCHMAN; STYLING: NICHOLE BRYANT

REVIEW

Dietary fat: From foe to friend?

David S. Ludwig[1,2]*, Walter C. Willett[2,3], Jeff S. Volek[4], Marian L. Neuhouser[5]

For decades, dietary advice was based on the premise that high intakes of fat cause obesity, diabetes, heart disease, and possibly cancer. Recently, evidence for the adverse metabolic effects of processed carbohydrate has led to a resurgence in interest in lower-carbohydrate and ketogenic diets with high fat content. However, some argue that the relative quantity of dietary fat and carbohydrate has little relevance to health and that focus should instead be placed on which particular fat or carbohydrate sources are consumed. This review, by nutrition scientists with widely varying perspectives, summarizes existing evidence to identify areas of broad consensus amid ongoing controversy regarding macronutrients and chronic disease.

A report by the U.S. Senate Select Committee on Nutrition and Human Needs in 1977 called on Americans to reduce consumption of total and saturated fat, increase carbohydrate intake, and lower calorie intake, among other dietary goals (*1*). This report, by elected members of Congress with little scientific training, was written against a backdrop of growing public concern about diet-related chronic disease, precipitated in part by attention surrounding President Eisenhower's heart attack in 1955.

Even then, the recommendations were hotly debated. The American Medical Association stated that "The evidence for assuming benefits to be derived from the adoption of such universal dietary goals as set forth in the report is not conclusive … [with] potential for harmful effects." Indeed, the lack of scientific consensus was reflected in the voluminous, 869-page "Supplemental Views" published contemporaneously by the committee. Nonetheless, reduction in fat consumption soon became a central principle of dietary guidelines from the U.S. government and virtually all nutrition- and health-related professional organizations. [Note that modern approaches to the study of diet-related chronic diseases were at that time in their infancy; previously, nutritional science was focused on individual nutrients for the prevention of deficiency diseases (*2*).]

The Surgeon General's Report on Nutrition and Health in 1988 identified reduction of fat consumption as the "primary dietary priority," with sugar consumption only a secondary concern for children at risk for dental caries (*3*). The 1992 Food Guide Pyramid of the U.S. Department of Agriculture advised eating 6 to 11 daily servings of starchy foods such as bread, cereal, rice, and pasta while limiting all fats and oils. To facilitate this goal, the U.S. Healthy People 2000 report of the Department of Health and Human Services called on the food industry to market thousands of new "processed food products that are reduced in fat and saturated fat" (*4*). This intensive focus on reducing dietary fat was driven by a prevailing belief that carbohydrates—all carbohydrates, including highly processed grains and sugar—were innocuous and possibly protective against weight gain, cancer, and cardiovascular disease through multiple mechanisms (*5*).

As a result, the proportion of fat in the U.S. diet decreased from about 42% in the 1970s to about 34% of total calories today (somewhat greater than the stated goal of <30%) and the proportion of dietary carbohydrates increased substantially (*6*). During this time, rates of obesity and diabetes increased greatly, contributing to the first nationwide decrease in life expectancy since the flu pandemic 100 years ago (*7*). These trends could be causally connected or unrelated.

If causal, how could some traditional societies, such as that of Okinawa, enjoy relative freedom from chronic disease and long lifespan when they consume a low-fat diet (*8*)? In Mexico, Brazil, and China, rates of obesity and diet-related chronic diseases have also increased without similar government dietary guidance to individuals and food manufacturers. Moreover, many other aspects of the American diet changed in the past 40 years, including increased portion sizes, greater consumption of foods away from home, and more extreme food processing. At the same time, labor-saving technology and the digital age have led to declines in occupational and recreational physical activity, and budget shortfalls in schools have led to curtailments in physical education classes, recess time, and after-school recreation opportunities.

Despite a lack of clear evidence specifically relating fat consumption (as a proportion of total energy intake) to the epidemics of diet-related disease—and a lack of high-quality, long-term trials focused on macronutrients in general—the pendulum has recently swung in the opposite direction, with rising consumer popularity of low-carbohydrate, high-fat diets. Among the current top-10 best-selling weight loss books on Amazon.com, four promote a ketogenic diet with energy intake derived mainly from fat. In support of higher fat intake, several meta-analyses found slightly greater weight loss on high-fat rather than low-fat diets (*9*, *10*), and preliminary data suggest the potential for excellent control of diabetes through carbohydrate restriction (*11*, *12*). But versions of low-carbohydrate, high-fat diets have been around at least as early as the 1800s, with no clear evidence of superiority for long-term obesity treatment at present. And regardless of body weight, high intakes of fat—especially from red meat and dairy products—might increase risk for heart disease or cancer.

Perhaps both high-carbohydrate, low-fat and low-carbohydrate, high-fat diets have benefit for different populations or for different clinical outcomes, and the critical issue is to identify the optimal macronutrient ratio for an individual. Or perhaps the focus on macronutrient quantity has been a distraction, and qualitative aspects (the particular sources of fat or carbohydrate) and overall eating patterns are more important.

To explore these issues, we have joined together as scientists with a diversity of expertise, perspectives, and prior research focus. Our aim is not to assemble a premature consensus among the like-minded, but rather to identify areas of general agreement and delineate a research agenda to address long-standing controversies.

The case for a low-fat, high-carbohydrate diet

Physiologic mechanisms

Among many societies worldwide, carbohydrate is the primary source of energy, providing 50% or more of daily energy, with lesser amounts from both fat and more expensive and scarce protein. Population-level or ecological studies comparing global chronic disease rates show that less developed countries have lower rates of cardiovascular disease, obesity, and cancer than more Westernized countries. When individuals move from countries with low chronic disease rates to Westernized countries, their incidence of chronic diseases approaches that of their new country within one to two generations. This rapid shift in chronic disease rates spurred thinking that environmental exposures, such as adoption of a higher-fat Western diet, may be causally related to disease risk patterns. [A low-fat diet typically contains <30% energy as fat, and a very-low-fat diet ≤20%, versus 32 to 36% in the United States (*6*).]

Humans ingest complex food mixtures that include macronutrients (fat, carbohydrate, and protein) and alcohol as energy sources. Macronutrients have highly regulated yet integrated metabolic interactions. One consideration for judging optimal macronutrient intake is the relative efficiency of substrate oxidation and interconversion. Humans preferentially oxidize carbohydrate over fat, a process that helps to maintain blood glucose within homeostatically controlled ranges. Further, carbohydrate consumption acutely increases carbohydrate oxidation, with only a quantitatively small increase in de novo lipogenesis under typical conditions (*13*–*16*). Humans have limited storage capacity for carbohydrate but also

[1]New Balance Foundation Obesity Prevention Center, Boston Children's Hospital, Boston, MA, USA. [2]Harvard Medical School, Boston, MA, USA. [3]Departments of Epidemiology and Nutrition, Harvard T. H. Chan School of Public Health and Channing Division of Network Medicine, Brigham and Women's Hospital, Boston, MA, USA. [4]Department of Human Sciences, The Ohio State University, Columbus, OH, USA. [5]Cancer Prevention Program, Division of Public Health Sciences, Fred Hutchinson Cancer Research Center, Seattle, WA, USA.
*Corresponding author. Email: david.ludwig@childrens.harvard.edu

have extensive adipose stores, thus favoring fat deposition with excess fat intake (*17*, *18*). Fat is also highly palatable and may have a weak effect on satiation, potentially leading to passive overconsumption (*18*). This excess intake, if not coupled with increased energy expenditure, results in weight gain. This effect may be enhanced because, by weight, fat provides more than twice as much energy (9 kcal/g) as carbohydrate or protein (4 kcal/g). Conversely, diets rich in whole grains, which are low in fat and have a relatively low glycemic load, promote satiety and reduce overconsumption, possibly by increasing concentrations of glucagon-like peptide–1 after eating (*19*). Of 29 diets with varying macronutrient composition tested in mice, only high-fat diets, but not high-carbohydrate diets, led to overconsumption and weight gain (*20*). Of particular interest, the high-fat diets increased expression of three serotonin receptors and both dopamine and opioid signaling pathways, components of the reward system in the hypothalamus.

Fat and specific fatty acids also have adverse metabolic effects independent of calorie content. High-fat diets up-regulate inflammatory mediators including tumor necrosis factor–α (TNF-α), interleukins (IL-1β, IL-6) (*21*), complement (*22*), and Toll-like receptors (*23*) in human and animal studies. In contrast, lower-fat diets reduce amounts of these and other inflammatory cytokines, as well as activity of the transcription factor NF-κB (*24*). Palmitic and stearic acids (abundant in animal foods) influence the structure and function of mitochondrial membranes, such that an increase in these saturated fatty acids leads to impaired membrane function (*25*). High-fat diets may also promote unfavorable epigenetic profiles. For example, excess saturated fat changes DNA methylation patterns in adipose tissue (*26*) and skeletal muscle, and alters histone acetylation (*27*, *28*). When acetyl–coenzyme A concentrations are high, such as under conditions of low glucose, histone acetylation increases according to in vitro human and animal studies (*28*).

High-fat diets also stimulate hepatic bile acid synthesis, which, after conversion into secondary bile acids in the colon, may promote tumorigenesis (*29*–*31*). Among Africans consuming a diet high in minimally processed carbohydrates, gut microbial communities were dominated by butyrate-producing bacteria, whereas genetically similar African Americans consuming a high-fat diet had a less healthful gut microbiome with high secondary bile acid production (*31*). Fat-stimulated production of bile acids was also unfavorably associated with inflammation and proliferation in colonic biopsy samples (*29*–*31*). Conversely, high-carbohydrate diets containing whole grains and other high-fiber foods provide the preferred fuel for colonic bacteria, with less secondary bile acid production and greater production of butyrate and other short-chain fatty acids that lower inflammation, decrease cellular proliferation, and enhance expression of genes with antineoplastic properties. Low-fat diets may also decrease serum estradiol and increase sex hormone–binding globulin (*32*, *33*) and may reduce other breast cancer risk factors such as mammographic density (*34*), although the persistence of these effects remains unclear.

Taken together, these multiple physiologic mechanisms suggest that higher dietary fat may be harmful for health. However, it is critically important to consider carbohydrate quality when fat intake is lowered. Refined grains provide negligible nutrition and their high glycemic load causes unhealthful spikes in postprandial glucose and insulin, promoting hunger, inflammation, insulin resistance, and dyslipidemia. However, with a lower-fat diet containing high-fiber, low-glycemic carbohydrates such as minimally processed grains, legumes, and nonstarchy fruits and vegetables, these measures improve. Whole plant foods are also rich sources of micronutrients, antioxidants, and phytochemicals with beneficial health effects.

Obesity and diabetes

Low-fat diets may favorably influence body weight and adiposity. In the Women's Health Initiative Dietary Modification Trial (WHI-DM), the low-fat intervention (20% energy as fat, as part of a healthy eating pattern) was associated with significant, small reductions in body weight, total fat mass, and percent body fat as measured by dual x-ray absorptiometry (*35*). Another randomized controlled trial (RCT) in postmenopausal women tested a lower-fat, higher-carbohydrate diet (20% and 65% energy, respectively), a lower-carbohydrate, higher-fat diet (45% and 35% energy, respectively), and a walnut-rich higher-fat, lower-carbohydrate diet (18%, 35%, and 45% energy, respectively) for weight loss. All three diets led to weight loss at 12 months, with slightly higher weight loss in the lower-fat diet group (*33*). A meta-analysis of dietary intervention trials showed that low-fat diets were effective for weight loss under ad libitum conditions (*36*); however, this was published prior to recent carbohydrate-restricted diet studies.

Although obesity has a dominant role in the development of diabetes, clinical trial evidence suggests benefit for low-fat eating patterns in risk reduction and disease management. The Diabetes Prevention Program (DPP) was an RCT of 3234 adults at risk for diabetes (*37*). DPP's primary goal was to compare the effect of at least 7% reduction in body weight achieved by following a low-calorie, low-fat diet and increasing physical activity, with that of the drug metformin or a placebo. Rates of diabetes incidence were reduced by 58% in the lifestyle intervention group and by 31% in those taking metformin, although the effects of dietary composition cannot be fully disentangled from weight loss and other factors. Numerous other trials and observational studies support the use of high-fiber whole grains and fiber supplements for diabetes prevention and control. A recent meta-analysis found that fiber, typically consumed in greater amounts in low-fat, high-carbohydrate diets, improved measures of glycemia and weight (*38*).

Cardiovascular disease

The effects of dietary macronutrient composition on cardiovascular disease (CVD) risk have been a subject of debate for more than 40 years. Ecological studies and controlled feeding trials supported associations of higher-fat diets with CVD or its biomarkers of risk. However, definitive trials have not been conducted that explicitly test this "diet-heart hypothesis." WHI-DM was not designed to test CVD endpoints; even so, participants in the low-fat group had significantly lower low-density lipoprotein (LDL) cholesterol and metabolic syndrome scores and no unfavorable changes to high-density lipoprotein (HDL) cholesterol or triglycerides relative to those of controls (*39*). Although the overall results of WHI-DM were negative for CVD, follow-up showed that women without baseline hypertension had a 30% reduced CVD risk, whereas

Box 1. Current controversies.

1. Do diets with various carbohydrate-to-fat proportions affect body composition (ratio of fat to lean tissue) independently of energy intake? Do they affect energy expenditure independently of body weight?

2. Do ketogenic diets provide metabolic benefits beyond those of moderate carbohydrate restriction? Can they help with prevention or treatment of cardiometabolic disease?

3. What are the optimal amounts of specific fatty acids (saturated, monounsaturated, polyunsaturated) in the context of a very-low-carbohydrate diet?

4. What is the relative importance for cardiovascular disease of the amounts of LDL cholesterol, HDL cholesterol, and triglycerides in the blood, or of lipoprotein particle size, for persons on diets with distinct fat-to-carbohydrate ratios? Are other biomarkers of equivalent or greater importance?

5. What are the effects of dietary fat amount and quality across the lifespan on risk of neurodegenerative, pulmonary, and other diseases that have not been well studied?

6. What are the long-term efficacies of diets with different carbohydrate-to-fat proportions in chronic disease prevention and treatment under optimal intervention conditions (designed to maximize dietary compliance)?

7. What behavioral and environmental interventions can maximize long-term dietary compliance?

8. What individual genetic and phenotypic factors predict long-term beneficial outcomes on diets with various fat-to-carbohydrate compositions? Can this knowledge inform personalized nutrition, with translation to prevention and treatment?

9. How does variation in the carbohydrate-to-fat ratio and in sources of dietary fat affect the affordability and environmental sustainability of diets?

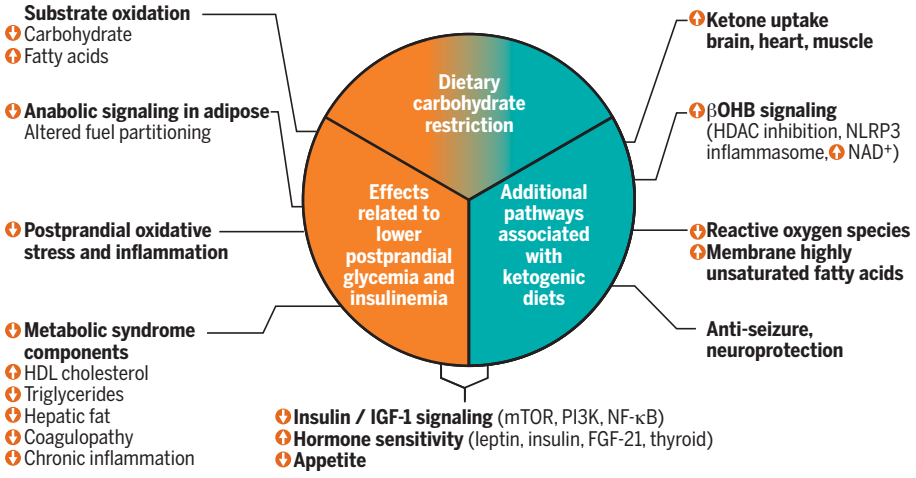

Fig. 1. Pleiotropic effects of low-carbohydrate, high-fat diets. Ketogenic diets (aqua) may enhance these effects and act through additional mechanisms. Abbreviations: βOHB, β-hydroxybutyrate; HDAC, histone deacetylase; NAD^+, nicotinamide adenine dinucleotide; mTOR, mechanistic target of rapamycin.

those with baseline hypertension or prior CVD had no benefit or increased CVD risk; these findings suggest that a low-fat diet might have a greater effect on prevention than treatment (*40*).

In a meta-analysis of RCTs, addition of at least 3 g of oat β-glucan per day reduced total and LDL cholesterol without unfavorable effects on triglycerides or HDL cholesterol (*41*), highlighting the benefits of a low-fat, grain-based diet. In another meta-analysis of examined RCTs, low-fat diets lowered LDL cholesterol, a major CVD risk factor, whereas low-carbohydrate diets lowered triglycerides (*42*).

Cancer

Cancer includes more than 100 disease types and subtypes, precluding a comprehensive assessment of potential diet effects here, but several major trials provide useful evidence. In the low-fat diet arm of WHI-DM, there was no significant effect on total breast cancer incidence, but estrogen receptor–positive, progesterone receptor–negative cancers were significantly reduced by 36% over a mean of 8.1 years of follow-up (*32*). Among women who had higher baseline fat intake (>36.8% of energy), overall risk of breast cancer was significantly reduced by 22% over a median of 11.5 years. For these women, total and breast cancer deaths were reduced by 22% and 14%, respectively. However, a low-fat, high-carbohydrate intervention conducted in high-risk women had no significant effect on incidence of invasive breast cancer in another study with a mean 10-year follow-up (*43*). Breast cancer patients in the Women's Intervention Nutrition Study randomly assigned to the low-fat diet group had a statistically significant 24% reduced risk of cancer relapse relative to controls over a median of 5 years (*44*). In another randomized trial among breast cancer patients with very low risk of recurrence, a low-fat, plant-based diet had no effect on recurrence or mortality (*45*).

Specific types of fats may influence prostate cancer risk, possibly as a result of effects on cell signaling and other cancer-related pathways. In the Prostate Cancer Prevention Trial and the Selenium and Vitamin E Cancer Prevention Trial, higher blood measures of omega-3 (N-3) fatty acids, particularly docosahexaenoic acid (DHA), were associated with increased risks of both total and high-grade prostate cancer (*46*, *47*). These findings are consistent with a study in which prostate cancer patients were randomly assigned to flaxseed supplements [a rich source of the N-3 fat α-linolenic acid (ALA)] or placebo (*48*). The supplement led to increased tumor proliferation and higher prostate-specific antigen (PSA) at prostatectomy. However, the clinical implications remain unknown; research is needed to determine whether specific fatty acids should be reduced in people at risk for specific cancers.

The case for a low-carbohydrate, high-fat diet

Carbohydrate-restricted diets vary in macronutrient composition, but the defining feature is that contributions to total energy are reduced for carbohydrate and increased for fat (≥40% of energy) relative to conventional diets. Emerging evidence suggests that a ketogenic diet—a special type of low-carbohydrate diet with fat typically ≥70% of energy—may have unique therapeutic effects beyond those of less restrictive regimens.

Physiological mechanism

Conventional lifestyle recommendations and existing drug treatments have failed to stem the twin epidemics of obesity and type 2 diabetes. Nearly three-fourths of U.S. adults are overweight or obese, and half have prediabetes or diabetes, despite a 40-year focus on reducing dietary fat. The most salient change in macronutrient intake over this period has been a marked increase in processed starches and added sugars, which suggests that they may have a role in the public health crisis of diet-related chronic disease (*49*).

As dietary carbohydrate is replaced by fat, postprandial spikes in the blood concentrations of glucose and insulin decrease, glucagon secretion increases, and metabolism shifts to a greater reliance on fat oxidation (Fig. 1). These metabolic and hormonal responses are associated with attenuated oxidative stress and inflammatory responses after eating (*50*, *51*), reduced hormone resistance [to insulin, leptin, fibroblast growth factor–21 (FGF-21), and thyroxine] (*52*, *53*), and improvements in many features of metabolic syndrome (*54*–*56*)—effects that increase throughout the range of carbohydrate restriction. Additional mechanisms arise as carbohydrate is restricted to a point that results in nutritional ketosis, in which serum concentrations of β-hydroxybutyrate increase from <0.1 mM to 0.5 to 5 mM. This normal physiological state differs from diabetic ketoacidosis, in which β-hydroxybutyrate concentrations exceed 10 mM. Ketones, an alternative fuel used by the brain (*57*) and heart, affect metabolic efficiency and a panoply of signaling functions, producing beneficial changes in gene expression, inflammation, oxidative stress, and possibly health span (*58*, *59*).

From a pathophysiological perspective, low-carbohydrate, high-fat diets may directly target underlying metabolic dysfunction in insulin resistance and type 2 diabetes, characterized by defects in the body's ability to oxidize ingested carbohydrate. With insulin resistance, dietary carbohydrate is diverted at increased rates into hepatic de novo lipogenesis, resulting in increased hepatic triglyceride synthesis and abnormal concentrations of lipids in the blood (*60*). From a historical perspective, some aboriginal hunting and fishing cultures (e.g., Inuit of the Arctic and First Nations groups in Canada) survived for millennia with little available dietary carbohydrate. In fact, mild ketosis was the "normal" metabolic state for many cultures before the advent of agriculture (i.e., for all but the last 1% or less of the existence of humans as a species). When these ethnic groups underwent a transition from their low-carbohydrate and high-fat traditional diets, the prevalence of obesity and type 2 diabetes increased markedly, although changes in other lifestyle factors may have also had a role.

Obesity, type 2 diabetes, and cardiovascular disease

The most recent systematic reviews and meta-analyses have concluded that carbohydrate-restricted diets tend to outperform low-fat diets for short- to medium-term weight loss, especially in trials that involved a ketogenic diet (*9*, *10*, *54*, *61*). Whereas individuals with insulin sensitivity seem to respond similarly to low-fat or low-carbohydrate diets, those with insulin resistance, glucose intolerance, or insulin hypersecretion may lose more weight on a low-carbohydrate, high-fat diet (*62*, *63*). The lower insulin concentrations and accelerated rates of adipose tissue lipolysis and ketogenesis may provide more stable metabolic fuel availability,

especially for the brain, resulting in greater satiety during weight loss; potential effects on energy expenditure remain a subject of investigation (*63*).

Metabolic syndrome—including central adiposity, high circulating concentrations of triglycerides, low levels of HDL cholesterol, high blood pressure, glucose intolerance, fatty liver, and chronic inflammation—comprises a constellation of clinical risk factors associated with insulin resistance that predispose to diabetes and CVD. Reduction in dietary carbohydrate may improve these markers more effectively than do low-fat diets (*54*–*56*, *64*). In an 8-week trial of patients with type 2 diabetes in Italy, a diet high in total (42% of energy) and monounsaturated (MUFA) fat decreased liver fat significantly more than did a low-fat (28% of energy), high-fiber diet (*65*). In a 2-year trial conducted at a worksite in Israel, participants in the low-carbohydrate diet group (fat approximately 40% of energy) lost more weight and experienced greater improvements in HDL cholesterol and triglycerides than did those in the low-fat diet group (fat approximately 30% of energy) (*66*). With restriction of carbohydrate to ketogenic levels (<50 g/day), individuals with metabolic syndrome lost more weight, total fat, and abdominal fat than did those consuming a low-fat (24% of energy), calorie-restricted diet (*56*). The ketogenic diet also significantly decreased serum triglycerides, increased HDL cholesterol concentration, lowered inflammatory markers, and reduced concentrations of circulating saturated fatty acids (*50*), consistent with metabolic benefits seen in other studies (*67*).

Carbohydrate restriction in general, and specifically a ketogenic diet, may provide exceptional benefits in the setting of diabetes, essentially a disease of carbohydrate intolerance. Historically, ketogenic diets were the treatment of choice for diabetes, but the discovery of insulin in the early 1920s allowed for control of acute symptoms on higher-carbohydrate diets. By the 1980s, low-fat diets with up to 60% energy from carbohydrate had become the standard of care, although current recommendations emphasize individualizing macronutrient composition. However, despite modern insulin analogs and glucose monitoring technologies, management of diabetes remains suboptimal. In a recent survey, 316 children and adults with type 1 diabetes following a low-carbohydrate, high-fat diet for a mean of >2 years reported exceptional glycemic control, low rates of complications, and excellent metabolic health markers (*12*). Among 262 participants with type 2 diabetes assigned to a ketogenic diet with intensive telemedicine support, 83% completed the 1-year intervention; in this group, weight was reduced by 12%, hemoglobin A1c (HbA1c, a measure of long-term average glucose concentration) was reduced by 1.3%, and a majority had HbA1c levels of <6.5% (i.e., below the diagnostic threshold for diabetes) while taking no medications other than metformin (*11*).

Low-carbohydrate diets are typically (but not necessarily) high in saturated fat. As discussed below, saturated fat is directly associated with cardiovascular and total mortality in the general population (although this relation has been a subject of controversy, related in part to the nature of the substituted calories) (*68*, *69*). However, with the higher rates of fatty acid oxidation and decreased de novo lipogenesis on a ketogenic diet, blood concentrations of saturated fatty acids and palmitoleic acid (a marker of de novo lipogenesis) may decrease (*50*, *55*, *56*), suggesting a lower risk of diabetes and CVD. Furthermore, any effects of increased LDL cholesterol (a risk marker for CVD that occurs in about half of individuals on a ketogenic diet) need to be considered together with improvements in triglycerides, HDL cholesterol, inflammatory markers, and other features of metabolic syndrome. However, there are no long-term studies tracking CVD outcomes.

Box 2. Points of consensus.

1. With a focus on nutrient quality, good health and low chronic disease risk can be achieved for many people on diets with a broad range of carbohydrate-to-fat ratios.

2. Replacement of saturated fat with naturally occurring unsaturated fats provides health benefits for the general population. Industrially produced trans fats are harmful and should be eliminated. The metabolism of saturated fat may differ on carbohydrate-restricted diets, an issue that requires study.

3. Replacement of highly processed carbohydrates (including refined grains, potato products, and free sugars) with unprocessed carbohydrates (nonstarchy vegetables, whole fruits, legumes, and whole or minimally processed grains) provides health benefits.

4. Biological factors appear to influence responses to diets of differing macronutrient composition. People with relatively normal insulin sensitivity and β cell function may do well on diets with a wide range of carbohydrate-to-fat ratios; those with insulin resistance, hypersecretion of insulin, or glucose intolerance may benefit from a lower-carbohydrate, higher-fat diet.

5. A ketogenic diet may confer particular metabolic benefits for some people with abnormal carbohydrate metabolism, a possibility that requires long-term study.

6. Well-formulated low-carbohydrate, high-fat diets do not require high intakes of protein or animal products. Reduced carbohydrate consumption can be achieved by substituting grains, starchy vegetables, and sugars with nonhydrogenated plant oils, nuts, seeds, avocado, and other high-fat plant foods.

7. There is broad agreement regarding the fundamental components of a healthful diet that can serve to inform policy, clinical management, and individual dietary choice. Nonetheless, important questions relevant to the epidemics of diet-related chronic disease remain. Greater investment in nutrition research should assume a high priority.

Cancer

Certain cancer cells rely on glycolysis for energy metabolism. By decreasing glucose flux into tumor cells, a ketogenic diet could target the defective mitochondrial oxidative phosphorylation specific to some cancers. Carbohydrate restriction might also help to prevent or treat cancer by lowering oxidative stress, inflammation, and cellular signaling involving anabolic hormones such as insulin (which is thought to mediate in part the association between obesity and cancer risk) (*70*, *71*). Preclinical data involving various models appear promising, including the use of a ketogenic diet to enhance the effectiveness of phosphoinositide 3-kinase (PI3K) inhibitors in cancer treatment (*72*). However, clinical reports are largely limited to small case series, with no high-quality RCTs.

Clinical translation

Moderately low-carbohydrate diets entail relatively simple changes in diet, focused primarily on substituting high-fat foods for processed carbohydrates while allowing several daily servings of whole fruits, legumes, and minimally processed grains. A ketogenic diet may include various nutrient-dense whole foods such as nonstarchy vegetables, nuts, eggs, cheese, butter/cream, fish, meats, oils, and select fruits. Proper formulation of a ketogenic diet entails restriction of carbohydrate, adequate but not high intake of protein, and sufficient sodium to offset the natriuretic effect of ketosis and reduced insulinemia. Recent data among motivated patients suggest the possibility of good compliance and improved quality of life through 1 year (*11*), although safety has not been fully assessed in long-term trials.

The case for dietary fat quality

At one time, dietary fat, primarily triglycerides, was considered simply a source of energy. However, the fatty acids in triglycerides can vary in chain length, number and position of double bonds, and whether the double bonds are in cis or trans configuration. These features profoundly affect the biological function of fatty acids, and thus their effects on heath, in complex, incompletely understood ways.

The position of double bonds, described by the number of carbons from the noncarboxyl end of the fatty acid to the first double bond, has particular importance. Two families of polyunsaturated fatty acids (PUFAs), the N-3 and N-6 fatty acids, are essential because they cannot be synthesized by humans. Both are critical components of every human cell membrane and are precursors of eicosanoid hormones that mediate inflammation, thrombosis, immunity, and insulin resistance. An increase in N-3 fatty acid intake alters expression of more than 6000 genes, underscoring this biological complexity (*73*).

A vast literature based on controlled feeding studies with physiologic endpoints, long-term epidemiologic studies, and randomized trials with clinical outcomes has documented that the type of dietary fat strongly influences human health independent of total fat intake. N-6 and N-3 fatty acids provide benefit at intakes above minimum levels to prevent essential fatty acid deficiency, and nonessential dietary fatty acids also have important metabolic effects.

Obesity and diabetes

Whereas the literature on total fat intake is extensive, little is known about the effects of specific types of fat on weight control and body composition. In a 7-week controlled overfeeding study, saturated fat increased hepatic and visceral fat storage relative to polyunsaturated fat (*74*). In a large cohort analysis (*75*), increases in the intakes of trans and saturated fat were positively associated with weight gain when compared isocalorically with carbohydrate, but intakes of MUFA and PUFAs did not influence weight. To our knowledge, no RCTs lasting 1 year or longer have compared the effects of different types of fat on body weight.

Consistent with the effects of trans fat on multiple components of metabolic syndrome (see below), higher intake was associated with risk of type 2 diabetes in a large cohort study with repeated measures of diet (*76*). In a 10-week randomized trial, consumption of PUFA reduced biomarkers of insulin resistance relative to consumption of saturated fat (*77*). In a large cohort study, the ratio of polyunsaturated to saturated fat intake was inversely associated with risk of type 2 diabetes (*76*), and relative blood levels of linoleic acid, which reflect intake, were inversely associated with risk of type 2 diabetes in a pooled analysis of 20 cohort studies (*78*).

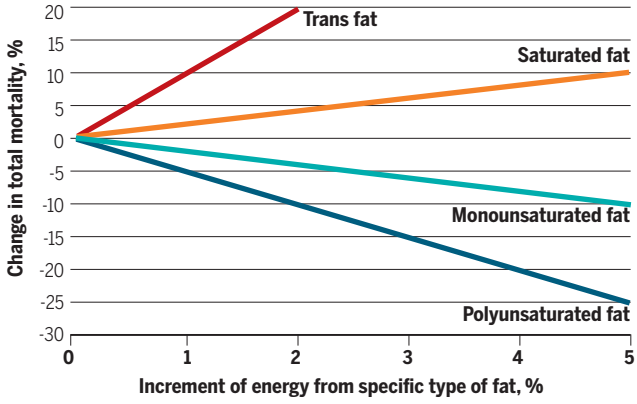

Fig. 2. Relation between increasing intakes of trans, saturated, unsaturated, monounsaturated, and polyunsaturated fatty acid (compared isocalorically with carbohydrate) in relation to total mortality. Data are based on 126,233 men and women followed for up to 32 years, with assessments every 4 years, as described in Wang *et al*. (*94*). The strong inverse association with polyunsaturated fatty acids was primarily due to N-6 polyunsaturated fatty acids; associations with N-3 polyunsaturated fatty acids were weaker.

Cardiovascular disease

Early evidence on dietary fats and CVD was based on comparisons of incidence and mortality rates across geographical areas, and on knowledge of the effects of dietary fats on blood cholesterol levels. In the Seven Countries Study (*79*), per capita intake of saturated fat, but not total fat, was strongly correlated with rates of CVD; although potentially confounded by other variables, this provided a strong incentive to understand the major geographical variation in CVD rates. In controlled feeding studies lasting several weeks, compared isocalorically to carbohydrate, saturated fat increased blood cholesterol concentrations, whereas PUFA reduced them (*80*, *81*). Thus, from the 1960s, dietary advice to reduce CVD emphasized replacing saturated fat with PUFAs, primarily N-6, and consumption of N-6 PUFA in the United States increased from approximately 3% to 7% of energy. Concurrently, age-adjusted coronary heart disease mortality decreased by about 75%, although lower rates of tobacco use and other prevention efforts (e.g., statins) contributed to this secular trend.

In subsequent epidemiologic studies, blood lipid subfractions predicted CVD better than did total cholesterol; higher amounts of LDL cholesterol and triglycerides are associated with higher risk, whereas higher amounts of HDL cholesterol predict lower risk (*82*). In further controlled feeding studies, replacement of saturated fat with carbohydrates reduced both LDL cholesterol and HDL cholesterol and increased blood concentrations of triglyceride during fasting, suggesting little or potentially adverse effects on risk of CVD. Replacement of monounsaturated or polyunsaturated fat with carbohydrate increased LDL cholesterol and had minimal effects on HDL cholesterol or triglycerides.

Consistent with the controlled feeding studies of blood lipids, in several randomized trials with CVD as the outcome, replacement of saturated fat with PUFA reduced the risk of CVD, whereas replacement with carbohydrate did not (*83*); however, these studies were small, short-term, and had other limitations (e.g., a lack of emphasis on carbohydrate quality). Long-term prospective cohort studies are also consistent with these findings: When compared isocalorically with saturated fat, N-6 PUFAs—but not typical carbohydrates in Western diets—are associated with lower risk of CVD (*84*–*86*). Controlled for other types of fat, MUFAs are also inversely associated with risk. This inverse association with PUFA is linear up to about 8% of energy, beyond which data are sparse. These epidemiologic studies also highlight the importance of carbohydrate quality; relative to saturated fat, whole grains are associated with lower CVD risk (*87*).

By the 1990s, the distinction between N-6 and N-3 PUFAs and between cis and trans isomers gained widespread recognition. In animals, N-3 fatty acids protect against cardiac arrhythmias, and in epidemiologic studies, intakes of N-3 fatty acids [DHA or eicosapentaenoic acid (EPA) from fish and ALA from plant sources] are inversely but nonlinearly associated with risk of sudden cardiac death (*88*). Specifically, risk decreases with intakes up to about 250 mg/day (equivalent to one or two servings of fish per week) but then plateaus. The inconsistent effects of supplements seen in these RCTs may relate to the variability in intakes within and among populations (intakes among some individuals in the United States and mean intakes in many countries remain very low) (*89*). At high dosage, fish oil supplements may reduce the risk of cardiovascular events such as heart attack and stroke among people with hypertriglyceridemia, according to preliminary data from a large trial (*90*)—a possibility that warrants further study.

The main N-6 PUFA in diets, linoleic acid, can be elongated and desaturated to form eicosanoids that are prothrombotic and proinflammatory. In addition, linoleic acid may competitively inhibit biosynthetic pathways shared by the N-3 fatty acid ALA in the formation of antithrombotic and anti-inflammatory eicosanoids. For these reasons, some have concluded that higher N-6 fatty acid intake should be minimized to prevent CVD and other diseases associated with chronic inflammation. However, this reasoning disregards evidence that N-6 PUFA intermediates in these pathways, such as arachidonic acid, are highly regulated (*91*). Although very high intakes of N-6 PUFA increase inflammatory measures in some animal models, this effect has not been convincingly demonstrated in humans (*92*); higher intake of linoleic acid in humans may actually have anti-inflammatory effects (*93*). Moreover, the ratio of N-6 to N-3 fatty acids has not been associated with risk of CVD, consistent with both being beneficial (*94*). Nonetheless, special effects in subgroups or at very low intakes of carbohydrate cannot be ruled out.

The process of partial hydrogenation, which creates trans isomers from the natural cis double bonds of fatty acids, was widely used to create margarine and vegetable shortening with favorable commercial properties (solidity at room temperature, long shelf life). This industrial process altered the structure and function of linoleic acid and ALA, the dominant fatty acids in many widely used oils, resulting in major health impacts. Trans fat has uniquely adverse effects on LDL, LDL particle size, HDL, triglycerides, and inflammatory factors (*95*). In multiple large-cohort studies, intake of trans fat is directly associated with risk of coronary heart disease and other chronic illnesses. Through regulations, education, and food labeling, trans fat was largely eliminated from the food supply in the United States and some European

countries. However, intake remains high in some parts of the world.

Cancer

Mechanistic studies have suggested that both N-6 and N-3 fatty acids could either increase or reduce cancer risk (*46*–*48*), and some animal studies have suggested that intakes of PUFA beyond the range of typical human diets might increase risks. In human studies, consumption of these fatty acids and other specific types of fat during midlife do not have consistent relationships to risks of various cancers, according to biomarkers of intake and assessments of diet (*96*). Higher intake of fat from animal sources, but not vegetable sources, during early adult life was associated with higher risk of breast cancer, which may reflect the type of fat or nonlipid factors (*97*). Because of long latencies and windows of vulnerability for carcinogenic influences, further studies of specific types of fat across the lifespan are desirable.

Other outcomes

Adequate intake of both N-6 and N-3 fatty acids in utero and during early life is critical for neurological development because these fatty acids constitute much of the lipid in the central nervous system. Low consumption of fish, the primary source of DHA and EPA, during pregnancy is associated with lower cognitive function and preterm birth (*98*, *99*). In later life, lower consumption of N-3 fatty acids and higher consumption of trans fats have been associated with greater risk of dementia (*100*).

In a recent prospective study, 126,233 men and women were followed for up to 32 years, with diet assessed every 4 years (*94*). Compared isocalorically to carbohydrate intake, intake of trans fat was strongly associated with higher mortality. Intakes of MUFA and N-3 PUFA were weakly associated with lower mortality, and intake of N-6 PUFA was strongly associated with lower mortality (Fig. 2). Because of reductions in saturated and trans fats over the study period, total fat intake was inversely associated with mortality.

Conclusion

The optimal proportion of carbohydrate to fat in the diet for obesity treatment and chronic disease prevention has been a topic of debate for decades, often generating more heat than light (*101*). Of course, any meaningful assessment of a diet's impact on health must extend far beyond macronutrient quantity, to include the myriad qualitative aspects of food and food combinations that influence hormonal response, gene expression, and metabolic pathways. Further complicating this issue is the likelihood that inherent or acquired biological differences among individuals or populations, especially related to glucose homeostasis, affect response to specific diets.

Unfortunately, the national nutrition research agenda has not been adequate to address important areas of controversy (Box 1). Currently, the United States invests a fraction of a cent on nutrition research for each dollar spent on treatment of diet-related chronic disease. All too often, scientific results in this field have been ambiguous: Macronutrient feeding studies have been too short and too small to distinguish transient from chronic effects; many behavioral trials have lacked the intensity to produce meaningful differences between dietary treatment groups; and observational studies can be affected by confounding, inability to distinguish cause and effect, and other methodological problems. Furthermore, despite promising preliminary data, few major studies of a ketogenic diet in the treatment of diabetes have been conducted. Additional questions related to sustainability for the individual (whether people can realistically remain on prescribed diets) and for the environment (the impacts of specific dietary patterns on natural resources and climate change) require more study. Given the enormous human and economic toll of diet-related disease, high-quality research into key controversies should be given priority.

The incomplete nature of research notwithstanding, data from multiple lines of investigation have led to important areas of consensus (Box 2). Current evidence indicates that no specific carbohydrate-to-fat ratio in the diet is best for the general population. Nor do all diets, and calorie sources, have similar metabolic effects in everyone. With attention to diet quality—and specifically a focus on reducing processed foods, including sugar and refined grains—many people do relatively well with substantial variation in macronutrient composition (*102*). For the rapidly rising proportion of the population with severe metabolic dysfunction or diabetes, a more specific dietary prescription may be needed.

REFERENCES AND NOTES

1. U. S. Senate Select Committee on Nutrition and Human Needs, *Dietary Goals for the United States, Second Edition* (U.S. Government Printing Office, 1977).
2. D. Mozaffarian, D. S. Ludwig, *JAMA* **304**, 681–682 (2010).
3. J. M. McGinnis, M. Nestle, *Am. J. Clin. Nutr.* **49**, 23–28 (1989).
4. Public Health Service, U.S. Department of Health and Human Services, *Healthy People 2000: National Health Promotion and Disease Prevention Objective* (1991).
5. J. O. Hill, A. M. Prentice, *Am. J. Clin. Nutr.* **62**, 264S–273S (1995).
6. G. L. Austin, L. G. Ogden, J. O. Hill, *Am. J. Clin. Nutr.* **93**, 836–843 (2011).
7. D. S. Ludwig, *JAMA* **315**, 2269–2270 (2016).
8. D. C. Willcox, B. J. Willcox, H. Todoriki, M. Suzuki, *J. Am. Coll. Nutr.* **28** (suppl.), 500S–516S (2009).
9. N. B. Bueno, I. S. de Melo, S. L. de Oliveira, T. da Rocha Ataide, *Br. J. Nutr.* **110**, 1178–1187 (2013).
10. D. K. Tobias *et al.*, *Lancet Diabetes Endocrinol.* **3**, 968–979 (2015).
11. S. J. Hallberg *et al.*, *Diabetes Ther.* **9**, 583–612 (2018).
12. B. S. Lennerz *et al.*, *Pediatrics* **141**, e20173349 (2018).
13. F. Diraison *et al.*, *J. Lipid Res.* **44**, 846–853 (2003).
14. L. C. Hudgins *et al.*, *J. Nutr. Biochem.* **19**, 237–245 (2008).
15. E. J. Parks, R. M. Krauss, M. P. Christiansen, R. A. Neese, M. K. Hellerstein, *J. Clin. Invest.* **104**, 1087–1096 (1999).
16. J. M. Schwarz, R. A. Neese, S. Turner, D. Dare, M. K. Hellerstein, *J. Clin. Invest.* **96**, 2735–2743 (1995).
17. A. Astrup, A. Raben, *Eur. J. Clin. Nutr.* **46**, 611–620 (1992).
18. J. E. Blundell, J. I. MacDiarmid, *J. Am. Diet. Assoc.* **97** (suppl.), S63–S69 (1997).
19. S. S. Runchey *et al.*, *Metabolism* **62**, 188–195 (2013).
20. S. Hu *et al.*, *Cell Metab.* **28**, 415–431.e4 (2018).
21. M. Valdearcos, A. W. Xu, S. K. Koliwad, *Annu. Rev. Physiol.* **77**, 131–160 (2015).
22. S. K. Doerner *et al.*, *Mol. Cancer Res.* **14**, 953–965 (2016).
23. R. G. Snodgrass, S. Huang, I. W. Choi, J. C. Rutledge, D. H. Hwang, *J. Immunol.* **191**, 4337–4347 (2013).
24. J. V. Heymach *et al.*, *Cancer Prev. Res.* **4**, 1590–1598 (2011).
25. E. M. Sullivan *et al.*, *Adv. Nutr.* **9**, 247–262 (2018).
26. A. Perfilyev *et al.*, *Am. J. Clin. Nutr.* **105**, 991–1000 (2017).
27. J. A. Martínez, F. I. Milagro, K. J. Claycombe, K. L. Schalinske, *Adv. Nutr.* **5**, 71–81 (2014).
28. B. Paul *et al.*, *Clin. Epigenetics* **7**, 112 (2015).
29. S. J. O'Keefe, *Nat. Rev. Gastroenterol. Hepatol.* **13**, 691–706 (2016).
30. S. Ocvirk, S. J. O'Keefe, *Curr. Nutr. Rep.* **6**, 315–322 (2017).
31. J. Ou *et al.*, *Am. J. Clin. Nutr.* **98**, 111–120 (2013).
32. R. L. Prentice *et al.*, *JAMA* **295**, 629–642 (2006).
33. C. L. Rock *et al.*, *Metabolism* **65**, 1605–1613 (2016).
34. N. F. Boyd *et al.*, *J. Natl. Cancer Inst.* **89**, 488–496 (1997).
35. C. L. Carty *et al.*, *Am. J. Clin. Nutr.* **93**, 516–524 (2011).
36. A. Astrup, G. K. Grunwald, E. L. Melanson, W. H. M. Saris, J. O. Hill, *Int. J. Obes.* **24**, 1545–1552 (2000).
37. Diabetes Prevention Program Research Group, *N. Engl. J. Med.* **346**, 393–403 (2002).
38. S. V. Thompson, B. A. Hannon, R. An, H. D. Holscher, *Am. J. Clin. Nutr.* **106**, 1514–1528 (2017).
39. B. V. Howard *et al.*, *JAMA* **295**, 655–666 (2006).
40. R. L. Prentice *et al.*, *Am. J. Clin. Nutr.* **106**, 35–43 (2017).
41. A. Whitehead, E. J. Beck, S. Tosh, T. M. Wolever, *Am. J. Clin. Nutr.* **100**, 1413–1421 (2014).
42. A. J. Nordmann *et al.*, *Arch. Intern. Med.* **166**, 285–293 (2006).
43. L. J. Martin *et al.*, *Cancer Res.* **71**, 123–133 (2011).
44. R. T. Chlebowski *et al.*, *J. Natl. Cancer Inst.* **98**, 1767–1776 (2006).
45. J. P. Pierce *et al.*, *JAMA* **298**, 289–298 (2007).
46. T. M. Brasky *et al.*, *J. Natl. Cancer Inst.* **105**, 1132–1141 (2013).
47. T. M. Brasky *et al.*, *Am. J. Epidemiol.* **173**, 1429–1439 (2011).
48. M. Azrad *et al.*, *PLOS ONE* **7**, e53104 (2012).
49. E. Cohen *et al.*, *Nutrition* **31**, 727–732 (2015).
50. C. E. Forsythe *et al.*, *Lipids* **43**, 65–77 (2008).
51. D. S. Ludwig, *JAMA* **287**, 2414–2423 (2002).
52. B. M. Hron, C. B. Ebbeling, H. A. Feldman, D. S. Ludwig, *Nutr. Metab.* **14**, 44 (2017).
53. C. B. Ebbeling *et al.*, *JAMA* **307**, 2627–2634 (2012).
54. N. Mansoor, K. J. Vinknes, M. B. Veierød, K. Retterstøl, *Br. J. Nutr.* **115**, 466–479 (2016).
55. J. S. Volek, M. L. Fernandez, R. D. Feinman, S. D. Phinney, *Prog. Lipid Res.* **47**, 307–318 (2008).
56. J. S. Volek *et al.*, *Lipids* **44**, 297–309 (2009).
57. S. C. Cunnane *et al.*, *Front. Mol. Neurosci.* **9**, 53 (2016).
58. G. F. Cahill Jr., *Annu. Rev. Nutr.* **26**, 1–22 (2006).
59. J. C. Newman, E. Verdin, *Annu. Rev. Nutr.* **37**, 51–76 (2017).
60. K. F. Petersen *et al.*, *Proc. Natl. Acad. Sci. U.S.A.* **104**, 12587–12594 (2007).
61. J. Sackner-Bernstein, D. Kanter, S. Kaul, *PLOS ONE* **10**, e0139817 (2015).
62. M. F. Hjorth, Y. Zohar, J. O. Hill, A. Astrup, *Annu. Rev. Nutr.* **38**, 245–272 (2018).
63. D. S. Ludwig, C. B. Ebbeling, *JAMA Intern. Med.* **178**, 1098–1103 (2018).
64. E. J. van Zuuren, Z. Fedorowicz, T. Kuijpers, H. Pijl, *Am. J. Clin. Nutr.* **108**, 300–331 (2018).
65. L. Bozzetto *et al.*, *Diabetes Care* **35**, 1429–1435 (2012).

66. I. Shai *et al*., *N. Engl. J. Med.* **359**, 229–241 (2008).
67. N. H. Bhanpuri *et al*., *Cardiovasc. Diabetol.* **17**, 56 (2018).
68. P. W. Siri-Tarino, Q. Sun, F. B. Hu, R. M. Krauss, *Am. J. Clin. Nutr.* **91**, 535–546 (2010).
69. M. Dehghan *et al*., *Lancet* **390**, 2050–2062 (2017).
70. A. Poff, A. P. Koutnik, K. M. Egan, S. Sahebjam, D. D'Agostino, *Semin. Cancer Biol.* 10.1016/j.semcancer.2017.12.011 (2017).
71. P. N. Hyde, M. B. Lustberg, V. J. Miller, R. A. LaFountain, J. S. Volek, *Cancer Treat. Res. Commun.* **12**, 32–39 (2017).
72. B. D. Hopkins *et al*., *Nature* **560**, 499–503 (2018).
73. A. Jans *et al*., *Am. J. Clin. Nutr.* **95**, 825–836 (2012).
74. F. Rosqvist *et al*., *Diabetes* **63**, 2356–2368 (2014).
75. A. E. Field, W. C. Willett, L. Lissner, G. A. Colditz, *Obesity* **15**, 967–976 (2007).
76. F. B. Hu *et al*., *N. Engl. J. Med.* **345**, 790–797 (2001).
77. H. Bjermo *et al*., *Am. J. Clin. Nutr.* **95**, 1003–1012 (2012).
78. J. H. Y. Wu *et al*., *Lancet Diabetes Endocrinol.* **5**, 965–974 (2017).
79. A. Keys, *Seven Countries: A Multivariate Analysis of Death and Coronary Heart Disease* (Harvard Univ. Press, 1980).
80. A. Keyes, J. T. Anderson, F. Grande, *Metabolism* **14**, 747–758 (1965).
81. D. M. Hegsted, *Am. J. Clin. Nutr.* **44**, 299–305 (1986).
82. R. P. Mensink, P. L. Zock, A. D. Kester, M. B. Katan, *Am. J. Clin. Nutr.* **77**, 1146–1155 (2003).
83. F. M. Sacks *et al*., *Circulation* **136**, e1–e23 (2017).
84. M. U. Jakobsen *et al*., *Am. J. Clin. Nutr.* **89**, 1425–1432 (2009).
85. F. B. Hu *et al*., *N. Engl. J. Med.* **337**, 1491–1499 (1997).
86. M. S. Farvid *et al*., *Circulation* **130**, 1568–1578 (2014).
87. G. Zong *et al*., *BMJ* **355**, i5796 (2016).
88. D. Mozaffarian, J. H. Wu, *J. Am. Coll. Cardiol.* **58**, 2047–2067 (2011).
89. S. Petrova, P. Dimitrov, W. C. Willett, H. Campos, *Public Health Nutr.* **14**, 1157–1164 (2011).
90. A. O'Connor, "Fish oil drug may reduce heart attack and stroke risks for some." *New York Times*, 25 September 2018; www.nytimes.com/2018/09/25/well/fish-oil-heart-attack-stroke-triglycerides-omega-3s.html.
91. B. S. Rett, J. Whelan, *Nutr. Metab.* **8**, 36 (2011).
92. H. Su, R. Liu, M. Chang, J. Huang, X. Wang, *Food Funct.* **8**, 3091–3103 (2017).
93. K. L. Fritsche, *Prostaglandins Leukot. Essent. Fatty Acids* **79**, 173–175 (2008).
94. D. D. Wang *et al*., *JAMA Intern. Med.* **176**, 1134–1145 (2016).
95. D. Mozaffarian, M. B. Katan, A. Ascherio, M. J. Stampfer, W. C. Willett, *N. Engl. J. Med.* **354**, 1601–1613 (2006).
96. World Cancer Research Fund and American Institute for Cancer Research, *Diet, Nutrition, Physical Activity and Cancer: A Global Perspective* (2018); www.wcrf.org/sites/default/files/Summary-third-expert-report.pdf.
97. E. Cho *et al*., *J. Natl. Cancer Inst.* **95**, 1079–1085 (2003).
98. E. Oken *et al*., *Am. J. Epidemiol.* **167**, 1171–1181 (2008).
99. A. Horvath, B. Koletzko, H. Szajewska, *Br. J. Nutr.* **98**, 253–259 (2007).
100. M. C. Morris, *Proc. Nutr. Soc.* **71**, 1–13 (2012).
101. J. Palfreman, producer, "Diet Wars" episode of *Frontline* (WGBH-TV, 2004); www.pbs.org/wgbh/pages/frontline/shows/diet/.
102. C. D. Gardner *et al*., *JAMA* **319**, 667–679 (2018).

ACKNOWLEDGMENTS

Funding: D.S.L. was supported in part by a career award from the National Institute of Diabetes and Digestive and Kidney Diseases (K24DK082730). **Competing interests:** D.S.L., W.C.W., and J.S.V. received royalties for books about obesity and nutrition that include recommendations on dietary fat. J.S.V. is a founder, stockholder, and consultant for VirtaHealth Corp. and a member of the advisory boards for Atkins Nutritionals Inc., UCAN Co., and Axcess Global.

10.1126/science.aau2096

REVIEW

A time to fast

Andrea Di Francesco, Clara Di Germanio, Michel Bernier, Rafael de Cabo*

Nutrient composition and caloric intake have traditionally been used to devise optimized diets for various phases of life. Adjustment of meal size and frequency have emerged as powerful tools to ameliorate and postpone the onset of disease and delay aging, whereas periods of fasting, with or without reduced energy intake, can have profound health benefits. The underlying physiological processes involve periodic shifts of metabolic fuel sources, promotion of repair mechanisms, and the optimization of energy utilization for cellular and organismal health. Future research endeavors should be directed to the integration of a balanced nutritious diet with controlled meal size and patterns and periods of fasting to develop better strategies to prevent, postpone, and treat the socioeconomical burden of chronic diseases associated with aging.

The worldwide increase in life expectancy has not been paralleled by an equivalent increase in healthy aging. Developed and developing countries are facing social and economic challenges caused by disproportional increases in their elderly populations and the accompanying burden of chronic diseases (*1*). Geriatricians and gerontologists have contributed greatly to our understanding of the consequences and processes that underlie aging from clinical, social, mental, physical, and biological perspectives. The primary goal of aging research is to improve the health of older persons and to design and test interventions that may prevent or delay age-related diseases. Besides socioeconomic status, energy, environmental quality, and genetics are the most powerful determinants of health and longevity. Although environmental quality and genetics are not under our direct control, energy intake is. The consumption of food provides energy and nutrients necessary to sustain life and allows growth, repair, and reproduction. Proper nutrition can influence health and survival and delay or, in some cases, prevent the onset and progression of chronic diseases. However, both hypo- and hypernutrition have the potential to increase the risk of chronic disease and premature death. Furthermore, manipulation of a nutritionally balanced diet, whether by altering caloric intake or meal timing, can lead to a delay of the onset and progression of diseases and to a healthier and longer life in most organisms (*2*–*4*). In general, both prolonged reduction in daily caloric intake and periodic fasting cycles have the power to delay the onset of disease and increase longevity. Data from experimental studies in short-lived species and emerging clinical and epidemiological observations indicate that dietary interventions are valuable strategies that can be applied to promote healthy aging. In model organisms, caloric restriction (CR) provides beneficial effects on health and survival, and there is an extensive literature that provides insights into its molecular mechanisms of action (*4*). However, chronic CR has been reported to exert adverse effects for a number of mouse strains (*5*) and could push humans to what one may consider a near anorexic state (*6*), underlying some cautionary negative outcomes pointed out by the eating-disorders field as well (*7*–*9*).

An emerging area of research is the investigation of the independent consequences of variations in meal size (through the control of energy intake) and meal frequency (by controlling the time of feeding and fasting) on the incidence or amelioration of multiple age-related diseases, including cardiovascular disease, diabetes, cancer, and dementia (*2*, *10*). These studies are starting to reveal that health-span and life-span extension can be achieved by interventions that do not require an overall reduction in caloric intake. Major challenges for the future include the design of well-controlled and randomized clinical trials to test whether these observations can be translated to humans, determination of the importance of individual genetic variant medicine, and implementation of health care policies in which new eating regimens can be integrated into clinical practice. We discuss four experimental strategies aimed at altering energy intake or the duration of fasting and feeding periods that result in improved aspects of health in mammals. These are (i) classical CR, in which daily caloric intake is typically decreased by 15 to 40%; (ii) time-restricted feeding (TRF), which limits daily intake of food to a 4- to 12-hour window; (iii) intermittent or periodic full or partial fasting, that is a periodic, full- or multiday decrease in food intake; and (iv) fasting-mimicking diets (FMDs) that use a strategy to maintain a physiological fasting-like state by reducing caloric intake and modifying diet composition but not necessarily fasting (Fig. 1). We also summarize the metabolic and cellular responses triggered by these feeding regimens and their impact on physiology, focusing on studies in rodents, monkeys, and humans. Finally, we discuss how these studies may provide a basis for future investigations on the role of various dietary interventions in the prevention of diseases and promotion of health throughout the life span.

Translational Gerontology Branch, National Institute on Aging, National Institutes of Health, Baltimore, MD 21224, USA.
*Corresponding author. Email: decabora@grc.nia.nih.gov

Caloric restriction

Early observations linking reduced food intake to improvements on health and survival are now a century old. Rous discovered that limiting food intake had an impact on cancer development (*11*), and Osborne *et al*. reported growth retardation and life-span extension by a reduction in food intake (*12*). McCay and colleagues later published a seminal paper showing that rats fed a limited amount of food lived much longer than their ad libitum (AL)–fed littermates (*13*). Nearly a century after these initial studies, the positive impact of CR on health span and life span has been documented in many model organisms that include unicellular yeast, nematode worms, fruitflies, mice, and primates, suggesting a strong evolutionary conservation of common mechanisms connecting food intake to longevity (*4*). CR interventions oppose several age-associated pathophysiological changes, including reduction of metabolic rate and oxidative damage (*14*), enhanced cellular turnover and protein homeostasis, and improvement of age-related metabolic disorders that include central obesity, insulin resistance, dyslipidemia, and hypertension. Studies seeking to unravel the link between metabolism and aging have demonstrated that CR induces profound metabolic and molecular changes in components of the nutrient-sensing and stress-responsive pathways, such as growth hormone, insulin and insulin-like growth factor (IGF) signaling, mechanistic target of rapamycin (mTOR), adenosine 5′-monophosphate–activated protein kinase (AMPK), forkhead box protein O (FOXO), sirtuins, and nuclear factor erythroid 2–related factor 2 (NRF2) (*15*, *16*) (Fig. 2). The identification of longevity-regulatory pathways led to studies of pharmacological interventions with U.S. Food and Drug Administration–approved drugs (for example, rapalogs and metformin) and other naturally occurring compounds (such as resveratrol and spermidine) that mimic changes observed in CR without the requirement of changes in food intake (*17*, *18*). We focus on the most relevant molecular and metabolic alterations elicited by dietary interventions that involve a reduction in caloric intake and fasting periods.

Numerous strides have been made to understand how the number of calories, diet composition, and timing of the intervention can be manipulated to effectively extend longevity and to translate these observations into feeding paradigms that can be applied to humans, with the goal of delaying the onset of age-associated conditions and promoting healthy aging. CR without malnutrition can be accomplished by chronically reducing energy intake by 15 to 40% from AL conditions, while maintaining adequate intake of vitamins and minerals. In rodents, under certain circumstances, CR can extend life span by up to 50% (*19*). Traditionally, diet composition and genetic background have been thought to have a marginal impact on life-span extension elicited by CR. More recently, studies in mice and nonhuman primates have revealed that the effect of CR on life-span extension is not universal (*20*). Indeed, certain mouse recombinant

Feeding regimen	Description	Macronutrient balance Fat Protein Carbohydrate	Feeding time Fasting Feeding	Median life-span increase	Effects on health
Caloric restriction (CR)	Daily reduction by 15 to 40% of caloric intake without malnutrition	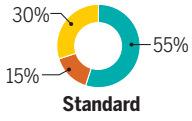	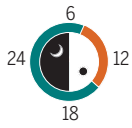	Yes 	Prevention of obesity, diabetes, oxidative stress, hypertension, cancer, cardiovascular disease
Time-restricted feeding (TRF)	Daily food consumption restriced to 4- to 12-hour window	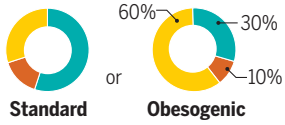		No data	Defense against type II diabetes, hepatic steatosis, hypercholesterolemia
Intermittent or periodic fasting (IF or PF)	**IF:** Alternation of 24-hour fasting or very low calories (25% of energy needs) with a 24-hour ad libitum eating period **PF:** 1 to 2 days fasting or very low calories followed by a 5-day ad libitum eating period (5:2)			Yes 	Protection against obesity, oxidative stress, cardiovascular disease, hypertension, neurodegeneration, diabetes
Fasting-mimicking diet (FMD)	Reduced caloric intake (~30% of energy needs) for five consecutive days before returning to normal eating cycles of FMD once a month or every 3 to 4 months per year	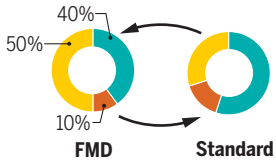		Yes 	Protection from cancer and diabetes, improved risk factors associated with multiple age-related diseases

Fig. 1. Experimental approaches used to improve fitness and promote health span. Description of different feeding regimens, their macronutrient balance, and feeding time during a 24-hour period. The feeding time represented in the day-night diagrams refers to eating time in humans and nonhuman primates. Mice undergoing a CR regimen tend to finish their food allotment quickly, self-imposing a continuous form of TRF. In human studies, people voluntarily reduce their food intake and mostly adhere to a three-meals-per-day schedule. Mean life-span extension is documented for all the treatments in the species depicted in the box, whereas maximum life span is only achieved after CR and IF or PF.

inbred strains show either little increase or deleterious effects on life span after CR (*5*). Analysis of body composition revealed that the best outcomes on survival were obtained in mice that preserved their fat stores during the second year of life, suggesting the necessity of a minimum level of adiposity for the full benefit of CR (*21*, *22*). In CR regimens, sex, age, and genetic background contribute to outcomes regarding health and survival in mice (*22*), and this may also be true for long-lived organisms, including humans. Data from two independent nonhuman primate studies, one at the National Institute on Aging (NIA) and the other at the University of Wisconsin–Madison (UW), challenged the association between life-span extension and health span by reporting similar improvements in health but contrasting survival benefits in response to CR (*23*, *24*). Possible explanations for the divergent outcomes emanating from these two studies have revealed important differences in genetic background, onset of the intervention, feeding practices, and diet composition (*25*).

In humans, short-term trials such as the multicenter CALERIE (Comprehensive Assessment of Long-Term Effects of Reducing Intake of Energy) study (*26*–*29*), the observational studies of centenarians residing in Okinawa who have been exposed to CR for most of their lives (*30*), and observations of the members of the Calorie Restriction Society (CRONies) who self-impose CR (*31*) have shown the occurrence of many of the same physiological, metabolic, and molecular benefits typically associated with long-lived animals on CR. These studies support the observation that long-term CR preserves a more youthful functionality by improving several markers of health, including decreases in body weight, metabolic rate, and oxidative damage (*14*); lower incidence of cardiovascular disease (*31*) and cancer; and decreased activity of the insulin-Akt-FOXO signaling pathway (*32*, *33*) (Fig. 2).

Although these findings clearly indicate that a reduction of caloric intake could be an effective intervention to improve health and prevent disease during aging in humans, there are several obstacles that halt the transition from experimental studies into standard medical practice: (i) the lack of clinical data supporting consistent effects of CR in older populations and the incomplete understanding of the age-specific effects of these interventions (*4*, *10*); (ii) safety concerns related to lack of reserve capacity upon exposure to infection (*34*), injury, or surgery (*35*) and about bone thinning that could lead to the development of osteoporosis in older individuals (*36*); (iii) the difficulty of compliance to extreme restriction; and (iv) the interindividual variability in body mass, especially lean mass, which strongly correlates with frailty (*23*). The current "obesogenic" social environment makes it difficult for individuals to adhere to strict dietary regimens and lifestyle modifications for long periods of time. Thus, there is interest in alternative feeding regimens that may recapitulate at least some of the beneficial effects of CR by controlling feeding-fasting patterns with little or no reduction in caloric intake.

Time-restricted feeding

Recent evidence indicates that the benefits of CR may not be entirely related to a reduction in calories. In many experimental models of CR, the reduction in energy intake encourages the animals to consume their entire daily food allowance in a very short interval, thus promoting a longer fasting period than when consuming standard or hypercaloric diets AL (*37*). Although (nocturnal) rodents with free access to food eat predominantly at night, they also tend to feed during the day, which correlates with gains in body weight (*37*). These observations raise the question of whether the timing of food consumption (either feeding duration or circadian timing) is a determinant of metabolic health, independent of total caloric intake and quality of calories. Thus, it is possible that triggering the fasting response on a daily basis or at specific times is in itself beneficial. This would explain why dietary dilution, a form of CR in which

mice eat all day to compensate for the low density of energy in their diet, does not result in life-span extension (*38*, *39*). Hence, chronic CR may improve health, at least in part, through an extended period of fasting.

TRF refers to daily limitations in the timing of food intake, spanning from 4 to 12 hours, without reduction in caloric intake (Fig. 1). Although data on the effects of TRF on longevity are not yet available, studies in rodents have shown that TRF can confer protection against several detrimental metabolic consequences of a typical western diet (high fat and high carbohydrates, particularly refined sugars) through reduction in body weight, increase in energy expenditure, improved glycemic control and lower insulin levels, decrease in hepatic fat and hyperlipidemia, and attenuated inflammatory outcomes, even when food intake or body weight or both are matched to the control group (*40*–*43*). The molecular mechanisms responsible for the effects of altered meal patterns on metabolic health appears to be related, at least in part, to the synchronization between the time of fasting-feeding and the circadian rhythm (*3*) (Fig. 3). The circadian clock provides a conserved mechanism that allows organisms to anticipate and respond to environmental changes. This perpetual rhythm leads to the timely expression of clock-controlled genes, especially those encompassing enzymes and regulatory molecules that mediate physiological and metabolic functions. A strong relation exists between the circadian clock and metabolism, as they share some common regulators. Indeed, TRF can restore cycling of metabolic regulators, such as nicotinamide phosphoribosyltransferase (NAMPT), cAMP response element–binding protein, mTOR, AMPK, or the insulin signaling pathway, all of which take part in the life-span and health-span benefits of CR (*40*) (Fig. 3).

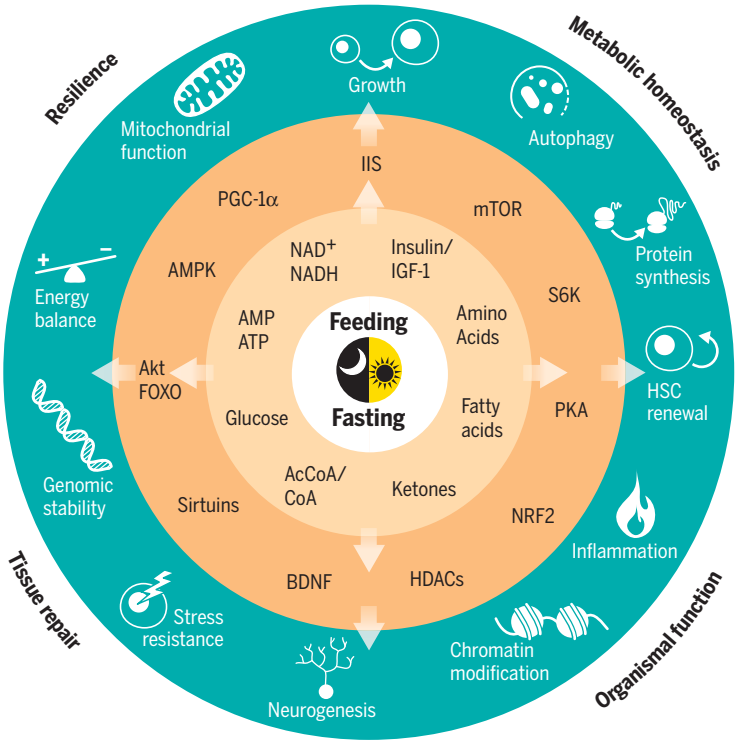

Fig. 2. Fasting time and energy restriction share biological responses implicated in metabolite-controlled longevity pathways. Reduction of calories by continuous energy restriction or prolonged fasting periods trigger metabolic adaptations characterized by increased amounts of circulating ketones, whereas circulating fatty acids, amino acids, glucose, and insulin are maintained at low concentrations. Adaptive cellular responses involve alterations in the ratios of adenosine monophosphate (AMP) to adenosine triphosphate (ATP), of oxidized nicotinamide adenine dinucleotide (NAD^+) to the reduced form NADH, and of acetyl-CoA to CoA. After a few hours of fasting, increased AMP to ATP ratios activate AMPK, which triggers repair and inhibits anabolic processes. Acetyl-CoA and NAD^+ serve as cofactors for epigenetic modifiers such as histone acetyltransferases and NAD^+-dependent deacetylases, the sirtuins, thus linking nutrition, energy metabolism, and post-translational modifications of histone proteins. Sirtuins deacetylate FOXOs and peroxisome proliferator-activated receptor γ coactivator 1α (PGC-1α), factors respectively involved in stress resistance and mitochondrial biogenesis. Production of ketone bodies such as β-hydroxybutyrate from fatty-acid catabolism may operate as endogenous histone deacetylase (HDAC) inhibitors and may contribute to epigenetic control of gene expression, DNA repair, and genome stability. Ketogenesis also promotes synaptic plasticity and neurogenesis by increasing the expression of brain-derived neurotrophic factor (BDNF). Periodic cycles of fasting have systemic anti-inflammatory effects and increase progenitor stem cells. Down-regulation of the insulin–IGF-1 signaling (IIS) pathway and reduction of circulating amino acids repress the activity of mTOR and its downstream effector, the ribosomal protein S6 kinase beta-1 (S6K). This mechanism inhibits global protein synthesis and promotes recycling of macromolecules by stimulation of autophagy. CR promotes the expression and activity of NRF2, which induces a number of antioxidative and carcinogen-detoxifying enzymes. Collectively, the organism responds to a low-energy challenge by minimizing anabolic processes (synthesis, growth, and reproduction), favoring maintenance systems, and enhancing stress resistance, tissue repair, and recycling of damaged molecules. Improvement in resilience, metabolic homeostasis, tissue repair, and organismal function can act as direct modifiers of the four domains of the aging phenotype: body composition (*1*); balance between energy availability and energy demand (*27*); signaling networks that maintain homeostasis (*81*); and neurodegeneration (*4*). Each of these domains can be assessed readily by routine clinical tests.

The NIA and UW CR monkey studies showed that the genetic background, age of onset of the intervention, and diet composition per se were not sufficient to explain the differences observed in longevity under both control diet and CR. Upon completion of the studies, the two research teams came to realize the notable differences in the feeding regimen (*25*), whereby UW monkeys were fed in the morning and the food was removed in the afternoon when another small treat, such as a piece of fruit, was offered. This protocol caused the animals to eat during the day and fast overnight. By contrast, NIA animals were fed twice daily, without removal of the second meal, thus virtually excluding the possibility of an overnight fast. To further shed light on the interaction between diet composition and eating patterns in a genetically homogeneous animal model, we recently compared the survival of mice fed the same diets used in the two nonhuman primate studies (NIA and UW) under AL, 30% CR, or a daily single meal feeding (MF) to match the calories consumed by the AL animals. Although both CR and MF mice showed increased life span compared with the AL groups, the effect was independent of the diet composition. Both the CR and MF mice self-imposed a TRF paradigm, and the life-span and health-span extension seen in those groups appeared to be directly proportional to the time spent fasting (*44*). Similar behavior was reported in mice under CR, which voluntarily adopted a TRF paradigm, as measured by an automated system that recorded time of food availability and consumption (*37*).

Outcomes from TRF trials in humans also appear to depend on the distribution of meals during the day and the duration of fasting (*45*–*49*). Limiting food intake to the middle of the day decreased body weight or body fat, fasting glucose

and insulin levels, insulin resistance, hyperlipidemia, and inflammation and produced mild caloric restriction and weight loss, without calorie counting (*46*, *47*, *50*, *51*). Similarly, metabolic markers were improved in a group of people eating an isocaloric diet with a bigger breakfast and a smaller dinner (*52*, *53*), and type 2 diabetic patients under hypocaloric diet obtained better metabolic outcome by eating most of their daily allotment in the first half of the day rather than divided into six meals throughout the day (*54*). On the contrary, restricting food intake to the late afternoon or evening either produced mostly null results or worsened glucose levels after eating, β cell responsiveness, blood pressure, and lipid levels (*45*, *48*, *49*). A strictly controlled feeding trial tested prediabetic subjects that were allowed to eat their meals in either a 6-hour time window in the morning (before 3 p.m.) or a 12-hour time window for 5 weeks. Early TRF ameliorated the metabolic markers of diabetes without a significant reduction of body weight (*55*). Individuals on a hypocaloric, three-meal-per-day diet lost more weight when the majority of the food was consumed in the morning, as opposed to the evening (*51*). However, no significant changes in glycemia, insulin sensitivity, or respiratory exchange ratio (RER, defined as the ratio between the amount of carbon dioxide produced and oxygen used during breathing) were observed when obese, insulin-resistant men were exposed to a hypocaloric diet with food provided in the morning (*56*). In the context of cancer, two studies found that a fasting period of more than 13 hours resulted in lower risk of breast cancer recurrence than that in subjects who fasted less than 13 hours (*57*, *58*). The discrepancies remain to be explained, but collectively, given the present body of knowledge, these studies indicate that both the amount of time spent eating during each day and the time at which food is consumed relative to the circadian rhythm are critically important to the effects of diet on health and longevity.

Intermittent and periodic fasting

An increasingly popular alternative to both continuous CR and TRF is intermittent fasting (IF), an eating pattern in which no or few calories are consumed for periods of time that range from one to several days, followed by AL feeding on the remaining days (*10*) (Fig. 1). One example of IF is the 24-hour water fast without solid food followed by a normal feeding period of 24 hours. This alternate-day fasting differs somewhat from the alternate-day modified fasting in which participants consume very few calories one day (e.g., 25% of usual intake) followed by a day without restrictions.

Both CR and fasting promote stress resistance in model organisms ranging from unicellular yeast to mammals, presumably by shifting energy from growth and reproduction to maintenance, recycling, and repair in order to increase cellular protection and survival (Fig. 2). There is an abundance of data that supports this hypothesis (*59*). From an evolutionary perspective, fasting is a natural phenomenon to which both humans and lower organisms were regularly exposed. Although many animals in the wild still encounter prolonged periods of time with little or no food, humans have rapidly transitioned into a sedentary lifestyle accompanied by a continuous and abundant supply of food. In a bygone era, the postabsorptive, or fasting, state triggered hunger and food-seeking behavior that took hours, sometimes days, to satisfy. Mechanisms to survive such periods of fasting are believed to have pleiotropic benefits. However, in our present-day civilization, hunger and food-seeking behavior result in instant gratification and alterations in eating patterns characterized by the consumption of high-energy meals as soon as the urge arises, thus negating the putative benefits that periods without food provide. This behavior might be a major contributor to the emergence of the obesity epidemic and obesity-related morbidities (*2*).

In rodents, IF extends life span (*60*) and protects against obesity, cardiovascular disease,

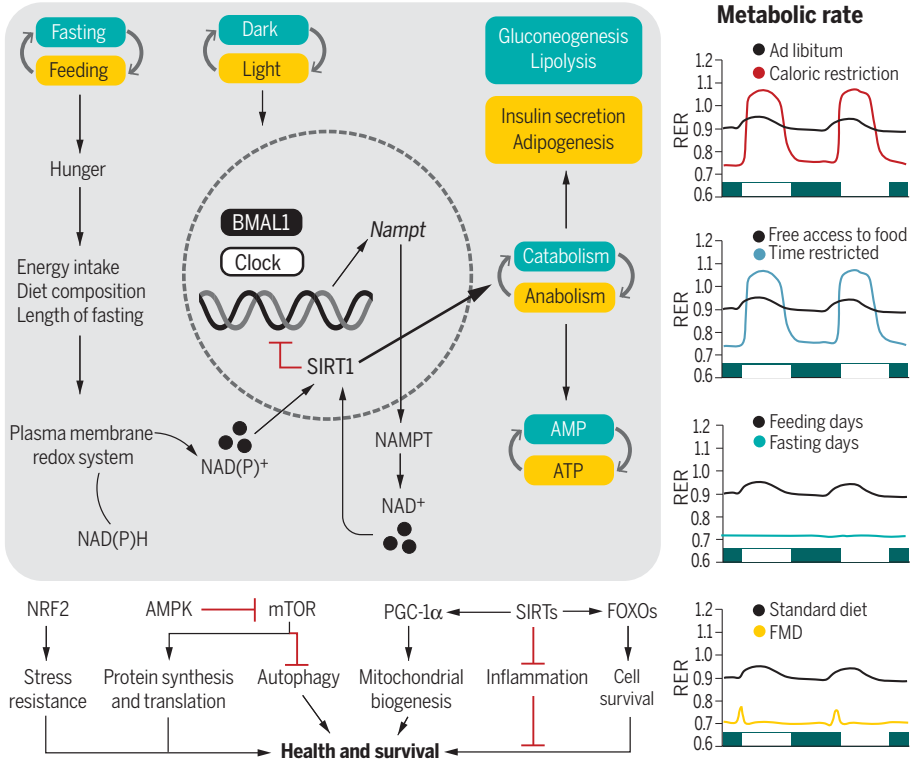

Fig. 3. Integration of the circadian rhythms and feeding-fasting cycles with metabolism. (**Left**) The transcriptional activators BMAL1 and CLOCK are at the core of a cell-autonomous molecular circuit that governs circadian rhythms. Fasting increases hunger, the extent of which depends on the overall energy intake, diet composition, and length of fasting. The internal circadian clock also increases hunger independent of food intake and other behaviors. Intermittent energy restriction increases concentrations of the plasma membrane redox system enzymes, NADH-cytochrome b5 reductase and NAD(P)H-quinone oxidoreductase, contributing to oscillations in the NAD(P)H [reduced form of $NAD(P)^+$] to $NAD(P)^+$ (nicotinamide adenine dinucleotide phosphate) ratio (*82*). The circadian rhythmicity of CLOCK and BMAL1 expression regulates the transcription of NAMPT, a key regulatory enzyme involved in the generation of NAD^+, a metabolite required for the deacetylase activity of SIRT1. Active SIRT1 influences metabolism through its effects on catabolic and anabolic reactions and mediates BMAL1 deacetylation, which inhibits the circadian clock machinery. During the active phase (yellow boxes), increased production of ATP sustains anabolic pathways. During the resting phase (green boxes), a shift toward AMP gears metabolism toward catabolic processes. These intermediate energy carriers activate downstream transcription factors, kinases, and deacetylases like NRF2, AMPK, PGC-1α, sirtuins, and FOXOs, whose activation influences health and survival. (**Right**) At the organismal level, fasting or feeding states are paralleled by changes in the metabolic rate. AL–fed animals set their RERs at around 0.9, showing an intermediate preference between fat and carbohydrate metabolism. Both CR and TRF regimens increase the amplitude of RER oscillations, characterized by higher RER (utilization of carbohydrates) during feeding and lower RER (utilization of lipids) during fasting. Under prolonged fasting, lipids are the only source of energy, as opposed to feeding time. The FMD diet results in lower RER with a slight peak after the meal. The RER traces are idealized and may be close to what is seen in nocturnal rodents.

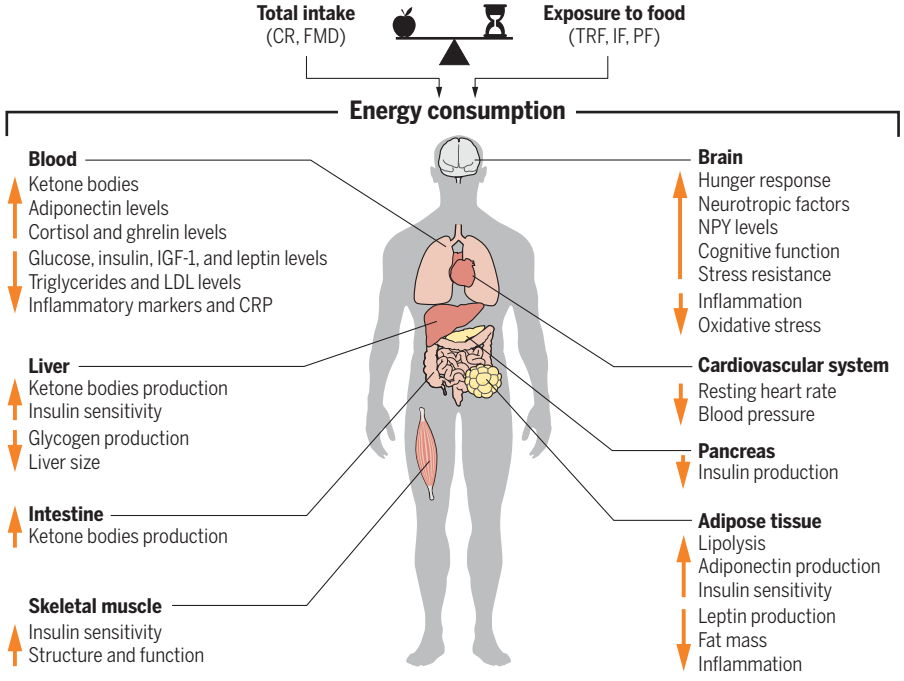

Fig. 4. Systemic effects of caloric restriction or intermittent fasting. The balance between reduction in total food intake and timing contributes to differences in energy consumption, leading to changes in circulating factors and organ function. The height of each arrow does not reflect the intensity level but instead highlights a grouping. Down arrows indicate decreased levels, and up arrows indicate increased levels.

hypertension, diabetes, and neurodegenerative diseases (*2*). It also retards the growth of tumors (*61*) and sensitizes a range of cancer cell types to chemotherapy (*62*). Additional benefits of IF include improvement in insulin sensitivity, independently of both total food intake and weight loss (*63*), and enhancement in brain function as evidenced by better performance on behavioral tests that assess motor responses to sensory stimuli (*64*). The behavioral responses to IF are associated with increased synaptic plasticity and increased production of new neurons from neural stem cells (*2*). Similar results were achieved when animals were fed a ketogenic diet (*65*) that is composed almost exclusively of fat. In mice, a ketogenic diet improved health span and delayed age-associated neurological decline, without an effect on longevity (*66*, *67*). In the study of Verdin and colleagues, feeding a ketogenic diet to mice caused weight gain without life-span extension when compared to the controls, but a cyclic ketogenic diet reduced midlife mortality, whereas in the second study, mice consuming a ketogenic diet isocaloric to that of the control group had increased life span despite having similar body weight (*66*, *67*). The benefits of fasting may be mediated by a highly conserved stress-response or nutrient-sensing pathway, whereby organismal metabolism switches from storage to mobilization, in part, by increasing autophagy and recycling at the cellular level. The ensuing production and utilization of fatty acid–derived ketones serve to preserve the brain and muscle function and allow the organism to withstand extended periods of food shortage. Production of ketone bodies (β-hydroxybutyrate and acetoacetate) by the liver and gut epithelial cells (*68*) during β-oxidation of fatty acids to acetyl–coenzyme A (CoA) or conversion of ketogenic amino acids or both, are released into the bloodstream to provide metabolic fuel to various organs (Fig. 4).

Several short-term human clinical trials have shown that alternate-day fasting can deliver benefits similar to CR in terms of weight loss and cardiometabolic health, including reduction in body weight and improved lipid profiles, lower blood pressure, and increased insulin sensitivity (*69*–*71*). In cancer patients, fasting selectively protects normal cells, but not cancerous cells, against toxicity related to chemotherapeutic agents, and fasting for up to 5 days followed by a normal diet appear to be a safe, feasible, and effective strategy in reducing common side effects associated with chemotherapy (*72*). Nevertheless, the challenges of implementing alternate-day fasting or similar interventions are real and can be a major burden by causing difficulties reminiscent to those encountered by individuals on chronic CR.

Fasting-mimicking diets

Implementing a long-term calorie restriction or complete fasting can be challenging in humans, and compliance tends to decrease with time. In a human study, the withdrawal rates of CR and periodic fasting (PF) participants from a 12-month study were about 40 and 30%, respectively (*73*). In the 2-year CALERIE clinical trial, the compliance rate was reduced to 82% with the restriction achieved averaging −12%, which was half the targeted reduction (*28*). The success of the long-term CRONies study in which individuals of the CR group ate nearly half of the calories compared to the AL subjects (1112 to 1958 kcal/day compared with 1976 to 3537 kcal/day) relied upon the strong motivation of its participants (*31*). There are side effects associated with prolonged periods of daily fasting (>15 hours) for human health. Studies associating such extended fasting periods and skipping breakfast with mortality and disease in humans have been reported (*74*, *75*), although most long-lived populations from around the globe do practice 12- to 13-hour TRF with little to no adverse effects (*5*).

To make fasting acceptable to most people, Longo and colleagues conceived a low-carbohydrate, high-fat diet that enhances compliance by avoiding complete deprivation of food. The diet coined as FMD (Fig. 1) has low calories and provides for plant-based soups, herbal tea, energy bars, nut-based snacks, and supplements to be gradually implemented in a 5-day cycle each month for 3 months (*76*). For the first day, the caloric amount is about 1090 kcal (10% protein, 56% fat, and 34% carbohydrate) and, for days 2 to 5, only 725 kcal are provided (9% protein, 44% fat, and 47% carbohydrate) (*76*). A similar diet was also designed for laboratory mice, whereby animals were allowed to consume 50% of the AL food supplied as a vegetable-based powder mixed with hydrogel on day 1 and reduced to 10% of AL on days 2 through 4. The main goal of the FMD is to maintain low circulating concentrations of IGF-1, insulin, and glucose, while increasing plasma concentrations of IGF-binding protein 1 and ketone bodies. Rejuvenating effects of FMD were initially reported through an increased number of progenitor stem cells (*77*). The FMD regimen also leads to improvement of markers of diseases and metabolic dysfunction, lowers cancer incidence, and extends health span in rodents, but without affecting maximum longevity (*76*, *78*). More recently, FMD has been proposed to exert a therapeutic, antidiabetic effect by fostering regeneration of pancreatic β cells and restoring insulin secretion and glucose homeostasis in mice through the regulation of protein kinase A (PKA) and mTOR pathways (*77*). Furthermore, this dietary intervention improves the control of autoimmune disease—for example, multiple sclerosis—through regulation of the immune system (*79*). Despite the positive results on health span, FMD did not increase maximum longevity in mice, and, when administered to very old animals, it may have been detrimental (*76*).

Conclusions

Pharmacological interventions with proven effectiveness are often accompanied by a range of unwanted side effects. Many elderly people take multiple medications, which can cause adverse geriatric outcomes linked to increases in morbidity and mortality (*80*). Dietary interventions that are accompanied by long fasting periods

have emerged as promising strategies to target a myriad of clinical parameters that constitute the foundation for metabolic syndrome, cardiovascular disease, cancer, and even neurodegenerative diseases (*2*). Although the specific mechanisms are far from being fully understood, this periodic absence of energy intake appears to improve multiple risk factors and, in some cases, reverse disease progression in mice and humans. Thus, the time is ripe to add to our understanding of the molecular mechanisms of action and efficacy of these dietary interventions to the foundation for future clinical trials. It will be important to understand and consider the differences in metabolic rate, equivalence of fasting times, role of diet composition, and the duration of the intervention as they relate to a particular disease or clinical target. Although current mouse models have not been very useful in identifying translatable therapies for some of the most common chronic diseases (e.g., Alzheimer's and cardiovascular disease), it should be acknowleged that most experiments have been limited to a few inbred stains. It may be important to move to other model organisms closer to human physiology and etiology—such as pigs, dogs, and nonhuman primates—to test, develop, and translate interventions. Strategies could use different forms of CR, FMD, PF, and TRF in combination with known pharmacological interventions and CR mimetics. We expect that these dietary interventions combined with classical pharmacology and clinical practice will yield interventions that will improve human health and enhance health span and quality of life as we grow old. Although promising, these approaches are still experimental in nature and should not be initiated without medical supervision.

REFERENCES AND NOTES

1. World Health Organization (WHO), "World health statistics 2018: Monitoring health for the SDGs" (WHO Report, WHO, 2018).
2. M. P. Mattson *et al*., *Proc. Natl. Acad. Sci. U.S.A.* **111**, 16647–16653 (2014).
3. S. Panda, *Science* **354**, 1008–1015 (2016).
4. J. R. Speakman, S. E. Mitchell, *Mol. Aspects Med.* **32**, 159–221 (2011).
5. C. Y. Liao, B. A. Rikke, T. E. Johnson, V. Diaz, J. F. Nelson, *Aging Cell* **9**, 92–95 (2010).
6. R. L. Walford, D. Mock, R. Verdery, T. MacCallum, *J. Gerontol. A Biol. Sci. Med. Sci.* **57**, B211–B224 (2002).
7. K. M. Vitousek, F. P. Manke, J. A. Gray, M. N. Vitousek, *Eur. Eat. Disord. Rev.* **12**, 338–360 (2004).
8. K. M. Vitousek, J. A. Gray, K. M. Grubbs, *Eur. Eat. Disord. Rev.* **12**, 279–299 (2004).
9. K. M. Vitousek, *Eur. Eat. Disord. Rev.* **12**, 275–278 (2004).
10. V. D. Longo, S. Panda, *Cell Metab.* **23**, 1048–1059 (2016).
11. P. Rous, *J. Exp. Med.* **20**, 433–451 (1914).
12. T. B. Osborne, L. B. Mendel, E. L. Ferry, *Science* **45**, 294–295 (1917).
13. C. M. McCay, M. F. Crowell, L. A. Maynard, *J. Nutr.* **10**, 63–79 (1935).
14. L. M. Redman *et al*., *Cell Metab.* **27**, 805–815.e4 (2018).
15. L. Fontana, L. Partridge, V. D. Longo, *Science* **328**, 321–326 (2010).
16. C. López-Otín, M. A. Blasco, L. Partridge, M. Serrano, G. Kroemer, *Cell* **153**, 1194–1217 (2013).
17. D. K. Ingram, G. S. Roth, *Ageing Res. Rev.* **20**, 46–62 (2015).
18. F. Madeo, F. Pietrocola, T. Eisenberg, G. Kroemer, *Nat. Rev. Drug Discov.* **13**, 727–740 (2014).
19. J. R. Speakman, C. Hambly, *J. Nutr.* **137**, 1078–1086 (2007).
20. D. K. Ingram, R. de Cabo, *Ageing Res. Rev.* **39**, 15–28 (2017).
21. C. Y. Liao *et al*., *Aging Cell* **10**, 629–639 (2011).
22. S. J. Mitchell *et al*., *Cell Metab.* **23**, 1093–1112 (2016).
23. R. J. Colman *et al*., *Science* **325**, 201–204 (2009).
24. J. A. Mattison *et al*., *Nature* **489**, 318–321 (2012).
25. J. A. Mattison *et al*., *Nat. Commun.* **8**, 14063 (2017).
26. L. K. Heilbronn *et al*., *JAMA* **295**, 1539–1548 (2006).
27. C. K. Martin *et al*., *JAMA Intern. Med.* **176**, 743–752 (2016).
28. E. Ravussin *et al*., *J. Gerontol. A Biol. Sci. Med. Sci.* **70**, 1097–1104 (2015).
29. J. Rochon *et al*., *J. Gerontol. A Biol. Sci. Med. Sci.* **66**, 97–108 (2011).
30. D. C. Willcox, B. J. Willcox, W.-C. Hsueh, M. Suzuki, *Age (Dordr.)* **28**, 313–332 (2006).
31. L. Fontana, T. E. Meyer, S. Klein, J. O. Holloszy, *Proc. Natl. Acad. Sci. U.S.A.* **101**, 6659–6663 (2004).
32. L. Fontana, S. Klein, *JAMA* **297**, 986–994 (2007).
33. E. M. Mercken *et al*., *Aging Cell* **12**, 645–651 (2013).
34. D. M. Kristan, *Age (Dordr.)* **30**, 147–156 (2008).
35. N. D. Hunt *et al*., *Age (Dordr.)* **34**, 1453–1458 (2012).
36. A. J. Dirks, C. Leeuwenburgh, *Mech. Ageing Dev.* **127**, 1–7 (2006).
37. V. A. Acosta-Rodríguez, M. H. M. de Groot, F. Rijo-Ferreira, C. B. Green, J. S. Takahashi, *Cell Metab.* **26**, 267–277.e2 (2017).
38. F. J. Roe *et al*., *Food Chem. Toxicol.* **33** (suppl. 1), S1–S100 (1995).
39. S. M. Solon-Biet *et al*., *Cell Metab.* **19**, 418–430 (2014).
40. M. Hatori *et al*., *Cell Metab.* **15**, 848–860 (2012).
41. H. Sherman *et al*., *J. Cell. Mol. Med.* **15**, 2745–2759 (2011).
42. L. N. Woodie *et al*., *Metabolism* **82**, 1–13 (2018).
43. A. Chaix, A. Zarrinpar, P. Miu, S. Panda, *Cell Metab.* **20**, 991–1005 (2014).
44. S. J. Mitchell *et al*., *Cell Metab.* S1550-4131(18)30512-6 (2018).
45. O. Carlson *et al*., *Metabolism* **56**, 1729–1734 (2007).
46. S. Gill, S. Panda, *Cell Metab.* **22**, 789–798 (2015).
47. T. Moro *et al*., *J. Transl. Med.* **14**, 290 (2016).
48. K. S. Stote *et al*., *Am. J. Clin. Nutr.* **85**, 981–988 (2007).
49. G. M. Tinsley *et al*., *Eur. J. Sport Sci.* **17**, 200–207 (2017).
50. K. Gabel *et al*., *Nutr. Healthy Aging* **4**, 345–353 (2018).
51. H. A. Raynor, F. Li, C. Cardoso, *Physiol. Behav.* **192**, 167–172 (2018).
52. D. Jakubowicz, M. Barnea, J. Wainstein, O. Froy, *Obesity (Silver Spring)* **21**, 2504–2512 (2013).
53. T. Yoshizaki *et al*., *Eur. J. Appl. Physiol.* **113**, 2603–2611 (2013).
54. H. Kahleova *et al*., *Diabetologia* **57**, 1552–1560 (2014).
55. E. F. Sutton *et al*., *Cell Metab.* **27**, 1212–1221.e3 (2018).
56. R. I. Versteeg *et al*., *J. Biol. Rhythms* **32**, 130–142 (2017).
57. C. R. Marinac *et al*., *Cancer Epidemiol. Biomarkers Prev.* **24**, 783–789 (2015).
58. C. R. Marinac *et al*., *JAMA Oncol.* **2**, 1049–1055 (2016).
59. T. Finkel, *Nat. Med.* **21**, 1416–1423 (2015).
60. C. L. Goodrick, D. K. Ingram, M. A. Reynolds, J. R. Freeman, N. Cider, *Mech. Ageing Dev.* **55**, 69–87 (1990).
61. K. Xie *et al*., *Nat. Commun.* **8**, 155 (2017).
62. C. Lee *et al*., *Sci. Transl. Med.* **4**, 124ra27 (2012).
63. R. M. Anson *et al*., *Proc. Natl. Acad. Sci. U.S.A.* **100**, 6216–6220 (2003).
64. R. Singh *et al*., *Age (Dordr.)* **34**, 917–933 (2012).
65. J. A. Baur *et al*., *Nature* **444**, 337–342 (2006).
66. J. C. Newman *et al*., *Cell Metab.* **26**, 547–557.e8 (2017).
67. M. N. Roberts *et al*., *Cell Metab.* **27**, 1156 (2018).
68. P. Puchalska, P. A. Crawford, *Cell Metab.* **25**, 262–284 (2017).
69. V. A. Catenacci *et al*., *Obesity (Silver Spring)* **24**, 1874–1883 (2016).
70. K. K. Hoddy *et al*., *Obesity (Silver Spring)* **22**, 2524–2531 (2014).
71. K. A. Varady, S. Bhutani, E. C. Church, M. C. Klempel, *Am. J. Clin. Nutr.* **90**, 1138–1143 (2009).
72. F. M. Safdie *et al*., *Aging* **1**, 988–1007 (2009).
73. J. F. Trepanowski *et al*., *JAMA Intern. Med.* **177**, 930–938 (2017).
74. Y. Yokoyama *et al*., *Yonago Acta Med.* **59**, 55–60 (2016).
75. I. Uzhova *et al*., *J. Am. Coll. Cardiol.* **70**, 1833–1842 (2017).
76. S. Brandhorst *et al*., *Cell Metab.* **22**, 86–99 (2015).
77. C.-W. Cheng *et al*., *Cell* **168**, 775–788.e12 (2017).
78. M. Wei *et al*., *Sci. Transl. Med.* **9**, eaai8700 (2017).
79. I. Y. Choi *et al*., *Cell Reports* **15**, 2136–2146 (2016).
80. A. J. McLean, D. G. Le Couteur, *Pharmacol. Rev.* **56**, 163–184 (2004).
81. B. A. Rikke *et al*., *Mech. Ageing Dev.* **124**, 663–678 (2003).
82. A. Diaz-Ruiz *et al*., *Aging Cell* **17**, e12767 (2018).

ACKNOWLEDGMENTS

We wish to thank L. Brick for excellent assistance with the art production of figures. We apologize for the omission of relevant works owing to space constraints. **Funding**: This work was supported by the Intramural Research Program of the NIA-NIH. **Competing interests:** The authors declare no competing interests, financial or otherwise.

10.1126/science.aau2095

REVIEW

The gut microbiota at the intersection of diet and human health

Christopher L. Gentile and Tiffany L. Weir*

Diet affects multiple facets of human health and is inextricably linked to chronic metabolic conditions such as obesity, type 2 diabetes, and cardiovascular disease. Dietary nutrients are essential not only for human health but also for the health and survival of the trillions of microbes that reside within the human intestines. Diet is a key component of the relationship between humans and their microbial residents; gut microbes use ingested nutrients for fundamental biological processes, and the metabolic outputs of those processes may have important impacts on human physiology. Studies in humans and animal models are beginning to unravel the underpinnings of this relationship, and increasing evidence suggests that it may underlie some of the broader effects of diet on human health and disease.

Controversy regarding what constitutes a healthful diet has persisted since the advent of nutrition as a scientific discipline and establishment of government nutritional guidelines (*1*). The emergence of the gut microbiota as a key regulator of health and disease has further complicated this issue. A mutualistic relation exists between diet and the gut microbiota so that dietary factors are among the most potent modulators of microbiota composition and function. Intestinal microbes in turn influence the absorption, metabolism, and storage of ingested nutrients, with potentially profound effects on host physiology.

The human gut microbiota consists of trillions of microbial cells and thousands of bacterial species. The specific compositional features differ among individuals, and although the mature microbiota is fairly resilient, it can be altered within individuals by both internal and external stimuli. Interindividual variability and the plasticity of the gut microbiota have hindered efforts to identify a "healthy" microbiota, although markers of microbial stability, such as richness and diversity, are often used as indicators of gut health because of their inverse association with chronic disease and metabolic dysfunction (*2*). Microbiota plasticity also creates a distinct opportunity; by manipulating various external factors, the potential exists to reshape the architecture and biological outputs of gut microbes for improved human health.

Diet is an important external factor affecting the gut microbiota, and diet's ability to alter microbial ecology was first recognized more than a century ago (*3*). Transient diet-induced alterations occur independently of body weight and adiposity and are detectable in humans within 24 to 48 hours after dietary manipulation (*4*). The effects of diet on microbial ecology are unsurprising when one considers that gut microbes, like their human hosts, use ingested nutrients as fuel for fundamental biological processes. Thus, changes to host dietary patterns alter bacterial metabolism and favor species most suited to use consumed fuel sources. What was not predicted after the initial observations a century ago, and has only come to light in recent decades, is the important effect that diet-induced changes in microbial structure have on human physiology and disease processes.

Department of Food Science and Human Nutrition, Colorado State University, Fort Collins, CO 80526, USA.
*Corresponding author. Email: tiffany.weir@colostate.edu

Nutrients

Microbiota-accessible carbohydrates

When studied in isolation, each of the major macronutrients and numerous micronutrients have been shown to modify the gut microbiome. Among the macronutrients, the effects of dietary carbohydrates (CHO) are best characterized. Simple CHO such as sucrose, both alone and as part of a Western-style high-fat high-sugar diet, cause rapid microbiota remodeling and metabolic dysfunction in experimental animals (*5*, *6*). Complex CHO exhibit a diverse array of monosaccharide linkages, many of which are indigestible by humans. Gut microbes, on the other hand, possess several hundredfold more CHO-degrading enzymes and thus use indigestible CHO as their primary energy source. The term "fiber" is commonly used to describe these indigestible CHO, although this designation is problematic given that some fibers are not used by gut microbes (such as cellulose), whereas other readily fermented CHO fall outside of the definition of fiber (such as resistant starches). Sonnenburg and colleagues (*7*) recently proposed the term "microbiota-accessible carbohydrate," or MAC, to describe CHO that are metabolically available to gut microbes, and we use that terminology hereafter.

Several lines of evidence indicate that alterations in dietary MACs have important effects on microbiota composition and function. Agronomic and nomadic hunter-gatherer societies that consume high levels of MACs display greater microbial richness and diversity as compared with those of industrialized societies (*8*, *9*). Diets high in MACs alter microbiota composition in humans within days or weeks (*10*, *11*). Mice fed a diet low in MACs experience decreases in numerous taxa, and loss of diversity is compounded over several generations of offspring and not recovered after reintroduction of MACs (*7*, *9*). Reductions in bacterial abundance with low MAC intake are not observed uniformly across all bacterial taxa because certain bacterial species that typically consume dietary glycoproteins can also use glycoproteins of the intestinal mucus layer as an alternative energy source. Over-grazing of the mucus layer by these species may be an important consequence of MAC restriction, as chronic foraging has been shown to compromise barrier integrity and enhance inflammation and pathogen susceptibility in animal studies (*12*, *13*).

Another consequence of MAC restriction is a reduction in short chain fatty acid (SCFA) production. SCFAs, the primary end products of bacterial fermentation, represent an excellent example of mutualism between humans and their bacterial symbionts. MACs provide a critical energy source for gut bacteria, and the consequent production of SCFAs benefits the host by serving as both recovered energy from otherwise inaccessible carbohydrates as well as potent regulatory molecules with vast physiological effects (Fig. 1). SCFAs signal via the central nervous system and several G protein–coupled receptors (GPCRs) to modulate a range of physiological processes, including energy homeostasis, lipid and carbohydrate metabolism, and suppression of inflammatory signals (*14*, *15*). Two SCFAs, butyrate and propionate, also act as histone deacetylase inhibitors, suggesting that they can epigenetically influence host gene expression (*16*). Thus, decreased SCFA production and increased mucus foraging represent two microbiota-dependent consequences of low MAC intake, and it is tempting to speculate that these processes underlie the long-recognized health benefits of high-fiber diets. It should be noted that the extent of mucus foraging in humans, and its importance in human disease processes, have not been directly examined. Furthermore, despite the protective effects of SCFAs observed in preclinical models, obese humans and genetically obese mice display increased fecal and caecal concentrations of SCFA (*17*), suggesting that they may contribute to enhanced energy harvest. Thus, energy balance status of an individual may determine whether the beneficial effects of SCFA signaling on metabolism outweigh the additional calories harvested (*18*).

It is important to recognize that MACs represent a diverse group of oligo- and polysaccharides with considerable structural heterogeneity and diverse effects on microbial ecology. A specific subset of MACs have been termed "prebiotic," which originally described a class of oligosaccharides that selectively enhance growth of *Bifidobacterium* and *Lactobacillus* (*19*). These canonical prebiotics, primarily fructo- and galactooligosaccharides of varying chain lengths, have been shown to alter members of the human gut microbiota and modulate inflammation and

markers of metabolic syndrome (*20*, *21*). Despite promising data on oligosaccharide use for appetite regulation and obesity-related complications, therapeutic efficacy of these prebiotics in treating gastrointestinal conditions is variable (*22*). Several studies have shown that restricting oligosaccharides and other fermentable sugars [a low-FODMAPs (fermentable oligosaccharides, disaccharides, monosaccharides, and polyols) diet] alleviates symptoms of irritable bowel syndrome (*23*).

Technological advances that allow for holistic examination of microbial responses to dietary components have led to a recent expansion of the prebiotic concept (*24*). Although selective use of a dietary substrate by specific microbial populations is still required, the list of potential substrates and microbial targets is more inclusive. For example, candidate prebiotic substrates now include nonpolysaccharide dietary components such as polyunsaturated fats, conjugated linoleic acid, and phytochemicals/phenolics (*24*, *25*). Likewise, prebiotics may be selectively used by bacteria other than *Bifidobacterium* and *Lactobacillus*, provided the net effects on host health are beneficial. As a result of these expanded inclusion criteria, studies that characterize distinct host-microbe-substrate interactions are of particular interest.

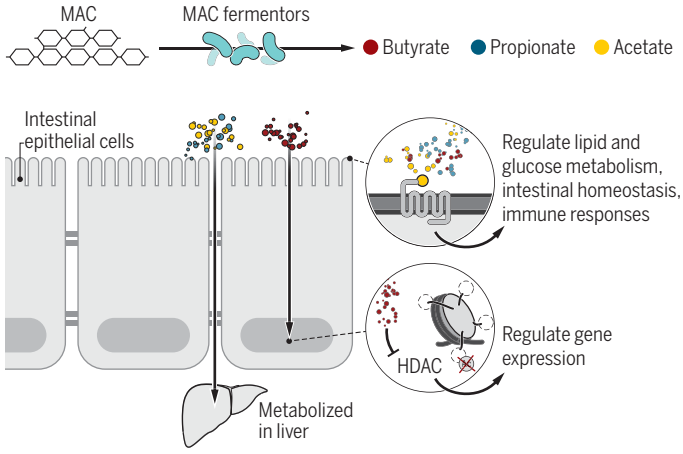

Fig. 1. MAC fermentors produce SCFAs that can have multiple interactions with host tissues. Butyrate is taken up by epithelial cells and used as a primary source of energy for these cells. Butyrate (and to a lesser degree, propionate) can block histone deacetylases (HDAC) to regulate gene expression. All of the SCFAs can bind with varying affinities to G protein receptors in the intestines and other cells to regulate energy metabolism, intestinal homeostasis, and immune responses. Acetate and propionate are primarily metabolized in the liver, where propionate is used as a substrate for gluconeogenesis and acetate is used as an energy source and for fatty acid synthesis.

Dietary fats

An increase in dietary fat also substantially alters microbiota composition. Experimental mice fed a high-fat diet (40 to 80% total caloric intake) exhibit decreases at the phyla-level in Bacteroidetes and increases in Firmicutes and Proteobacteria. These changes were observed in mice resistant to weight gain, implying a direct effect of dietary lipids on the microbiota (*26*, *27*). Germ-free (GF) mice are protected from the metabolic consequences of high-fat diets, suggesting that gut microbes may be important mediators of lipid-induced metabolic dysfunction (*28*). The metabolic protection in GF mice may be due to enhanced fat oxidation or reduced absorption in the small intestine (*29*). Microbes in the small intestine were recently found to be highly susceptible to fat load and essential for lipid digestion and absorption (*17*). These data suggest that regional specificity of microbiota composition may have important functional consequences and highlight the need for spatially distinct analyses along the gastrointestinal tract. Importantly, not all studies have found that GF mice are protected from the metabolic consequences of high-fat feeding, and the cholesterol content of the diet may be an important determining factor (*30*). As with carbohydrates, lipid-mediated effects on the microbiota are dependent on the lipid type and source. For example, mice fed an isocaloric diet rich in long-chain saturated fats derived primarily from meat products displayed greater insulin resistance and adipose tissue inflammation as compared with that of mice fed a high–fish oil diet. These metabolic disturbances were accompanied by reductions in phylogenetic diversity in the saturated fat–fed mice, and receipt of transplanted microbiota from mice fed fish oil abrogated saturated fat–induced inflammation (*31*). Furthermore, transgenic mice that constitutively produce ω3 polyunsaturated fatty acids possess a microbiome with enhanced phylogenetic diversity that offers protection against the metabolic consequences of a high-saturated-fat, high-sugar diet (*32*).

One mechanism by which gut microbes may mediate the metabolic consequences of high-fat intake is through translocation of lipopolysaccharide (LPS), a cell-wall component of gram-negative bacteria. Increases in circulating LPS have been reported in humans after a high-fat meal, with exacerbated effects in obese individuals (*33*). Once in circulation, LPS elicits a potent inflammatory response via Toll-like 4 receptor signaling, which has been implicated in the development of cardiovascular and metabolic disease (*34*). Although existing data that link circulating LPS to cardiometabolic disturbances are compelling, progress in this area has been hindered by the inability of available assays to distinguish between stimulatory and non-stimulatory LPS, as well as by circulating inhibitors that reduce accuracy of LPS quantification (*35*). Furthermore, although circulating LPS has been reported in obese individuals and correlates with markers of metabolic disease, a direct causal role in human disease has not been examined (*36*).

Primary bile acids are produced in the liver from cholesterol and facilitate the digestion of dietary lipids. Once generated, primary bile acids are secreted into the small intestine, where they facilitate the solubilization and absorption of lipids. Microbial alterations to primary bile acids include hydrolysis of conjugated amino acids, 7α/β-dehydroxylation, and oxidation and epimerization of hydroxyl groups at various positions (Fig. 2) (*37*). GF mice display increased abundance and reduced diversity of bile acids compared with that of conventional mice (*38*), and enrichment of specific secondary bile acids has been observed in colorectal cancer cases (*39*). In addition to their canonical role in aiding lipid digestion, bile acids act as dynamic signaling molecules via the farnesoid X receptor (FXR) and the G protein–coupled bile acid receptor 1 (TGR5). Like SCFAs, bile acids have been shown to regulate energy homeostasis, glucose metabolism, and innate immunity (*40*). More recent data suggest that gut microbes also have direct effects on FXR and TGR5 expression and signaling (*40*, *41*). Thus, the gut microbiota helps regulate bile acid composition, abundance, and signaling, and this regulation may have important implications not only for lipid digestion and absorption but also for the development and prevention of metabolic disease. Several bile acid–directed therapeutics are currently being examined for obesity-related conditions, and as the clinical utility of these therapeutics is tested, it will be important to consider microbiota composition in determining interindividual efficacy and safety.

Dietary protein

Dietary proteins also modulate microbial composition and metabolite production, with amino acids providing gut microbes essential carbon and nitrogen. Amino acid catabolism yields numerous metabolites that affect host physiology (Fig. 3). For example, although SCFAs are derived mainly from MAC fermentation, they are also by-products of bacterial metabolism of amino acids. The relative contribution of amino acid metabolism to total SCFA production is unclear, but total protein and fiber intake are influencing factors. Additional metabolites of amino acid catabolism include branched chain fatty acids, indoles, phenols, ammonia, and amines, all of which can affect human health. For example, phenols, indoles, and amines can combine with nitric oxide to form genotoxic N-nitroso compounds that are associated with gastrointestinal

cancers in human populations (*42*). By contrast, indolepropionic acid, a microbial metabolite of tryptophan, maintains intestinal homeostasis and protects from experimental colitis (*43*). Indole-3-acetate, another bacterially derived tryptophan metabolite, was recently shown to reduce hepatocyte and macrophage inflammation (*44*). The source of dietary protein also determines the nature of microbiota-dependent metabolic outputs. This is perhaps best exemplified by production of the compound trimethylamine oxide (TMAO) from the amino acid L-carnitine, which is abundant in animal but not vegetable protein. TMAO is predictive of cardiovascular events in various populations (*45*) and has been implicated in the development of fatty liver disease (*46*). A recently developed inhibitor of TMAO production reduced platelet aggregation and thrombus formation in experimental animals, enhancing the potential of TMAO-directed therapies (*47*). Collectively, these data highlight that the vast effects of microbiota-derived amino acid metabolites on host physiology are only now beginning to emerge and represent an area ripe for future research.

Micronutrients

In addition to major macronutrients, the gut microbiota regulates both synthesis and metabolic output of various micronutrients. The B vitamins, for example, can be synthesized by more than 100 bacterial species, and analysis of the synthesis pathways involved suggests that bacteria cooperatively exchange B vitamins to ensure survival (*48*). The relation between vitamins and the microbiota appears to be bidirectional because several vitamins supplied by the host shape microbial composition and provide critical functions within bacteria. Riboflavin, for example, regulates bacterial extracellular electron transfer and redox status (*49*), and vitamin D and its receptor help regulate intestinal inflammation, in part by shaping microbial ecology (*50*). Like vitamins, metals are required cofactors for numerous mammalian and bacterial physiological processes and can dramatically alter the microbiota. Zinc deficiency, which is a strong risk factor for potentially fatal childhood diarrhea in developing countries, enhances populations of pathogenic bacteria (*51*). Iron is an essential micronutrient for pathogen growth, and restricting iron intake is an effective form of nutritional immunity against pathogen establishment. Human breastmilk transmits lactoferrin, an iron-binding glycoprotein, to protect the undeveloped infant gut from pathogen colonization, and iron supplementation in infants can increase pathogen growth and intestinal inflammation (*52*). Despite observed bacteriogenic effects of iron, supplementation in experimental mice was recently found to suppress virulence of the rodent enteric pathogen *Citrobacter rodentium*, essentially converting the pathogen to a commensal microbe (*53*). High salt intake has been implicated in the cardiovascular consequences of Western diets. Recent data suggest that the hypertensive effects of high-salt diets in experimental animals and humans are mediated by reduced levels of *Lactobacillus* and subsequent increases in proinflammatory T helper 17 cells (*54*). Collectively, the interactions identified thus far between the microbiota and micronutrients, as well as the myriad other interactions that undoubtedly await discovery, represent an important avenue of future research. The data also highlight the importance of monitoring micronutrient composition in microbiota-focused dietary intervention studies and beget the need for clinical trials in populations at risk for vitamin and mineral deficiencies.

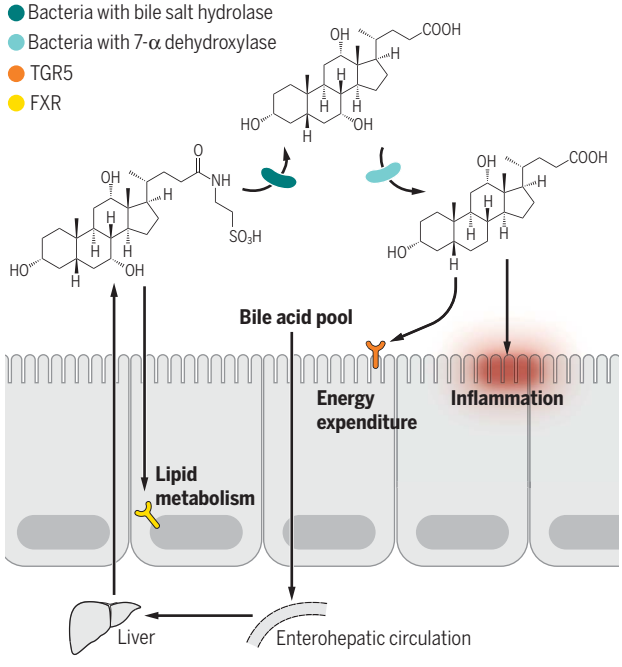

Fig. 2. Gut bacteria play an important role in bile acid modification. Primary bile acids deposited into the small intestine are deconjugated and dehydroxylated by enzymes from bile-modifying bacteria. These changes influence total bile acid pools available for reabsorption and recycling through enterohepatic circulation. In addition, bile acids can act as regulatory molecules by binding to cell surface or nuclear receptors, influencing host factors such as energy expenditure and lipid metabolism.

Food additives

The impact of food additives on the gut microbiota and intestinal homeostasis represents another understudied area with potential implications for human health. Although microbial and health consequences of Western diets are typically attributed to macronutrient composition, several studies suggest that the detrimental effects may be driven by food additives. For example, administration of two dietary emulsifiers, polysorbate-80 and carboxymethyl cellulose, induced obesity, intestinal inflammation, and metabolic dysfunction in the absence of other dietary manipulations in mice. The microbiota was both required and sufficient for these effects as GF mice were protected from detrimental consequences, and microbiota transfer from emulsifier-treated mice was sufficient to recapitulate the metabolic derangements (*55*). These results are particularly striking given the wide range of foods in which these emulsifiers are found (such as gluten-free and reduced-fat products, ice cream, wine, and pickles), and that the doses used in the study are well within the amount consumed by humans. In addition to emulsifiers, non-nutritive sweeteners (NNS) have been linked to gut-associated metabolic alterations. In a series of experiments that used rodents and humans, NNS consumption induced glucose intolerance in a microbiota-dependent manner (*56*). However, the collective data regarding the effects of NNS on the gut microbiota and metabolic function are equivocal, and it is important to recognize that NNS represent a broad class of substances with tremendous structural and functional diversity. Thus, the physiological effects of a particular NNS should not be generalized, and additional human intervention studies examining the impact of individual NNS are needed.

Dietary patterns

One obvious limitation to studying the health effects of individual nutrients is that those nutrients are rarely consumed in isolation; thus, experimental manipulation of an individual macronutrient invariably alters intake of other macronutrients that may have metabolic effects unto themselves. For example, high-fat diets are commonly low in fiber, and it may be this latter feature, and its downstream effects on the microbiota, that drives some of the metabolic consequences of the diet rather than the elevated fat content by itself. Given the limitations of studying nutrients in isolation, there is increasing focus away from this experimental reductionism and toward examining the health effects of broader dietary patterns.

Ketogenic diet

The ketogenic diet is characterized by very low CHO consumption (5 to 10% of total caloric intake), sufficient to enhance ketone production. It was originally developed as a treatment for refractory childhood epilepsy, and response of the gut microbiota to a ketogenic diet appears to play a role in the efficacy of this intervention in epileptic children (*57*). Animal data suggest that the neuroprotective effects are mediated through modulation of specific gut bacteria that enhance

hippocampal γ-aminobutyric acid/glutamate levels (*58*). In recent years, the benefits of ketogenic diets have extended beyond seizure control, and the diets are commonly adopted for weight loss and have been shown to enhance longevity and reduce disease onset in experimental animals (*59*). Conversely, some human studies that examined ketogenic diets suggest negative impacts on microbial ecology and gut health. However, these studies were conducted in small cohorts with specific metabolic conditions (*60*, *61*), limiting generalization to larger populations. Because modified versions of ketogenic diets are rapidly growing in popularity, it is necessary to examine their long-term safety and impacts on the gut microbiota and intestinal environment.

Paleolithic diet

The Paleolithic diet, which seeks to mimic the dietary patterns of pre-agricultural societies, is often implemented as a high-protein/low-CHO diet for weight loss by individuals in Western societies. Clinically, the Paleolithic diet is being explored for management of inflammatory bowel disease (IBD), and although initial findings were promising, the study was conducted in a small cohort, and additional nutrient supplementation was required to curtail iron and vitamin D deficiencies (*62*). Although there is a paucity of intervention studies that examine microbiota-specific effects of replacing a Western diet with a Paleolithic diet, comparative studies between industrialized populations and modern-day hunter-gatherer societies have provided some insight. The Hadza, a hunter-gatherer tribe whose lifestyle has been described as mimicking that of Paleolithic communities, experience few metabolic diseases that plague industrialized societies, and their microbiota is characterized by greater microbial diversity (*9*, *63*). However, it is difficult to ascribe these microbiota and health benefits to lower CHO intake by itself because the Hadza diet is rich in plant-derived MACs, and their microbiota contains a high abundance of CHO-metabolizing bacteria (*63*). Furthermore, diets of Western societies lack many of the traditional foods and seasonal variation of the Hadza, highlighting the limited parallels between traditional hunter-gatherer diets and modern-day Paleolithic diets adopted by individuals in Western societies.

Vegan/vegetarian diets

Plant-rich diets have long been a key feature of dietary recommendations, and vegan/vegetarian diets are associated with positive health outcomes and reduced disease risk (*64*). These beneficial effects may extend to the gut microbiota. Plant-based foods constitute the primary source of dietary MACs, and the microbiota of individuals who consume vegetarian or predominantly plant-based diets exhibit greater capacity for MAC fermentation. However, some intervention and cross-sectional studies have observed only modest microbiota differences between omnivores and vegetarians and suggest that the effects of dietary pattern on the microbiota are greatest at the genus and species level and relatively minimal on broader compositional features, such as diversity and richness (*65*–*67*). Despite the absence of global microbiota compositional shifts, the species-level changes appear sufficient to alter metabolic outputs because SCFA production is typically increased in vegetarians. The extent to which these microbial metabolic outputs mediate the beneficial effects of vegetarian diets is unclear.

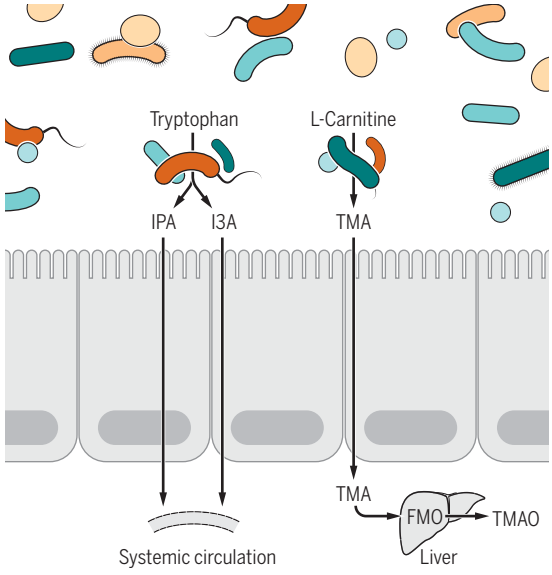

Fig. 3. Interactions between amino acids and the gut microbiota. Microbial metabolism of the amino acid carnitine produces trimethylamine (TMA), which is subsequently oxidized in the liver to TMAO in a reaction catalyzed by flavin-containing monooxygenase (FMO). Increased levels of circulating TMAO have been linked to metabolic disease. Gut microbes metabolize the amino acid tryptophan into various substances, including indolepropionic acid (IPA) and indole-3-acetic acid (I3A), both of which can enter the general circulation. The metabolic effects of IPA, I3A, and other microbially derived amino acid metabolites are only now beginning to emerge.

In addition to providing MACs, plant-based foods provide a diverse source of phytochemicals, biologically active small molecules with the potential to affect human health. Within the plant, many phytochemicals are glycosylated, reducing their bioavailability and bioactivity when consumed. As a result, phytochemicals often reach the lower intestinal tract and can have direct antimicrobial and anti-inflammatory effects in the gut. In addition, phytochemicals can be modified by microbial enzymes into metabolites with increased bioavailability and altered bioactivity (*68*). A prominent example includes the bioconversion of naturally occurring soy isoflavones to equol (*69*), which exhibits increased bioavailability compared with that of the parent compounds. Thus, microbe-mediated alterations in phytochemical bioavailability may represent an additional mechanism underlying the beneficial effects of plant-based diets.

Mediterranean diet

The Mediterranean diet emphasizes consumption of a variety of foods (fruits, vegetables, legumes, unsaturated fats, and limited red meat intake) rather than the exclusion of particular food groups or confinement to specific macronutrient ratios. Numerous epidemiologic studies and clinical trials have demonstrated that following a Mediterranean diet reduces the risk of all-cause mortality and multiple chronic diseases (*64*, *70*). Although only a few of these studies have examined the effects on microbiota composition, existing data indicate that the Mediterranean diet elicits favorable microbiota profiles and metabolite production, with microbial diversity paralleling levels of dietary adherence (*71*–*73*). For example, closer adherence to the Mediterranean dietary pattern was associated with lower ratios of Firmicutes:Bacteroidetes and higher fecal SCFA detection (*73*). Collectively, these studies suggest that emphasis should be placed on sufficient inclusion of a variety of plant-based foods rather than exclusion of animal-based food and supports the concept that diet diversity is a driver of microbiota stability.

Microbiota-targeted diets

A number of microbiota-targeted diets have recently emerged with the growing public awareness of the gut microbiota and its potential to influence human health. Although the scientific premise of many of these diets is logically rooted in prevailing paradigms, they fail to acknowledge the many gaps in our knowledge regarding diet-microbiome-host interactions. The specific carbohydrate diet (SCD) restricts complex carbohydrates and refined sugar under the premise that these compounds are malabsorbed in the gastrointestinal tract, leading to bacterial overgrowth and gut dysbiosis. Like the low-FODMAPs diet, there is some evidence to suggest that individuals with IBD experience benefits when following a SCD (*74*), although long-term adherence to this restrictive diet is difficult. A derivative of the SCD is the gut and psychology syndrome (GAPS) diet, which expands beyond dietary exclusion of specific foods by adding foods claimed to have gut-healing potential. This includes consumption of nutrient-rich bone broth to regenerate the intestinal lining and antimicrobial foods such as garlic to reduce pathogen loads. Although this diet is frequently prescribed by alternative medicine practitioners for conditions ranging from autism to depression, there is only anectotal rather than scientific evidence to support that adherence produces the intended effects on health outcomes. A study supporting the use of a similar diet was recently retracted from the journal *PLOS ONE* because of several issues, including the absence of a control group, inadequate description of methods, and lack of microbiota analysis (*75*). Last, although not a diet in itself, there is a common belief that probiotic-containing fermented foods modify the

gut microbiota and confer host health benefits. However, fermented foods rarely contain adequate amounts of specific probiotic organisms. Moreover, there is limited evidence for the role of probiotics as modulators of the human gut microbiota, and recent data suggest that even supplemental quantities of probiotics exert limited effects on human gut ecology (*76*) and may even be detrimental with regard to recolonization of the microbiota after antibiotic use (*77*). With the exception of yogurt, benefits of fermented foods have not been clinically tested, and studies examining the effects of yogurt for weight management are equivocal (*78*). Evidence suggests that acetic acid, a metabolic by-product of fermentation, suppresses appetite and reduces postprandial insulin response and glucose excursions (*79*). In addition, some fermented foods have higher nutrient content and elevated B vitamins as compared with those of nonfermented forms of the same food (*80*), suggesting that any added benefits may be due to microbial metabolites rather than the microbes themselves.

Perspectives and future directions

Data collected over the past decade have identified the gut microbiota as an important factor defining interindividual variation in disease risk and dietary response. The ascension of the gut microbiota as a key regulator of human physiology has generated tremendous excitement within and beyond the scientific community, as exemplified by the exponential increase in microbiota-focused publications and by the growth of the probiotic market into a multibillion-dollar industry. The rapidity of this ascension, however, poses a substantial challenge in that commercialization and popularity of microbiota-targeted therapies have accelerated despite the fact that fundamental questions regarding the microbiota and its relation to diet and human health remain unresolved. For example, much of the current data linking the microbiota to disease processes have been generated in animal models, and human feeding studies are needed to confirm their relevance before they can be translated to practical nutrition advice.

The plasticity of the microbiota makes microbiome-targeted interventions an attractive approach for disease prevention and treatment. However, despite reported alterations of the gut microbiota in response to short-term dietary interventions, long-term dietary patterns are associated with stable microbiota conformations that are difficult to alter (*81*–*83*). Additionally, diet-responsive members of the microbiota often represent a small proportion of the total community, necessitating a better understanding of whether changes in tractable populations are sufficient to elicit physiological outcomes in the host. Last, the degree of microbiota plasticity, and thus the potential for response to microbiota-directed interventions, may be dependent on baseline microbial populations (*76*) and past dietary patterns (*82*). For example, recent data from mice colonized by human bacteria indicate that diets associated with reduced microbial diversity may have impaired responsiveness to dietary interventions, requiring reexposure to diet-responsive microorganisms (*82*). Thus, identifying presence of key diet-responsive microorganisms may be important in predicting success of dietary interventions in humans.

Although plasticity offers an opportunity for microbiota-targeted therapeutics, it represents a double-edged sword in that it also catalyzes deleterious effects of external stressors, such as an unhealthful diet. Dysbiosis, an alteration in the composition of the microbiota associated with a disease state, has been linked with poor diet and numerous chronic diseases. However, determination of an absolute, rather than comparative, definition of dysbiosis remains a fundamental unresolved question. The recently proposed "Anna Karenina hypothesis" suggests that dysbiosis is not a definitive pattern but rather the loss of microbiota stability, resulting in dispersion from the norm (*84*). This indicates the need to define a healthy microbiota, which is problematic on an individual basis, given that factors such as environment, genetics, past diet, exercise, and geography all play a role in shaping the microbiota, and these individual influences may or may not translate to tangible health outcomes.

Despite current unresolved questions that limit practical and clinical translation of microbiota research, several new developments promise continued advancement of the field. Integration of proteomic and metabolomic data with existing DNA-based methods of microbiota assessment could circumvent the need to define healthy versus unhealthy microbial populations as more accurate functional profiling emerges. To this end, the Integrated Human Microbiome Project was recently launched to functionally characterize human cohorts in various life stages and at the onset of specific disease states (*85*). Additionally, new bioinformatics tools and modeling algorithms are improving our ability to apply microbiota data to human outcomes. Examples of recent successes include the development of algorithms that incorporate microbiota profiles to predict post-dieting weight gain (*86*) and develop personalized diet recommendations for control of postprandial glycemic responses (*87*). These examples demonstrate how realization of the potential for microbiota-diet interactions could change future approaches to nutrition.

REFERENCES

1. J. Mayer, *Science* **176**, 237–241 (1972).
2. A. Cotillard *et al.*, *Nature* **500**, 585–588 (2013).
3. C. A. Herter, A. I. Kendall, *J. Biol. Chem.* **7**, 203–236 (1910).
4. L. A. David *et al.*, *Nature* **505**, 559–563 (2014).
5. K. H. Collins *et al.*, *Sci. Rep.* **6**, 37278 (2016).
6. R. Mastrocola *et al.*, *J. Nutr. Biochem.* **55**, 185–199 (2018).
7. E. D. Sonnenburg *et al.*, *Nature* **529**, 212–215 (2016).
8. T. Yatsunenko *et al.*, *Nature* **486**, 222–227 (2012).
9. S. L. Schnorr *et al.*, *Nat. Commun.* **5**, 3654 (2014).
10. C. L. F. Walker *et al.*, *Lancet* **381**, 1405–1416 (2013).
11. T. V. Maier *et al.*, *MBio* **8**, e01343-17 (2017).
12. K. A. Earle *et al.*, *Cell Host Microbe* **18**, 478–488 (2015).
13. M. S. Desai *et al.*, *Cell* **167**, 1339–1353.e21 (2016).
14. B. S. Samuel *et al.*, *Proc. Natl. Acad. Sci. U.S.A.* **105**, 16767–16772 (2008).
15. F. De Vadder *et al.*, *Cell* **156**, 84–96 (2014).
16. M. Waldecker, T. Kautenburger, H. Daumann, C. Busch, D. Schrenk, *J. Nutr. Biochem.* **19**, 587–593 (2008).
17. P. J. Turnbaugh *et al.*, *Nature* **444**, 1027–1031 (2006).
18. G. den Besten *et al.*, *J. Lipid Res.* **54**, 2325–2340 (2013).
19. G. R. Gibson, M. B. Roberfroid, *J. Nutr.* **125**, 1401–1412 (1995).
20. J. Vulevic, A. Juric, G. Tzortzis, G. R. Gibson, *J. Nutr.* **143**, 324–331 (2013).
21. P. Dehghan, B. Pourghassem Gargari, M. Asghari Jafar-abadi, *Nutrition* **30**, 418–423 (2014).
22. W. Bridgette *et al.*, *J. Gastroenterol. Hepatol.* **32**, 64–68 (2017).
23. E. P. Halmos, V. A. Power, S. J. Shepherd, P. R. Gibson, J. G. Muir, *Gastroenterology* **146**, 67–75.e5 (2014).
24. G. R. Gibson *et al.*, *Nat. Rev. Gastroenterol. Hepatol.* **14**, 491–502 (2017).
25. A. Duda-Chodak, T. Tarko, P. Satora, P. Sroka, *Eur. J. Nutr.* **54**, 325–341 (2015).
26. M. A. Hildebrandt *et al.*, *Gastroenterology* **137**, 1716–24.e1, 2 (2009).
27. S. Ramos-Romero *et al.*, *Am. J. Physiol. Endocrinol. Metab.* **314**, E552–E563 (2018).
28. S. Rabot *et al.*, *FASEB J.* **24**, 4948–4959 (2010).
29. S. El Aidy, G. Hooiveld, V. Tremaroli, F. Bäckhed, M. Kleerebezem, *Gut Microbes* **4**, 118–124 (2013).
30. R. Kübeck *et al.*, *Mol. Metab.* **5**, 1162–1174 (2016).
31. K. Martinez-Guryn *et al.*, *Cell Host Microbe* **23**, 458–469.e5 (2018).
32. C. Bidu *et al.*, *Diabetes* **67**, 1512–1523 (2018).
33. C. Vors *et al.*, *J. Clin. Endocrinol. Metab.* **100**, 3427–3435 (2015).
34. P. D. Cani *et al.*, *Diabetes* **56**, 1761–1772 (2007).
35. R. S. Munford, *J. Leukoc. Biol.* **100**, 687–698 (2016).
36. K. A. Kallio *et al.*, *Acta Diabetol.* **52**, 395–404 (2015).
37. V. Urdaneta, J. Casadesús, *Front. Med.* **4**, 163 (2017).
38. J. R. Swann *et al.*, *Proc. Natl. Acad. Sci. U.S.A.* **108** (suppl. 1), 4523–4530 (2011).
39. J. M. Ridlon, P. G. Wolf, H. R. Gaskins, *Gut Microbes* **7**, 201–215 (2016).
40. C. Thomas *et al.*, *Cell Metab.* **10**, 167–177 (2009).
41. S. I. Sayin *et al.*, *Cell Metab.* **17**, 225–235 (2013).
42. Y. Zhu *et al.*, *Br. J. Nutr.* **111**, 1109–1117 (2014).
43. E. E. Alexeev *et al.*, *Am. J. Pathol.* **188**, 1183–1194 (2018).
44. S. Krishnan *et al.*, *Cell Rep.* **23**, 1099–1111 (2018).
45. W. H. Tang *et al.*, *N. Engl. J. Med.* **368**, 1575–1584 (2013).
46. M.-E. Dumas *et al.*, *Proc. Natl. Acad. Sci. U.S.A.* **103**, 12511–12516 (2006).
47. A. B. Roberts *et al.*, *Nat. Med.* **24**, 1407–1417 (2018).
48. S. Magnúsdóttir, D. Ravcheev, V. de Crécy-Lagard, I. Thiele, *Front. Genet.* **6**, 148 (2015).
49. M. T. Khan, W. R. Browne, J. M. van Dijl, H. J. M. Harmsen, *Antioxid. Redox Signal.* **17**, 1433–1440 (2012).
50. J. Wang *et al.*, *Nat. Genet.* **48**, 1396–1406 (2016).
51. C. A. Lopez, E. P. Skaar, *Cell Host Microbe* **23**, 737–748 (2018).
52. T. Jaeggi *et al.*, *Gut* **64**, 731–742 (2015).
53. K. K. Sanchez *et al.*, *Cell* **175**, 146–158.e15 (2018).
54. N. Wilck *et al.*, *Nature* **551**, 585–589 (2017).
55. B. Chassaing *et al.*, *Nature* **519**, 92–96 (2015).
56. J. Suez *et al.*, *Nature* **514**, 181–186 (2014).
57. Y. Zhang *et al.*, *Epilepsy Res.* **145**, 163–168 (2018).
58. C. A. Olson *et al.*, *Cell* **173**, 1728–1741.e13 (2018).
59. M. N. Roberts *et al.*, *Cell Metab.* **26**, 539–546.e5 (2017).
60. A. Swidsinski *et al.*, *Front. Microbiol.* **8**, 1141 (2017).
61. A. Tagliabue *et al.*, *Clin. Nutr. ESPEN* **17**, 33–37 (2017).
62. G. G. Konijeti *et al.*, *Inflamm. Bowel Dis.* **23**, 2054–2060 (2017).
63. S. A. Smits *et al.*, *Science* **357**, 802–806 (2017).
64. J. Salas-Salvadó *et al.*, *Ann. Intern. Med.* **160**, 1–10 (2014).
65. C. Zhang *et al.*, *Front. Immunol.* **9**, 908 (2018).
66. C. Losasso *et al.*, *Front. Microbiol.* **9**, 317 (2018).
67. G. D. Wu *et al.*, *Gut* **65**, 63–72 (2016).
68. J. van Duynhoven *et al.*, *Proc. Natl. Acad. Sci. U.S.A.* **108** (suppl. 1), 4531–4538 (2011).
69. X.-L. Wang, H.-G. Hur, J. H. Lee, K. T. Kim, S.-I. Kim, *Appl. Environ. Microbiol.* **71**, 214–219 (2005).
70. F. Sofi, R. Abbate, G. F. Gensini, A. Casini, *Am. J. Clin. Nutr.* **92**, 1189–1196 (2010).
71. F. De Filippis *et al.*, *Gut* **65**, 1812–1821 (2016).
72. D. Pastori *et al.*, *J. Am. Heart Assoc.* **6**, e005784 (2017).
73. I. Garcia-Mantrana, M. Selma-Royo, C. Alcantara, M. C. Collado, *Front. Microbiol.* **9**, 890 (2018).
74. S. A. Cohen *et al.*, *J. Pediatr. Gastroenterol. Nutr.* **59**, 516–521 (2014).
75. K. Lawrence, J. Hyde, *PLOS ONE* **12**, e0179017 (2017).
76. N. Zmora *et al.*, *Cell* **174**, 1388–1405.e21 (2018).
77. J. Suez *et al.*, *Cell* **174**, 1406–1423.e16 (2018).
78. K. A. Kaiser *et al.*, *FASEB J.* **30**, 905 (2016).
79. E. Östman, Y. Granfeldt, L. Persson, I. Björck, *Eur. J. Clin. Nutr.* **59**, 983–988 (2005).
80. J. G. LeBlanc *et al.*, *J. Appl. Microbiol.* **111**, 1297–1309 (2011).
81. R. N. Carmody *et al.*, *Cell Host Microbe* **17**, 72–84 (2015).
82. N. W. Griffin *et al.*, *Cell Host Microbe* **21**, 84–96 (2017).
83. G. D. Wu *et al.*, *Science* **334**, 105–108 (2011).
84. J. R. Zaneveld, R. McMinds, R. Vega Thurber, *Nat. Microbiol.* **2**, 17121 (2017).
85. Integrative HMP (iHMP) Research Network Consortium, *Cell Host Microbe* **16**, 276–289 (2014).
86. C. A. Thaiss *et al.*, *Nature* **540**, 544–551 (2016).
87. D. Zeevi *et al.*, *Cell* **163**, 1079–1094 (2015).

10.1126/science.aau5812

REVIEW

Swifter, higher, stronger: What's on the menu?

Louise M. Burke[1,2]* and John A. Hawley[2]

The exploits of elite athletes delight, frustrate, and confound us as they strive to reach their physiological, psychological, and biomechanical limits. We dissect nutritional approaches to optimal performance, showcasing the contribution of modern sports science to gold medals and world titles. Despite an enduring belief in a single, superior "athletic diet," diversity in sports nutrition practices among successful athletes arises from the specificity of the metabolic demands of different sports and the periodization of training and competition goals. Pragmatic implementation of nutrition strategies in real-world scenarios and the prioritization of important strategies when nutrition themes are in conflict add to this variation. Lastly, differences in athlete practices both promote and reflect areas of controversy and disagreement among sports nutrition experts.

Ancient Olympians manipulated their diets according to prevailing beliefs, with Pythagoras being credited (probably incorrectly) for introducing athletes to meat and protein-rich foods in place of traditional figs, cereals, and cheese (*1*). Meanwhile, modern-day athletes are bombarded with social media "warriors" who evangelize vegan, Paleo, and low-carb "keto" diets for peak performance. In contrast to the battle over the perfect menu, contemporary sports nutrition embraces diversity in dietary practices, underpinning the demands of training and competition with the philosophies of specificity, periodization, and personalization (*2*).

The metabolic demands of elite sport are complex, with events lasting from seconds (jumps, throws, and lifts) to several weeks (Grand Tour cycling races). Performance outcomes culminate from deliberate, sport-specific training aimed at maximizing adaptations toward the fulfilment of individual genetic potential (*3*). Although some elite athletes benefit from systematic, science-driven advice on training adaptation and competition performance, others use trial-and-error approaches under the guidance of experienced coaches, leaving scientists to explain post hoc how diet might have contributed to their performance peaks (*3*).

Solving the fuel crisis

Energy for competitive sports is provided by transforming chemical energy (intramuscular glycogen and lipids) into mechanical energy (contraction), with adenosine triphosphate (ATP) being the metabolic intermediary (*4*). Because intramuscular ATP stores are small, exercise-associated increases in ATP turnover within active myocytes (up to 100 times the resting turnover rate) pose a major energetic challenge. Metabolic pathways for resynthesizing ATP are rapidly activated during short-term (<30-s) sprints, primarily through substrate-level phosphorylation: phosphocreatine (PCr) breakdown and the conversion of muscle glycogen to lactate. However, as ATP production becomes unable to match rates of utilization, a range of metabolic by-products accumulates. Some of these, such as hydrogen ions, appear to exert negative feedback on the pathways that produce them to prevent further disruption to homeostasis, whereas others, including adenosine monophosphate (AMP) and organic phosphate, stimulate energy sensors, such as the 5′-AMP–activated protein kinase, to maintain cellular homeostasis by regulating anabolic and catabolic pathways, thereby ensuring a balance between energy supply and demand.

Sporting activities lasting several minutes to several hours and performed either as a steady state (e.g., marathon running) or with intermittent high-intensity bursts (e.g., team sports) are fueled principally by the oxidation of intramuscular glycogen and, to a lesser extent, lipids, whereas the mobilization of extramuscular substrates [plasma glucose from the liver and gut and free fatty acids (FFAs) released from adipocytes] becomes more important as exercise duration increases. Training enhances the metabolic flexibility of the myocyte, enhancing the size of substrate pools and the capacity to rapidly switch between carbohydrate (CHO)– and fat-based fuels to meet the demands of the working muscles.

The location- or fiber-specific depletion of muscle glycogen stores is often associated with fatigue, and since the introduction of the percutaneous needle biopsy technique to exercise science in the 1960s (*5*), numerous investigations have examined strategies to promote the storage of glycogen before or between exercise bouts. The key factor in the synthesis of this macromolecule is the quantity of dietary CHO consumed (*6*), but because maximal hourly synthesis rates are equivalent to ~5% of the size of normalized stores, athletes need to plan adequate time as well as sufficient CHO intake to increase

Box 1. Move over, muscle: The brain's the boss!

The brain and CNS are implicit in skilled tasks and events requiring concentration and decision-making. Only recently, however, have we recognized their role in the performance of even simple locomotor events, including strategies around pacing. A century ago, Bainbridge wrote, "There appear, however, to be two types of fatigue, one arising entirely within the central nervous system, the other in which fatigue of the muscles themselves is superadded to that of the nervous system" (*71*). Despite this early insight, sports nutrition has evolved with a bias toward studying peripheral mechanisms of fatigue and their role in performance, possibly because of the opportunities provided by available research tools (*72*). Exceptions are noted; hypoglycemia has long been recognized as a cause of fatigue during endurance sports (*73*), and brain astrocytes are now known to have labile glycogen stores (*74*). Furthermore, we now explain the ergogenic benefits of caffeine through central roles (reduced perception of effort and increased neural recruitment of muscle fibers) rather than a metabolic origin (muscle glycogen sparing because of increased availability and oxidation of plasma FFAs) (*75*).

An intriguing theme in modern sports nutrition involves the CNS and nutrients that can enhance performance without even being absorbed (*76*). This interest emerged from the recognition that exogenous CHO intake could improve ~1-hour cycling time trial performance, even though muscle substrate (glycogen) availability is not rate limiting for this event (*76*). The same performance benefits were detected when the mouth was simply rinsed with a glucose or maltodextrin solution (*77*), exposing receptors in the oral cavity to CHO and stimulating reward centers in the brain to increase pace or work output (*78*). The "oral sensing" benefits of CHO have been shown to be robust and repeatable when undertaken throughout an event, offering new performance nutrition strategies and a different range of targeted sports (*76*). Although this science is still in its infancy, evidence shows benefits of oral sensing from other tastants (e.g., fluid and caffeine), and effects have been reported for menthol (perception of cooling), quinine [activation of the autonomic nervous system and/or corticomotor excitability for brief events (*79*)], and capsaicin, acetic acid, cinnamaldehyde, and other plant chemicals that are known transient receptor potential channel activators and may prevent exercise-associated muscle cramps (*80*).

[1]Australian Institute of Sport, Belconnen ACT 2616, Australia. [2]Exercise and Nutrition Research Program, The Mary MacKillop Institute for Health Research, Australian Catholic University, Melbourne 3000, Australia.
*Corresponding author. Email: louise.burke@ausport.gov.au

glycogen to levels commensurate with the demands of the upcoming session (*6*). Factors reducing the efficiency of glycogen synthesis from a given CHO intake include muscle damage and inadequate energy intake, whereas other factors (training status, the severity of glycogen depletion, intake within the hours following strenuous exercise, and co-ingestion of protein) can increase synthesis rates or absolute stores (*6*). The resting glycogen concentrations in endurance-trained muscle are higher than those in sedentary individuals; furthermore, glycogen supercompensation ("CHO loading") can be achieved in trained muscle with as little as 24 to 48 hours of reduced activity and high intakes of CHO [10 to 12 g per kilogram of body mass (BM) per 24 hours] (*6*). For at least 50 years, such techniques have been used by athletes to enhance their performance in endurance events in which glycogen depletion would otherwise occur (*7*).

Of course, the fuel demands of many sports exceed muscle glycogen storage capacity or the athlete's opportunity to replete endogenous stores between events. Exogenous CHO (CHO consumed in the hours before and/or throughout exercise) maintains euglycemia by "sparing" hepatic glucose production (*8*), with blood glucose making an increasing contribution to rates of muscle CHO oxidation as glycogen stores become depleted (*9*). Strong evidence suggests that performance in a range of sports and exercise scenarios is enhanced by consuming CHO during exercise, with intakes targeted to the muscle's need to supplement its diminishing glycogen reserves [30 to 60 g/hour in endurance events of up to 2 to 3 hours duration and 60 to 90 g/hour in ultra-endurance events lasting 8 to 10 hours (*10*)]. Intestinal CHO absorption is likely the rate-limiting step in the oxidation of ingested CHO (*11*). However, to some extent this can be overcome by "training the gut": increasing CHO intake in the diet and during exercise to increase tolerance and the activity of sodium-dependent glucose transporter SGLT-1 (*12*, *13*). The use of glucose-fructose mixtures that utilize different gut transporters can also increase total intestinal absorption and rates of muscle oxidation of ingested CHO (*14*).

The relatively large lipid stores in even the leanest of athletes have, understandably, intrigued sports scientists as a potential source of fuel for prolonged aerobic exercise. However, whereas CHO oxidation is closely geared to the energetic demands of the working muscles, no mechanisms exist for closely regulating the availability and metabolism of FFAs to the prevailing energy expenditure. Short-term strategies [overnight fasting or low-CHO, high-fat (LCHF) eating] have proven unsuccessful in enhancing performance, despite increasing FFA availability: The small increase in FFA oxidation is insufficient to replace the contribution of CHO after near depletion of liver and muscle CHO stores (*15*). An alternative strategy (*16*) to potentially boost the use of both substrate pools involves exposure (5 days) to LCHF (60 to 70% fat) diets to promote muscle retooling to enhance FFA transport and utilization, followed with restoration of endogenous and exogenous CHO availability (24 hours of high-CHO diet and CHO intake before and during exercise). Despite substantial increases in rates of fat oxidation after such protocols, benefits to endurance performance have been, at best, limited to specific scenarios or individuals (*17*).

More notably, the observed reduction in the utilization of CHO during submaximal exercise ("glycogen sparing"), initially thought to be advantageous in preserving this fuel for later oxidation, was discovered to be impaired CHO oxidation, caused by reduced muscle glycogenolysis and the down-regulation of flux through the citric acid cycle secondary to reduced pyruvate dehydrogenase activity (*18*). In sports where success is determined by high-intensity aerobic exercise, either throughout the event (such as in a cycling time trial or 10,000-m run) or at critical stages [within team sports or the "breakaways" and finishes in marathons, Ironman triathlons (*19*), and longer cycle races (*20*)], the highest sustainable rates of muscle energy turnover require the better economy of ATP production from CHO oxidation. Short-term fat adaptation strategies, or even long-term adaptation to ketogenic LCHF diets (80% fat, <50 g of CHO/day), which can increase normal rates of fat oxidation by two or three times (*21*, *22*), are limited in application to a small range of sporting events in which utilization is low enough for muscle energy to be provided by fat oxidation (*21*, *23*). To date, it appears that protocols that substantially increase fat oxidation also decrease metabolic flexibility by reducing CHO substrate pools and/or the ability to rapidly oxidize them. The bottom line is that when elite athletes train for and compete in most sporting events, CHO fuels are the predominant and critical substrate for the working muscles, and the availability of CHO (*22*, *24*), rather than fat, wins gold medals. We propose that the increased rates of fat oxidation observed after endurance training and "train-low" strategies (see When less is more) are a proxy for an increase in mitochondrial density; for competition success, this machinery is best utilized by harnessing it to enhance the oxidation of CHO-based fuels.

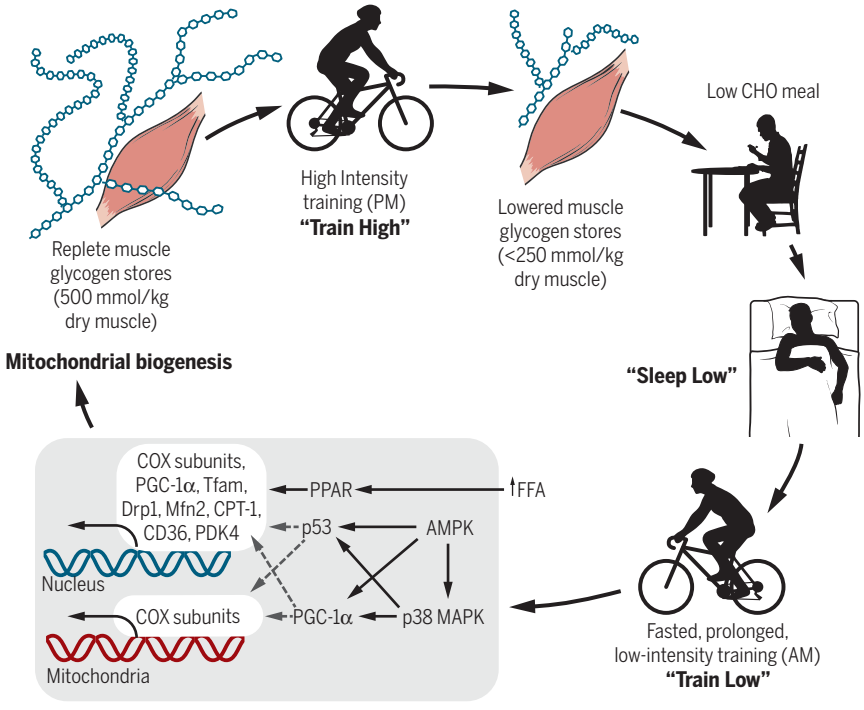

Fig. 1. Periodized nutrition: Evolution of a nutritional practice. Commencing endurance training with lowered muscle glycogen stores (training low) results in greater transcriptional activation of enzymes involved in CHO and fat oxidation, as well as greater mitochondrial biogenesis, than undertaking exercise with a normal or elevated glycogen content (*29*, *30*). Restricting CHO availability during the early (1 to 5 hours) postexercise recovery period also acutely up-regulates various markers of substrate metabolism and endurance training adaptation in skeletal muscle (*45*). Against this background, we formulated a novel approach in which we can undertake high-quality, high-intensity training and then prolong the duration of low CHO availability during recovery and subsequent aerobic exercise, thereby potentially extending the time course of transcriptional activation of metabolic genes and their target proteins. We have termed this practice "train high, sleep low" (*45*, *46*). PPAR, peroxisome proliferator–activated receptor; AMPK, 5′-AMP–activated protein kinase; MAPK, mitogen-activated protein kinase; COX, cyclooxygenase.

ILLUSTRATION: V. FALCONIERI BASED ON L. M. BURKE AND J. A. HAWLEY

Training nutrition: A balancing act

A reductionist view of training identifies a range of interdependent adaptations that permit athletes to sustain the highest rate and yield of energy production, optimize economy of motion, defend cellular homeostasis, and delay the onset of fatigue while simultaneously attaining the optimal physique and technical skills specific to their events (*3*, *25*). To achieve these ends, elite athletes and their coaches integrate a series of workouts that individually target important competition performance traits into a periodized training program composed of (weekly) microcycles and (3- to 6-week) mesocycles, culminating in targeted competition peaks within the (annual) macrocycle. The long-term adaptations to exercise training, such as those observed in elite athletes, result from the cumulative effect of the many transient increases in mRNA transcripts encoding various proteins after each acute exercise session (*26*, *27*). These repeated bursts in mRNA expression appear to be essential to drive the chronic intracellular adaptive response to exercise training (*27*).

With regard to the training diet, early nutrition guidelines promoted a singular and somewhat static approach, focusing predominantly on CHO-based fuels as the major energy source for muscle. However, contemporary guidelines acknowledge differences in the requirements and goals of different sessions or phases of training, leading to a periodization of the athlete's diet (*2*, *28*). In principle, nutrient support is organized around each training session to maximize physiological outcomes within a framework that addresses larger nutrition goals. Recommendations target total energy and fuel availability, with a focus on protein and CHO intakes and their distribution throughout the day (*2*). For high-intensity or high-quality training sessions, high endogenous and exogenous CHO availability is recommended, with the timing and intake of CHO matching or exceeding the muscle fuel requirements to support training quality (*2*, *28*, *29*). Some training sessions should develop competition fluid and CHO intake plans, incorporating practice of event-specific behaviors as well as training the gut function needed to tolerate and deliver these nutrients into the bloodstream. CHO intake can be reduced for lighter training loads (*2*, *29*); furthermore, adaptations to endurance training may be enhanced by deliberately commencing some sessions under conditions of low exogenous and endogenous CHO availability (*28*–*30*) (see When less is more and Fig. 1). As a result, daily CHO intakes typically vary from 2 to 12 g per kilogram of BM among athletes and across training cycles (*31*).

New perspectives on protein intake target the daily consumption of useful amounts (~0.3 g per kilogram of BM) of high-quality sources at four to six meals or snacks, particularly during the 1- to 3-hour window after key training sessions (*32*, *33*) and, perhaps, a double dose before sleep (*34*). This approach extends previous recognition that athletes have total daily protein requirements in excess of the standard Recommended Dietary Allowances to optimize the sustained (~24-hour) increase in contraction-stimulated synthesis of muscle protein that occurs after strength or endurance exercise by supplying leucine to further up-regulate the mammalian target of rapamycin complex 1 (mTORC1) pathway (*32*, *33*). Attention to nutrients for which athletes have increased requirements [such as water, electrolytes, and iron (*35*)] or risks of deficiency [such as vitamin D (*36*)] is also important in maximizing training adaptation, especially during training blocks undertaken in the heat or at high altitude (*3*).

Elite athletes straddle a thin line between maximizing overall training stimulus to promote sport-specific adaptation and remaining free of illness or injury. Within the framework of any periodized training program, each acute exercise session is an integral part of a long-term goal, with the training impulse (the sum of the intensity, duration, and frequency of sessions) being finely balanced to underpin optimal adaptation for a specific competition peak. The integration of nutrition goals for a specific training session or phase within the larger nutrition plan often creates tension between opposing themes. Athletes, both males and females, can develop relative energy deficiency in sport (RED-S), with a mismatch between energy intake and the energy expended in exercise leading to impairments in metabolic rate, bone health, protein synthesis, production of reproductive hormones, and performance gains (*37*). Yet, RED-S can occur secondarily to the body fat manipulation and very high training volumes that typically underpin success (*38*); this necessitates careful implementation and scheduling of such phases into the annual plan (*39*). Other strategies that need to be balanced or strategically managed include training with low CHO availability, which increases the inflammatory (interleukin-6) response to exercise, with acute disturbances to the immune system (*40*) and bone metabolism (*41*) that appear to persist with long-term exposure (*42*). Similarly, the use of antioxidant supplements acutely reduces free oxygen radical damage to muscle fibers but potentially dampens the training response by interfering with redox-sensitive signaling pathways; this has also been seen to translate into a reduction in performance (*43*).

When less is more

The application of molecular biology techniques to exercise science has identified the complexity and breadth of intracellular signaling networks by which different exercise modes drive adaptive changes that underpin the athletic phenotype (*3*, *25*). Altering nutrient availability, particularly endogenous CHO stores, selectively modulates gene expression and intracellular signaling within the muscle; mechanisms include alterations in cell osmolality and increased activity of molecules within the regulatory CHO-binding domain of the AMP-activated protein kinase, as well as perturbations to circulating FFAs and hormones in concert with plasma glucose and

Box 2. Performance in a bottle.

Sports products represent a lucrative portion of the worldwide explosion in the manufacture and marketing of supplements; according to one report, sports supplements generated global revenue of $9 billion in 2017, with a doubling of this value forecasted by 2025 (*81*). Surveys confirm the high prevalence of sports food and supplement use among athletes, including greater use at higher levels of competition (*82*). Despite earlier reluctance, many expert groups, including the International Olympic Committee (*83*), now pragmatically accept the use of supplements passing a risk-benefit analysis as being safe, effective, legal, and appropriate to an athlete's age and maturation in their sport. Supplements used by athletes fall into different categories (*83*): nutrient supplements for the treatment or prevention of deficiencies (e.g., iron and vitamin D); sports foods providing energy or nutrients when it is impractical to consume everyday foods (e.g., sports drinks and protein supplements); performance supplements that directly enhance exercise capacity; and supplements that provide indirect benefits through recovery, body composition management, and other goals. Despite enthusiastic marketing, from the latter two groups, only a few products enjoy robust evidence of efficacy [e.g., caffeine, creatine monohydrate, bicarbonate, β-alanine, and nitrate (*84*)] (Fig. 2).

Any benefits associated with supplement use must be balanced against the expense, the potential for adverse outcomes due to poor protocols for use (e.g., excessive doses or interactions with other supplements), and the dangers inherent with products whose manufacture and marketing are less regulated than those of foods or pharmaceutical goods. There are safety issues around dietary supplements in general, which accounted for ~23,000 notifiable emergency department visits in the United States in 2015 (*85*). Elite athletes also need to consider that supplements have been found to contain contaminants or undeclared ingredients that are prohibited by the antidoping codes (*86*) under which they compete; these include stimulants, anabolic agents, selective androgen receptor modulators, diuretics, anorectics, and β_2 agonists (*87*). Strict liability codes mean that a positive urine test can trigger an Adverse Doping Rule Violation with potentially serious effects on the athlete's career, livelihood, and reputation, despite unintentional intake or minute (ineffective) doses. Third-party auditing of products can help elite athletes make informed choices about supplement use but cannot provide an absolute guarantee of product safety (*83*).

insulin concentrations (*3*, *29*). Within their repertoire of training nutrition strategies, athletes can now include practices that augment adaptive processes in skeletal muscle; these include commencing training with low exogenous CHO availability (fasting overnight and/or withholding CHO during a session) or the more potent train-low strategy of deliberately commencing selected training sessions with lowered muscle glycogen stores (e.g., using a first session to deplete glycogen and then training for a second time after withholding CHO to prevent glycogen restoration) (*29*, *30*).

Although studies consistently report augmented cellular responses as a result of train-low strategies, the translation to performance enhancement has been less clear (*29*, *30*). Early investigations failed to detect superior performance outcomes; this was attributed to the overemphasis of such sessions within the training program and their resultant impairment of training intensity (*44*). These sessions need to be appropriately placed into a periodized program to complement high-quality training (*7*). A recent, clever sequencing of practices (Fig. 1) integrates a performance-promoting session and an adaptation-focused session while adding the benefits of a prolonged increase in exercise-stimulated cellular signaling and posttranscriptional regulation during glycogen-depleted recovery and exercise (*45*). In subelite populations at least, better integration of train-low and train-high sessions into the training sequence (Fig. 1) has been associated with superior performance compared with the same training undertaken with normal CHO availability (*46*). So far, however, this does not seem to be the case in studies involving elite populations (*22*, *47*), although it is often incorporated into real-world training sessions (*48*). Although further studies are needed, part of the challenge in advancing this area of research is the lack of agreement with regard to the terminology and implementation of the practices involved; we have tried to address this in a separate commentary (*7*).

Fighting fatigue: Eating to win

Each sport has distinct features, but characteristics shared by all competitors are a desire to pace their performance to achieve the highest sustainable outputs or speeds and maintain technical proficiency, with the likelihood of a reduction in some performance metrics intermittently, toward the end of the event, or both. "Fatigue" is defined operationally as a periodic or sustained decline in the athlete's ability to optimally perform the tasks required of their sport. Although fatigue is often characterized as muscular (decreased force or power production) or mental (increased ratings of perceived exertion or loss of skill and cognitive abilities), there is interplay between these phenomena. Muscular fatigue has both peripheral (related to the exercising muscle) and central [related to the ability of the central nervous system (CNS) to enervate the muscle fibers] input. Although some events require maximum performance to break world records or personal bests, others reward a superior performance relative to those of other competitors. The factors underpinning fatigue or performance power or speed are specific to the event, the environment in which it is undertaken, and the individual athlete.

Figure 2 provides a simplified summary of the most common fatigue factors in competitive sport to which evidence-based nutrition strategies can be applied to reduce or delay the onset. Such strategies can involve chronic protocols that work synergistically with training to make the body more resilient to these factors. For example, in team sports involving repetition of short (e.g., 6-s) high-intensity sprints, a progressive decay in speed related to the failure to fully recover PCr stores in the intervening recovery periods (>30 to 120 s) can be addressed by supplementation with creatine monohydrate to increase the size of the muscle PCr pool (*49*). This may not only directly enhance match performance by altering the sprint decay profile (*50*) but also allow the athlete to train harder (i.e., complete more sprints during training sessions) to increase adaptations in other physiological systems. Acute pre-event strategies such as CHO loading (24 to 48 hours of preparation) to increase the muscle glycogen stores or glycerol-assisted hyperhydration (2 hours of preparation) to increase body water storage can enhance performance in specific events if they can increase the time of optimal output before the body reaches a critical level of glycogen depletion (*51*) or fluid deficit (*52*), respectively. Intake of CHO (*10*) or fluid (*53*) during the event can also address these peripherally limiting factors but, intriguingly, may provide a benefit though a CNS effect associated with the oral sensing of these nutrients (Boxes 1 and 2).

Lastly, for real-world events, the development of a competition nutrition plan is challenged by the complexity of addressing a multitude and overlay of these fatigue factors, the practical constraints imposed by the event or the nature of the exercise, and the beliefs and tolerance of the athlete. This is covered in Box 3 and illustrated by recent activities around the marathon (42.2 km). In 2017, in a carefully orchestrated attempt to break the 2-hour barrier (*54*) and after much scientific banter (*55*), Kenyan Eliud Kipchoge came within 25 s of a sub-2-hour performance. Kipchoge already had two of the three "success factors" for prolonged endurance events: high aerobic power and the ability to run at a very high proportion of his aerobic capacity for prolonged periods without losing metabolic control (*56*). His attempt, albeit outside the International Association of Athletics Federations rules, targeted mainly the third factor: running economy (achieving the highest speed for the lowest oxygen cost). Strategies to improve economy included running on a flat motor racing track without sharp corners to preserve speed, running in aerodynamic formation behind other runners, using a car-mounted time clock to provide a windshield as well as pacing assistance, and wearing shoes developed to return 4% extra energy via carbon-fiber inserts (*57*).

Nutritional strategies were also used to enhance economy, and future improvements are likely. The beneficial effects of beetroot juice, a popular performance aid providing a supplemental source of inorganic nitrate, are mediated through the enhancement of exercise economy: A secondary nitric oxide (NO)–generating pathway (nitrate-nitrite-NO) is believed to enhance NO-mediated increases in capillary O_2 delivery to the muscle and reduce mitochondrial proton leakage (*58*). Furthermore, despite current claims that ketogenic LCHF diets provide unlimited substrate for prolonged exercise (*21*), both century-old empirical data (*59*) and recent interventions involving world-class race walkers (*22*) remind us that the oxidation of CHO yields ~5% more ATP per unit of O_2 than fat. Future nutrition strategies for the marathon may focus on increasing CHO availability and oxidation by shifting away from the use of fat from the mitochondrial furnace. Tactics include achieving maximally supercompensated glycogen stores, increasing the opportunities for aggressive in-race feedings, and training the gut to use multiple CHO sources to increase overall intestinal absorption of CHO (*12*).

"...the decisive day of this race,...over a challenging mountainous terrain, was achieved with a nutrition plan providing 6663 kcal and 18.9 g of CHO per kilogram (a total of 1.3 kg, equivalent to ~85 slices of bread)..."

Elite athletes are different

Scrutiny of the evidence base for current sports nutrition guidelines reveals that the individuals who contribute blood, sweat, and tears to scientific investigations are at best well trained, often male, and almost always subelite. Interventions with world-class athletes are rare: By definition, such athletes are few in number, and they are generally disinclined to interrupt successful training or nutrition programs or submit to invasive experimental techniques for the sake of science. It is reasonable to ask, therefore, whether the results of studies on nonelite populations apply to their elite counterparts. Issues include application of the intervention to the specific scenarios in which elite athletes train or compete, the inability of underpowered studies to detect small but worthwhile differences or changes in performance that could alter the outcomes of elite sport, and the translation of putative mechanisms to athletes who undertake substantially larger volumes of specialized training and potentially possess favorable genetic

traits (*60*). In relation to some nutrition interventions, evidence suggests a diminished response in elite competitors. For example, beetroot juice supplementation appears to be less effective in achieving economy or performance improvements in elite athletes (*61*); explanations for nonresponsiveness to this supplement in higher-caliber athletes include their different muscle fiber composition and the legacy of physiological adaptations attained through extensive training, such as greater activity of the primary arginine-NO pathway (*62, 63*). Nevertheless, because this pathway is oxygen dependent, scenarios can be identified in which elite athletes could benefit from activity from the alternative (oxygen- and pH-independent) nitrate-derived NO production, justifying beetroot juice supplementation; these include training or competing at high altitude and competing in sports involving small muscle groups, such as the arms, in which lower blood flow increases the likelihood of local hypoxia and acidosis (*62*, *63*).

The challenge remains to determine whether elite athletes are successful because, or in spite, of their nutrition practices. There are few studies of such groups or individuals, although elite East African athletes who have dominated middle-distance and distance running for the past decades have received scientific inquiry (*64*, *65*). Their dietary patterns include consistencies with current athlete guidelines [high CHO intakes (~60 to 80% of energy) but regular use of training in a fasted state to achieve train-low sessions],

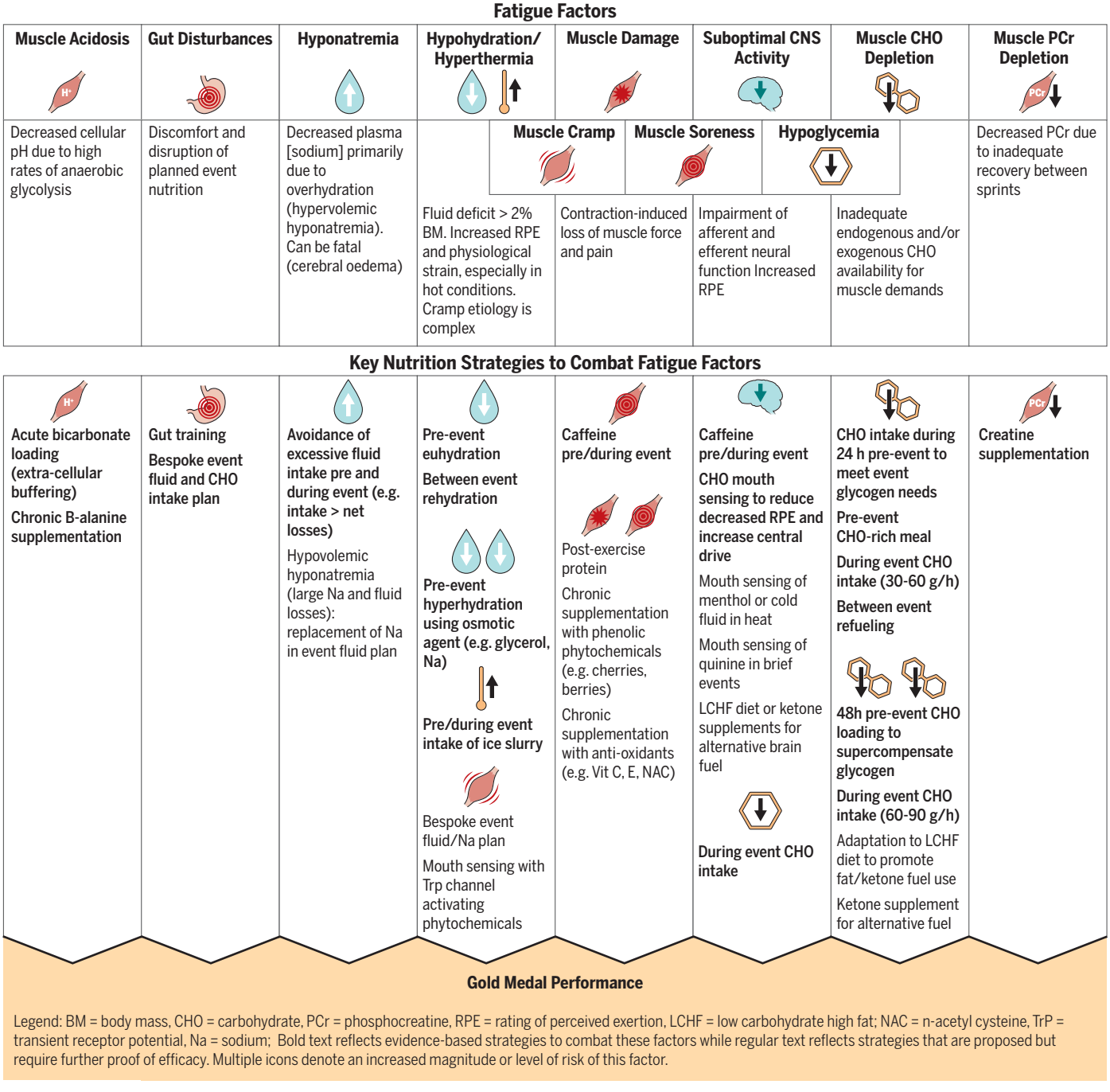

ILLUSTRATION: V. FALCONIERI BASED ON L. M. BURKE AND J. A. HAWLEY

Fig. 2. Nutrition can beat competition fatigue. Many factors that commonly cause fatigue (a periodic or sustained decline in the athlete's ability to optimally perform) in sporting events can be addressed by nutritional strategies that reduce the effects of these factors or delay their onset.

as well as inconsistencies with either the guidelines or typical practices of other elite athletes [reliance on vegetable (80 to 90% of diet) rather than animal food sources, very limited food variety, distribution of energy to a small number of meals in the day, and chronic periods of low energy availability]. Case histories of scientist-devised approaches to performance for elite competitors, such as "weight making" for a professional boxer (*66*) or a complex nutrition plan followed by the winner of the 3-week Giro d'Italia cycling race, do not necessarily allow firm and reproducible conclusions about the benefits of these strategies but show how practices can be achieved within the complexities of the sporting environment (see Box 3 and Fig. 3). In the latter case, the competition plan manipulated BM (by slight energy restriction and the use of a low-residue diet to reduce gastrointestinal contents) according to the benefits of being lighter on hilly sections and fluctuated daily energy and CHO intakes according to the estimated metabolic cost of each stage (*67*). Notably, the decisive day of this race, involving a solo ride over a challenging mountainous terrain, was achieved with a nutrition plan providing 6663 kcal and 18.9 g of CHO per kilogram

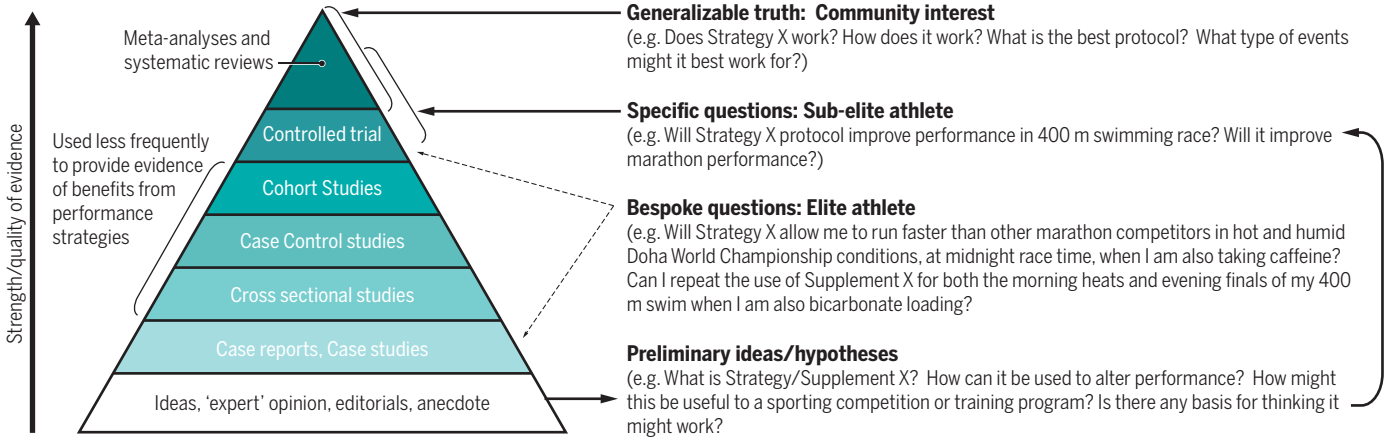

Fig. 3. Perspectives on the evidence base for elite athlete practices. Developing an evidence base for the nutritional practices of elite athletes requires acknowledgment that specific answers to research questions and interpretations of guidelines are needed. [Adapted from (*60*)]

Box 3. Specificity and practicality require bespoke solutions.

The practical implementation of nutrition strategies by athletes in real-world settings confounds the establishment of an evidence base by traditional research methods and the development of generalizable (and uncontroversial) guidelines. In most sports, performance is limited by a number of interdependent factors, typically addressed by a coordinated plan. We often consider several independently valuable nutrition strategies in combination, despite the potential for redundancy, amplification, attenuation, and competition between effects. The individual benefits of fluid and CHO replacement for performance in the heat are additive (*88*), caffeine is less effective when CHO intake is also used to attenuate the performance decline during prolonged exercise (*89*), and combining caffeine and bicarbonate supplementation impairs the benefits of the former because of gastrointestinal disturbances (*90*). However, because it is impractical to investigate the many permutations and combinations of evidence-based nutrition strategies (*90*), the overall effects on performance are unknown.

Environmental conditions and competition schedules add further practical challenges. Premiere championships can be hosted under "hostile" conditions (such as high altitude in the 1968 Mexico City Olympic Games or heat in the 2019 Doha Athletics World Championships) or with unusual timetables (such as late-night swimming at the 2016 Rio Olympic Games to coincide with primetime television in the United States). Thus, athletes often need bespoke strategies for different iterations of the same event. Lastly, sport involves rules, logistical considerations, and cultures that dictate opportunities for nutrient intake before, during, and between events (*91*). Some provide adequate opportunities for beneficial intake (e.g., basketball players drink during substitutions and time-outs). However, conditions in other events, such as weight-division sports, encourage substantial pre-event dehydration and energy restriction to "make weight" (*92*). Soccer prohibits breaks or access to fluids during each half, and the practical challenge of drinking while running at ~21 km/hour in a marathon limits the volumes ingested (*68*).

It is important to consider whether the traditional conduct and evaluation of scientific research adequately inform elite athletes. In many areas of our lives, we are content with generalizable truths (strategy X is good) and guidelines (we should all implement strategy X by doing Y). Figure 3 illustrates a hierarchy of types of scientific evidence. The types of studies that provide the strongest or highest-quality evidence (such as randomized controlled trials) are extremely hard to achieve with high-caliber competitors or may provide generic information inappropriate for a specific task. Lack of appreciation of these concepts has caused angst within the sports science community and an unfair dismissal of the integrity of its outputs.

Sports science was criticized in an assessment by epidemiologically trained scientists (*93*, *94*). Although valid methodological issues were raised, the analysis failed to appreciate that sports scientists working in elite sport typically seek highly context-specific information (Fig. 3). Evidence-based but bespoke solutions for small numbers of individuals require special designs and research tools; the validity, reliability, and sensitivity of measurements are critical. We must consider repeatability in study design or case history approaches to account for small sample sizes. Even individual responsiveness to interventions may vary. New or refined statistical approaches may be required (*60*, *90*).

Controversy regarding guidelines for fluid intake during sport exemplifies a lack of appreciation for context. Critics of current guidelines for an individualized approach (*95*) who argue that athletes should be told to drink only when thirsty during events (*96*) fail to recognize that opportunities for fluid intake are often beyond the athlete's control and unrelated to need. Therefore, it is reasonable to develop a bespoke plan for specific events that optimizes opportunities to consume fluid and CHO before and throughout the event to integrate gut comfort, fuel needs, a tolerable fluid deficit, and thirst management.

ILLUSTRATION: V. FALCONIERI BASED ON L. M. BURKE AND J. A. HAWLEY

(a total of 1.3 kg, equivalent to ~85 slices of bread), with race supplies being provided by *domestique* teammates and a support crew at planned intervals to avoid the need for the cyclist to carry the weight burden (*67*). We can never know how much this plan contributed to the rider's eventual success. Equally, we need to intellectualize that athletic success can be achieved in the face of apparently suboptimal practice. For example, that the winner of an elite marathon incurred a loss of 10% of BM over the race (*68*) fails to disprove that hypohydration impairs performance; rather, it demonstrates that this athlete was faster than other competitors on that day and potentially was best able to tolerate the conditions.

Although elite athletes can learn from sports science, many lessons have also flowed in the opposite direction. Sports nutrition recommendations have often been updated when practices observed among elite athletes were found to be beneficial. For example, caffeine guidelines for sport changed when the flat cola beverages consumed by elite cyclists toward the end of prolonged races (~1 to 2 mg of caffeine per kilogram at the onset of fatigue) were found to be as effective as the "scientifically proven" protocols (6 to 9 mg/kg taken 1 hour pre-event) (*69*). Ammunition to update guidelines for CHO intake during prolonged (>2.5 hours) events came from observations that the intakes of many elite cyclists and triathletes (~90 g/hour) were higher than the earlier recommendations (30 to 60 g/hour) and correlated with success (*70*). Clearly, future outcomes will be best achieved with a two-way interaction between sports scientists and elite athletes and their coaches.

In the final analyses, modern sports nutrition offers a feast of opportunities to assist elite athletes to train hard, optimize adaptation, stay healthy and injury free, achieve their desired physique, and fight against fatigue factors that limit success. Although there will be challenges and changes to sports nutrition guidelines as they evolve beyond the frontiers of current knowledge and practice, we can be excited to know that sports science in many guises contributes to the outcomes that delight and amaze us from our sofas and the grandstand.

REFERENCES AND NOTES

1. L. E. Grivetti, E. A. Applegate, *J. Nutr.* **127** (Suppl), 860S–868S (1997).
2. D. T. Thomas, K. A. Erdman, L. M. Burke, *Med. Sci. Sports Exerc.* **48**, 543–568 (2016).
3. J. A. Hawley, C. Lundby, J. D. Cotter, L. M. Burke, *Cell Metab.* **27**, 962–976 (2018).
4. B. Egan, J. A. Hawley, J. R. Zierath, *Cell Metab.* **24**, 342–342.e1 (2016).
5. J. Bergström, E. Hultman, *Nature* **210**, 309–310 (1966).
6. L. M. Burke, L. J. C. van Loon, J. A. Hawley, *J. Appl. Physiol.* **122**, 1055–1067 (2017).
7. L. M. Burke *et al*., *Int. J. Sport Nutr. Exerc. Metab.* **28**, 451–463 (2018).
8. A. N. Bosch, S. C. Dennis, T. D. Noakes, *J. Appl. Physiol.* **76**, 2364–2372 (1994).
9. E. F. Coyle, A. R. Coggan, M. K. Hemmert, J. L. Ivy, *J. Appl. Physiol.* **61**, 165–172 (1986).
10. T. Stellingwerff, G. R. Cox, *Appl. Physiol. Nutr. Metab.* **39**, 998–1011 (2014).
11. J. A. Hawley, A. N. Bosch, S. M. Weltan, S. C. Dennis, T. D. Noakes, *Pfluegers Arch.* **426**, 378–386 (1994).
12. A. E. Jeukendrup, *Sports Med.* **47** (suppl. 1), 101–110 (2017).
13. R. J. S. Costa *et al*., *Appl. Physiol. Nutr. Metab.* **42**, 547–557 (2017).
14. A. E. Jeukendrup, *Curr. Opin. Clin. Nutr. Metab. Care* **13**, 452–457 (2010).
15. L. M. Burke, J. A. Hawley, *Med. Sci. Sports Exerc.* **34**, 1492–1498 (2002).
16. L. M. Burke *et al*., *Med. Sci. Sports Exerc.* **34**, 83–91 (2002).
17. L. M. Burke, *Sports Med.* **45** (suppl. 1), 33–49 (2015).
18. T. Stellingwerff *et al*., *Am. J. Physiol. Endocrinol. Metab.* **290**, E380–E388 (2006).
19. E. Maunder, A. E. Kilding, D. J. Plews, *Sports Med.* **48**, 2219–2226 (2018).
20. L. Havemann *et al*., *J. Appl. Physiol.* **100**, 194–202 (2006).
21. J. S. Volek *et al*., *Metabolism* **65**, 100–110 (2016).
22. L. M. Burke *et al*., *J. Physiol. (London)* **595**, 2785–2807 (2017).
23. S. D. Phinney, B. R. Bistrian, W. J. Evans, E. Gervino, G. L. Blackburn, *Metabolism* **32**, 769–776 (1983).
24. J. A. Hawley, J. J. Leckey, *Sports Med.* **45**, S5–S12 (2015).
25. J. A. Hawley, M. Hargreaves, M. J. Joyner, J. R. Zierath, *Cell* **159**, 738–749 (2014).
26. V. G. Coffey, J. A. Hawley, *Sports Med.* **37**, 737–763 (2007).
27. C. G. Perry *et al*., *J. Physiol. (London)* **588**, 4795–4810 (2010).
28. A. E. Jeukendrup, *Sports Med.* **47** (suppl. 1), 51–63 (2017).
29. S. G. Impey *et al*., *Sports Med.* **48**, 1031–1048 (2018).
30. J. D. Bartlett, J. A. Hawley, J. P. Morton, *Eur. J. Sport Sci.* **15**, 3–12 (2015).
31. L. M. Burke, G. R. Cox, N. K. Culmmings, B. Desbrow, *Sports Med.* **31**, 267–299 (2001).
32. T. Stokes, A. J. Hector, R. W. Morton, C. McGlory, S. M. Phillips, *Nutrients* **10**, 180 (2018).
33. D. R. Moore, D. M. Camera, J. L. Areta, J. A. Hawley, *Appl. Physiol. Nutr. Metab.* **39**, 987–997 (2014).
34. P. T. Res *et al*., *Med. Sci. Sports Exerc.* **44**, 1560–1569 (2012).
35. G. Clénin *et al*., *Swiss Med. Wkly.* **145**, w14196 (2015).
36. D. J. Owens, R. Allison, G. L. Close, *Sports Med.* **48** (suppl. 1), 3–16 (2018).
37. M. Mountjoy *et al*., *Int. J. Sport Nutr. Exerc. Metab.* **28**, 316–331 (2018).
38. L. M. Burke, B. Lundy, I. L. Fahrenholtz, A. K. Melin, *Int. J. Sport Nutr. Exerc. Metab.* **28**, 350–363 (2018).
39. T. Stellingwerff, *Int. J. Sport Nutr. Exerc. Metab.* **28**, 428–433 (2018).
40. S. Bermon *et al*., *Exerc. Immunol. Rev.* **23**, 8–50 (2017).
41. C. Sale *et al*., *J. Appl. Physiol.* **119**, 824–830 (2015).
42. A. K. A. McKay *et al*., *Med. Sci. Sports Exerc.* 10.1249/MSS.0000000000001816 (2018).
43. T. L. Merry, M. Ristow, *J. Physiol. (London)* **594**, 5135–5147 (2016).
44. W. K. Yeo *et al*., *J. Appl. Physiol.* **105**, 1462–1470 (2008).
45. S. C. Lane *et al*., *J. Appl. Physiol.* **119**, 643–655 (2015).
46. L. A. Marquet *et al*., *Med. Sci. Sports Exerc.* **48**, 663–672 (2016).
47. K. D. Gejl *et al*., *Med. Sci. Sports Exerc.* **49**, 2486–2497 (2017).
48. T. Stellingwerf, *Int. J. Sport Nutr. Exerc. Metab.* **22**, 392–400 (2012).
49. D. Bishop, *Sports Med.* **40**, 995–1017 (2010).
50. G. Cox, I. Mujika, D. Tumilty, L. Burke, *Int. J. Sport Nutr. Exerc. Metab.* **12**, 33–46 (2002).
51. J. A. Hawley, E. J. Schabort, T. D. Noakes, S. C. Dennis, *Sports Med.* **24**, 73–81 (1997).
52. E. D. B. Goulet, M. Aubertin-Leheudre, G. E. Plante, I. J. Dionne, *Int. J. Sport Nutr. Exerc. Metab.* **17**, 391–410 (2007).
53. R. W. Kenefick, *Sports Med.* **48** (suppl. 1), 31–37 (2018).
54. M. Z. Donahue, "Runner comes excruciatingly close to breaking two-hour marathon banner," 6 May 2017; https://news.nationalgeographic.com/2017/05/extreme-running-marathon-nike-science/.
55. M. J. Joyner, J. R. Ruiz, A. Lucia, *J. Appl. Physiol.* **110**, 275–277 (2011).
56. M. J. Joyner, E. F. Coyle, *J. Physiol. (London)* **586**, 35–44 (2008).
57. W. Hoogkamer *et al*., *Sports Med.* **48**, 1009–1019 (2018).
58. A. M. Jones, *Appl. Physiol. Nutr. Metab.* **39**, 1019–1028 (2014).
59. A. Krogh, J. Lindhard, *Biochem. J.* **14**, 290–363 (1920).
60. L. M. Burke, P. Peeling, *Int. J. Sport Nutr. Exerc. Metab.* **28**, 159–169 (2018).
61. R. K. Boorsma, J. Whitfield, L. L. Spriet, *Med. Sci. Sports Exerc.* **46**, 2326–2334 (2014).
62. K. L. Jonvik, J. Nyakayiru, L. J. van Loon, L. B. Verdijk, *J. Appl. Physiol.* **119**, 759–761 (2015).
63. M. Hultström *et al*., *J. Appl. Physiol.* **119**, 762–769 (2015).
64. L. Y. Beis *et al*., *J. Int. Soc. Sports Nutr.* **8**, 7 (2011).
65. V. O. Onywera, F. K. Kiplamai, P. J. Tuitoek, M. K. Boit, Y. P. Pitsiladis, *Int. J. Sport Nutr. Exerc. Metab.* **14**, 709–719 (2004).
66. J. P. Morton, C. Robertson, L. Sutton, D. P. MacLaren, *Int. J. Sport Nutr. Exerc. Metab.* **20**, 80–85 (2010).
67. T. Fordyce, "Chris Froome: Team Sky's unprecedented release of data reveals how British rider won Giro d'Italia," 4 July 2018; https://www.bbc.com/sport/cycling/44694122.
68. L. Y. Beis, M. Wright-Whyte, B. Fudge, T. Noakes, Y. P. Pitsiladis, *Clin. J. Sport Med.* **22**, 254–261 (2012).
69. G. R. Cox *et al*., *J. Appl. Physiol.* **93**, 990–999 (2002).
70. A. Jeukendrup, *Sports Med.* **44** (suppl. 1), S25–S33 (2014).
71. F. A. Bainbridge, *The Physiology of Muscular Exercise* (Longmans, Green & Co., 1919).
72. J. A. Hawley, R. J. Maughan, M. Hargreaves, *Cell Metab.* **22**, 12–17 (2015).
73. S. A. Levine, B. Gordon, C. L. Derick, *JAMA* **82**, 1778–1779 (1924).
74. T. Matsui *et al*., *J. Physiol. (London)* **590**, 607–616 (2012).
75. L. L. Spriet, *Sports Med.* **44** (suppl. 2), S175–S184 (2014).
76. L. M. Burke, R. J. Maughan, *Eur. J. Sport Sci.* **15**, 29–40 (2015).
77. J. M. Carter, A. E. Jeukendrup, D. A. Jones, *Med. Sci. Sports Exerc.* **36**, 2107–2111 (2004).
78. E. S. Chambers, M. W. Bridge, D. A. Jones, *J. Physiol. (London)* **587**, 1779–1794 (2009).
79. S. Gam, K. J. Guelfi, P. A. Fournier, *Sports Med.* **46**, 1385–1390 (2016).
80. D. H. Craighead *et al*., *Muscle Nerve* **56**, 379–385 (2017).
81. Persistence Market Research, "Global market study on sports supplements: Non-protein products to witness substantial growth during 2017 – 2025" (Rep. PMRREP3034, Persistence Market Research, January 2018); https://www.persistencemarketresearch.com/market-research/sports-supplements-market.asp.
82. I. Garthe, R. J. Maughan, *Int. J. Sport Nutr. Exerc. Metab.* **28**, 126–138 (2018).
83. R. J. Maughan *et al*., *Int. J. Sport Nutr. Exerc. Metab.* **28**, 104–125 (2018).
84. P. Peeling, M. J. Binnie, P. S. R. Goods, M. Sim, L. M. Burke, *Int. J. Sport Nutr. Exerc. Metab.* **28**, 178–187 (2018).
85. A. I. Geller *et al*., *N. Engl. J. Med.* **373**, 1531–1540 (2015).
86. World Anti-Doping Agency, The Code; https://www.wada-ama.org/en/what-we-do/the-code.
87. J. M. Martínez-Sanz *et al*., *Nutrients* **9**, 1093 (2017).
88. P. R. Below, R. Mora-Rodríguez, J. González-Alonso, E. F. Coyle, *Med. Sci. Sports Exerc.* **27**, 200–210 (1995).
89. S. A. Conger, G. L. Warren, M. A. Hardy, M. L. Millard-Stafford, *Int. J. Sport Nutr. Exerc. Metab.* **21**, 71–84 (2011).
90. L. M. Burke, *Sports Med.* **47** (suppl. 1), 79–100 (2017).
91. A. K. Garth, L. M. Burke, *Sports Med.* **43**, 539–564 (2013).
92. R. Reale, G. Slater, L. M. Burke, *Int. J. Sports Physiol. Perform.* **13**, 459–466 (2018).
93. C. Heneghan, R. Perera, D. Nunan, K. Mahtani, P. Gill, *BMJ* **345**, e4797 (2012).
94. C. Heneghan *et al*., *BMJ* **345**, e4848 (2012).
95. M. N. Sawka *et al*., *Med. Sci. Sports Exerc.* **39**, 377–390 (2007).
96. D. Cohen, *BMJ* **345**, e4737 (2012).

ACKNOWLEDGMENTS

Competing interests: L.M.B. is a director of the International Olympic Committee Diploma in Sports Nutrition program and has been funded by the Australian Institute of Sport High Performance Research Funds, Australian Catholic University, and the Australian Research Council, as well as industry partners including the Alliance for Potato Research and Education (APRE), South African Potato Producers Organisation, Dairy Health and Nutrition Research Consortium, Dairy Australia, Nestle Research Centre, Nestle Australia, Kellogg's Australia, Mars Australia, and Gatorade Australia. L.M.B. was a member of the Gatorade Sports Science Expert Panel from 2014 to 2015, for which her workplace received an honorarium. J.A.H. has received funding for studies in nutritional metabolism from APRE; the Novo Nordisk Foundation; the Australian Sports Commission; Dairy Health and Nutrition Research Consortium, Australia; the Australian Research Council; Nestec, Switzerland; the National Heart Foundation of Australia; the Diabetes Australia Research Trust; Uncle Ben's of Australia, a division of EFFEM Foods; Polar Electro, Finland; SmithKline Beecham Consumer Healthcare (Nutrition), United Kingdom; the South African Potato Board; Bromor Foods, South Africa; the Sugar Association of South Africa; and Wander Research and Development, Switzerland. J.A.H. was a member of the Gatorade Sports Science Expert Panel from 2014 to 2015.

10.1126/science.aau2093

RESEARCH

Nanoparticles boost yeast as bioreactor

Guo et al., *p. 813*

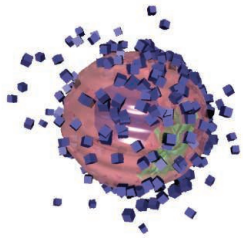

IN *SCIENCE* JOURNALS

Edited by **Stella Hurtley**

TROPICAL STORMS

Warm water and big winds

Tropical storm Nate caused extensive damage in Costa Rica in October 2017.

The 2017 North Atlantic hurricane season was highly active, with six major storms—nearly two standard deviations above the normal number. Three of those storms made landfall over the Gulf Coast and the Caribbean, causing terrible damage and loss. Why was the season so fierce? Murakami *et al*. used a suite of high-resolution model experiments to show that the main cause was pronounced warm sea surface conditions in the tropical North Atlantic. This effect was distinct from La Niña conditions in the Pacific Ocean that were involved in other years. It remains unclear how important anthropogenic forcing may be in causing such increased hurricane activity. —HJS

Science, this issue p. 794

NETWORK SCIENCE

The science of art advancement

Art appreciation is highly subjective. Fraiberger *et al*. used an extensive record of exhibition and auction data to study and model the career trajectory of individual artists relative to a network of galleries and museums. They observed a lock-in effect among highly reputed artists who started their career in high-prestige institutions and a long struggle for access to elite institutions among those who started their career at the network periphery. —BJ

Science, this issue p. 825

MASS SPECTROMETRY

Innovating to be nondisruptive

Insights into the architecture and stoichiometry of membrane complexes have grown with advances in cryo–electron microscopy and native mass spectroscopy. However, most of these studies are not in the context of native membrane. Chorev *et al*. released intact membrane complexes directly from native lipid membrane vesicles into a mass spectrometer. They analyzed components of the *Escherichia coli* inner and outer membranes and the bovine mitochondrial inner membrane. For several identified complexes, they found a stoichiometry that differs from published results and, in some cases, confirmed interactions that could not be characterized structurally. —VV

Science, this issue p. 829

BIOTECHNOLOGY

A programmable type of CRISPR system

CRISPR-Cas9 systems have been causing a revolution in biology. Harrington *et al*. describe the discovery and technological implementation of an additional type of CRISPR system based on an extracompact effector protein, Cas14. Metagenomics data, particularly from uncultivated samples, uncovered the CRISPR-Cas14 systems containing all the components necessary for adaptive immunity in prokaryotes. At half the size of class 2 CRISPR effectors, Cas14 appears to target single-stranded DNA without class 2 sequence restrictions. By leveraging this activity, a fast and high-fidelity nucleic acid detection system enabled detection of single-nucleotide polymorphisms. —SYM

Science, this issue p. 839

POLYMERS

Patterned fiber formation

The ability of liquid crystalline materials to order spontaneously has driven many innovations, from display technologies to extremely tough polymer fibers. Cheng *et al*. exploited this preponderance toward long-range ordering to direct the growth of nonliquid crystalline polymers into sheets of highly ordered fibers. Small changes to the processing conditions could be used to tweak the arrangement of the liquid crystals to generate a wide

range of polymer mats or sheets for potential use in sensing or filtration applications. —MSL

Science, this issue p. 804

INFLAMMATION

DNA binding as an anti-inflammatory

Mice that lack the gene encoding 8-oxoguanine DNA glycosylase 1 (OGG1) show resistance to inflammation. This enzyme binds to sites of oxidative DNA damage and initiates DNA base excision repair. Visnes *et al*. developed a small-molecule drug that acts as a potent and selective active-site inhibitor that stops OGG1 from recognizing its DNA substrate (see the Perspective by Samson). The drug inhibited DNA repair and modified OGG1 chromatin dynamics, which resulted in the inhibition of proinflammatory pathway genes. The drug was well tolerated by mice and suppressed lipopolysaccharide- and tumor necrosis factor–α–mediated neutrophilic inflammation in the lungs. —STS

Science, this issue p. 834; see also p. 748

DYNAMIC MATERIALS

Chemically reversible hydrogels

The dynamic reorganization of some cellular biopolymers in response to signals has inspired efforts to create artificial materials with similar properties. Freeman *et al*. created hydrogels based on peptide amphiphiles that can bear DNA strands that assemble into superstructures and that disassemble in response to chemical triggers. The addition of DNA conjugates induced transitions from micelles to fibers and bundles of fibers. The resulting hydrogels were used as an extracellular matrix mimic for cultured cells. Switching the hydrogel between states also switched astrocytes between their reactive and naïve phenotypes. —PDS

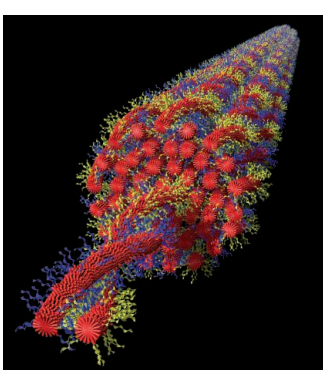

Illustration of triggered superstructure changes

Science, this issue p. 808

GEOLOGY

Impact crater under ice

Ancient meteorite impact craters have been found across the surface of Earth. Kjær *et al*. performed an ice-penetrating radar analysis of the Hiawatha Glacier in northwest Greenland and discovered an impact crater under Earth's ice sheets. The oldest ice in this crater is debris-ridden or heavily disturbed, suggesting that the impact postdates initiation of the ice sheet. Sediments carried by a river draining out of the Hiawatha Glacier included grains that were physically shocked in an impact by a relatively rare iron meteorite. Models suggest that the meteorite must have been on the scale of a kilometer wide. The crater may have formed relatively recently during the Pleistocene. —PJB

Sci. Adv. 10.1126/sciadv.aar8173 (2018).

CANCER

Lung cancer search and destroy

Like many cancer types, lung cancer is easier to treat when it is detected in its early stages. Scafoglio *et al*. discovered that a glucose transporter called sodium-dependent glucose transporter 2 is specifically found in early-stage lung tumors. They used a receptor-specific, radiolabeled tracer to perform positron emission tomography to identify early tumors. Furthermore, a class of diabetes drugs called gliflozins, which target the same receptor, effectively targeted these lung tumors in mouse models. —YN

Sci. Transl. Med. **10**, eaat5933 (2018).

IN OTHER JOURNALS

Edited by **Caroline Ash** *and* **Jesse Smith**

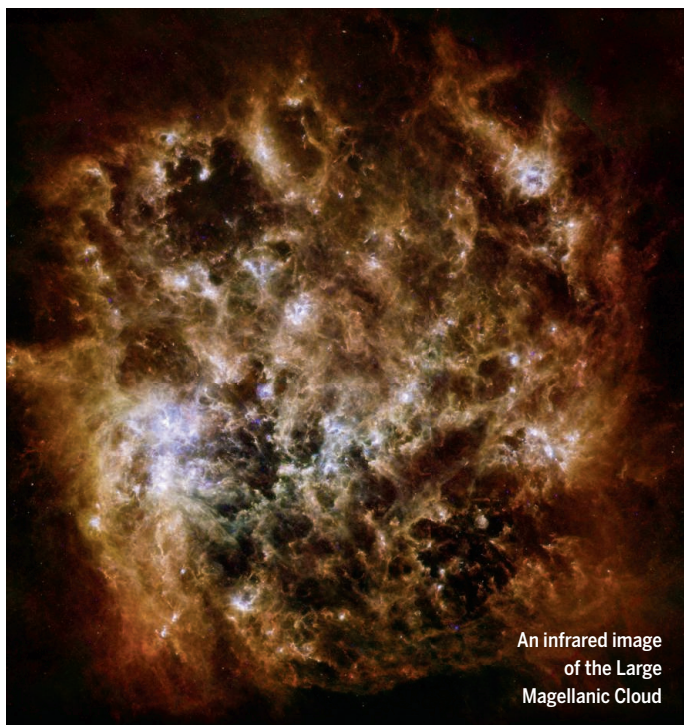

An infrared image of the Large Magellanic Cloud

GALAXIES

Big dwarfs have little dwarfs

Galaxies grow hierarchically: Small galaxies merge into bigger ones. Large galaxies like our Milky Way are surrounded by dozens of satellite dwarf galaxies, which are still in the process of merging. Those satellite galaxies should themselves be accompanied by even smaller dwarfs, but there is little observational evidence for this. Kallivayalil *et al.* examined 32 recently discovered dwarf galaxies by comparing astrometric data from the *Gaia* mission to simulations. They show that at least four of the dwarfs are associated with the Large Magellanic Cloud, the largest satellite galaxy of the Milky Way. This is consistent with standard cosmology. —KTS

Astrophys. J. **867**, 19 (2018).

IMMUNOLOGY

A new immune syndrome identified

The causes of later-onset immune deficiencies are elusive, but the symptoms can be distressing. A new syndrome that leads to global immune dysregulation has been discovered independently in two unrelated patients, one from Australia and the other in Japan. Using whole-genome sequencing, Cardinez *et al*. found that both patients had a mutation in a gene called inhibitor of nuclear factor kappa-B kinase subunit beta (*IKBKB*). The mutation causes the destruction of white blood cells known as lymphocytes, leading to excessive inflammation and recurrent infections. CRISPR-Cas technology was used to precisely engineer the same mutation into mice and generate immunodeficiency similar to that observed in human patients. This discovery highlights the value of rare-disease research and offers

The American crocodile (shown here) has been hybridizing with the Morelet's crocodile for millions of years.

CONSERVATION

Hybrid history

Hybridization between species has long presented a problem for the identification of biological species boundaries and, more recently, for establishing conservation priorities. Although the strict biological definition of a species states that it is reproductively isolated, many clearly defined species regularly hybridize, to the point that new species may emerge. Despite this, classifying hybrids and identifying their conservation status has been problematic. Pacheco-Sierra *et al*. attempted to address this challenge in the case of two species of crocodile (American and Morelet's), which have been hybridizing for millions of years. Although more "pure" populations of each species exist, there is considerable hybridization throughout their range of overlap. Hence, conservation focus on only the nonhybridized populations would exclude a range of natural, and presumably adaptive, hybrids and millions of years of diversity. —SNV

Front. Ecol. Evol. **6**, 138 (2018).

hope to patients with conditions that have escaped diagnosis. —PNK

J. Exp. Med. **215**, 2715 (2018).

SYNTHETIC BIOLOGY

Controls for a synthetic RNA circuit

Gene therapy generally relies on delivering DNA into cells along with strategies to control its expression. Synthetic messenger RNA (mRNA) is an attractive alternative gene therapy vehicle for applications that require transient protein expression, but controlling this expression remains challenging. One approach is to add a degradation domain to the protein, but this may compromise its proper function. Wagner *et al*. engineered small-molecule-responsive RNA binding proteins (RBPs) to control expression of proteins from synthetic mRNA. By regulating binding of the RBPs, they can regulate the timing and magnitude of expression of reporter proteins in engineered circuits that use either synthetic RNAs with base modifications (modRNA) designed to decrease immunogenicity or self-replicating RNAs (replicons) that give high levels of expression. —VV

Nat. Chem. Biol. **14**, 1043 (2018).

FOREST ECOLOGY

Declining wood in disturbed forest

The wood density of forest trees is an indicator of their potential to store carbon. Berenguer *et al*. compared the wood densities of trees and saplings in disturbed and undisturbed primary and secondary forests in eastern Amazonia. They found that wood density within disturbed forest is not recovering to the predisturbance values, with reductions as great as 33% in secondary forest. Key factors contributing to these reductions are proximity to forest edges, which impedes the recovery of high–wood density tree species, and infestation by lianas (woody vines) in disturbed forest, which also have an inhibitory effect on tree growth. As forests are increasingly disturbed in Amazonia and other tropical areas, their capacity to act as carbon sinks will diminish. —AMS

J. Ecol. **106**, 2190 (2018).

METABOLIC PATHWAYS

Roadblocks removed by rapid evolution

Cellular metabolism is an interconnected network of chemical reactions, each step catalyzed by dedicated enzymes. Inhibition or intentional removal of an enzyme should grind the pathway to a halt, a fact exploited by many drugs. However, given an adequate level of variation, cells inevitably circumvent such roadblocks. Pontrelli *et al*. challenged a strain of *Escherichia coli* with increased mutation rates to overcome a blocked biosynthetic pathway for the essential cofactor coenzyme A. Not one, not two, but three independent shortcuts around the roadblock were selected for, each after removal of the former. Such plasticity underlies the well-known ability of microorganisms to evade antibiotics. —MAF

Nat. Chem. Biol. **14**, 1005 (2018).

ORGANIC CHEMISTRY

A radical approach to asymmetric amines

Converting aliphatic C–H bonds into C–N bonds is a broadly useful reaction in pharmaceutical research. A persistent challenge is to obtain just one of the two possible mirror-image products, or enantiomers, in this context. Li *et al*. report an odd-electron cobalt porphyrin complex that catalyzes highly enantioselective intramolecular C–H amination in a variety of substrates with pendant sulfamoyl azides. The reaction selectively targets carbon centers that are five atoms away from the activated nitrogen, producing six-membered rings that can be opened by hydrolytic sulfonyl removal. Isotopic labeling and trapping studies implicate a radical mechanism. —JSY

Angew. Chem. Int. Ed. 10.1002/anie.201808923 (2018).

PHOTO: BORUT FURLAN/GETTY IMAGES

ALSO IN *SCIENCE* JOURNALS

Edited by **Stella Hurtley**

CELL METABOLISM

Mitochondrial serine transporter identified

One-carbon (1C) metabolism is a universal metabolic process that is required for purine synthesis and supports the high levels of proliferation in cancer cells. The transport of serine into mitochondria supplies most of the 1C units needed for biosynthesis. Kory *et al*. used a genetic screen to identify the long-sought-after mitochondrial serine transporter. Elucidating the key step of serine transport is important for our understanding of metabolism and has potential implications for cancer treatment. —SYM

Science, this issue p. 791

NEUROGENOMICS

Mapping the brain, one neuron at a time

Spatial transcriptomics can link molecularly described cell types to their anatomical positions and functional roles. Moffitt *et al*. used a combination of single-cell RNA-sequencing and MERFISH (multiplexed error-robust fluorescence in situ hybridization) to map the identity and location of specific cell types within the mouse preoptic hypothalamus and surrounding areas of the brain (see the Perspective by Tasic and Nicovich). They related these cell types to specific behaviors via gene activity. The approach provides an unbiased description of cell types of the preoptic area, which are important for sleep, thermoregulation, thirst, and social behavior. —LMZ

Science, this issue p. 792; see also p. 749

NEURODEVELOPMENT

Development of human brain neurons

The earliest stages of human brain development are very difficult to monitor, but using induced pluripotent stem cells (iPSCs) can help to elucidate the process. Real *et al*. transplanted neural progenitors derived from human iPSCs into the brains of adult mice. They used intravital imaging to visualize how resulting neurons grew and connected. The human cells produced neurons that integrated and developed synaptic networks with oscillatory activity. Dendritic pruning was observed and involved a process of branch retraction, not degeneration. Cells derived from individuals with Down syndrome, upon transplantation into the mouse brain, produced neurons that grew normally but showed reduced dendritic spine turnover and less network activity. —PJH

Science, this issue p. 793

ORGANIC CHEMISTRY

Heterocycles meet and marry on phosphorus

Metals such as palladium are routinely used to link together carbon rings in pharmaceutical synthesis. However, the presence of nitrogen in both rings can trip up this process. Hilton *et al*. report a versatile alternative process in which phosphorus takes the place of the metal. The phosphorus binds successively to both rings at the sites opposite the nitrogen, and treatment with acidic ethanol then pushes them off, bound to each other. Theory implicates a five-coordinate phosphorus intermediate that kinetically favors coupling of the two nitrogen-bearing rings over reactions of the other all-carbon substituents. —JSY

Science, this issue p. 799

BIOHYBRID MICROBES

Light-powered cell factories

Bacteria and fungi are used industrially to produce commodity fine chemicals at vast scale. Sugars are an economical feedstock, but many of the desired products require enzymatic reduction, meaning that some of the sugar must be diverted to regenerate the cellular reductant NADPH (reduced form of nicotinamide adenine dinucleotide phosphate). Guo *et al*. show that electrons from light-sensitive nanoparticles can drive reduction of cellular NADPH in yeast, which can then be used for reductive biosynthetic reactions. This system can reduce diversion of carbon to NADPH regeneration and should be compatible with many existing engineered strains of yeast. —MAF

Science, this issue p. 813

NANOMATERIALS

Wafer-scale hBN crystalline films

Although wafer-scale polycrystalline films of insulating hexagonal boron nitride (hBN) can be grown, the grain boundaries can cause both scattering or pinning of charge carriers in adjacent conducting layers that impair device performance. Lee *et al*. grew wafer-scale single-crystal films of hBN by feeding the precursors into molten gold films on tungsten substrates. The low solubility of boron and nitrogen in gold caused micrometer-scale grains of hBN to form that coalesced into single crystals. These films in turn supported the growth of epitaxial wafer-scale films of graphene and tungsten disulfide. —PDS

Science, this issue p. 817

ULTRAFAST DYNAMICS

Physics and chemistry in concert

Shining a short, intense light pulse on a material can cause a transition in both its atomic and electronic structures. The dynamics of the electronic structure in such transitions can be monitored using, for example, time-resolved photoemission spectroscopy. Nicholson *et al*. observed a photoinduced metal-insulator transition in indium nanowires on a silicon surface. They monitored both the physics and the chemistry of the system after the initial photoexcitation and correlated the closing of the electronic bandgap with the rearrangement of chemical bonds. The results showcase the wealth of information that time-resolved tools can reveal about the dynamics of complex systems. —JS

Science, this issue p. 821

CELL BIOLOGY

Cell transitions in pathology

Endothelial cells line the vasculature. These plastic cells can undergo a cell fate transition to produce mesenchymal cells, known as the endothelial-to-mesenchymal transition (EndMT). This transition is important in embryonic heart development and has also been observed in vascular pathologies, such as atherosclerosis. In a Perspective, Dejana and Lampugnani discuss the debate surrounding how EndMT contributes to disease and whether it can be targeted to treat various pathologies associated with vascular and extracellular matrix dysfunction. —GKA

Science, this issue p. 746

CONSERVATION

Impacts of outdoor artificial light

The use of artificial light at night is increasing around the world, causing both direct emissions, mostly in the vicinity of the light, and a brightening of the night sky called skyglow. In a Perspective, Gaston explains that this light is changing the activity patterns of many animal species and can even affect the timing of budburst in temperate

trees. Outdoor artificial light at night may also affect human sleep patterns and human health. The ongoing shift to light-emitting diode (LED) lamps with a broader and colder light spectrum is exacerbating these problems. —JFU

Science, this issue p. 744

CARDIAC DYSFUNCTION

Breaking mitochondria and hearts

Blocking the excessive mitochondrial fission mediated by dynamin-related protein 1 (Drp1) that occurs after myocardial infarction prevents cardiac dysfunction from developing. Nishimura *et al*. found that the cytoskeletal regulator filamin increased Drp1 activity after myocardial infarction and that the filamin-Drp1 interaction was inhibited by the U.S. Food and Drug Administration–approved drug cilnidipine (see the Focus by Boyer and Eguchi). Administering cilnidipine to mice after myocardial infarction reduced mitochondrial fission and cardiac dysfunction, suggesting that this drug could be repurposed to reduce heart attack–induced damage. —WW

Sci. Signal. **11**, eaat5185, eaav3267 (2018).

IMMUNOGENETICS

Fine-tuning CD8$^+$ T cell responses

Human cytotoxic CD8$^+$ T cells are important for defense against viral infections. Boelen *et al*. investigated whether inhibitory killer cell immunoglobulin-like receptors (iKIRs) carried by patients with chronic viral infections affected the efficacy of their CD8$^+$ T cell responses. Possession of an iKIR gene along with a gene encoding a KIR ligand enhanced protective and detrimental human leukocyte antigen (HLA) class I associations for HIV-1, hepatitis C virus, and human T cell leukemia virus type 1. Analysis of virus dynamics, in vitro survival assays, and mathematical modeling suggested that iKIR ligation enhances HLA associations by increasing T cell survival. In contrast to many reported iKIR-disease associations, these observations applied to all iKIRs and the three viral infections studied. —IW

Sci. Immunol. **3**, eaao2892 (2018).

RESEARCH ARTICLE SUMMARY

CELL METABOLISM

SFXN1 is a mitochondrial serine transporter required for one-carbon metabolism

Nora Kory, Gregory A. Wyant*, Gyan Prakash*, Jelmi uit de Bos, Francesca Bottanelli, Michael E. Pacold, Sze Ham Chan, Caroline A. Lewis, Tim Wang, Heather R. Keys, Yang Eric Guo, David M. Sabatini†

INTRODUCTION: One-carbon metabolism generates the one-carbon units required to synthesize many critical metabolites, including nucleotides, amino acids, and lipids. The pathway has cytosolic and mitochondrial branches, and a key step is the entry, through an unknown mechanism, of serine into mitochondria, where it is converted into glycine and formate.

In dividing mammalian cells, the mitochondrial catabolism of serine supplies most of the one-carbon units needed for biosynthesis. Indeed, many cancers rely on the one-carbon units generated from serine for proliferation, and mitochondrial serine catabolism enzymes are commonly up-regulated in tumors. Given that the entry of serine into mitochondria is a critical step in the generation of one-carbon units, it is surprising that the mitochondrial transporter(s) for serine remains unknown.

RATIONALE: To seek the transporter responsible for serine import into mitochondria, we designed a CRISPR-Cas9–mediated genetic screen in human cells based on the likelihood that loss of mitochondrial serine transport will reduce the proliferation of cells lacking the cytosolic branch of the one-carbon metabolism pathway. Therefore, we aimed to identify genes that are synthetic lethal with serine hydroxymethyl transferase–1 (SHMT1), a key cytosolic enzyme of the pathway. Moreover, we reasoned that even if there are redundant mechanisms for serine transport, we can sensitize cells to its partial inhibition by lowering cytosolic serine concentrations, which is easily achieved by removing exogenous serine. Thus, we sought genes required for the optimal proliferation of cells lacking the cytosolic one-carbon pathway when cultured in serine-free media. We picked the human blood Jurkat and K562 cancer cell lines for our screen because of their high mitochondrial one-carbon metabolism activity and suitability for screening and transduced cells with a lentiviral single guide RNA (sgRNA) library that targets ~3000 metabolic enzymes, small-molecule transporters, and metabolism-related transcription factors.

RESULTS: This screen yielded genes in the pathways for serine and purine biosynthesis and with known functions in one-carbon metabolism. In both cell lines, only one gene of unknown molecular function scored, sideroflexin 1 (SFXN1), a multipass mitochondrial membrane protein. *Sfxn1* was originally identified as the gene mutated in a mouse mutant with anemia and axial skeletal abnormalities, and is part of the sideroflexin family of proteins conserved throughout eukaryotes. In humans, *SFXN1* is highly expressed in the blood, liver, and kidney, which are tissues with high one-carbon metabolism activity. STED super-resolution microscopy confirmed that SFXN1 localizes to the inner and not outer mitochondrial membrane, in agreement with a potential role as a metabolite transporter. The proliferation defect of *SFXN1*-null cells in serine-depleted media was completely reversed by adding formate, the product of the mitochondrial one-carbon pathway, which directly implicates an insufficient supply of one-carbon units in their defective proliferation. Notably, expression of an sgRNA-resistant *SFXN1* cDNA restored the proliferation rate of the *SFXN1*-null cells to that of the wild-type cells.

ON OUR WEBSITE

Read the full article at http://dx.doi.org/10.1126/science.aat9528

Serine tracing experiments place SFXN1 in the mitochondrial branch of the one-carbon pathway. Like cells missing mitochondrial components of one-carbon metabolism, those null for SFXN1 are defective in glycine and purine synthesis and have reduced levels of charged folate species. Cells lacking SFXN1 and one of its four homologs, SFXN3, have more severe defects, including mitochondrial dysfunction and being auxotrophic for glycine. Several human SFXN family members can complement SFXN1-3 double loss, as can their yeast and *Drosophila* orthologs. These results were confirmed when *SFXN3* emerged as one of the top synthetic lethal genes with *SFXN1* in the absence of exogenous glycine. To test whether SFXN1 can directly transport serine, we purified the FLAG-tagged protein from mammalian cells and reconstituted it into liposomes. Recombinant SFXN1 mediated serine uptake into liposomes. Conversely, serine uptake into mitochondria isolated from *SFXN1*-null cells was decreased. SFXN1 may have other physiologically relevant transport substrates besides serine, including cysteine and alanine.

CONCLUSION: SFXN1 functions as a mitochondrial serine transporter in one-carbon metabolism. As there are multiple sideroflexins and their expression varies across tissues, SFXN1 and its homologs may turn out to be important nodes for regulating the fate of serine in cells. Because SFXN1 is expressed in many cancers and its expression is likely regulated by the Myc transcription factor, it may also have unexplored roles in cancer cell growth. ■

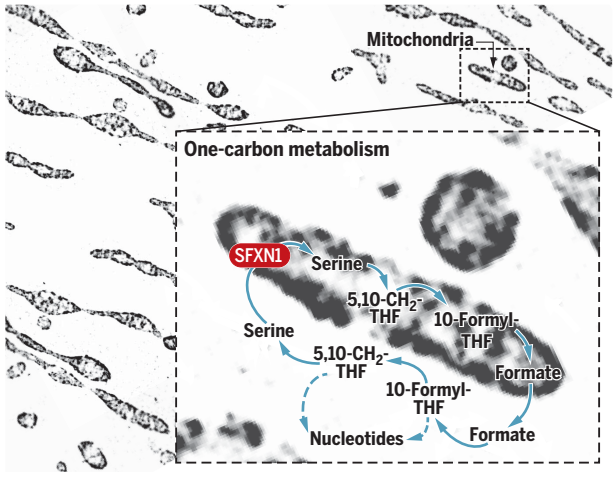

SFXN1 transports serine into mitochondria and is a component of the one-carbon metabolism pathway. Serine is converted to formate in mitochondria, which is then exported to the cytosol to generate one-carbon units carried on tetrahydrofolate (THF) for nucleotide synthesis and other processes. In this diagram, the mitochondria are represented by STED super-resolution images of cells stained both for FLAG-SFXN1 and the outer mitochondrial membrane marker Tom20.

The list of author affiliations is available in the full article online.
*These authors contributed equally to this work.
†Corresponding author. Email: sabatini@wi.mit.edu
Cite this article as N. Kory *et al.*, *Science* **362**, eaat9528 (2018). DOI: 10.1126/science.aat9528

RESEARCH ARTICLE

CELL METABOLISM

SFXN1 is a mitochondrial serine transporter required for one-carbon metabolism

Nora Kory[1,2,3,4], Gregory A. Wyant[1,2,3,4]*, Gyan Prakash[1]*, Jelmi uit de Bos[1], Francesca Bottanelli[5]†, Michael E. Pacold[1,2,3,4,6]‡, Sze Ham Chan[1], Caroline A. Lewis[1], Tim Wang[1,2,3,4], Heather R. Keys[1], Yang Eric Guo[1], David M. Sabatini[1,2,3,4]§

One-carbon metabolism generates the one-carbon units required to synthesize many critical metabolites, including nucleotides. The pathway has cytosolic and mitochondrial branches, and a key step is the entry, through an unknown mechanism, of serine into mitochondria, where it is converted into glycine and formate. In a CRISPR-based genetic screen in human cells for genes of the mitochondrial pathway, we found sideroflexin 1 (SFXN1), a multipass inner mitochondrial membrane protein of unclear function. Like cells missing mitochondrial components of one-carbon metabolism, those null for SFXN1 are defective in glycine and purine synthesis. Cells lacking SFXN1 and one of its four homologs, SFXN3, have more severe defects, including being auxotrophic for glycine. Purified SFXN1 transports serine in vitro. Thus, SFXN1 functions as a mitochondrial serine transporter in one-carbon metabolism.

One-carbon metabolism uses serine to generate the reactive one-carbon donors, such as 5,10-methylene-tetrahydrofolate, required for many basic processes, including nucleotide and lipid synthesis [reviewed in (*1*–*3*)]. An interesting aspect of the one-carbon pathway is that although partially redundant isozymes exist in the cytosol and mitochondrial matrix, in most proliferating cells, the pathway primarily flows from the cytosol into mitochondria and back out (Fig. 1A). Cytosolic serine enters the mitochondrial matrix and is converted to glycine and formate, which then exits to the cytosol where it is used to generate the charged folates that serve as one-carbon donors (*4*) (Fig. 1A). In dividing mammalian cells, the mitochondrial catabolism of serine supplies most of the one-carbon units needed for biosynthesis (*5*–*9*), but the cytosolic branch can compensate for its loss (*8*).

Given that the entry of serine into mitochondria is a critical step in the generation of one-carbon units, it is surprising that the mitochondrial transporter(s) for serine remains unknown (*5*, *10*–*12*). To seek such a transporter, we designed a CRISPR-Cas9–mediated genetic screen based on the likelihood that loss of mitochondrial serine transport will reduce the proliferation of cells lacking the cytosolic branch of one-carbon metabolism. Moreover, we reasoned that even if there are redundant mechanisms for serine transport, we can sensitize cells to its partial inhibition by lowering cytosolic serine concentrations, which is easily achieved by removing exogenous serine (fig. S1A) (*13*). Thus, we sought genes required for the optimal proliferation of cells lacking the cytosolic one-carbon pathway when cultured in serine-free media.

A genetic screen for components of the mitochondrial one-carbon metabolism pathway yields SFXN1

To implement such a screening strategy, we first generated human Jurkat leukemic T cells and K562 erythroleukemic cells null for serine hydroxymethyltransferase 1 (SHMT1), an isozyme of mitochondrial SHMT2 and a key component of the cytosolic one-carbon pathway that interconverts serine and glycine (Fig. 1A). We chose Jurkat and K562 cells because they are suitable for screening (*14*, *15*) and have high mitochondrial one-carbon pathway activity (*8*, *16*). We transduced the *SHMT1*-null cells with a lentiviral single guide RNA (sgRNA) library that targets ~3000 metabolic enzymes, small-molecule transporters, and metabolism-related transcription factors (~10 sgRNAs per gene) and also contains 499 control sgRNAs (*15*). The transduced cells were cultured in RPMI media with or without serine, and for each gene, we generated a gene score by calculating the mean $\log_2$ fold-change in the abundance from the beginning to end of the culture period of all the sgRNAs targeting the gene (*15*) (Fig. 1B). We also obtained a differential gene score that reflects the relative importance of the gene in the presence or absence of serine.

As expected, most genes, as well as the control sgRNAs, had similar scores in cells cultured under both media conditions (Fig. 1C). Multiple classes of genes behaved as predicted. For example, in both cell lines, the three genes in the serine synthesis pathway (*PHGDH*, *PSAT1*, *PSPH*) were required for proliferation in serine-free media, as were components of the purine synthesis pathway, which is downstream of one-carbon metabolism (Fig. 1D and fig. S1B). Established components of the mitochondrial one-carbon pathway, such as SHMT2 and the mitochondrial folate transporter (MFT), scored differentially in Jurkat cells, as did 5,10-methenyltetrahydrofolate synthetase (MTHFS), which returns 5-formyl-tetrahydrofolate to the tetrahydrofolate (THF) cofactor pool (*17*), in K562 cells.

Notably, the only gene of unknown molecular function that scored differentially in both cell lines was the mitochondrial transmembrane protein sideroflexin 1 (SFXN1) (Fig. 1, C and D, and fig. S1, B and C). *Sfxn1* was originally identified as the gene mutated in a mouse mutant with anemia and axial skeletal abnormalities and is part of the sideroflexin family of proteins conserved throughout eukaryotes (*18*, *19*). In humans, *SFXN1* is highly expressed in the blood, liver, and kidney, which are tissues with high one-carbon metabolism activity (fig. S2, A and B).

To follow up the screen, we generated Jurkat and K562 cells lacking SFXN1 alone or in combination with SHMT1 (fig. S1D). In the absence of serine, the *SFXN1*-null Jurkat cells proliferated more slowly than the wild-type or AAVS1-targeted control cells, and the loss of SHMT1 exacerbated the defect, consistent with the screening results (Fig. 1E). The *SFXN1*-null K562 cells proliferated less well than their Jurkat counterparts, but SHMT1 deletion did not exacerbate the defect, likely because K562 cells express very low levels of SHMT1 to begin with (Fig. 4C). The addition of formate, the product of the mitochondrial one-carbon pathway, completely reversed the slow proliferation of the Jurkat and K562 single- and double-null cells in the serine-free media, directly implicating an insufficient supply of one-carbon units in their defective proliferation (Fig. 1E). Notably, expression of an sgRNA-resistant *SFXN1* cDNA restored the proliferation rate of the *SFXN1*-null cells to that of the wild-type cells (Fig. 1F). *SHMT2*-null cells exhibited similar albeit more profound proliferation defects than the cells lacking *SFXN1* (Fig. 1E).

Loss of SFXN1 phenocopies mutants in mitochondrial one-carbon metabolism

SFXN1 localizes to the inner mitochondrial membrane and is predicted to have five transmembrane domains [(*18*) and our analysis with Protter (*20*)], with its N terminus in the matrix and C terminus

[1]Whitehead Institute for Biomedical Research, 455 Main Street, Cambridge, MA 02142, USA. [2]Howard Hughes Medical Institute, Department of Biology, Massachusetts Institute of Technology, Cambridge, MA 02139, USA. [3]Koch Institute for Integrative Cancer Research, Massachusetts Institute of Technology, Department of Biology, 77 Massachusetts Avenue, Cambridge, MA 02139, USA. [4]Broad Institute of Harvard and Massachusetts Institute of Technology, 415 Main Street, Cambridge, MA 02142, USA. [5]Department of Cell Biology, Yale University School of Medicine, New Haven, CT 06520, USA. [6]Department of Radiation Oncology at NYU Langone Medical Center, New York, NY 10016, USA.
*These authors contributed equally to this work. †Present address: Freie Universität Berlin, Faculty of Biology, Chemistry and Pharmacy, 14195 Berlin, Germany. ‡Present address: NYU Langone Medical Center, 522 First Avenue, Smilow 907, New York, NY 10016, USA.
§Corresponding author. Email: sabatini@wi.mit.edu

in the intermembrane space (Fig. 2A) (*21*). As expected, in HeLa cells, FLAG-tagged SFXN1 colocalized with the inner mitochondrial membrane protein COX4 (Fig. 2B), and endogenous SFXN1 was enriched in mitochondria purified from Jurkat and K562 cells (fig. S5B). Using super-resolution microscopy, we confirmed that SFXN1 localizes to the inner and not outer mitochondrial membrane (Fig. 2C). The outer mitochondrial membrane, which can be marked by Tom20 (Fig. 2C), is permeable to most small metabolites owing to the presence of the VDAC porins. Given these attributes and its emergence from our screen, SFXN1 was an excellent candidate to be a mitochondrial serine transporter.

If this were the case, cells lacking SFXN1 should have metabolic defects similar to those of cells missing SHMT2 or MTHFD2, the enzymes needed to convert serine to glycine and formate in mitochondria. Indeed, loss of SFXN1, SHMT2, or MTHFD2, but not SHMT1, caused the depletion of glycine in Jurkat cells, an increase in the serine-to-glycine ratio, and a reduction in

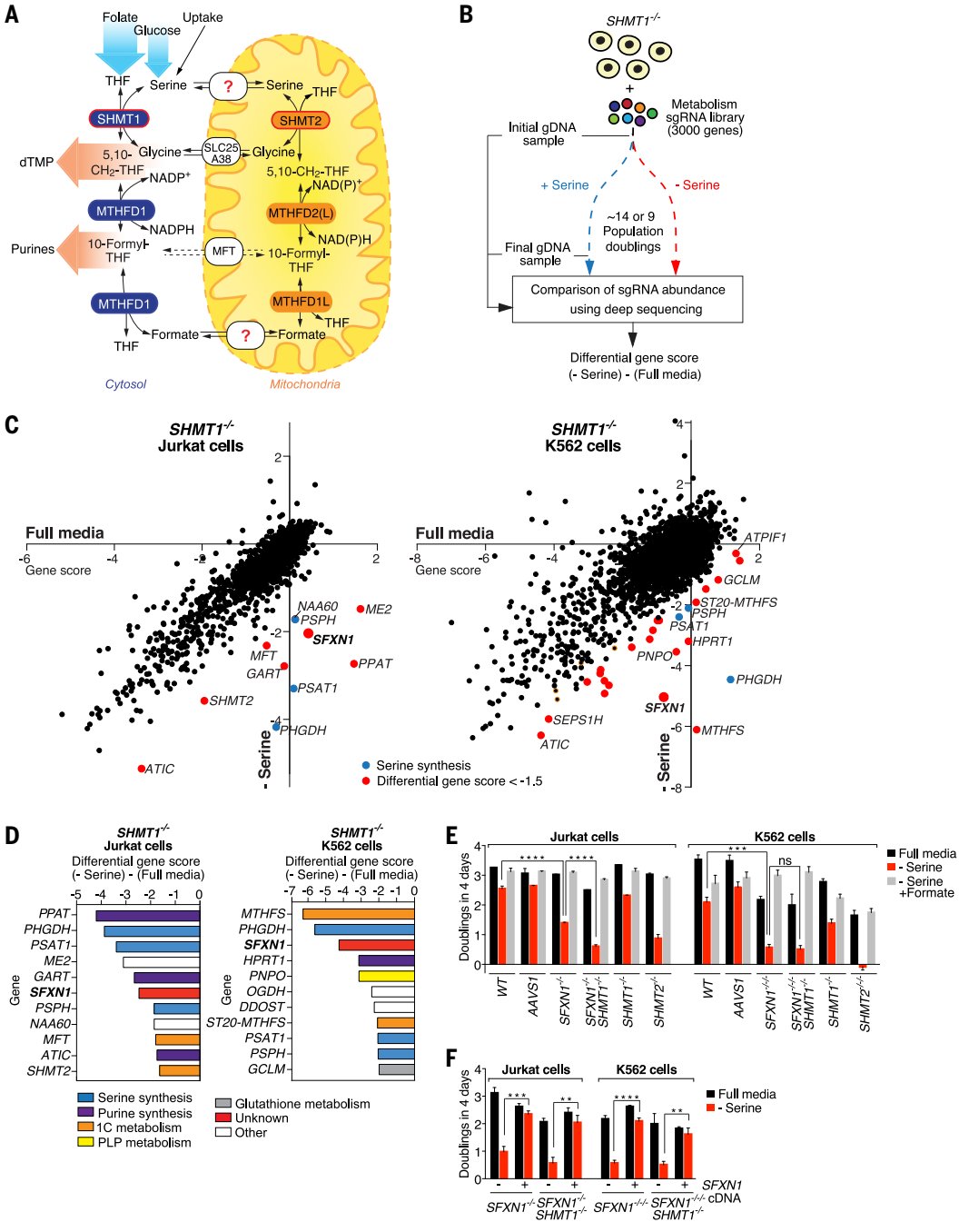

Fig. 1. A genetic screen for components of the one-carbon metabolism pathway yields *SFXN1*. (**A**) Schematic of the one-carbon metabolism pathway. dTMP, deoxythymidine monophosphate; THF, tetrahydrofolate; CH2THF, methyleneTHF. NAD(P)H, nicotinamide adenine dinucleotide (phosphate); SHMT, serine hydroxymethyltransferase; MFT, mitochondrial folate transporter/carrier; MTHFD, methylenetetrahydrofolate dehydrogenase. The dashed arrows indicate that the exact nature of the substrate for MFT is unknown. (**B**) CRISPR-Cas9–based screening strategy designed to identify new components of the mitochondrial one-carbon pathway. The cells in the serine-free media were collected after ~9 population doublings because they proliferated more slowly than cells in full media, which were collected after ~14 doublings. For each gene, we calculated its gene score as the mean $\log_2$ fold-change in the abundance of the 10 sgRNAs targeting the gene. The differential gene score is the difference in scores in the absence versus presence of serine. sgRNA, single guide RNA; gDNA, genomic DNA. (**C**) *SFXN1* emerges as a hit in both the Jurkat and K562 screens. Gene scores in full media were plotted against those in serine-deficient media. Genes with a differential score of <−1.5 are shown in red or blue (for serine synthesis genes). The full list of genes that scored in K562 cells is shown in fig. S1B. (**D**) Top-scoring genes from both screens. Genes were ranked according to the differential gene score in full versus serine-deficient media. 1C, one-carbon; PLP, pyridoxal phosphate. (**E**) *SFXN1*-null cells have a proliferation defect in the absence of serine, which is rescued by the addition of 1 mM formate to the media. Additional loss of *SHMT1* exacerbates the proliferation defect in the Jurkat cells (mean ± SD; $n = 3$; n denotes biological replicates; this is true for every main and supplementary figure except fig. S6D; ***$P < 0.001$, ****$P < 0.0001$; ns, not significant). AAVS1 indicates control cells that were treated with an sgRNA targeting the AAVS1 locus as described previously (*14*). SFXN1- and SHMT2-null K562 cells are designated as -/-/- as they are triploid for these genes. (**F**) Expression of an sgRNA-resistant cDNA for SFXN1 in the *SFXN1*-null cells restores their proliferation rate in serine-deficient media (mean ± SD; $n = 3$; **$P < 0.01$, ****$P < 0.0001$). Two-tailed t tests were used for comparisons between groups.

the amount of de novo–synthesized glycine secreted into the media as measured in tracing experiments with labeled serine (Fig. 2, D and E, and fig. S3A). The null cells also had lower levels of the charged folate species that we were able to detect (5,10-methenyl-THF and 5-formyl-THF), and this was not secondary to a drop in THF or folate levels (Fig. 2F and fig. S3B). The sgRNA-resistant *SFXN1* cDNA complemented all the metabolic defects of the *SFXN1*-null cells.

To determine if loss of SFXN1 affects pathways that consume one-carbon donors, we examined purine synthesis, as it uses large amounts of 10-formyl-THF as a cofactor (Fig. 2G). Indeed, the purine synthesis intermediates 5′-phosphoribosylglycinamide (GAR), phosphoribosylaminoimidazolesuccinocarboxamide (SAICAR), and 5-aminoimidazole-4-carboxamide ribonucleotide (AICAR) accumulated in *SFXN1*-null cells to similar extents as in cells lacking SHMT2 and MTHFD2 (*8*) (Fig. 2H and fig. S3C). In this respect, loss of SFXN1 mimicked serine starvation, which in wild-type cells also caused an accumulation of the intermediates (fig. S3D). Consistent with SFXN1 acting upstream of formate production, formate abolished the accumulation of the intermediates in the *SFXN1*-null cells but did not rescue the defects in glycine levels (Fig. 2, I and J).

To monitor the relative contributions of the cytosolic and mitochondrial pathways to the synthesis of one-carbon units in *SFXN1*-null cells, we used a reported strategy to trace [2,3,3-$^2H_3$]-serine to thymidine triphosphate (TTP) (*8*, *22*). The deuterated serine will give rise to TTP shifted by two mass units (TTP M+2) when catabolized through the cytosolic pathway but only by one mass unit (TTP M+1) if via the mitochondrial pathway (Fig. 2K). In wild-type cells, the M+1 form was the predominant species of newly synthesized TTP, as expected in cells generating most of their one-carbon donors through mitochondria. By contrast, in cells lacking SFXN1, SHMT2, or MTHFD2, most of the newly synthesized TTP was of the M+2 species (Fig. 2L), consistent with SFXN1 being important for the function of the mitochondrial one-carbon pathway.

To corroborate this conclusion, we used our metabolism-focused sgRNA library to screen for genes important for the optimal proliferation of *SFXN1*-null but not wild-type cells. Gratifyingly, among the top hits were many components of the cytosolic one-carbon pathway, including *SHMT1*, which was the most differentially required gene (Fig. 2, M and N, and fig. S3E). We conclude that SFXN1 is part of the mitochondrial one-carbon pathway and its loss, like that of established components, makes cells more dependent on the cytosolic branch of the pathway.

SFXN1 transports serine in vitro

To test if SFXN1 can directly transport serine, we purified the FLAG-tagged protein from mammalian cells (fig. S4A) and reconstituted it into liposomes. Recombinant SFXN1 mediated serine uptake into liposomes (Fig. 3A). Both L- and D-serine competed with the transport of the labeled serine, as did other amino acids, including the structurally related amino acids alanine, cysteine, and glycine, whereas other metabolites did so to negligible extents (Fig. 3B). Neither formate nor citrate competed with serine transport. In vitro, SFXN1 transports serine with a Michaelis constant (K_m) of ~170 μM (Fig. 3C), which suggests that SFXN1 can transport serine at the estimated cellular serine concentration of 300 μM. Consistent with these findings, serine uptake by mitochondria isolated from *SFXN1*-null cells was reduced compared to that by wild-type mitochondria, whereas the uptake of the structurally unrelated amino acid glutamate was unaffected (Fig. 3D).

Because alanine, cysteine, and glycine partially competed with serine in the in vitro transport assay, we tested whether SFXN1 can also transport these amino acids. Indeed, SFXN1 transported alanine at the physiologically relevant concentration of 371 μM (Fig. 3E). We could not reliably measure cysteine and glycine transport by SFXN1 and suspect that further optimization of the assay might be necessary to determine whether SFXN1 can also directly transport these amino acids. To begin to assess a potential role for SFXN1 in the metabolism of these amino acids, we incubated cells in media with or without them. Although the presence or absence of alanine or glycine did not affect the proliferation of *SFXN1*-null cells, they proliferated better than their wild-type counterparts in media with low concentrations of cystine, suggesting that SFXN1 may play a role in intracellular cysteine transport (fig. S4C and fig. S5A) (see Discussion).

Homologs of SFXN1 can compensate for its loss

Cells lacking components of the mitochondrial one-carbon pathway are auxotrophic for glycine (*6*, *23*–*25*), which we confirmed using our *SHMT2*- and *MTHFD2*-null cells (fig. S5A). Because loss of SFXN1 did not cause glycine auxotrophy, we reasoned that there must be genes that can partially compensate for it. In mammals there are five sideroflexins, with SFXN3 being the closest homolog of SFXN1 (88% protein sequence similarity) (Fig. 4A). Budding yeast has only one sideroflexin (FSF1), while *Drosophila melanogaster* has two, one most similar to SFXN1 and SFXN3 (Sfxn1-3) and the other to SFXN2 (Sfxn2) (Fig. 4A). The human, fly, and yeast sideroflexins that we examined localized to mitochondria when expressed in HeLa cells (Fig. 4D).

Because Jurkat and K562 cells, like other commonly used cell lines, express multiple sideroflexins (Fig. 4, B and C), we hypothesized that one or more family members might partially compensate for the loss of SFXN1, thus explaining why the *SFXN1*-null cells are not auxotrophic for glycine. To explore this possibility, we used the metabolism-focused sgRNA library to screen for genes required for *SFXN1*-null Jurkat cells to proliferate in the absence of glycine. In addition to several genes in the mitochondrial (*MTHFD2, SHMT2, MFT*) and cytosolic (*MTHFS*) one-carbon pathways, the only other gene to score was *SFXN3* (Fig. 4E), suggesting that it has redundant functions with *SFXN1*.

Indeed, like cells lacking *SHMT2* or *MTHFD2*, cells null for both *SFXN1* and *SFXN3* [*SFXN1&3* DKO (double knockout) cells] did not proliferate in the absence of glycine (Fig. 4F). Consistent with these cells having a severe defect in glycine synthesis, the addition of formate to the glycine-free media did not reverse their proliferation defect (Fig. 4F), whereas expression of either SFXN1 or SFXN3 did (fig. S5, D and E). Purine synthesis intermediates accumulated to greater extents in the DKO cells than in those lacking only *SFXN1*, whereas the single or combined deletions of *SFXN3* and *SFXN2* did not affect these metabolites (Fig. 4G). Compared to the *SFXN1*-null and wild-type cells, the DKO cells proliferated slowly even in full media, suggesting that beyond experiencing one-carbon unit stress, these cells have limiting amounts of one-carbon donors and/or glycine.

Whereas mitochondrial mass, morphology, and function were not affected in *SFXN1*-null cells, *SFXN1&3* DKO cells did have defects in these parameters (fig. S6). Mitochondrial one-carbon metabolism, as well as serine itself, is needed for mitochondrial protein synthesis and, indeed, the DKO cells had reduced levels of mitochondrially encoded proteins, likely explaining their mitochondrial dysfunction (fig. S6G) (*26*–*29*). Despite multiple attempts and the supplementation of full media with formate, we failed to isolate *SFXN1&2&3* triple knockout cells, suggesting that such cells are not viable. However, we were able to obtain one cell clone lacking SFXN1 and SFXN2 and containing low levels of SFXN3 as a result of an in-frame deletion (fig. S5C), and these cells were also unable to proliferate in the absence of glycine (Fig. 4F).

Because SFXN1 and SFXN3 are among the most highly expressed sideroflexins in Jurkat cells (Fig. 4B), we asked if other homologs can compensate for them if expressed at higher levels. With the exception of SFXN4, overexpression of any of the human sideroflexins reversed the glycine auxotrophy of the Jurkat *SFXN1&3* DKO cells, as did heterologous expression of yeast FSF1 and *Drosophila* Sfxn1-3 and Sfxn2 (Fig. 4H and fig. S5F). However, besides SFXN1 and SFXN3, only SFXN2, FSF1, and Sfxn1-3 (the closest *Drosophila* homolog of SFXN1) ameliorated, to differing degrees, the defects in purine synthesis (Fig. 4I). These results suggest that serine transport is an evolutionarily conserved feature of the sideroflexins but that their kinetic properties and likely substrate specificities vary so that not all can support the high rate of mitochondrial serine import required to fulfill the demand for one-carbon units of proliferating cells. In vitro transport assays optimized for each sideroflexin will be required to test this idea.

Discussion

Our work reveals SFXN1 as a previously missing component of the one-carbon metabolism pathway that functions as a mitochondrial serine transporter. We propose that SFXN1 and SFXN3 (and perhaps SFXN2) are the main mitochondrial serine transporters in human cells and that

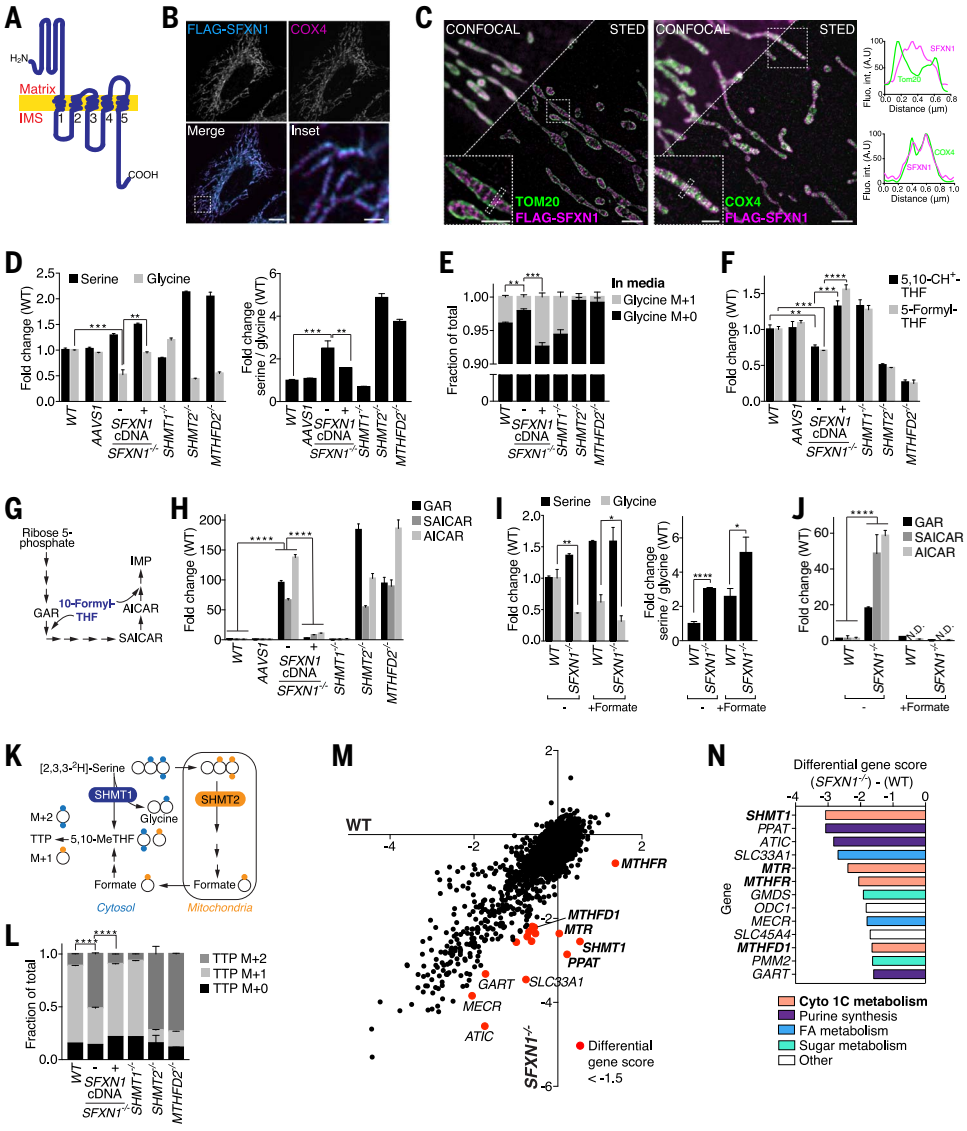

Fig. 2. Loss of SFXN1 phenocopies mutants in mitochondrial one-carbon metabolism. (**A**) Model of the predicted topology of SFXN1 in the mitochondrial inner membrane. Transmembrane helices are indicated by numbers. IMS, intermembrane space. (**B**) FLAG-tagged SFXN1 localizes to mitochondria. Wild-type HeLa cells transiently expressing FLAG-SFXN1 were processed for immunofluorescence detection of the FLAG epitope (cyan) and the mitochondrial inner membrane marker cytochrome c oxidase subunit 4 (COX4) (magenta). The merged image shows the overlap of both channels in white. Scale bar is 10 μm in the full image and 2 μm in the inset. (**C**) Super-resolution microscopy confirms SFXN1 localization to the inner membrane of mitochondria. Wild-type HeLa cells transiently expressing FLAG-SFXN1 were processed for immunofluorescence detection of the FLAG epitope (magenta) and the outer mitochondrial membrane marker Tom20 (left panel, green) or the mitochondrial inner membrane marker cytochrome c oxidase subunit 4 (COX4) (right panel, green) and imaged by STED microscopy. Overlap of magenta and green channels is shown in white, and line profiles show fluorescent signals of each channel across mitochondria where marked by the dotted rectangles. Scale bars are 2 μm in the full images and 1 μm in the insets. (**D**) As in cells lacking known components of the mitochondrial one-carbon pathway, glycine levels are reduced and the cellular serine/glycine ratio is increased in *SFXN1*-null cells. Serine and glycine levels were measured by gas chromatography–mass spectrometry (GC-MS) in extracts from wild-type Jurkat cells or single-cell–derived control and knockout clones (mean ± SD; $n = 3$; $^{**}P < 0.01$, $^{***}P < 0.001$). (**E**) Loss of SFXN1 causes a glycine synthesis defect. GC-MS was used to measure glycine in the culture media of wild-type Jurkat cells or single-cell–derived knockout clones incubated for 12 hours with 2,3,3-$^{2}H_3$-serine as the only serine source. The glycine M+0 species is the unlabeled species. The glycine M+1 species is derived from 2,3,3-$^{2}H_3$-serine (mean ± SD; $n = 3$; $^{**}P < 0.01$, $^{***}P < 0.001$). (**F**) Levels of charged folate species are decreased in *SFXN1*-null cells. Metabolites were measured by LC-MS in extracts from wild-type Jurkat cells or single-cell–derived control and knockout clones (mean ± SD; $n = 3$; $^{**}P < 0.01$, $^{***}P < 0.001$, $^{****}P < 0.0001$). 5,10-CH^{+}-THF, 5,10-methenyl-THF. (**G**) Schematic of the purine synthesis pathway, indicating steps using one-carbon units in the form of 10-formyl-THF. GAR, 5′-phosphoribosyl-glycinamide. SAICAR, phosphoribosylaminoimidazolesuccinocarboxamide. AICAR, 5-aminoimidazole-4-carboxamide ribonucleotide. IMP, inosine monophosphate. (**H**) The purine synthesis intermediates GAR, SAICAR, and AICAR accumulate in *SFXN1*-null cells. Purine synthesis intermediates were measured by LC-MS in extracts from wild-type Jurkat cells or single-cell–derived control and knockout clones (mean ± SD; $n = 3$; $^{****}P < 0.0001$). (**I**) Addition of 1 mM formate does not rescue glycine levels and serine/glycine ratio of *SFXN1*-null cells. Serine and glycine levels were measured by LC-MS in extracts from wild-type Jurkat cells or single-cell–derived *SFXN1*-null cells incubated for 24 hours in the indicated media (mean ± SD; $n = 3$; $^{*}P < 0.05$, $^{**}P < 0.01$). (**J**) Addition of 1 mM formate reverses the accumulation

Sfxn1-3 also has this function in *D. melanogaster*. SFXN1 and SFXN3 likely have other physiologically relevant substrates besides serine, such as alanine or cysteine, a notion supported by our in vitro transport results, the finding that cells lacking both have more severe proliferation defects than those missing established components of the mitochondrial one-carbon pathway, and that cells lacking SFXN1 have a proliferation advantage in media containing low cystine, the oxidized dimer of cysteine present in RPMI media and taken up by cells (fig. S4C). A major use of cysteine is cytosolic glutathione synthesis, and it is possible that loss of SFXN1 and thus a reduction in mitochondrial cysteine import should increase its availability for this use, which is known to be limiting for cell proliferation (*30*). Two reports proposed that SFXN1 can transport citrate in vitro (*31*, *32*), but the physiological relevance of this remains unclear because SLC25A1 is well established as the mitochondrial citrate carrier (*33*–*35*) and citrate did not compete with serine in our in vitro assays (Fig. 3B). Moreover, these previous studies used purified endogenous rather than recombinant protein, raising the possibility that the observed activity was due to a copurifying contaminating protein. In addition, we excluded another potential substrate for the sideroflexins, pyridoxine (*36*), which is a precursor for the pyridoxal 5′-phosphate cofactor of SHMT2, ALAS2, and mitochondrial transaminases, because the levels of pyridoxal-conjugated proteins were unchanged in the mitochondria of *SFXN1*- or *SFXN1&3*-null cells (fig. S6H). Furthermore, SLC25A39 is likely responsible for pyridoxal 5′-phosphate transport into mitochondria (*37*).

When overexpressed, SFXN5 only partially complements loss of SFXN1, and we suspect that its main function is not as a serine transporter—similarly to SFXN4, which in our experimental systems cannot substitute for SFXN1. It is interesting that budding yeast only has one sideroflexin (FSF1), perhaps suggesting that is has broader functions than its homologs in other species.

Mice with a loss-of-function mutation in *Sfxn1* have a sideroblastic-like anemia characterized by iron accumulation in mitochondria (*18*, *39*). Although *Sfxn1* has been challenged as the causative gene (*39*), our work does provide a possible explanation for the phenotype. In humans, mutations that impair the part of the heme synthesis pathway that occurs in mitochondria, which requires glycine, cause sideroblastic anemia (*40*). Given that mitochondria make glycine from serine, we speculate that in the *Sfxn1*-mutant mice, an insufficient import of serine into mitochondria results in a decrease in glycine and thus heme synthesis. Iron itself is unlikely to be a direct substrate of SFXN1 as the mitoferrins are reported mitochondrial iron transporters (*41*). There are multiple sideroflexins, and their expression varies across tissues (fig. S2 A, B). Like other genes of the mitochondrial one-carbon

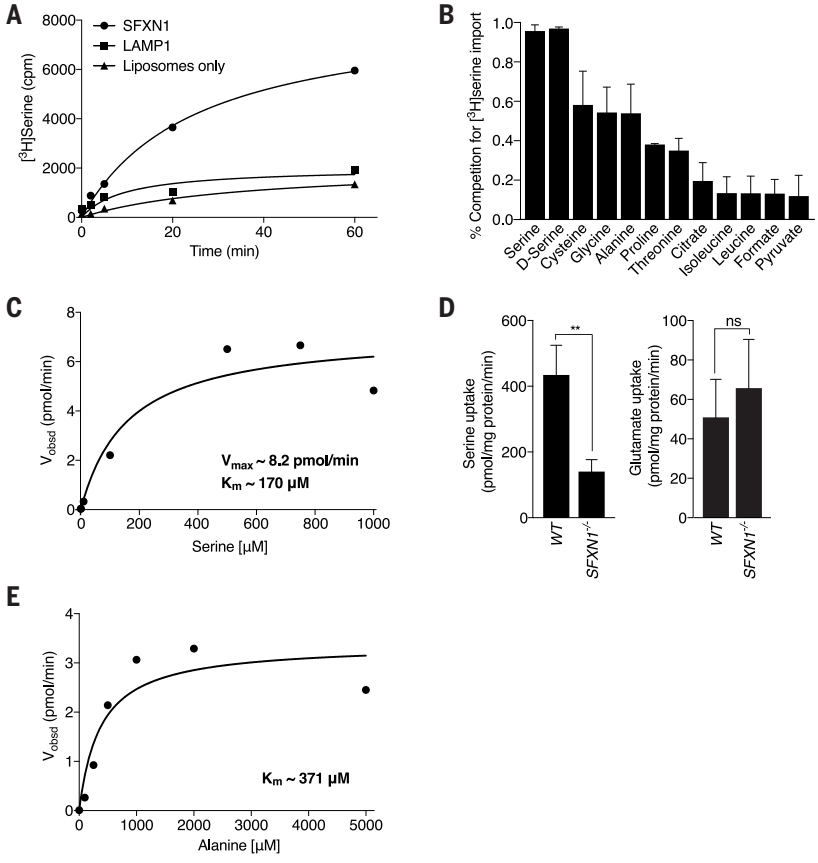

Fig. 3. SFXN1 transports serine in vitro. (**A**) Time course of radioactive serine uptake into proteoliposomes containing SFXN1. LAMP1-containing or empty liposomes were used as controls. Values are the averages of two replicates. Cpm, counts per minute. (**B**) Competition of serine uptake after 60 min by different metabolites at 500 μM (mean ± SD; $n = 3$). (**C**) Steady-state kinetic analysis of SFXN1-mediated serine transport reveals a V_{max} of ~ 8.2 pmol/min and a K_m of ~170 μM. Velocity, as shown, was calculated as a function of the serine concentration. Each data point was calculated from three replicate data points. (**D**) Radioactive serine uptake into mitochondria purified from *SFXN1*-null cells is reduced compared to that into mitochondria purified from wild-type cells, whereas glutamate uptake is unchanged (mean ± SD; $n = 3$, $^{**}P < 0.01$; ns, not significant). (**E**) Steady-state kinetic analysis of SFXN1-mediated alanine transport reveals a K_m of ~371 μM for alanine. Each data point was calculated from three replicate data points.

of purine synthesis intermediates in *SFXN1*-null cells. Intermediates were measured by LC-MS in extracts from wild-type Jurkat cells or single-cell–derived *SFXN1*-null cells incubated for 24 hours in the indicated media (mean ± SD; $n = 3$; $^{****}P < 0.0001$; N.D., not detected). (**K**) Tracing strategy to differentiate contribution of cytosolic and mitochondrial pathways to cytosolic TTP synthesis. Oxidation of 2,3,3-$^2H_3$-serine by SHMT2 and subsequent enzymes in mitochondria gives rise to a singly labeled formate species, and thus singly labeled (one mass unit heavier, M+1) TTP. Oxidation by SHMT1 in the cytosol gives rise to doubly labeled (two mass units heavier, M+2) TTP. The difference between unlabeled (M+0), M+1, and M+2 TTP can be resolved on a high-resolution mass spectrometer. The ratio of M+1 to M+2 is indicative of the contribution of mitochondria- versus cytosol-derived one-carbon units to nucleotide synthesis. Adapted from (*8*). TTP, thymidine triphosphate. (**L**) The relative contribution of the cytosolic and mitochondrial one-carbon pathways to TTP synthesis is inverted in *SFXN1*-null compared to wild-type cells. Wild-type Jurkat or single-cell-derived knockout cells were cultured for 12 hours in media containing 2,3,3-$^2H_3$-serine as the only serine source before harvesting and LC-MS analysis (mean ± SD; $n = 3$, $^{****}P < 0.0001$). (**M**) Genes of the cytosolic one-carbon pathway are selectively required for the optimal proliferation of *SFXN1*-null cells. Gene scores in wild-type cells were plotted against those in *SFXN1*-null cells. Genes with a differential gene score of <−1.5 are shown in red. (**N**) *Serine Hydroxymethyltransferase 1* (*SHMT1*) was the top hit from the *SFXN1* synthetic lethality screen. Genes were ranked according to differential gene score between wild-type and *SFXN1*-null cells. Cyto 1C metabolism, cytosolic one-carbon metabolism; FA, fatty acid. Two-tailed *t* tests were used for comparisons between metabolites.

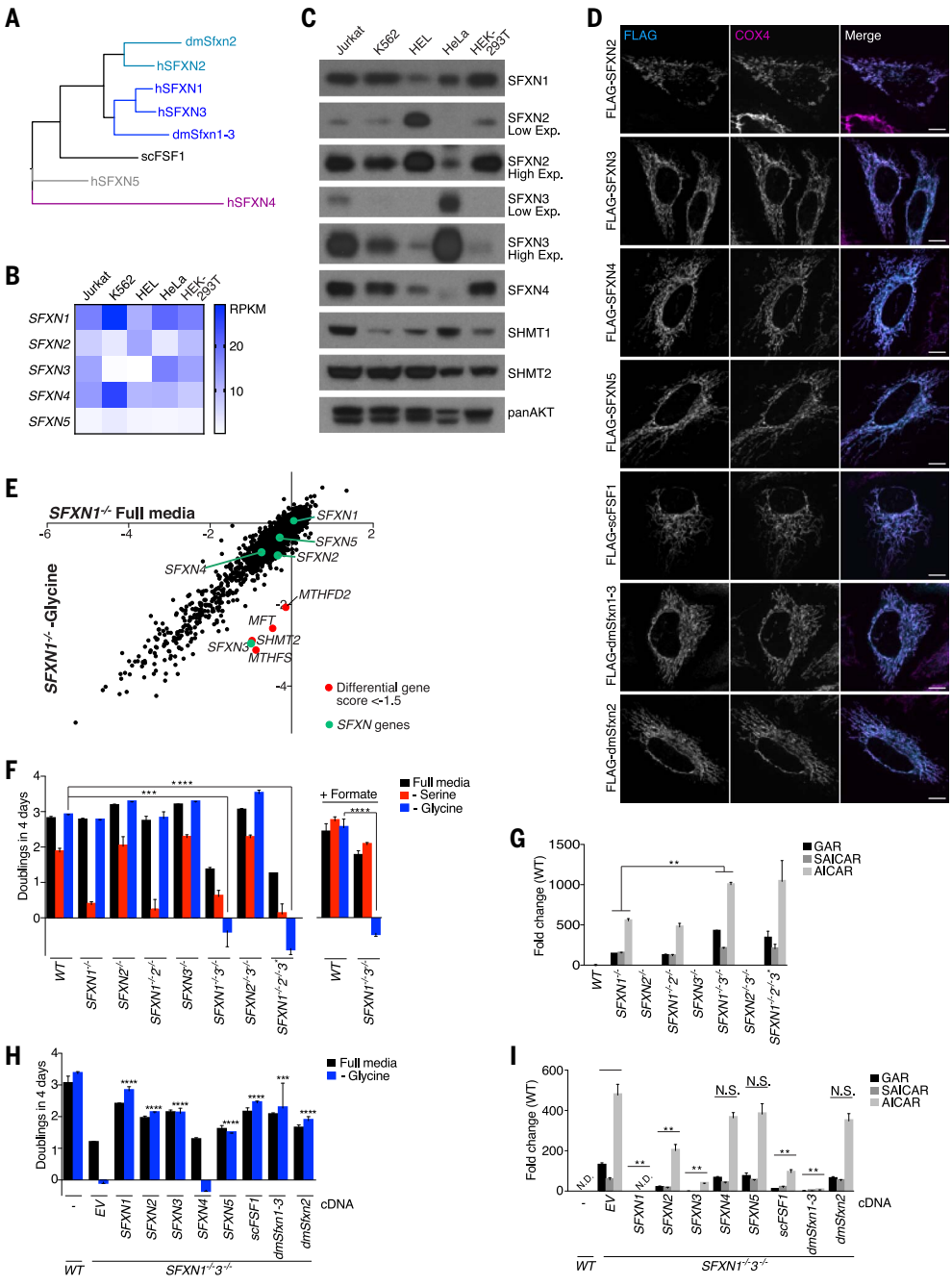

Fig. 4. SFXN3 and fly and yeast sideroflexin homologs can substitute for SFXN1 loss. (**A**) Phylogenetic tree of human, *Drosophila melanogaster*, and *Saccharomyces cerevisae* sideroflexins. (**B**) mRNA levels of the five human sideroflexins in commonly used cell lines. RPKM (reads per kilobase million) levels were extracted from the Cancer Cell Line Encyclopedia. (**C**) Sideroflexin protein levels in commonly used cell lines. Cell lysates were equalized for total protein amounts and analyzed by immunoblotting for the levels of the indicated proteins. (**D**) FLAG-tagged sideroflexin homologs localize to mitochondria. Wild-type HeLa cells transiently expressing FLAG-sideroflexin homologs were processed for immunofluorescence detection of the FLAG epitope (cyan) and the mitochondrial inner membrane marker COX4 (magenta). The merged image shows the overlap of both channels in white. (**E**) CRISPR-Cas9–based genetic screen reveals that SFXN3 is required for proliferation in the absence of SFXN1 and glycine. Gene scores in *SFXN1*-null cells cultured in the presence or absence of glycine were plotted against each other. Except for *SFXN3*, genes with a differential gene score of <−1.5 are shown in red. All sideroflexins are shown in green. (**F**) Cells lacking both SFXN1 and SFXN3 are glycine auxotrophs and formate does not rescue their proliferation. The asterisk denotes a cell clone lacking SFXN1 and SFXN2 and with incomplete deletion of *SFXN3*. Proliferation of wild-type Jurkat or single-cell–derived knockout cells was assayed in full, serine- or glycine-deficient media, as indicated. For the formate rescue, cells were cultured in media with 1 mM formate for 2 days before initiating the experiment (mean ± SD; $n = 3$; $^{***}P < 0.001$, $^{****}P < 0.0001$). (**G**) The accumulation of purine synthesis intermediates is exacerbated in cells lacking both SFXN1 and SFXN3 compared to their single-knockout counterparts. The asterisk denotes a cell clone lacking SFXN1 and SFXN2 and with incomplete deletion of *SFXN3*. Purine intermediates were measured by LC-MS in extracts from the indicated cells (mean ± SD; $n = 3$; $^{**}P < 0.01$). Abbreviations as in Fig. 2C. (**H**) Human, yeast, and *Drosophila* sideroflexin homologs, with the exception of SFXN4, rescue the glycine auxotrophy of cells lacking both SFXN1 and SFXN3. Single cell–derived double-knockout Jurkat cells were transduced with an empty vector (EV) or cDNAs of human, yeast, and *Drosophila* sideroflexin homologs. Asterisks denote statistically significant differences in proliferation in media lacking glycine between the cells expressing the empty vector and the sideroflexin homologs. Mean ± SD; $n = 3$; $^{***}P < 0.001$, $^{****}P < 0.0001$). (**I**) Sideroflexin homologs rescue to varying degrees the purine synthesis defects of cells lacking SFXN1 and SFXN3. Purine intermediates were measured by LC-MS in extracts from wild-type Jurkat cells or the double-knockout Jurkat cells expressing an empty vector (EV) or cDNAs of human, yeast, and *Drosophila* sideroflexin homologs. Asterisks denote statistically significant differences between the cells expressing the empty vector and the sideroflexin homologs. Values were normalized to the average value of the wild-type samples in (G) because purine synthesis intermediates were not detected in the wild-type samples in this experiment (mean ± SD; $n = 3$, $^{**}P < 0.01$; N.D., not detected; N.S., not significant). Two-tailed *t* tests were used for comparisons between metabolites.

pathway, *SFXN1*, *2*, and *3* expression is likely regulated by the Myc transcription factor, as we found 34, 20, and 14 Myc-binding sites in the promoters of *SFXN1*, *SFXN2*, and *SFXN3*, respectively. *SFXN1* is expressed in many cancers, most highly in leukemias and lymphomas (fig. S2C), Thus, SFXN1 and its homologs may turn out to be important nodes for regulating the fate of serine in cells and also play unexplored roles in cancer cell growth.

Methods summary

CRISPR screens performed in human SHMT1-null Jurkat and K562 cells identified SFXN1 as one of the most differentially scoring genes in media with and without serine in both cell lines. The proliferation and metabolism of single-cell–derived *SFXN1*-null cells generated using CRISPR-Cas9 was analyzed by using Cell Titer Glo assays and mass spectrometry–based metabolite profiling and compared with mutants of the known one-carbon metabolism genes *SHMT1*, *SHMT2*, and *MTHFD2*. The localization of SFXN1 and its homologs was analyzed by spinning disk confocal and stimulated emission depletion (STED) super-resolution microscopy. In vitro transport assays and uptake assays into isolated mitochondria confirmed SFXN1 as a serine transporter. The redundancy of genes homologous to SFXN1 (the sideroflexins) was analyzed by using a SFXN1 synthetic lethality CRISPR screen, by studying double deletion cells, and in complementation assays.

REFERENCES AND NOTES

1. M. Yang, K. H. Vousden, Serine and one-carbon metabolism in cancer. *Nat. Rev. Cancer* **16**, 650–662 (2016). doi: 10.1038/nrc.2016.81; pmid: 27634448
2. J. W. Locasale, Serine, glycine and one-carbon units: Cancer metabolism in full circle. *Nat. Rev. Cancer* **13**, 572–583 (2013). doi: 10.1038/nrc3557; pmid: 23822983
3. G. S. Ducker, J. D. Rabinowitz, One-Carbon Metabolism in Health and Disease. *Cell Metab.* **25**, 27–42 (2017). doi: 10.1016/j.cmet.2016.08.009; pmid: 27641100
4. A. S. Tibbetts, D. R. Appling, Compartmentalization of Mammalian folate-mediated one-carbon metabolism. *Annu. Rev. Nutr.* **30**, 57–81 (2010). doi: 10.1146/annurev.nutr.012809.104810; pmid: 20645850
5. C. K. Barlowe, D. R. Appling, In vitro evidence for the involvement of mitochondrial folate metabolism in the supply of cytoplasmic one-carbon units. *Biofactors* **1**, 171–176 (1988). pmid: 2475123
6. W. Pfendner, L. I. Pizer, The metabolism of serine and glycine in mutant lines of Chinese hamster ovary cells. *Arch. Biochem. Biophys.* **200**, 503–512 (1980). doi: 10.1016/0003-9861(80)90382-3; pmid: 6776895
7. M. R. Narkewicz, S. D. Sauls, S. S. Tjoa, C. Teng, P. V. Fennessey, Evidence for intracellular partitioning of serine and glycine metabolism in Chinese hamster ovary cells. *Biochem. J.* **313**, 991–996 (1996). doi: 10.1042/bj3130991; pmid: 8611185
8. G. S. Ducker *et al*., Reversal of Cytosolic One-Carbon Flux Compensates for Loss of the Mitochondrial Folate Pathway. *Cell Metab.* **23**, 1140–1153 (2016). doi: 10.1016/j.cmet.2016.04.016; pmid: 27211901
9. T. F. Fu, J. P. Rife, V. Schirch, The role of serine hydroxymethyltransferase isozymes in one-carbon metabolism in MCF-7 cells as determined by (13)C NMR. *Arch. Biochem. Biophys.* **393**, 42–50 (2001). doi: 10.1006/abbi.2001.2471; pmid: 11516159
10. C. Yu, D. L. Claybrook, A. H. Huang, Transport of glycine, serine, and proline into spinach leaf mitochondria. *Arch. Biochem. Biophys.* **227**, 180–187 (1983). doi: 10.1016/0003-9861(83)90361-2; pmid: 6416178
11. R. L. Cybulski, R. R. Fisher, Mitochondrial neutral amino acid transport: Evidence for a carrier mediated mechanism. *Biochemistry* **16**, 5116–5120 (1977). doi: 10.1021/bi00642a026; pmid: 911815
12. R. L. Cybulski, R. R. Fisher, Intramitochondrial localization and proposed metabolic significance of serine transhydroxymethylase. *Biochemistry* **15**, 3183–3187 (1976). doi: 10.1021/bi00660a004; pmid: 952851
13. C. F. Labuschagne, N. J. van den Broek, G. M. Mackay, K. H. Vousden, O. D. Maddocks, Serine, but not glycine, supports one-carbon metabolism and proliferation of cancer cells. *Cell Reports* **7**, 1248–1258 (2014). doi: 10.1016/j.celrep.2014.04.045; pmid: 24813884
14. T. Wang *et al*., Identification and characterization of essential genes in the human genome. *Science* **350**, 1096–1101 (2015). doi: 10.1126/science.aac7041; pmid: 26472758
15. K. Birsoy *et al*., An Essential Role of the Mitochondrial Electron Transport Chain in Cell Proliferation Is to Enable Aspartate Synthesis. *Cell* **162**, 540–551 (2015). doi: 10.1016/j.cell.2015.07.016; pmid: 26232224
16. Y. Pikman *et al*., Targeting MTHFD2 in acute myeloid leukemia. *J. Exp. Med.* **213**, 1285–1306 (2016). doi: 10.1084/jem.20151574; pmid: 27325891
17. M. S. Field, D. M. Szebenyi, P. J. Stover, Regulation of de novo purine biosynthesis by methenyltetrahydrofolate synthetase in neuroblastoma. *J. Biol. Chem.* **281**, 4215–4221 (2006). doi: 10.1074/jbc.M510624200; pmid: 16365037
18. M. D. Fleming, D. R. Campagna, J. N. Haslett, C. C. Trenor 3rd, N. C. Andrews, A mutation in a mitochondrial transmembrane protein is responsible for the pleiotropic hematological and skeletal phenotype of flexed-tail (f/f) mice. *Genes Dev.* **15**, 652–657 (2001). doi: 10.1101/gad.873001; pmid: 11274051
19. G. Miotto, S. Tessaro, G. A. Rotta, D. Bonatto, In silico analyses of Fsf1 sequences, a new group of fungal proteins orthologous to the metazoan sideroblastic anemia-related sideroflexin family. *Fungal Genet. Biol.* **44**, 740–753 (2007). doi: 10.1016/j.fgb.2006.12.004; pmid: 17240176
20. U. Omasits, C. H. Ahrens, S. Müller, B. Wollscheid, Protter: Interactive protein feature visualization and integration with experimental proteomic data. *Bioinformatics* **30**, 884–886 (2014). doi: 10.1093/bioinformatics/btt607; pmid: 24162465
21. S. Y. Lee *et al*., APEX Fingerprinting Reveals the Subcellular Localization of Proteins of Interest. *Cell Reports* **15**, 1837–1847 (2016). doi: 10.1016/j.celrep.2016.04.064; pmid: 27184847
22. K. Herbig *et al*., Cytoplasmic serine hydroxymethyltransferase mediates competition between folate-dependent deoxyribonucleotide and S-adenosylmethionine biosyntheses. *J. Biol. Chem.* **277**, 38381–38389 (2002). doi: 10.1074/jbc.M205000200; pmid: 12161434
23. F. T. Kao, T. Puck, Mutagenesis and genetic analysis with Chinese hamster auxotrophic cell markers. *Genetics* **79** (Suppl), 343–352 (1975). pmid: 1171046
24. M. W. McBurney, G. F. Whitmore, Isolation and biochemical characterization of folate deficient mutants of Chinese hamster cells. *Cell* **2**, 173–182 (1974). doi: 10.1016/0092-8674(74)90091-9; pmid: 4547236
25. H. Patel, E. D. Pietro, R. E. MacKenzie, Mammalian fibroblasts lacking mitochondrial NAD+-dependent methylenetetrahydrofolate dehydrogenase-cyclohydrolase are glycine auxotrophs. *J. Biol. Chem.* **278**, 19436–19441 (2003). doi: 10.1074/jbc.M301718200; pmid: 12646567
26. R. Bianchetti, G. Lucchini, P. Crosti, P. Tortora, Dependence of mitochondrial protein synthesis initiation on formylation of the initiator methionyl-tRNAf. *J. Biol. Chem.* **252**, 2519–2523 (1977). pmid: 323247
27. N. Takeuchi *et al*., Recognition of tRNAs by Methionyl-tRNA transformylase from mammalian mitochondria. *J. Biol. Chem.* **276**, 20064–20068 (2001). doi: 10.1074/jbc.M101007200; pmid: 11274157
28. R. J. Morscher *et al*., Mitochondrial translation requires folate-dependent tRNA methylation. *Nature* **554**, 128–132 (2018). doi: 10.1038/nature25460; pmid: 29364879
29. D. R. Minton *et al*., Serine Catabolism by SHMT2 Is Required for Proper Mitochondrial Translation Initiation and Maintenance of Formylmethionyl-tRNAs. *Mol. Cell* **69**, 610–621.e5 (2018). doi: 10.1016/j.molcel.2018.01.024; pmid: 29452640
30. G. S. Ducker *et al*., Human SHMT inhibitors reveal defective glycine import as a targetable metabolic vulnerability of diffuse large B-cell lymphoma. *Proc. Natl. Acad. Sci. U.S.A.* **114**, 11404–11409 (2017). doi: 10.1073/pnas.1706617114; pmid: 29073064
31. S. Miyake *et al*., Identification and characterization of a novel mitochondrial tricarboxylate carrier. *Biochem. Biophys. Res. Commun.* **295**, 463–468 (2002). doi: 10.1016/S0006-291X(02)00694-0; pmid: 12150972
32. A. Azzi, M. Glerum, R. Koller, W. Mertens, S. Spycher, The mitochondrial tricarboxylate carrier. *J. Bioenerg. Biomembr.* **25**, 515–524 (1993). doi: 10.1007/BF01108408; pmid: 8132491
33. F. Bisaccia, A. De Palma, F. Palmieri, Identification and purification of the tricarboxylate carrier from rat liver mitochondria. *Biochim. Biophys. Acta* **977**, 171–176 (1989). doi: 10.1016/S0005-2728(89)80068-4; pmid: 2804096
34. R. S. Kaplan, J. A. Mayor, D. O. Wood, The mitochondrial tricarboxylate transport protein. cDNA cloning, primary structure, and comparison with other mitochondrial transport proteins. *J. Biol. Chem.* **268**, 13682–13690 (1993). pmid: 8514800
35. F. Palmieri, The mitochondrial transporter family SLC25: Identification, properties and physiopathology. *Mol. Aspects Med.* **34**, 465–484 (2013). doi: 10.1016/j.mam.2012.05.005; pmid: 23266187
36. X. Ye *et al*., Isolation and characterization of a novel human putative anemia-related gene homologous to mouse sideroflexin. *Biochem. Genet.* **41**, 119–125 (2003). doi: 10.1023/A:1022026001114; pmid: 12670026
37. M. M. Whittaker, A. Penmatsa, J. W. Whittaker, The Mtm1p carrier and pyridoxal 5′-phosphate cofactor trafficking in yeast mitochondria. *Arch. Biochem. Biophys.* **568**, 64–70 (2015). doi: 10.1016/j.abb.2015.01.021; pmid: 25637770
38. H. Grüneberg, The anaemia of flexed-tailed mice (*Mus musculus* L.) II. Siderocytes. *J. Genet.* **44**, 246–271 (1942). doi: 10.1007/BF02982831
39. L. E. Lenox, J. M. Perry, R. F. Paulson, BMP4 and Madh5 regulate the erythroid response to acute anemia. *Blood* **105**, 2741–2748 (2005). doi: 10.1182/blood-2004-02-0703; pmid: 15591122
40. M. D. Fleming, Congenital sideroblastic anemias: Iron and heme lost in mitochondrial translation. *Hematology* **2011**, 525–531 (2011). doi: 10.1182/asheducation-2011.1.525; pmid: 22160084
41. P. N. Paradkar, K. B. Zumbrennen, B. H. Paw, D. M. Ward, J. Kaplan, Regulation of mitochondrial iron import through differential turnover of mitoferrin 1 and mitoferrin 2. *Mol. Cell. Biol.* **29**, 1007–1016 (2009). doi: 10.1128/MCB.01685-08; pmid: 19075006

ACKNOWLEDGMENTS

We thank all members of the Sabatini lab for helpful insights, suggestions, and discussion, in particular G. Sienski. We thank T. Kunchok from the Whitehead Institute Metabolite Profiling Facility, P. Thiru from BARC, the Whitehead Institute FACS facility, Genome Technology Core, and MIT MicrobioCenter for technical assistance, and the Vander Heiden laboratory for access to a GC-mass spectrometer. We thank A. Mennone and the Center for Cellular and Molecular Imaging (CCMI) imaging facilities at Yale University, supported by NIH grant S10 OD020142, as well as the W. M. Keck microscopy facility at the Whitehead Institute. **Funding:** This work was supported by grants from the NIH to D.M.S (R01 CA103866, R01 CA129105, and R37 AI47389), and by the Department of Defense (W81XWH-07-0448) and a Cancer Research Institute Irvington Fellowship (Y.E.G.). N.K. is an HHMI fellow of the Damon-Runyon Cancer Research Foundation. D.M.S. is an investigator of the Howard Hughes Medical Institute and an ACS Research Professor. **Author contributions**: N.K. and D.M.S. designed the research plan and interpreted experimental results. N.K. designed and analyzed most of the experiments and N.K., G.P., and J.u.d.B. performed experiments. G.W. established and performed the in vitro transport assays. M.E.P. and S.H.C. validated the screening approach. F.B. performed STED imaging. T.W. analyzed the Jurkat serine-depletion CRISPR-Cas9 screen, H.R.K. helped with analysis of the *SFXN1* synthetic lethality screen data, and C.A.L. helped with the design and analysis of tracing experiments. Y.E.G. performed the transcription factor binding analysis. N.K. wrote and D.M.S. edited the manuscript. **Competing interests:** N.K. and D.M.S. are inventors on a patent application filed by the Whitehead Institute relating to work described in this paper. None of the authors have a competing interest. **Data and materials availability:** All data are available in the manuscript or the supplementary materials. All expression plasmids were deposited at Addgene.

SUPPLEMENTARY MATERIALS

www.sciencemag.org/content/362/6416/eaat9528/suppl/DC1
Materials and Methods
Figs. S1 to S6
Tables S1 and S2
References (*42*–*56*)

24 April 2018; accepted 17 September 2018
10.1126/science.aat9528

RESEARCH ARTICLE SUMMARY

NEUROGENOMICS

Molecular, spatial, and functional single-cell profiling of the hypothalamic preoptic region

Jeffrey R. Moffitt*, Dhananjay Bambah-Mukku*, Stephen W. Eichhorn†, Eric Vaughn†, Karthik Shekhar, Julio D. Perez, Nimrod D. Rubinstein, Junjie Hao, Aviv Regev, Catherine Dulac‡§, Xiaowei Zhuang‡§

INTRODUCTION: A mechanistic understanding of brain function requires the identification of distinct cell types in the brain at a molecular, spatial, and functional level. The preoptic region of the hypothalamus comprises multiple nuclei and controls many social behaviors and homeostatic functions. Discrete neuronal types within the preoptic region have been associated with specific hypothalamic behaviors and homeostatic controls, yet the organizational principles of the underlying circuits remain elusive. Further progress requires methods that can identify molecularly distinct cell types and map their spatial and functional organization in the tissue.

RATIONALE: Single-cell RNA sequencing (scRNA-seq) has revolutionized the understanding of many tissues by allowing a systematic, genome-wide molecular identification of cell types. However, scRNA-seq requires cell dissociation, leading to a loss of spatial context that is essential to understand the cellular architecture of brain circuits. Image-based approaches to single-cell transcriptomics enables gene expression profiling of individual cells within their native tissue and offers opportunities for simultaneous in situ cell-type identification and spatial mapping, as well as functional characterization when combined with activity marker imaging. The combination of these complementary techniques would allow us to generate a molecular inventory of neuronal types while mapping their spatial and functional organization.

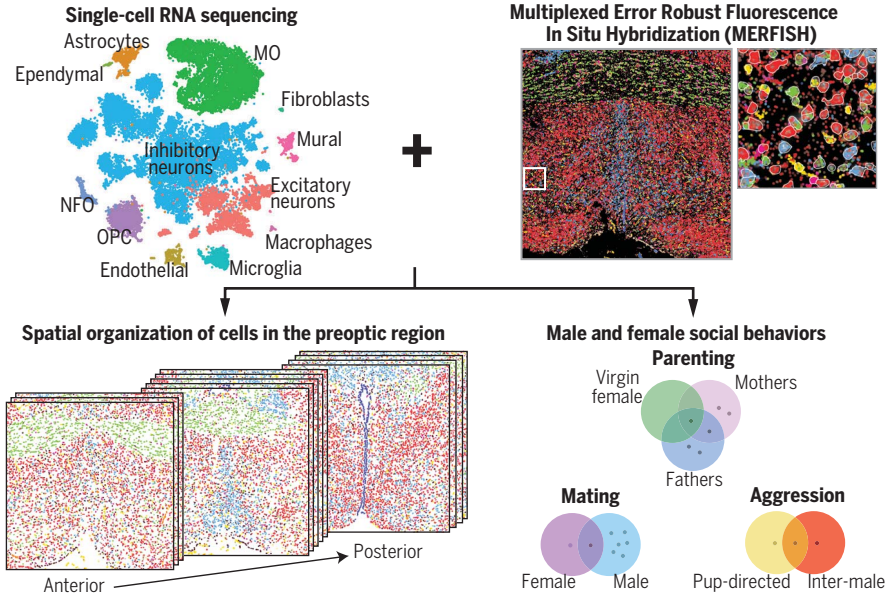

In situ single-cell profiling reveals the molecular and cellular organization of the hypothalamic preoptic region. The combination of MERFISH with scRNA-seq to profile the gene expression of 1 million cells in situ revealed ~70 neuronal populations in the preoptic region, each with distinct molecular signatures and spatial organizations, providing insights into neuromodulatory signaling pathways. Further combination with activity marker imaging led to the identification of discrete neuronal types activated by key social behaviors, including parenting, aggression, and mating.

RESULTS: We combined scRNA-seq and multiplexed error robust fluorescence in situ hybridization (MERFISH), a single-cell transcriptome imaging method, to investigate the molecular, spatial, and functional organization of the mouse hypothalamic preoptic region. We profiled ~31,000 cells using scRNA-seq and imaged ~1.1 million cells within intact tissues using MERFISH. Our data revealed a remarkable diversity of neurons in this region, comprising ~70 different neuronal populations, many of which were previously unknown. These neuronal types exhibited distinct neuromodulatory signatures and revealed a striking heterogeneity within cell populations that were previously thought to be functionally unitary. MERFISH measurements further allowed us to map the spatial organization of these neuronal types, determine the cellular composition of distinct nuclei, and provide insights into the functional organization of neuron populations, including topographical relationships that underlie sex hormone signaling.

ON OUR WEBSITE

Read the full article at http://dx.doi.org/10.1126/science.aau5324

Last, we combined MERFISH with immediate-early-gene expression imaging to identify specific neuronal populations activated by social behaviors, including parenting, mating, and aggression. Several neuronal populations were selectively activated in each of these behaviors, supporting the notion that transcriptionally distinct neuronal types control specific hypothalamic functions. We identified a core neuronal population activated in all animals that exhibit parenting, as well as cell populations differentially activated in mothers and fathers, providing insights into how physiological state may affect parental behavior. Moreover, we identified cells associated with sexual behavior in males and females as well as male aggression toward infants and conspecific males.

CONCLUSION: By combining MERFISH with scRNA-seq, we have revealed the molecular, spatial, and functional organization of neurons within the hypothalamic preoptic region. These results provide a framework for mechanistic investigation of behavior circuits with high molecular and spatial resolution and opens avenues for identifying and mapping cell types in a diverse range of tissues and organisms. ■

The list of author affiliations is available in the full article online.
*These authors contributed equally to this work.
†These authors contributed equally to this work.
‡These authors contributed equally to this work.
§Corresponding author. Email: dulac@fas.harvard.edu (C.D.); zhuang@chemistry.harvard.edu (X.Z.)
Cite this article as J. R. Moffitt *et al.*, *Science* **362**, eaau5324 (2018). DOI: 10.1126/science.aau5324

RESEARCH ARTICLE

NEUROGENOMICS

Molecular, spatial, and functional single-cell profiling of the hypothalamic preoptic region

Jeffrey R. Moffitt[1,2,3,4]*, Dhananjay Bambah-Mukku[1,4,5]*, Stephen W. Eichhorn[1,2,3,4]†, Eric Vaughn[1,4,5]†, Karthik Shekhar[6], Julio D. Perez[1,4,5], Nimrod D. Rubinstein[1,4,5], Junjie Hao[1,2,3,4], Aviv Regev[1,6,7], Catherine Dulac[1,4,5]‡§, Xiaowei Zhuang[1,2,3,4]‡§

The hypothalamus controls essential social behaviors and homeostatic functions. However, the cellular architecture of hypothalamic nuclei—including the molecular identity, spatial organization, and function of distinct cell types—is poorly understood. Here, we developed an imaging-based in situ cell-type identification and mapping method and combined it with single-cell RNA-sequencing to create a molecularly annotated and spatially resolved cell atlas of the mouse hypothalamic preoptic region. We profiled ~1 million cells, identified ~70 neuronal populations characterized by distinct neuromodulatory signatures and spatial organizations, and defined specific neuronal populations activated during social behaviors in male and female mice, providing a high-resolution framework for mechanistic investigation of behavior circuits. The approach described opens a new avenue for the construction of cell atlases in diverse tissues and organisms.

A mechanistic understanding of brain function requires a systematic assessment of cell types and their spatial organization, connectivity, and functional properties. A case in point is the preoptic region of the hypothalamus, which comprises multiple nuclei and controls essential social behaviors such as parenting, mating, and aggression as well as homeostatic functions such as thermoregulation, thirst, and sleep (*1*, *2*). Because these are evolutionarily conserved functions, it has been proposed that the associated neural circuits are genetically defined and thus composed of transcriptionally distinct neuronal types (*1*–*3*). Indeed, several neuronal populations within the preoptic region, each defined by discrete molecular markers, have been linked to distinct behavioral and homeostatic functions (*4*–*11*). However, the number of cell types present in the preoptic region as well as their molecular signatures, spatial organizations, and functional roles remain unclear, hampering our ability to investigate the underlying neural circuits.

[1]Howard Hughes Medical Institute, Harvard University, Cambridge, MA 02138, USA. [2]Department of Chemistry and Chemical Biology, Harvard University, Cambridge, MA 02138, USA. [3]Department of Physics, Harvard University, Cambridge, MA 02138, USA. [4]Center for Brain Science, Harvard University, Cambridge, MA 02138, USA. [5]Department of Molecular and Cellular Biology, Harvard University, Cambridge, MA 02138, USA. [6]Klarman Cell Observatory, Broad Institute of MIT and Harvard, Cambridge, MA 02139, USA. [7]Koch Institute of Integrative Cancer Biology, Department of Biology, MIT, Cambridge, MA 02139, USA.

*These authors contributed equally to this work. †These authors contributed equally to this work. ‡These authors contributed equally to this work. §Corresponding author. Email: dulac@fas.harvard.edu (C.D.); zhuang@chemistry.harvard.edu (X.Z.)

Single-cell RNA-sequencing (scRNA-seq) provides a powerful means for the identification of cell types and cell states through genome-wide expression profiling of individual cells, offering rich insights into the cellular diversity of many tissues, including the brain (*12*–*15*). However, scRNA-seq requires cell dissociation and thus results in the loss of the spatial context of cells that is critical for understanding tissue function (*15*, *16*). Recently, image-based single-cell transcriptomic approaches have been developed that quantify gene expression by directly imaging individual RNA molecules within intact cells and tissues with multiplexed fluorescence in situ hybridization (FISH) or in situ sequencing (*15*, *17*–*22*). These approaches offer new opportunities to identify cell populations within complex tissues while simultaneously mapping their spatial organization and uncovering their functions by combining gene expression profiling with imaging of activity markers, such as the induction of immediate early genes (IEGs) (*22*, *23*). Among these, multiplexed error-robust FISH (MERFISH) detects individual RNA molecules with single-molecule FISH (smFISH) (*24*, *25*) and uses error-robust barcoding, combinatorial labeling, and sequential imaging to multiplex smFISH measurements, enabling transcriptome-scale RNA imaging of individual cells in situ (*20*, *26*).

We developed a MERFISH-based imaging and analysis platform for in situ cell-type identification and mapping and used this approach, in combination with scRNA-seq, to create a cell atlas of the preoptic region of the mouse hypothalamus. We used scRNA-seq to catalog cell populations and identify their marker genes. We then performed MERFISH imaging of these marker genes together with genes of known functional importance to identify cell populations and map their spatial organization in situ. Last, we combined MERFISH with measurements of IEG expression in order to identify discrete cell populations activated by specific social behaviors—including parenting, aggression, and mating—in both sexes and different physiological states.

Results

scRNA-seq of the preoptic region

We dissected a rostral part of the mouse hypothalamus that contains the preoptic region (Fig. 1A)—the medial preoptic area (MPOA) and surrounding nuclei (~2.5 by 2.5 by 1.1 mm, Bregma +0.5 to −0.6)—from adult female and male brains and dissociated the tissue using a custom protocol that improved cell survival and capture (fig. S1). We collected scRNA-seq profiles from 31,299 cells across three replicates of each sex using droplet-based scRNA-seq (*27*–*29*).

We used unsupervised, graph-based, community-detection methods (*28*, *30*, *31*) modified by us (fig. S2) to cluster cells (*29*). This led to the delineation of major cell classes, including inhibitory and excitatory neurons, microglia, astrocytes, immature oligodendrocytes (newly formed oligodendrocytes and oligodendrocyte progenitor cells), mature oligodendrocytes, ependymal cells, endothelial cells, fibroblasts, macrophages, and mural cells, as well as subdivisions within these cell classes (Fig. 1B and table S1).

Further clustering of inhibitory neurons (15,042 cells) and excitatory neurons (3511 cells) separately revealed 43 and 23 subpopulations, respectively (Fig. 1B; fig. S3, A and B; and tables S1 and S2). Hereafter, we denote excitatory and inhibitory neuronal clusters as e1, e2, …, and i1, i2, …, respectively. We also provide specific names for these clusters based on marker genes (Fig. 1, C and D, and figs. S4 and S5, the latter emphasizing neuropeptide expression) (*29*).

Although the majority of the identified clusters expressed either excitatory or inhibitory neuronal markers, we observed expression of the γ-aminobutyric acid (GABA) synthetic genes Gad1 and Gad2 in many excitatory neuronal clusters classified on the basis of expression of Vglut2 (Slc17a6), with Gad2 expression being particularly widespread (fig. S3C). By contrast, very few Slc17a6-positive clusters expressed the GABA transporter gene Vgat (Slc32a1). These data suggest that Slc17a6 and Slc32a1 are better discriminators for excitatory versus inhibitory neurons, corroborating evidence from other brain areas (*32*). Cells in two neuronal clusters originally designated as inhibitory and one originally designated as excitatory coexpressed Slc17a6 (or Slc17a8, vGlut3) and Slc32a1. These cells were unlikely to be a clustering artifact because individual cells coexpressed both markers, nor did they correspond to doublets (*29*); hence, they potentially represent hybrid neurons capable of GABA/glutamate corelease, as characterized in the hypothalamus and a few other brain

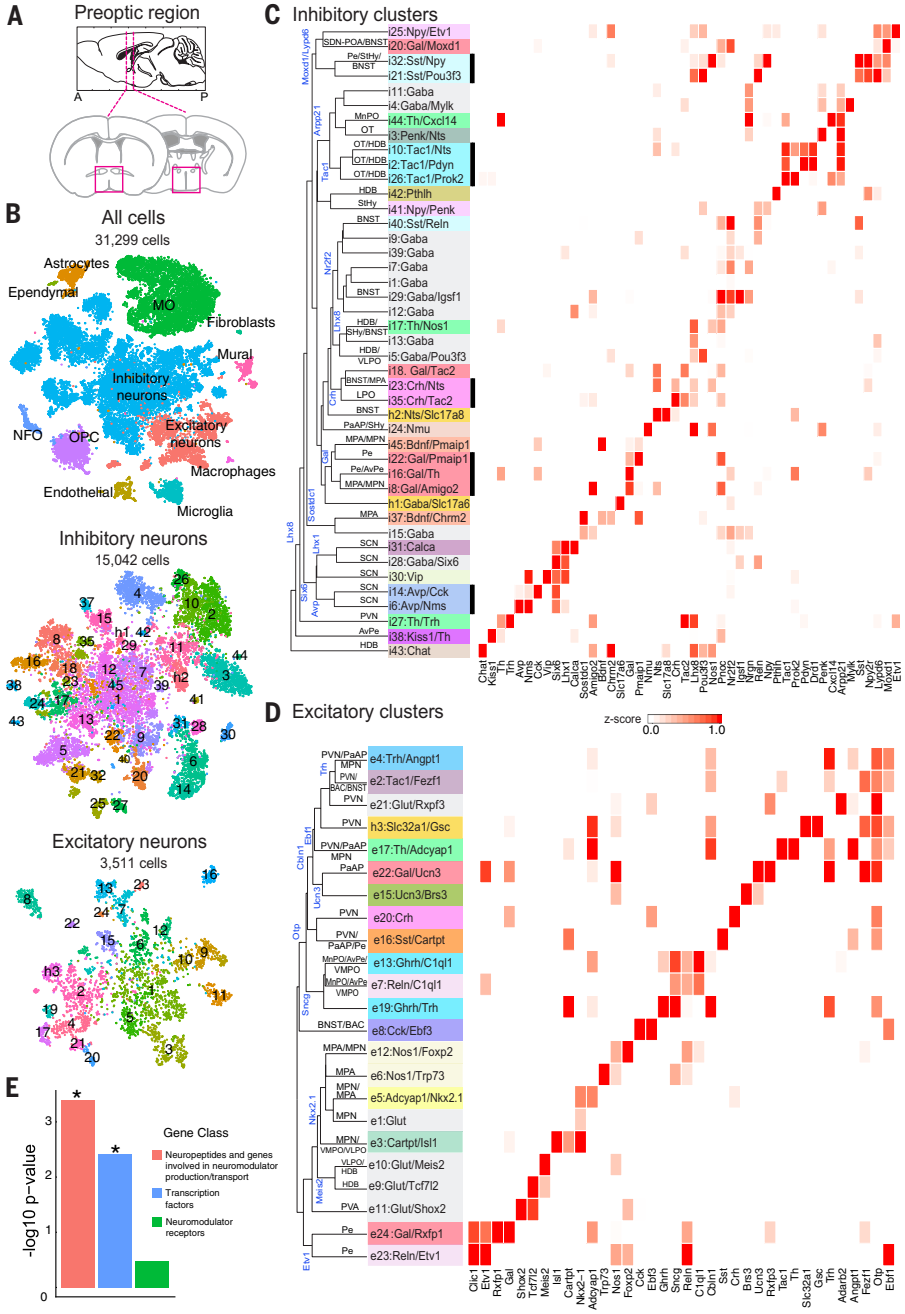

Fig. 1. scRNA-seq of the preoptic region in the mouse hypothalamus. (**A**) Schematic of the preoptic region of the hypothalamus. Magenta boxes indicate the area dissected for scRNA-seq (Bregma +0.5 to −0.6). (**B**) *t*-distributed stochastic neighbor embedding (tSNE) for all cells and inhibitory and excitatory neurons, with cells colored by cluster. Numbers superimposed on the tSNE indicate the cluster ID. Total cell numbers for each tSNE plot are indicated. NFO, newly formed oligodendrocytes; OPC, oligodendrocyte progenitor cells; MO, mature oligodendrocytes. (**C**) Heat map of *z*-scores of expression for select genes within inhibitory neuronal clusters. Clusters are organized on the basis of the hierarchical tree constructed with expression in principal component space, with some of the genes differentially expressed between branches indicated (blue). The nomenclature of clusters uses a numeric indicator of excitatory or inhibitory cluster followed by one or two marker genes, with the first marker typically a neuromodulator (*29*). Inhibitory and excitatory clusters that lack a notable neuromodulator marker gene were designated as Gaba and Glut, respectively, with an additional marker gene to help differentiate among these clusters when possible. Cluster names are colored according to the first gene. Predicted anatomical locations for the clusters are listed on the tree, and the unlabeled lines indicate that such prediction was not possible. Thick black lines underscore clusters grouped by common neuropeptide expression. (**D**) As in (C) but for excitatory neurons. The hybrid neuronal clusters h1/h2 and h3 are listed in (C) and (D), respectively, because they were initially classified as inhibitory and excitatory, respectively. (**E**) $-\log_{10}$(*P* value) for the enrichment of gene categories in differentially expressed genes that mark neuronal clusters calculated based on a gene-set enrichment analysis as shown in fig. S6. **P* < 0.05.

regions (*32*–*34*). We denote these clusters as h1, h2, and h3 (Figs. 1, C and D, and fig. S3C).

To determine the gene categories that best discriminate neuronal clusters, we examined the top five most differentially expressed genes in each cluster and observed enrichment for neuropeptides and molecules involved in neuromodulator production and transport, as well as for transcription factors, but not for neuromodulator (neuropeptide and hormone) receptors. Quantitative analyses of enrichment profiles of these three gene classes among differentially expressed genes further support this notion (Fig. 1E, fig. S6, and table S3). Neuromodulator receptors did discriminate some clusters (for example, Npr1, Rxfp1, Brs3, and Drd1) (Fig. 1, C and D, and figs. S4 and S5). However, on average, neuromodulator receptors were expressed more widely and at lower levels than neuromodulators and transcription factors, limiting their use as potential markers for functional studies. Most clusters were discriminated by combinations of genes rather than by single markers.

Hierarchical tree analyses (*29*) showed that inhibitory neuronal clusters that express a common neuromodulator were often grouped together on the tree—for example, clusters expressing Avp, Gal, Crh, Tac1, and Sst (Fig. 1C)—suggesting potential functional or developmental commonality among them. By contrast, neuromodulators largely failed to group excitatory neuronal clusters (Fig. 1D). Instead, predicted locations of individual clusters on the basis of spatial expression patterns of their marker genes observed in the Allen Brain Atlas (*35*) and our own in situ hybridization data (fig. S7) suggest that excitatory clusters tended to be grouped on the tree by anatomical structures or nuclei (Fig. 1D). For example, markers of clusters e4, e2, e21, h3, and e17 defined a node in the tree located in the PVN and adjacent nuclei (MPN, PaAP, BAC, and BNST), markers of node-sharing clusters e13 and e7 placed these populations in the MnPO/AvPe/VMPO region, whereas markers of e12, e6, e5, and e1 placed these cells in the MPN/MPA region (Fig. 1D) (full names of the nuclei described in this work are provided in table S4). We thus hypothesize that excitatory neuron types tend to be spatially segregated

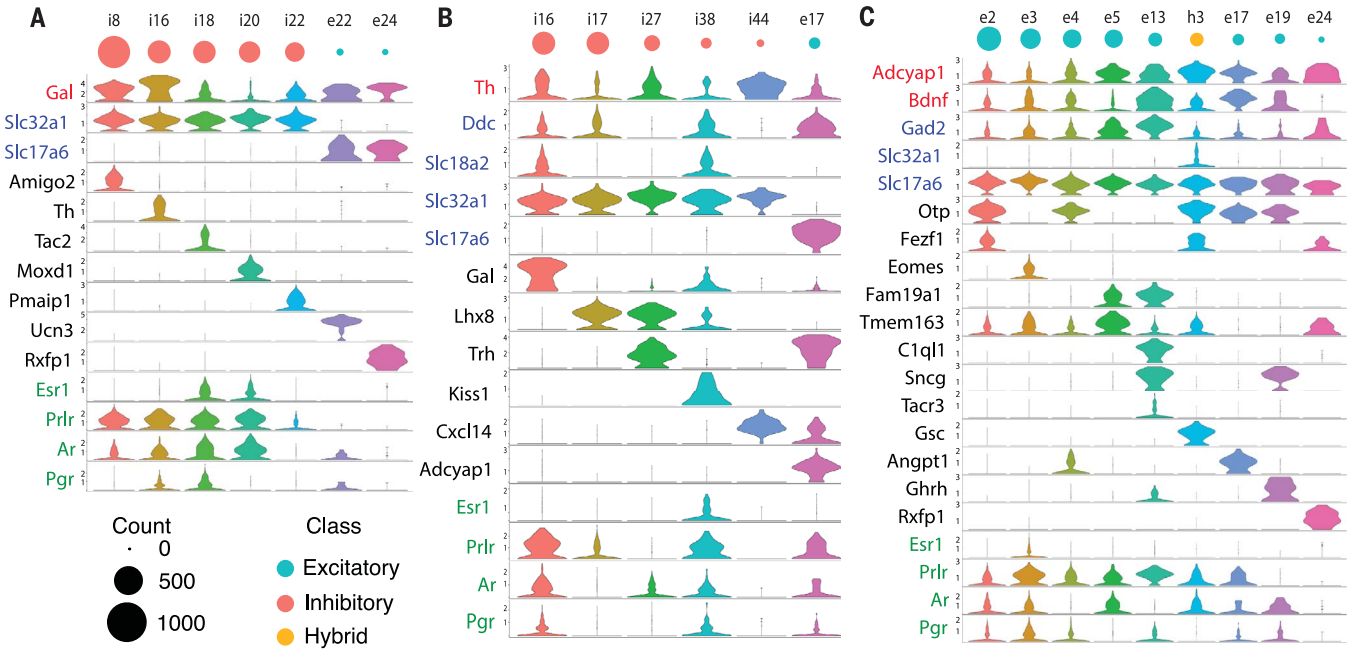

Fig. 2. scRNA-seq identifies subdivisions of cells that express markers previously associated with single neuronal populations. (**A** to **C**) Expression distributions of selected marker genes and genes of interest in all neuronal clusters that are statistically enriched [Model-based Analysis of Single-cell Transcriptomics (MAST) (*75*), false discovery rate <0.01] in (A) galanin (Gal), (B) tyrosine hydroxylase (Th), or (C) Bdnf and Adcyap1. Gene names in black indicate differentially expressed genes for each selected neuronal cluster. Gene names in blue indicate inhibitory (Gad1, Gad2, Slc32a1) and excitatory (Slc17a6) neuronal markers, as well as dopaminergic markers (Ddc, Slc6a3, and Slc18a2). Gene names in green indicate sex hormone receptors. The *y* axis on each violin plot depicts the log transformed counts with the range set to the 95% expression quantile of the cluster with the highest expression (*29*). The sizes of red, cyan, and yellow circles correspond to the cell abundance of the inhibitory, excitatory, and hybrid clusters, respectively.

in distinct anatomical structures of the preoptic region, in a manner similar to the spatial segregation of different types of excitatory neurons in various layers of the cortex (*36*). Similar analysis with the inhibitory neuronal tree suggests that although some groups of clusters were defined by spatially restricted transcription factor expression—for example, Six6 marking the SCN (Fig. 1C)—such spatial grouping of transcriptionally similar clusters appeared to be less pronounced than with excitatory clusters. Additionally, transcription factors tended to mark groups of neuronal clusters further subdivided by neuromodulator expression (Fig. 1, C and D), which is consistent with earlier reports of hypothalamic parcellation by transcription factors during early development (*37*).

Specific neuronal clusters identified with scRNA-seq

Previous studies of the preoptic region have defined cell populations associated with the regulation of specific homeostatic and behavioral functions on the basis of the expression of one or more marker genes (table S5). Clusters that express these marker combinations were identified in our scRNA-seq data (figs. S4 and S5), together with many previously unknown cell populations. Moreover, we uncovered a high level of molecular heterogeneity among a number of previously reported singular cell types, thus partitioning them into multiple distinct populations, as illustrated below on specific examples.

The neuropeptide galanin (Gal) has been associated with behaviorally relevant cell populations of the preoptic region (*4*, *5*, *38*) in the MPOA (parenting and feeding) (*5*, *38*) and VLPO (sleep) (*4*). Our scRNA-seq data revealed seven neuronal clusters that were statistically enriched in Gal expression, each characterized by distinct marker genes (Fig. 2A) validated with two-color in situ hybridization (fig. S7A). These clusters were each associated with different hormonal modulations, ranging from cluster i20:Gal/Moxd1, predicted to lie in the sexually dimorphic nucleus of the POA (Fig. 1C) and expressing a wide range of sex steroid and neuropeptide receptors, to cluster e24:Gal/Rxfp1, expressing no sex steroid receptor (Fig. 2A).

Second, cells that express tyrosine hydroxylase (Th), a key enzyme involved in catecholamine synthesis, have been viewed as a single population involved in several social behaviors (*6*, *39*). We identified six Th-enriched neuronal clusters (Fig. 2B and fig. S7B), among which only i16:Gal/Th and i38:Kiss1/Th expressed both Dopa decarboxylase (Ddc) and the vesicular monoamine transporter Vmat2 (Slc18a2), genes required for dopaminergic function (Fig. 2B).

Last, the neuropeptide adenylate cyclase activating polypeptide 1 (Adcyap1) and brain-derived neurotrophic factor (Bdnf) have recently been identified as combined markers for preoptic neurons sensing warm temperature (*8*). Our data revealed nine Adcyap1- and Bdnf-enriched clusters (Fig. 2C). Although the warm-sensitive neurons have been previously considered as inhibitory neurons on the basis of their functional properties and expression of Gad2, all nine Adcyap1- and Bdnf-enriched clusters identified here coexpressed Gad2 and Slc17a6, and only one of them also expressed Slc32a1 (Fig. 2C), identifying these clusters as excitatory or hybrid neurons. We further identified one of these clusters as representing warm-sensitive neurons with the help of MERFISH. A recent study has revealed that a neuronal population that controls thirst-motivated behavior also expresses Adcyap1 and Bdnf (*10*), further supporting the notion that Adcyap1 and Bdnf are imperfect markers for warm-sensitive cells.

MERFISH measurements of the preoptic region

Next, we performed MERFISH measurements of the preoptic region (1.8 by 1.8 by 0.6 mm, Bregma +0.26 to −0.34), within the area characterized with scRNA-seq, targeting a set of 155 genes (Fig. 3A and table S6) (*29*). These genes were composed of two groups: (i) 85 preselected genes that were either known markers for major cell classes or relevant to neuronal functions of the hypothalamus, such as neuropeptides and neuromodulator receptors, and (ii) 70 additional genes that were identified with scRNA-seq as neuronal cluster markers but not already included in the 85 preselected genes. Among these 155 genes, 135 genes were imaged by using combinatorial smFISH with an error-robust barcoding scheme, as demonstrated previously for MERFISH (*20*, *26*, *40*). The

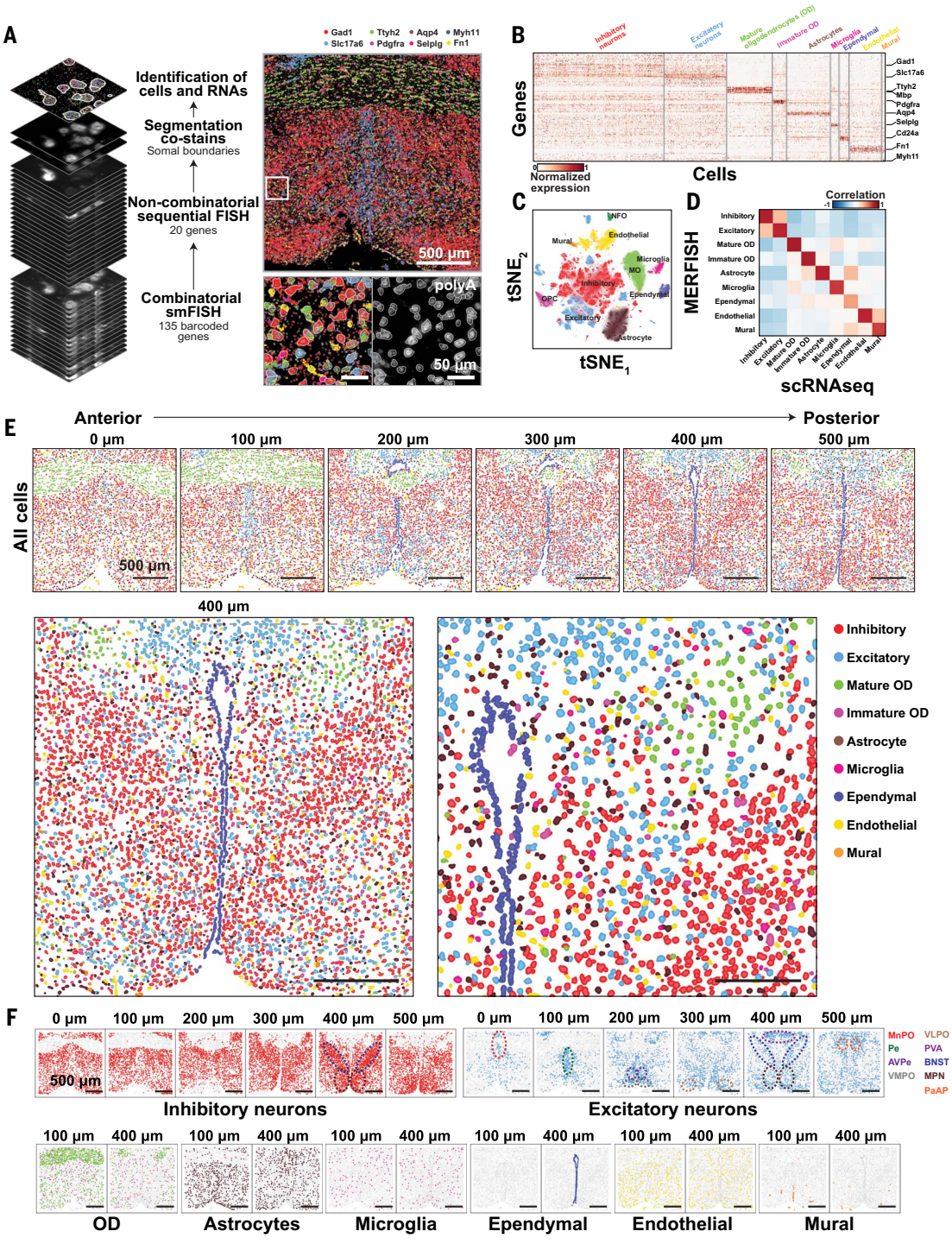

Fig. 3. Major cell classes and their spatial organizations in the preoptic region as revealed with MERFISH. (**A**) (Left) Schematic of the MERFISH measurements. Combinatorial smFISH imaging was used to identify 135 genes, followed by sequential rounds of two-color FISH to identify 20 additional genes. Total polyadenylated mRNA and nuclei costains then allowed cell boundary segmentation. (Top right) Pseudo-colored dots marking localizations of individual molecules of eight example RNA species, each marking a distinct major cell class, in a 10-μm-thick, 1.8- by 1.8-mm slice. (Bottom right) Magnification of the white boxed region (left) and the total mRNA image and the segmented cell boundaries of the same region (right). The raw and decoded MERFISH images of the same field of view (FOV) for all 135 genes measured by using combinatorial smFISH are shown in fig. S9; the total mRNA and nuclei costain images and segmented cell boundaries for the same FOV are shown in fig. S10. The segmented cell boundaries represent the boundaries of the cell soma (*29*). A subset of identified RNA molecules fell outside these boundaries and are thus candidates for RNAs in neuronal or glial processes. (**B**) Expression of all genes measured with MERFISH for ~500,000 cells imaged in multiple naïve animals. Expression for each gene is normalized to the 95% expression quantile for that gene across all cells. Cells are grouped by major classes, and markers of each major cell class are listed on the right. OD, oligodendrocytes. (**C**) tSNE plot of these cells. (**D**) Pairwise Pearson correlation coefficients between the average expression profiles (in *z*-scores) of individual cell classes identified with MERFISH and scRNA-seq. (**E**) (Top) Spatial distribution of all major cell classes across sections at different anterior-posterior positions from a single female mouse. Cells are marked with cell segmentation boundaries and colored by cell classes as indicated. Six of the twelve 1.8- by 1.8-mm imaged slices are shown. The 0, 100, 200, 300, 400, and 500 μm labels indicate the distance from the anterior position (Bregma +0.26). (Bottom) Enlarged image of the slice at 400 μm from the anterior position (left) and a further magnified image of the region shown in the gray dashed box (right). Scale bars, 500 μm (left), 250 μm (right). (**F**) Spatial distributions of individual cell classes are shown as colored dots on the background of all cells shown as gray dots. Dashed ovals indicate several specific hypothalamic nuclei and are colored identically to the nuclei abbreviations listed to the right. BNST, bed nucleus of the stria terminalis; MPN, medial preoptic nucleus; MnPO, median preoptic nucleus; Pe, periventricular hypothalamic nucleus; AvPe, anteroventral periventricular nucleus; VMPO, ventromedial preoptic nucleus; VLPO, ventrolateral preoptic nucleus; PVA, paraventricular thalamic nucleus; PaAP, paraventricular hypothalamic nucleus, anterior parvicellular.

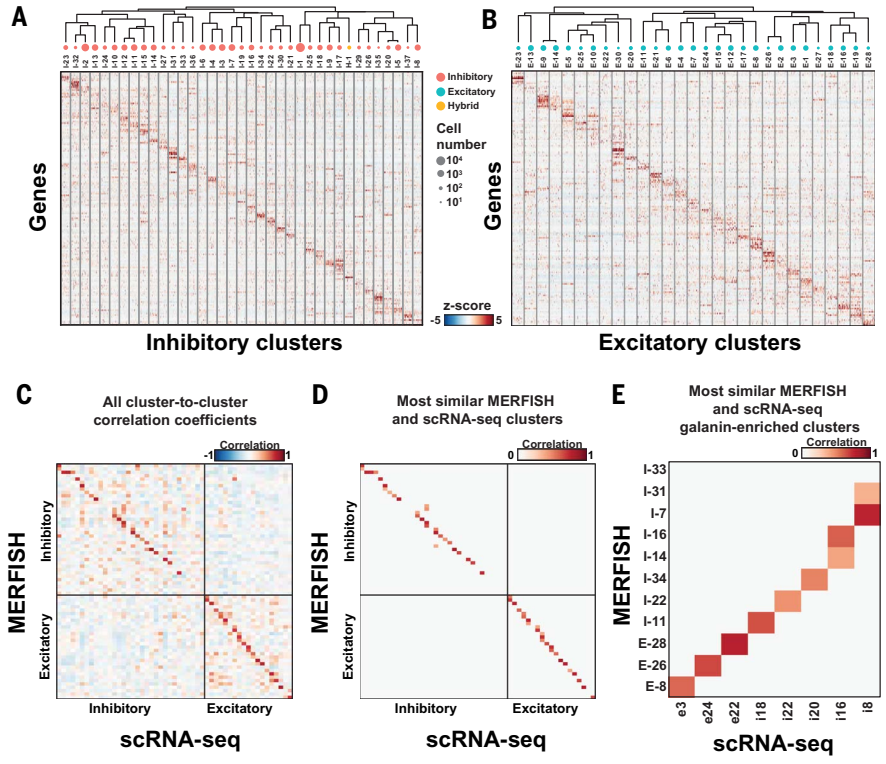

Fig. 4. Neuronal clusters in the preoptic region as revealed with MERFISH. (**A** and **B**) *z*-scores of expression profiles for (A) inhibitory and (B) excitatory neuronal clusters identified with MERFISH. Depicted are 100 random cells from each cluster. The neuronal clusters are organized on the basis of similarity in their expression profiles, as depicted by the dendrogram. The sizes of red, cyan, and yellow circles indicate the abundance of neuronal clusters, and only clusters with more than 100 cells are depicted. H-1 is grouped with the inhibitory clusters because it was initially classified as inhibitory neurons. (**C**) The pairwise Pearson correlation coefficients between the expression profile (in *z*-score) of the MERFISH and scRNA-seq clusters. The order of the clusters in (C) is not the same as in (A) and (B). (**D**) As in (C) but with only scRNA-seq cluster(s) most similar to each MERFISH cluster shown, identified as the cluster(s) with the highest Pearson correlation coefficient(s) (fig. S14 and table S9) (*29*). When multiple scRNA-seq clusters show statistically indistinguishable, highest correlation coefficients to a MERFISH cluster (*29*), all of them are indicated. scRNA-seq clusters outside the region imaged with MERFISH, as assessed by the expression patterns of the marker genes in the Allen Brain Atlas (*35*) and our own in situ data (fig. S7) (*29*), are excluded from this analysis (*29*). (**E**) Same as (D) but for clusters enriched in galanin (Gal).

remaining 20 genes were relatively short and/or expressed at high levels, which is challenging for combinatorial smFISH detection, and hence were measured in sequential rounds of multicolor FISH after the combinatorial run. The sexually dimorphic expression previously reported for 11 genes (*41*, *42*) was confirmed here (fig. S8).

We sectioned the preoptic region into 60 evenly spaced slices along the anterior-posterior axis and performed three-dimensional MERFISH imaging on every fifth slice (*29*). Individual RNA molecules were clearly detected and identified (fig. S9), and individual cells were segmented based on 4′,6-diamidino-2-phenylindole (DAPI) and total mRNA staining (fig. S10) (*29*). In total, we profiled >400,000 cells from three to four replicates in naïve male and female animals, as well as >500,000 additional cells from three to five replicates of animals subjected to behavioral stimuli (*29*). MERFISH expression data showed high reproducibility between replicates (fig. S11A), good correlation with bulk RNA-seq data of the preoptic region (*43*) (fig. S11B), and a low false-detection rate (fig. S11C). For the targeted genes, MERFISH detected on average six- to eightfold more transcript copies per cell than did scRNA-seq (fig. S12, A to D), underscoring the high sensitivity of MERFISH.

We used an unsupervised, community-detection–based clustering approach similar to that applied to scRNA-seq data to identify transcriptionally distinct cell populations in MERFISH data (Fig. 3, B and C, and table S7) (*29*). MERFISH identified all major cell classes (Fig. 3, B and C), except for macrophages and fibroblasts, potentially because the corresponding marker genes were not included in the MERFISH gene library. The expression profiles of cell classes measured with MERFISH were strongly correlated with those determined by using scRNA-seq (Fig. 3D). However, the relative abundance of cells in various cell classes differed in the two datasets (fig. S12E). In particular, astrocytes, endothelial cells, and ependymal cells were depleted in our scRNA-seq data, presumably because of cell loss during tissue dissociation.

MERFISH also provided a direct measurement of the spatial distribution of major cell classes. As expected, mature oligodendrocytes were enriched in the anterior commissure and the fornix–major myelinated fiber tracts of the rostral hypothalamus, whereas immature oligodendrocytes, astrocytes, microglia, and endothelial cells were dispersed throughout (Fig. 3, E and F). Ependymal cells formed a single layer lining the more caudal aspects of the third ventricle, and mural cells were organized in vermiform structures that resemble blood vessels (Fig. 3, E and F). Notably, inhibitory and excitatory neurons exhibited distinct distributions (Fig. 3, E and F). Inhibitory neurons, the more abundant neuronal type in the preoptic region, were widely dispersed across this region but enriched in specific posterior nuclei, including the BNST and MPN. By contrast, excitatory neurons were specifically enriched in a few nuclei anteriorly but became more dispersed posteriorly and, in agreement with previous reports (*44*), were depleted in the posterior BNST.

MERFISH analyses of specific neuronal types

Clustering analyses of inhibitory neurons and excitatory neurons separately identified ~40 inhibitory and ~30 excitatory neuronal populations (Fig. 4, A and B, and tables S7 and S8). We investigated the impact of the number of genes used to cluster cells in MERFISH data and found that ~90% of the identified neuronal clusters were recovered by using the ~75 genes that were most informative among the 155 (fig. S13). Beyond this point, cluster recovery increased more slowly with the number of genes added (fig. S13). Hereafter, we denote excitatory and inhibitory neuronal clusters identified with MERFISH as E-1, E-2, ... and I-1, I-2, ..., respectively, and the one identified hybrid cluster as H-1.

The expression profiles of most neuronal clusters determined with MERFISH correlated well with those of scRNA-seq clusters (Fig. 4C and fig. S14, A and B). This observation allowed us to infer, for each MERFISH cluster, the putative corresponding or most similar scRNA-seq cluster(s), defined as the cluster(s) with the highest correlation coefficient(s) (Fig. 4D, fig. S14C, and table S9) (*29*), which could help expand our knowledge of the expression profiles of the MERFISH clusters. Similar correspondence was observed by using a neural network classifier (fig. S14, D and E). Correlations between MERFISH and scRNA-seq clusters were only moderately weaker than those between scRNA-seq clusters derived from bootstrapped replicates (fig. S14, F and G). Many MERFISH clusters had a distinct, most similar scRNA-seq cluster (Fig. 4D, fig. S14, and table S9). However, in some instances, multiple MERFISH clusters exhibited the highest correlation to the same scRNA-seq cluster; in addition, a small fraction of MERFISH clusters lacked a statistically significant correlation to any scRNA-seq cluster (Figs. 4D, fig. S14, and table S9). Both of these

scenarios suggest that some clusters identified with MERFISH were not discriminated by scRNA-seq. Conversely, a small fraction of scRNA-seq clusters lacked a statistically significant correlation to any MERFISH cluster (Fig. 4D, fig. S14, and table S9), suggesting that these clusters were not identifiable by the MERFISH gene panel or were located outside the MERFISH-imaged area (*29*).

As a specific illustration, MERFISH identified 10 clusters enriched in Gal expression, some showing one-to-one correspondences to Gal-enriched scRNA-seq clusters (Fig. 4E; fig. S15, A and B; and table S9). We also observed instances in which two Gal-enriched MERFISH clusters putatively corresponded to the same Gal-enriched scRNA-seq cluster (for example, I-14 and I-16 to i16) (Fig. 4E and table S9), suggesting that MERFISH resolved subpopulations within the scRNA-seq cluster. Indeed, we identified two subsets of cells within the scRNA-seq cluster i16, each respectively expressing markers of the MERFISH clusters I-14 and I-16 (fig. S15, C and D). The calcitonin receptor (Calcr)– and bombesin receptor (Brs3)–positive I-14 and the Th-positive I-16 were found to be differentially activated in specific social behaviors, as described later (table S9), supporting the resolution of these cells into two distinct populations. We also observed a similar resolution of i8 into I-7 and I-31 (Fig. 4E; fig. S15, E and F; and table S9). A Gal-enriched scRNA-seq cluster could also be split into Gal-enriched and non–Gal-enriched MERFISH clusters [for example, i20 into Gal-enriched cluster I-34 and non–Gal-enriched clusters I-2 and I-32 (fig. S15, G and H, and table S9)].

Examination of the MERFISH or scRNA-seq clusters that were not discriminated by the other method showed several trends. Some of the MERFISH clusters not detected with scRNA-seq had relatively low abundance and thus might not be sufficiently represented in our scRNA-seq data, which profiled 4% as many neurons as we did in MERFISH. Some of the MERFISH clusters not discriminated by scRNA-seq had lowly expressed marker genes, which may not be reliably detected with scRNA-seq. Conversely, some scRNA-seq clusters not identified with MERFISH had marker genes that were not included in the MERFISH gene library. Some of the extremely low-abundance MERFISH or scRNA-seq clusters that lack correspondence may not represent well-identified clusters. These results thus demonstrate the complementary nature of MERFISH and scRNA-seq and an increased ability to characterize cell populations when both approaches are combined. Nevertheless, some clusters still exhibited heterogeneity in gene expression associated with distinct spatial locations (fig. S16), suggesting either spatial gradients in gene expression within the same cluster or the presence of unresolved cell subpopulations.

Spatial organization of specific neuronal cell types

Next, we examined the spatial distributions of individual neuronal clusters (Fig. 5A and figs. S17 and S18) within the framework of major anatomically defined nuclei of the preoptic region

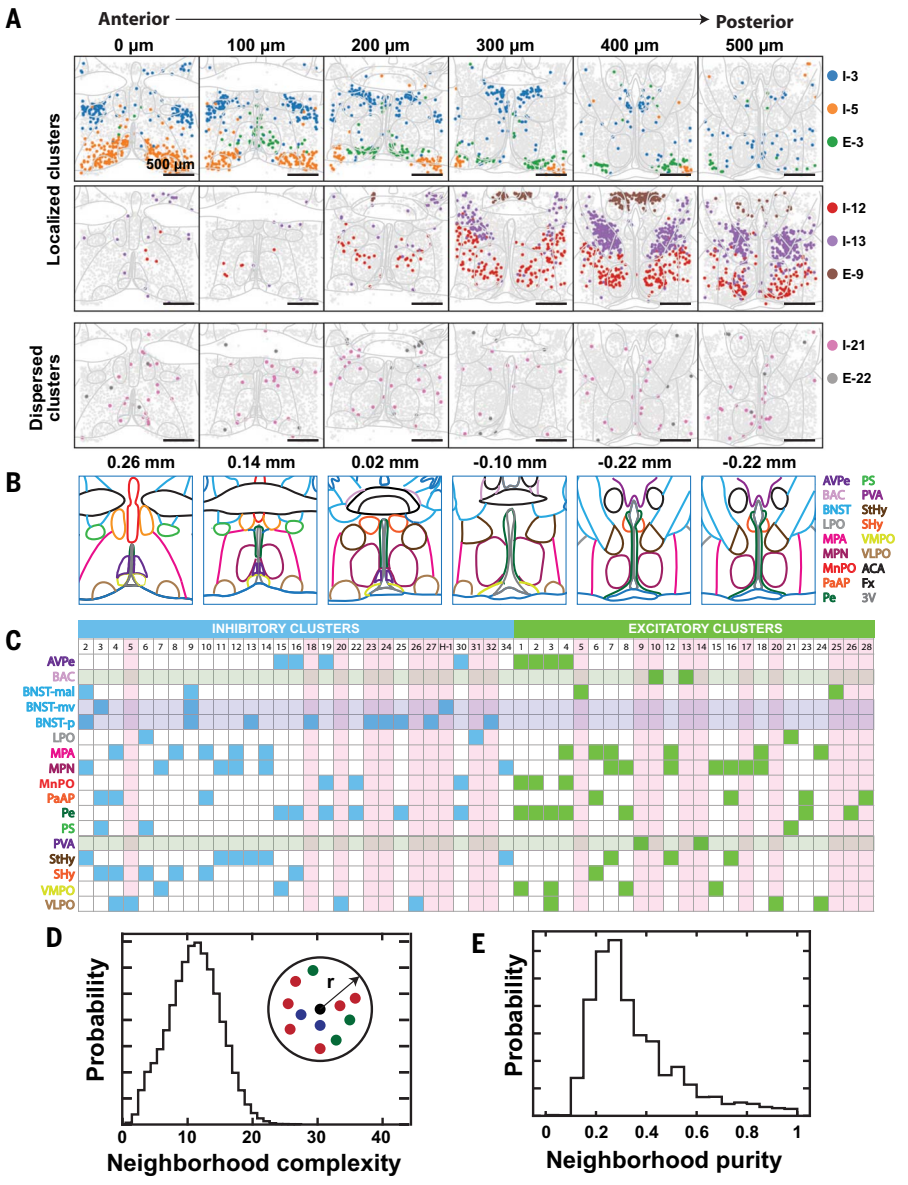

Fig. 5. The spatial organization of neuronal clusters in the preoptic region. (**A**) Spatial distribution of example neuronal clusters that are localized (top and middle) or dispersed (bottom). Depicted are six of the 12 slices imaged from a female mouse. Colored markers indicate cells of the specified neuronal clusters, and gray markers indicate all other neurons. Nuclei boundaries depicted in light gray are drawn according to (*45*) and aligned to the tissue slices according to the locations of landmarks, such as the anterior commissure, fornix, and ventricle. The 0, 100, 200, 300, 400, and 500 μm labels indicate the distance from the anterior position (Bregma +0.26). (**B**) Illustration of major hypothalamic nuclei spanning the imaged region and colored according to legend on the right (*45*). Nuclei abbreviations are as defined in Fig. 3F, and additionally, BAC, bed nucleus of the anterior commissure; LPO, lateral preoptic area; MPA, medial preoptic area; PS, parastrial nucleus; StHy, striohypothalamic nucleus; SHy, septohypothalamic nucleus; ACA, anterior commissure; Fx, fornix; 3V, third ventricle. Bregma locations are listed on top and the map at Bregma −0.22 is duplicated. (**C**) Summary of nuclei in which inhibitory (blue) or excitatory (green) neuronal clusters are enriched. Translucent horizontal bars indicate nuclei that contain only inhibitory (blue) or excitatory (green) clusters. Vertical pink bars highlight clusters primarily enriched in single nuclei. BNST-mal, BNST, medial division, anterolateral part; BNST-mv, BNST, medial division, ventral part; BNST-p, BNST, posterior part. (**D** and **E**) Analysis of spatial mixing of distinct neuronal clusters. We define the complexity of the neighborhood surrounding any given neuron as the number of distinct neuronal clusters present within that neighborhood, and the purity of that neighborhood as the fraction of all cells within the given neighborhood that are part of the most abundant cluster. Probability distributions of the complexity (D) and purity (E) of the 100-μm-radius neighborhood surrounding any given neuron are depicted.

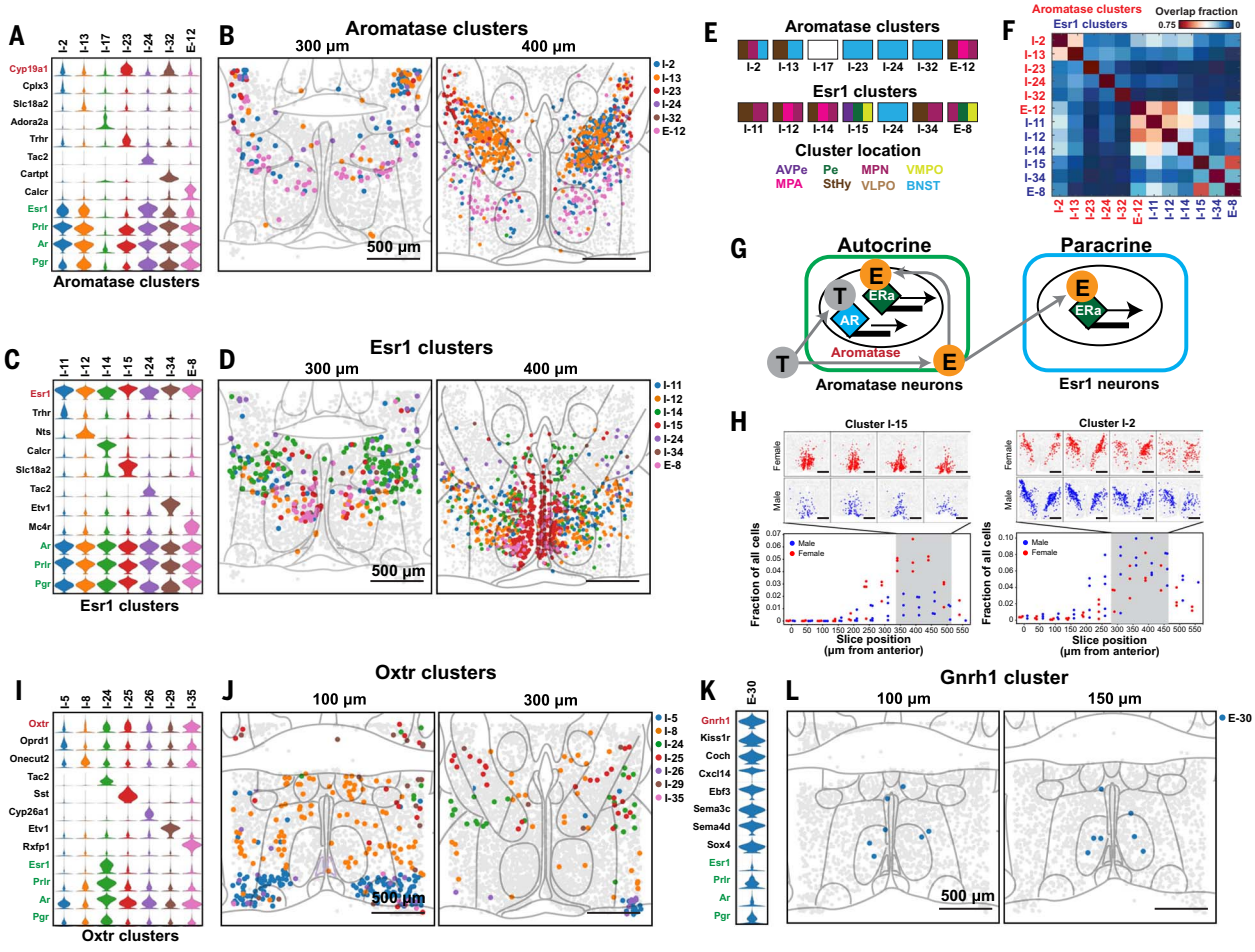

Fig. 6. Spatial and molecular organization of neuronal clusters enriched in genes relevant to social behaviors. (**A**) Expression distributions of selected marker genes and genes of interest for neuronal clusters enriched in aromatase (Cyp19a1). Expression distributions are calculated as in Fig. 2. (**B**) Spatial distributions of neuronal clusters depicted in (A). Two of the 12 slices from a female mouse sample are depicted. Nuclei boundaries depicted in light gray are as defined in Fig. 5A. (**C** and **D**) As in (A) and (B) but for clusters enriched in estrogen receptor α (Esr1). (**E**) Schematic showing the nuclei spanned by individual clusters, as indicated by the color subdivisions of the rectangles, colored identically to the nuclei abbreviations listed below. The nuclei abbreviations are as defined in Figs. 3F and 5B. I-17 is not colored because it was found at the edge of our imaged region and falls outside of the boundaries of the nearest imaged nuclei, the VLPO (table S9). (**F**) Average overlap fraction between aromatase-enriched clusters and Esr1-enriched clusters for all measured animals. Cluster I-24 is enriched in both aromatase and Esr1 and listed only once. (**G**) Models of autocrine and paracrine signaling. Circulating testosterone (gray T) can activate cells expressing androgen receptor (AR) or, in cells expressing aromatase, can be converted to estrogen (orange E). Autocrine: In cells co-expressing aromatase and Esr1, estrogen produced in these cells can activate estrogen receptor (ERa) in the same cells. Paracrine: Estrogen produced by aromatase-enriched cells can activate ERa in nearby cells enriched with Esr1. (**H**) Comparison of the fraction of cells that belong to the specified neuronal clusters (I-15 or I-2) for all male (blue) and female (red) replicates as a function of the anterior-posterior position of the slices. Above each panel are the spatial distribution of the cluster in four slices from a single female (red) and male (blue) replicate. (**I** and **J**) As in (A) and (B) but for clusters enriched in oxytocin receptor (Oxtr). (**K** and **L**) As in (A) and (B) but for a cluster enriched in gonadotropin releasing hormone 1 (Gnrh1). MERFISH revealed 8, 15, and 19 aromatase-, Esr1- and Oxtr-enriched clusters, respectively, with only the seven most enriched clusters depicted for each.

as depicted in Fig. 5B (*45*). About 30% of the MERFISH clusters were enriched primarily in a single nucleus (Fig. 5C, pink shading)—for example, cluster I-5 primarily in the VLPO and cluster E-9 in the PVA (Fig. 5, A to C)—whereas approximately half of the clusters were distributed over a few (two to four), often physically contiguous nuclei (Fig. 5C, unshaded clusters)—for example, cluster I-3 in the BNST-mv, PaAP, PS, and SHy and cluster I-12 in the StHy, MPA, and MPN (Fig. 5, A to C). This anatomical dispersion may reflect a similar function of the same cell type across distinct nuclei or a developmental relationship of spatially distinct cells. By contrast, a small fraction of the neuronal clusters were dispersed and not enriched in any given nucleus, such as I-21 and E-22 (Fig. 5A). Whereas most nuclei were populated by both excitatory and inhibitory neurons, the PVA and BAC only contained excitatory clusters (Fig. 5C, green shaded row), and the BNST-p and BNST-mv contained only inhibitory clusters (Fig. 5C, blue shaded rows), which is consistent with previous observations of high expression of Slc17a6 and Slc32a1 in these regions, respectively (*35*, *44*).

Neuronal clusters of the preoptic region appeared highly intermixed, with multiple clusters occupying any given nucleus. To quantify the degree of intermixing, we calculated the neighborhood composition for each neuron. This analysis showed that each neighborhood contained multiple clusters and was typically not dominated by a single cell population (Fig. 5, D and E).

These direct spatial measurements allowed us to provide an anatomy-based taxonomy for the identified neuronal clusters, except for the dispersed clusters, which we named on the basis of marker genes (table S9). The putative correspondence between these MERFISH clusters and scRNA-seq clusters allowed us to further assess the spatial locations of scRNA-seq clusters and compare them with our earlier predictions

shown in Fig. 1, C and D. In nearly all cases, the predicted locations matched or partially overlapped those of the corresponding MERFISH clusters (table S9), lending additional support to our earlier observations on the spatial relationship between transcriptionally similar clusters (Fig. 1, C and D). However, we caution that the predicted scRNA-seq cluster locations represent rough approximations because of the relatively low resolution of available in situ hybridization data and suffer from occasional ambiguity in the spatial patterns of some marker genes. Moreover, because of the remaining heterogeneity in some of the identified scRNA-seq and MERFISH clusters, the putative correspondence may only represent similarity between subsets of cells within these clusters.

Spatial and molecular organization of socially relevant cell populations

Neuromodulators, hormones, and associated signaling pathways play critical roles in hypothalamic functions, but analyses with cellular resolution have been limited owing to the low expression level of many of the corresponding receptors. MERFISH enabled us to examine the distribution of these genes throughout the preoptic region, providing functional insights into the associated cell populations.

Sex steroid hormones are essential to the development and modulation of social behaviors and reproduction. We examined the distribution of enzymes and receptors essential for steroid hormone signaling in the preoptic region. The enzyme aromatase (Cyp19a1) converts testosterone to estrogen and thus modulates steroid function (*39*). MERFISH revealed aromatase-enriched clusters with distinct repertoires of sex hormone receptors (Fig. 6, A and B). Several of these clusters (such as I-2, I-13, I-24, I-32, and E-12) expressed both androgen receptor (Ar) and estrogen receptor α (Esr1), suggesting that in these cell populations, circulating testosterone can be converted into estrogen and thus affect gene expression in a cell-autonomous manner through Esr1 activation. In addition, the aromatase-enriched clusters E-12 and I-2 substantially overlapped with locations of several Esr1-enriched clusters (Fig. 6, C to F), suggesting that estrogen synthesized by these aromatase-expressing cells may also act in a paracrine manner on cells of the nearby Esr1-enriched clusters, in addition to the autocrine signaling mode described above (Fig. 6G).

Some Esr1-enriched and aromatase-enriched clusters exhibited differences in cell abundance of varying extent between males and females. For example, the Esr1-enriched cluster I-15 showed an appreciable enrichment in female animals, whereas the aromatase-enriched cluster I-2 showed a more modest male enrichment (Fig. 6H). I-2 overlapped with the sexually dimorphic nucleus of the preoptic area (SDN-POA), and its marker gene Cplx3 was co-expressed with MoxD1 [a canonical SDN-POA marker (*46*) not in our MERFISH gene library] in cells of the SDN-POA and BNST (fig. S19). However, I-2:BNST/StHy/MPN spatially extended beyond the boundaries of the SDN-POA,

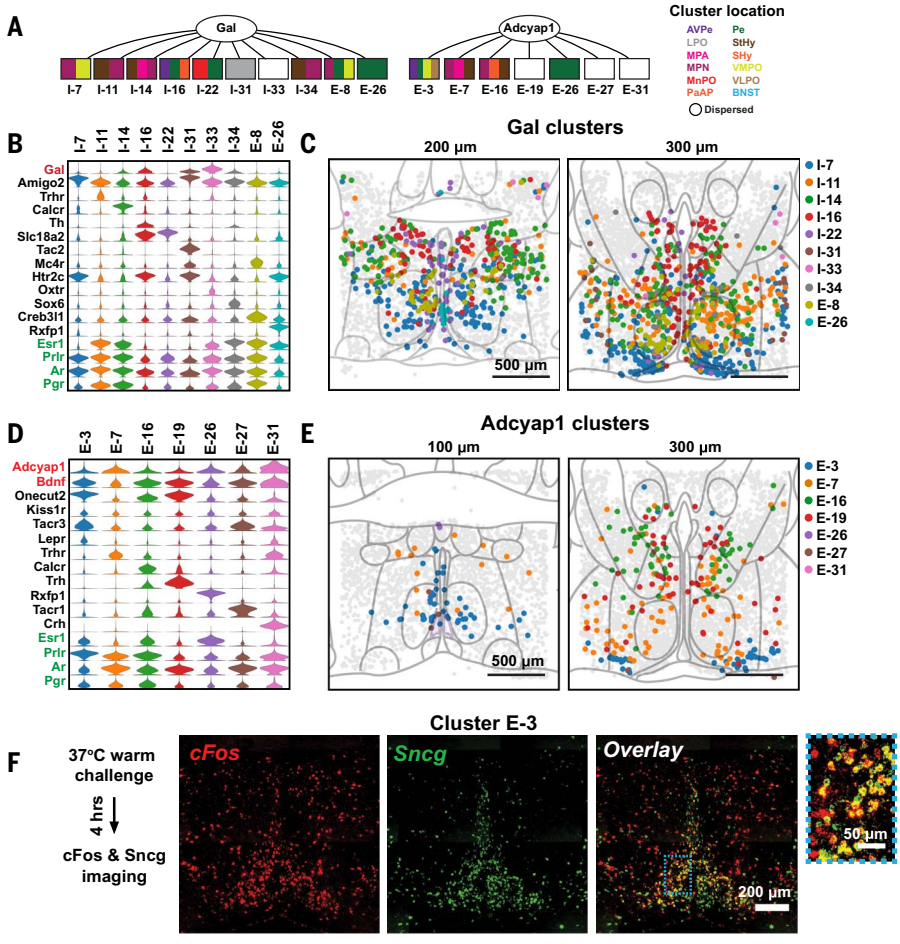

Fig. 7. Subdivisions of neuronal populations expressing Gal or Adcyap1 revealed with MERFISH. (**A**) MERFISH subdivides galanin- and Adycap1-expressing cells into multiple transcriptionally and spatially distinct clusters. Color subdivision of the rectangles shows the nuclei spanned by individual clusters, colored identically to the nuclei abbreviations listed on the right. The nuclei abbreviations are as defined in Figs. 3F and 5B. (**B**) Expression distributions of selected marker genes and genes of interest for all neuronal clusters enriched in galanin (Gal). Expression distributions are calculated as in Fig. 2. (**C**) Spatial distributions of all inhibitory and excitatory Gal-enriched clusters. (**D** and **E**) As in (B) and (C) but for Adcyap1- and Bdnf-enriched clusters. The seven most enriched of the 14 Adcyap1- and Bdnf-enriched clusters are shown. (**F**) in situ hybridization images of cFos (red), Sncg (green), and overlay of an anterior slice of the preoptic region taken from a heat-stressed animal. The blue boxed region is magnified and shown on the right. Sncg is a marker for the scRNA-seq cluster e13 that corresponds to the MERFISH cluster E-3 (table S9).

suggesting that it may contain unresolved subpopulations, which may partially mask a sexual dimorphism in SDN-POA cell populations.

We next considered clusters enriched in the expression of oxytocin receptor (Oxtr), an important modulator of social behaviors that exerts its effects broadly throughout the brain (*47*). Although the low expression level of Oxtr has previously made it challenging to identify oxytocin targets, the high sensitivity of MERFISH allowed us to detect enrichment of Oxtr in multiple clusters (Fig. 6, I and J). For example, the Oxtr-enriched BNST cluster I-24 coexpressed multiple sex hormone receptors as well as the neuropeptide Tac2 implicated in social isolation stress (*48*), aggression, and fear (*48*, *49*), suggesting the involvement of oxytocin signaling in these functions. This cluster was specifically activated after pup-directed aggression by virgin males as described below, corroborating studies that implicate the BNST in this function (*50*). This highlights a seemingly paradoxical role for Oxtr in agonistic pup encounters versus its known roles in affiliative behaviors (*47*). Oxtr was also found in the VLPO cluster I-5, implying that oxytocin might have a role in the modulation of VLPO functions such as sleep or temperature sensing (*4*, *51*–*53*).

The high throughput of MERFISH measurements allowed us to identify some extremely rare cell types. GnRH-expressing cells (E-30) represent a rare cell population dispersed within the preoptic area and basal forebrain that integrates and orchestrates peripheral and central aspects of reproduction (*54*–*56*). Only a few cells were

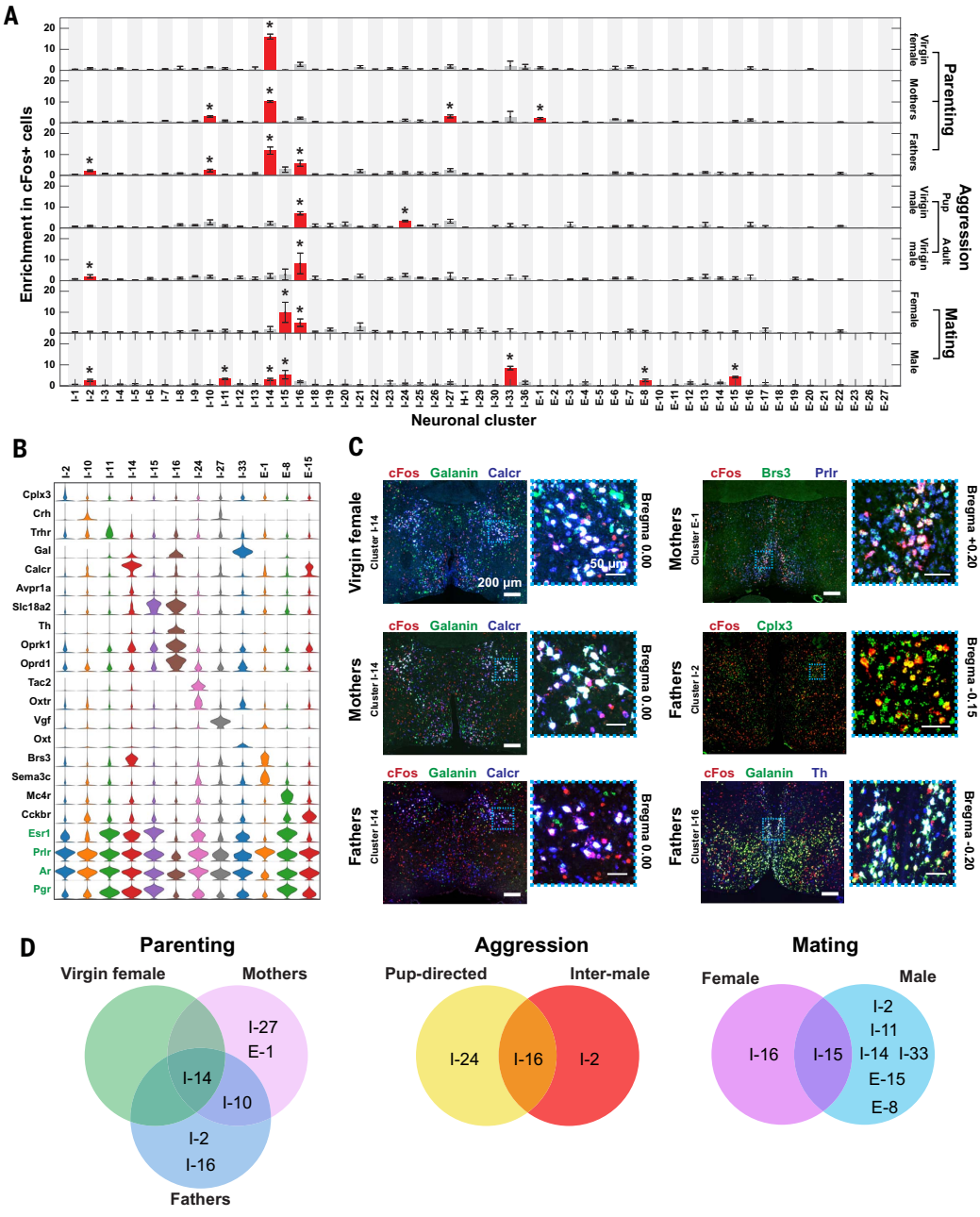

Fig. 8. Neuronal clusters activated during specific social behaviors revealed with MERFISH. (**A**) Enrichment in cFos-positive cells within each neuronal cluster observed in males or females after displaying a given social behavior. Red bars marked with asterisks are clusters with statistically significant enrichment in cFos-positive cells, as compared with the fraction of cFos-positive cells in all cells (binomial test; false-discovery rate < 5%). Error bars represent standard error of the mean (n = 3 to 5 replicates). We measured fewer slices in behaviorally stimulated animals than in naive animals (4 versus 12 slices per animal) (*29*), and only clusters in which at least 10 cells are present in two or more behavior replicates are depicted. (**B**) Expression distributions of selected marker genes and genes of interest for neuronal clusters enriched in cFos-positive cells in the tested social behaviors. Expression distributions are calculated as in Fig. 2. (**C**) Representative in situ hybridization images of 16-µm-thick sections from the preoptic region showing cFos expression in cells expressing markers of neuronal clusters activated during parenting, in virgin females, mothers, and fathers. Regions in blue dashed boxes are magnified and shown on the right. Red, green, and blue mark the listed genes, and white (or yellow for I-2) indicates coexpression in the merged images. Clusters that cannot be distinguished by a combination of two marker genes plus their spatial location (I-27 and I-10) were not tested. (**D**) Venn diagrams summarizing the clusters that were activated during specific behaviors in different sexes or physiological states.

found to express appreciable GnRH in our scRNA-seq data and did not form a distinct cluster. By contrast, MERFISH identified a GnRH-enriched cluster (Fig. 6, K and L), which expressed remarkably low levels of Esr1 and Ar (Fig. 6K), suggesting that GnRH neurons may receive indirect feedback from circulating hormones within the hypothalamic–pituitary–gonadal (HPG) axis, potentially through synaptic input from hormone-responsive cell-types such as Kisspeptin (Kiss)–expressing cells (*57*).

Partition of previously defined cell types into multiple cell populations

Our MERFISH data also partitioned a number of previously reported single cell types—for example, Gal-expressing and Adcyap1-expressing neurons—into multiple distinct cell populations (Fig. 7A). We observed 10 Gal-enriched MERFISH clusters, several of which were scattered across multiple nuclei, such as cluster I-14:MPA/MPN/StHy (Fig. 7, A to C). I-14 was strongly activated during parenting, as shown below, revealing that molecularly and functionally defined cell types can spread across multiple nuclei.

Similarly, MERFISH identified 14 clusters enriched in Adcyap1 and Bdnf (Fig. 7, A, D, and E), which were previously designated as markers for warm-sensitive neurons (*8*). Yet only one of these clusters, E-3:AvPe/Pe/VMPO/VLPO, displayed the established spatial location of warm-sensitive cells (Fig. 7E) (*8*). Indeed, upon heat stress (*29*), a high level of the IEG cFos was expressed in cells in the region covered by E-3, and Sncg, a marker gene of E-3's corresponding scRNA-seq cluster e13 (table S9), was highly enriched in these cFos-positive cells (Fig. 7F). E-3 expressed the leptin and prolactin receptors (Lepr and Prlr) (Fig. 7D), suggesting a mechanism by which metabolic and reproductive states may modulate thermoregulation. Preoptic cells receiving projections from Arcuate Nucleus Kiss1 cells were recently implicated in the regulation of hormonally induced hot flashes via the activation of the receptor Tacr3 (*58*). E-3 and e13 expressed both Kiss1 receptor and Tacr3, implicating the warm-sensitive cluster in the generation of hot flashes.

Neuronal cell types activated by key social behaviors

To investigate the role of specific neuronal populations in discrete social behaviors, we included cFos in MERFISH measurements and characterized animals after parenting, aggression, or mating. We performed clustering analysis of these behavioral samples together with naïve samples not subjected to behavioral stimuli and did not observe any cluster that was present only in behavioral samples. For each behavior, only a few neuronal clusters, each characterized by key markers, exhibited a statistically significant enrichment in cFos-positive cells (Fig. 8, A and B, and fig. S20). In addition, many other clusters showed a small fraction of cFos-positive cells, which together accounted for a substantial subset of all cFos-positive cells (Fig. 8A and fig. S20B). Activated neurons in all tested behaviors were predominately inhibitory.

We first examined clusters preferentially activated after pup exposure, which elicits parenting behaviors in virgin females, mothers, and fathers but triggers aggression in virgin males (*5*, *59*). We identified, with MERFISH, preferentially activated clusters—clusters enriched in cFos-positive cells (referred to as cFos enrichment hereafter) (Fig. 8, A and B, and fig. S20)—and validated, by use of two- or three-color in situ hybridization, all clusters that could be specifically defined by two marker genes and spatial location (Fig. 8C). In all animal groups that display parenting, I-14:MPA/MPN/StHy had substantially higher cFos enrichment than that of any other cluster (Fig. 8A and fig. S20). The expression of Gal and vasopressin receptor (Avpr1a) within this cluster (Fig. 8B) is consistent with the established role of Gal neurons in parenting (*5*) and their recently documented vasopressinergic input (*60*). Moreover, this cluster expressed a large set of hormone and peptide receptors (Fig. 8B), substantiating the complex neuromodulation of parenting (*61*). In addition to I-14, we observed a preferential activation of clusters by pup exposure in a state-dependent manner. In mothers and fathers, cFos enrichment was observed in Oxtr-expressing cluster I-10:MPA/PaAP/SHy, and mothers additionally showed modest cFos enrichment in I-27:BNST and E-1:AvPe/Pe/MnPO/VMPO (Fig. 8 and fig. S20). Fathers additionally showed cFos enrichment in clusters I-2:BNST/StHy/MPN and in I-16:AvPe/Pe/SHy (Fig. 8 and fig. S20).

By contrast, I-14 was not preferentially activated in virgin males exposed to pups, which is consistent with their aggressive responses toward pups (*5*). Instead, I-16:AvPe/Pe/SHy and I-24:BNST exhibited cFos enrichment after pup-directed aggression (Fig. 8 and figs. S20 and S21). I-16 was also preferentially activated in virgin males that display inter-male aggression, as was I-2 (Fig. 8 and figs. S20 and S21), suggesting that I-16 is broadly involved in aggressive responses, whereas I-24 and I-2 may mediate differential responses to pups and adults. I-16 was also activated in fathers during parenting, which might indicate that the switch from pup-directed aggression to parenting (*59*, *61*) occurs in circuit nodes downstream of I-16, or that the role of I-16 in aggression is inhibited by pro-parenting circuits. The Gal- and Th-enriched cluster I-16 expressed Vmat2 (Slc18a2) and showed correspondence to the scRNA-seq cluster i16:Gal/Th (table S9), which additionally expressed Ddc, suggesting that this cell population is dopaminergic. The activation of a dopaminergic neuronal population during aggression may provide a cellular basis to understand the observations that dopamine is released during aggression and modulates aggressive behavior (*6*). I-16 also expressed the opioid receptors Oprd1 and Oprk1 (Fig. 8B), supporting the effects of opioid receptor ligands on aggressive encounters in mice and other rodents (*62*).

Next, we examined clusters activated by successful mating (*29*) to capture neural activity associated with appetitive and consummatory aspects of sexual behavior. The cluster I-15: AvPe/Pe/VMPO, which displayed a cell abundance enrichment in female mice compared with males (Fig. 6H), was preferentially activated in females and to a lesser extent in males after mating (Fig. 8 and figs. S20 and S21). Both I-14 and I-15—activated by parenting and mating, respectively—expressed Esr1 (Fig. 8B), which is consistent with recent findings on the involvement of Esr1-expressing cells in parenting and mating behaviors (*63*, *64*). However, our data showed that cells activated by parenting and mating belong to two distinct cell populations localized to distinct preoptic nuclei. More generally, we found Esr1 expression in nearly all behaviorally activated clusters, suggesting that this gene alone cannot define specific behaviorally relevant cell types. In addition to I-15, which was activated in both sexes after mating, we also observed a few clusters that exhibited sexually dimorphic cFos enrichment, such as I-16 in female mating and I-2, I-11, I-14, I-33, E-8, and E-15 in male mating (Fig. 8 and figs. S20 and S21). The weak activation of the parenting cluster I-14 after male sexual behavior is consistent with our previous finding that a small subset of Gal neurons are activated in both mating and parenting (*5*) and may suggest a mechanism underlying the mating-dependent switch to parental behavior in virgin male mice. Intriguingly, the Th-enriched cluster I-16 was activated by different behaviors in animals of different sexes, mating in females and aggression in males, similarly to the functional sexual dimorphism observed in a recent study of AvPe Th cells (*6*).

Discussion

Here, we combined the power of scRNA-seq and MERFISH to create a spatially resolved and functionally aware cell atlas of the preoptic region of the mouse hypothalamus. These methods identified major cell classes and neuronal subpopulations with correlated gene expression profiles, providing cross-validations for both methods. Moreover, the two methods are complementary: scRNA-seq measured more genes than MERFISH and helped define marker genes for MERFISH, whereas MERFISH provided spatial context of cells at high resolution as well as more accurate detection and quantification of weakly expressed genes, including functionally important genes such as neuropeptide and hormone receptors. As a result, the combined data provided a more complete picture of the transcriptional diversity and spatial organization of individual cells in the preoptic region.

We observed a remarkable diversity of neurons in this region, comprising ~70 different neuronal clusters. Transcription factors and cell-surface markers have been observed as markers of neuronal identity in the mouse spinal cord (*65*) and cortex (*66*) and the *Drosophila* olfactory system (*67*). In the mouse preoptic region, genes discriminating neuronal clusters were enriched for neuropeptides and molecules involved in neuromodulator synthesis and transport and for transcription factors. By contrast, neuromodulator receptors were weaker discriminators of these neuronal populations or were expressed at low levels, providing a useful note of caution in using these genes for targeted functional studies in the preoptic region. Many of these neuronal populations were defined by a combination of multiple genes, indicating that genetic intersectional approaches will be most useful in the functional interrogation of specific cell types (*67*).

The list of cell populations identified in this work substantially expands and further defines previously reported cell types in this region. We observed specific clusters enriched in genes previously identified as markers of functionally important preoptic cells (for example, cells involved in parenting, aggression, thermoregulation, sleep, or thirst), such as Galanin, Th, Adcyap1, Nts, Crh, Tac1, Cck, Agtr1a, Nos1, and aromatase (tables S5 and S9). Our data also resolved many of the previously described singular cell types into multiple cell populations. We observed good correlation between our data and recent scRNA-seq analyses of the whole mouse hypothalamus (*68*) and of the whole mouse brain (*69*). In the latter study, which we compared with ours in more detail because it had a larger whole hypothalamic dataset, 15 neuronal clusters were identified from ~2000 profiled hypothalamic neurons (fig. S22) (*69*). However, because we used ~10 times more neuronal scRNA-seq profiles to characterize about one-fifth of the whole hypothalamus (the preoptic region), we were able to analyze the preoptic region with a greater depth and thus gain finer delineation of cell populations (fig. S22B). The neuronal populations that we uncovered in the preoptic region also largely differed from cell clusters described in scRNA-seq studies of other hypothalamic areas (*33*, *70*), perhaps suggesting a molecular and cellular distinctiveness of this brain area.

MERFISH further allowed us to map the spatial organization of cell populations. Structural features of the hypothalamus are not as visibly apparent as in laminated parts of the brain, and hypothalamic nuclei have largely been defined by subtle differences in neuronal density together with specific connectivity and functional roles (*1*). However, the differences versus similarities

in the cell-type composition and function of distinct nuclei in the hypothalamus remains unclear (*71*). MERFISH allowed us to examine the organization of distinct cell populations within individual hypothalamic nuclei, providing a framework with which to explore the molecular basis of their anatomical segregation. The spatial organizations of neuronal clusters were diverse: Many of the neuronal clusters were each primarily enriched in one or a few nuclei, whereas several clusters were substantially more dispersed. Moreover, individual nuclei were composed of multiple neuronal clusters. We also observed specific topographical organizations that can support defined modes of function; for example, the spatial proximity of aromatase- and Esr1-expressing cells may support paracrine estrogen signaling. Although aromatase- and Esr1-enriched cell populations regulate sex hormone production and signaling, rarely any of them appeared to be exclusively expressed in either sex, which is consistent with behavioral evidence that males and females are capable of exhibiting behaviors typical of the opposite sex (*5*, *72*).

Last, the ability of MERFISH to interrogate intact tissue allowed us to include activity-dependent IEGs in our measurements, allowing the identification of neuronal populations activated by specific behaviors. Using this approach to study several social behaviors—including parenting, aggression, and mating—we observed that only a small number of neuronal clusters displayed statistically significant enrichment in cFos-positive cells after each behavior. This observation supports a model in which genetically encoded circuits composed of transcriptionally distinct neuronal types control specific hypothalamic functions. However, in all three behaviors, we also observed widespread activation of many neuronal clusters at a substantially weaker level, suggesting a secondary role for many different neuronal types in these behaviors and possibly reflecting necessary cross-talk between different behavior circuits. We caution that the large range of cFos expression levels seen in our samples suggests that some activated clusters with low levels of activity-dependent cFos induction may not have been identified if their cFos levels were below the background noise in our measurements.

This study also extended our previous work on circuits that underlie parenting behavior (*5*, *60*) by resolving preoptic Gal neurons into several distinct subpopulations, with only one of them involved in both male and female parenting. In addition, we identified distinct cell populations that were differentially activated in mothers and fathers during parenting, providing insights into how physiological state may affect parental behavior. Moreover, we identified cell populations associated with sexual behavior in males and females as well as those involved in male aggression toward infants and conspecific males. Together, our data defined functionally relevant cell populations that underlie social behavior with a high molecular and spatial resolution.

Overall, our study demonstrates the power of combining scRNA-seq and MERFISH to map cell types and their organization in the brain, reveal their functional roles in diverse behaviors, and generate hypotheses about structure-function relationships in neural circuits. The identification of marker gene combinations and spatial locations defining the neuronal populations in the preoptic region provides necessary tools for the precise targeting and perturbation of these neurons, thus enabling future functional studies. As an imaging-based approach, we envision that MERFISH can be combined with diverse imaging methods for anatomical tracing and functional interrogation to provide insights into how distinct cell types communicate to form functional circuits in the healthy and diseased brain, as well as in other tissues.

Methods summary

scRNA-seq of the preoptic region was performed by using protocols modified from (*70*) to increase neuronal survival. Tissue fixation and sectioning as well as MERFISH probe construction, staining, and imaging were performed by using established protocols (*26*). We imaged 155 genes in MERFISH measurements, with 135 genes imaged by using combinatorial smFISH measurements and 20 additional genes imaged by using sequential rounds of noncombinatorial FISH. The sequences of all probes used for MERFISH are provided in tables S10 and S11. Individual cells were segmented with a seeded watershed algorithm by using DAPI and total mRNA costains (*29*). Cell clusters were identified by using Louvain community detection on a nearest-neighbor graph built on the statistically significant principle components of gene expression (*28*, *31*, *73*) modified to allow an optimized choice of the number of nearest neighbors in the graph. Behavioral stimuli were applied to animals by using established protocols (*5*, *72*, *74*), and only animals scored as displaying the desired behavior were used for MERFISH measurements.

REFERENCES AND NOTES

1. L. W. Swanson, Cerebral hemisphere regulation of motivated behavior. *Brain Res.* **886**, 113–164 (2000). doi: 10.1016/S0006-8993(00)02905-X; pmid: 11119693
2. R. B. Simerly, in *The Rat Nervous System*, G. Paxinos, Ed. (Elsevier, ed. 3, 2004), pp. 335–368.
3. S. M. Sternson, Hypothalamic survival circuits: Blueprints for purposive behaviors. *Neuron* **77**, 810–824 (2013). doi: 10.1016/j.neuron.2013.02.018; pmid: 23473313
4. J. Lu *et al*., Selective activation of the extended ventrolateral preoptic nucleus during rapid eye movement sleep. *J. Neurosci.* **22**, 4568–4576 (2002). doi: 10.1523/JNEUROSCI.22-11-04568.2002; pmid: 12040064
5. Z. Wu, A. E. Autry, J. F. Bergan, M. Watabe-Uchida, C. G. Dulac, Galanin neurons in the medial preoptic area govern parental behaviour. *Nature* **509**, 325–330 (2014). doi: 10.1038/nature13307; pmid: 24828191
6. N. Scott, M. Prigge, O. Yizhar, T. Kimchi, A sexually dimorphic hypothalamic circuit controls maternal care and oxytocin secretion. *Nature* **525**, 519–522 (2015). doi: 10.1038/nature15378; pmid: 26375004
7. K. Sokolowski *et al*., Specification of select hypothalamic circuits and innate behaviors by the embryonic patterning gene dbx1. *Neuron* **86**, 403–416 (2015). doi: 10.1016/j.neuron.2015.03.022; pmid: 25864637
8. C. L. Tan *et al*., Warm-sensitive neurons that control body temperature. *Cell* **167**, 47–59.e15 (2016). doi: 10.1016/j.cell.2016.08.028; pmid: 27616062
9. D. E. Leib *et al*., The forebrain thirst circuit drives drinking through negative reinforcement. *Neuron* **96**, 1272–1281.e4 (2017). doi: 10.1016/j.neuron.2017.11.041; pmid: 29268095
10. W. E. Allen *et al*., Thirst-associated preoptic neurons encode an aversive motivational drive. *Science* **357**, 1149–1155 (2017). doi: 10.1126/science.aan6747; pmid: 28912243
11. S. Chung *et al*., Identification of preoptic sleep neurons using retrograde labelling and gene profiling. *Nature* **545**, 477–481 (2017). doi: 10.1038/nature22350; pmid: 28514446
12. J. F. Poulin, B. Tasic, J. Hjerling-Leffler, J. M. Trimarchi, R. Awatramani, Disentangling neural cell diversity using single-cell transcriptomics. *Nat. Neurosci.* **19**, 1131–1141 (2016). doi: 10.1038/nn.4366; pmid: 27571192
13. A. Tanay, A. Regev, Scaling single-cell genomics from phenomenology to mechanism. *Nature* **541**, 331–338 (2017). doi: 10.1038/nature21350; pmid: 28102262
14. H. Zeng, J. R. Sanes, Neuronal cell-type classification: Challenges, opportunities and the path forward. *Nat. Rev. Neurosci.* **18**, 530–546 (2017). doi: 10.1038/nrn.2017.85; pmid: 28775344
15. E. Lein, L. E. Borm, S. Linnarsson, The promise of spatial transcriptomics for neuroscience in the era of molecular cell typing. *Science* **358**, 64–69 (2017). doi: 10.1126/science.aan6827; pmid: 28983044
16. N. Crosetto, M. Bienko, A. van Oudenaarden, Spatially resolved transcriptomics and beyond. *Nat. Rev. Genet.* **16**, 57–66 (2015). doi: 10.1038/nrg3832; pmid: 25446315
17. J. M. Levsky, S. M. Shenoy, R. C. Pezo, R. H. Singer, Single-cell gene expression profiling. *Science* **297**, 836–840 (2002). doi: 10.1126/science.1072241; pmid: 12161654
18. R. Ke *et al*., In situ sequencing for RNA analysis in preserved tissue and cells. *Nat. Methods* **10**, 857–860 (2013). doi: 10.1038/nmeth.2563; pmid: 23852452
19. J. H. Lee *et al*., Highly multiplexed subcellular RNA sequencing in situ. *Science* **343**, 1360–1363 (2014). doi: 10.1126/science.1250212; pmid: 24578530
20. K. H. Chen, A. N. Boettiger, J. R. Moffitt, S. Wang, X. Zhuang, Spatially resolved, highly multiplexed RNA profiling in single cells. *Science* **348**, aaa6090 (2015). doi: 10.1126/science.aaa6090; pmid: 25858977
21. S. Shah, E. Lubeck, W. Zhou, L. Cai, In situ transcription profiling of single cells reveals spatial organization of cells in the mouse hippocampus. *Neuron* **92**, 342–357 (2016). doi: 10.1016/j.neuron.2016.10.001; pmid: 27764670
22. X. Wang *et al*., Three-dimensional intact-tissue sequencing of single-cell transcriptional states. *Science* **361**, eaat5691 (2018). doi: 10.1126/science.aat5691; pmid: 29930089
23. M. E. Greenberg, E. B. Ziff, L. A. Greene, Stimulation of neuronal acetylcholine receptors induces rapid gene transcription. *Science* **234**, 80–83 (1986). doi: 10.1126/science.3749894; pmid: 3749894
24. A. M. Femino, F. S. Fay, K. Fogarty, R. H. Singer, Visualization of single RNA transcripts in situ. *Science* **280**, 585–590 (1998). doi: 10.1126/science.280.5363.585; pmid: 9554849
25. A. Raj, P. van den Bogaard, S. A. Rifkin, A. van Oudenaarden, S. Tyagi, Imaging individual mRNA molecules using multiple singly labeled probes. *Nat. Methods* **5**, 877–879 (2008). doi: 10.1038/nmeth.1253; pmid: 18806792
26. J. R. Moffitt *et al*., High-performance multiplexed fluorescence in situ hybridization in culture and tissue with matrix imprinting and clearing. *Proc. Natl. Acad. Sci. U.S.A.* **113**, 14456–14461 (2016). doi: 10.1073/pnas.1617699113; pmid: 27911841
27. A. M. Klein *et al*., Droplet barcoding for single-cell transcriptomics applied to embryonic stem cells. *Cell* **161**, 1187–1201 (2015). doi: 10.1016/j.cell.2015.04.044; pmid: 26000487
28. E. Z. Macosko *et al*., Highly parallel genome-wide expression profiling of individual cells using nanoliter droplets. *Cell* **161**, 1202–1214 (2015). doi: 10.1016/j.cell.2015.05.002; pmid: 26000488
29. Materials and methods are available as supplementary materials.
30. J. H. Levine *et al*., Data-driven phenotypic dissection of AML reveals progenitor-like cells that correlate with prognosis. *Cell* **162**, 184–197 (2015). doi: 10.1016/j.cell.2015.05.047; pmid: 26095251
31. K. Shekhar *et al*., Comprehensive classification of retinal bipolar neurons by single-cell transcriptomics. *Cell* **166**, 1308–1323.e30 (2016). doi: 10.1016/j.cell.2016.07.054; pmid: 27565351
32. S. M. Wojcik *et al*., A shared vesicular carrier allows synaptic corelease of GABA and glycine. *Neuron* **50**, 575–587 (2006). doi: 10.1016/j.neuron.2006.04.016; pmid: 16701208
33. R. A. Romanov *et al*., Molecular interrogation of hypothalamic organization reveals distinct dopamine neuronal subtypes.

Nat. Neurosci. **20**, 176–188 (2017). doi: 10.1038/nn.4462; pmid: 27991900
34. S. J. Shabel, C. D. Proulx, J. Piriz, R. Malinow, GABA/glutamate co-release controls habenula output and is modified by antidepressant treatment. *Science* **345**, 1494–1498 (2014). doi: 10.1126/science.1250469; pmid: 25237099
35. E. S. Lein *et al*., Genome-wide atlas of gene expression in the adult mouse brain. *Nature* **445**, 168–176 (2007). doi: 10.1038/nature05453; pmid: 17151600
36. B. Tasic *et al*., Adult mouse cortical cell taxonomy revealed by single cell transcriptomics. *Nat. Neurosci.* **19**, 335–346 (2016). doi: 10.1038/nn.4216; pmid: 26727548
37. T. Shimogori *et al*., A genomic atlas of mouse hypothalamic development. *Nat. Neurosci.* **13**, 767–775 (2010). doi: 10.1038/nn.2545; pmid: 20436479
38. Z. A. Knight *et al*., Molecular profiling of activated neurons by phosphorylated ribosome capture. *Cell* **151**, 1126–1137 (2012). doi: 10.1016/j.cell.2012.10.039; pmid: 23178128
39. R. B. Simerly, Wired for reproduction: Organization and development of sexually dimorphic circuits in the mammalian forebrain. *Annu. Rev. Neurosci.* **25**, 507–536 (2002). doi: 10.1146/annurev.neuro.25.112701.142745; pmid: 12052919
40. J. R. Moffitt *et al*., High-throughput single-cell gene-expression profiling with multiplexed error-robust fluorescence in situ hybridization. *Proc. Natl. Acad. Sci. U.S.A.* **113**, 11046–11051 (2016). doi: 10.1073/pnas.1612826113; pmid: 27625426
41. M. V. Wu *et al*., Estrogen masculinizes neural pathways and sex-specific behaviors. *Cell* **139**, 61–72 (2009). doi: 10.1016/j.cell.2009.07.036; pmid: 19804754
42. X. Xu *et al*., Modular genetic control of sexually dimorphic behaviors. *Cell* **148**, 596–607 (2012). doi: 10.1016/j.cell.2011.12.018; pmid: 22304924
43. C. Gregg *et al*., High-resolution analysis of parent-of-origin allelic expression in the mouse brain. *Science* **329**, 643–648 (2010). doi: 10.1126/science.1190830; pmid: 20616232
44. T. Kudo *et al*., Three types of neurochemical projection from the bed nucleus of the stria terminalis to the ventral tegmental area in adult mice. *J. Neurosci.* **32**, 18035–18046 (2012). doi: 10.1523/JNEUROSCI.4057-12.2012; pmid: 23238719
45. G. Paxinos, K. Franklin, *The Mouse Brain in Stereotaxic Coordinates* (Academic Press, ed. 3, 2007).
46. Y. Tsuneoka *et al*., Moxd1 is a marker for sexual dimorphism in the medial preoptic area, bed nucleus of the stria terminalis and medial amygdala. *Front. Neuroanat.* **11**, 26 (2017). doi: 10.3389/fnana.2017.00026; pmid: 28396628
47. B. J. Marlin, R. C. Froemke, Oxytocin modulation of neural circuits for social behavior. *Dev. Neurobiol.* **77**, 169–189 (2017). doi: 10.1002/dneu.22452; pmid: 27626613
48. M. Zelikowsky *et al*., The neuropeptide Tac2 controls a distributed brain state induced by chronic social isolation stress. *Cell* **173**, 1265–1279.e19 (2018). doi: 10.1016/j.cell.2018.03.037; pmid: 29775595
49. R. Andero, B. G. Dias, K. J. Ressler, A role for Tac2, NkB, and Nk3 receptor in normal and dysregulated fear memory consolidation. *Neuron* **83**, 444–454 (2014). doi: 10.1016/j.neuron.2014.05.028; pmid: 24976214
50. Y. Tsuneoka *et al*., Functional, anatomical, and neurochemical differentiation of medial preoptic area subregions in relation to maternal behavior in the mouse. *J. Comp. Neurol.* **521**, 1633–1663 (2013). doi: 10.1002/cne.23251; pmid: 23124836
51. T. Gallopin *et al*., Identification of sleep-promoting neurons in vitro. *Nature* **404**, 992–995 (2000). doi: 10.1038/35010109; pmid: 10801127
52. J. Lu, M. A. Greco, P. Shiromani, C. B. Saper, Effect of lesions of the ventrolateral preoptic nucleus on NREM and REM sleep. *J. Neurosci.* **20**, 3830–3842 (2000). doi: 10.1523/JNEUROSCI.20-10-03830.2000; pmid: 10804223
53. Z. D. Zhao *et al*., A hypothalamic circuit that controls body temperature. *Proc. Natl. Acad. Sci. U.S.A.* **114**, 2042–2047 (2017). doi: 10.1073/pnas.1616255114; pmid: 28053227
54. C. L. Sisk, D. L. Foster, The neural basis of puberty and adolescence. *Nat. Neurosci.* **7**, 1040–1047 (2004). doi: 10.1038/nn1326; pmid: 15452575
55. H. Yoon, L. W. Enquist, C. Dulac, Olfactory inputs to hypothalamic neurons controlling reproduction and fertility. *Cell* **123**, 669–682 (2005). doi: 10.1016/j.cell.2005.08.039; pmid: 16290037
56. U. Boehm, Z. Zou, L. B. Buck, Feedback loops link odor and pheromone signaling with reproduction. *Cell* **123**, 683–695 (2005). doi: 10.1016/j.cell.2005.09.027; pmid: 16290036
57. J. T. George, S. B. Seminara, Kisspeptin and the hypothalamic control of reproduction: Lessons from the human. *Endocrinology* **153**, 5130–5136 (2012). doi: 10.1210/en.2012-1429; pmid: 23015291
58. S. L. Padilla, C. W. Johnson, F. D. Barker, M. A. Patterson, R. D. Palmiter, A neural circuit underlying the generation of hot flushes. *Cell Reports* **24**, 271–277 (2018). doi: 10.1016/j.celrep.2018.06.037; pmid: 29996088
59. F. S. vom Saal, Time-contingent change in infanticide and parental behavior induced by ejaculation in male mice. *Physiol. Behav.* **34**, 7–15 (1985). doi: 10.1016/0031-9384(85)90069-1; pmid: 4041052
60. J. Kohl *et al*., Functional circuit architecture underlying parental behaviour. *Nature* **556**, 326–331 (2018). doi: 10.1038/s41586-018-0027-0; pmid: 29643503
61. C. Dulac, L. A. O'Connell, Z. Wu, Neural control of maternal and paternal behaviors. *Science* **345**, 765–770 (2014). doi: 10.1126/science.1253291; pmid: 25124430
62. G. C. Teskey, M. Kavaliers, Effects of opiate agonists and antagonists on aggressive encounters and subsequent opioid-induced analgesia, activity and feeding responses in male mice. *Pharmacol. Biochem. Behav.* **31**, 43–52 (1988). doi: 10.1016/0091-3057(88)90309-7; pmid: 3252259
63. Y.-Y. Fang, T. Yamaguchi, S. C. Song, N. X. Tritsch, D. Lin, A hypothalamic midbrain pathway essential for driving maternal behaviors. *Neuron* **98**, 192–207.e10 (2018). doi: 10.1016/j.neuron.2018.02.019; pmid: 29621487
64. Y.-C. Wei *et al*., Medial preoptic area in mice is capable of mediating sexually dimorphic behaviors regardless of gender. *Nat. Commun.* **9**, 279 (2018). doi: 10.1038/s41467-017-02648-0; pmid: 29348568
65. S. Arber, Motor circuits in action: Specification, connectivity, and function. *Neuron* **74**, 975–989 (2012). doi: 10.1016/j.neuron.2012.05.011; pmid: 22726829
66. A. Paul *et al*., Transcriptional architecture of synaptic communication delineates GABAergic neuron identity. *Cell* **171**, 522–539.e20 (2017). doi: 10.1016/j.cell.2017.08.032 pmid: 28942923
67. H. Li *et al*., Classifying *Drosophila* olfactory projection neuron subtypes by single-cell RNA sequencing. *Cell* **171**, 1206–1220.e22 (2017). doi: 10.1016/j.cell.2017.10.019; pmid: 29149607
68. R. Chen, X. Wu, L. Jiang, Y. Zhang, Single-cell RNA-seq reveals hypothalamic cell diversity. *Cell Reports* **18**, 3227–3241 (2017). doi: 10.1016/j.celrep.2017.03.004; pmid: 28355573
69. A. Zeisel *et al*., Molecular architecture of the mouse nervous system. *Cell* **174**, 999–1014.e22 (2018). doi: 10.1016/j.cell.2018.06.021; pmid: 30096314
70. J. N. Campbell *et al*., A molecular census of arcuate hypothalamus and median eminence cell types. *Nat. Neurosci.* **20**, 484–496 (2017). doi: 10.1038/nn.4495; pmid: 28166221
71. S. Blackshaw *et al*., Molecular pathways controlling development of thalamus and hypothalamus: From neural specification to circuit formation. *J. Neurosci.* **30**, 14925–14930 (2010). doi: 10.1523/JNEUROSCI.4499-10.2010; pmid: 21068293
72. T. Kimchi, J. Xu, C. Dulac, A functional circuit underlying male sexual behaviour in the female mouse brain. *Nature* **448**, 1009–1014 (2007). doi: 10.1038/nature06089; pmid: 17676034
73. S. Pandey, K. Shekhar, A. Regev, A. F. Schier, Comprehensive identification and spatial mapping of habenular neuronal types using single-cell RNA-seq. *Curr. Biol.* **28**, 1052–1065.e7 (2018). doi: 10.1016/j.cub.2018.02.040; pmid: 29576475
74. L. Stowers, T. E. Holy, M. Meister, C. Dulac, G. Koentges, Loss of sex discrimination and male-male aggression in mice deficient for TRP2. *Science* **295**, 1493–1500 (2002). doi: 10.1126/science.1069259; pmid: 11823606
75. G. Finak *et al*., MAST: A flexible statistical framework for assessing transcriptional changes and characterizing heterogeneity in single-cell RNA sequencing data. *Genome Biol.* **16**, 278 (2015). doi: 10.1186/s13059-015-0844-5; pmid: 26653891
76. J. R. Moffitt *et al*., Data from: Molecular, spatial and functional single-cell profiling of the hypothalamic preoptic region. Dryad (2018); doi: 10.5061/dryad.8t8s248

ACKNOWLEDGMENTS

We thank Y. Sigal and H. Babcock for advice on sample preparation and assistance with instrumentation and J. Fan for assistance in the gene set enrichment analysis. **Funding:** This work is in part supported by the National Institutes of Health (R01MH113094 to X.Z and C.D.; R01MH111502 to C.D., X.Z., and A.R.; and R01HD082131 to C.D.). D.B.-M. and K.S. are supported in part by the National Institutes of Health Pathway to Independence Award (K99HD092542 to D.B-M. and K99EY028625 to K.S.). A.R. was supported by the Klarman Cell Observatory. A.R., C.D., and X.Z. are Howard Hughes Medical Institute Investigators. **Author contributions:** J.R.M., D.B-M., C.D., and X.Z. conceived the study; J.R.M., D.B-M., and S.W.E. performed experiments with help from J.H. and J.D.P.; J.R.M., D.B.-M., S.W.E., and E.V. analyzed data, with help from K.S. and N.D.R.; K.S. and A.R. provided some of the analysis tools; J.R.M., D.B-M., S.W.E., E.V., C.D., and X.Z. wrote the manuscript, with input from A.R., K.S., J.D.P., N.D.R., and J.H. **Competing interests:** J.R.M. and X.Z. are inventors on patents applied for by Harvard University related to MERFISH. A.R. is a founder of Celsius Therapeutics and a SAB member of Thermo Fisher Scientific, Driver Group, and Syros Pharmaceuticals. **Data and materials availability:** scRNA-seq data are available at Gene Expression Omnibus (GEO) (GSE113576). MERFISH data are available at Dryad (*76*), and the analysis software is available at https://github.com/ZhuangLab/MERFISH_analysis.

SUPPLEMENTARY MATERIALS

www.sciencemag.org/content/362/6416/eaau5324/suppl/DC1
Materials and Methods
Figs. S1 to S22
Tables S1 to S11
References (*77*–*98*)

20 June 2018; accepted 21 September 2018
Published online 1 November 2018
10.1126/science.aau5324

RESEARCH ARTICLE SUMMARY

NEURODEVELOPMENT

In vivo modeling of human neuron dynamics and Down syndrome

Raquel Real*, Manuel Peter*, Antonio Trabalza*, Shabana Khan, Mark A. Smith, Joana Dopp, Samuel J. Barnes, Ayiba Momoh, Alessio Strano, Emanuela Volpi, Graham Knott, Frederick J. Livesey†, Vincenzo De Paola†

INTRODUCTION: Scientists are building detailed maps of the cellular composition in the human brain to learn about its development. In the human cortex, the largest area of the mammalian brain, neural circuits are formed through anatomical refinement, including axon and synaptic pruning, and the emergence of complex patterns of network activity during early fetal development. Cellular analyses in the human brain are restricted to postmortem material, which cannot reveal the process of development. Model organisms are, therefore, commonly used for studies of brain physiology, development, and pathogenesis, but the results from model organisms do not always translate to humans.

RATIONALE: Systems to model human neuron dynamics and their dysfunction in vivo are needed. While biopsy specimens and the generation of neurons from induced pluripotent stem cells (iPSCs) could provide the necessary human genetic background, two- and three-dimensional cultures lack factors that normally support neuronal development, including blood vessels, immune cells, and interaction with innervating neurons from other brain areas. On the basis of previous stem cell transplantation studies in mice, we reasoned that the physiological microenvironment of the adult mouse brain could support the growth of human cortical tissue grafts that had been generated from iPSC-derived neuronal progenitors. With human neurons implanted into the mouse brain, high-resolution, real-time in vivo monitoring of human neuron dynamics for periods of time spanning the range from subseconds to several months becomes feasible.

ON OUR WEBSITE

Read the full article at http://dx.doi.org/10.1126/science.aau1810

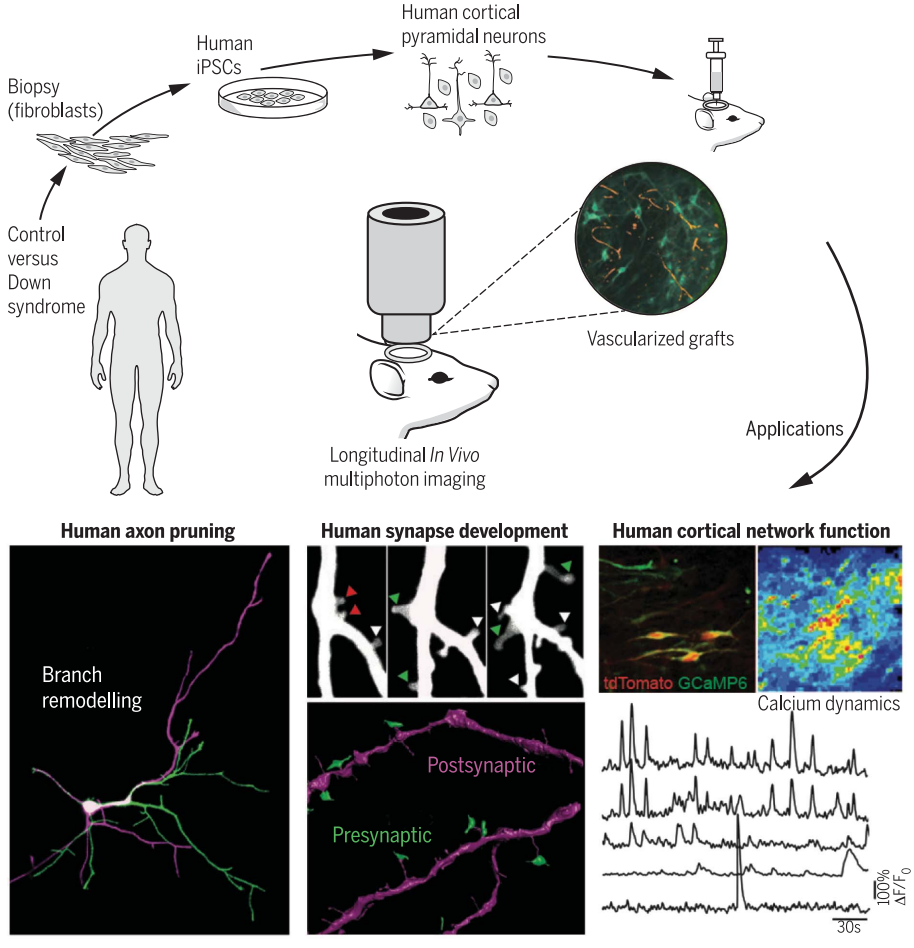

Human neuron dynamics imaged in vivo. We combined a human-specific genetic background with live imaging in cortical tissue grafts to investigate the earliest stages of human axon, synaptic, and network activity development and model Down syndrome.

RESULTS: We found that transplanted human iPSC–derived neuronal progenitors consistently assembled into vascularized territories with complex cytoarchitecture, mimicking key features of the human fetal cortex, such as its large size and cell diversification. Single-cell-resolution intravital microscopy showed that human neuronal arbors were refined via branch-specific retraction, rather than degeneration. Human synaptic networks restructured over the course of 4 months, while maintaining balanced rates of synapse formation and elimination. Human functional neurons rapidly and consistently acquired oscillatory population activity, which persisted over the 5-month observation period. Lastly, we used cortical tissue grafts derived from the fibroblasts of two individuals with Down syndrome, caused by supernumerary chromosome 21. We found that neuronal synapses in cells derived from these individuals were overly stable and that oscillatory neural activity was reduced in these grafts, revealing in vivo cellular phenotypes not otherwise apparent.

CONCLUSION: By combining live imaging in a multistructured tissue environment in mice with a human-specific genetic background, we provide insights into the earliest stages of human axon, synaptic, and network activity development and uncover cellular phenotypes in Down syndrome. Our work provides an alternative experimental system that can be used to study other disorders affecting the developing human cortex. ■

The list of author affiliations is available in the full article online.
*These authors contributed equally to this work.
†Corresponding author. Email: vincenzo.depaola@imperial.ac.uk (V.D.P.); r.livesey@ucl.ac.uk (F.J.L.)
Cite this article as R. Real *et al.*, *Science* **362**, eaau1810 (2018). DOI: 10.1126/science.aau1810

RESEARCH ARTICLE

NEURODEVELOPMENT

In vivo modeling of human neuron dynamics and Down syndrome

Raquel Real[1,2,3]*, Manuel Peter[4]*, Antonio Trabalza[1,3]*, Shabana Khan[1,3], Mark A. Smith[1,3], Joana Dopp[1], Samuel J. Barnes[5], Ayiba Momoh[4], Alessio Strano[4], Emanuela Volpi[6], Graham Knott[7], Frederick J. Livesey[4,8]†, Vincenzo De Paola[1,3]†

Harnessing the potential of human stem cells for modeling the physiology and diseases of cortical circuitry requires monitoring cellular dynamics in vivo. We show that human induced pluripotent stem cell (iPSC)–derived cortical neurons transplanted into the adult mouse cortex consistently organized into large (up to ~100 mm^3) vascularized neuron-glia territories with complex cytoarchitecture. Longitudinal imaging of >4000 grafted developing human neurons revealed that neuronal arbors refined via branch-specific retraction; human synaptic networks substantially restructured over 4 months, with balanced rates of synapse formation and elimination; and oscillatory population activity mirrored the patterns of fetal neural networks. Lastly, we found increased synaptic stability and reduced oscillations in transplants from two individuals with Down syndrome, demonstrating the potential of in vivo imaging in human tissue grafts for patient-specific modeling of cortical development, physiology, and pathogenesis.

Cellular analyses in the human brain are restricted mainly to postmortem material, which cannot provide direct observation of dynamic events, such as anatomical refinement (*1*) and the emergence of complex patterns of network activity. This limitation raises the question of how to model human neuron dynamics and their dysfunction in the many incurable disorders that affect the developing cortex (*2*).

Rodent models have been valuable for understanding the pathophysiology of complex genetic disorders, such as Down syndrome (DS) (*3*–*5*), which is associated with neurodevelopmental alterations and is caused by trisomy of chromosome 21 (Ts21), but certain phenotypes are better captured in the context of a human genetic background (*6*).

Human induced pluripotent stem cell (iPSC)–derived neurons can be used in patient-specific studies to model human cortical development (*7*), but in vitro two-dimensional (2D) and 3D cultures (*8*, *9*) lack key interactions with neuroglia and vasculature (*10*). Therefore, systems that more closely recapitulate the complex cellular dynamics of the living brain by using patient-specific cells are urgently needed.

Building on previous transplantation work (*11*), we hypothesized that the existing physiological microenvironment in the adult mouse brain could support the expansion of human cortical tissue grafts from iPSC-derived neurons, thus allowing high-resolution, real-time in vivo monitoring of human neuron dynamics for extended periods of time.

In this study, we used single-cell-resolution intravital microscopy (*12*) in human tissue grafts to gain insights into the dynamics of pruning, synaptogenesis, and network activity during the earliest stages of cortical neuron development and demonstrated this approach by modeling human neuron structural and functional dynamics in DS. This research was approved by the U.K. Stem Cell Bank Steering Committee and the U.K. Home Office, in accordance with the U.K. Code of Practice for the Use of Human Stem Cell Lines and the U.K. Animals (Scientific Procedures) Act 1986, respectively.

Complex cytoarchitecture in human cortical tissue grafts

To study the dynamics of human axon and synaptic development and population activity in vivo, we generated cortical excitatory neurons from a control human iPSC line (*13*) (fig. S1) and transplanted them into the adult mouse somatosensory cortex (SCx1) for chronic multiphoton imaging (Fig. 1A). Cells were transplanted after 36 to 38 days of differentiation, a stage at which cultures contained ~50% neural progenitor cells and ~50% deep-layer cortical neurons [of which ~15% expressed T-box, brain 1 (TBR1+), and ~85% expressed COUP transcription factor–interacting protein 2 (CTIP2+)] (fig. S2, A and B). As expected, and consistent with ongoing neurogenesis after engraftment, upper-layer cortical excitatory neurons and a small proportion of astrocytes and oligodendrocytes could also be found at both 3 and 5 months posttransplantation (mpt) (fig. S2, C and D). Electron microscopy (EM) confirmed that human grafts resembled immature cortical tissue at 130 days posttransplantation (dpt) (fig. S3, A to C), with few synapses and few myelinated axons, and showed no detectable boundary with the mouse brain (fig. S3C), suggestive of structural integration (*14*). The grafts contained proliferating cells (fig. S3, C and D), enlarged with time (movie S1), and consisted of multiple human- and host-derived cell types (figs. S2 and S3). The cell types from the host included microglial cells, oligodendrocytes, astrocytes, and both excitatory neurons and inhibitory interneurons (fig. S3, D to F), whereas no interneurons of human origin were found (n = 3 transplants). Microglia recruitment in the graft was minimal (fig. S4). Postmortem analysis revealed that the human tissue grafts developed organizational features resembling the structural arrangement of the early fetal cortex (fig. S5) (*15*, *16*).

At earlier stages (<2 mpt), cortical tissue grafts contained areas with ventricular zone–like territories, with cells positive for Paired box protein 6 (PAX6), a marker of neuronal progenitors, and Nestin, a marker for radial glia, which extended processes both radially outward from the core of the rosette-like structures (fig. S5A) and arranged in parallel (fig. S5B), mimicking the organization of radial fibers in the intermediate zone of the human fetal cortex (*15*). Ki67-expressing proliferating cells were found in the inner apical layer, with doublecortin (DXC)-positive immature neurons toward the basal part, extending out into the rest of the graft (*16*) (fig. S5A). After 2 mpt, the rosettes did not persist, and although discrete cortical laminae were not clearly visible, consistent with their formation in late embryonic development (~7 months postconception) (*17*), immunostaining for deep- and upper-layer cortical neurons with antibodies for TBR1 and Special AT-rich sequence–binding protein 2 (SATB2), respectively, showed that these cell populations can segregate in vivo (fig. S5C). Human astrocytes were homogenously distributed in the cortical tissue grafts (fig. S5D). Lastly, human tissue grafts were vascularized, as shown in vivo and by the endothelial marker cluster of differentiation 31 (CD31) (Fig. 1, B to D), suggesting that the adult mouse brain microenvironment can support the development of a multicellular transplant.

Human axon pruning imaged in vivo

To track human neurons in vivo, we engineered them to express green fluorescent protein (GFP) via lentivirus-mediated transduction before transplantation. Human neurons were present for the duration of our experimental time course,

[1]Institute of Clinical Sciences, Faculty of Medicine, Imperial College London, London W12 0NN, UK. [2]Graduate Program in Areas of Basic and Applied Biology, Instituto de Ciencias Biomedicas Abel Salazar, Universidade do Porto, 4050-313 Porto, Portugal. [3]Medical Research Council London Institute of Medical Sciences, London W12 0NN, UK. [4]Gurdon Institute and ARUK Stem Cell Research Centre, University of Cambridge, Tennis Court Rd., Cambridge CB2 1QN, UK. [5]UK Dementia Research Institute, Division of Brain Sciences, Faculty of Medicine, Imperial College London, London W12 0NN, UK. [6]University of Westminster, 115 New Cavendish St., London W1W 6UW, UK. [7]EPFL, Lausanne CH-1015, Switzerland. [8]UCL Great Ormond Street Institute of Child Health, 30 Guilford St., London WC1N 1EH, UK.
*These authors contributed equally to this work.
†Corresponding author. Email: vincenzo.depaola@imperial.ac.uk (V.D.P.); r.livesey@ucl.ac.uk (F.J.L.)

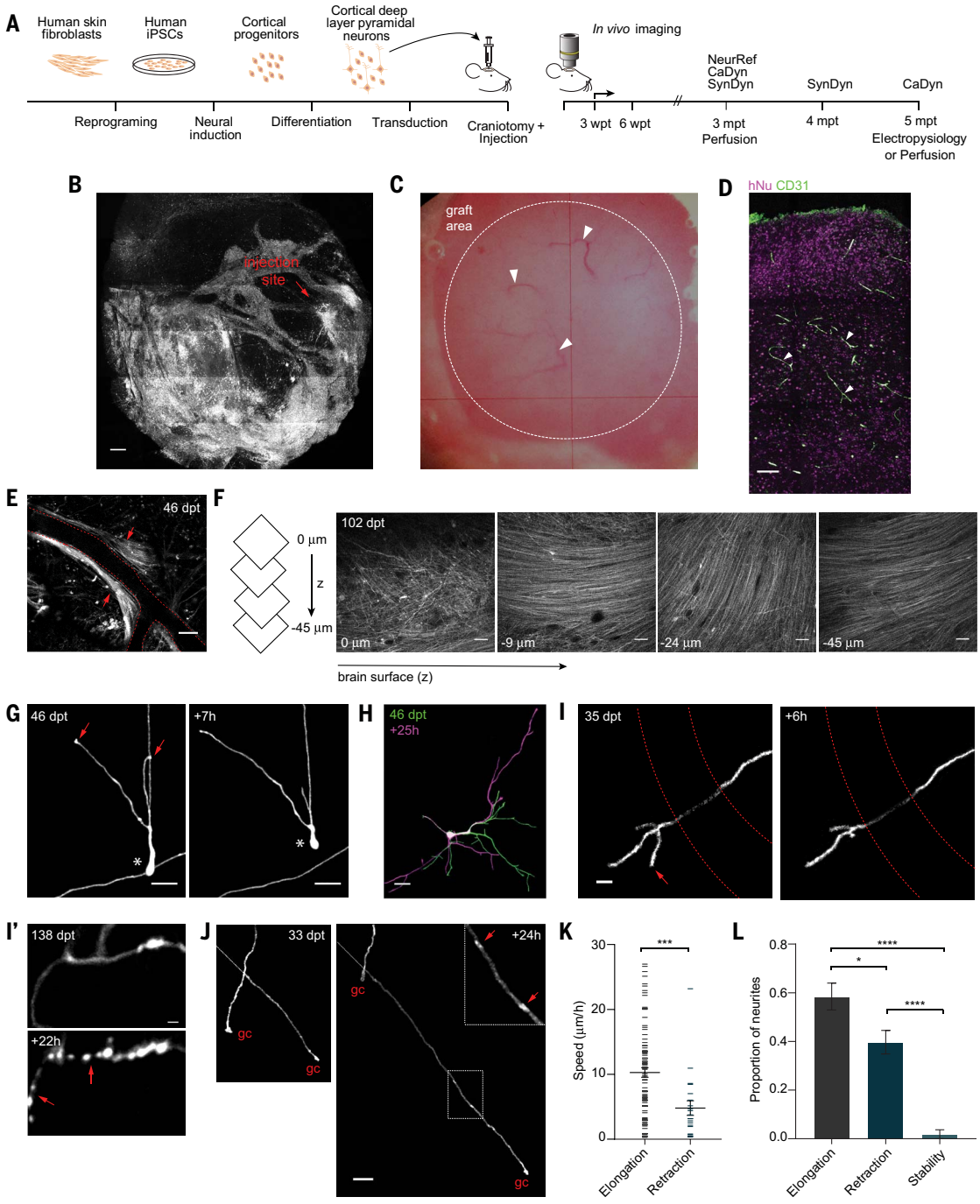

Fig. 1. Single-cell-resolution in vivo imaging of human cortical tissue grafts reveals mechanisms of pruning. (**A**) Schematic of experimental design (left) and two-photon in vivo imaging time line (right). NeurRef, neurite refinement; CaDyn, calcium dynamics; SynDyn, synaptic dynamics. (**B**) Representative two-photon overview of the cranial window over the injection site at 3 mpt. (**C**) Bright-field view of a cranial window (~15 mm^2) at 5 mpt. Arrowheads indicate blood vessels. (**D**) Representative immunostaining of endothelial marker CD31 in the human graft at 5 mpt. Arrowheads indicate blood vessels. hNu, human nucleus marker. (**E**) Representative example of axonal bundles (arrows) along blood vessels. Dashed red lines represent a blood vessel. (**F**) Representative example of axonal layering in human grafts. The example shown is the same as that in movie S3. (**G**) Example of a human neuron migrating (*) and remodeling the leading processes (arrows) over 7 hours. (**H**) Representative example of extensive remodeling of a dendritic arbor in a human pyramidal neuron over 25 hours. (**I**) Pruning of axonal branch over 6 hours. Dashed red lines represent a blood vessel. (**I'**) Neurite degeneration over 22 hours. Arrows indicate axonal fragments. (**J**) Representative examples of axon elongation and retraction over 24 hours. The boxed area in the right panel is magnified in the inset. The arrows in the inset indicate EPBs. gc, growth cone. (**K**) Speed of neurite elongation and retraction at 3 mpt (n = 113 neurites from 104 cells in six animals, average 17 cells per animal). Means and SEM are indicated. Mann-Whitney U test, ***$P < 0.001$. (**L**) Proportion of neurites elongating, retracting, and stable in 24-hour intervals at 3 mpt (n = 92 neurites from 88 cells in six animals, average 15 cells per animal). Error bars indicate SEM. Bonferroni's multiple comparisons test after one-way analysis of variance (ANOVA), $F_{2,15} = 43.74$, $P < 0.0001$; *$P < 0.05$; ****$P < 0.0001$. Scale bars, 500 µm (B), 100 µm (D), 50 µm [(E) and (F)], 20 µm [(G), (H), and (J)], 10 µm (I), and 2 µm (I').

which spanned up to 6 months, and spread away from the injection site (Fig. 1B) [on average, up to 1.2 ± 0.6 mm (mean ± SD) from the bregma in the rostral direction over the first 3 mpt (n = 4 mice)]. Consistent with the immature brain cell-cell interactions (*10*), human axons grew along blood vessels and as fiber bundles (Fig. 1E and movie S2), and parallel and radially oriented axonal layers could be detected below the dura mater (Fig. 1F and movie S3), similar to the ones found in the human cortex (*18*).

Given the widespread axonal extension outside the graft area, we asked which brain regions human neurons target 5 mpt. Main SCx1 target areas showed a higher number of human fibers than in areas known to receive fewer projections from SCx1 (fig. S6), suggesting that the direction of axon elongation is targeted. For example, the ipsilateral motor cortex, striatum, thalamus, and contralateral SCx1 received more fibers than the cerebellum and substantia nigra, and the corpus callosum had more axonal tracts than the internal capsule and cerebral peduncle (fig. S6), as expected from rodent tracing experiments (*19*). These data provide evidence for long-range (over centimeters) axon growth of grafted human neurons through the mouse adult brain and indicate that, although human axons are either not responsive to or can overcome the inhibitory signals present in the adult mouse brain, they may be directed by existing guidance cues or paths.

After an initial phase of growth (*20*), the selective pruning of axons and dendrites is thought to occur normally via retraction and degeneration during early development (*2*, *21*). We explored the mechanisms of human neurite pruning up to 3 mpt (Fig. 1, G to L, and fig. S7, A and B). At this stage, neurons were still migrating (Fig. 1G) and developing neural processes in a highly dynamic mode (Fig. 1, G to L). We tracked the fate of 92 human neurites from 88 cells in six mice at 3 mpt (Fig. 1, G to L). Whereas most neurites (58.4% ± 5.5%) elongated in 24 hours, neurite refinement was dynamic, and interchanging retraction and elongation of individual neurites (31.0% ± 2.1%) over 24 hours were observed (Fig. 1, I to L). Developmental neurite degeneration involves cytoskeletal destruction with widespread fragmentation over a time scale of 12 to 48 hours (*22*), whereas retracting axons do not leave fluorescent fragments behind (*23*). Reducing the imaging interval from 24 hours to 8 hours showed that branch pruning (Fig. 1I) occurred mainly by retraction (91%), rather than degeneration (Fig. 1I′) (9%). Axonal en passant boutons (EPBs), one of the two types of presynaptic specialization on cortical axons (*24*), could be observed in branches with a growth cone elongating (Fig. 1J). Neural processes extended long distances (maximum neurite extension = 462.769 μm in 24 hours) at a speed of 10.29 ± 0.73 μm/hour (Fig. 1K), comparable to that observed in the neonatal mouse brain (*23*). Results were validated with tissue grafts from an independent control line (fig. S7, A and B).

Human synaptic development imaged in vivo

Next, we studied the dynamics of synaptogenesis up to 4 mpt. Hallmarks of developing synaptic networks are an increase in synaptic density over time, followed by pruning, and the acquisition of a steady state with balanced rates of synaptic gain and loss (*25*). However, when and how human synaptic networks acquire these properties is unclear. We first considered dendritic spine formation and elimination (Fig. 2, A to F).

After the initial phase of cell migration and neurite remodeling (Fig. 1, G and H), neurons stabilized, allowing us to track the same cells over time (Fig. 2A and fig. S8). Dendritic spines, the structural correlates of mammalian excitatory synapses (*26*), were seen as early as 20 dpt (32.8 ± 5.5 dpt for either dendritic filopodia, considered to be the precursors of dendritic spines, or spines; n = 3 mice) (*27*, *28*). We monitored >500 dendritic segments from six mice over days. However, for most dendrites, the density of synapses was too low to quantitatively study the dynamics of dendritic spines before 3 mpt, as expected from previous human fetal cerebral cortex postmortem work (*29*) and the early developmental stage modeled in this study. Eight neurons had sufficient dendritic spine numbers at 3 mpt to calculate spine density and turnover during three to four consecutive sessions of 48-hour intervals (up to 6 days). The average spine density was similar to that in the human early fetal cerebral cortex (*29*) and constant over the imaging period (Fig. 2C) (0.043 ± 0.006 spines/μm; n = 70 spines present in the first session, 176 in total; Kruskal-Wallis test, P > 0.05). Synaptic structures were added and eliminated at equal rates, even at these early developmental stages (Fig. 2D) (Wilcoxon matched-pairs signed-rank test, P > 0.05). The turnover ratio (TOR), a function of both spine gain and loss (*30*), was 46.9% ± 5.3% over 4 days (Fig. 2E), indicating synaptic reorganization.

To investigate the development of synaptic remodeling over time, we repeated the same experiment after 1 month. Again, spine density was constant over time (Fig. 2C) (0.112 ± 0.024 spines/μm; n = 171 spines present in the first session, 291 in total; Kruskal-Wallis test, P > 0.05). However, the average spine density was increased at 4 mpt. The majority of dendrites had balanced rates of dendritic spine gain and loss (Fig. 2D) (paired two-tailed t test, P > 0.05), and only in one cell were we able to capture net synaptic pruning over 2 days (Fig. 2C, thick dashed line), consistent with the idea that a major phase of synaptic pruning occurs only at later developmental stages (*28*).

The TOR over 4 days was 27.6% ± 3.7%, which was lower than at 3 mpt (Fig. 2E). Consistently, the survival fraction, defined as the fraction of spines surviving as a function of time, was higher at 4 mpt (Fig. 2F), suggesting stabilization of dendritic spine dynamics over time.

To more thoroughly assess synaptic dynamics, we also studied presynaptic terminals along human cortical axons (Fig. 2, G to L). The density of boutons remained stable over time (Fig. 2I) (0.051 ± 0.0075 EPBs/μm; n = 69 EPBs in the first session, 145 in total), indicating that axonal boutons were also added and eliminated at equal rates (Fig. 2L). The TOR over 4 days was 45.1% ± 3.6% (Fig. 2, J and K), denoting comparable dynamics between dendritic spines and axonal boutons (at 3 mpt, Mann-Whitney U test, P = 0.34).

In summary, we were able to study early events of human cortical neuron synaptogenesis over the first 4 mpt. Despite the low synaptic density, consistent with the primordial stage modeled in this study (*29*), we can draw a number of conclusions about early in vivo human synaptic network development. First, transplanted human neurons initially formed synaptic structures within 4 to 12 weeks of in vivo development, similar to the human fetal cerebral cortex (*29*). Second, they underwent synaptic reorganization. Third, they progressively increased dendritic spine density over 1 month. Finally, human neurons balanced the rates of synaptic gain and loss over a time scale of a few days.

Functional human cortical networks imaged in vivo

Patterned neural activity is thought to be fundamental to neural circuit development in the immature brain (*31*, *32*). Although spontaneous and sparse activity can be detected in human cortical network preparations in vitro, recapitulating patterns typical of early human cortical population activity, such as recurrent oscillatory bursts (*32*), remains challenging (*33*, *34*).

We first investigated the electrophysiological properties of transplanted cells. We performed ex vivo whole-cell recordings in coronal brain slices containing the grafts (fig. S9). Current-clamp recordings were made from 18 pyramidal neurons (n = 4 mice), as identified by using differential interference contrast microscopy and expression of either GFP or tdTomato and by filling neurons with Lucifer yellow dye before post hoc anatomical inspection (fig. S9A). Patched grafted pyramidal neurons were at different stages of biophysical maturation and development, with an average resting membrane potential of −53.8 ± 1.7 mV, average capacitance of 19.4 ± 2.2 pF, and average input resistance of 1.4 ± 0.1 gigaohms. Although cells were quiescent at resting membrane potentials, depolarizing current steps evoked action potential firing in all pyramidal neurons tested (fig. S9B), with average action potential amplitudes of 91.3 ± 2.6 mV and half-widths of 2.2 ± 0.2 ms.

Immunohistochemistry showed glutamatergic and GABAergic terminals within the human graft (fig. S10, A and B). To confirm that human neurons received both excitatory and inhibitory input, pyramidal neurons were voltage clamped (−70 mV) and spontaneous miniature excitatory postsynaptic currents (mEPSCs) were observed at a frequency of 0.30 ± 0.05 Hz (5 of 18 neurons) with an amplitude of 20.1 ± 3.2 pA, which were completely blocked by the α-amino-3-hydroxy-5-methyl-4-isoxazolepropionic acid receptor

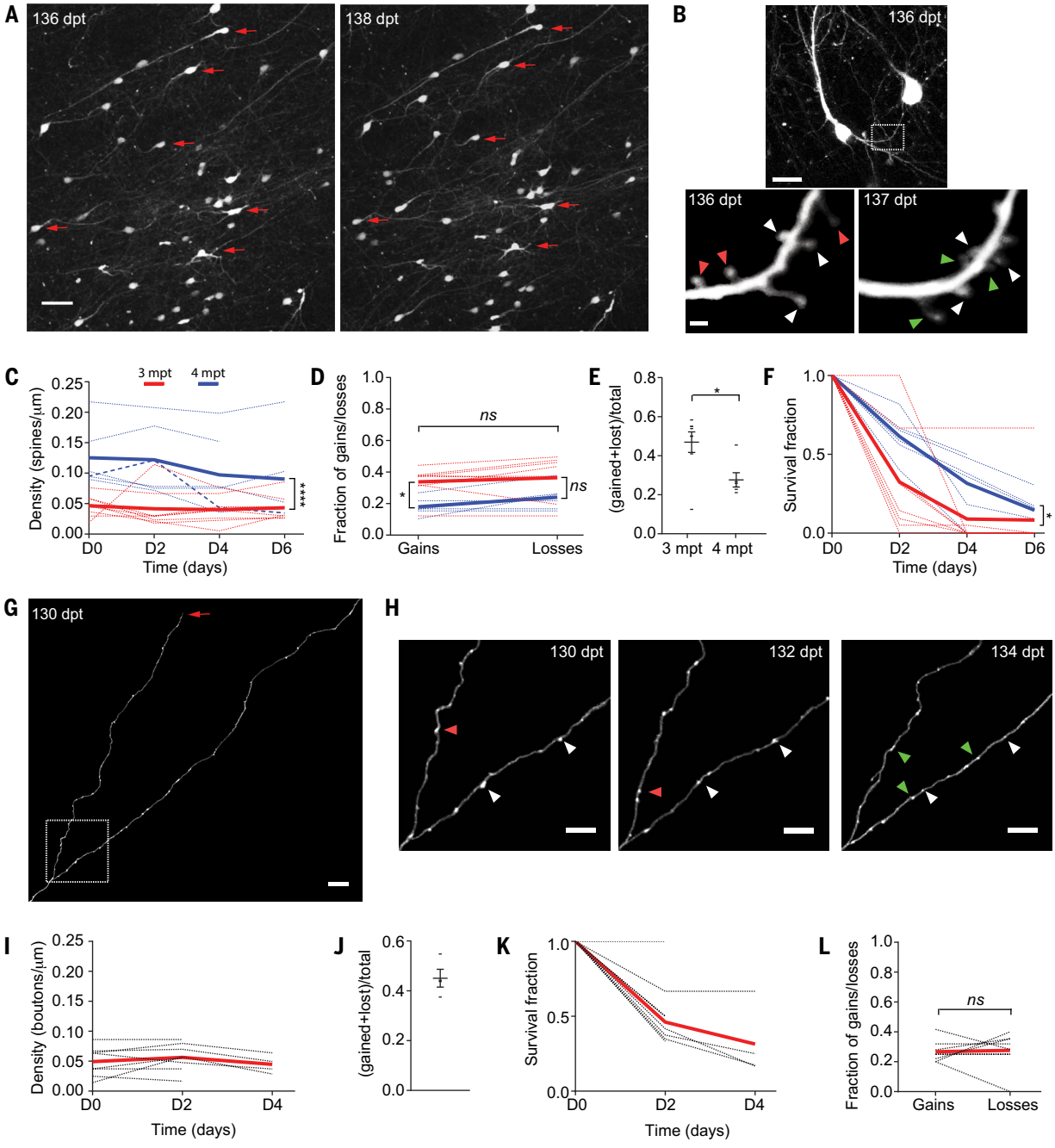

Fig. 2. Developing human synaptic networks are characterized by substantial restructuring and balanced rates of gains and losses. (**A**) Overview of cranial window at 136 and 138 dpt. Red arrows point to examples of cells with a stable location over a 48-hour period. (**B**) Detail of a representative dendrite imaged over 24 hours (white box in the top panel and red box in fig. S8A). Green, red, and white arrowheads indicate gained, lost, and stable dendritic spines, respectively. (**C**) Dendritic spine density over 4 to 6 days at 3 mpt (n = 8 cells, 1.40 mm of total dendritic length, from three animals) and 4 mpt (n = 6 cells, 0.93 mm of total dendritic length, from two animals). Two-way ANOVA, interaction $F_{3,46}$ = 0.4357, P = 0.73. ****P < 0.0001. (**D**) Average fractions of dendritic spines gained and lost over 48 hours at 3 mpt (red, n = 8 cells) and 4 mpt (blue, n = 6). Two-way ANOVA, interaction $F_{1,24}$ = 0.1894, P = 0.67. Sidak's multiple comparisons test, *P < 0.05 (gains); P = 0.063 (losses). ns, not significant. (**E**) Dendritic spine TOR over 4 days at 3 mpt (n = 8 cells) and 4 mpt (n = 6 cells). Mann-Whitney U test, *P < 0.05. Each data point represents a cell. (**F**) Dendritic spine survival fraction at 3 mpt (red, n = 7 cells) and 4 mpt (blue, n = 6 cells). Two-way ANOVA, interaction $F_{3,47}$ = 1.513, P = 0.22; *P < 0.05. (**G**) Representative example of a branched human axon at 130 dpt. The arrow indicates a growth cone. The boxed area is magnified in subsequent panels. (**H**) Detail of the axon shown in the boxed area in (G), imaged every 48 hours over 4 days. Green, red, and white arrowheads indicate gained, lost, and stable EPBs, respectively. (**I**) EPB density over 2 to 4 days at 3 mpt (n = 8 cells, 1.3 mm of total axonal length, from three animals). One-way ANOVA, $F_{2,17}$ = 0.4014; P = 0.68. (**J**) Quantification of EPB TOR over 4 days at 3 mpt (n = 4 cells). Each data point represents an axon. (**K**) Quantification of EPB survival fraction at 3 mpt (n = 8 cells). (**L**) Average fractions of EPB gains and losses over 48 hours at 3 mpt (n = 8 cells). Wilcoxon matched-pairs signed-rank t test; ns, not significant. [(C), (D), (F), (I), (K), and (L)] Dashed lines represent individual cells, and solid lines represent means. Scale bars, 50 µm (A), 20 µm [(B), top panel], 2 µm [(B), bottom panel], 10 µm (G), and 5 µm (H).

antagonist 2,3-dihydroxy-6-nitro-7-sulfamoyl-benzo-quinoxaline-2,3-dione (NBQX) (n = 4). Although synaptic events were observed in the remaining neurons, spontaneous frequency was insufficient to acquire enough events for statistical analysis (figs. S7, C and D, and S9C). By using a high-chloride (130 mM) internal solution and in the presence of NBQX, spontaneous miniature inhibitory postsynaptic currents were observed at a frequency of 0.24 ± 0.12 Hz (three of six neurons) with an amplitude of −73.3 ± 21.0 pA, which were fully inhibited by bicuculline (fig. S9C). Similar to mEPSCs, inhibitory synaptic events were observed in the remaining neurons, but insufficient events were acquired for detailed kinetic analysis. In summary, grafted neurons are excitable and fire action potentials. In addition, they receive both excitatory and inhibitory input, suggesting functional network connectivity.

To determine the origin of the afferent synaptic input to the functionally active neurons, we performed monosynaptic retrograde tracing by using a modified rabies virus. This virus lacks a glycoprotein needed for replication and can infect only cells expressing the avian tumor virus receptor A (TVA) (fig. S11). Human iPSC–derived cortical progenitors and neurons were transduced with a lentiviral vector containing the TVA, nuclear GFP, and glycoprotein under the control of the human synapsin promoter (fig. S11A). Five months after the transplantation, the modified mCherry expressing–rabies virus was injected in the same location, where only grafted cells expressing the TVA are susceptible to infection. Cells that are monosynaptically connected to the infected human cells also become infected and express mCherry, allowing for accurate tracing of the neural input to the cells in the human grafts (fig. S11B). We observed that whereas most of the input to the transplanted human neurons comes from other human neurons (92.5% ± 1.5%, n = 4333 cells in two brains), host neurons also innervate the human graft (7.5% ± 1.5%, n = 397 cells in two brains) (fig. S11C). The traced host neurons were located within the graft, in the cortical areas adjacent to the graft, in the contralateral cortex, and in the ipsilateral CA1 hippocampal region (fig. S11B). Although no traced neurons were found in other subcortical regions, thalamocortical terminals were present in the graft (fig. S10; see also fig. S12) (*20*). These results provide evidence that most synaptic input to the grafts comes from other human neurons. Furthermore, as no interneurons of human origin were found, these data, together with the demonstration that human neurons in the graft receive inhibitory input (fig. S9C, bottom), suggest that inhibition in the human grafts comes from the host.

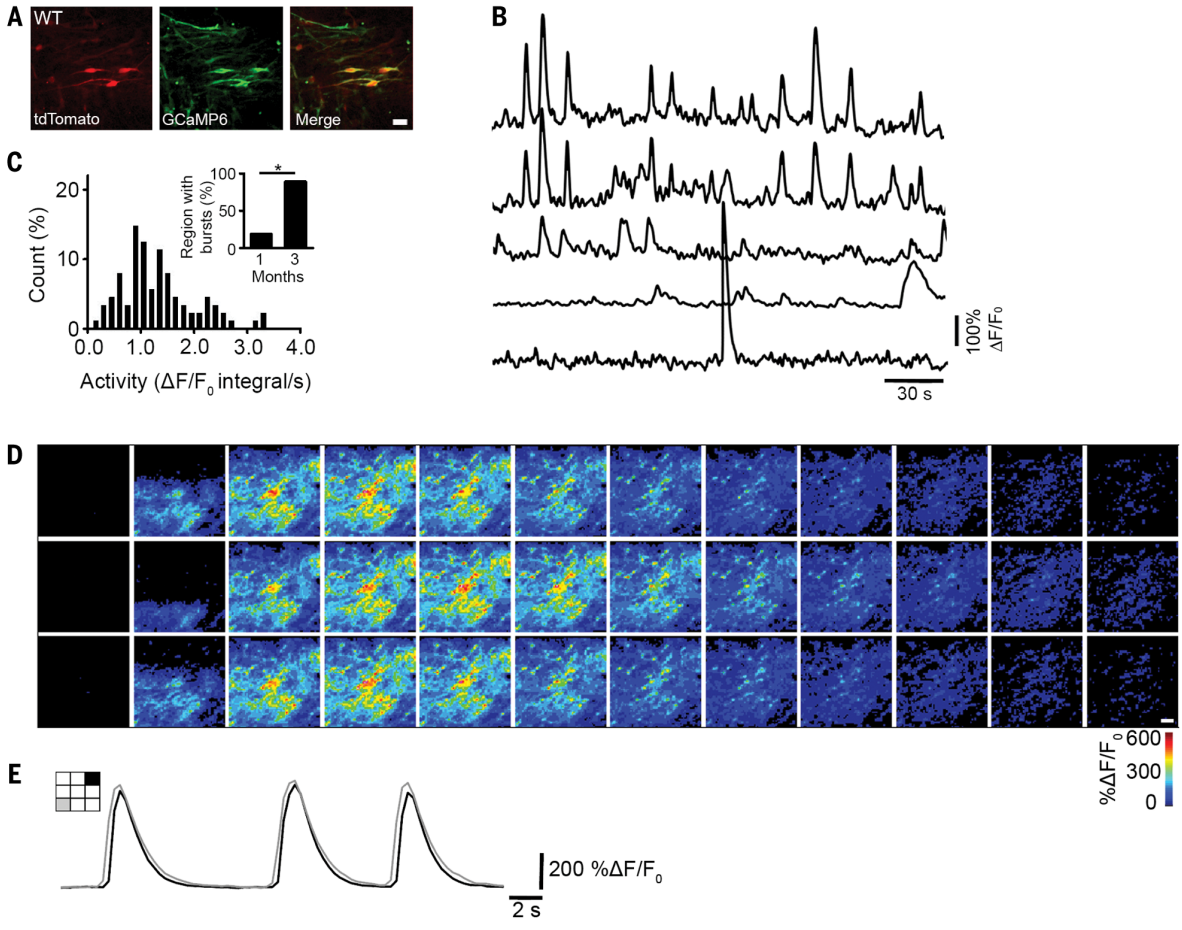

Fig. 3. In vivo calcium imaging shows that patterned population activity emerges early and has a defined spatiotemporal order. (**A**) Example of an imaged cortical region taken from a WT-1 graft at 1 mpt in the somatosensory cortex of an adult mouse. Neurons express tdTomato (red) and GCaMP6 (green). GCaMP-positive neurons are shown as a maximum-intensity projection of activity over a 4-min period of spontaneous activity. Active neurons (yellow) are shown by overlaying the images (merge). (**B**) Representative $\Delta F/F_0$ calcium traces (where $\Delta F/F_0$ is the ratio of the change in fluorescence to the baseline fluorescence) from five active neurons imaged in a WT-1 graft at 1 mpt. (**C**) Distribution of spontaneous calcium activity in WT-1 grafts at 1 to 2 mpt. Activity was measured as the integral of the average $\Delta F/F_0$ signal over the entire region of interest (ROI), normalized to the total duration of the recording in seconds (n = 88 cells, six ROIs, three mice). (Inset) Percentage of ROIs in WT-1 grafts at 1 to 2 mpt (3 of 16 ROIs, 18.8%; n = 4 mice) and 3 mpt (31 of 35 ROIs, 89.0%; n = 5 mice) that exhibit bursts. Chi-square test, $^*P < 0.05$. (**D**) Montage of image frames from a typical recurrent burst in a WT-1 graft. (**E**) Example of burst activity over two different spatial regions (gray and black) shown on the left, taken from the bursts in (D). Scale bars, 10 μm (A) and 20 μm (D).

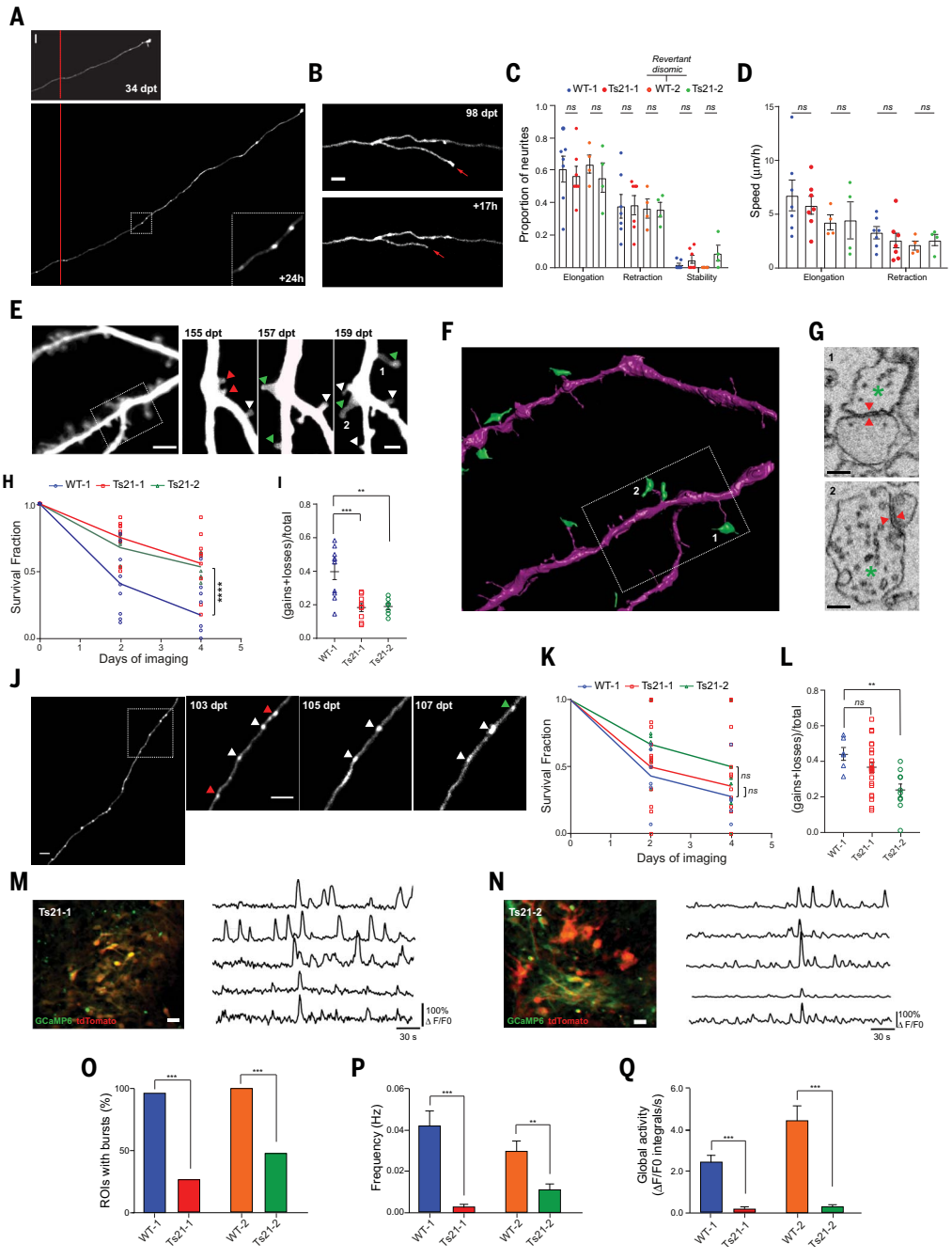

Fig. 4. In vivo modeling of structural and functional neuronal dynamics in tissue grafts from individuals with DS. (**A**) Representative example of axon elongation in a Ts21-1 neuron over a 24-hour period. The inset corresponds to the boxed area and highlights the presence of EPBs. The red line indicates alignment between the top and bottom images. (**B**) Example of axonal branch retraction (arrows) in a Ts21-1 neuron over 17 hours. (**C**) Proportion of elongating, retracting, and stable neurites in 24-hour intervals in WT-1 (n = 96 neurites from 79 cells, seven grafted animals, average 11 cells per animal), Ts21-1 (n = 65 neurites from 60 cells, seven grafted animals, average 9 cells per animal), WT-2 (n = 65 neurites from 53 cells, four grafted animals, average 13 cells per animal), and Ts21-2 (n = 60 neurites from 51 cells, four grafted animals, average 13 cells per animal) grafts at 3 wpt. WT-2 is a revertant disomic cell line from Ts21-2. Unpaired two-tailed t test; ns, not significant. Each data point represents an animal. (**D**) Speed of neurite elongation and retraction in WT-1 (n = 96 neurites from 73 cells, average 10 cells per animal), Ts21-1 (n = 62 neurites from 54 cells, average 8 cells per animal), WT-2 (n = 53 neurites from 47 cells, average 12 cells per animal), and Ts21-2 (n = 54 neurites from 46 cells, average 12 cells per animal) grafts at 3 wpt. Unpaired multiple t test; ns, not significant. Each data point represents an animal. (**E**) Example of dendritic branches and spines on a Ts21-1 neuron, imaged at 48-hour intervals for 4 days. The boxed region in the left panel is magnified in subsequent panels. Green, red, and white arrowheads indicate gained, lost, and stable dendritic spines, respectively. (**F**) 3D rendering of the same dendritic region imaged in vivo in (E), obtained from EM reconstruction. Presynaptic terminals are shown in green. (**G**) EM images of the dendritic spines marked with 1 and 2 in (E). Arrowheads indicate the location of synapses. Asterisk, presynaptic terminal. (**H**) Dendritic spine survival fraction over 4 days in WT-1 (n = 10 cells from two animals), Ts21-1 (n = 9 cells from four animals), and Ts21-2 (n = 7 cells from two animals) grafts at 3 to 4 mpt. Two-way ANOVA, interaction $F_{4,69}$ = 5.435, P = 0.0007; Tukey's multiple comparisons test, ****P < 0.0001. Each data point represents a cell. (**I**) Quantification of dendritic spine TOR over 4 days in WT-1 (n = 10 cells from two animals), Ts21-1 (n = 9 cells from four animals), and Ts21-2 (n = 7 cells from two animals) grafts at 3 to 4 mpt. Sidak's multiple comparisons test after one-way ANOVA, $F_{2,23}$ = 3.078, **P < 0.01; ***P < 0.001. Each data point represents a cell. (**J**) Representative example of an axon on a Ts21-2 neuron imaged at 48-hour intervals for 4 days. The arrowheads in the insets indicate stable (white), new (green), and lost (red) EPBs. (**K**) EPB survival fraction over 4 days in WT-1 (n = 6 cells), Ts21-1 (n = 24 cells), and Ts21-2 (n = 10 cells) grafts from three mice each at 3 to 4 mpt. Two-way ANOVA, interaction $F_{4,111}$ = 0.8211, P = 0.51; ns, not significant. Each data point represents an axon. (**L**) EPB TOR over 4 days in WT-1 (n = 6 cells), Ts21-1 (n = 24 cells), and Ts21-2 (n = 10 cells) grafts from three mice each at 3 to 4 mpt. Sidak's multiple comparisons test after one-way ANOVA, $F_{2,37}$ = 5.588, **P < 0.01; ns, not significant. Each data point represents an axon. (**M** and **N**) (Left) Example of imaged cortical regions taken from Ts21-1 (M) and Ts21-2 (N) grafts in the somatosensory cortices of adult mice. Neurons express tdTomato (red) and GCaMP6s (green). Active neurons (yellow) are shown by overlaying the images. (Right) Representative $\Delta F/F_0$ calcium traces from five active neurons imaged in Ts21-1 (M) and Ts21-2 (N) grafts. Note weak synchronized burst activity across different neurons compared with the traces in fig. S7E. (**O**) Percentage of ROIs in WT-1 (50 of 52 ROIs, 96.1%, six grafted mice), Ts21-1 (10 of 38 ROIs, 26.3%, three grafted mice), WT-2 (34 of 34 ROIs, 100%, three grafted mice), or Ts21-2 (11 of 23 ROIs, 47.8%, three grafted mice) grafts that exhibit bursts at 3 to 5 mpt. Z test, ***P < 0.001. (**P**) Frequency of burst events in WT-1, Ts21-1, WT-2, and Ts21-2 grafts measured at 3 to 5 mpt. Kruskal-Wallis test, **P < 0.01; ***P < 0.001. (**Q**) Global ROI activity in WT-1, Ts21-1, WT-2, and Ts21-2 grafts measured at 3 to 5 mpt. Kruskal-Wallis test, ***P < 0.001. Error bars in (P) and (Q) indicate SEM. Scale bars, 10 µm [(A) and (B)], 5 µm [(E), left, and (J)], 2 µm [(E), right], 0.2 µm (G), and 20 µm [(M) and (N)].

To assess the functional development of cortical networks in vivo, we engineered neurons to express the genetically encoded calcium indicator GCaMP6s (*35*) before grafting and studied calcium-mediated neuronal activity in vivo (Fig. 3) (n = 8 mice). Spontaneous, sparse activity (Fig. 3, A to C) was detected as early as 2 weeks post-transplantation (wpt) and persisted up to 3 mpt (Fig. 3C). In addition, bursts of activity synchronized across the neuropil and multiple cells (*31*) were also detected at 1 mpt (Fig. 3C, inset) and persisted in all grafts tested up to 5 mpt (fig. S7, E to H, and movies S4 and S5).

Many of these bursts had a defined spatiotemporal order (Fig. 3, D and E), as well as recurrent oscillatory behavior (<1 Hz between events) (Fig. 3D and fig. S7, E to I), with different incidences between 1 and 3 mpt (Fig. 3C, inset), resembling activity recorded in the developing human cortex (*36*, *37*) and consistent with a report on transplanted human cerebral organoids (*38*).

Recordings of calcium signals with air-puff stimulation of the animal's whiskers and facial skin revealed that grafted neurons in the primary somatosensory cortex can be responsive to sensory stimulation (fig. S12) (~30% of the stimulation trials in one mouse; neither of the other two animals tested showed sensory-evoked activity), indicating that thalamocortical synapses can functionally drive activity in the human graft at 6 mpt.

Imaging human neuron structural and functional dynamics in DS

So far, we have characterized the structural and functional dynamics of human cortical neurons during the earliest phases of their development in vivo (Figs. 1 to 3) and validated the main results with neurons from an independent control iPSC line [designated WT-2 (for wild-type line 2)] (fig. S7). To model the in vivo dynamics of pruning, synaptogenesis, and network activity in a complex genetic disorder, we first generated iPSC-derived progenitors and neurons from two individuals with DS (fig. S1) and then transplanted the cells into adult immunodeficient mice. During the reprogramming process of one of these lines [designated Ts21-2 (Ts21 line 2)], we identified a disomic clone that had lost one extra copy of human chromosome 21 (Hsa21) (yielding a WT-2 population) (*39*–*41*). We used a microsatellite short tandem repeat (STR) assay to confirm that the parental fibroblast population was not mosaic for disomy and trisomy of chromosome 21 and that Ts21-2 and WT-2 are otherwise identical to each other and the initial fibroblasts (fig. S13). This revertant disomic line (WT-2) allowed us to highlight phenotypes caused by an extra copy of Hsa21, rather than by genetic differences between individuals, without the need for multiple control lines, which are typically required to control for genetic variations or diverse differentiation potencies observed in genetically distinct human iPSC lines (*42*). A genome-wide copy number single-nucleotide polymorphism assay confirmed that the two Ts21 iPSC lines (Ts21-1 and Ts21-2) had normal karyotypes, except for the extra copy of Hsa21 (fig. S14). Fluorescence in situ hybridization (FISH) on cortical tissue grafts further verified the presence of the extra copy of Hsa21 (fig. S15). The Ts21 lines generated progenitors, neurons, and proliferating cells similarly to control grafts at 5 mpt (figs. S16 and S17). Astroglia, however, were overproduced in Ts21 grafts (fig. S16), recapitulating the human pathology (*43*). Ts21 neurons were also present in stable locations to the end of our experimental time line, allowing for in vivo single-cell tracking (fig. S18). Chronic in vivo imaging revealed that Ts21 neurons had rates of axon growth and retraction similar to those of control neurons at 3 wpt (Fig. 4, A to D), suggesting normal early developmental axon refinement. In addition, Ts21 neurons in the graft formed morphologically mature synaptic structures, which were plastic over time (Fig. 4, E to L). To determine whether dendritic spine growth was associated with synapse formation in Ts21 neurons, we reconstructed in one transplant, with EM, a subset of the same dendrites after long-term in vivo imaging (Fig. 4, E to G). We found that newly formed dendritic spines formed synapses in 14 of 34 cases (41%) and six of them (6 of 14, 43%) within 48 hours of their first appearance. Serial EM reconstructions revealed that human dendritic spines and presynaptic terminals contained a postsynaptic density and synaptic vesicles, respectively, suggestive of complete synaptic maturation (Fig. 4G). Whole-cell recordings from coronal brain slices containing the Ts21 grafts showed normal synaptic input on the DS donor–derived neurons compared to the control (fig. S19, A to D), suggesting functional synaptic connections. Longitudinal in vivo imaging, however, showed that dendritic spines, and to a lesser extent synaptic boutons (Fig. 4, J to L), were more stable in neurons from both individuals with DS than in the control, as demonstrated by higher survival and reduced turnover (Fig. 4, H and I, and fig. S20). High density of GFP-positive neurons prevented a quantitative analysis of synaptic dynamics in the WT-2 line. To understand whether the higher dendritic spine survival rates in Ts21 lines lead to higher spine density, we quantified dendritic spine density across the four lines (Ts21-1, Ts21-2, WT-1, and WT-2). We found an increase in dendritic spine density in neurons from the Ts21-1 line compared with WT-1 (fig. S21A), although this increase did not reach significance, consistent with postmortem fetal DS brain analysis at ~5 to 8 gestational months (*27*). However, we found higher spine densities in Ts21-2 than in WT-2, our most reliable comparison (fig. S21A). Putting the data from the two Ts21 and WT lines together highlighted a significant spine density increase in the Ts21 cells (fig. S21B). Overall, these data raise the possibility that spine density in DS cortical neurons is higher than in the control, at least at the early developmental stages tested. No difference in EPB density was found across the four lines (fig. S21, C and D).

To further investigate the increased synaptic stability phenotype, we studied neural population activity, a main regulator of postnatal synaptic refinement and stabilization (*26*), through in vivo calcium imaging of GCaMP6-expressing Ts21 grafts (Fig. 4, M and N). We measured both burst and global activity (see methods). These measures were reduced in Ts21 grafts (Fig. 4, O to Q). Together, these data highlight in vivo synaptic stability and functional early cortical network phenotypes in DS.

Conclusion

We investigated the earliest stages of human axon, synaptic, and network activity development in a complex genetic disorder by combining live imaging in a multistructured tissue environment and a patient-specific genetic background.

Transplanted human neurons continued to develop and mature in vivo, in a microenvironment that retained features reminiscent of the human fetal cortex, such as large size (up to ~100 mm^3 at 5 mpt) (movie S1), temporal order and duration (i.e., many months) of neurogenesis (*20*), vascularization, and cell diversification (human-derived cortical progenitors, neurons, oligodendrocytes, and astrocytes together with host-derived microglia and vessels), as well as complex cytoarchitecture. However, the extent to which neurons in human cortical tissue grafts, generated from either human iPSCs (present study) or embryonic stem cells (ESCs) (*20*, *38*, *44*), can mimic the maturation, complexity, and functionality of early human fetal cortical networks remains to be fully established.

Repeated imaging of single human neurons in cortical tissue grafts enabled us to gain insights on pruning, synaptic refinement, and functional neural network formation in vivo. We found that pruning occurred mainly by branch-specific retraction, rather than degeneration.

Nascent human excitatory synaptic networks already had balanced rates of synaptic gain and loss over ~1 week at the single-cell level, suggesting that immature human neurons possess intrinsic programs of synaptic turnover regulation over relatively short time scales. Human synaptogenesis and axon growth were concurrent, rather than happening at different times, confirming previous postmortem static analysis (*28*) and revealing conservation of this developmental growth program between species (*45*).

Oscillatory population activity had marked neuropil and soma synchronization, which became more prominent over 2 months, underscoring on-going modifications of cortical circuits. Results were robust across two independent control lines, providing a basis for applying this approach, which combines live imaging in a multistructured tissue environment with a patient-specific genetic background (*46*), to many other neurodevelopmental diseases affecting the cortex.

In this study, we modeled a complex genetic disorder and saw that whereas developmental axon refinement was normal, synapses were more stable and neural network activity was

reduced in tissue grafts from two individuals with DS, suggesting a possible role for patterned activity in regulating synaptic lifetimes in the early stages of human cortical circuit development (*32*). These deficits were evident even after Ts21 cells were exposed to the in vivo physiological microenvironment of the mouse brain for several months, indicating cell-intrinsic deficits. By using a revertant disomic iPSC line, we showed that the population activity deficits were rescued by the loss of an extra copy of Hsa21, indicating that heightened expression of Hsa21 genes is both necessary and sufficient to disrupt oscillatory burst activity in developing cortical DS networks in vivo.

In most previous work, human ESC– or iPSC–derived neurons have been transplanted into the damaged cortex (*38*, *47*), spinal cord (*48*), striatum (*49*, *50*), or retina (*51*), with the aim of cell replacement (*11*) rather than for disease modeling (*6*, *52*), as demonstrated in our study. Transplantation and in vivo imaging for disease modeling in mice is advantageous over that in higher species such as primates, as larger numbers of animals can be used to track cells in the grafts over long periods of time and the model provides a microenvironment containing vessels, immune cells, and innervation, not present in common in vitro preparations.

In summary, we established a new in vivo experimental model of DS to study how the chromosomal abnormality affects the earliest stages of human axon, synaptic, and functional neural network development. We expect that this single-cell-resolution intravital microscopy approach will advance the knowledge of cellular pathophysiology in this and other neurodevelopmental disorders, particularly valuable in light of the scarcity of early human fetal brain tissue material.

REFERENCES AND NOTES

1. W. M. Cowan, J. W. Fawcett, D. D. O'Leary, B. B. Stanfield, Regressive events in neurogenesis. *Science* **225**, 1258–1265 (1984). doi: 10.1126/science.6474175; pmid: 6474175
2. L. K. Low, H. J. Cheng, Axon pruning: An essential step underlying the developmental plasticity of neuronal connections. *Philos. Trans. R. Soc. London Ser. B* **361**, 1531–1544 (2006). doi: 10.1098/rstb.2006.1883; pmid: 16939973
3. Y. Herault *et al*., Rodent models in Down syndrome research: Impact and future opportunities. *Dis. Model. Mech.* **10**, 1165–1186 (2017). doi: 10.1242/dmm.029728; pmid: 28993310
4. A. O'Doherty *et al*., An aneuploid mouse strain carrying human chromosome 21 with Down syndrome phenotypes. *Science* **309**, 2033–2037 (2005). doi: 10.1126/science.1114535; pmid: 16179473
5. M. Gupta, A. R. Dhanasekaran, K. J. Gardiner, Mouse models of Down syndrome: Gene content and consequences. *Mamm. Genome* **27**, 538–555 (2016). doi: 10.1007/s00335-016-9661-8; pmid: 27538963
6. I. Espuny-Camacho *et al*., Hallmarks of Alzheimer's disease in stem-cell-derived human neurons transplanted into mouse brain. *Neuron* **93**, 1066–1081.e8 (2017). doi: 10.1016/j.neuron.2017.02.001; pmid: 28238547
7. J. van den Ameele, L. Tiberi, P. Vanderhaeghen, I. Espuny-Camacho, Thinking out of the dish: What to learn about cortical development using pluripotent stem cells. *Trends Neurosci.* **37**, 334–342 (2014). doi: 10.1016/j.tins.2014.03.005; pmid: 24745669
8. Y. Shi, P. Kirwan, J. Smith, H. P. Robinson, F. J. Livesey, Human cerebral cortex development from pluripotent stem cells to functional excitatory synapses. *Nat. Neurosci.* **15** (S471), 477–486, S1 (2012). doi: 10.1038/nn.3041; pmid: 22306606
9. M. A. Lancaster *et al*., Cerebral organoids model human brain development and microcephaly. *Nature* **501**, 373–379 (2013). doi: 10.1038/nature12517; pmid: 23995685
10. P. Carmeliet, M. Tessier-Lavigne, Common mechanisms of nerve and blood vessel wiring. *Nature* **436**, 193–200 (2005). doi: 10.1038/nature03875; pmid: 16015319
11. L. H. Thompson, A. Björklund, Reconstruction of brain circuitry by neural transplants generated from pluripotent stem cells. *Neurobiol. Dis.* **79**, 28–40 (2015). doi: 10.1016/j.nbd.2015.04.003; pmid: 25913029
12. J. S. Barbosa *et al*., Live imaging of adult neural stem cell behavior in the intact and injured zebrafish brain. *Science* **348**, 789–793 (2015). doi: 10.1126/science.aaa2729; pmid: 25977550
13. Y. Shi, P. Kirwan, F. J. Livesey, Directed differentiation of human pluripotent stem cells to cerebral cortex neurons and neural networks. *Nat. Protoc.* **7**, 1836–1846 (2012). doi: 10.1038/nprot.2012.116; pmid: 22976355
14. M. E. Emborg *et al*., Induced pluripotent stem cell-derived neural cells survive and mature in the nonhuman primate brain. *Cell Rep.* **3**, 646–650 (2013). doi: 10.1016/j.celrep.2013.02.016; pmid: 23499447
15. X. Qian *et al*., Brain-region-specific organoids using mini-bioreactors for modeling ZIKV exposure. *Cell* **165**, 1238–1254 (2016). doi: 10.1016/j.cell.2016.04.032; pmid: 27118425
16. A. Hoerder-Suabedissen, Z. Molnár, Development, evolution and pathology of neocortical subplate neurons. *Nat. Rev. Neurosci.* **16**, 133–146 (2015). doi: 10.1038/nrn3915; pmid: 25697157
17. T. Saito *et al*., Neocortical layer formation of human developing brains and lissencephalies: Consideration of layer-specific marker expression. *Cereb. Cortex* **21**, 588–596 (2011). doi: 10.1093/cercor/bhq125; pmid: 20624841
18. N. Palomero-Gallagher, K. Zilles, Cortical layers: Cyto-, myelo-, receptor- and synaptic architecture in human cortical areas. *Neuroimage* S1053-8119(17)30682-1 (2017). doi: 10.1016/j.neuroimage.2017.08.035; pmid: 28811255
19. I. M. Zakiewicz, J. G. Bjaalie, T. B. Leergaard, Brain-wide map of efferent projections from rat barrel cortex. *Front. Neuroinform.* **8**, 5 (2014). doi: 10.3389/fninf.2014.00005; pmid: 24550819
20. I. Espuny-Camacho *et al*., Pyramidal neurons derived from human pluripotent stem cells integrate efficiently into mouse brain circuits in vivo. *Neuron* **77**, 440–456 (2013). doi: 10.1016/j.neuron.2012.12.011; pmid: 23395372
21. L. Luo, D. D. O'Leary, Axon retraction and degeneration in development and disease. *Annu. Rev. Neurosci.* **28**, 127–156 (2005). doi: 10.1146/annurev.neuro.28.061604.135632; pmid: 16022592
22. A. Nikolaev, T. McLaughlin, D. D. O'Leary, M. Tessier-Lavigne, APP binds DR6 to trigger axon pruning and neuron death via distinct caspases. *Nature* **457**, 981–989 (2009). doi: 10.1038/nature07767; pmid: 19225519
23. C. Portera-Cailliau, R. M. Weimer, V. De Paola, P. Caroni, K. Svoboda, Diverse modes of axon elaboration in the developing neocortex. *PLOS Biol.* **3**, e272 (2005). doi: 10.1371/journal.pbio.0030272; pmid: 16026180
24. V. De Paola *et al*., Cell type-specific structural plasticity of axonal branches and boutons in the adult neocortex. *Neuron* **49**, 861–875 (2006). doi: 10.1016/j.neuron.2006.02.017; pmid: 16543134
25. V. De Paola, S. Arber, P. Caroni, AMPA receptors regulate dynamic equilibrium of presynaptic terminals in mature hippocampal networks. *Nat. Neurosci.* **6**, 491–500 (2003). doi: 10.1038/nn1046; pmid: 12692557
26. P. Caroni, F. Donato, D. Muller, Structural plasticity upon learning: Regulation and functions. *Nat. Rev. Neurosci.* **13**, 478–490 (2012). doi: 10.1038/nrn3258; pmid: 22714019
27. T. L. Petit, J. C. LeBoutillier, D. P. Alfano, L. E. Becker, Synaptic development in the human fetus: A morphometric analysis of normal and Down's syndrome neocortex. *Exp. Neurol.* **83**, 13–23 (1984). doi: 10.1016/0014-4886(84)90041-4; pmid: 6228436
28. P. R. Huttenlocher, A. S. Dabholkar, Regional differences in synaptogenesis in human cerebral cortex. *J. Comp. Neurol.* **387**, 167–178 (1997). doi: 10.1002/(SICI)1096-9861(19971020)387:2<167::AID-CNE1>3.0.CO;2-Z; pmid: 9336221
29. M. E. Molliver, I. Kostović, H. van der Loos, The development of synapses in cerebral cortex of the human fetus. *Brain Res.* **50**, 403–407 (1973). doi: 10.1016/0006-8993(73)90741-5; pmid: 4705508
30. A. Holtmaat *et al*., Long-term, high-resolution imaging in the mouse neocortex through a chronic cranial window. *Nat. Protoc.* **4**, 1128–1144 (2009). doi: 10.1038/nprot.2009.89; pmid: 19617885
31. O. Garaschuk, J. Linn, J. Eilers, A. Konnerth, Large-scale oscillatory calcium waves in the immature cortex. *Nat. Neurosci.* **3**, 452–459 (2000). doi: 10.1038/74823; pmid: 10769384
32. R. Khazipov, H. J. Luhmann, Early patterns of electrical activity in the developing cerebral cortex of humans and rodents. *Trends Neurosci.* **29**, 414–418 (2006). doi: 10.1016/j.tins.2006.05.007; pmid: 16713634
33. P. Kirwan *et al*., Development and function of human cerebral cortex neural networks from pluripotent stem cells in vitro. *Development* **142**, 3178–3187 (2015). doi: 10.1242/dev.123851; pmid: 26395144
34. G. Quadrato *et al*., Cell diversity and network dynamics in photosensitive human brain organoids. *Nature* **545**, 48–53 (2017). doi: 10.1038/nature22047; pmid: 28445462
35. T. W. Chen *et al*., Ultrasensitive fluorescent proteins for imaging neuronal activity. *Nature* **499**, 295–300 (2013). doi: 10.1038/nature12354; pmid: 23868258
36. S. Vanhatalo *et al*., DC-EEG discloses prominent, very slow activity patterns during sleep in preterm infants. *Clin. Neurophysiol.* **113**, 1822–1825 (2002). doi: 10.1016/S1388-2457(02)00292-4; pmid: 12417237
37. P. J. Uhlhaas, F. Roux, E. Rodriguez, A. Rotarska-Jagiela, W. Singer, Neural synchrony and the development of cortical networks. *Trends Cogn. Sci.* **14**, 72–80 (2010). doi: 10.1016/j.tics.2009.12.002; pmid: 20080054
38. A. A. Mansour *et al*., An in vivo model of functional and vascularized human brain organoids. *Nat. Biotechnol.* **36**, 432–441 (2018). doi: 10.1038/nbt.4127; pmid: 29658944
39. C. Chen *et al*., Role of astroglia in Down's syndrome revealed by patient-derived human-induced pluripotent stem cells. *Nat. Commun.* **5**, 4430 (2014). doi: 10.1038/ncomms5430; pmid: 25034944
40. G. A. MacLean *et al*., Altered hematopoiesis in trisomy 21 as revealed through in vitro differentiation of isogenic human pluripotent cells. *Proc. Natl. Acad. Sci. U.S.A.* **109**, 17567–17572 (2012). doi: 10.1073/pnas.1215468109; pmid: 23045682
41. J. P. Weick *et al*., Deficits in human trisomy 21 iPSCs and neurons. *Proc. Natl. Acad. Sci. U.S.A.* **110**, 9962–9967 (2013). doi: 10.1073/pnas.1216575110; pmid: 23716668
42. K. Plona, T. Kim, K. Halloran, A. Wynshaw-Boris, Chromosome therapy: Potential strategies for the correction of severe chromosome aberrations. *Am. J. Med. Genet. C Semin. Med. Genet.* **172**, 422–430 (2016). doi: 10.1002/ajmg.c.31530; pmid: 27813255
43. E. Dossi, F. Vasile, N. Rouach, Human astrocytes in the diseased brain. *Brain Res. Bull.* **136**, 139–156 (2018). doi: 10.1016/j.brainresbull.2017.02.001; pmid: 28212850
44. K. Møllgård, J. J. Lundberg, B. K. Beebe, A. Björklund, U. Stenevi, The intracerebrally cultured 'microbrain': A new tool in developmental neurobiology. *Neurosci. Lett.* **8**, 295–301 (1978). doi: 10.1016/0304-3940(78)90139-8; pmid: 19605176
45. S. Falkner *et al*., Transplanted embryonic neurons integrate into adult neocortical circuits. *Nature* **539**, 248–253 (2016). doi: 10.1038/nature20113; pmid: 27783592
46. J. A. Korecka, S. Levy, O. Isacson, In vivo modeling of neuronal function, axonal impairment and connectivity in neurodegenerative and neuropsychiatric disorders using induced pluripotent stem cells. *Mol. Cell. Neurosci.* **73**, 3–12 (2016). doi: 10.1016/j.mcn.2015.12.004; pmid: 26691153
47. D. Tornero *et al*., Synaptic inputs from stroke-injured brain to grafted human stem cell-derived neurons activated by sensory stimuli. *Brain* **140**, 692–706 (2017). pmid: 28115364
48. P. Lu *et al*., Long-distance growth and connectivity of neural stem cells after severe spinal cord injury. *Cell* **150**, 1264–1273 (2012). doi: 10.1016/j.cell.2012.08.020; pmid: 22980985
49. V. Tabar *et al*., Migration and differentiation of neural precursors derived from human embryonic stem cells in the rat brain. *Nat. Biotechnol.* **23**, 601–606 (2005). doi: 10.1038/nbt1088; pmid: 15852001
50. M. Wernig *et al*., Neurons derived from reprogrammed fibroblasts functionally integrate into the fetal brain and improve symptoms of rats with Parkinson's disease. *Proc. Natl. Acad. Sci. U.S.A.* **105**, 5856–5861 (2008). doi: 10.1073/pnas.0801677105; pmid: 18391196
51. M. Mandai *et al*., Autologous induced stem-cell-derived retinal cells for macular degeneration. *N. Engl. J. Med.* **376**,

1038–1046 (2017). doi: 10.1056/NEJMoa1608368; pmid: 28296613
52. H. Q. Huo *et al*., Modeling Down syndrome with patient iPSCs reveals cellular and migration deficits of GABAergic neurons. *Stem Cell Rep.* **10**, 1251–1266 (2018). doi: 10.1016/j.stemcr.2018.02.001; pmid: 29526735

ACKNOWLEDGMENTS

We thank K. Alvian, R. Festenstein, T. Keck, and M. Lancaster for comments on the manuscript; S. Papadoupoulou for help with immunohistochemistry; C. Bass and A. A. Bharath (Imperial College London) for help with the calcium imaging analysis; C. Whilding for developing a customized FIJI script for image analysis; M. Tortora for help with the immunohistochemistry experiments and analysis and C. Pernaci for help with the analysis; M. Lavrov and M. Rakowska for help with synaptic dynamics analysis; E. Mustafa, A. Czerniak, K. Horan, A. Matthews, and E. Rowley for assistance with animal care and monitoring; M. Tripodi (LMB, Cambridge) for the kind gift of the modified rabies transynaptic tracer; and G. Stamp for the analysis of hematoxylin and eosin–stained material. **Funding:** This work was supported by the Medical Research Council (V.D.P.); the GABBA Ph.D. program (FCT fellowship PD/BD/52198/2013), the Rosetrees Trust, and ARUK (R.R.); the UK Dementia Research Institute (grant code DRIImp17/18 Q3 to S.J.B.); a Wellcome Senior Investigator award (F.J.L.); and the Alborada Trust of the ARUK Stem Cell Research Centre (M.P. and F.J.L.). **Author contributions:** V.D.P. conceived and planned the live imaging, characterization, and analysis of transplanted patient-derived neurons and brought F.J.L. into the project; F.J.L. independently generated the iPSC-derived neurons, conceived the in vitro aspects of the project, and contributed to the study design; R.R., A.T., and V.D.P. performed the grafting and the two-photon imaging experiments, analyzed the data, and prepared the related figures and text; M.P. performed the human iPSC–derived neuron differentiation and in vitro characterization, the copy number assay, and the lentiviral vector transductions and provided input on the design of the experiments; R.R. and S.K. performed cell marker immunohistochemistry, imaging, and analysis for the characterization of cell identity after transplantation and prepared the relevant figures with input from V.D.P.; R.R. conducted and analyzed the whole-brain rabies tracing reconstructions; M.A.S. performed the electrophysiology recordings in acute brain slices containing the human grafts and prepared the relevant figure and text; S.J.B. analyzed the in vivo calcium imaging data and prepared the relevant figures and text with input from R.R. and V.D.P.; A.M. generated and characterized the Ts21-2, WT-2, and WT-2′ lines with input from F.J.L.; A.S. analyzed the gene expression, copy number variation, and STR data and prepared the relevant figures; J.D. and S.K. characterized the graft size; J.D. characterized the axon projections from the grafts; E.V. provided input on the Hsa21 FISH experiment and analyzed the FISH data with input from V.D.P.; G.K. performed and analyzed the EM reconstructions and prepared the relevant figures; V.D.P. led the project; and V.D.P and R.R. wrote the paper with contributions from all authors. **Competing interests:** None. **Data and materials availability:** All data needed to evaluate the conclusions in the paper are present in the paper or the supplementary materials.

SUPPLEMENTARY MATERIALS

www.sciencemag.org/content/362/6416/eaau1810/suppl/DC1
Materials and Methods
Figs. S1 to S21
Table S1
References (*53*–*60*)
Movies S1 to S6

24 May 2018; accepted 26 September 2018
Published online 11 October 2018
10.1126/science.aau1810

RESEARCH ARTICLE

TROPICAL STORMS

Dominant effect of relative tropical Atlantic warming on major hurricane occurrence

H. Murakami[1,2]*†, E. Levin[3], T. L. Delworth[1,2], R. Gudgel[1], P.-C. Hsu[4]

Here we explore factors potentially linked to the enhanced major hurricane activity in the Atlantic Ocean during 2017. Using a suite of high-resolution model experiments, we show that the increase in 2017 major hurricanes was not primarily caused by La Niña conditions in the Pacific Ocean but rather triggered mainly by pronounced warm sea surface conditions in the tropical North Atlantic. Further, we superimpose a similar pattern of North Atlantic surface warming on data for long-term increasing sea surface temperature (a product of increases in greenhouse gas concentrations and decreases in aerosols) to show that this warming trend will likely lead to even higher numbers of major hurricanes in the future. The key factor controlling Atlantic major hurricane activity appears to be the degree to which the tropical Atlantic warms relative to the rest of the global ocean.

The 2017 hurricane season in the North Atlantic Ocean was highly active, with six major hurricanes (MHs) causing widespread damage over the Gulf Coast and the Caribbean (*1*, *2*) (Fig. 1, A and C). Considering the mean seasonal MH number (2.7) and its standard deviation (1.9) during the period 1979–2017 (Fig. 1B), the positive anomaly of MHs was almost two standard deviations above normal. Specifically, among these six MHs in 2017, Hurricanes Harvey, Irma, and Maria made landfall over the Gulf Coast and the Caribbean (Fig. 1, A and C), causing substantial damage in these coastal regions (*2*). Moreover, Hurricane Harvey ended a 12-year period of no landfalling MHs in the United States [the so-called "MH landfall drought" (*3*, *4*)], with the most recent landfalling MH (Hurricane Wilma) having occurred in 2005. The highly active MH season in 2017 has attracted considerable attention throughout the scientific community (*5*), as well as broader society (*6*), in terms of its causes and also whether anthropogenic forcing played a role (*2*).

A number of factors might have caused the active MH season. The boreal summer season in 2017 was characterized by a developing moderate La Niña and associated conditions [see region A in Fig. 1D; the Niño3.4 index was 0.4 standard deviations below normal (Fig. 1B)]. It is known that, during summers with a developing La Niña, hurricanes are more active over the North Atlantic due to a weakening of the vertical shear of the zonal winds over the tropical Atlantic relative to climatology (*7*, *8*). The correlation coefficient (hereafter, *r*) between the Niño3.4 index and the observed MH frequency for the period 1979–2017 is −0.45, which is statistically significant (*P* value < 0.01) (Fig. 1B). It is also apparent that the surface ocean in boreal summer 2017 was substantially warmer than the climatological mean in the tropical North Atlantic, where most tropical cyclones are generated [the sea surface temperature anomaly (SSTA) was 1.5 standard deviations above normal in region B in Fig. 1D, hereafter referred to as the main developing region (MDR); fig. S1]. On the basis of observations made over the past 60 years, Kossin (*9*) reported that ambient environmental vertical wind shear (*10*–*12*), defined as wind speed difference between upper troposphere (200 hPa) and lower troposphere (850 hPa) and considered a detrimental factor for tropical cyclone genesis and intensification, tends to be stronger off the east coast of the United States (region C in Fig. 1D) when sea surface temperature (SST) is higher over region B, leading to fewer MHs over region C. However, this relationship is not clear for the 2017 summer. Observations for the 2017 summer within region C show a mixture of wind shear anomalies (fig. S2A): weaker in the Gulf of Mexico and stronger along the Canadian coast despite the positive SSTA over region B. Meanwhile, a substantial positive SSTA was also observed over region C. It is expected that tropical cyclones obtain more energy from warmer oceans and then further develop into MHs during their westward propagation from the MDR.

Overall, the SSTA spatial pattern in 2017 over the North Atlantic resembles a positive phase of the Atlantic Multidecadal Oscillation (AMO) (*13*). The observed AMO index is 1.5 standard deviations above its long-term mean for the 2017 summer season (Fig. 1B). Indeed, the AMO index is moderately and positively correlated with the number of MHs for the period 1979–2017 (r = +0.50; P value < 0.01) (Fig. 1B). There is, however, another mode of variability over the region: the Atlantic Meridional Mode (AMM) (*14*). The AMM has substantial variability at the interannual time scale in the North Atlantic, characterized by a meridional contrast in the SSTA across the Equator, as well as associated surface wind anomalies. The correlation coefficient between the observed AMM index and MH frequency is +0.62 (P value < 0.01) (Fig. 1B), and the observed AMM index for the 2017 summer season was 1.2 standard deviations above normal. These high positive indices imply a possible impact of internal natural variability on this active MH season in 2017 (*15*). However, it is also possible that greenhouse gas–induced global warming might have caused the emergence of the pronounced MH activity in the 2017 hurricane season. This supposition is based on the findings of several previous modeling studies that commonly projected an increase in intense storms such as MHs under conditions of increased anthropogenic forcing (*16*–*18*). In this study, using a suite of high-resolution model experiments (*19*, *20*), we attempted to elucidate the physical reasons for the occurrence of the active 2017 MH season and to anticipate possible future changes in MH activity, given conditions similar to those of summer 2017 but with increased anthropogenic forcing.

Successful prediction of active 2017 MHs

The particularly active MH season in 2017 was forecast well in real-time seasonal predictions starting from initial conditions on 1 July, using a high-resolution global coupled model [HiFLOR (*19*, *20*)] developed at the Geophysical Fluid Dynamics Laboratory. Previous studies have shown that HiFLOR can simulate the observed interannual variation of MH frequency in historical simulations (*19*) and offers skill in retrospective seasonal predictions (*20*) (the r between the predicted and observed MH frequency is +0.74 for the period 1980–2017; see fig. S3). Figure 1E shows the predicted 2017 seasonal-mean MH density anomaly (July to November) from initial conditions on 1 July 2017 (i.e., lead month = 0 to 4), which can be contrasted with the corresponding observations shown in Fig. 1C. HiFLOR successfully predicted the observed higher MH density along the eastern coast of the Caribbean and Florida, although the predicted density anomalies were underestimated. HiFLOR realistically predicted the spatial pattern of the MH density anomaly over the Pacific Ocean as well. Because in these real-time seasonal predictions the oceanic conditions were initialized but the atmospheric and land surface were not, the successful prediction mainly derives from the oceanic state, along with the prescribed boundary conditions of anthropogenic forcing (*8*, *20*). Indeed, HiFLOR predicted

[1]Geophysical Fluid Dynamics Laboratory, National Oceanic and Atmospheric Administration, Princeton, NJ, USA. [2]Atmospheric and Oceanic Sciences Program, Princeton University, Princeton, NJ, USA. [3]Paul D. Schreiber High School, Port Washington, NY, USA. [4]Key Laboratory of Meteorological Disaster of Ministry of Education, Nanjing University of Information Science and Technology, Nanjing, China.
*Corresponding author. Email: hir.murakami@gmail.com
†Present address: Cooperative Programs for the Advancement of Earth System Science, University Corporation for Atmospheric Research, Boulder, CO, USA.

a higher SSTA over the Atlantic, especially over the MDR and off the east coast of the United States, in addition to the moderate La Niña conditions as observed (Fig. 1, D and F). However, the amplitude of the La Niña conditions was underestimated in the real-time predictions. HiFLOR also largely predicted the spatial pattern of vertical wind shear anomalies (fig. S2, B and C) compared with observations (fig. S2A); however, there are some differences between predictions and observations at small regional scales.

Observations show that the MHs in 2017 primarily occurred during a confined period in the late summer season (26 August to 14 October; black solid line in fig. S4), which is a subset of the climatological MH season (July to October; black dashed line in fig. S4). This clustering indicates an important role for subseasonal oscillations for the timing of 2017 MHs (*21*, *22*). HiFLOR failed to predict the timing of active MHs in 2017. Figure S4 shows that 2017 MHs (blue thick line) were predicted to occur earlier than the modeled climatological mean MH season (red thick line). However, we did not expect that HiFLOR could predict the timing of the active MHs for 2017 because the atmosphere was not initialized in the predictions. Because a few ensemble members show active MHs during the late 2017 summer season (blue thin lines in fig. S4), it appears that HiFLOR is able to simulate subseasonal oscillations comparable to those observed (*19*) and that inclusion of atmospheric initialization may potentially improve predictions of MH timing during 2017.

Reasons for the active 2017 MH season

To elucidate the relative importance of SSTAs in various regions for the occurrence of this highly active 2017 MH season, we used HiFLOR to conduct a series of idealized seasonal predictions for the period 1 July through 30 November. In these idealized predictions, SST in the model was restored to the SSTs from the original HiFLOR seasonal predictions initialized from 1 July 2017, but with some modifications [we refer to the SST-restoring experiments as "nudging experiments" (*19*) (see supplementary method c)]. In the first nudging experiment, which we call CLIM, we

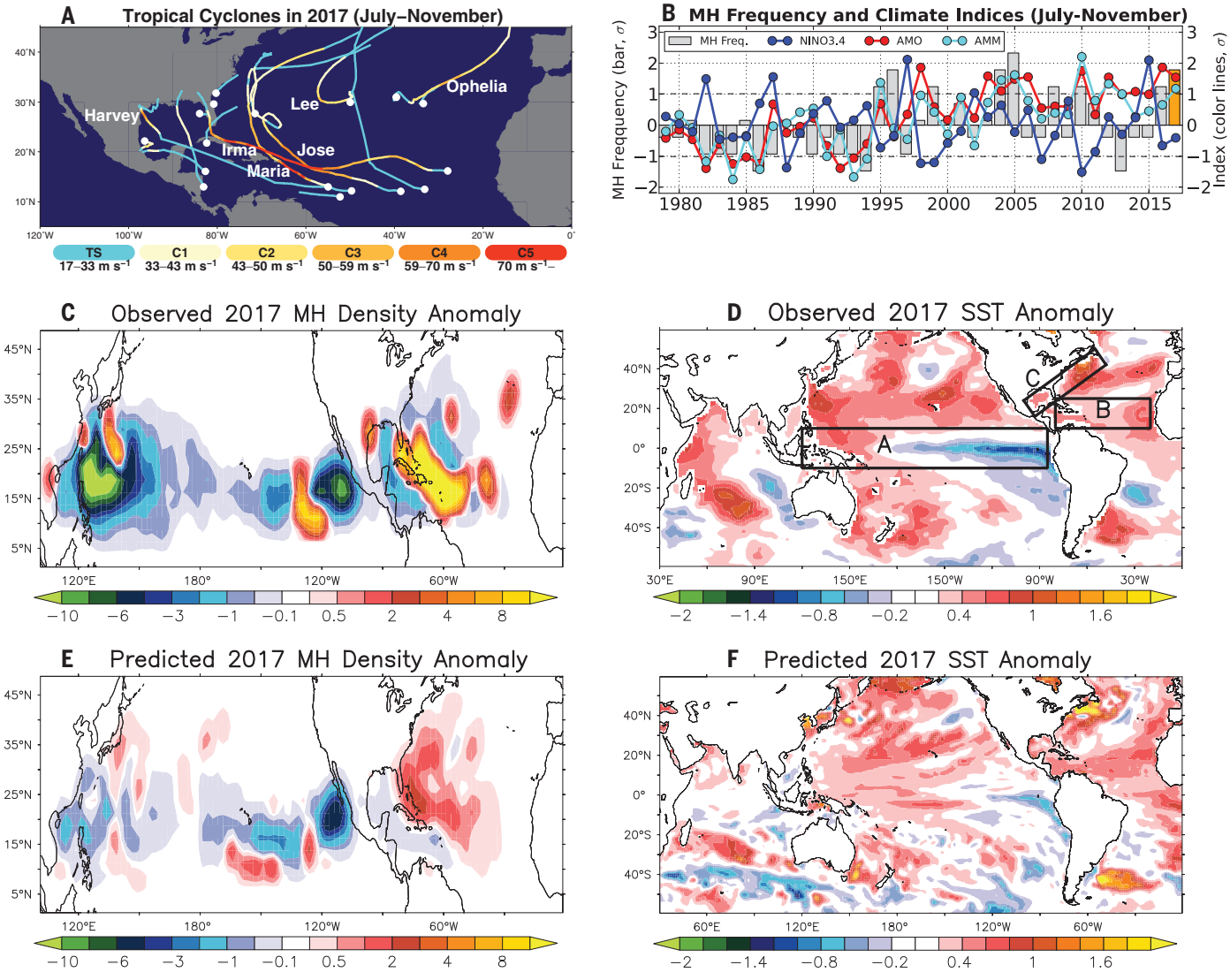

Fig. 1. Observed and predicted major hurricanes (MHs) and SSTs in 2017. (**A**) Observed tropical cyclones during the 2017 hurricane season. Storm tracks are colored according to the intensities of the storms, as categorized by the Saffir-Simpson hurricane wind scale (TS, tropical storm; C1 to C5, category 1 to category 5 hurricanes). Labeled storms denote MHs. (**B**) Standardized index (σ) for the observed anomaly of MH frequency (gray bars), along with the observed standardized index (σ) of the natural variability (colored lines) for the Niño3.4 (blue), AMO (red), and AMM (cyan) indices. The orange bar highlights the observed 2017 MH anomaly. (**C**) Observed MH density anomaly in the 2017 hurricane season relative to the mean of 1980–2017 (number per 2.5°-by-2.5° grid box per season). (**D**) Observed SST anomaly (SSTA; units: K) in the 2017 hurricane season relative to the mean of the period 1982–2012. The black frames demarcate the possible key regions for the unusually high MH activity in 2017. (**E** and **F**) As in (C) and (D) but for ensemble mean of real-time seasonal predictions from 1 July 2017 initial conditions, as predicted by HiFLOR.

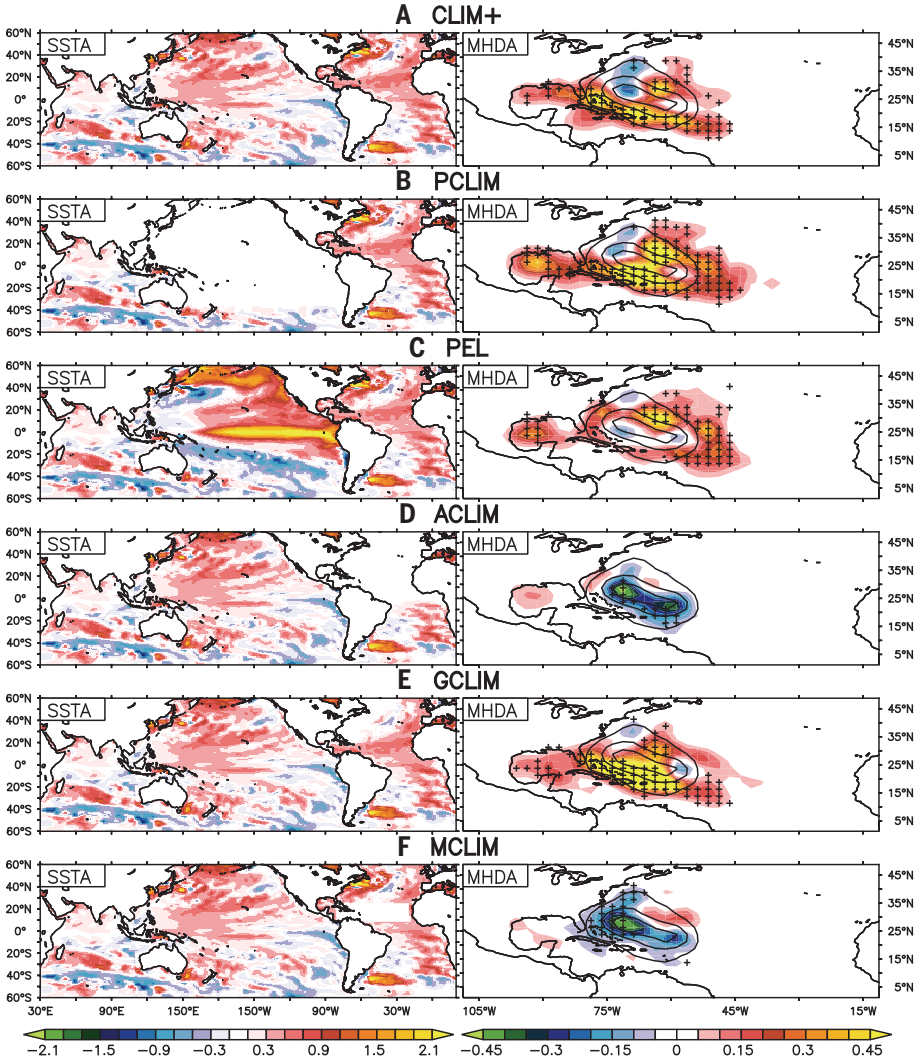

Fig. 2. Prescribed idealized SSTA and predicted MH density. Idealized seasonal forecasts were conducted by prescribing the idealized SSTs in which SSTAs (left panels; units: K) are superimposed onto the climatological mean SST (CLIM). The resultant predicted MH density anomalies (MHDAs) relative to the CLIM experiment are shown by the shading in the right panels (units: number per season). The prescribed SSTAs are: (**A**) all 2017 anomalies (CLIM+); (**B**) as in CLIM+, except the Pacific SSTAs are set to zero (PCLIM); (**C**) as in CLIM+, except the Pacific SSTA is replaced with the SSTA predicted from initial conditions on 1 April 2017, predicting El Niño conditions (PEL); (**D**) as in CLIM+, except the Atlantic SSTA is set to zero (ACLIM); (**E**) as in CLIM+, except the SSTA off the coast of North America is set to zero (GCLIM); and (**F**) as in CLIM+, except the SSTA in the tropical Atlantic is set to zero. Contours in the panels at right denote the mean MH density predicted from the CLIM experiment. The contour interval is 0.6 per season. Cross symbols in the right panels indicate that the predicted change relative to the CLIM experiment is statistically significant at the 90% confidence level or above [bootstrap method proposed by Murakami *et al*. (*32*)].

restored the SST to the predicted climatological mean SST computed over the period 1982–2012. In the second experiment, called CLIM+, we restored the SST to that predicted for 2017 (Fig. 2A). The CLIM and CLIM+ simulations yielded about three and six MHs, respectively (Fig. 3). These simulated values were close to the observed values for the climatology (2.7) and the 2017 season (6). Moreover, the pattern of the predicted MH density anomaly in CLIM+ (right panel of Fig. 2A) reflected the observed 2017 MH density anomaly in the North Atlantic (Fig. 1C). The fidelity of the MH prediction by HiFLOR gave us confidence in carrying out further sensitivity experiments with the model.

In the next sensitivity experiment, we used the SSTs from CLIM+, except the SSTs over the Pacific Ocean were replaced with those from CLIM. We refer to this experiment as PCLIM, and the results are shown in Fig. 2B. If the 2017 La Niña conditions indeed led to the particularly active MH season in 2017, the predicted MH frequency should have been reduced in the PCLIM experiment. However, the results (Figs. 2B and 3) show that this was not the case. Therefore, the moderate 2017 La Niña conditions were not the key factor for the highly active MH season in 2017. Unlike the predictions started from initial conditions on 1 July 2017, the HiFLOR real-time seasonal predictions started from initial conditions on 1 April 2017 predicted a strong El Niño development for the 2017 summer season. This false alarm was also predicted by other seasonal models (*23*), possibly associated with the so-called "spring predictability barrier" (*24*). In our next sensitivity test, which we refer to as experiment PEL, we replaced the CLIM+ SST over the Pacific Ocean with the predicted SST from the April forecasts to emulate a strong El Niño condition. Although the MH frequency in PEL decreased slightly relative to CLIM+, the PEL prediction still showed active MHs over the North Atlantic (Fig. 2C and 3), indicating the possibility of high MH activity in the Atlantic, even with El Niño conditions during summer 2017. These experiments support the assertion that the Pacific SSTA in 2017 was not a critical factor for the particularly active MH season in the North Atlantic that year.

Next, we conducted an experiment similar to CLIM+ but with the Atlantic SST replaced by the CLIM SST (ACLIM; Fig. 2D). The ACLIM prediction showed substantial reductions in both MH number and density (Figs. 2D and 3), suggesting that the local Atlantic SSTA was critical for the high MH activity in 2017. Furthermore, we separately replaced the SST with the CLIM SST in the region off the east coast of the United States (GCLIM; Fig. 2E) and in the MDR (MCLIM; Fig. 2F) and found that replacing the MDR SSTA substantially reduced the MH frequency and MH density (Figs. 2F and 3). In contrast, results from GCLIM led us to conclude that the SSTA off the East Coast of the United States was not a major factor controlling the unusually high MH activity in the 2017 hurricane season, in terms of the number of MHs.

Note that we utilized the predicted SSTs, rather than observed SSTs, for the lower boundary conditions throughout this study (supplementary method c). This is because we started this attribution study before the end of the 2017 hurricane season (i.e., real-time event attribution study), when observed SSTs were unavailable. Meanwhile, we confirmed that the same conclusions could be obtained even by using observed SSTs (figs. S5 and S6).

Effect of anthropogenic forcing on active MH season

Another open question is to what extent the increase in anthropogenic forcing influenced the emergence of this particularly active MH season in 2017. To investigate this, we followed the idealized seasonal-prediction framework but additionally considered potential future conditions (see supplementary method c). The representative concentration pathway 4.5 (RCP4.5) and RCP8.5 experiments, in which future changes in mean SSTs according to CMIP5 models (fig. S7) were superimposed onto the CLIM SST, respectively resulted in more-frequent MHs relative to CLIM by about 1.5 and 2.0, with statistical significance (P values of < 0.05 and < 0.01) (Fig. 3), and a

basin-wide increase in MH density (Fig. 4, A and B), albeit with both RCP4.5 and RCP8.5 also showing a marked increase in MH density in the northern Atlantic and Gulf of Mexico. These results imply a general increase in MH occurrence induced by anthropogenic forcing. The RCP4.5 and RCP8.5 runs showed a slight reduction in MH density along the location of maximum MH density in CLIM (i.e., maximum contour in Fig. 4, A and B), but the reduction was not statistically significant. This noisy spatial pattern of changes may have been caused by the small sampling size in the predictions (i.e., 12 ensemble members). To increase the sample size, we conducted another set of long-term (200-year) control simulations by fixing the level of anthropogenic forcing to those in 2015 (2015Cntl) and 1940 (1940Cntl) (see supplementary method b). These simulations showed a basin-wide increase in MH density in 2015Cntl relative to 1940Cntl (Fig. 4C).

In addition to the RCP4.5 and RCP8.5 experiments, we superimposed the 2017 SSTA (Fig. 2A) onto the SSTs from the RCP4.5 and RCP8.5 experiments to mimic the impact of the 2017 spatial distribution of SSTAs if that pattern were to occur in a future warmer climate. These experiments, which we refer to as RCP4.5+ and RCP8.5+, showed an increase in the number of MHs by about three relative to their future mean-state experiments (i.e., RCP4.5 and RCP8.5) (Fig. 3). The increase of three MHs was similar to that from the present-day experiments (i.e., CLIM+ minus CLIM in Fig. 3), suggesting that the increase in MH activity induced by the 2017 SSTA was not highly sensitive to the mean climate state. The increase in MHs induced by the 2017 SSTA (i.e., +3 MHs) was larger than that by the mean-state changes (i.e., +1.5 to 2.0 MHs; Fig. 3), indicating that the 2017 SSTA had a greater influence than the mean-state change on the unusually high MH activity that year. The MH density anomalies projected by RCP4.5+ and RCP8.5+ relative to their mean-state experiments (Fig. 4, D and E) show a spatial pattern similar to that of the 2017 MH anomaly (Fig. 4F) but with a higher MH density over the Caribbean and near the U.S. coast, amplifying the risk of MHs over these regions, as well as a higher MH density over the open ocean in the northern North Atlantic.

Another possible factor responsible for the unusually active MH season in 2017 was the external influence of anthropogenic aerosols. Dunstone *et al.* (*25*) reported that their dynamical model revealed that anthropogenic aerosols lowered the frequency of tropical storms during the 20th century, whereas sharp declines in anthropogenic aerosol levels over the North Atlantic at the end of the 20th century increased the number of tropical storms. On the basis of climate model simulations, recent studies (*26*, *27*) also reported that the potential intensity, the theoretical upper limit of the storm intensity given the large-scale environment, recently started to increase because of reductions in anthropogenic aerosols over the global domain (*27*) as well as in the North Atlantic (*26*), indicating potential increases in MH frequencies due to decreases in

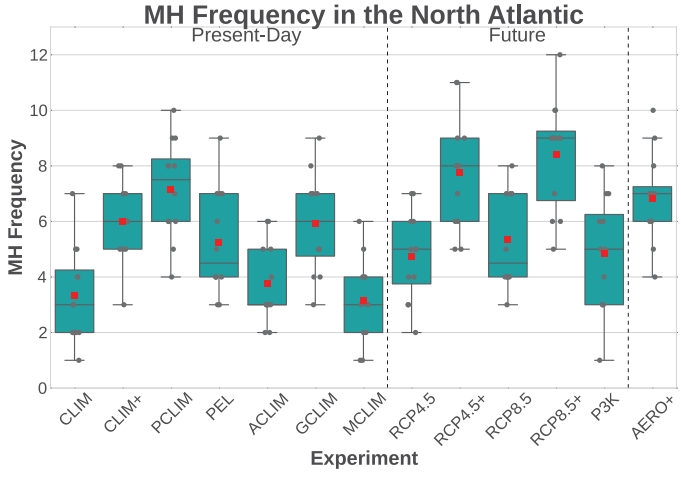

Fig. 3. Box plots for the predicted MH frequency over the North Atlantic, according to various prescribed SSTA patterns. Red squares denote the ensemble mean, whereas the black dots represent each ensemble member. The boxes indicate the lower and upper quartiles, the horizontal lines in the middle show the median value, and the horizontal end lines show the lowest (highest) datum still within the 1.5 interquartile range of the lower (upper) quartile.

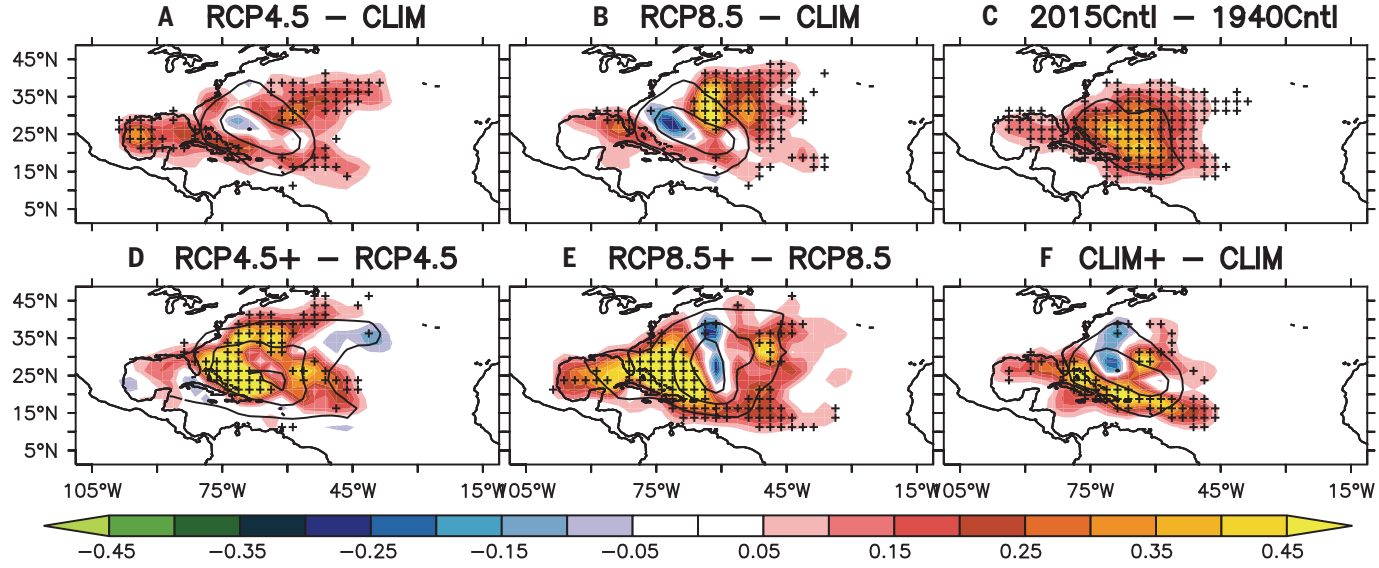

Fig. 4. Projected changes in MH density in the future experiments. Projected change in the July to November mean MH density (number per season), on the basis of (**A**) RCP4.5 relative to CLIM, (**B**) RCP8.5 relative to CLIM, (**C**) 2015Cntl relative to 1940Cntl, (**D**) RCP4.5+ relative to RCP4.5, (**E**) RCP8.5+ relative to RCP8.5, and (**F**) CLIM+ relative to CLIM. Cross symbols indicate that the predicted change is statistically significant at the 90% confidence level or above [bootstrap method (*32*)]. Contours show the predicted values for the reference experiment [i.e., CLIM for (A), (B), and (F); 1940Cntl for (C); RCP4.5 for (D); and RCP8.5 for (E)]. The contour interval is 0.6 per season.

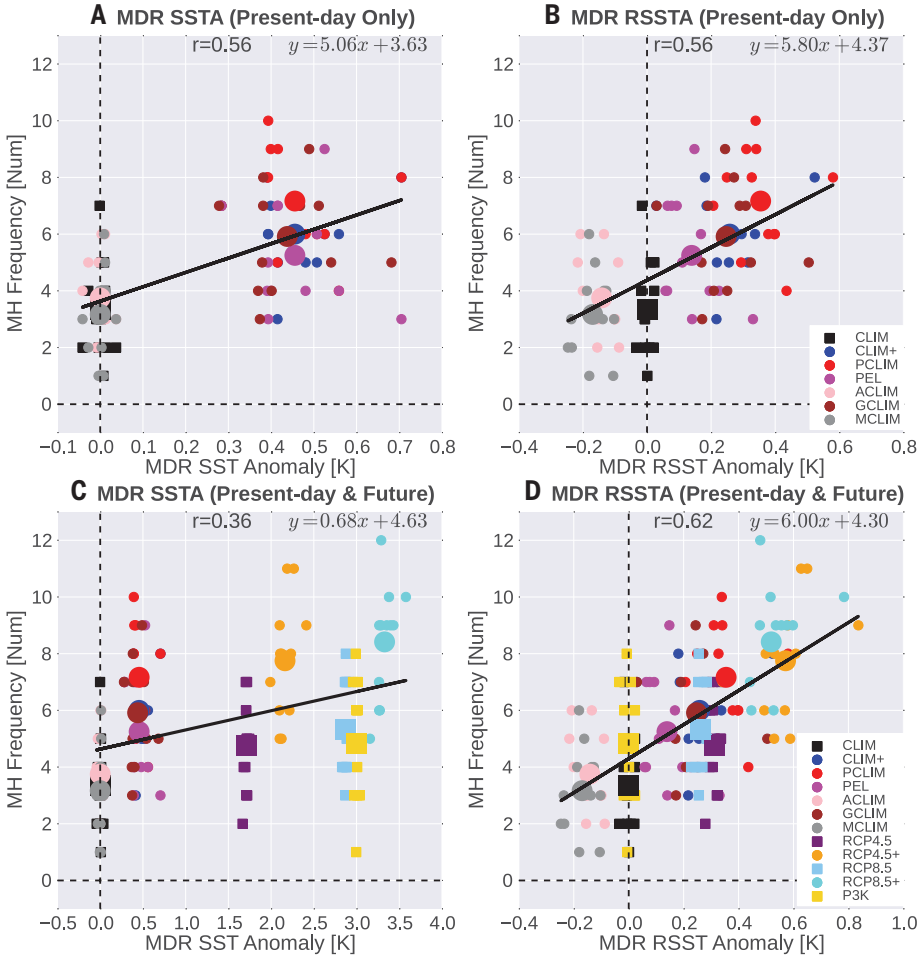

Fig. 5. Relationship between predicted MH frequency and prescribed MDR SSTA or RSSTA. (**A**) MH frequency and MDR SSTA for the present-day experiments. (**B**) As in (A) but for the MH frequency and MDR RSST (relative SST). (**C** and **D**) As in (A) and (B) but with the future experiments as well as the present-day experiments included. The small (large) symbols denote each ensemble member (the ensemble mean). The black line is the linear regression line. The correlation coefficient (r) and linear regression equation are displayed at the top of each panel.

anthropogenic aerosol forcing. To investigate the influence of aerosols on the MH frequency, we conducted an additional idealized seasonal nudging prediction, with settings to those of CLIM+, except that the estimated SSTA due to a reduced concentration of anthropogenic aerosols (fig. S8) was superimposed onto the CLIM+ SST (hereafter, AERO+; see supplementary method c). The AERO+ experiment did increase the MH frequency slightly (by +0.8) relative to the CLIM+ experiment (Fig. 3), qualitatively supporting the conclusion of previous studies (*25*–*27*), even for the MH frequency. However, the increase is not statistically significant (P value = 0.19). As discussed by Murakami *et al.* (*28*), the projected impact of aerosols on MH frequency may be underestimated in HiFLOR because the model may underestimate the radiative forcing by aerosols due to a lack of representation of the indirect effects of aerosols. Further refinement of the model's physics is necessary to better estimate the impact of aerosols on MH frequency.

Relative importance of relative SSTAs on active MH season

Previous studies (*29*, *30*) have reported the frequency of hurricanes (i.e., those weaker than MHs) to be positively correlated with the MDR SSTA (the SSTA in domain B in Fig. 1C; 10° to 25°N, 80° to 20°W), as well as the relative SSTA (RSSTA), which is defined as the difference between the mean SST over the MDR and the mean SST over the global tropics (30°S to 30°N). This is also true for MHs. The correlation coefficient between observed MH frequency and MDR SSTA (RSSTA) was +0.50 (+0.61) for the period 1979–2017. The standardized value for MH frequency for the 2017 summer season was 1.1 (0.8) standard deviations above its long-term mean (fig. S1). A recent study (*15*) also reported a positive correlation between the observed MH frequency and the RSSTA on the decadal time scale. However, it is uncertain whether these positive correlations will hold true for MHs in the future. The response of MHs to anthropogenic warming might differ from that of weaker storms because, as reported in several previous studies, the global number of weaker storms will likely decrease in a warmer environment in the future, whereas the number of intense storms will increase (*16*–*18*). Figure 5, A and B, shows a moderate and positive correlation of the predicted MH frequency with both the MDR SSTA and RSST, on the basis of a series of idealized nudging experiments in the present-day framework (the RCP experimental results are not included in these figure panels). The correlation (r) between the MH frequency and MDR SSTA was +0.56 and the slope of linear regression (hereafter, a) was +5.06 K^{-1}, similar to the values for the RSSTA (r = +0.56 and a = +5.80 K^{-1}). However, when we included the RCP experiments in this analysis, the values of r and a for the MDR SSTA dropped sharply from the original values (Fig. 5, A and C), whereas for RSSTA they remained almost the same (Fig. 5, B and D). To further clarify these relationships, we conducted an additional nudging experiment (P3K; see supplementary method c) with the CLIM SST plus a globally uniform +3 K (i.e., zero RSSTA change) with other settings identical to the RCP8.5 experiment. P3K showed a slight increase in MH frequency relative to CLIM (Fig. 3), but not as large as that of RCP8.5+, resulting in a lowering of the positive correlation between the MDR SSTA and MH frequency. Overall, our results support the hypothesis that the MH frequency over the North Atlantic is highly correlated with the RSST—at least with this model.

Discussions

Overall, the results from our series of idealized experiments show that the enhanced MH activity in the Atlantic in 2017 was mainly caused by the larger SSTA over the MDR relative to the rest of the global ocean, rather than by the moderate La Niña conditions. However, this does not mean that the MH frequency and spatial distribution in the Atlantic are always insensitive to the El Niño–Southern Oscillation (ENSO). As documented in previous studies (*19*, *31*), HiFLOR can capture the observed contrast in MH activity in the North Atlantic in different ENSO phases. We speculate that in 2017 the effect of the MDR SSTA was large enough to increase the MH activity regardless of the remote effects of any phase of ENSO. The higher tropical North Atlantic SSTA was possibly associated with a specific phase of natural variability, like the positive phase of the AMO or AMM. However, it is also possible that to some degree the 2017 SSTA contained the effects of anthropogenic forcing too, although we cannot separate the two factors at this moment. It also remains uncertain whether we will see more of these active hurricane seasons, like that of 2017, in the ensuing decades, despite the arguably strong indicator of having experienced two successive active MH seasons since 2016 (Fig. 1B). This is because a recent study (*15*) suggested a marked reduction in MHs since 2005 on the decadal time scale in association with a weakening of the Atlantic meridional overturning circulation (AMOC). Monitoring AMOC and RSST anomalies is key

to predicting the MH activity of the future, although, according to the moderate correlation in our study (r = +0.61) between the RSST anomaly and MH frequency in observations (fig. S1), the RSST anomaly is not the only factor determining the MH frequency in the North Atlantic. Further research is necessary to address the physical mechanisms underpinning highly active MH seasons.

REFERENCES AND NOTES

1. A. J. Willingham, "A look at four storms from one brutal hurricane season" (2017); www.cnn.com/2017/10/10/weather/hurricane-nate-maria-irma-harvey-impact-look-back-trnd/index.html.
2. K. Emanuel, *Proc. Natl. Acad. Sci. U.S.A.* **114**, 12681–12684 (2017).
3. T. Hall, K. Hereid, *Geophys. Res. Lett.* **42**, 3482–3485 (2015).
4. B. E. Hart, D. R. Chavas, M. P. Guishard, *Bull. Am. Meteorol. Soc.* **97**, 713–722 (2016).
5. E. Shuckburgh, D. Mitchell, P. Stott, *Weather* **72**, 353–354 (2017).
6. B. Resnick, "Hurricane season 2017: What the hell just happened?" (2017); www.vox.com/energy-and-environment/2017/10/25/16504488/hurricane-season-2017-what-the-hell.
7. S. B. Goldenberg, L. J. Shapiro, *J. Clim.* **9**, 1169–1187 (1996).
8. D. M. Smith *et al.*, *Nat. Geosci.* **3**, 846–849 (2010).
9. J. P. Kossin, *Nature* **541**, 390–393 (2017).
10. M. DeMaria, *J. Atmos. Sci.* **53**, 2076–2088 (1996).
11. R. L. Elsberry, R. A. Jeffries, *Mon. Weather Rev.* **124**, 1374–1387 (1996).
12. M. L. M. Wong, J. C. L. Chan, *J. Atmos. Sci.* **61**, 1859–1876 (2004).
13. T. L. Delworth, M. E. Mann, *Clim. Dyn.* **16**, 661–676 (2000).
14. D. J. Vimont, J. P. Kossin, *Geophys. Res. Lett.* **34**, L07709 (2007).
15. X. Yan, R. Zhang, T. R. Knutson, *Nat. Commun.* **8**, 1695 (2017).
16. T. R. Knutson *et al.*, *Nat. Geosci.* **3**, 157–163 (2010).
17. H. Murakami *et al.*, *J. Clim.* **25**, 3237–3260 (2012).
18. T. R. Knutson *et al.*, *J. Clim.* **28**, 7203–7224 (2015).
19. H. Murakami *et al.*, *J. Clim.* **28**, 9058–9079 (2015).
20. H. Murakami *et al.*, *J. Clim.* **29**, 7977–7989 (2016).
21. E. D. Maloney, D. L. Hartmann, *Science* **287**, 2002–2004 (2000).
22. P. J. Klotzbach, *J. Clim.* **23**, 282–293 (2010).
23. North American Multi-Model Ensemble (NMME), NMME relative forecast archive, Season 2 tmpsfc forecast; www.cpc.ncep.noaa.gov/products/NMME/archive/2017040800/current/tmpsfc_Seas2.html.
24. W. Duan, C. Wei, *Int. J. Climatol.* **33**, 1280–1292 (2013).
25. N. J. Dunstone, D. M. Smith, B. B. B. Booth, L. Hermanson, R. Eade, *Nat. Geosci.* **6**, 534–539 (2013).
26. M. Ting, S. J. Camargo, C. Li, Y. Kushnir, *J. Clim.* **28**, 3926–3942 (2015).
27. A. H. Sobel *et al.*, *Science* **353**, 242–246 (2016).
28. H. Murakami, G. A. Vecchi, S. Underwood, *Nat. Clim. Chang.* **7**, 885–889 (2017).
29. G. A. Vecchi, B. J. Soden, *Nature* **450**, 1066–1070 (2007).
30. G. A. Vecchi *et al.*, *J. Clim.* **26**, 5337–5357 (2013).
31. W. Zhang *et al.*, *J. Clim.* **29**, 1391–1415 (2016).
32. H. Murakami, B. Wang, T. Li, A. Kitoh, *Nat. Clim. Chang.* **3**, 749–754 (2013).

ACKNOWLEDGMENTS

We thank X. Yan, M. Bushuk, K. Gao, and two anonymous reviewers for suggestions and comments. **Funding:** H.M. prepared this report under awards NA14OAR4320106 (the Cooperative Institute for Climate Science) and NA14OAR4830101 (the Sandy Supplemental) from the National Oceanic and Atmospheric Administration, U.S. Department of Commerce. The statements, findings, conclusions, and recommendations are those of the authors and do not necessarily reflect the views of the National Oceanic and Atmospheric Administration or the U.S. Department of Commerce. **Author contributions:** H.M. designed the study, carried out the experiments, analyzed the results, and wrote the manuscript. R.G. carried out the retrospective and real-time seasonal forecasts. E.L analyzed the observed MH frequency and climate indices. R.G., T.L.D and P.-C.H. discussed the results with H.M. and made comments on the manuscript. **Competing interests:** The authors declare no competing interests. **Data and materials availability:** The source code of the climate model can be accessed at www.gfdl.noaa.gov/cm2-5-and-flor/. The predicted tropical cyclone tracks through the idealized experiments are available online at ftp://nomads.gfdl.noaa.gov/users/Hiroyuki.Murakami/GFDL-HiFLOR/2017MH/.

SUPPLEMENTARY MATERIALS

www.sciencemag.org/content/362/6416/794/suppl/DC1
Materials and Methods
Figs. S1 to S8
Tables S1 and S2
References (*33*–*44*)

22 March 2018; accepted 14 September 2018
Published online 27 September 2018
10.1126/science.aat6711

ORGANIC CHEMISTRY

Heterobiaryl synthesis by contractive C–C coupling via P(V) intermediates

Michael C. Hilton[1], Xuan Zhang[1]*, Benjamin T. Boyle[1]*, Juan V. Alegre-Requena[1], Robert S. Paton[1,2]†, Andrew McNally[1]†

Heterobiaryls composed of pyridine and diazine rings are key components of pharmaceuticals and are often central to pharmacological function. We present an alternative approach to metal-catalyzed cross-coupling to make heterobiaryls using contractive phosphorus C–C couplings, also termed phosphorus ligand coupling reactions. The process starts by regioselective phosphorus substitution of the C–H bonds para to nitrogen in two successive heterocycles; ligand coupling is then triggered via acidic alcohol solutions to form the heterobiaryl bond. Mechanistic studies imply that ligand coupling is an asynchronous process involving migration of one heterocycle to the ipso position of the other around a central pentacoordinate P(V) atom. The strategy can be applied to complex drug-like molecules containing multiple reactive sites and polar functional groups, and also enables convergent coupling of drug fragments and late-stage heteroarylation of pharmaceuticals.

Reactions that couple two aromatic rings to make biaryls are among the most widely used processes in the pharmaceutical industry (*1*, *2*). Coupling of pyridines and diazines results in heterobiaryls, a privileged pharmacophore found in commercial drugs as well as numerous therapeutic candidates, such as the examples shown in Fig. 1A (*3*–*5*). These heterocycles often play a key role in drug-receptor binding and impart other important properties such as net polarity, aqueous solubility, and resistance to oxidative metabolism. Most conceivable aryl-aryl couplings can be accomplished using metal-catalyzed cross-coupling reactions; these processes feature exceptional chemoselectivity, precise regioselectivity, and sufficient robustness to be applied to both drug discovery and manufacture (*6*–*8*). However, the same synthetic prowess is not transferable to heteroaryl-heteroaryl coupling, particularly for complex substrates. An alternative strategy that addresses the shortcomings in this fundamental bond construction would therefore offer new opportunities to incorporate heterobiaryls into therapeutic candidates.

For de novo synthesis of heterobiaryls, a schematic for metal-catalyzed cross-couplings is shown in Fig. 1B (*9*–*15*). A minimum of three steps are required, and there are challenges in the coupling step, such as catalyst poisoning and decomposition of starting materials (*16*). Furthermore, drug-like molecules and intermediates often have multiple reactive sites and a high proportion of polar functional groups, such as basic amines, that interfere with catalytic processes and cause a considerable number of them to fail (*15*, *17*). Another serious problem arises from the lack of methods to prepare the cross-coupling precursors. Although simple heteroaryl halides are commercially available or can be straightforwardly prepared, direct and selective halogenation of pyridine and diazine derivatives encountered during drug development remains an unsolved challenge (*18*, *19*). Similarly, synthesizing nucleophilic coupling partners such as heteroaryl boronic acids, stannanes, and organozinc or magnesium compounds is challenging, and they are often prepared from the corresponding heteroaryl halides to begin with (*20*). Cross-dehydrogenative couplings of heteroarenes have shown some promise but are currently limited to specific pyridine combinations and are not applicable in complex settings (*21*).

Reaction development

The limitations of current heterocycle coupling methods can potentially be overcome by contractive phosphorus C–C couplings, often termed phosphorus ligand coupling reactions; a test system is shown in Fig. 1C (*22*–*24*). The strategy does not rely on heteroaryl halides or partners such as boronic acids, but instead regioselectively substitutes the C–H bond in each heterocyclic coupling partner by successive C–P bond formations to produce a bis-azaarene phosphonium salt; phosphorus ligand coupling is then triggered to form the heterobiaryl bond via a P(V) intermediate. Heteroaryl-heteroaryl coupling has previously been observed at phosphorus centers, but an inability to transform a generic set of pyridines and diazine precursors into the required bis-azaarene phosphonium salts has restricted these processes to specialized cases (*25*–*29*). In our test system, stage A combined the first heterocycle, 2-phenylpyridine, with Tf_2O at low temperature to form an intermediate pyridinium triflyl salt (not shown); adding fragmentable phosphine **1** (prepared on large scale from diphenyl phosphine and methyl acrylate) (*30*) results in a para-selective reaction to form dearomatized intermediate **Int-I** (*31*–*37*). Two equivalents of DBU (1,8-diazabicyclo[5.4.0]undec-7-ene) eliminate first the triflyl anion to form phosphonium ion **Int-II**, and then methyl acrylate to form heteroaryl phosphine **2a** in good yield. Pyridine was chosen as the second coupling partner in stage B with phosphine **2a** as a nucleophile, resulting in bis-heteroaryl phosphonium salt **3a**, with complete regiocontrol. Several nucleophiles are known to initiate phosphorus ligand coupling, including alkoxides, Grignard reagents, and acidic alcohol solutions (*22*, *25*–*29*); for stage C, we found the latter to be most effective and two equivalents of HCl in EtOH at 80°C to be optimal, forming heterobiaryl **4a** in excellent yield with diphenylphosphine oxide as a by-product (see table S1). We did not observe products from heteroaryl-phenyl or phenyl-phenyl coupling, nor ethoxylation of either heterocycle, in this protocol.

Mechanistic investigation

To investigate the reasons for selective heterocycle-heterocycle coupling and the kinetics of the ligand-coupling process, we performed a series of experimental and computational studies. We hypothesized that ethanol attacks the phosphorus center and a P(V) species is formed. Subjecting salt **3a** to a solution of DCl in d_4-methanol results in successive shifts of pyridine proton resonances per equivalent of acid by ^{1}H NMR (nuclear magnetic resonance) and ^{31}P NMR spectroscopy, and indicates that both pyridines are protonated (see figs. S17 and S18). However, no P(V) intermediates were detected in a ^{31}P NMR study under the reaction conditions. Computational studies do predict that intramolecular ligand coupling occurs from P(V) intermediate **Int-III** in a stepwise fashion (see below) and that there is a substantial barrier-lowering effect ($\Delta G^{\ddagger}$) upon successive protonation of **Int-III** (Fig. 2A) (*38*). Transition state energies considerably favor pyridine-pyridine coupling over pyridine-phenyl coupling for each protonation state; ΔG^{react} values show that the process is similarly exergonic and irreversible in each case, reinforcing the conclusion that selective pyridine-pyridine coupling results from kinetic differences in the ligand-coupling transition state rather than thermodynamic factors. The intrinsic reaction coordinate (IRC; Fig. 2B) shows no involvement of alkoxy lone pairs and negligible changes to the other three equatorial P–C bonds. In the C–C bond-forming transition structure [**TS-I·2H**]$^{2+}$, a single P–C bond breaks, allowing one ligand to migrate to the ipso-carbon of another (Fig. 2C). The intermediate formed in this key step ([**Int-IV·2H**]$^{2+}$) is a dearomatized adduct characteristic of nucleophilic aromatic substitution, which is predicted to collapse irreversibly (ΔG = −39 kcal/mol) and with considerable ease (see figs. S9 to S11). This stepwise ligand coupling is therefore mechanistically distinct from the concerted cleavage of two σ-bonds during reductive elimination at, for example, Pd(II) or in dihydrogen formation from PH_5. This latter

[1]Department of Chemistry, Colorado State University, Fort Collins, CO 80523, USA. [2]Chemistry Research Laboratory, University of Oxford, Oxford OX1 3TA, UK.
*These authors contributed equally to this work.
†Corresponding author. Email: robert.paton@chem.ox.ac.uk (R.S.P.); andy.mcnally@colostate.edu (A.M.)

detail is important because concerted coupling of apical-equatorial substituents from a (D_{3h}) trigonal bipyramidal compound is symmetry-forbidden (fig. S6) (*24*): in contrast, this stepwise-coupling mechanism permits, and indeed favors, the migration of an apical ligand to an equatorial one ([**TS-I·2H**]$^{2+}$) (fig. S7).

The computed structures of P(V) intermediates, such as [**Int-III·2H**]$^{2+}$, are characterized by stronger, shorter ($d_{P–C(py)}$ = 1.86 Å) bonds to equatorial ligands and weaker, longer ($d_{P–C(py)}$ = 1.99 Å) bonds to those in apical positions. This is a result of three-center, four-electron bonding between the apical ligands and the central phosphorus atom. Accordingly, the relative stability of P(V) stereoisomeric forms can be readily predicted on the basis of each ligand's capacity to stabilize the buildup of electron density at the apical positions: σ-electron–withdrawing alkoxy and heteroaryl groups preferentially occupy the apical sites (fig. S5). Weaker and more polar apical P–L bonds favor migration in nucleophilic 1,2-rearrangements, in which an equatorial ligand acts as the electrophilic acceptor (fig. S7), leading to ligand coupling. Phenyl ligands are unfavorable for both donor and acceptor roles in ligand coupling: Apical positions (donors) favor more σ-electron–withdrawing substituents, whereas pyridyl substituents are superior acceptors. This explains the complete absence of biphenyl and phenyl-heterobiaryl coupled products. N-protonation decreases the activation barrier considerably, from 30 to 20 kcal/mol, increasing the electrophilicity of the equatorial pyridyl group. Successive N-protonation further reduces the activation barrier to 14 kcal/mol by increasing the σ-electron–withdrawing power of the axial donor ligand and weakening the P–C bond ($d_{P–C(py)}$ increases from 1.95 Å in [**Int-III·H**]$^{+}$ to 1.99 Å in [**Int-III·2H**]$^{2+}$), whereas equatorial P–C bonds are largely unchanged ($d_{P–C(py)}$ is 1.87 Å in [**Int-III·H**]$^{+}$ and 1.86 Å in [**Int-III·2H**]$^{2+}$). Computed values of C–O coupling from **Int**-[**Int-III·2H**]$^{2+}$ are also disfavored relative to pyridine-pyridine coupling ($\Delta G^{\ddagger(C–O)}$ = 18 kcal/mol versus $\Delta G^{\ddagger(py\text{-}py)}$ = 14 kcal/mol; fig. S8) (*31*).

Figure 2D examines the effect of phosphorus electrophilicity on the rate of heterobiaryl formation. The low energy barrier for ligand coupling in [**Int-III·2H**]$^{2+}$ implies that the rate-determining step precedes this event and involves attack of the alcoholic solvent at the phosphonium center. We prepared a set of salts with substituted aryl groups that would change the electrophilicity at

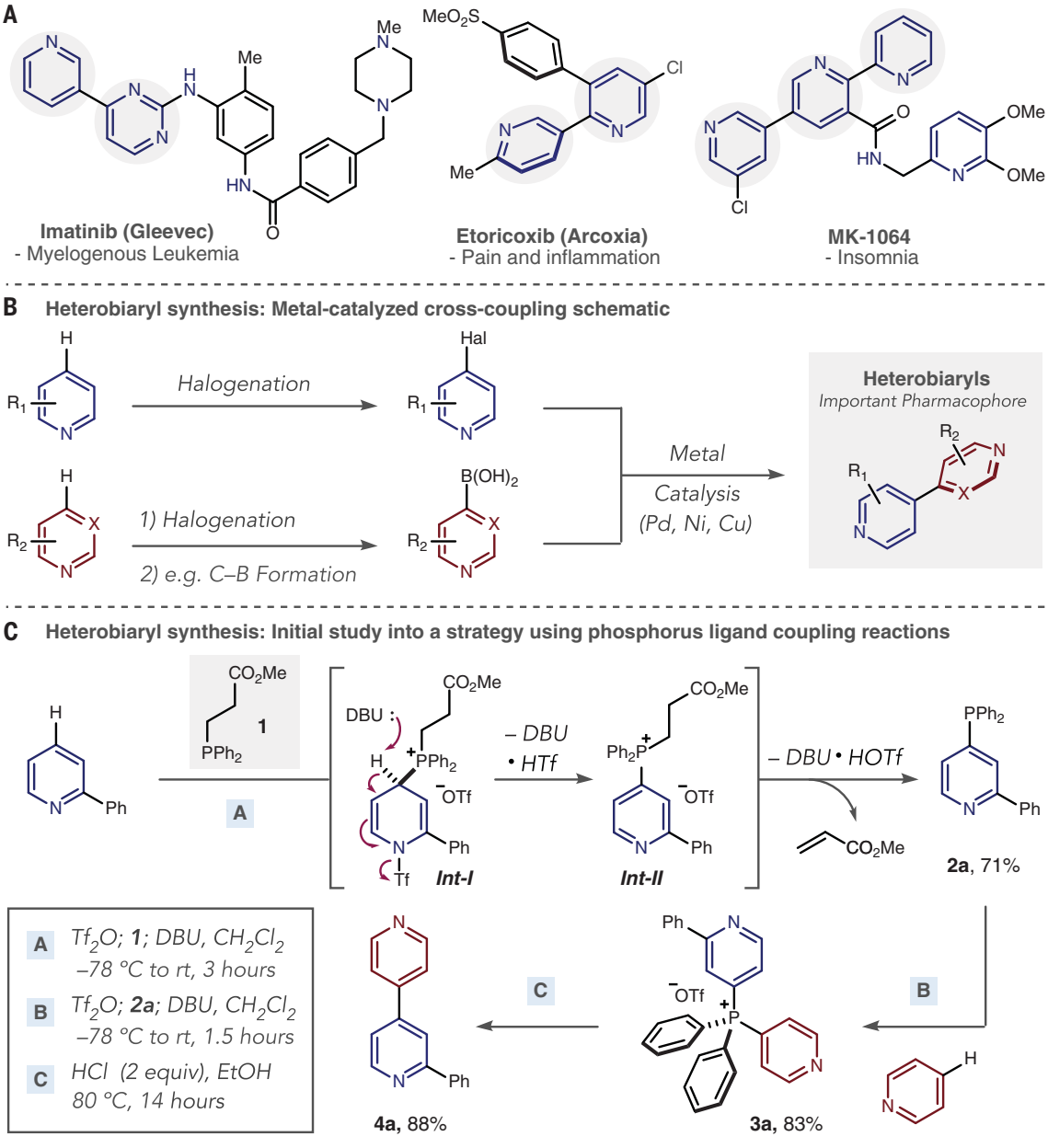

Fig. 1. Important heterobiaryl-containing drugs and synthetic strategies. (**A**) Heterobiaryls in drugs. (**B**) Heterobiaryls via metal-catalyzed cross-coupling reactions. R denotes a general organic group; Hal, halogen substituent. (**C**) Test system for heterobiaryl synthesis via phosphorus ligand coupling reactions. Ph, phenyl; Me, methyl; Et, ethyl; Tf, trifluoromethylsulfonyl; DBU, 1,8-diazabicyclo[5.4.0]undec-7-ene; rt, room temperature.

phosphorus; rate data show faster heterobiaryl formation as the electrophilicity of the phosphonium increases, in line with the above hypothesis. Further experimental verification of the low barriers for ligand coupling is shown in Fig. 2E. Acidic alcohol solutions are inefficient for heterobiaryl formation at lower temperatures (table S1); however, when ethoxide is used as a nucleophile for facile addition to the phosphonium ion (fig. S24), heterobiaryl synthesis occurs in minutes at room temperature, with trace amounts of C–O coupling also observed. Substantial amounts of products resulting from protiodephosphination are formed under these conditions, making this protocol less practical than that under acidic conditions.

Substrate scope exploration

We next selected a set of pyridines and diazines to examine which substitution patterns and functional groups could be tolerated in the ligand coupling process (Fig. 3). The reaction is completely selective for the 4-position of pyridines in the vast majority of cases studied, unless a 4-substituent is present, which switches selectivity to the 2-position. A variety of 4,4′-bipyridines are accessible using this strategy (**4b**–**4f**); functional groups such as esters, trifluoromethyl groups, and methoxy groups are accommodated, as are halides that would normally be active in metal-catalyzed reactions. Substituents can be present at the 2- or 3-positions of pyridines, and example **4e** shows that a 2-position substituent is not a requirement (see below). A fluorinated 2,4′-quinoline-pyridine was also synthesized by phosphorus ligand coupling (**4g**) (*39*). Examples of 2,2′-systems, **4h** and **4i**, showcase an alternative to Suzuki couplings, where 2-pyridyl and quinolyl boronic acids often decompose during metal-catalyzed reactions (*16*). Pyrimidine- and pyrazine-containing heterobiaryls **4j** and **4k** were formed via the three-step sequence, with lower yields in the coupling step relative to pyridine examples.

Reaction guidelines

During these studies, we have established a general set of reaction guidelines and limitations. First, when coupling 2-substituted pyridines to 3-substituted pyridines, it is important to perform the salt-forming sequence in the correct order (Fig. 3). Taking heterobiaryl **4b** as a representative example, if heteroaryl phosphine **2b′** is used instead in stage B, then salt **3b** is not formed. We believe that a biased Tf-salt equilibrium rapidly develops, and pyridinium-phosphine [**2b′-Tf**]$^+$ is favored on steric grounds; the 2-substituted pyridine is then not activated for nucleophilic addition, and the desired salt is not formed (fig. S25). Instead, the 2-substituted pyridine should be converted into the corresponding phosphine

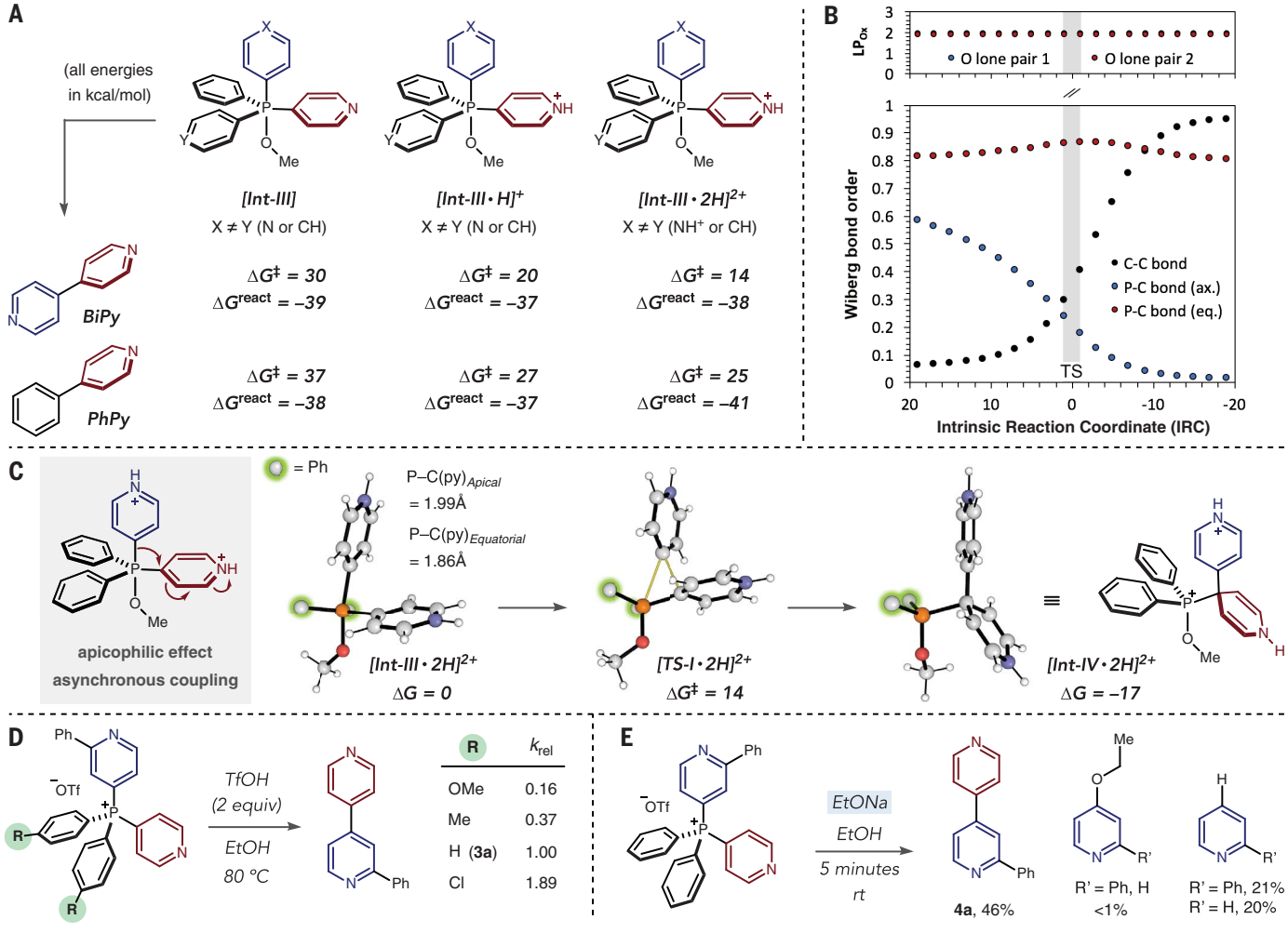

Fig. 2. Computational and experimental investigation of phosphorus ligand coupling. (**A**) Biaryl-coupling activation barriers [coupled cluster/density functional theory SMD-DLPNO-CCSD(T)/cc-pV(DT)Z//ωB97XD/6-31+G(d), kcal/mol] decrease upon protonation and consistently favor heterobiaryl formation. Py, pyridine. (**B**) Computed bond orders show a single (apical) P–C(py) bond breaking along the reaction coordinate, with little involvement of oxygen lone pairs. LP_{Ox}, number of electrons in each oxygen lone pair. (**C**) Optimized structures for [**Int-III·2H**]$^{2+}$, [**TS-I·2H**]$^{2+}$, and [**Int-IV·2H**]$^{2+}$ show stepwise apical-equatorial ligand coupling. (**D**) A kinetic study indicates that alcohol addition is rate-limiting. TfOH was used in place of HCl because of poor solubility of aryl derivatives. Yields after complete consumption of the phosphonium salts were approximately the same in each case (89 to 94%). (**E**) Room-temperature coupling using ethoxide as a nucleophile.

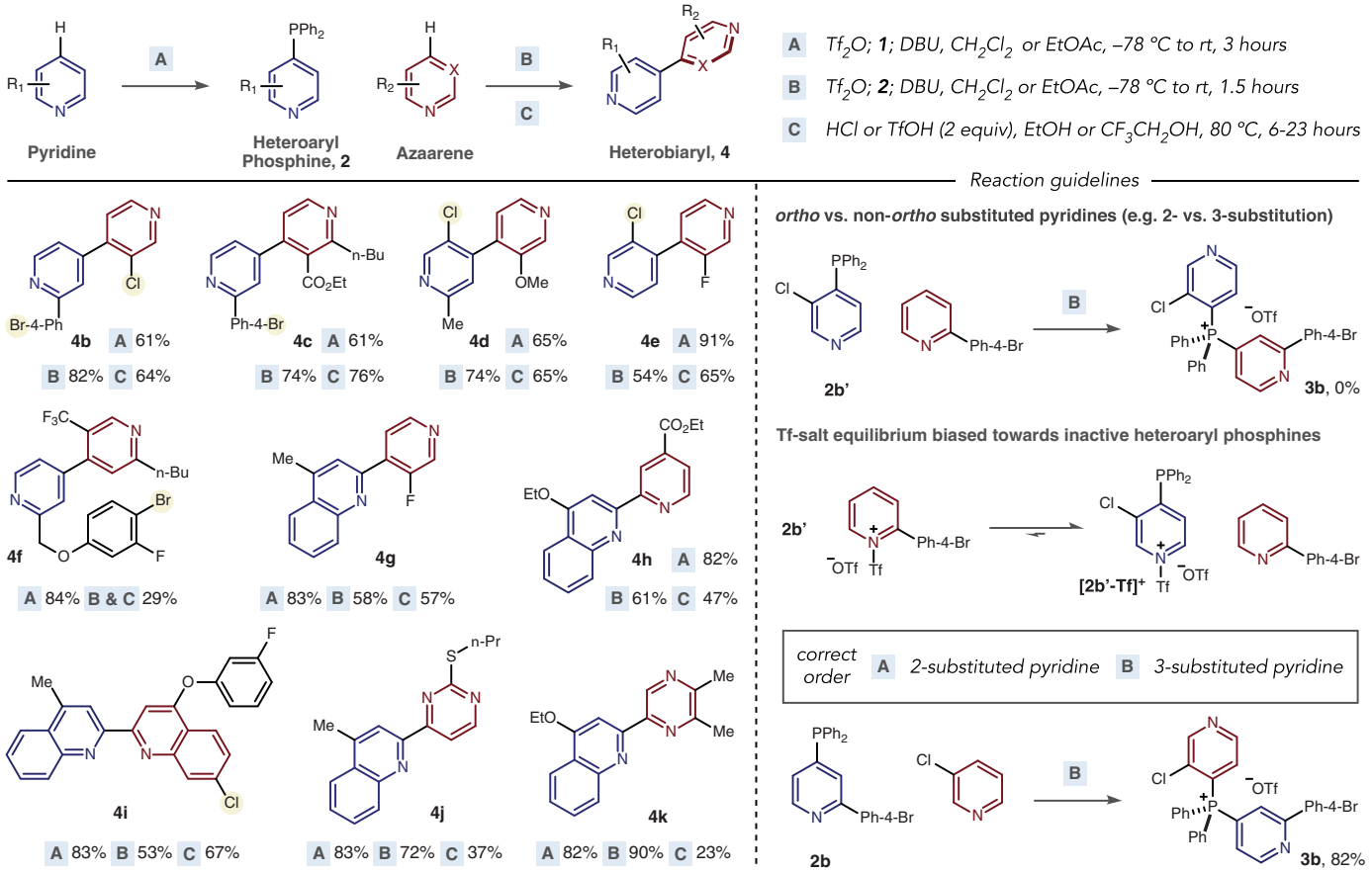

Fig. 3. Azaarene scope and guidelines for phosphonium salt formation. Yields of isolated products after each stage are shown. *n*-Bu, normal butyl group; *n*-Pr, normal propyl group. Reaction guidelines are shown for phosphonium salt formation involving ortho and non-ortho substituted pyridines as partners. Further details of challenges and limitations are highlighted in fig. S25.

and used as a nucleophile with the 3-substituted pyridine in stage B. Second, problematic substrates for heteroaryl phosphine and salt formation include pyridines with 2-trifluoromethyl groups, 4-alkyl or aryl substituents, and 2,6-disubstituted pyridines. In general, pyridines and diazines with more than two electron-withdrawing groups or electron-donating groups can result in low yields or no phosphonium salt formation. During ligand coupling, we have observed that pyridines substituted with bromides and iodides can be dehalogenated, that 2-chloro- or 2-fluoropyridines are not successful, and that 2-methoxypyridines proceed with slower rates. For pyridines containing electron-withdrawing groups, using EtOH and HCl can result in ethoxylation. Changing the acid to TfOH avoids this problem and leads us to believe that ethoxylation results from chlorination followed by ethoxylation via nucleophilic aromatic substitution. Trifluoroethanol is preferred when molecules contain functional groups such as amides and esters that are susceptible to ethanolysis. In general, one equivalent of acid per basic nitrogen is optimal (see below).

Application to complex intermediates

Our attention then turned to ligand couplings involving complex azaarenes (Fig. 4). Convergent couplings of pyridine-containing fragments were first examined; these molecules are representative of drug leads, which are promising candidates for a therapeutic target but have suboptimal pharmacokinetic and pharmacodynamic properties (*40*). A convergent coupling strategy would enable rapid access to complex heterobiaryls from compounds common in pharmaceutical libraries (*41*, *42*). Four examples in Fig. 4 are shown where the corresponding halide precursors are not commercially available or would be challenging to prepare (**4l**–**4o**). Heterobiaryl bonds are formed with precise regioselectivity, and the presence of additional saturated and unsaturated nitrogen heterocycles is tolerated in this approach. Three or four equivalents of acid are used in the coupling step in these cases to ensure adequate reaction rates.

Next, we investigated whether the ligand-coupling strategy could be applied to advanced intermediates in drug development. Success in this endeavor would offer distinct strategies to introduce heterobiaryls into complex molecules and alleviate concerns over metal contamination in subsequent biological testing. To demonstrate the feasibility of this approach, we chose a set of existing drug molecules with diverse structures, substitution patterns, and functional groups (*43*).

The use of previously synthesized heteroaryl phosphines (Fig. 4) shows that heteroarylation is possible in these complex systems with complete control of regioselectivity and site selectivity. Chlorphenamine, a common antihistamine, and loratadine, an allergy medicine, are competent substrates for this protocol, with the resulting heterobiaryls isolated in good overall yields (**4p** and **4q**) that again highlight how halides can be tolerated during the coupling procedure. Vismodegib was converted into a 2,4′-quinoline-pyridine system in moderate yield (**4r**). A widely applied fungicide, quinoxyfen, was also compatible with the reaction protocol (**4s**). Etoricoxib and imatinib are challenging examples because they contain multiple reactive sites (*34*). The structural features in etoricoxib enable selective transformation of the 2,5-disubstituted pyridine (**4t**), and heteroarylation of the pyridine occurs selectively over the pyrimidine in imatinib to form **4u**.

Outlook

This phosphorus ligand coupling method overcomes major limitations of metal-catalyzed approaches by virtue of its compatibility with polar functionalities found in drug-like molecules and its circumvention of preformed heteroaryl halides and boronic acids. As well as

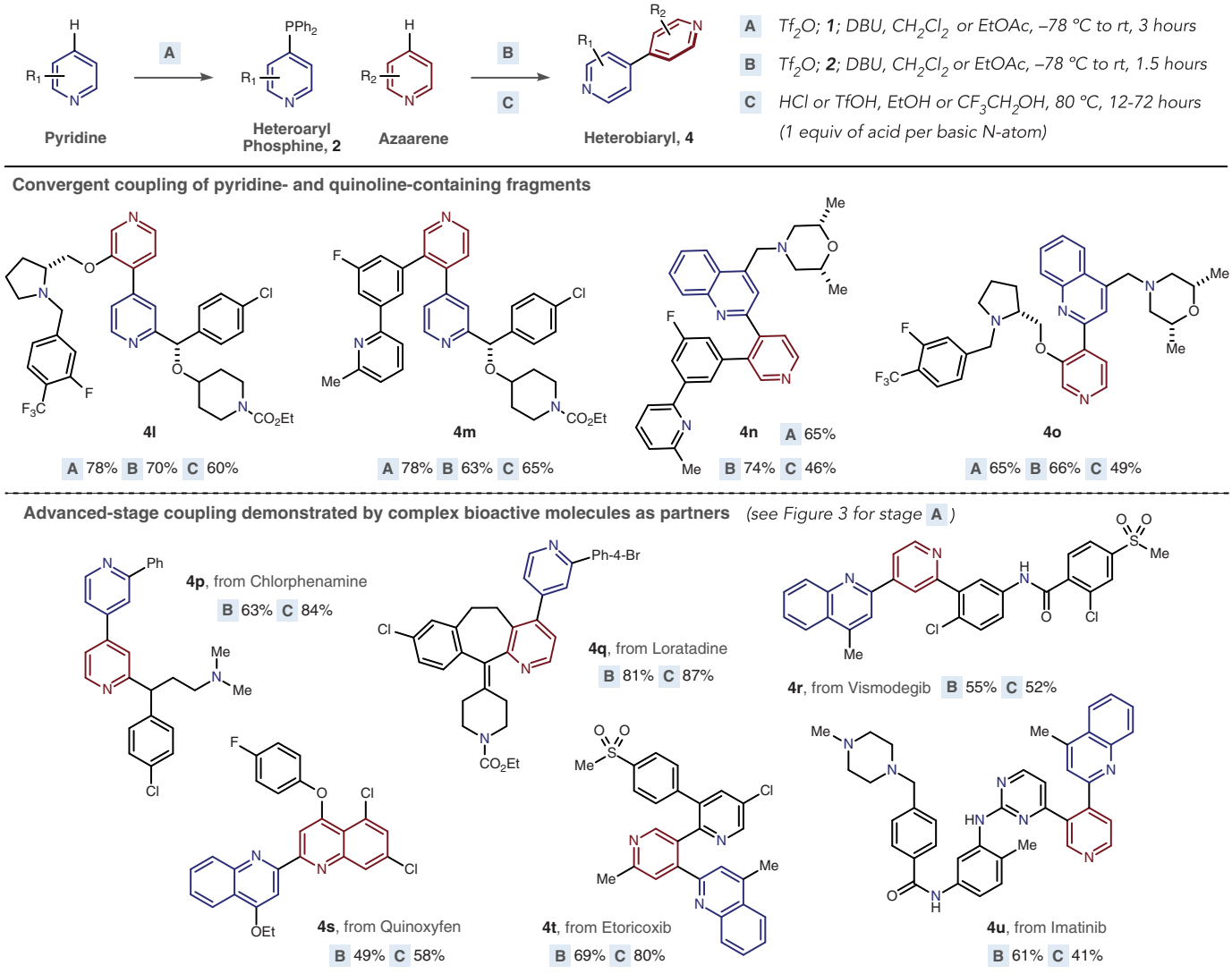

Fig. 4. Heterobiaryl synthesis in complex molecules. Yields of isolated products after each stage are shown. Further examples of advanced stage couplings are shown in fig. S26.

transforming building block compounds, convergent coupling of drug fragments and heteroarylation of complex pharmaceuticals were demonstrated. The protocol uses readily available reagents under simple conditions and is immediately applicable in medicinal chemistry.

REFERENCES AND NOTES

1. D. G. Brown, J. Boström, *J. Med. Chem.* **59**, 4443–4458 (2016).
2. S. D. Roughley, A. M. Jordan, *J. Med. Chem.* **54**, 3451–3479 (2011).
3. R. Capdeville, E. Buchdunger, J. Zimmermann, A. Matter, *Nat. Rev. Drug Discov.* **1**, 493–502 (2002).
4. A. J. Roecker *et al.*, *ChemMedChem* **9**, 311–322 (2014).
5. S. D. Martina, K. S. Vesta, T. L. Ripley, *Ann. Pharmacother.* **39**, 854–862 (2005).
6. M. L. Crawley, B. M. Trost, *Applications of Transition Metal Catalysts in Drug Discovery and Development: An Industrial Perspective* (Wiley, 2012), pp. 25–96.
7. A. de Meijere, F. Diederich, *Metal-Catalyzed Cross-Coupling Reactions* (Wiley-VCH, ed. 2, 2004).
8. J. Hassan, M. Sévignon, C. Gozzi, E. Schulz, M. Lemaire, *Chem. Rev.* **102**, 1359–1470 (2002).
9. L.-C. Campeau, K. Fagnou, *Chem. Soc. Rev.* **36**, 1058–1068 (2007).
10. D. Zhao, J. You, C. Hu, *Chem. Eur. J.* **17**, 5466–5492 (2011).
11. K. L. Billingsley, K. W. Anderson, S. L. Buchwald, *Angew. Chem. Int. Ed.* **45**, 3484–3488 (2006).
12. N. Kudo, M. Perseghini, G. C. Fu, *Angew. Chem. Int. Ed.* **45**, 1282–1284 (2006).
13. A. S. Guram *et al.*, *J. Org. Chem.* **72**, 5104–5112 (2007).
14. U. Kiehne, J. Bunzen, A. Lützen, *Synthesis* 1061–1069 (2007).
15. T. Markovic, B. N. Rocke, D. C. Blakemore, V. Mascitti, M. C. Willis, *Chem. Sci.* **8**, 4437–4442 (2017).
16. P. A. Cox *et al.*, *J. Am. Chem. Soc.* **139**, 13156–13165 (2017).
17. D. C. Blakemore *et al.*, *Nat. Chem.* **10**, 383–394 (2018).
18. J. A. Joule, K. Mills, *Heterocyclic Chemistry* (Wiley-Blackwell, ed. 5, 2013).
19. M. R. Grimmett, *Adv. Heterocycl. Chem.* **58**, 271–345 (1993).
20. M. A. Larsen, J. F. Hartwig, *J. Am. Chem. Soc.* **136**, 4287–4299 (2014).
21. H.-Q. Do, O. Daugulis, *J. Am. Chem. Soc.* **133**, 13577–13586 (2011).
22. J.-P. Finer, in *Ligand Coupling Reactions with Heteroaromatic Compounds, Vol. 18* (Pergamon, 1998), chap. 4.
23. K. D. Reichl, A. T. Radosevich, *Chem. Commun.* **50**, 9302–9305 (2014).
24. R. Hoffmann, J. M. Howell, E. L. Muetterties, *J. Am. Chem. Soc.* **94**, 3047–3058 (1972).
25. F. G. Mann, J. Watson, *J. Org. Chem.* **13**, 502–531 (1948).
26. G. R. Newkome, D. C. Hager, *J. Am. Chem. Soc.* **100**, 5567–5568 (1978).
27. Y. Uchida, K. Onoue, N. Tada, F. Nagao, S. Oae, *Tetrahedron Lett.* **30**, 567–570 (1989).
28. Y. Uchida, H. Kozawa, S. Oae, *Tetrahedron Lett.* **30**, 6365–6368 (1989).
29. Y. Uchida, N. Echikawa, S. Oae, *Heteroatom Chem.* **5**, 409–413 (1994).
30. F. Alonso, Y. Moglie, G. Radivoy, M. Yus, *Green Chem.* **14**, 2699–2702 (2012).
31. M. C. Hilton, R. D. Dolewski, A. McNally, *J. Am. Chem. Soc.* **138**, 13806–13809 (2016).
32. X. Zhang, A. McNally, *Angew. Chem. Int. Ed.* **56**, 9833–9836 (2017).
33. J. L. Koniarczyk, D. Hesk, A. Overgard, I. W. Davies, A. McNally, *J. Am. Chem. Soc.* **140**, 1990–1993 (2018).
34. R. D. Dolewski, P. J. Fricke, A. McNally, *J. Am. Chem. Soc.* **140**, 8020–8026 (2018).
35. R. G. Anderson, B. M. Jett, A. McNally, *Angew. Chem. Int. Ed.* **57**, 12514–12518 (2018).
36. E. Anders, F. Markus, *Tetrahedron Lett.* **28**, 2675–2676 (1987).
37. P. S. Fier, *J. Am. Chem. Soc.* **139**, 9499–9502 (2017).
38. Both DLPNO-CCSD(T)/cc-pV(DT)Z and ωB97XD/def2-QZVPP results are in close-agreement. Full details in the supplementary materials.
39. O. Afzal *et al.*, *Eur. J. Med. Chem.* **97**, 871–910 (2015).
40. R. B. Silverman, M. W. Holladay, in *The Organic Chemistry of Drug Design and Drug Action* (Academic Press, ed. 3, 2014), chap. 2.

41. D. A. Erlanson, S. W. Fesik, R. E. Hubbard, W. Jahnke, H. Jhoti, *Nat. Rev. Drug Discov.* **15**, 605–619 (2016).
42. C. W. Murray, D. C. Rees, *Nat. Chem.* **1**, 187–192 (2009).
43. T. Cernak, K. D. Dykstra, S. Tyagarajan, P. Vachal, S. W. Krska, *Chem. Soc. Rev.* **45**, 546–576 (2016).

ACKNOWLEDGMENTS

Funding: Supported by startup funds from Colorado State University and by NIH award R01 GM124094-01 (A.M., M.C.H., X.Z., and B.T.B.). We acknowledge the RMACC Summit supercomputer, supported by NSF grants ACI-1532235 and ACI-1532236, the University of Colorado Boulder, Colorado State University, and the Extreme Science and Engineering Discovery Environment (XSEDE) through allocations TG-CHE180006 and TG-CHE180056. XSEDE is supported by NSF grant ACI-1548562. **Author contributions:** M.C.H., X.Z., and B.T.B. performed the experimental work; the computational studies were performed by J.V.A.-R. and R.S.P.; all authors contributed to the design of the experimental and computational work and to data analysis, discussed the results, and commented on the manuscript; and A.M. and R.S.P. wrote the manuscript. **Competing interests:** The authors declare no competing interests; **Data and materials availability:** All data are available in the main text or the supplementary materials.

SUPPLEMENTARY MATERIALS

www.sciencemag.org/content/362/6416/799/suppl/DC1
Materials and Methods
Figs. S1 to S26
Tables S1 to S22
NMR Spectra
References (*44*–*97*)
Movies S1 and S2

8 January 2018; resubmitted 3 July 2018
Accepted 25 September 2018
10.1126/science.aas8961

REPORT

POLYMERS

Templated nanofiber synthesis via chemical vapor polymerization into liquid crystalline films

Kenneth C. K. Cheng[1,2]*†, Marco A. Bedolla-Pantoja[3]*, Young-Ki Kim[3,4]*, Jason V. Gregory[1,5], Fan Xie[1,5], Alexander de France[1,5], Christoph Hussal[6], Kai Sun[2], Nicholas L. Abbott[3,4]‡, Joerg Lahann[1,2,5,6]‡

Extrusion, electrospinning, and microdrawing are widely used to create fibrous polymer mats, but these approaches offer limited access to oriented arrays of nanometer-scale fibers with controlled size, shape, and lateral organization. We show that chemical vapor polymerization can be performed on surfaces coated with thin films of liquid crystals to synthesize organized assemblies of end-attached polymer nanofibers. The process uses low concentrations of radical monomers formed initially in the vapor phase and then diffused into the liquid-crystal template. This minimizes monomer-induced changes to the liquid-crystal phase and enables access to nanofiber arrays with complex yet precisely defined structures and compositions. The nanofiber arrays permit tailoring of a wide range of functional properties, including adhesion that depends on nanofiber chirality.

Surfaces decorated with oriented arrays of fibers are ubiquitous in the natural world because they can provide functions such as sensing [hair cells (*1*)], thermal insulation [polar bear fur (*2*)], enhanced mass transport [microtubules (*3*)], extreme wetting properties [lotus leaf (*4*)], and reversible adhesion [gecko foot (*5*)]. However, re-creation of these functions in synthetic materials requires multiscale engineering of the composition, shape, and morphology of individual fibers, as well as control of higher-order organization of fibers into arrays. We address this challenge by building from studies reported in 1916 by T. Svedberg (*6*), who used the long-range molecular order and fluidity inherent to liquid crystals (LCs) to control chemical reactions, principles that have since been exploited in a wide range of transformations based on unimolecular reactions (*7*), molecular self-assembly (*8*), or polymerizations (*9*, *10*). A key limitation of LC-templated polymerization, however, has been perturbation of the LC phase by monomers that are dissolved into the LC before the polymerization and then consumed during polymerization (*9*, *10*).

Chemical vapor polymerization (CVP) is a versatile process that is compatible with a range of polymerization modes (Fig. 1A), including reaction pathways using [2.2]paracyclophanes (*11*–*13*) (Gorham process) or halogenated xylene precursors (Gilch process) (*14*, *15*) and free-radical ring-opening copolymerization (ROP) using 5,6-benzo-2-methylene-1,3-dioxepane and [2.2]paracyclophanes (*16*). CVP is widely used for fabrication of consumer products (e.g., electronics and packaging) because it enables rapid and inexpensive conformal coating of large surface areas with polymer films (*12*). Whereas past studies used CVP to form continuous

[1]Biointerfaces Institute, University of Michigan, Ann Arbor, MI, USA. [2]Department of Materials Science and Engineering, University of Michigan, Ann Arbor, MI, USA. [3]Department of Chemical and Biological Engineering, University of Wisconsin–Madison, Madison, WI, USA. [4]Robert Frederick Smith School of Chemical and Biomolecular Engineering, Cornell University, Ithaca, NY, USA. [5]Department of Chemical Engineering, University of Michigan, Ann Arbor, MI, USA. [6]Institute of Functional Interfaces, Karlsruhe Institute of Technology, Karlsruhe, Germany.
*These authors contributed equally to this work.
†Present address: IBM Research, Albany, NY, USA.
‡Corresponding author. Email: nabbott@cornell.edu (N.L.A.); lahann@umich.edu (J.L.)

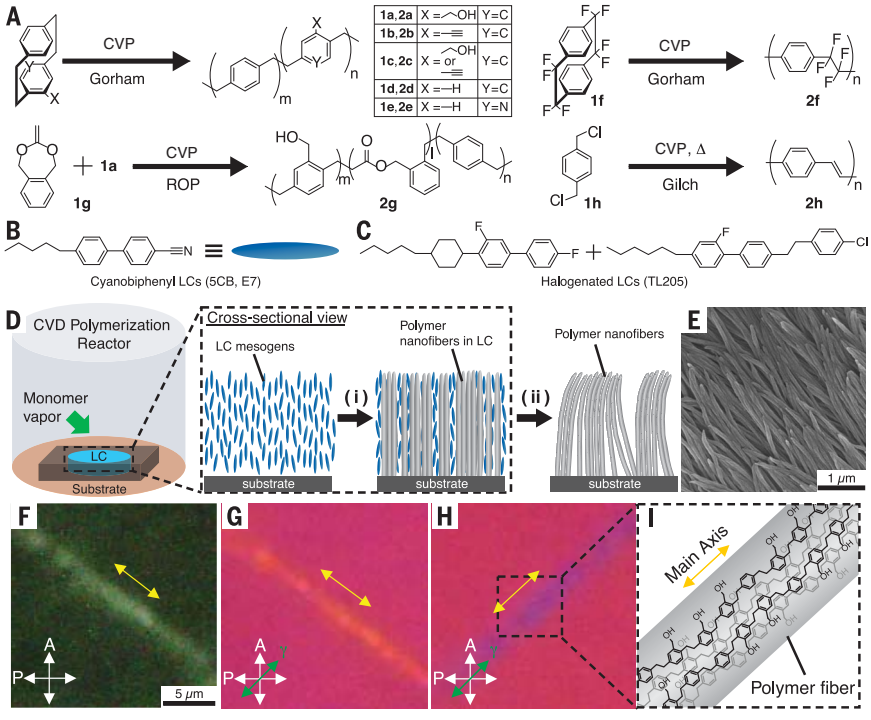

Fig. 1. Templated synthesis of nanofiber arrays via CVP into anisotropic media. (**A**) CVP of **1a** to **1h** yields polymers **2a** to **2h**. m, n, and l: copolymer repeat units; Δ: 250°C. (**B** and **C**) Representative chemical structures of cyanobiphenyl-based (5CB and E7) (B) and halogenated (TL205) (C) LCs. (**D**) Fabrication of polymer nanofibers via CVP into a LC phase aligned perpendicular to the substrate. (i) CVP; (ii) LC removal. (**E**) Scanning electron microscopy (SEM) images of nanofibers polymerized from **1a** (10 mg) in 5CB. After the nanofiber synthesis, the LC template was removed. (**F**) Optical micrograph (crossed polars) of a nanofiber. Orientations of the analyzer (A) and polarizer (P) are shown in the white double-arrow cross. The yellow double arrow indicates the main axis of the nanofiber. (**G** and **H**) Micrographs (crossed polars) of the nanofiber with a quarter-wave plate with its slow axis (γ, green double arrow) perpendicular (G) or parallel (H) to the fiber axis; lower-order interference colors [yellow in (G)] indicate a decrease in retardance. (**I**) Analysis of interference colors of the nanofiber in (G) and (H) indicates that the polymer chains are aligned along the fiber axis.

polymeric films on surfaces (*11*–*16*), we found that CVP of compound **1a** into micrometer-thick supported films of nematic LCs (Fig. 1, B and C) resulted in the formation of surfaces decorated with aligned arrays of nanofibers (Fig. 1, D and E). When nematic 4′-pentyl-4-biphenylcarbonitrile (5CB) was anchored on a silane-functionalized glass surface in a perpendicular orientation (i.e., homeotropic anchoring, Fig. 1D), the nanofibers were straight and aligned perpendicular to the surface. Removal of the LC [confirmed by Fourier transform infrared (FTIR) spectroscopy and solid-state ^{13}C nuclear magnetic resonance (NMR) spectroscopy, figs. S1 and S2] revealed that the nanofibers were made of insoluble polymer, were anchored at one end to the surface, and were structurally amorphous (fig. S3) yet optically birefringent, as confirmed by cross-polarized light microscopy (Fig. 1F). Insertion of a quarter-wave plate between crossed polarizers (Fig. 1, G and H) revealed that the refractive index was greatest along the fiber axis, consistent with electron diffraction patterns (fig. S3B), indicating alignment of polymer chains along the main axis of the nanofibers (Fig. 1I) (*17*).

CVP into films that lacked fluidity (crystalline solid 5CB, Fig. 2A) or long-range order (isotropic liquid 5CB, Fig. 2C; or silicone oil, Fig. 2D) did not yield nanofibers, indicating that long-range order and fluidity are both necessary requirements for the shape-controlled synthesis of nanofiber arrays (Fig. 2B). Replacement of 5CB with nematic E7 (a mixture of cyanobiphenyls, Fig. 1B), TL205 (a mixture of halogenated molecules, Fig. 1C), or other nematic LCs (fig. S4) yielded organized assemblies of nanofibers with well-defined yet distinct diameters (D) of 142 ± 11 nm in 5CB, 85 ± 9 nm in E7, and 69 ± 7 nm in TL205 (Fig. 2E). We hypothesized that the nanofiber diameter is controlled by the extrapolation length ξ, which is defined as K/W, where K is the average Frank elastic constant for splay and bend of the LC and W is the surface anchoring energy density. If an inclusion (here, nanofiber) in a LC grows to a size that exceeds ξ, the orientation-dependent interfacial energy associated with interaction of the LC with the surface of the inclusion (WD^2, where diameter D is the inclusion size) exceeds the energetic cost of elastic deformation of the LC (KD), and the LC will elastically deform around the inclusion (*18*, *19*). We tested the hypothesis that $D \approx K/W$ by using literature values of K at temperature (T) = 25°C (*18*, *20*) and our experimental values of D to calculate W (Fig. 2E). Calculated values of W were ~10^{-4} J/m^2 (*21*), with $W_{TL205} > W_{E7} > W_{5CB}$, a ranking that is consistent with (i) the theoretical prediction that $W \propto (T_{NI} - T)^{2\beta}$, where the material constant β = 0.4 to 0.5 (*22*, *23*) and T_{NI} is the nematic-isotropic phase-transition temperature of the LCs (Fig. 2E), and (ii) independent experiments that measured the relative values of W of these LCs (fig. S5). We also found the average diameters of the nanofibers to depend on the temperature of the LC during CVP. For example, D increased with T (Fig. 2E and fig. S6), as theoretically predicted by $\xi = K/W \propto (T_{NI} - T)^{-\beta}$ (*22*, *23*). Overall, these results are consistent with a mechanism of growth in which the elastic energy of the LC defines the nanofiber diameter (via ξ) and promotes preferential growth of the nanofibers along the alignment direction of the LCs.

We performed CVP of **1a** using homeotropically oriented E7 films with thicknesses ranging from 5 to 22 μm and found that the lengths of the fibers closely matched the LC film thicknesses (Fig. 2F). The result confirms growth of the nanofibers along the LC (figs. S7 and S8). We also found that monomers with a wide range of chemical functional groups could be polymerized in LCs by CVP (Gorham process), yielding (i) ethynyl-functionalized nanofibers

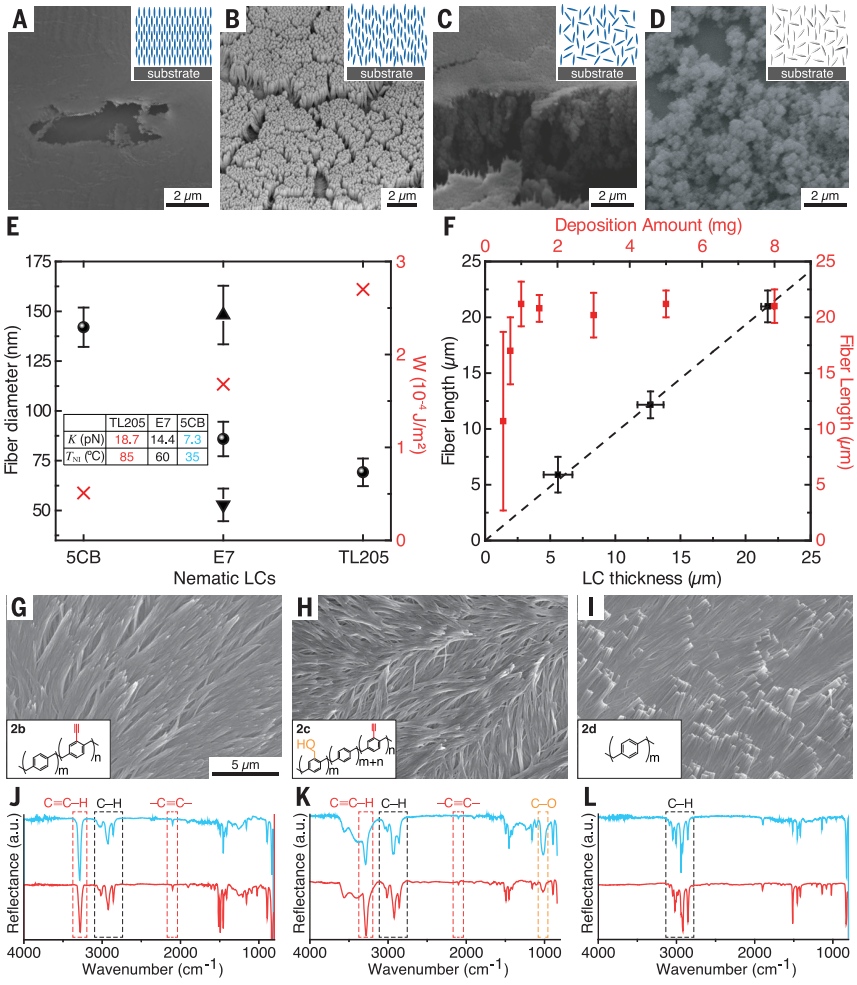

Fig. 2. Templated CVP of nanofibers with precise lengths, diameters, and surface chemistries. (**A** to **D**) SEM images of nanofibers formed by CVP of **1a** (10 mg) with the indicated templates (see insets): crystalline 5CB at 13°C (A), nematic 5CB at 25°C (B), isotropic 5CB at 37°C (C), and isotropic silicone oil at 25°C (D). The LC thickness was 21.7 ± 0.5 μm. (**E**) Nanofiber diameters (left axis) obtained by CVP of **1a** (6 mg) into E7 at 13°C (down triangle), 25°C (circle), 30°C (up triangle), and 5CB and TL205 at 25°C (circles). Red X's are the calculated surface anchoring energy densities (W, right axis) for each LC at 25°C. The inset table shows elastic constants (K) at 25°C and the nematic-isotropic phase transition temperatures (T_{NI}) of TL205, E7, and 5CB. (**F**) Nanofiber length as a function of either nematic E7 film thickness (black points) or mass of polymerized **1a** for a LC film with thickness of 21.7 ± 0.5 μm (red points). Mean ± SD, $n \geq 10$ measurements. (**G** to **I**) Representative SEM images of **2b** (G), **2c** (H), and **2d** (I) templated into TL205. (**J** to **L**) Representative FTIR spectra of **2b** (J), **2c** (K), and **2d** (L) templated into TL205. FTIR spectra of the nanofibers (red) are compared to polymer films synthesized without the LC phase (blue). LCs were removed before imaging and FTIR spectroscopy. a.u., arbitrary units.

for click-based reactions with azide derivatives (**2b**, Fig. 2G), (ii) nanofibers that simultaneously present ethynyl and hydroxyl groups for reaction with azides and activated carboxylic acids (**2c**, Fig. 2H), (iii) nanofibers without functional groups (**2d**, Fig. 2I) as a nonreactive reference, (iv) polycationic pyridine-functionalized nanofibers (**2e**, fig. S9A), and (v) water-repelling perfluoro-functionalized nanofibers (**2f**, fig. S9B). Additionally, we used CVP into LCs to generate polymeric nanofibers with distinct main chains, including (vi) biodegradable polyester nanofibers (**2g**, ROP process, fig. S9C) and (vii) semiconducting poly(phenylene vinylene) nanofibers (**2h**, Gilch process, fig. S9D). When templated by nematic TL205, nanofibers made of polymers **2b** to **2h** were morphologically similar (Fig. 2, G to I, and fig. S9, A to D) and possessed infrared spectroscopic signatures of the constituent chemical groups (Fig. 2, J to L, and fig. S9, E to H).

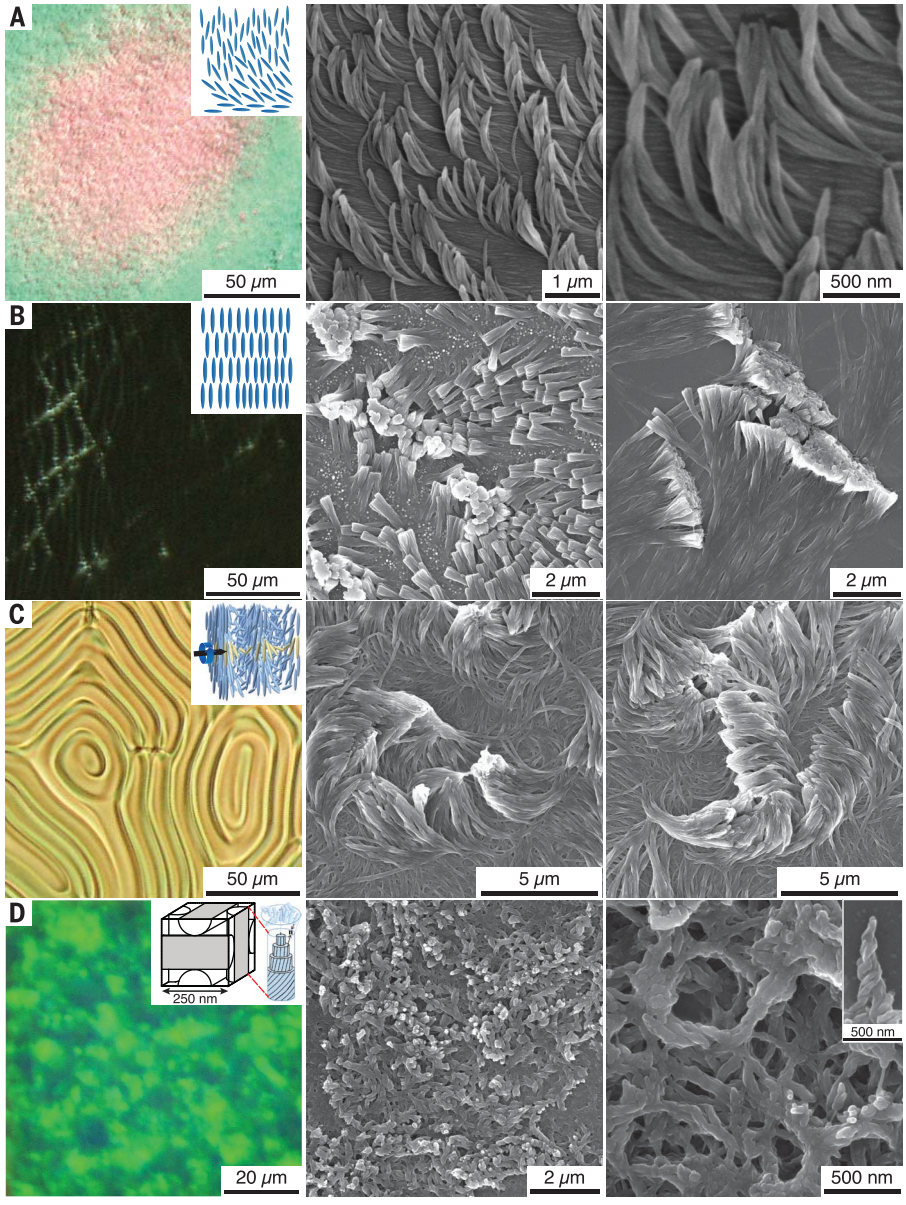

Fig. 3. Influence of LC template on nanofiber morphology and organization. (**A** to **D**) The left column shows optical micrographs (top view, crossed polars) of LC templates; insets are schematic illustrations (side view) of molecular order within the LC templates. The right two columns show SEM images of nanofibers templated from the LCs. (A) Nematic film of E7 with hybrid anchoring and resulting banana-shaped nanofibers. (B) Homeotropically oriented film of a smectic A LC phase and the resulting polymeric nanostructures. (C) Micrograph showing cholesteric LC phase of E7 doped with a left-handed chiral dopant (S-811). SEM images in middle and right columns show nanofibers templated from E7 containing left-handed (S-811) and right-handed (R-811) dopants, respectively. The black and blue arrows in the inset indicate the helical axis and handedness of the twist, respectively. (D) Blue phase LC (BP1) with a cubic lattice spacing of ~250 nm and the resulting polymeric nanostructure. The inset in the far-right column shows a bundle of helical nanofibers.

LC ordering within films is influenced by interactions with confining surfaces, LC elastic moduli, and molecular properties of LCs, including chirality (*19*), thus offering access to a diverse range of LC templates for CVP. For example, a film of nematic 5CB prepared with planar and homeotropic anchoring at bottom and top LC surfaces, respectively, leads to a bent and splayed internal ordering of the LC that templates banana-shaped nanofibers (Fig. 3A). Smectic LCs, with a statistical layering of oriented molecules (*19*), templated straight nanofibers with broadened tips arranged in conical fan-like morphologies (Fig. 3B) (*24*). Chiral nematic phases (cholesteric) yielded shape-controlled and chiral nanofiber assemblies with micrometer-scale periodicities (11.5 ± 1.5 and 11.3 ± 1.5 μm for *S*- and *R*-templated nanofibers, respectively) and an organization consistent with the fingerprint pattern characteristic of cholesteric films (periodicity of 10.8 ± 1.2 and 10.7 ± 1.1 μm for *S*- and *R*-handed cholesteric phases, respectively; Fig. 3C and fig. S10). The chirality of the LC also influenced the handedness of the nanofibers, as confirmed by circular dichroism spectroscopy of surface-immobilized and solvent-dispersed nanofibers (figs. S11 and S12) (*25*). In contrast to all other LC phases, a three-dimensional network of helical nanofibers was formed by CVP into blue-phase LCs, reflecting nanofiber growth templated by a three-dimensional network of double-twisted LC and line defects (Fig. 3D) (*26*). Overall, these results reveal that the shape, interfacial orientations, and morphologies of the nanofiber arrays are templated by the structure of the LC phase. The LC transition temperatures remain almost unaltered by CVP (fig. S13), consistent with our conclusion (fig. S14) that the monomer concentration in the templating LC phase during nanofiber formation is low. These findings differ from conventional polymerizations in LCs, in which the dynamic interplay between the polymerization process and the LC template phase behavior makes control of the resulting polymeric nanostructures difficult and often leaves unreacted monomers in the sample (*26*–*28*).

Figure 4, A to D, shows that CVP into conformal films of nematic E7 formed over the outer or inner surfaces of a hollow cylinder yielded arrays of nanofibers (97.5 ± 17.5 nm in diameter) anchored on the curved surfaces of the cylinder. On the inner surface, the density of the nanofibers decreased with increasing distance from the open end (Fig. 4D). Mesoscopic nanofiber islands were templated from micrometer-sized LC droplets electrosprayed onto surfaces, thus providing a scalable approach for fabrication of arrays (Fig. 4, E and F). We also found that free-standing LC films formed within metallic meshes or at the ends of capillaries (Fig. 4G) templated organized nanofiber assemblies (Fig. 4, H and I). Additionally, microbeads dispersed in LC phases before CVP supported

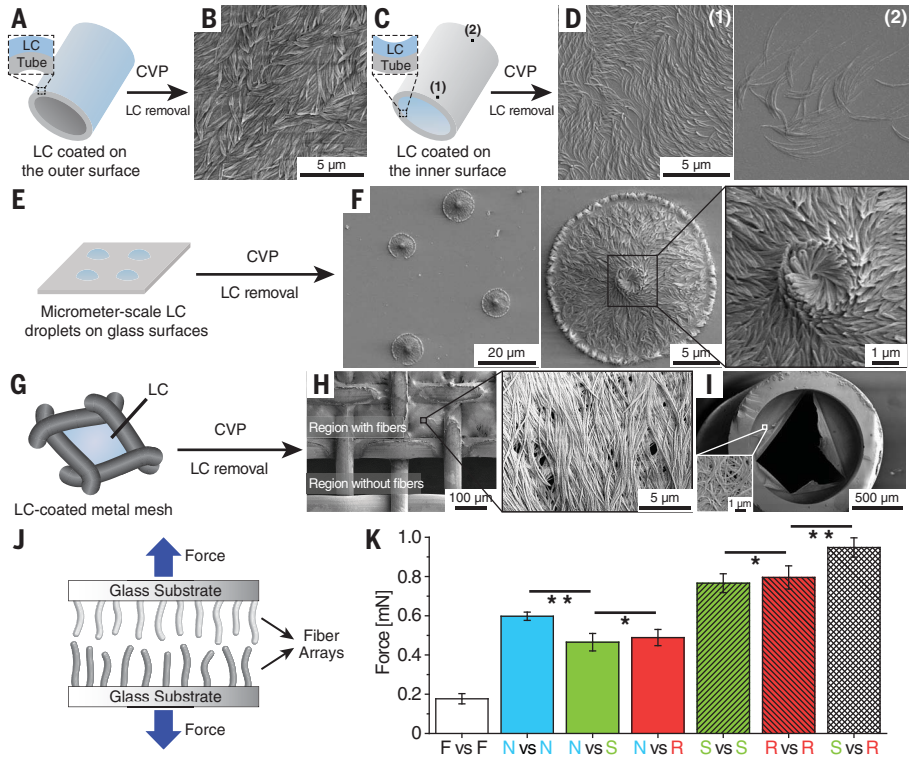

Fig. 4. Templated CVP of polymeric nanofibers in complex geometries. (**A** to **D**) CVP of **1a** into nematic E7 films coated on either the exterior (A) or interior (C) surfaces of glass capillaries and SEM images [(B) and (D)] of corresponding nanofibers [(1) indicates the region closest to the orifice and (2) indicates the region 1.5 mm from (1) inside the cylinder]. (**E** and **F**) CVP of **1a** into E7 microdroplets on a glass surface (E) and SEM images of the nanofiber assemblies (F). (**G** and **H**) CVP of **1a** into free-standing films of E7 hosted within a stainless-steel mesh (G) and SEM image of suspended nanofiber film (H). (**I**) SEM image of a nanofiber membrane spanning the tip of a glass capillary, which was initially intact but was opened during microscopy, revealing an ultrathin nanofiber array. (**J**) Schematic illustration of two substrates coated with nanofiber arrays prepared by CVP. (**K**) Adhesion forces between pairs of substrates decorated by flat CVP films (F) or nanofiber arrays templated from nematic (N), left-handed cholesteric (*S*) or right-handed cholesteric (*R*) LC phases. Data are means ± SD; $n \geq 5$ measurements. Statistical analyses were performed between groups using Tukey's test; * indicates statistically identical results, $P > 0.4$; ** indicates statistically different results, $P < 0.002$.

growth of nanofibers, and copolymerization was used to create nanofibers for coimmobilization of different biomolecules (fig. S15).

Overall, our results reveal that CVP into LC templates enables scalable fabrication of arrays of polymeric nanofibers with programmable shapes, chemistries, and long-range lateral organization, yielding interfacial properties currently unavailable by other techniques. For example, we found that it was possible to manipulate nanofiber chirality to control adhesion between surfaces. As shown in Fig. 4, J and K, we measured adhesion to be higher for surfaces decorated with nanofibers than the corresponding flat CVP films, with the relative chirality of the nanofibers presented by the two surfaces also influencing the magnitude and selectivity of adhesion (Fig. 4K). Other properties designed into nanofiber arrays prepared by LC-templated CVP include wettability, intrinsic photoluminescence, biodegradability, and surface charge (Fig. 4, J and K, and fig. S16). We envisage that additional functional properties can be realized by exploiting the full diversity of LC templates (*17*, *19*) along with other polymerization mechanisms using vapor-phase delivery of monomers.

REFERENCES AND NOTES

1. A. J. Hudspeth, *Nat. Rev. Neurosci.* **15**, 600–614 (2014).
2. H. E. M. Liwanag, A. Berta, D. P. Costa, S. M. Budge, T. M. Williams, *Biol. J. Linn. Soc. Lond.* **107**, 774–787 (2012).
3. N. Hirokawa, *Science* **279**, 519–526 (1998).
4. W. Barthlott, C. Neinhuis, *Planta* **202**, 1–8 (1997).
5. K. Autumn *et al.*, *Nature* **405**, 681–685 (2000).
6. T. Svedberg, *Kolloid Z* **18**, 54–56 (1916).
7. A. Matsumoto, S. Nagahama, T. Odani, *J. Am. Chem. Soc.* **122**, 9109–9119 (2000).
8. X. Wang, D. S. Miller, E. Bukusoglu, J. J. de Pablo, N. L. Abbott, *Nat. Mater.* **15**, 106–112 (2016).
9. T. J. White, D. J. Broer, *Nat. Mater.* **14**, 1087–1098 (2015).
10. K. Akagi, *Chem. Rev.* **109**, 5354–5401 (2009).
11. F. Bally-Le Gall *et al.*, *Chem. Eur. J.* **23**, 13342–13350 (2017).
12. X. P. Deng, J. Lahann, *J. Appl. Polym. Sci.* **131**, 40315 (2014).
13. W. F. Gorham, *J. Polym. Sci. A1* **4**, 3027–3039 (1966).
14. K. M. Vaeth, K. F. Jensen, *Macromolecules* **31**, 6789–6793 (1998).
15. O. Schäfer *et al.*, *Synth. Met.* **82**, 1–9 (1996).
16. F. Xie *et al.*, *Angew. Chem. Int. Ed.* **56**, 203–207 (2017).
17. D. Demus, J. Goodby, G. W. Gray, H.-W. Spiess, V. Vill, *Handbook of Liquid Crystals* (Wiley-VCH, 1998), vol. 2.
18. Y.-K. Kim, X. Wang, P. Mondkar, E. Bukusoglu, N. L. Abbott, *Nature* **557**, 539–544 (2018).
19. P. G. de Gennes, J. Prost, *The Physics of Liquid Crystals* (Clarendon Press, 1993).
20. N. Podoliak *et al.*, *RSC Advances* **4**, 46068–46074 (2014).
21. W. Iglesias, N. L. Abbott, E. K. Mann, A. Jákli, *ACS Appl. Mater. Interfaces* **4**, 6884–6890 (2012).
22. H. Wang, T. X. Wu, S. Gauza, J. R. Wu, S. Wu, *Liq. Cryst.* **33**, 91–98 (2006).
23. S. Faetti, M. Gatti, V. Palleschi, T. J. Sluckin, *Phys. Rev. Lett.* **55**, 1681–1684 (1985).
24. V. Designolle, S. Herminghaus, T. Pfohl, Ch. Bahr, *Langmuir* **22**, 363–368 (2006).
25. R. Kuroda, T. Honma, *Chirality* **12**, 269–277 (2000).
26. F. Castles *et al.*, *Nat. Mater.* **11**, 599–603 (2012).
27. M. Mizusaki, K. Nakai, S. Enomoto, Y. Hara, S. Yusa, *Polym. J.* **49**, 457–463 (2017).
28. Y. Nakanishi, K. Okamoto, *Jpn. J. Appl. Phys.* **51**, 041701 (2012).

ACKNOWLEDGMENTS

We thank Y. Dong, C. Lu, S. Rahmani, and B. Plummer for help with SEM and transmission electron microscopy; V. Subramanian and the University of Michigan Biophysics NMR center for help with the solid-state NMR analysis; and N. Kotov for insightful comments on the manuscript. **Funding:** This study was supported by the Army Research Office (W911NF-11-1-0251 and W911NF-17-1-0575). We thank the Michigan Center for Materials Characterization and University of Wisconsin Materials Research Science and Engineering Center (DMR-1720415). The experiments performed with blue-phase liquid crystals at University of Wisconsin–Madison were supported by the U.S. Department of Energy (DE-SC0004025). J.L. and C.H. acknowledge support from the German Science Foundation (SFB 1176, Project B3), and F.X. acknowledges funding from the China Scholarship Council and Northwestern Polytechnical University, China. **Author contributions:** N.L.A. and J.L. proposed and supervised the project; K.C.K.C., M.A.B.-P., and Y.-K.K. conducted experiments with assistance from J.V.G., F.X., A.d.F., C.H., and K.S.; and K.C.K.C., M.A.B.-P., Y.-K.K., N.L.A., and J.L. analyzed the data and wrote the manuscript with input from all coauthors. **Competing interests:** The University of Wisconsin–Madison and University of Michigan have filed a patent application (PCT/US17/27764) on the work described in this manuscript. F.X. is also affiliated with the Department of Applied Chemistry, School of Science, Northwestern Polytechnical University, Xi'an 710072, China, and the College of Bioresources Chemical and Materials Engineering, Shaanxi University of Science and Technology, Xi'an 710021, China. **Data and materials availability:** All data supporting the findings of this study are available in the manuscript or the supplementary materials.

SUPPLEMENTARY MATERIALS

www.sciencemag.org/content/362/6416/804/suppl/DC1
Materials and Methods
Figs. S1 to S16
References (*29*–*31*)

22 December 2017; resubmitted 9 June 2018
Accepted 8 October 2018
10.1126/science.aar8449

DYNAMIC MATERIALS

Reversible self-assembly of superstructured networks

Ronit Freeman[1]*, Ming Han[2], Zaida Álvarez[1], Jacob A. Lewis[3], James R. Wester[1], Nicholas Stephanopoulos[1]†, Mark T. McClendon[1], Cheyenne Lynsky[1], Jacqueline M. Godbe[4], Hussain Sangji[3], Erik Luijten[5,6,7]‡, Samuel I. Stupp[1,3,4,5,8]‡

Soft structures in nature, such as protein assemblies, can organize reversibly into functional and often hierarchical architectures through noncovalent interactions. Molecularly encoding this dynamic capability in synthetic materials has remained an elusive goal. We report on hydrogels of peptide-DNA conjugates and peptides that organize into superstructures of intertwined filaments that disassemble upon the addition of molecules or changes in charge density. Experiments and simulations demonstrate that this response requires large-scale spatial redistribution of molecules directed by strong noncovalent interactions among them. Simulations also suggest that the chemically reversible structures can only occur within a limited range of supramolecular cohesive energies. Storage moduli of the hydrogels change reversibly as superstructures form and disappear, as does the phenotype of neural cells in contact with these materials.

Nature exploits self-assembly processes to promote the formation of highly organized structures in a hierarchical manner (*1*, *2*). These structures often reorganize dynamically as interactions among their constituents change, which affects their functions (*3*–*5*). The design of weak and reversible interactions between molecules provides, in principle, a strategy to synthesize supramolecular architectures that can rearrange dynamically to impart changes in functionality. Despite recent advances in creating artificial hierarchical systems through self-assembly (*6*–*10*), approaches to manipulate these structures reversibly across length scales that reach macroscopic dimensions remain elusive. Collagen-mimetic peptides that form hierarchical structures have been designed in which triple helices of molecules interact to create fibrillar networks (*11*). However, these structures are neither tunable nor reversible. Another relevant recent example demonstrated dynamic changes in the unit cell of a microscopic colloidal crystal, in which gold nanoparticles were spatially reconfigured through chemically driven changes in surface organic ligands (*12*). Synthetic bundled fibrous networks with the dimensional tunability and dynamic reversibility of collagen would greatly enhance our ability to design functional soft matter.

We report on fibrous supramolecular networks that form reversible superstructures controlled externally by the addition of soluble molecules. The system consists of nanofibers formed by co-assembly of alkylated peptides (monomer **1**) with a similar monomer containing a covalently linked oligonucleotide terminal segment (monomer **2**; see fig. S1). Mixing **1** with **2** in molar concentrations ranging from 0.1% to 10% led to the formation of fibers with a stochastic distribution of monomers along its length (fig. S2). The original objective of this work was to create hydrogels in which small amounts of complementary oligonucleotides in separate fibers would lead to reversible cross-linking through Watson-Crick base pairing (Fig. 1A). When we mixed an aqueous solution containing fibers with complementary oligonucleotides (**1**/**2** and **1**/**2′**, tables S1 and S2), we observed the expected formation of a gel that could be liquefied by adding a soluble single-stranded DNA that breaks the cross-links via the well-known toehold-mediated strand displacement (*13*) (fig. S3). However, we were surprised to find by scanning electron microscopy (SEM) a superstructure in which large micrometer-sized bundles of fibers segregated within a network of individual fibers (Fig. 1B and fig. S4). Small-angle x-ray scattering (SAXS) also confirmed the formation of higher-order structures (fig. S5).

To investigate possible differences in composition between the two apparent phases, we labeled oligonucleotides with a fluorescent dye (Cy3) to probe their distribution in the hydrogel. Confocal optical microscopy revealed that most of the DNA-containing monomers were concentrated within the bundled regions (Fig. 1C). We first hypothesized that the system contained supramolecular polymers differing in content of DNA-bearing monomers, which in turn spatially segregated to create the bundled regions. However, we gelled solutions containing fibers with either monomer **2** or monomer **2′** by adding calcium chloride (electrostatic cross-linking) and did not find any domains with concentrated fluorescence characteristic of the bundled regions (fig. S6).

We then considered whether the formation of bundled regions involved large-scale spatial redistribution of monomers within and among the fibers. Stochastic optical reconstruction microscopy revealed such dynamic exchange of monomers in supramolecular copolymers (*14*). To confirm that DNA hybridization among neighboring fibers was involved in the formation of the bundles, we mixed aqueous solutions of fibers containing noncomplementary oligonucleotides, which did not yield bundled structures (fig. S7A).

To establish that large-scale redistribution of monomers can give rise to bundle formation in a network of fibers, we carried out coarse-grained molecular dynamics simulations using a model that accounts for the hybridization of complementary DNA segments (fig. S8 and tables S3 and S4). In the simulation, each fiber is a chain of overlapping spheres that represent peptide amphiphile (PA) monomers, and some of the monomers are randomly grafted with DNA side chains. Complementary side chains can hybridize by forming reversible bonds while dynamic exchange of molecules among fibers is either disabled or permitted (by fixing monomers within the fibers or allowing them to be mobile, respectively). A detailed description of the model and the simulation procedure is provided in the supplementary materials. Snapshots (Fig. 1, D and E) show that dynamic molecular exchange among the supramolecular polymers is essential for the formation of DNA-rich bundles. Förster resonance energy transfer (FRET) experiments on mixtures of assemblies containing complementary DNA strands and labeled with either a donor or an acceptor moiety confirmed that monomers from the two separate fiber populations exchange and hybridize (fig. S9).

The simulations also provide important insights into the mechanism and kinetics of bundle formation. From a kinetic point of view, a hybridization event between fibers is likely to facilitate additional cross-linking locally of other DNA segments in neighboring locations. Furthermore, hybridized monomers have a lower tendency to escape to other fibers, measured in the simulations as "trapping time" (fig. S10A). Likewise, the diffusivity of DNA monomers decreased once they were recruited into the incipient bundles of the superstructure (fig. S10B). We infer that such mechanisms should lead to the growth of stable bundled regions. In experiments using monomers labeled with the cyanine dye Cy3, we followed the kinetics of bundle formation and found that micrometer-scale bundles formed within 10 min (fig. S9, A and B).

The simulations also showed that the bundle growth rate (fig. S11) is sensitively controlled by the relative strength of molecular attraction

[1]Simpson Querrey Institute, Northwestern University, Chicago, IL 60611, USA. [2]Applied Physics Graduate Program, Northwestern University, Evanston, IL 60208, USA. [3]Department of Biomedical Engineering, Northwestern University, Evanston, IL 60208, USA. [4]Department of Chemistry, Northwestern University, Evanston, IL 60208, USA. [5]Department of Materials Science and Engineering, Northwestern University, Evanston, IL 60208, USA. [6]Department of Engineering Sciences and Applied Mathematics, Northwestern University, Evanston, IL 60208, USA. [7]Department of Physics and Astronomy, Northwestern University, Evanston, IL 60208, USA. [8]Department of Medicine, Northwestern University, Chicago, IL 60611, USA.
*Present address: Department of Applied Physical Sciences, University of North Carolina, Chapel Hill, NC 27599, USA.
†Present address: School of Molecular Sciences, Biodesign Center for Molecular Design and Biomimetics, Arizona State University, Tempe, AZ 85287, USA.
‡Corresponding author. Email: s-stupp@northwestern.edu (S.I.S.); luijten@northwestern.edu (E.L.)

among monomers within the fiber versus the energy associated with hybridization. Molecular attraction within the fibers is controlled by the energy associated with β-sheet formation and hydrophobic collapse of aliphatic segments in PA molecules (E_{intra}), whereas interaction between fibers is mediated by hybridization energy (E_{inter}). Additionally, the simulation predicted that fiber bundles form through redistribution of monomers when E_{intra} lies within the remarkably narrow range of 5 to 10 k_BT, where k_BT is the thermal energy (the product of the Boltzmann constant k_B and temperature T) (Fig. 1F). Thus, cohesion among molecules needs to be strong enough to create stable fibers but not too strong to prevent dynamic exchange. Within this range, the model also showed that interfiber cross-linking requires a threshold energy to create bundled regions ($E_{inter} > 5\ k_BT$; fig. S12A). Below this threshold, the DNA monomers are predicted to distribute randomly along fibers, resulting in a homogeneous disorganized structure (fig. S12B). By explicit estimation of the free-energy differences (see supplementary materials), we confirmed that the molecular design of monomers **2** and **2′** indeed fell in the predicted regime for bundle formation. When dynamic exchange was suppressed ($E_{intra} > 10\ k_BT$), very small bundles could still form, provided that cross-links could break and rehybridize (fig. S12C). As redistribution of monomers does not occur, the growth rate is naturally limited by the low density of DNA monomers in the fibers. Additional experiments varying E_{intra} and E_{inter} using different molecules supported our computational predictions and demonstrated the experimental tunability of the system investigated (figs. S13 to S18).

We also explored, both experimentally and through simulations, the effect of molar concentration of DNA monomers on bundle formation (figs. S7, B to D, and S19). When DNA densities were too low, few fibers were cross-linked and the resulting monomer redistribution was not sufficient to support appreciable bundling. As the density increased, the clustering of DNA-containing monomers drove formation of larger bundles. Above a given DNA concentration, the system "froze" kinetically into a three-dimensional (3D) gel without any bundled structures.

Having obtained evidence that the superstructures form when the systems contain low amounts of DNA-containing monomers, we were interested in investigating supramolecular assemblies in which all of the molecules are functionalized with complementary oligonucleotides. These systems would experimentally mimic the final DNA-rich superstructures created dynamically in the hydrogels. We followed the time evolution of these systems using electron microscopy and discovered that both DNA-containing monomers in pure form self-assembled into spherical micelles (fig. S20, A and B). In our view, this result is not surprising given the large size and charge of the DNA segments. However, when **2** and **2′** were mixed and annealed, the spherical micelles metamorphosed into large twisted bundles of fibers (fig. S20, C and D). These structures resembled the bundles observed in the hydrogels formed by co-assembled fibers in which DNA was only present in a small percentage of the monomers. This result implies that the drastic shape transformation from micelles to filaments was driven by DNA hybridization.

We then considered what would be the role of charge in the formation of such structures and designed monomers **3** and **3′** (tables S1 and S2), which contained complementary shorter DNA sequences that would experience weaker electrostatic forces. In these systems, we observed the formation of similar filamentous structures starting from spherical aggregates (fig. S21). To reduce electrostatic interactions further, we synthesized monomer **4** lacking the charges associated with nucleotides by replacing DNA with a peptide nucleic acid (PNA) sequence (table S1 and fig. S1) while keeping hybridization energy constant, as confirmed by the melting temperature (table S2). We found that monomer **4** self-assembled into filaments (fig. S22), which indicates that charge density is an important factor in the formation of spherical aggregates. We then combined monomer **4** with a complementary DNA-containing monomer **4′**. Much to our surprise, within 24 hours after mixing **4** and **4′**, we observed formation of pairs of intertwining fibers with a regular pitch (Fig. 2A). As solutions were allowed to age further (5 and 7 days), we discovered further growth of twisted structures containing many fibers. These results suggest that the pairs formed at early time points contained nonhybridized oligonucleotide segments,

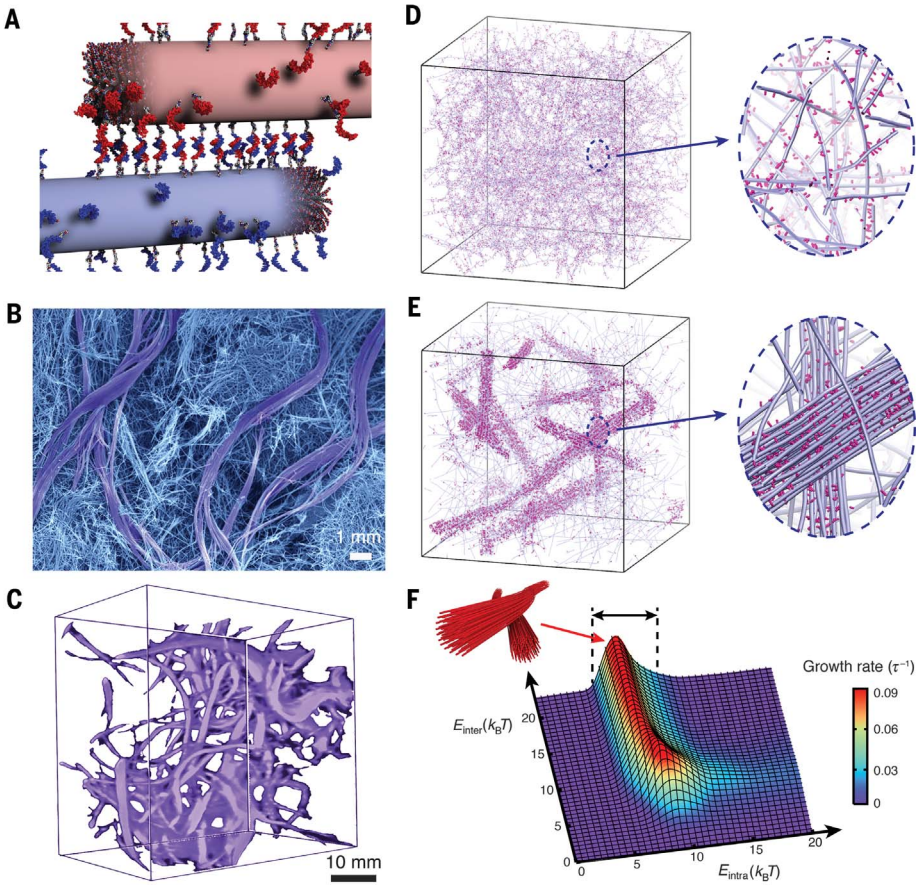

Fig. 1. Dynamics in DNA-peptide amphiphiles drives the formation of hierarchical structures. (**A**) Illustration of peptide amphiphile fibers cross-linked by DNA hybridization; fibers are shown in their initial state prior to monomer exchange. (**B**) SEM micrograph of the hydrogel formed upon DNA cross-linking. Two populations within the gel are shown, consisting of twisted bundles (diameter ~1 to 3 μm) and single fibers (diameters between 10 and 15 nm). (**C**) Confocal reconstruction image of a section of the gel containing DNA monomers modified with the fluorescent dye Cy3. Bundles are shown in purple. (**D**) Simulation snapshots showing a homogeneous hydrogel when molecular exchange of DNA monomers between peptide amphiphile fibers is prohibited. Magnified view shows individual fibers (blue) with a stochastic distribution of DNA monomers (pink) along the fibers. (**E**) Simulation snapshots showing the emergence of bundles of fibers when molecular exchange is allowed. Magnified view shows bundle of fibers (blue) enriched with DNA (pink) in a matrix of individual fibers depleted of DNA monomers. (**F**) Bundle growth rate as a function of intra- and interfiber energies (E_{intra}, E_{inter}). Bundles form within the energy range $5\ k_BT < E_{intra} < 10\ k_BT$ (black arrows).

which created attachment points that then allowed further growth of the intertwined bundles.

To investigate the mechanism of intertwining, we simulated the interaction between complementary PNA and DNA filaments meeting at an arbitrary angle (Fig. 2B). The simulation showed that oligonucleotides hybridize first at the contact point, rapidly followed by further hybridization events as the fibers bend around each other to create an intertwined pair (movie S1). Because the intertwined state requires bending of the fibers (~1 k_BT/nm), we hypothesized that the observed structure is thermodynamically less favorable than hybridization among two parallel fibers. However, to achieve parallel arrangement, the intertwined structure faces an enormous energy barrier (>10 k_BT/nm) involving the breaking (and subsequent reforming) of hybridized oligonucleotides. This was confirmed by a free-energy analysis (fig. S23) and by the observation that the twist state of two complementary fibers was determined by their initial contact angle (fig. S24). When deformation of the soft fibers was taken into account, the degree of hybridization increased (thereby raising the free-energy barrier), but parallel alignment remained favorable (fig. S25). Thus, we concluded that the observed intertwined structure is likely a kinetically trapped state. Future atomistic simulations may reveal that the intertwined architecture can be driven by the nature of intermolecular packing within the supramolecular polymer. The simulation also showed that intertwined pairs display a relatively uniform pitch of approximately 300 nm, consistent with our experimental observations. In fact, the pitch saturated at a constant value for most initial contact angles between fibers (>25°; Fig. 2B) and sufficiently high DNA densities (>30%; Fig. 2C). However, the saturated pitch could be controlled by varying DNA length (Fig. 2D), fiber stiffness (fig. S26), or oligonucleotide type (DNA or PNA; fig. S27).

The work described above in solutions containing complementary filaments provided us with mechanistic insight into the origin of bundle formation in hydrogels. The superstructure observed in the hydrogels containing fiber bundles can be viewed as a hierarchical structure with multiple levels of molecular organization. The first level of structure involves the interactions leading to filament formation (hydrogen bonding and hydrophobic collapse), followed by intertwining of fibers through DNA hybridization as a second level of structure. At even larger length scales in the hierarchical structure, bundle formation occurs via further hybridization among multiple intertwined fiber pairs, which then twist collectively. This description of the hierarchical structure is consistent with the large bundles dispersed in a matrix of DNA-depleted PA nanofibers as shown in Fig. 1B.

Given the possibility of melting interfiber DNA duplexes or breaking them using a competitive single-stranded oligonucleotide, we proceeded to investigate the reversibility of the hierarchical structure. First, we tested the effect of temperature and found that bundle-containing hydrogels could be liquefied at 95°C. We then rapidly fixed the structure at elevated temperature by electrostatic gelation with calcium chloride and analyzed its structure by SEM (fig. S28). In samples treated this way, large bundles completely disappeared and only a network of individual fibers was visible (fig. S28B). In contrast, when the liquefied hydrogel was cooled slowly and imaged by SEM, superstructures reformed (fig. S28A). We infer that monomers once again redistributed in space, hybridized, and recreated the bundles. To further probe the thermal melting of bundles, we performed SAXS experiments, which indicated that at 95°C the fiber morphology persisted but the hierarchical bundling did not (fig. S29).

We also investigated the use of a toehold-mediated strand-displacement mechanism to destroy interfiber DNA duplexes. Monomers **2** and **2′** were designed to have an overhang sequence that is not complementary. Thus, adding an "invader" oligonucleotide that is fully complementary to monomer **2** should reverse interfiber hybridization events. After simply adding a drop of solution containing the invader molecules to the hydrogel, we observed the complete disappearance of the bundled structures (fig. S28D). The invader strand also contained a short overhang sequence, which, upon addition of an anti-invader (fully complementary to the invader strand), allowed the hierarchical structures to reform (fig. S28C).

The observed hierarchical structures appear to be chemically reversible by adding molecules or through changes in temperature. By adjusting the stoichiometry of invader oligonucleotides, we could form intermediate structures with small rather than large fiber bundles (fig. S30). The reversible transformation from bundled structures to individual fiber networks also led to reversible changes in the bulk mechanical properties of the hydrogels (see fig. S30). Hydrogels with superstructures had bulk storage moduli that were 15 times those of materials containing individual fiber networks. Furthermore, atomic force

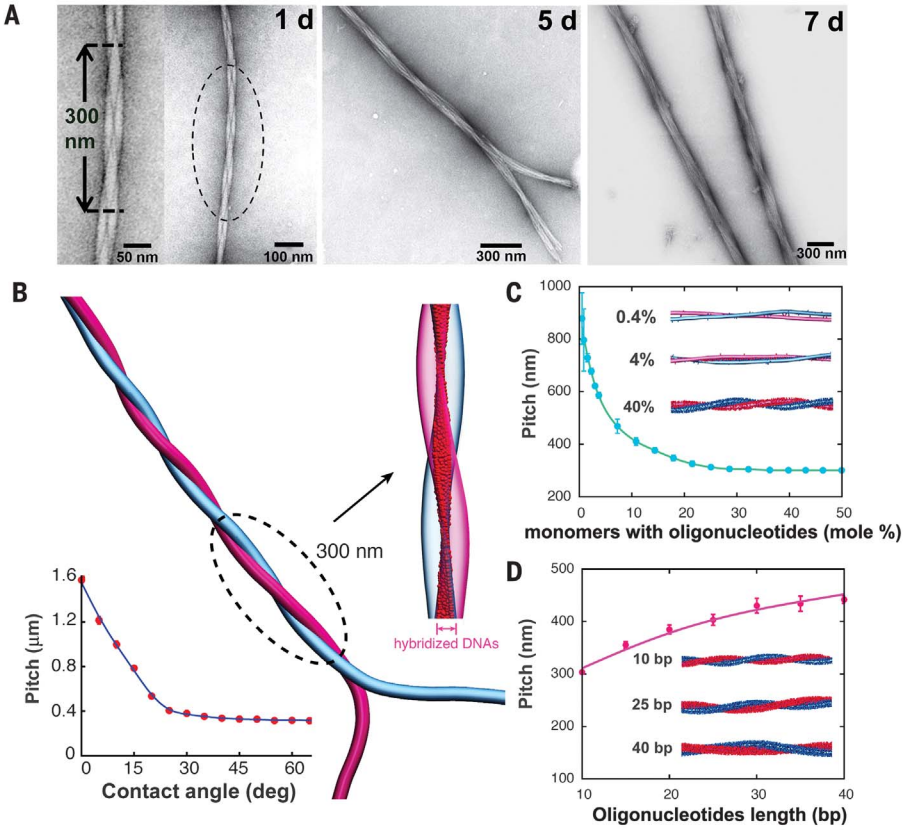

Fig. 2. Programming the growth of intertwined bundles of fibers. (**A**) Transmission electron microscopy images after mixing complementary DNA- and PNA-terminated peptide amphiphiles show the time-dependent evolution of twisted bundles over 24 hours, 5 days, and 7 days. (**B**) Simulation snapshot of two intertwined complementary fibers. The intertwining pitch saturates for most initial contact angles (inset, bottom left). Hybridized DNA-PNA pairs between the two fibers (magnified view) form a twisted ribbon pattern. (**C**) Dependence of the pitch on the fraction of monomers with oligonucleotides. Simulation snapshots are shown for systems with 0.4%, 4%, and 40% oligonucleotide-modified monomers. (**D**) Dependence of the pitch on the length of oligonucleotides. Simulation snapshots are shown for duplexes with 10, 25, and 40 DNA-PNA base pairs (bp).

microscopy (AFM) nano-indentation studies confirmed that the bundled fibers were stiffer than individual fibers by a factor of ~6 on average (fig. S31).

The coarse-grained rather than atomistic nature of our simulations suggested that the observed phenomena should not be limited to oligonucleotides and could be encoded in other systems without the use of DNA chemistry. For this purpose, we designed various PA sequences (**5**–**7**) each containing at their termini two oppositely charged peptide domains (Fig. 3, table S1, and fig. S32). We reasoned that electrostatic interdigitation of such "sticky ends" would mimic DNA duplex formation (Fig. 3A). Co-assembly of these monomers with **1** yielded bundles of intertwined fibers similar to those in DNA-containing systems (Fig. 3, B to D). Longer sequences of both charged residues and spacers resulted in greater bundle dimensions (Fig. 3, B to D). When pH was either raised or lowered by adding NaOH or HCl, the bundles disappeared owing to the lack of electrostatic complementarity (figs. S33 to S35). However, simply mixing two different fibers bearing oppositely charged peptide domains did not result in bundle formation (fig. S36). This difference most likely arose because the fibers were kinetically trapped by electrostatic forces in a 3D gel. Alternatively, monomer exchange could reduce the thermodynamic driving force for bundling by mixing oppositely charged monomers on individual fibers.

The system investigated here has structural features that are biomimetic of mammalian extracellular matrices (ECMs), a physical space that is known to undergo constant remodeling (*15*, *16*). In natural ECMs, the networks of fibers vary widely in their organization and stiffness depending on the tissue (*17*). Often, these features are controlled by the extent of bundling of fibers. Because our experimental ECM mimic effectively remodels reversibly upon addition of a water-soluble and biocompatible molecule, we chose to investigate how dynamic organization of fibers within a hydrogel network affects cells in culture. We selected cortical astrocytes from the central nervous system (CNS) for these experiments because they are subjected to a changing matrix environment after injury to the brain or spinal cord, yet much remains to be learned about how these changes affect their behavior. In this injury environment, astrocytes become reactive, undergoing drastic morphological changes and upregulating glial fibrillary acidic protein (GFAP) and vimentin (*18*, *19*), a process known as astrogliosis. The glial scar after injury to the CNS is spatiotemporally dynamic and contains a variety of macromolecules, including collagens, laminins, fibronectin, and proteoglycans among others. The glial scar contains increased concentrations of fibrillar collagen type I, an ECM component not usually found in the normal brain, which is composed of nonfibrillar collagen IV and glycosaminoglycans (*20*, *21*).

Because our system can mimic aspects of the morphological changes in the brain microenvironment, we used it as a culture substrate for cortical astrocytes isolated from postnatal mice. We tested the two states of the system—one with the superstructures consisting of bundled fibers and the other containing only individual fibers—and switched from one to the other by adding the invader strand. Figure 4A shows confocal micrographs of the cells labeled with GFAP and the nuclear stain 4′,6-diamidino-2-phenylindole (DAPI) after 10 days in culture. To our surprise, astrocytes cultured on bundled fiber (BF) hydrogels developed a reactive morphology and up-regulation of GFAP and vimentin (see Western blot data in Fig. 4, B to D), whereas those cultured on individual fiber (IF) substrates had the naïve morphology observed under control conditions (glass) and lacked overexpression of both proteins. As a positive control, we added dibutyryl cyclic adenosine monophosphate, which is well known to induce the reactive phenotype of astrocytes (*22*, *23*). The data show that the resulting phenotype was similar to the one achieved on BF substrates (fig. S37). In addition, cells with the reactive phenotype were observed to upregulate phospho-histone 3 (PH3), a marker of cell proliferation (Fig. 4, B to E). Proliferation was also demonstrated through staining with 5-ethynyl-2′-deoxyuridine (fig. S38), which is only incorporated into actively dividing cells. Further confirmation of the reactive phenotype on BF substrates was provided, as expected, by an increase in reactive oxygen species (ROS) (Fig. 4F and fig. S39) (*24*, *25*).

We then considered that changes in phenotype were linked to differences in mechanical properties between BF and IF substrates. However, cells exhibited the naïve phenotype when cultured on non–DNA-containing hydrogels formed by self-assembly of monomer **1**, which has a bulk modulus similar to that of the BF structure (fig. S40). Although these hydrogels had similar bulk moduli, stiffness could be a factor in the phenotypic change observed because AFM revealed that the superstructures were locally stiffer than individual fibers (fig. S31). However, stiffness cannot be the sole factor in the observed behavior, because cells cultured on glass (obviously a very stiff substrate) also exhibited the naïve phenotype. Moreover, glial scars where the reactive phenotype of astrocytes is observed are actually softer rather than stiffer relative to the normal CNS environment (*26*). Our results therefore suggest that the structural organization of the newly formed extracellular matrix after injury elicits astrocyte activation, and that this phenomenon is reversible if the matrix environment reverts back to the pre-injury structure.

Having established the two distinct cell phenotypes on BF and IF substrates, we tested the response of the cells to the chemical reversibility of the artificial matrix from one state to the other by addition of the invader strand. Cells were cultured for 5 days on BF and IF substrates. At the end of this period, we added solutions of the invader and anti-invader strands to morphologically remodel the matrix. Five days later, cells had switched from the reactive to the naïve phenotype when the invader strand was added to BF substrates, and from naïve to reactive when the anti-invader strand was added to IF scaffolds. As indicated in Fig. 4, A to F, these changes in phenotype driven by dynamic changes of the substrate were accompanied by variation in protein expression and ROS. Figure 4G shows SEM images revealing the morphological differences between reactive and naïve astrocytes on bundled "terrain" versus single-fiber matrices. Moreover, in the case of BF substrates, cells appeared to interact closely with the bundles. Although astrogliosis was thought to be unidirectional and irreversible, glial cells transplanted from an injured

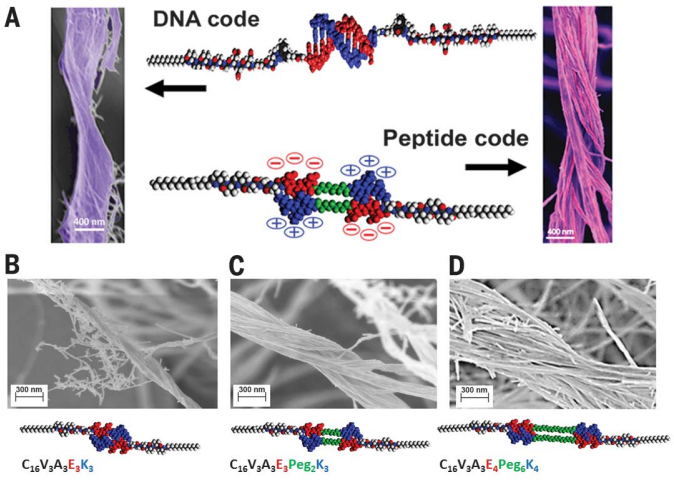

Fig. 3. Programming hierarchical structures with a peptide code. (**A**) Molecular graphics representation of the complementary interactions between the DNA (top) and DNA-mimetic peptide amphiphiles (bottom), and the corresponding morphologies of bundled fibers observed in both systems by SEM. (**B** to **D**) SEM micrographs of bundled and twisted fiber morphologies of varying diameters: (B) 140.5 ± 15 nm, (C) 332 ± 37 nm, and (D) 905 ± 190 nm. Also shown are the corresponding dimer molecular graphics and chemical sequences of the DNA-mimetic peptide amphiphiles that form the superstructures (C_{16} is the number of carbons in the aliphatic terminus of the amphiphiles; eg, ethylene glycol). Quantification of bundle diameters used a minimum of 15 randomly selected images (taken from three independent batches) for each system.

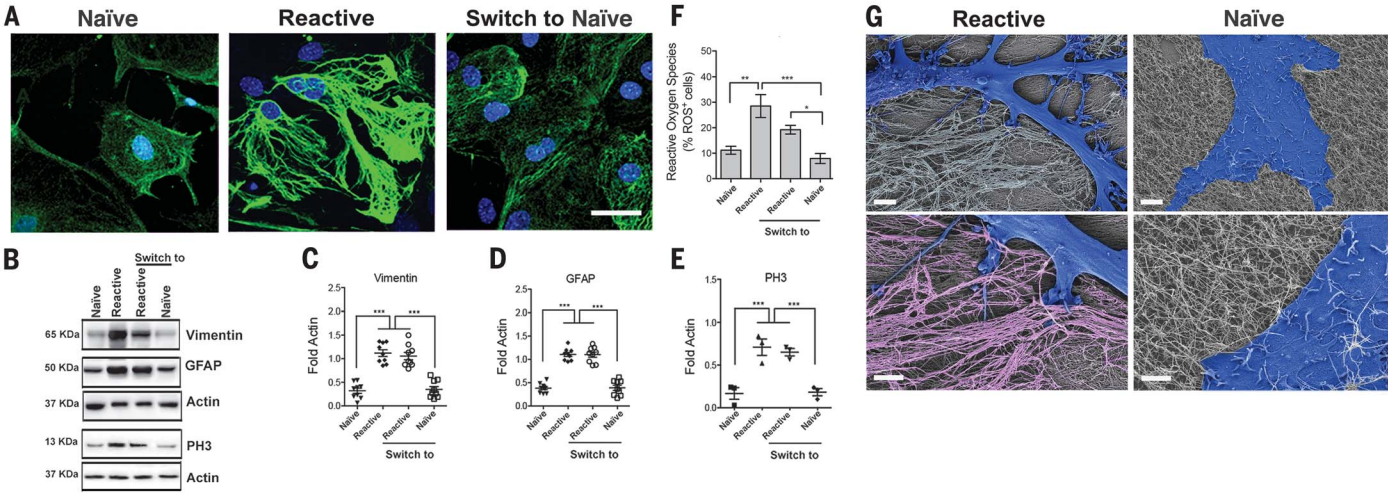

Fig. 4. Modulating the phenotype of astrocytes on reversible hierarchical ECM mimetic. (**A**) Confocal microscopy images of astrocytes plated on individual fibers (left), on bundled fibers (center), and after switching from bundles to individual fibers (right). Staining for GFAP (green) and cell nuclei (DAPI, blue) reveals cells with naïve morphology on substrates of individual fibers and reactive morphology on substrates of bundled fibers. Scale bar, 50 μm. (**B**) Western blot analysis of protein expression (related to cytoskeleton and cell proliferation) in astrocytes on indicated substrates. (**C** to **E**) Relative expression of proteins derived from Western blots in (B). All values were normalized to actin expression; three experiments were analyzed. ***$P < 0.001$ (least significant difference test). Error bars denote SD. (**F**) Reactive oxygen species (ROS) quantification on the different substrates relative to cell number. *$P < 0.05$, **$P < 0.01$, ***$P < 0.001$. Error bars denote SD. (**G**) SEM micrographs of a reactive cell on bundled fibers and a naïve cell on individual fibers. Cells are false-colored in blue. The magnified view (lower images) shows the cell-substrate interaction. Bundles are falsely colored in pink. Scale bars, 5 μm (upper images), 2 μm (lower images).

spinal cord to an uninjured one (known to be stiffer than the injured one) reverted from the reactive to the naïve phenotype (*20*), which suggests that architectural cues and not matrix stiffness can reversibly control astrogliosis. Future therapeutic strategies that "defibrillate" glial scars could be explored to reverse neural pathologies through astrocytic fate decisions.

Our work shows that reversible superstructures can be formed in supramolecular materials when their large-scale dynamics are directed by the formation of strong noncovalent bonds that can be externally disrupted. Mechanistic insights for this phenomenon were obtained using a computational model that also identified the molecular parameters that enable the bonding-directed spatial redistribution of monomers to form and disassemble the superstructures. Our initial observations used DNA hybridization as the strong interaction in the experimental system, but we showed that the principles learned can be applied to other strongly interacting chemical structures such as charged peptides. The dynamic supramolecular systems enabled us to discover how changes in architectural features in fibrous hydrogel networks can modulate important phenotypic transformations in astrocytes linked to brain and spinal cord injury as well as neurological diseases.

REFERENCES AND NOTES

1. G. M. Whitesides, B. Grzybowski, *Science* **295**, 2418–2421 (2002).
2. S. Zhang, *Nat. Biotechnol.* **21**, 1171–1178 (2003).
3. D. Needleman, Z. Dogic, *Nat. Rev. Mater.* **2**, 17048 (2017).
4. A. J. Ridley, A. Hall, *Cell* **70**, 389–399 (1992).
5. C. G. dos Remedios *et al.*, *Physiol. Rev.* **83**, 433–473 (2003).
6. H. Qiu, Z. M. Hudson, M. A. Winnik, I. Manners, *Science* **347**, 1329–1332 (2015).
7. R. M. Capito, H. S. Azevedo, Y. S. Velichko, A. Mata, S. I. Stupp, *Science* **319**, 1812–1816 (2008).
8. A. Aggeli *et al.*, *Proc. Natl. Acad. Sci. U.S.A.* **98**, 11857–11862 (2001).
9. S. Zhang *et al.*, *Nat. Mater.* **9**, 594–601 (2010).
10. M. Kumar *et al.*, *Nat. Chem.* **10**, 696–703 (2018).
11. L. E. O'Leary, J. A. Fallas, E. L. Bakota, M. K. Kang, J. D. Hartgerink, *Nat. Chem.* **3**, 821–828 (2011).
12. Y. Kim, R. J. Macfarlane, M. R. Jones, C. A. Mirkin, *Science* **351**, 579–582 (2016).
13. G. Seelig, D. Soloveichik, D. Y. Zhang, E. Winfree, *Science* **314**, 1585–1588 (2006).
14. R. M. da Silva *et al.*, *Nat. Commun.* **7**, 11561 (2016).
15. W. P. Daley, S. B. Peters, M. Larsen, *J. Cell Sci.* **121**, 255–264 (2008).
16. C. Bonnans, J. Chou, Z. Werb, *Nat. Rev. Mol. Cell Biol.* **15**, 786–801 (2014).
17. L. D. Muiznieks, F. W. Keeley, *Biochim. Biophys. Acta* **1832**, 866–875 (2013).
18. D. Sun, T. C. Jakobs, *Neuroscientist* **18**, 567–588 (2012).
19. S. A. Liddelow, B. A. Barres, *Immunity* **46**, 957–967 (2017).
20. K. Pogoda, P. A. Janmey, *Front. Cell. Neurosci.* **12**, 25 (2018).
21. M. Hara *et al.*, *Nat. Med.* **23**, 818–828 (2017).
22. S. Fedoroff, W. A. McAuley, J. D. Houkle, R. M. Devon, *J. Neurosci. Res.* **12**, 14–27 (1984).
23. V. W. Wu, J. P. Schwartz, *J. Neurosci. Res.* **51**, 675–681 (1998).
24. S. Robel, B. Berninger, M. Götz, *Nat. Rev. Neurosci.* **12**, 88–104 (2011).
25. W. S. Sheng, S. Hu, A. Feng, R. B. Rock, *Neurochem. Res.* **38**, 2148–2159 (2013).
26. E. Moeendarbary *et al.*, *Nat. Commun.* **8**, 14787 (2017).

ACKNOWLEDGMENTS

We thank M. Karver of the Peptide Synthesis Core Facility of the Simpson Querrey Institute at Northwestern University for assistance and key insights into the synthesis and purification of the peptide amphiphiles; M. Seniw for the preparation of graphic illustrations shown in the figures; and L. K. Frederick for assistance with the analysis of the time-lapse video of bundle formation.

Funding: The experimental work was primarily supported by the U.S. Department of Energy, Office of Science, Basic Energy Sciences, under award DE-FG02-00ER45810. Additional support on the synthesis and characterization of peptide-DNA conjugates was provided by Center for Bio-Inspired Energy Sciences (CBES), an Energy Frontiers Research Center (EFRC) funded by the U.S. Department of Energy, Office of Science, Office of Basic Energy Sciences, under award DE-SC0000989. All biological experiments reported were supported by a Catalyst Award from the Center for Regenerative Nanomedicine (CRN) at the Simpson Querrey Institute. The modeling work was supported by NSF award DMR-1610796 and NIH grant 1R01 EB018358-01A1. The U.S. Army Research Office, the U.S. Army Medical Research and Materiel Command, and Northwestern University provided funding to develop the Peptide Synthesis Core Facility (peptide synthesis) and the Analytical BioNanoTechnology Core Facility (biological and chemical analysis) that were used for this work, both of the Simpson Querrey Institute at Northwestern University, and ongoing support is being received from the Soft and Hybrid Nanotechnology Experimental (SHyNE) Resource (NSF NNCI-1542205). This work also made use of the EPIC facility of Northwestern NUANCE Center at Northwestern University, which has received support from the Soft and Hybrid Nanotechnology Experimental (SHyNE) Resource (NSF NNCI-1542205); the MRSEC program (NSF DMR-1121262) at the Materials Research Center; the International Institute for Nanotechnology (IIN); the Keck Foundation; and the State of Illinois, through the IIN. Imaging work was performed at the Northwestern University Center for Advanced Molecular Imaging, supported by NCI CCSG P30 CA060553 awarded to the Robert H. Lurie Comprehensive Cancer Center. J.A.L. was supported by a NSF Graduate Research Fellowship (grant DGE-1324585). Z.A. received postdoctoral support from the Beatriu de Pinós Fellowship 2014 BP-A 00007 (Agència de Gestió d'Ajust Universitaris i de Recerca, AGAUR) and grant PVA17_RF_0008 from the Paralyzed Veterans of America Research Foundation. **Author contributions:** R.F. designed and contributed to all the experiments, analyzed data, and wrote the manuscript; M.H. and E.L. designed the model, performed the simulation, and wrote the manuscript; Z.A. performed the experiments with the astroglial cells and analyzed the related data; J.A.L. contributed to the synthesis and purification of the materials, the characterization of mechanical properties, and SAXS measurements; J.R.W. contributed to the synthesis, purification, and characterization of the peptide-mimetic system; N.S.

contributed to developing synthetic approaches and self-assembly of oligonucleotide-peptide amphiphiles; M.T.M. acquired all SEM images; C.L. contributed to the synthesis and characterization of the oligonucleotide-peptide amphiphiles; J.M.G. contributed to the rheology measurements; H.S. performed the AFM nano-indentation measurements; and S.I.S. supervised the research and wrote the manuscript. **Competing interests:** None declared. **Data and materials availability:** All data needed to evaluate the conclusions in the paper are present in the paper or the supplementary materials.

SUPPLEMENTARY MATERIALS

www.sciencemag.org/content/362/6416/808/suppl/DC1
Materials and Methods
Figs. S1 to S40
Tables S1 to S4
Movie S1
References (*27*–*34*)

16 March 2018; resubmitted 29 May 2018
Accepted 24 September 2018
Published online 4 October 2018
10.1126/science.aat6141

BIOHYBRID MICROBES

Light-driven fine chemical production in yeast biohybrids

Junling Guo[1*†], Miguel Suástegui[1†], Kelsey K. Sakimoto[2,3], Vanessa M. Moody[4], Gao Xiao[1,5], Daniel G. Nocera[2], Neel S. Joshi[1,5*]

Inorganic-biological hybrid systems have potential to be sustainable, efficient, and versatile chemical synthesis platforms by integrating the light-harvesting properties of semiconductors with the synthetic potential of biological cells. We have developed a modular bioinorganic hybrid platform that consists of highly efficient light-harvesting indium phosphide nanoparticles and genetically engineered *Saccharomyces cerevisiae*, a workhorse microorganism in biomanufacturing. The yeast harvests photogenerated electrons from the illuminated nanoparticles and uses them for the cytosolic regeneration of redox cofactors. This process enables the decoupling of biosynthesis and cofactor regeneration, facilitating a carbon- and energy-efficient production of the metabolite shikimic acid, a common precursor for several drugs and fine chemicals. Our work provides a platform for the rational design of biohybrids for efficient biomanufacturing processes with higher complexity and functionality.

Inorganic-biological hybrid systems combine the light-harvesting efficiency of inorganic systems with established biosynthetic pathways in live cells, thus promising a sustainable and efficient biochemical synthesis platform (*1*, *2*). Comprehensive solar-to-chemical production has been investigated with bioinorganic hybrid systems, including semiconductor-conjugated hydrogenases for biohydrogen production (*3*–*5*), long-wavelength–absorbing nanomaterials integrated into plants for enhanced photosynthetic efficiency (*6*), and photoelectrodes coupled with whole cells for hydrogenation reactions (*7*) as well as atmospheric CO_2 and N_2 fixation (*8*–*11*).

Microorganisms are used in biomanufacturing because of their rapid proliferation and ability to convert renewable carbon sources into higher-value chemicals through genetically programmable multistep catalysis (*12*). In the context of inorganic-biological hybrids, autotrophic bacteria have been investigated intensively, with a focus on simple organic molecules (*7*–*14*). Interfacing heterotrophic organisms with light-harvesting inorganics may provide advantages, such as increased efficiency in the production of high-value chemicals (*15*–*17*). Common heterotrophs (e.g., *Saccharomyces cerevisiae*) are already used widely in industrial settings because of the large catalog of target metabolites accessible through genetic manipulation tools (*18*). The well-studied biology of canonical model organisms may provide access to better genetic and analytical tools to unravel the mechanisms governing electron transport and metabolic flux in biohybrid systems (*19*).

Of particular interest is the regeneration of the redox cofactor NADPH (reduced form of nicotinamide adenine dinucleotide phosphate), owing to its central role as a cosubstrate in biosynthetic pathways (*20*). This process is strongly intertwined with biomass production and is a common bottleneck in the production of metabolites through microbial cell factories (*21*). The primary source of NADPH in yeasts is the pentose phosphate pathway (PPP), which oxidizes a hexose sugar with concomitant loss of two equivalents of CO_2, decreasing theoretical carbon yields (*22*). Therefore, decoupling NADPH generation from central carbon metabolism may help maximize carbon flux for the production of desired metabolites (*20*).

We developed a *S. cerevisiae*–indium phosphide (InP) hybrid system, which combines rationally designed metabolic pathways and the electron donation capabilities of illuminated semiconductors (Fig. 1 and fig. S1). InP was selected as a photosensitizer in this biohybrid system because its direct bandgap (E_g = 1.34 eV) enables efficient absorption of a large fraction of the solar spectrum and is positioned appropriately to accept electrons from various species in the culture medium (fig. S2) (*23*). Additionally, its stability to oxygen and biocompatibility suggest that InP is an ideal material for biological integration (*24*). InP nanoparticles were prepared independently (fig. S3) and subsequently assembled on genetically engineered yeast cells by means of a biocompatible, polyphenol-based assembly method (*25*) (Fig. 1A and fig. S1). Yeast strain *S. cerevisiae* Δ*zwf1* was selected for the engineering of the biohybrid system. The deletion of the gene *ZWF1*, encoding the glucose-6-phosphate dehydrogenase enzyme, disrupts the oxidative portion of the PPP (*22*), causing a marked decrease in cytosolic NADPH generation capacity (Fig. 1B). We examined the integrated function of the biohybrid system to regenerate NADPH, which is essential for the biosynthesis of shikimic acid (SA), a precursor of aromatic amino acids (Fig. 1, C and D). *S. cerevisiae* Δ*zwf1* was genetically engineered to overexpress four genes to enhance carbon flux through the SA pathway (Fig. 1B) (*22*). The pentafunctional protein Aro1, which catalyzes the reduction of 3-dehydroshikimic acid (DHS) to SA, is selective for NADPH, and a low availability of cytosolic NADPH directly affects the production of SA, leading to elevated accumulation of its precursor, DHS. In previous examples of biohybrid systems, light-harvesting semiconductor particles attached to the surface of bacteria were able to provide reducing equivalents to central metabolic processes (*12*). We rationalized that the *S. cerevisiae* Δ*zwf1*–InP hybrid system (fig. S4) could operate similarly, with electrons flowing from the illuminated, surface-bound InP particles to the regeneration of NADPH from $NADP^+$ (nicotinamide adenine dinucleotide phosphate) inside the cell (Fig. 1, C and D). This regenerated NADPH can fuel the ultimate conversion of DHS to SA (*26*). Therefore, the *S. cerevisiae* Δ*zwf1*–InP hybrids both enable us to evaluate the efficiency of NADPH regeneration and lead to the enhanced biosynthesis of a highly sought-after molecule through photon energy conversion.

We designed a series of control experiments in which the presence of light and InP nanoparticles was varied (fig. S5). After 72 hours of aerobic growth, *S. cerevisiae* Δ*zwf1*–InP hybrids under illumination (5.6 mW cm^{-2}) (fig. S6) achieved the highest DHS-to-SA conversion rate with a SA/DHS ratio of 23.5 ± 1.6 (Fig. 2A and figs. S7 to S9). In contrast, a control experiment without illumination led to a ratio of only 0.67 ± 0.3 (fig. S10). Similarly, a low SA/DHS ratio was observed in the presence of InP nanoparticles that were not assembled on the cell surface, suggesting the importance of proximity in enabling photochemical synthesis. This is in line with recent reports describing the ability of cell wall–bound components in yeasts to contribute to extracellular electron transport through electron "hopping" mechanisms (*27*). In the absence of InP, *S. cerevisiae* Δ*zwf1* also showed a lower SA/DHS ratio, regardless of illumination scheme (figs. S11 and S12). The total SA production of the illuminated biohybrid system was superior to all other conditions, with a final titer of 48.5 ± 2.1 mg l^{-1}, showing an 11-fold increase compared with its counterpart with no illumination and a 24-fold increase compared with engineered cells in the presence of unattached InP nanoparticles (Fig. 2B). DHS-to-SA conversion yield also increased, to a point, with higher light intensities but decreased under the highest light intensity, possibly as a result of metabolic saturation or photodamage to the cells (fig. S13).

The SA/DHS ratio has previously been shown to serve as a metabolic readout for cytosolic levels

[1]Wyss Institute for Biologically Inspired Engineering, Harvard University, Boston, MA 02115, USA. [2]Department of Chemistry and Chemical Biology, Harvard University, Cambridge, MA 02138, USA. [3]Department of Systems Biology, Harvard Medical School, Boston, MA 02115, USA. [4]Department of Bioengineering, School of Engineering and Applied Sciences, University of Pennsylvania, PA 19104, USA. [5]John A. Paulson School of Engineering and Applied Sciences, Harvard University, Cambridge, MA 02138, USA. ***Corresponding author. Email: junling.guo@wyss.harvard.edu (J.G.); neel.joshi@wyss.harvard.edu (N.S.J.)**
†These authors contributed equally to this work.

of NADPH/NADP$^+$ (*28*). The highest NADPH/NADP$^+$ ratio calculated for the illuminated biohybrid experiment reaches a value of 87.1 ± 6.0 (Fig. 2C). Notably, this value was higher than even that measured for InP-free and -integrated wild-type *S. cerevisiae*, which possesses the fully functional machinery to produce NADPH through the oxidative PPP (fig. S14). *S. cerevisiae* Δ*zwf1* in darkness showed the lowest NADPH/NADP$^+$ ratios, regardless of the presence of InP. These results support the contention that irradiated, cell surface–assembled InP can drive the regeneration of cofactor NADPH, facilitating the conversion of DHS to SA. As determined from colony-forming unit (CFU) assays on nutrient-rich solid media, cell viability did not differ before and after the assembly of InP nanoparticles (Fig. 2D), confirming the biocompatibility of the particle assembly protocol. During fermentation in selective minimal media, cell count decreased for the biohybrids, regardless of the illumination scheme (see supplementary materials for additional discussion).

To further evaluate the metabolic performance of the biohybrid systems, we characterized their ability to consume glucose and variations in carbon flux. Glucose was fully consumed by the bare cells during the first 24 hours, whereas nearly 25% of the total initial glucose remained unused in the complete biohybrid scheme (Fig. 3A). The SA production kinetics in the *S. cerevisiae* Δ*zwf1*–InP hybrids showed that the conversion of DHS to SA occurred throughout the entire illumination period (Fig. 3B), suggesting a continuous supply of NADPH and potential accumulation of biosynthetic intermediates along the SA pathway that lags behind glucose consumption (*29*). This finding was also supported by the consistently high mass fractions of SA (~90%). The specific SA yields of *S. cerevisiae* Δ*zwf1*–InP hybrids surpassed those of the *S. cerevisiae* Δ*zwf1* and the wild-type bare cells cultured in darkness (Fig. 3C). The light-to-SA conversion efficiency reached a maximum of 1.58 ± 0.05% 12 hours after the start of fermentation and dropped as SA production plateaued (fig. S15). To unravel the variations in the central carbon metabolism caused by the illumination of InP in the biohybrids, we measured the production of secreted by-products, including ethanol and glycerol, linked to other pathways (figs. S16 and S17). Figure 3D shows that the concentration of these by-products produced by the illuminated biohybrids (C_L) was lower than its counterpart under dark conditions (C_D). This implies that the surface-assembled, photoexcited InP shunts carbon in *S. cerevisiae* Δ*zwf1* toward the desired SA pathway, with less activity in alternative pathways for NADPH regeneration (e.g., pathways catalyzed by aldehyde dehydrogenase) (Fig. 3E).

Though membrane-bound hydrogenases have been invoked to explain the ability of previously reported analogous bacterial systems to make use of photogenerated electrons (*29*–*31*), *S. cerevisiae* is surrounded by a cell wall composed of extracellular polymeric substances that would prevent direct contact between membrane-bound proteins and the InP particles. The need for proximity between InP particles and the cells suggests that the cell wall might mediate electron transfer in our biohybrids (*27*). Differential pulse voltammetry performed on the spent medium after fermentation (Fig. 3F and fig. S18) exhibited peaks more negative of the thermodynamic potential for NADP$^+$/NADPH [E° = −0.324 V versus normal hydrogen electrode (NHE) at pH 7]. This higher redox activity after *S. cerevisiae* Δ*zwf1* growth suggests that soluble redox-active species likely also play a role in electron transfer, as has been reported for yeast-based microbial fuel cells without exogenous mediators (*32*). The electron transfer mechanism in these *S. cerevisiae* Δ*zwf1*–InP hybrids remains an active subject of investigation, as multiple possible mechanisms (e.g., soluble mediators and cell wall–bound redox mediators) could exist in our biohybrid system.

The development of inorganic-biological hybrid systems in yeast will enable expansion of this overall approach to the production of higher-value metabolites. For example, the production of benzylisoquinoline alkaloids, which is already established in yeast, requires the activity of more than 10 membrane-bound cytochrome P450 oxidoreductases that depend on NADPH as an electron donor (*18*). The technology presented in this work may thus elevate the production efficiency of alkaloid natural products and other drugs and nutraceuticals, though practical implementation

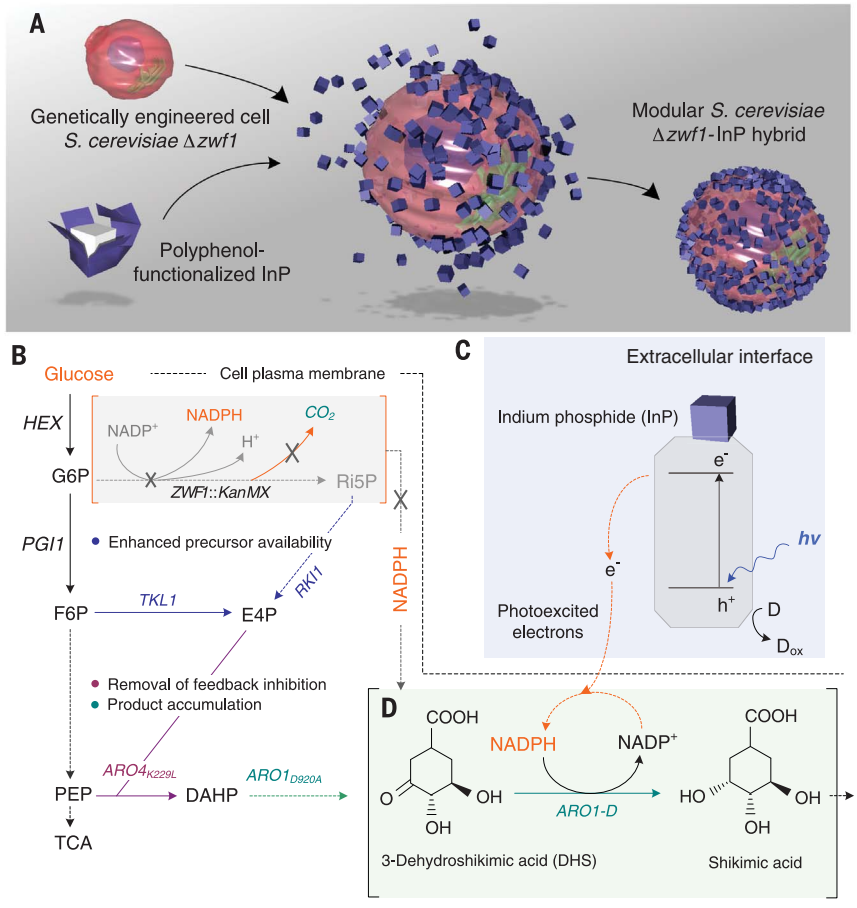

Fig. 1. Assembly of *S. cerevisiae*–InP hybrids and rationally designed metabolic pathways. (**A**) InP nanoparticles were first functionalized with polyphenol moieties and then assembled on the surface of genetically engineered yeast to form modular inorganic-biological hybrids. (**B**) Metabolic engineering scheme for overproduction of SA. *S. cerevisiae* Δ*zwf1* has the oxidative PPP disrupted (*ZWF1*), leading to low cytosolic NADPH pools, which directly affects the SA pathway and reduces carbon loss in the form of CO_2. (**C** and **D**) Schematic of cellular NADPH regeneration and SA biosynthesis assisted by photogenerated electrons from InP nanoparticles. G6P, glucose-6-phosphate; F6P, fructose-6-phosphate; Ri5P, ribulose-5-phosphate; E4P, erythrose-4-phosphate; PEP, phosphoenolpyruvate; DAHP, 3-deoxy-D-arabinoheptulosonate-7-phosphate; HEX, hexokinase; ZWF1, glucose-6-phosphate 1-dehydrogenase; PGI1, phosphoglucose isomerase; RKI1, ribose-5-phosphate ketol-isomerase; TKL1, transketolase; $ARO4_{K229L}$, feedback-insensitive DAHP synthase; $ARO1_{D920A}$, mutant pentafunctional aromatic enzyme; TCA, tricarboxylic acid cycle; h, Planck's constant; ν, frequency; h^+, electron hole; e^-, electron; D, putative electron donors in the cell culture medium; D_{ox}, oxidized electron donor species.

will require the development of illumination sources that interface with scaled-up fermenters. Our synthetic scheme is highly modular, enabling a mix-and-match approach; makes use of cheap components; and is compatible with existing workhorse cellular chassis and a wide range of particle-cell combinations. A more thorough understanding of electron transport mechanisms and global changes to metabolic flux will undoubtedly facilitate design and implementation of even better biohybrid systems. These systems would make use of alternative energy sources to streamline metabolic efficiency. With an ever-growing set of genetic tools, functional nanoparticles, and cell types, modular biohybrid platforms are likely to enable efficient and economical biochemical production of valuable and challenging targets.

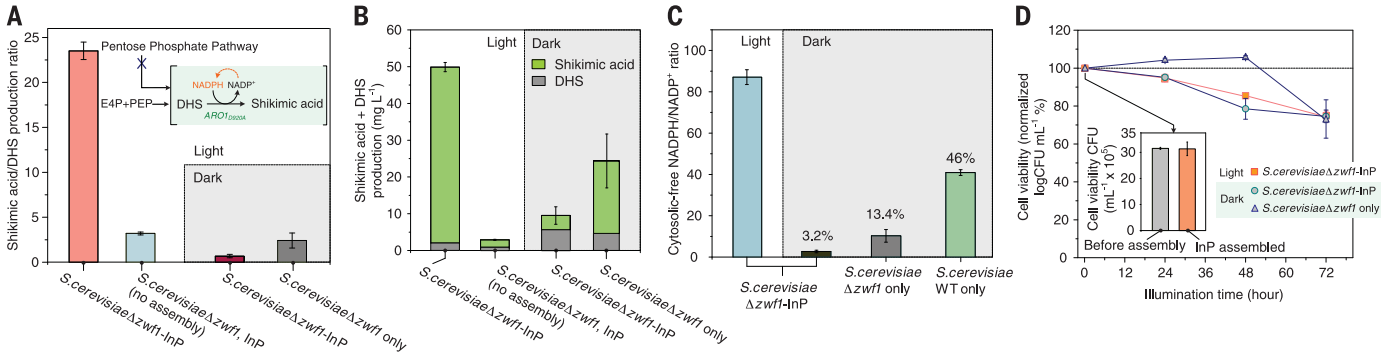

Fig. 2. Physiological and metabolic characterization of the *S. cerevisiae*–InP hybrid system. (**A**) Comparison of SA/DHS ratios in biohybrids and in yeast-only fermentations with light and dark conditions. (**B**) Total accumulation of SA and DHS after 72 hours of growth. (**C**) Estimation of cytosolic-free NADPH/NADP$^+$ ratio, based on the conversion of DHS to SA. (**D**) Cell viability assay based on counting of CFU, performed on rich solid media. The inset shows that the preparation of the biohybrids does not affect the initial CFU amount. Variation is represented by SE (error bars) from three independent replicates for all data points.

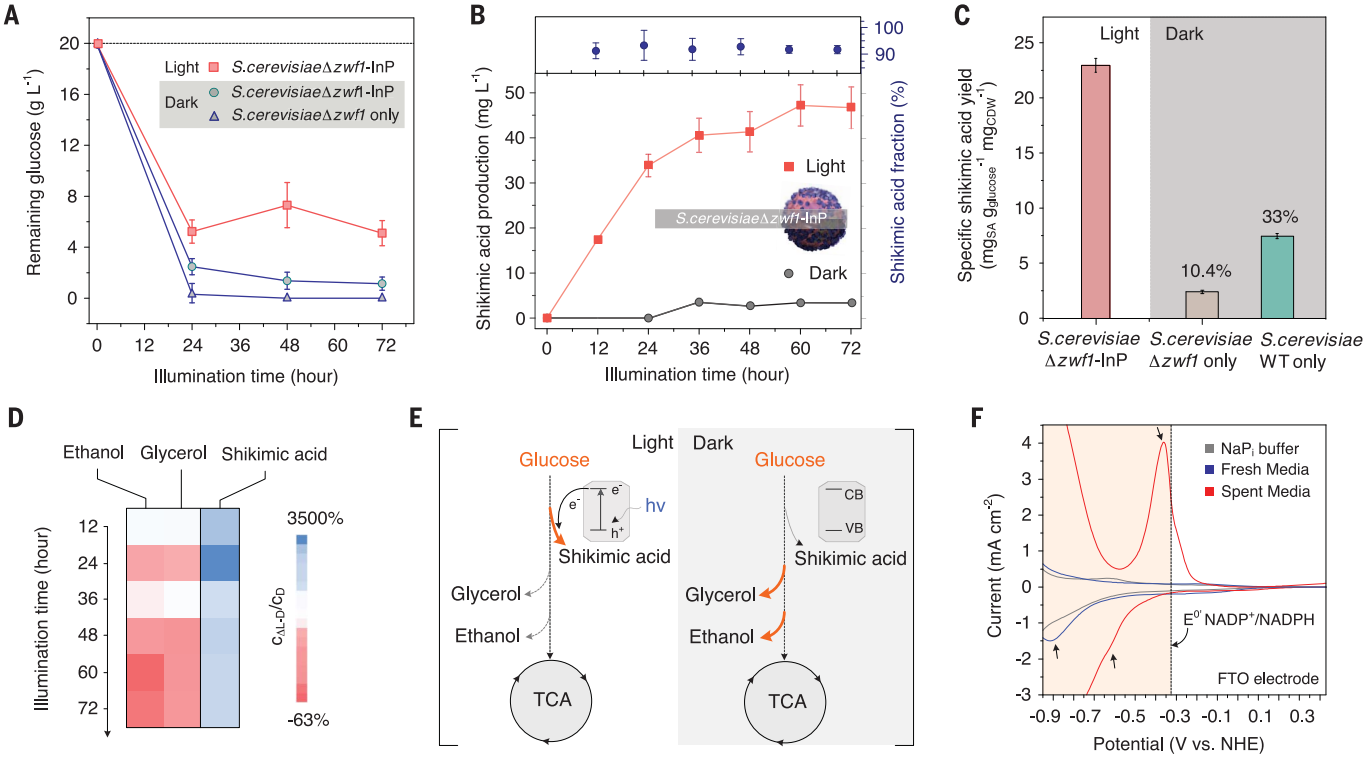

Fig. 3. Carbon utilization, cytosolic-free NADPH, and electron transfer in the *S. cerevisiae*–InP hybrid system. (**A**) Glucose consumption over the course of 72-hour culture. (**B**) SA production profiles in light and dark conditions. SA/DHS conversion yield was expressed as a mass fraction: [SA]/([SA] + [DHS]). (**C**) Specific SA yield based on consumed glucose and cell dry weight (CDW). (**D**) Percent variation in SA and by-product formation of the biohybrids under light (C_L) versus dark (C_D) conditions over time. (**E**) Proposed metabolic flux distributions based on total SA plus DHS concentrations and by-product (glycerol and ethanol) formation. CB, conduction band; VB, valence band. (**F**) Differential pulse voltammetry of culture medium before and after *S. cerevisiae* Δ*zwf1* growth. Arrows indicate electrochemical signatures from possible species with sufficient reducing potential to convert NADP$^+$ to NADPH. NaPi, sodium phosphate; FTO, fluorine-doped tin oxide. Variation is represented by SE (error bars) from three independent replicates for all data points.

REFERENCES AND NOTES

1. R. E. Blankenship *et al.*, *Science* **332**, 805–809 (2011).
2. K. K. Sakimoto, N. Kornienko, P. Yang, *Acc. Chem. Res.* **50**, 476–481 (2017).
3. A. Le Goff *et al.*, *Science* **326**, 1384–1387 (2009).
4. E. Reisner, D. J. Powell, C. Cavazza, J. C. Fontecilla-Camps, F. A. Armstrong, *J. Am. Chem. Soc.* **131**, 18457–18466 (2009).
5. K. A. Brown, M. B. Wilker, M. Boehm, G. Dukovic, P. W. King, *J. Am. Chem. Soc.* **134**, 5627–5636 (2012).
6. J. P. Giraldo *et al.*, *Nat. Mater.* **13**, 400–408 (2014).
7. S. F. Rowe *et al.*, *ACS Catal.* **7**, 7558–7566 (2017).
8. C. Liu, K. K. Sakimoto, B. C. Colón, P. A. Silver, D. G. Nocera, *Proc. Natl. Acad. Sci. U.S.A.* **114**, 6450–6455 (2017).
9. K. A. Brown *et al.*, *Science* **352**, 448–450 (2016).
10. C. Liu, B. C. Colón, M. Ziesack, P. A. Silver, D. G. Nocera, *Science* **352**, 1210–1213 (2016).
11. E. M. Nichols *et al.*, *Proc. Natl. Acad. Sci. U.S.A.* **112**, 11461–11466 (2015).
12. K. K. Sakimoto, A. B. Wong, P. Yang, *Science* **351**, 74–77 (2016).
13. H. Li *et al.*, *Science* **335**, 1596 (2012).
14. W. Wei *et al.*, *Sci. Adv.* **4**, eaap9253 (2018).
15. M. J. Herrgård *et al.*, *Nat. Biotechnol.* **26**, 1155–1160 (2008).
16. J. Förster, I. Famili, P. Fu, B. Ø. Palsson, J. Nielsen, *Genome Res.* **13**, 244–253 (2003).
17. J. D. Keasling, *Science* **330**, 1355–1358 (2010).
18. S. Galanie, K. Thodey, I. J. Trenchard, M. Filsinger Interrante, C. D. Smolke, *Science* **349**, 1095–1100 (2015).
19. J. Nielsen, J. D. Keasling, *Cell* **164**, 1185–1197 (2016).
20. X. Wang *et al.*, *Chem* **2**, 621–654 (2017).
21. S. Li, Y. Li, C. D. Smolke, *Nat. Chem.* **10**, 395–404 (2018).
22. M. Suástegui *et al.*, *Metab. Eng.* **42**, 134–144 (2017).
23. A.-M. Van Wezemael, W. Laflere, F. Cardon, W. Gomes, *J. Electroanal. Chem. Interfacial Electrochem.* **87**, 105–109 (1978).
24. K. K. Sakimoto *et al.*, *J. Am. Chem. Soc.* **140**, 1978–1985 (2018).
25. J. Guo *et al.*, *Nat. Nanotechnol.* **11**, 1105–1111 (2016).
26. M. Suástegui, W. Guo, X. Feng, Z. Shao, *Biotechnol. Bioeng.* **113**, 2676–2685 (2016).
27. Y. Xiao *et al.*, *Sci. Adv.* **3**, e1700623 (2017).
28. J. Zhang *et al.*, *Sci. Rep.* **5**, 12846 (2015).
29. N. Kornienko *et al.*, *Proc. Natl. Acad. Sci. U.S.A.* **113**, 11750–11755 (2016).
30. M. B. Wilker *et al.*, *J. Am. Chem. Soc.* **136**, 4316–4324 (2014).
31. K. Pandey, S. T. Islam, T. Happe, F. A. Armstrong, *Proc. Natl. Acad. Sci. U.S.A.* **114**, 3843–3848 (2017).
32. Y. Hubenova, M. Mitov, *Bioelectrochemistry* **106**, 177–185 (2015).

ACKNOWLEDGMENTS

We thank J. Richardson, G. Bazan, C. Catania, B. Tardy, and Y. Klyachina for helpful discussions; the group of Z. Shao at Iowa State University for providing the shikimic acid constructs; and E. Benecchi and M. Ericsson at the Harvard Medical School electron microscopy facility for help on microtoming techniques. Work was performed in part at the Center for Nanoscale Systems at Harvard University and the NSF's National Nanotechnology Infrastructure Network (NNIN). **Funding:** Work in the N.S.J. laboratory is supported by the National Institutes of Health (1R01DK110770-01A1) and the Wyss Institute for Biologically Inspired Engineering at Harvard University. D.G.N. acknowledges funding support from the National Institutes of Health (GM 47274). K.K.S. acknowledges the Harvard University Center for the Environment Fellowship for support. **Authors contributions:** J.G., M.S., and N.S.J. conceived of the idea. All authors performed research and/or analyzed data. J.G., M.S., N.S.J., K.K.S., and D.G.N. wrote and/or edited the manuscript. **Competing interests:** J.G., N.S.J., and M.S. are inventors on patent application 62691397 submitted by Harvard University and the Wyss Institute that covers photochemical biosynthesis enabled by biohybrids of the type described in this paper. **Data and materials availability:** All data are available in the main text or the supplementary materials. The primary strain used in this study, *S. cerevisiae* BY4741 zwf1Δ (MATa, his3Δ1, leu2Δ0, met15Δ0, ura3Δ0, zwf1Δ::KanMX), was obtained under an MTA from Iowa State University.

SUPPLEMENTARY MATERIALS

www.sciencemag.org/content/362/6416/813/suppl/DC1
Materials and Methods
Supplementary Text
Figs. S1 to S19
References (*33*–*35*)

14 June 2018; accepted 1 October 2018
10.1126/science.aat9777

NANOMATERIALS

Wafer-scale single-crystal hexagonal boron nitride film via self-collimated grain formation

Joo Song Lee[1,2], Soo Ho Choi[3], Seok Joon Yun[4], Yong In Kim[5], Stephen Boandoh[6], Ji-Hoon Park[4,5], Bong Gyu Shin[4,7,8], Hayoung Ko[1,5], Seung Hee Lee[2], Young-Min Kim[4,5], Young Hee Lee[4,5]*, Ki Kang Kim[6]*, Soo Min Kim[1]*

Although polycrystalline hexagonal boron nitride (PC-hBN) has been realized, defects and grain boundaries still cause charge scatterings and trap sites, impeding high-performance electronics. Here, we report a method of synthesizing wafer-scale single-crystalline hBN (SC-hBN) monolayer films by chemical vapor deposition. The limited solubility of boron (B) and nitrogen (N) atoms in liquid gold promotes high diffusion of adatoms on the surface of liquid at high temperature to provoke the circular hBN grains. These further evolve into closely packed unimodal grains by means of self-collimation of B and N edges inherited by electrostatic interaction between grains, eventually forming an SC-hBN film on a wafer scale. This SC-hBN film also allows for the synthesis of wafer-scale graphene/hBN heterostructure and single-crystalline tungsten disulfide.

Hexagonal boron nitride (hBN), called white graphite, consists of atomically flat layers of alternating hexagonal B and N atoms held together by van der Waals interaction between layers. The insulating hBN plays a role in a variety of fundamental science and technology fields, serving, for example, as a platform for charge fluctuation, contact resistance, gate dielectric, passivation layer, Coulomb drag, and atomic tunneling layer (*1*–*6*). Although micrometer-sized hBN grains have been commonly employed for fundamental studies, wafer-scale single-crystalline hBN (SC-hBN) films are not yet available for practical applications. One approach to reach SC-hBN film is to start with grains of a triangular shape at random orientations and eventually merge them to form the polycrystalline hBN (PC-hBN) film. However, grain boundaries between randomly oriented hBN grains inevitably yield PC-hBN film. An alternative to achieve SC-hBN film is therefore desired.

The concept for the synthesis of SC-hBN film is schematically shown in Fig. 1, A to C. Au is liquefied at high temperatures (~1100°C) and robustly anchored on W foil still holding in solid state owing to the high melting temperature (~3422°C). The key idea is to retain a flat liquid Au with high surface tension to allow for strong adhesion to borazine precursors (Fig. 1A, i). The solubility of B and N atoms in liquid Au (at 1100°C) is ~0.5 and ~0 atomic %, respectively (*7*, *8*), ensuring prevalent surface diffusion of B and N atoms rather than bulk diffusion (Fig. 1A, ii). At the initial growth stage (~30 s), the diameter sizes of circular hBN grains are irregularly distributed from approximately a few micrometers to ~14.0 μm (Fig. 1C, i, and supplementary materials and methods). The circular hBN grains increase to a regular size of 14.5 μm after 10 min of growth (Fig. 1C, ii). These circular hBN grains are also observed on liquid Cu substrate at high temperatures, rather than triangular hBN grains on solid substrates at low temperatures (*9*–*12*). The detailed edge structures and the corresponding edge energy of circular hBN grains should be investigated further. High diffusion of adatoms on a smooth liquid surface at high temperatures provokes the circular hBN domains. The size and uniformity of hBN grains are strongly influenced by the content of borazine and H_2 (fig. S1).

After a prolonged growth of 20 min (Fig. 1C, iii), the density of hBN grains further increases without a noticeable progressive change in size. Moreover, the well-regulated sizes of hBN grains are linearly aligned in some regions, indicated by white arrows. When two hBN grains merge, the individual grains are rotated by less than 60° with respect to each other by means of attractive Coulomb interaction between B (Lewis acid) and N (Lewis base) atoms, leading to a seamless stitching by the self-collimated hBN grains (Fig. 1A, iii and iv, and fig. S2), which is as a result of the cohesive energy of a B–N bond being much higher than that of an N–N or B–B bond at a high growth temperature (1100°C) (fig. S3). In addition, the orientation of the hBN grains is not commensurate with the lattice orientation of the underlying Au substrate, which is confirmed by electron backscatter diffraction measurements (fig. S4). The hBN grains are transformed further into a hexagonal close-packed structure at 30-min growth time through the self-collimation of hBN grains (Fig. 1C, iv). The seamless stitching of aligned hBN grains with the absence of grain boundary was further confirmed by the statistical analysis of a series of selected-area electron diffraction (SAED) patterns in transmission electron microscopy (TEM) by means of hBN transfer on a graphene-supported (or MoS_2-supported) TEM grid (figs. S5 to S8). Even at a longer growth time (~90 min), hBN grains were not fully merged with the presence of nanopores observed at a fixed precursor flow rate (fig. S9). We were able to achieve the full coverage of wafer-scale hBN film through two-step growth of elevated growth time and additional precursor flow rate (Fig. 1A, vi, and Fig. 1C, v to vi, and supplementary materials and methods). A wafer-scale full SC-hBN film is obtained with a size of 3 cm by 3 cm, followed by transfer to an SiO_2/Si wafer (Fig. 1B).

The grain size distribution and coverage as a function of growth time are displayed in Fig. 1D. The grain size rapidly increases to saturate at ~14.5 μm within 5-min growth time, whereas the standard deviation of the grain size abruptly decreases. The hBN grains are rapidly grown at a rate of ~283 μm^2/s owing to the high-temperature process (1100°C), which is ~10^6 times higher than the typical growth rate of hBN on solid substrate at lower temperature (~1000°C) (*10*). Meanwhile, the hBN coverage gradually increases and saturates to a full coverage at 60-min growth time. We emphasize that monolayer SC-hBN is achieved on a wafer scale with no appreciable multilayer hBN islands, confirmed by scanning electron microscope (SEM) images (fig. S10). This implies that monolayer hBN film is grown exclusively by means of surface-mediated growth on catalytic metal substrate under the current growth conditions. The stoichiometry of B and N atoms is 1:1.03, confirmed by x-ray photoelectron spectroscopy (XPS) (fig. S11). Furthermore, the expensive Au foil can be reused for the repeated growth of SC-hBN film (fig. S12).

We characterized the single crystallinity of hBN film on a large scale by three different methods: electron diffraction in TEM, liquid crystal (LC)–assisted polarized optical microscope (POM), and low-energy electron diffraction (LEED). The monolayer nature of hBN film is identified at the edge of hBN grains prepared on a TEM grid (Fig. 2, A and B), again confirming the results of atomic force microscopy analysis (fig. S13). Furthermore, the high-resolution TEM displays clear hexagonal B and N atoms (Fig. 2C). Fast Fourier transform spots from the

[1]Institute of Advanced Composite Materials, Korea Institute of Science and Technology (KIST), Wanju-Gun, 55324, Republic of Korea. [2]Applied Materials Institute for BIN Convergence, Department of BIN Fusion Technology and Department of Polymer-Nano Science and Technology, Chonbuk National University, Jeonju, 54896, Republic of Korea. [3]Department of Physics, Dongguk University-Seoul, Seoul, 04620, Republic of Korea. [4]Center for Integrated Nanostructure Physics (CINAP), Institute for Basic Science (IBS), 16419, Republic of Korea. [5]Department of Energy Science, Sungkyunkwan University, Suwon, 16419, Republic of Korea. [6]Department of Energy and Materials Engineering, Dongguk University-Seoul, Seoul, 04620, Republic of Korea. [7]Center for Quantum Nanoscience (QNS), Institute for Basic Science (IBS), Ewha Womans University, Seoul, 03760, Republic of Korea. [8]Department of Physics, Sungkyunkwan University, Suwon, 16419, Republic of Korea.
*Corresponding author. Email: kkkim@dongguk.edu (K.K.K.); leeyoung@skku.edu (Y.H.L.); smkim@kist.re.kr (S.M.K.)

whole image (inset of Fig. 2C) demonstrate only one set of hexagonal spots, assuring the hexagonal structure of the sample. The d-spacings of the $(10\bar{1}0)$ and $(11\bar{2}0)$ planes are 2.17 and 1.26 Å, respectively, confirming SC-hBN, in good agreement with reported values (*13*). The aberration-corrected dark field in the scanning tunneling electron microscopy image and intensity profile along the white-dashed line clearly distinguish the B and N atoms in the hexagonal lattice, with higher intensity of N atoms than that of B atoms (Fig. 2, D and E) (*14*, *15*). The bond length between B and N atoms is 1.45 Å (*16*). A series of SAED patterns vertically stacked by nine frames from regions I to IX in Fig. 2A (fig. S14) exhibit identical six hexagonal dots (Fig. 2F), ensuring that the hBN film is single crystalline in a selected area of ~300 μm by 300 μm. By spin-coating nematic LC on hBN film, the POM patterns in the absence of grains are not altered, regardless of polarized angles, again demonstrating the single crystallinity of hBN on a large scale (Fig. 2G and fig. S15). This is contrasted with inhomogeneous grain speckles with polarized angles due to the presence of multi-hBN grains in the PC-hBN film (fig. S16) (*17*). LEED images from 16 different regions in a 4 mm by 4 mm area with a separation of 1 mm display identical distorted hexagonal spots with the same rotation angle (Fig. 2H), indicating that the hBN film is indeed a single crystal over the whole area. An elongated uniaxial strain of ~14% is observed, similar to that noted in previous reports (*18*–*20*). The hBN lattice is relaxed after hBN transfer on the TEM grid and, consequently, the regular hexagonal lattice is preserved by restoring the strain without provoking fracture.

Our SC-hBN film can serve as a platform growth substrate for construction of a vertical, two-dimensional (2D) heterostructure or single-crystal 2D material on a wafer scale (*21*). We now demonstrate the synthesis of a single-crystal vertical graphene/hBN heterostructure (SC/Gr-hBN) and single-crystal WS_2 (SC-WS_2) film on a wafer scale. Epitaxial graphene is successively grown in situ on SC-hBN film at 1100°C under methane atmosphere (Fig. 3A and supplementary materials and methods). The orientationally aligned hexagonal graphene domains on SC-hBN film are clearly visible (Fig. 3B), eventually achieving the monolayer graphene film in a large area at a prolonged growth time while preserving SC-hBN film (Fig. 3C). SC-Gr/hBN film is transferred onto the SiO_2-Si substrate and onto the TEM grid for further characterizations. The G-band (~1585 cm^{-1}) and 2D-band (~2686 cm^{-1}) peaks in the Raman spectrum are clearly detected without a noticeable D-band (~1330 cm^{-1}) (Fig. 3D). Moreover, the E_{2g} phonon mode of monolayer hBN film is observed near 1370 cm^{-1} (inset of Fig. 3D). The SC-Gr/hBN film stacked at eight different regions in SAED patterns in TEM (fig. S17) shows an identical set of six hexagonal dots (Fig. 3E). This proves that the well-defined structure between graphene and SC-hBN is constructed by means of AA′-stacking with two distinct dots assigned to the $(10\bar{1}0)$ planes of graphene and hBN (inset of Fig. 3E) and the relative rotation angle between two dots of 0.64 ± 0.34° obtained from eight different regions (fig. S17). Furthermore, the moiré pattern of Gr/hBN heterostructure is clearly observed with a wavelength of ~9.20 nm rotated by 1.2° (Fig. 3, F and G, and fig. S18), ensuring the successful synthesis of SC-Gr/hBN film through van der Waals epitaxy (*22*). The distinct B-K, C-K, and N-K edges in the electron energy loss spectroscopy with preserved stoichiometry of B and N of 1.03:1 further support the growth of SC-Gr/hBN film (fig. S18C).

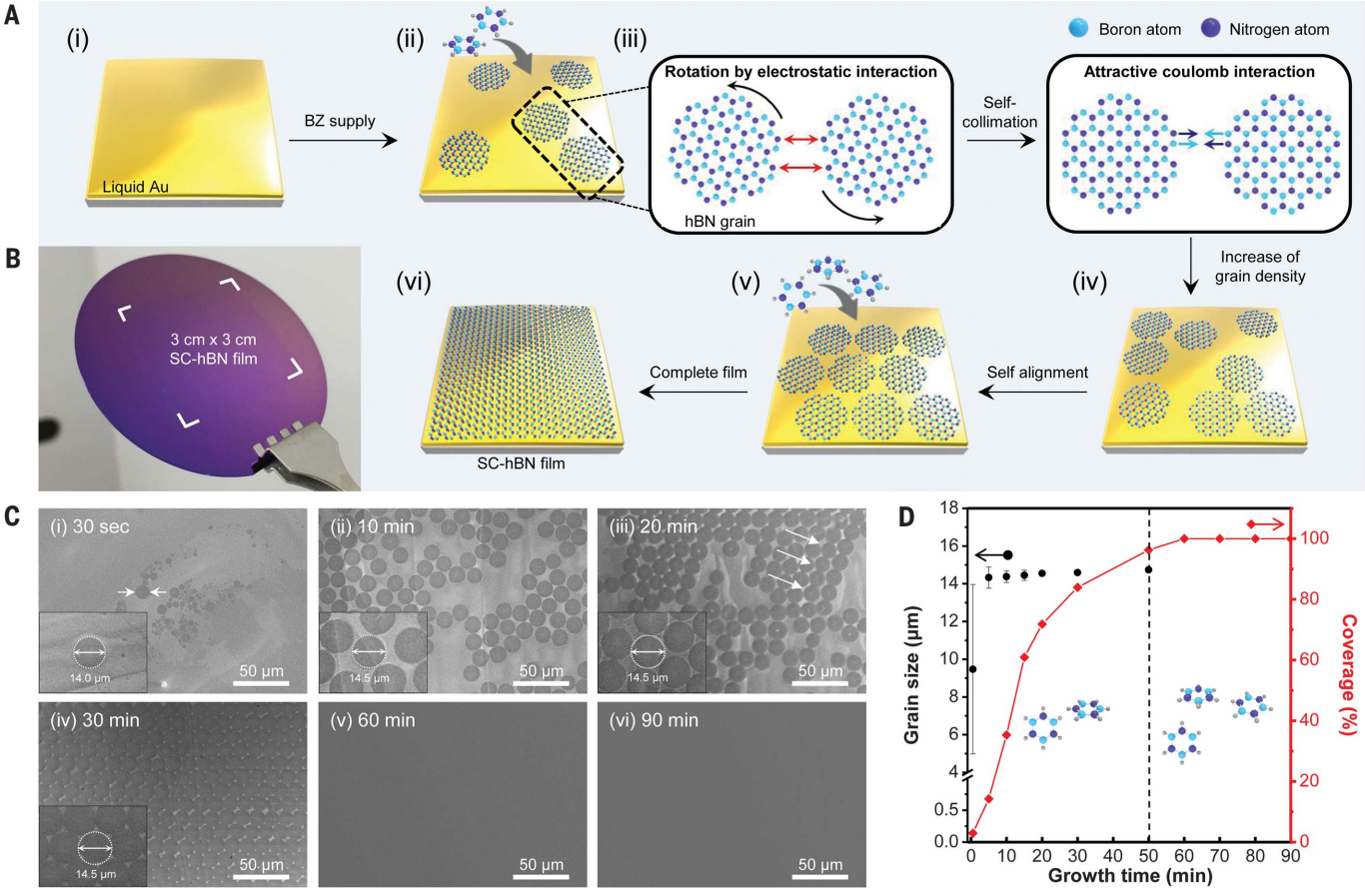

Fig. 1. Synthesis of single-crystal hBN film. (**A**) Schematic illustration for the growth of SC-hBN film by means of self-collimated circular hBN grains with a rotation invoked by the attractive Coulomb interaction of B and N edges between grains (i to vi). BZ, borazine. (**B**) Photograph of a wafer-scale SC-hBN film on a SiO_2-Si wafer. (**C**) Growth evolution of SEM images of hBN film. Single-headed arrows indicate linear alignment of hBN grains. (**D**) Time evolution of hBN grain size and coverage. Full coverage of monolayer hBN film is achieved at 60-min growth time. Error bars indicate the size deviation of hBN grains.

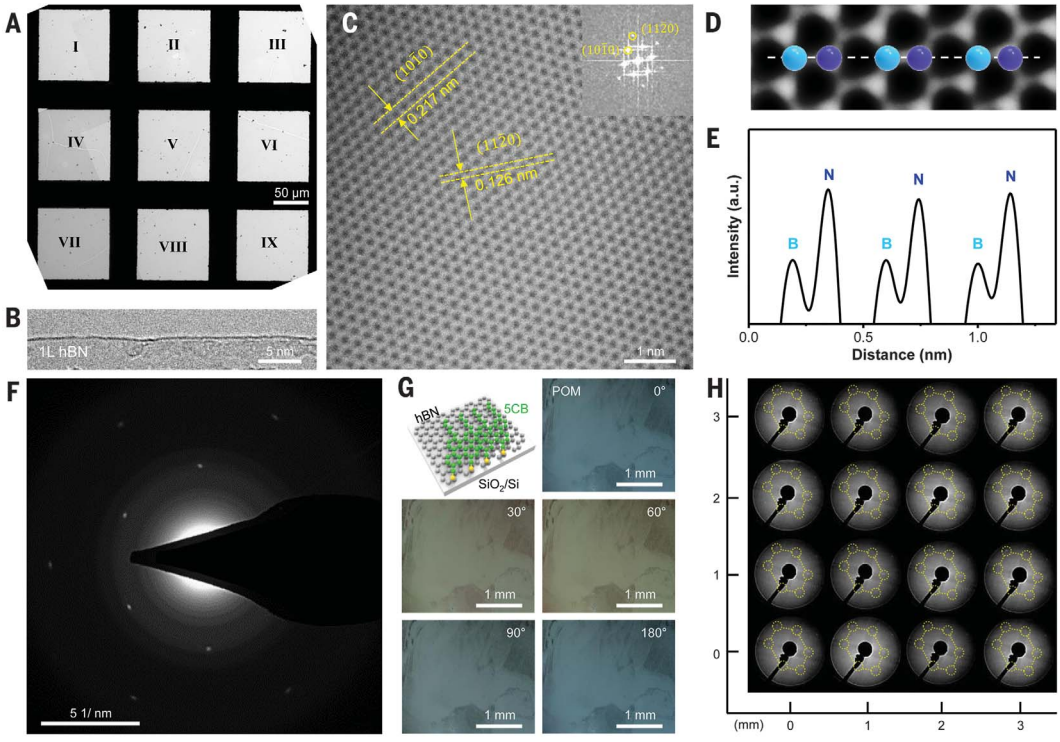

Fig. 2. Atomic structures of SC-hBN film. (**A**) TEM image of SC-hBN film transferred onto TEM grid divided into nine regions. (**B**) The folded edge of a monolayer (1L) SC-hBN film. (**C**) High-resolution TEM image of SC-hBN film. The inset shows the fast Fourier transform of the whole image. The d-spacings of (10$\bar{1}$0) and (11$\bar{2}$0) planes of hBN are 0.217 and 0.126 nm, respectively. (**D**) Aberration-corrected dark-field TEM image of SC-hBN film. Cyan and blue balls indicate B and N atoms, respectively. (**E**) Intensity profile along white-dashed line in (D). a.u., arbitrary units. (**F**) Vertically stacked SAED pattern image of nine segments from regions I to IX in (A). (**G**) Schematic illustration of aligned LC (5CB) on SC-hBN and optical images of 5CB-coated SC-BN film as a function of the polarized light angles: 0, 30, 60, 90, and 180°. (**H**) LEED pattern images of SC-hBN film on Au substrate over an area of 4 mm by 4 mm.

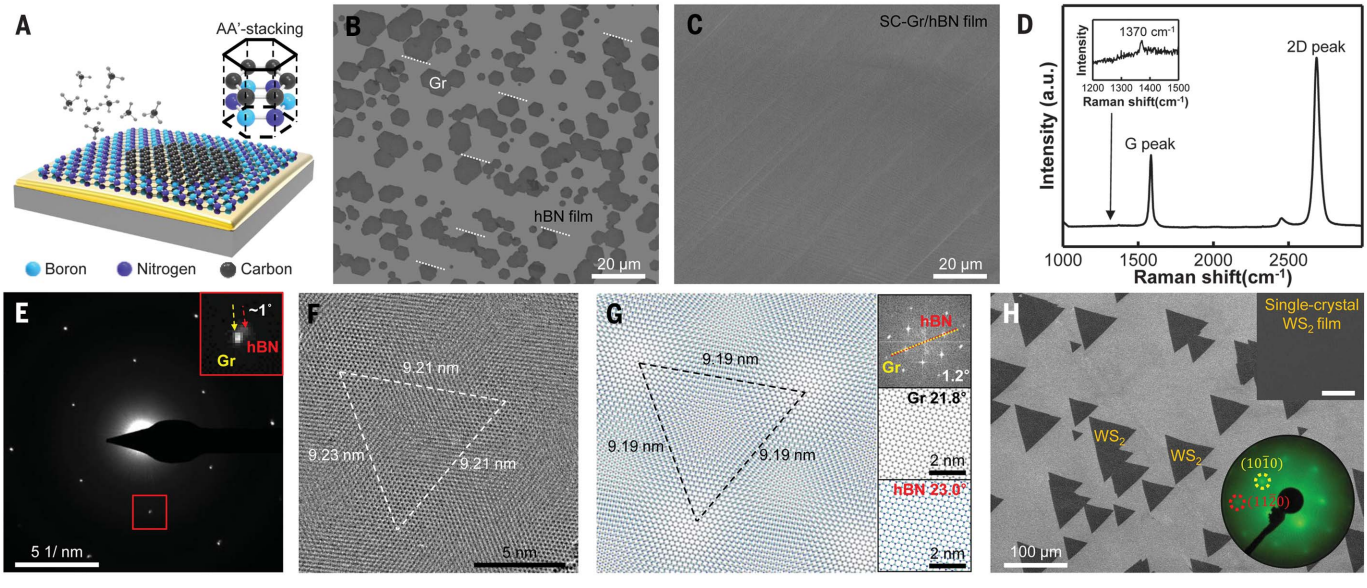

Fig. 3. Direct growth of vertical SC-Gr/hBN heterostructure and single-crystal WS_2 film. (**A**) Schematic for the direct growth of commensurate epitaxial graphene on SC-hBN film. (**B**) SEM image of as-grown hexagonal graphene domains on SC-Gr-BN film and (**C**) the corresponding large-area SC-Gr/hBN film. The dashed lines in (B) indicate the aligned orientation of individual hexagons. (**D**) Representative Raman spectrum of graphene/hBN heterostructure after transfer onto SiO_2/Si substrate. The inset shows the Raman spectrum near 1370 cm^{-1}, assigned to the E^1_{2g} phonon mode of hBN. (**E**) Combined SAED pattern stacked vertically by eight SAED patterns for graphene/hBN heterostructure. The inset shows a zoomed-in SAED pattern of one of the hexagonal spots, revealing an angle deviation of ~1° between two spots. (**F**) Representative moiré pattern of graphene on hBN, with a rotation angle of ~1.2° between the components, and (**G**) the corresponding simulated moiré pattern. The wavelength of the moiré pattern is ~9.20 nm. The three insets depict the diffraction pattern and schematics of graphene and hBN lattices, each rotated 21.8° and 23.0° from the horizon. (**H**) SEM image of triangular WS_2 domains grown on SC-hBN film. The right top and bottom insets show the SEM image of as-grown single-crystal monolayer WS_2 film with a scale bar of 100 μm and the corresponding LEED pattern image with (11$\bar{2}$0) and (10$\bar{1}$0) planes of monolayer WS_2.

Meanwhile, the ex situ growth of SC-WS_2 film on SC-hBN film is performed. To synthesize SC-WS_2, SC-hBN film is coated with a W precursor, and the growth of WS_2 film is further carried out at 900°C under Ar, H_2, and ammonium sulfide atmosphere (supplementary materials and methods). The aligned triangular WS_2 domains are clearly observed (Fig. 3H), and large-scale monolayer WS_2 film successfully proceeds at a prolonged growth time (right-top inset of Fig. 3H). This is markedly distinct from a previous report that both on-top and inverse triangular WS_2 domains are mixed on bare Au, leading to polycrystalline WS_2 film (figs. S19A and S20) (*23*). Therefore, SC-hBN film plays a crucial role to attain homogeneous orientation of the triangular WS_2 domains. The synthesis of such homogeneous triangular WS_2 domains is further confirmed by Raman spectroscopy, photoluminescence, and scanning tunneling electron microscopy (fig. S21). All triangular WS_2 domains have similar aligned orientations within ±1.33° (fig. S19, C and D), and a single set of six hexagonal dots of SC-WS_2 film (LEED) is clearly observed (Fig. 3H), revealing that the large-area monolayer WS_2 film is indeed a single crystal. The growth of MoS_2 domains with similar orientations is also achieved (fig. S22), further supporting universal growth of SC-hBN film as a substrate for the transition metal dichalcogenides. In contrast with SC-Gr-hBN heterostructure film, the presence of hBN after growth of WS_2 film is not detected, indicating that the hBN film might have been substituted or etched away during the growth of WS_2 film. Further study is required to understand the growth mechanism for SC-WS_2 film on SC-hBN film.

We further demonstrate that the wafer-scale SC-hBN film can serve as a protecting layer against metal oxidation and a gas-diffusion barrier for water vapor transmission (*24*, *25*). Cu foil is chosen as a test metal, which is easily oxidized in air. For the oxidation test, hBN film is transferred onto Cu foil (supplementary materials and methods). For comparison, PC-hBN film synthesized on solid Au substrate is used (fig. S9). The Cu surface covered by SC-hBN film is not noticeably changed after the oxidation test at 300°C in air, whereas both PC-hBN–covered and bare Cu surfaces are severely oxidized (Fig. 4, A, F, K and B, G, L), indicative of the change

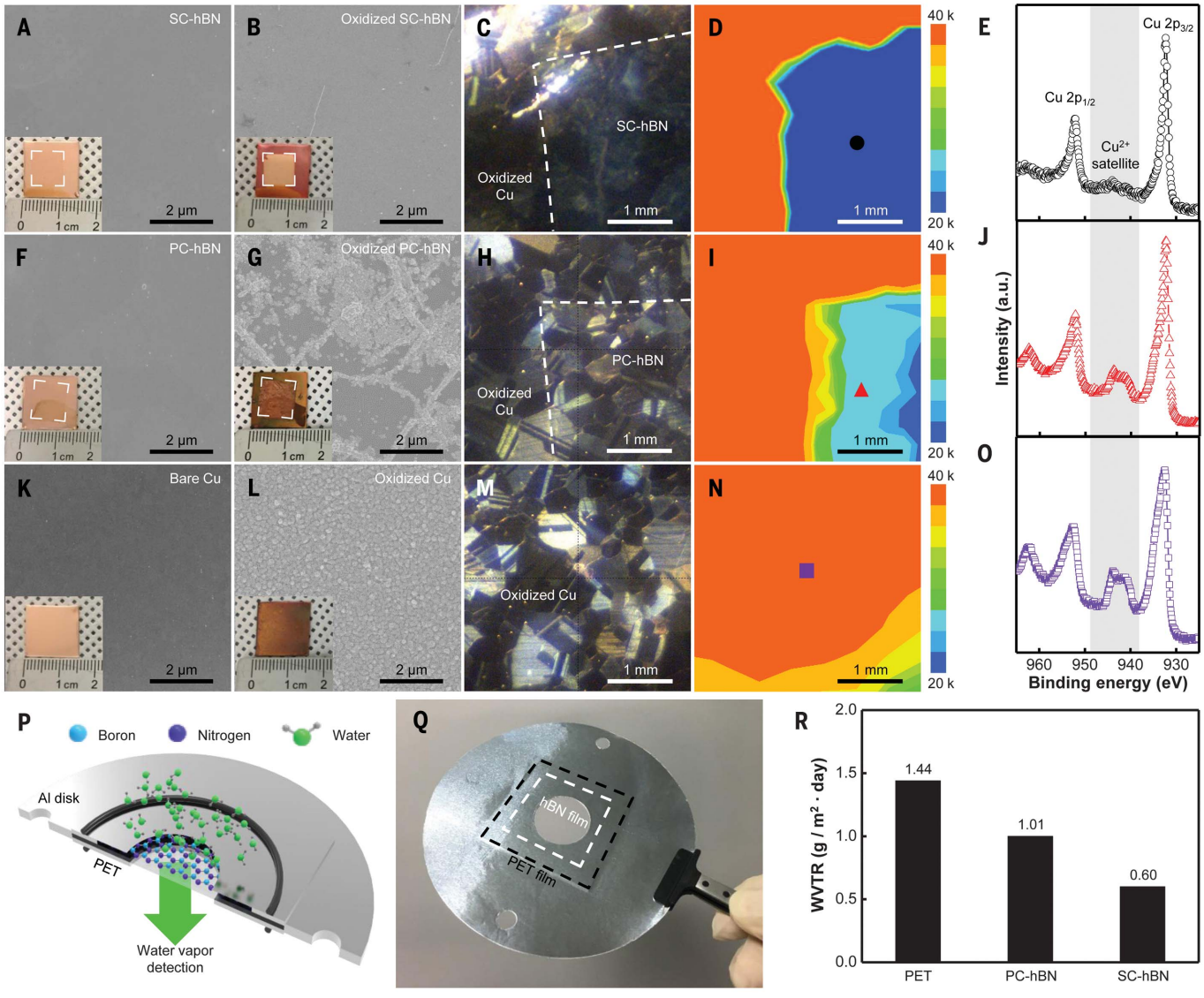

Fig. 4. Protecting layer against Cu oxidation and water vapor barrier applications of wafer-scale SC-hBN film. SEM images of SC-hBN–, PC-hBN–covered, and bare Cu foils before (**A**, **F**, and **K**) and after (**B**, **G**, and **L**) oxidation in air at 300°C for 1 hour. Optical (**C**, **H**, and **M**) and corresponding XPS (**D**, **I**, and **N**) mapping images of SC-hBN, PC-hBN, and bare Cu samples after oxidation. (**E**, **J**, and **O**) Representative Cu 2p core level spectra from the circle, triangle, and square symbols from (D), (I), and (N). The peaks near 952.2 and 932.3 eV in the spectra are assigned to Cu $2p_{1/2}$ and Cu $2p_{3/2}$, respectively. (**P** and **Q**) Schematic and photograph for the WVTR measurement. (**R**) WVTR values of PET, PC-hBN, and SC-hBN samples.

of color from orange to dark orange in each photograph. Some regions of PC-hBN–covered Cu surface withstand oxidation because of the presence of hBN grains (Fig. 4G), but O_2 or H_2O gases easily permeate through the structural defects such as grain boundary or point defect, leading to Cu oxidation. For quantitative analysis of Cu oxidation, the samples are characterized by optical microscope and corresponding XPS mapping for the Cu^{2+} satellite peak near 943 eV in Cu 2p core-level spectra, related to CuO (Fig. 4, C, H, M and D, I, N) (*26*). The XPS mapping image for the SC-hBN sample is quite uniform with low intensity of the CuO peak (Fig. 4D), whereas PC-hBN and bare Cu samples show prominent CuO peaks (Fig. 4, I and N). The representative CuO peak in Cu 2p core-level spectra for SC-hBN sample is negligible, whereas it appears developed for both PC-hBN and bare Cu samples (Fig. 4, E, J, and O). For gas-diffusion barrier application, water vapor transmission rate (WVTR) measurement is carried out for hBN film transferred onto polyethylene terephthalate (PET) film (Fig. 4, P to R and supplementary materials and methods). The WVTR values of PC-hBN and SC-hBN monolayer films are obtained to be 1.01 and 0.60 g/m^2·day, respectively, which are 30% and 58% less than that of PET (1.44 g/m^2·day). The SC-hBN monolayer film outperforms the PC-hBN monolayer film by approximately a factor of 2. The obtained WVTR value is comparable to that of monolayer polycrystalline graphene film (*27*), but it is envisaged to be further improved after optimization of the transfer technique. The wafer-scale SC-hBN film does not have any grain boundary, resulting in a water vapor barrier and the complete protection against Cu oxidation.

In summary, we have synthesized SC-hBN film by means of self-collimation between self-regulated circular hBN grains without a grain boundary. The key step is the facile rotation of circular hBN grains on the liquid Au substrate, regulated by attractive electrostatic interaction between B and N atoms at the perimeter of each grain that eventually leads to the single-crystal growth of hBN film on a wafer scale. The SC-hBN film serves as a promising substrate for the single-crystal growth of the graphene/hBN heterostructure and WS_2 film on a wafer scale. Our strategy for the synthesis of SC-hBN film opens a new horizon for the single-crystal growth of other 2D materials and their heterostructures on a wafer scale.

REFERENCES AND NOTES

1. J. Xue *et al.*, *Nat. Mater.* **10**, 282–285 (2011).
2. J. Wang *et al.*, *Adv. Mater.* **28**, 8302–8308 (2016).
3. S. K. Jang, J. Youn, Y. J. Song, S. Lee, *Sci. Rep.* **6**, 30449 (2016).
4. H.-S. Ra, A.-Y. Lee, D.-H. Kwak, M.-H. Jeong, J.-S. Lee, *ACS Appl. Mater. Interfaces* **10**, 925–932 (2018).
5. B. Amorim, J. Schiefele, F. Sols, F. Guinea, *Phys. Rev. B* **86**, 125448 (2012).
6. L. Britnell *et al.*, *Nano Lett.* **12**, 1707–1710 (2012).
7. R. W. Cahn, *ASM Handbook: Binary Alloy Phase Diagrams–Second edition* (ASM International, 1990).
8. H. Okamoto, T. B. Massalski, "Au-B (Gold-Boron)" in *Binary Alloy Phase Diagrams* (ASM International, ed. 2, 1990), pp. 340–342.
9. L. Tan *et al.*, *Adv. Electron. Mater.* **1**, 1500223 (2015).
10. K. K. Kim *et al.*, *Nano Lett.* **12**, 161–166 (2012).
11. Y. Liu, S. Bhowmick, B. I. Yakobson, *Nano Lett.* **11**, 3113–3116 (2011).
12. X. Fu, R. Zhang, *Nanoscale* **9**, 6734–6740 (2017).
13. Y. Xue *et al.*, *Nanoscale Res. Lett.* **8**, 49 (2013).
14. N. Alem *et al.*, *Phys. Rev. B* **80**, 155425 (2009).
15. M. L. Odlyzko, K. A. Mkhoyan, *Microsc. Microanal.* **18**, 558–567 (2012).
16. L. Wirtz, A. Rubio, R. A. de la Concha, A. Loiseau, *Phys. Rev. B* **68**, 045425 (2003).
17. J.-H. Park *et al.*, *ACS Nano* **8**, 8520–8528 (2014).
18. E. A. Soares, G. S. Leatherman, R. D. Diehl, M. A. Van Hove, *Surf. Sci.* **468**, 129–136 (2000).
19. R. C. Paul *et al.*, "Study of uniaxial tensile properties of hexagonal boron nitride nanoribbons" in *TENCON 2017 – 2017 IEEE Region 10 Conference* (IEEE, 2017), p. 2783.
20. A. Falin *et al.*, *Nat. Commun.* **8**, 15815 (2017).
21. W. Yang *et al.*, *Nat. Mater.* **12**, 792–797 (2013).
22. S. Tang *et al.*, *Sci. Rep.* **3**, 2666 (2013).
23. F. Hanke, J. Björk, *Phys. Rev. B* **87**, 235422 (2013).
24. Z. Liu *et al.*, *Nat. Commun.* **4**, 2541 (2013).
25. J. Meyer *et al.*, *Adv. Mater.* **21**, 1845–1849 (2009).
26. S. Poulston, P. M. Parlett, P. Stone, M. Bowker, *Surf. Interface Anal.* **24**, 811–820 (1996).
27. T. H. Seo *et al.*, *Sci. Rep.* **6**, 24143 (2016).

ACKNOWLEDGMENTS

We thank H. Jung in the Department of Chemistry at Dongguk University for the discussion about the self-collimation of hBN grains. **Funding:** S.M.K. acknowledges support by the Basic Science Research Program through the National Research Foundation of Korea (NRF) funded by the Ministry of Science, ICT and Future Planning (2018R1A2B2002859), and the Korea Institute of Science and Technology (KIST) Institutional Program. K.K.K. acknowledges support by the Basic Science Research Program through the National Research Foundation of Korea (NRF) funded by the Ministry of Science, ICT and Future Planning (2015R1C1A1A02037083) and (2018R1A2B2002302). Y.-M.K. acknowledges support by the Institute for Basic Science (IBS-R011-D1) and Creative Materials Discovery Program (NRF-2015M3D1A1070672) through the NRF grant. S.J.Y. and Y.H.L. acknowledge support by the Institute for Basic Science (IBS-R011-D1). **Author contributions:** J.S.L., K.K.K., and S.M.K. designed and developed this work. S.H.C. and S.B. performed the growth of SC-WS_2. S.J.Y. performed Raman and PL measurements. Y.-M.K. and Y.I.K. performed TEM measurements. J.H.P. performed POM measurement. B.G.S. performed the LEED measurement. H.K. performed the experiments of the protecting layer and WVTR measurement. S.H.L. and Y.H.L. guided and analyzed the work. J.S.L, K.K.K., Y.H.L., and S.M.K. wrote the manuscript. All authors participated in the manuscript review. **Competing interests:** The authors have no competing interests. **Data and materials availability:** All data are available in the main text or the supplementary materials.

SUPPLEMENTARY MATERIALS

www.sciencemag.org/content/362/6416/817/suppl/DC1
Materials and Methods
Figs. S1 to S22
Table S1
References (*28–39*)

30 May 2018; accepted 3 October 2018
10.1126/science.aau2132

ULTRAFAST DYNAMICS

Beyond the molecular movie: Dynamics of bands and bonds during a photoinduced phase transition

C. W. Nicholson[1]*†, A. Lücke[2], W. G. Schmidt[2], M. Puppin[1], L. Rettig[1], R. Ernstorfer[1], M. Wolf[1]*

Ultrafast nonequilibrium dynamics offer a route to study the microscopic interactions that govern macroscopic behavior. In particular, photoinduced phase transitions (PIPTs) in solids provide a test case for how forces, and the resulting atomic motion along a reaction coordinate, originate from a nonequilibrium population of excited electronic states. Using femtosecond photoemission, we obtain access to the transient electronic structure during an ultrafast PIPT in a model system: indium nanowires on a silicon(111) surface. We uncover a detailed reaction pathway, allowing a direct comparison with the dynamics predicted by ab initio simulations. This further reveals the crucial role played by localized photoholes in shaping the potential energy landscape and enables a combined momentum- and real-space description of PIPTs, including the ultrafast formation of chemical bonds.

Reactive events in nature are associated with the formation or breaking of chemical bonds. Within the Born-Oppenheimer approximation (*1*), a description of reactions that separates the atomic and electronic degrees of freedom is used, such that the atomic system evolves across a potential energy surface defined by the transient electronic structure. To test the validity of this nonequilibrium approach, whether in finite or extended systems, requires knowledge of both atomic and electronic structure on ultrafast time scales. The ultrafast dynamics of insulator-to-metal phase transitions offer an especially promising route because the change in electronic structure during these events is particularly extreme, and typically accompanied by a structural distortion. Ultrafast techniques have opened up avenues for exploring the interplay between the atomic and electronic subsystems (*2*–*5*), including during photoinduced insulator-to-metal transitions (*6*–*9*); these techniques additionally enabled the making of reciprocal space movies charting electronic structure dynamics (*7*, *10*) and "molecular movies" (*4*, *11*), which follow the real-time position of atoms during structural changes. Uniting these concepts to examine not only atomic positions, but also the underlying electronic structure determining the reaction pathway along the potential energy surface (PES), has been a long-pursued goal (*12*). Time- and angle-resolved photoemission spectroscopy (trARPES) is ideally suited for accessing the nonequilibrium electronic structure, as it allows direct access to the electronic band structure on ultrafast time scales and its occupation in momentum space ($\boldsymbol{k}$). Furthermore, this picture of electronic bands in periodic systems, often favored by physicists, is Fourier-equivalent to a real-space ($\boldsymbol{r}$) description of chemical bonds (*13*, *14*), which suggests the possibility of following ultrafast bond dynamics in $\boldsymbol{r}$-space (*15*) based on measurements in $\boldsymbol{k}$-space (*16*). We realize this by determining the reaction pathway—including the full electronic structure dynamics—during an ultrafast structural phase transition at a surface, thereby going beyond the molecular movie concept.

Our model phase transition system consists of atomic indium nanowires on the (111) surface of silicon, denoted In/Si(111). The system undergoes an order-order structural transition accompanied by an electronic insulator-to-metal transition (*17*, *18*). A close interplay between the electronic structure and specific lattice motions during the phase transition has been predicted that, in addition to a detailed knowledge of the equilibrium structure (*19*–*21*), makes this system ideal for investigating ultrafast changes in both $\boldsymbol{k}$- and $\boldsymbol{r}$-space. Recent time-resolved electron diffraction measurements have revealed that the structural photoinduced phase transition (PIPT) is completed within 1 ps (*22*), but such a technique does not give direct access to the underlying transient electronic dynamics.

Here we use trARPES to follow the ultrafast evolution of the electronic band structure during the PIPT in In/Si(111), which, combined with ab initio molecular dynamics (AIMD) simulations, allows access to the microscopic forces and mechanisms driving the structural transition and the dynamics of chemical bonds. To measure the dynamics of the electronic structure of In/Si(111), we have developed a 500-kHz repetition rate extreme ultraviolet (XUV) source at 22 eV (*23*), representing a substantial advance compared with the state of the art (*24*, *25*). This allows efficient access to the full, or even multiple, Brillouin zones (BZs) in many materials. A schematic trARPES experiment is shown in Fig. 1A: The pump pulse ($h\nu$ = 1.55 eV) excites electrons above the Fermi level (E_F); the electrons are then ejected from the sample after a variable delay time Δt by the probe pulse ($h\nu$ = 22 eV). A cross-correlation of 40 fs between pump and probe pulses is obtained. In contrast to traditional ARPES (*26*), this allows simultaneous access to the electronic structure above and below E_F (Fig. 1B).

In/Si(111) undergoes a transition from an insulating (8 × 2) to a metallic (4 × 1) structure above 130 K (*27*, *28*) (Fig. 1, C and D). The bonding motif in the insulating phase (Fig. 1C) consists of distorted hexagons, whereas in the conducting phase, the In atoms rearrange into zig-zagging chains (Fig. 1D). The $\boldsymbol{k}$-space band structures of the two phases calculated within the *GW* approximation are given in Fig. 1, E and F. In contrast to the (4 × 1) phase, which has three metallic bands (m_1 to m_3) that cross E_F (*17*) (Fig. 1F), the (8 × 2) phase is gapped at the $\bar{\Gamma}_{8\times2}$ and $\bar{X}_{8\times2}$ points (Fig. 1E). Upon increasing the temperature across the (8 × 2) to (4 × 1) phase transition, the states initially lying far above E_F at $\bar{\Gamma}_{8\times2}$ shift down in energy and eventually cross E_F, forming the metallic m_1 band of the (4 × 1) phase. Concurrently the energy gap in the m_2 and m_3 bands at the $\bar{X}_{8\times2}$ point closes, and the bands shift apart in momentum along the k_x direction (*23*). We note that the three metallic bands predicted from the calculation in the (4 × 1) phase are clearly observed in Fig. 1B. The Fermi surface of the (4 × 1) phase in Fig. 1G shows the momentum cut along which our data are obtained.

To investigate the PIPT, we cooled the sample to 25 K and photoexcited it by a pump pulse with incident fluence F = 1.35 mJ cm^{-2}, which corresponds to an excitation density in the surface In layer of around one electron per unit cell, implying a homogeneous excitation far from a dilute limit. Selected snapshots following excitation are shown in Fig. 2, A to D. At Δt = −450 fs (Fig. 2A), the XUV pulse arrives before the pump pulse; hence, the band structure reflects the unperturbed (8 × 2) phase with only states below E_F occupied. Shortly after excitation, at Δt = 50 fs (Fig. 2B), previously unoccupied states above E_F become clearly visible. An evolution of electronic states occurs, most clearly observed for the states around $\bar{\Gamma}_{8\times2}$ (k_x = 0.75 Å^{-1}), which shift down in energy between Δt = 50 and Δt = 250 fs (Fig. 2C). At Δt = 900 fs (Fig. 2D), the system has fully transformed into the (4 × 1) phase. The overlaid *GW* band structure for the two phases highlights the occurrence of the PIPT.

The dynamics of selected spectral features chart the progress of the PIPT (Fig. 2E). The arrows in Fig. 2, A to D, mark the positions and the direction along which one-dimensional slices of the data are analyzed and fitted to obtain the band positions presented in Fig. 2E as a function of time delay [see also (*23*)]. The fastest dynamics are found at $\bar{X}_{8\times2}$ (red arrow in Fig. 2A), where the band gap closes within 200 fs, thus defining the ultrafast insulator-to-metal transition. As a second step, the conduction band edge at the BZ

[1]Department of Physical Chemistry, Fritz-Haber-Institut der Max-Planck-Gesellschaft, Faradayweg 4-6, 14195 Berlin, Germany. [2]Department of Physics, University of Paderborn, Warburger Strasse 100, 33098 Paderborn, Germany.
*Corresponding author. Email: christopher.nicholson@unifr.ch (C.W.N.); wolf@fhi-berlin.mpg.de (M.W.)
†Present address: Department of Physics, University of Fribourg, Chemin du Musée 3, 1700 Fribourg, Switzerland.

zone center (orange arrow) is found to reach E_F after 500 fs. Finally, the structural transition, as measured by the splitting between bands m_2, m_3 (Fig. 2D, blue arrows), is completed after ~700 fs. This third time scale is in excellent agreement with the structural transition time scale observed by time-resolved electron diffraction, which is completed after ~700 fs with a time constant τ = 350 fs (*22*). It is notable that even before the structural transition is completed, two physically meaningful electronic transitions have occurred.

The distinct time scales of these three spectral features reveal a detailed pathway of the phase transition as it evolves along the electronic PES. To gain microscopic insight into the evolution of the atomic structure, electronic properties, and bond strengths along this pathway, we have performed AIMD simulations based on density functional theory (DFT) within the local density approximation (LDA), constrained by the experimental results. Because the experiment reveals the transient changes to the electronic states and their occupation, these can be used to simulate realistic excitation scenarios with AIMD. We have mapped the experimental ***k***-space distribution of excited carriers across multiple BZs in Fig. 3. This reveals that electrons are strongly delocalized throughout the BZ, in contrast to photoholes, which are localized at the BZ boundary. Such a distribution is substantially different from that of the excitation conditions assumed in a previous study, which forced excited electrons to be confined to the BZ center (*22*). In a first attempt, we assume transiently hot electronic distributions in the AIMD simulations based on the

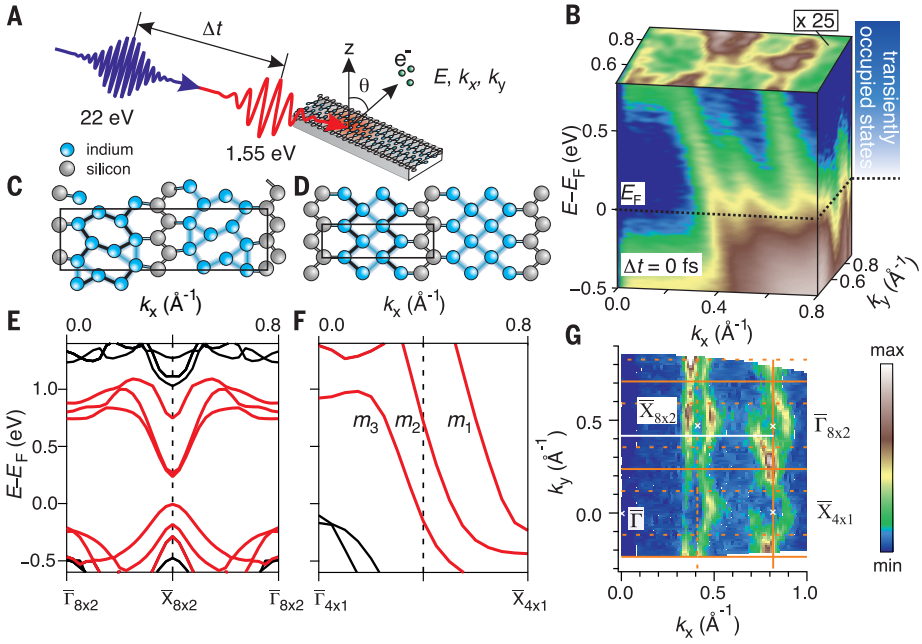

Fig. 1. Experiment overview and material system. (**A**) Schematic trARPES experiment, where Δt is the variable delay between pump (red) and probe (purple) pulses. (**B**) Excited-state photoemission data (log-color scale) obtained at T = 150 K in the metallic (4 × 1) phase with an excitation fluence F = 2 mJ cm^{-2}. (**C**) Schematic ***r***-space structure in the (8 × 2) phase and (**D**) in the (4 × 1) phase. Solid black lines highlight the structural motifs of the two phases, blue lines represent bonds. (**E**) Electronic band structure (***k***-space) calculated within the *GW* approximation in the (8 × 2) phase and in (**F**) for the (4 × 1) phase, corresponding to the structures in (C) and (D). The experimental characterization of the two phases is shown in (*23*). (**G**) Fermi surface obtained at 150 K with the 22-eV laser revealing the cut along which time-resolved measurements were obtained (white line). Solid orange lines mark the (4 × 1) BZ boundaries, whereas dashed lines mark the boundaries of the (8 × 2) BZ. High-symmetry points in the two phases are marked with crosses.

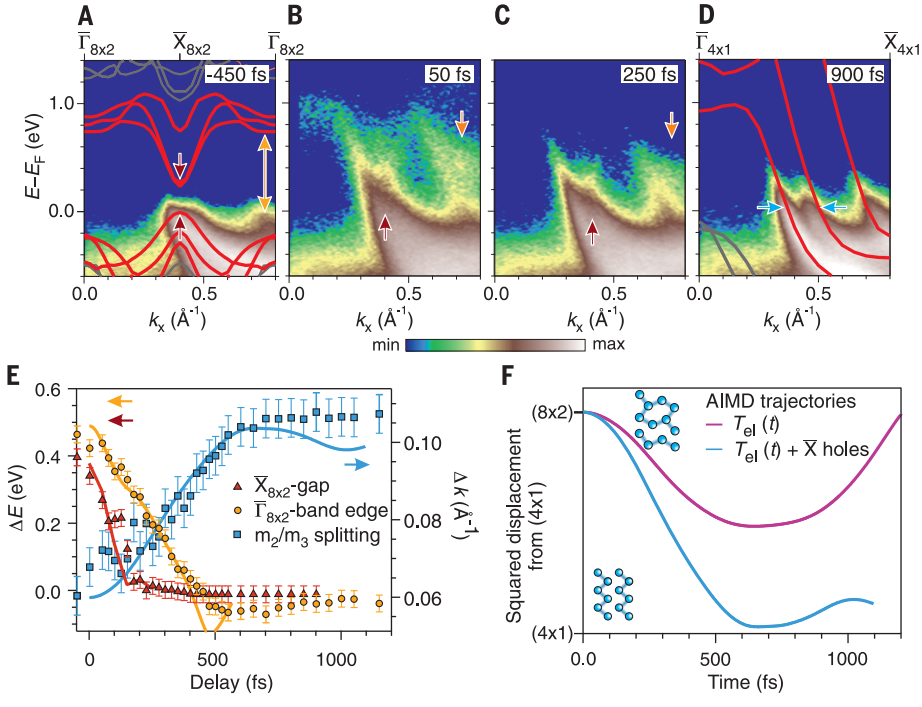

Fig. 2. Electronic and atomic structure during photoinduced phase transition. (**A** to **D**) trARPES data (F = 1.35 mJ cm^{-2}) on a logarithmic color scale at selected delays at a base temperature of T = 25 K. Arrows highlight the positions of the features of interest, which are followed in (E). (**E**) Dynamics of the features marked by arrows in (A) and (D). Red data points track the size of the band gap at the zone boundary over time, whereas the orange data mark the position of the band edge at the zone center with respect to the Fermi level. The blue data reveals the change of splitting between the two innermost bands marked in (D). Solid curves are the dynamics of the relevant spectral features from AIMD simulations, rescaled with respect to the GW band structure. For further details, see (*23*). (**F**) Evolution of the atomic structure (AIMD trajectories) through the PIPT, showing the mean squared displacement of the atomic positions from the (4 × 1) phase following excitation: $\sum_i |R_i - R_{i,4\times1}|^2$. Trajectories for two initial excitation conditions are shown, including (blue) and not including (purple) the observed localized hole population; only the former drives the PIPT. During the PIPT, the relevant atomic modes evolve with an average speed of 0.1 pm fs^{-1} (*23*).

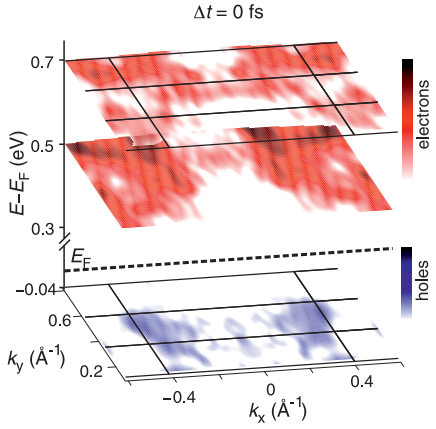

Fig. 3. *k*-space distribution of excited carriers. Experimentally measured difference map of the photoemission signal throughout multiple BZs in the (8 × 2) phase, revealing the distribution of excited electrons (red) and holes (blue) following photoexcitation (F = 0.7 mJ cm^{-2}). The distribution is obtained from the difference between spectra before excitation (Δt = −1000 fs) and Δt = 0 fs.

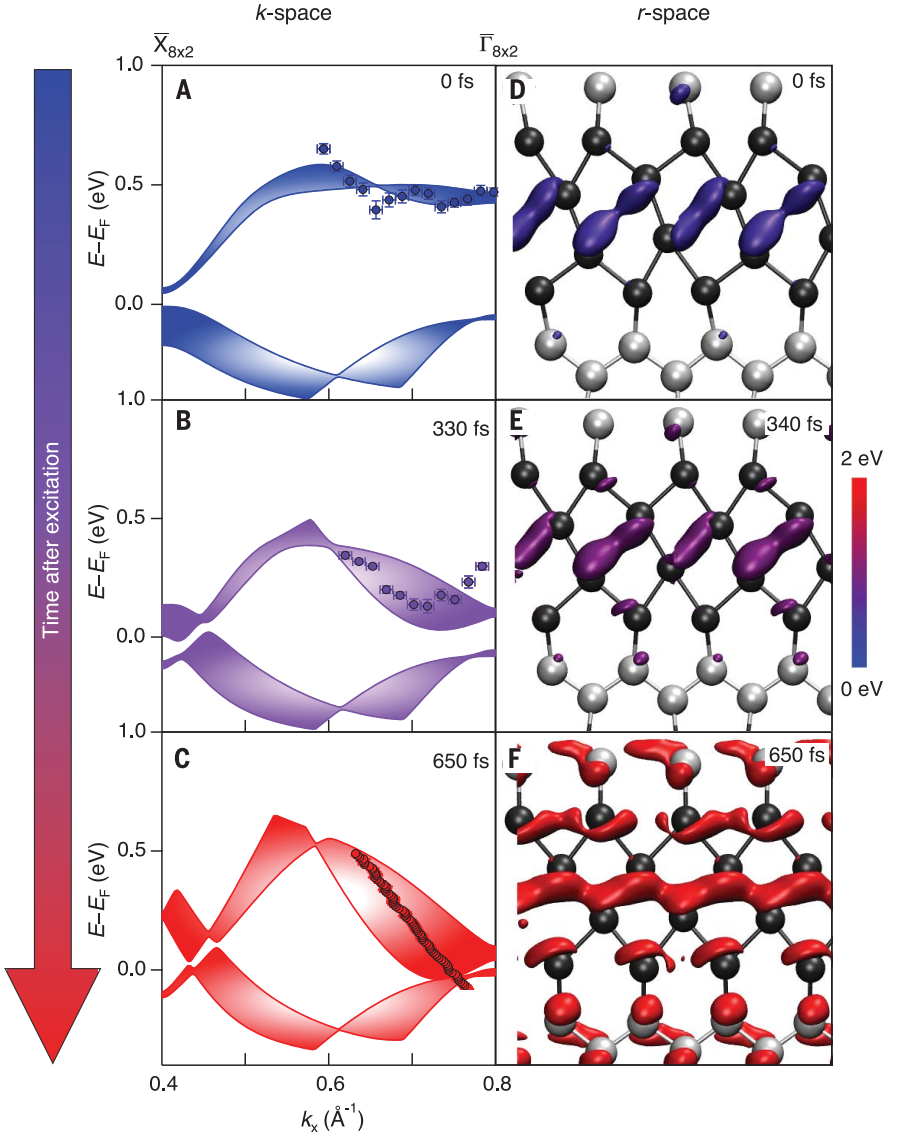

Fig. 4. Dynamics of bands and bonds during the insulator-to-metal transition. (**A** to **C**) Position of the ***k***-space bands close to the $\bar{\Gamma}_{8\times2}$ point at selected time delays extracted from the trARPES data, overlaid on the calculated LDA band structure (color-filled for clarity). Error bars mark a 95% confidence level. (**D** to **F**) Corresponding ***r***-space dynamics of the orbital, obtained from the Fourier transform of the ***k***-space band structures associated with the $\bar{\Gamma}_{8\times2}$ band in (A) to (C). Both the shape of the orbital distribution and the bond strength—indicated by the color scale—change during the phase transition, as a bond across the indium hexagon is formed. A complementary picture of charge transfer during the bond formation and breaking, as well as movies of the full ***k***- and ***r***-space dynamics (movies S1 and S2), can be found in (*23*).

experimentally determined time-dependent electronic temperature (fig. S6). However, the corresponding calculated trajectory (purple curve in Fig. 2F) describes an incomplete phase transition: The system starts to evolve from the (8 × 2) phase toward the (4 × 1) phase, but finally returns to the (8 × 2) ground state. This indicates that the LDA-DFT electronic structure is not sufficiently accurate. Indeed, the inclusion of electronic self-energy effects within the *GW* approximation raises the energy of the uppermost zone boundary valence state by about 0.2 eV with respect to the zone center states (fig. S7). Self-energy effects beyond the LDA thus lead to the preferential confinement of photoholes at the BZ boundary as experimentally observed (Fig. 3). Unfortunately, AIMD simulations based on a self-energy corrected electronic structure are computationally prohibitively expensive. Therefore, we compensate the misalignment of the valence state energies on an ad hoc basis by fixing the occupation numbers (on top of the thermal occupation) in the AIMD simulations such that holes occur at the BZ boundary and the zone center valence states are occupied (*23*). The AIMD simulation based on this excitation scenario now indeed results in a complete phase transition (Fig. 2F, blue curve). This underlines the role of zone-boundary photoholes as a key driving force in the structural transition. Moreover, the corrected AIMD simulation reproduces all three time scales observed in the ***k***-space experiment (Fig. 2E, solid lines), revealing a high level of accuracy in the simulated PES and the corresponding trajectory, even on these ultrafast time scales. The excellent agreement between our data and the simulations is strong evidence for the coherent directed motion of atoms within all unit cells during the PIPT, in accord with the previous electron diffraction study (*22*). Such ultrafast directed dynamics cannot be explained by a statistical picture of the phase transition where different regions of the sample evolve incoherently (*23*).

To further exemplify the high level of agreement between experiment and theory, in Fig. 4, A to C, we compare the calculated band structure at three snapshots during the PIPT with the corresponding band position at $\bar{\Gamma}_{8\times2}$ extracted from our data. Both the calculated energetic position and the slope of the dispersion are observed to change in agreement with the experimental data. This agreement enables us to extract the ***r***-space dynamics of nuclei and chemical bonds during the PIPT from the simulation. To do so, we plot the electronic orbitals associated with the bands discussed above at the BZ center ($\bar{\Gamma}_{8\times2}$) in Fig. 4, D to F, again for three snapshots. A transition from an orbital localized between opposite In hexagon atoms to a delocalized metallic state along the In chains is clearly seen during the PIPT.

To describe chemical bond formation additionally requires a measure of the bond strength. A quantitative understanding of bond strengths in extended systems can be gained from the crystal overlap Hamiltonian population (COHP)

(*29*, *30*), which resolves each band into bonding and antibonding contributions as a function of energy—essentially a bonding character density of states for each electronic band. By performing a COHP analysis along the AIMD trajectory, we obtain the evolution of the surface bond strengths during the phase transition (*23*). In Fig. 4, D to F, we show the formation of an In-In bond across the neighboring chains. A gradual evolution of the bond strength up to 2 eV is observed, encoded in the blue-to-red color scale applied to the orbitals in Fig. 4, D to F. Combined with the orbital distribution, this reveals the ultrafast formation of an In-In bond during the transition into the (4 × 1) structure, on the same time scale as the closing of the electronic gap in this region, i.e., within 500 fs. The buildup of bond strength thus parallels the transition from a localized molecular orbital (insulator) to a delocalized (metallic) state during the phase transition.

From our analysis, the following complete microscopic mechanism for the PIPT emerges: Upon excitation, holes are created in the bonding states at $\bar{X}_{8\times2}$, which correspond to In-In dimer bonds between the outer In chain atoms (*23*). Consequently, the dimer bonds characteristic for the hexagon structure weaken and break. At the same time, a sizable fraction of excited electrons populates the states at $\bar{\Gamma}_{8\times2}$ that are formed by a bonding combination of In states from neighboring In chains. Population of these excited states leads to interatomic forces that transform the hexagons into zig-zag chains, resulting in bond formation (Fig. 4, D to F). The electron band related to these bonds (m_1) is lowered in energy as the In atoms contributing to this bond approach each other, further populating those states and strengthening the bond. It finally crosses the Fermi energy as shown in Fig. 4C, resulting in the metallic state of the (4 × 1) phase.

Our combined experimental and theoretical approach extends the molecular movie concept by revealing the ultrafast electronic structure dynamics that govern a nonequilibrium structural transition. This unifying description bridges two fundamental concepts of physics and chemistry—band structure and chemical bonds—during ultrafast reactions. Besides elucidating the effect of the nonequilibrium electronic structure on structural dynamics, understanding the potential energy landscape induced by excitation paves the way for reaction pathways engineered via tailored excitation, potentially allowing optical control over such dynamic processes.

REFERENCES AND NOTES

1. M. Born, J. R. Oppenheimer, *Ann. Phys.* **389**, 457–484 (1927).
2. H. Petek, M. J. Weida, H. Nagano, S. Ogawa, *Science* **288**, 1402–1404 (2000).
3. H. Öström *et al.*, *Science* **347**, 978–982 (2015).
4. T. Ishikawa *et al.*, *Science* **350**, 1501–1505 (2015).
5. S. Gerber *et al.*, *Science* **357**, 71–75 (2017).
6. D. Wegkamp, J. Stähler, *Prog. Surf. Sci.* **90**, 464–502 (2015).
7. F. Schmitt *et al.*, *Science* **321**, 1649–1652 (2008).
8. T. Rohwer *et al.*, *Nature* **471**, 490–493 (2011).
9. C. Monney *et al.*, *Phys. Rev. B* **94**, 165165 (2016).
10. X. Cui *et al.*, *Nat. Phys.* **10**, 505–509 (2014).
11. J. R. Dwyer *et al.*, *Philos. Trans. A. Math. Phys. Eng. Sci.* **364**, 741–778 (2006).
12. J. C. Polanyi, A. H. Zewail, *Acc. Chem. Res.* **28**, 119–132 (1995).
13. Ashcroft, N. W. & Mermin, N. D. *Solid State Physics*. (Brooks/Cole, 1976).
14. R. Hoffmann, *Rev. Mod. Phys.* **60**, 601–628 (1988).
15. T. L. Cocker, D. Peller, P. Yu, J. Repp, R. Huber, *Nature* **539**, 263–267 (2016).
16. P. Puschnig *et al.*, *Science* **326**, 702–706 (2009).
17. H. Yeom *et al.*, *Phys. Rev. Lett.* **82**, 4898–4901 (1999).
18. P. C. Snijders, H. H. Weitering, *Rev. Mod. Phys.* **82**, 307–329 (2010).
19. C. González, J. Ortega, F. Flores, *New J. Phys.* **7**, 100 (2005).
20. S. Wippermann, W. G. Schmidt, *Phys. Rev. Lett.* **105**, 126102 (2010).
21. E. Jeckelmann, S. Sanna, W. G. Schmidt, E. Speiser, N. Esser, *Phys. Rev. B* **93**, 241407 (2016).
22. T. Frigge *et al.*, *Nature* **544**, 207–211 (2017).
23. Further details are available in the supplementary materials.
24. C. M. Heyl, J. Güdde, A. L'Huiller, U. Höfer, *J. Phys. At. Mol. Opt. Phys.* **45**, 074020 (2012).
25. H. Wang *et al.*, *Nat. Commun.* **6**, 7459 (2015).
26. S. Hüfner, *Photoelectron Spectroscopy: Principles and Applications* (Springer, 1995).
27. T. Tanikawa, I. Matsuda, T. Kanagawa, S. Hasegawa, *Phys. Rev. Lett.* **93**, 016801 (2004).
28. Y. Sun *et al.*, *Phys. Rev. B* **77**, 125115 (2008).
29. R. Dronskowski, P. E. Blöchl, *J. Phys. Chem.* **97**, 8617–8624 (1993).
30. S. Maintz, V. L. Deringer, A. L. Tchougréeff, R. Dronskowski, *J. Comput. Chem.* **34**, 2557–2567 (2013).

ACKNOWLEDGMENTS

We thank P. Kirchmann, C. Monney, and Y. Deng for their contributions to developing the infrastructure of the trARPES experiment. **Funding:** We gratefully acknowledge funding from the Max-Planck-Gesellschaft and the Deutsche Forschungsgemeinschaft through FOR1700 and TRR142. The Paderborn Center for Parallel Computing (PC^2) and the Höchstleistungs-Rechenzentrum Stuttgart (HLRS) are acknowledged for grants of high-performance computer time. **Author contributions:** C.W.N. prepared and characterized the samples. C.W.N., M.P., and L.R obtained the experimental data. C.W.N. analyzed the data. A.L. and W.G.S. performed the electronic structure calculations. W.G.S., R.E., and M.W. provided the project infrastructure. All authors discussed the results and their interpretation. C.W.N. wrote the manuscript with input and discussion from all authors. R.E. and M.W. were responsible for the overall project planning and direction. **Competing interests:** The authors declare no competing interests. **Data and materials availability:** The data that underpin the findings of this study are available at https://edmond.mpdl.mpg.de/imeji/collection/ph48BTv9YHGw49oc

SUPPLEMENTARY MATERIALS

www.sciencemag.org/content/362/6416/821/suppl/DC1
Materials and Methods
Supplementary Text
Figs. S1 to S8
Movies S1 and S2
References (*31*–*47*)

6 November 2017; accepted 3 October 2018
10.1126/science.aar4183

NETWORK SCIENCE

Quantifying reputation and success in art

Samuel P. Fraiberger[1,2], Roberta Sinatra[1,3,4,5], Magnus Resch[6,7], Christoph Riedl[1,2]*, Albert-László Barabási[1,3,8,9]*

In areas of human activity where performance is difficult to quantify in an objective fashion, reputation and networks of influence play a key role in determining access to resources and rewards. To understand the role of these factors, we reconstructed the exhibition history of half a million artists, mapping out the coexhibition network that captures the movement of art between institutions. Centrality within this network captured institutional prestige, allowing us to explore the career trajectory of individual artists in terms of access to coveted institutions. Early access to prestigious central institutions offered life-long access to high-prestige venues and reduced dropout rate. By contrast, starting at the network periphery resulted in a high dropout rate, limiting access to central institutions. A Markov model predicts the career trajectory of individual artists and documents the strong path and history dependence of valuation in art.

The Man with the Golden Helmet, an 18th-century painting attributed to Rembrandt, was Berlin's most famous artwork for decades. Once evidence emerged, in the 1980s, that the painting was not by Rembrandt, it lost much of its artistic and economic value, even though the artwork itself had not changed (*1*). Quality in art is elusive; art appeals to individual senses, pleasures, feelings, and emotions. Recognition depends on variables external to the work itself, like its attribution, the artist's body of work, the display venue, and the work's relationship to art history as a whole (*2*, *3*). Recognition and value are shaped by a network of experts, curators, collectors, and art historians whose judgments act as gatekeepers for museums, galleries, and auction houses (*4*). Given the fragmented and often secretive nature of transaction records, quantitative analyses of the art world have been difficult (*5*, *6*). Although artists' reputation is known to affect auction outcomes, our current understanding of these processes is based on small samples spanning short periods and limited to a country or region (*7*–*9*).

Our dataset was collected by Magnus (www.magnus.net) and combines information on artists' exhibitions, auction sales, and primary market quotes. It offers information on 497,796 exhibitions in 16,002 galleries, 289,677 exhibitions in 7568 museums, and 127,208 auctions in 1239 auction houses, spanning 143 countries and 36 years (1980 to 2016, fig. S1), allowing us to reconstruct the artistic career of 496,354 artists (see supplementary text S1 for additional description and validation and fig. S1a for an example) (*10*, *11*). The number of exhibitions for an artist followed a fat-tailed distribution; whereas 52% of the artists had one recorded show, a few high-profile artists were exhibited at an exceptional number of venues (fig. S1, c and d). Although half of the auctioned artworks sold for less than $4000, the price for art was as high as $110,500,000 (fig. S1f).

Prestigious institutions have access to well-regarded artists, and influential artists in turn tend to seek out prestigious institutions. Yet, institutional prestige is also highly subjective, determined by factors like history, leadership, resources, and geographic location. Given that major institutions act as art portfolios, we can uncover the slowly changing institutional prestige from frequent artwork exchanges, an approach called "adiabatic approximation" (*12*). For this, we define an order τ coexhibition network, whose nodes are museums and galleries, connected by weighted directed links (i, j) that represent the number of artists that exhibited first in i then in j within a window of τ exhibits (fig. S2, a and b) (*13*). The obtained order $\tau = \infty$ coexhibition network, connecting 16,002 galleries and 7568 museums as nodes via 19,031,332 links, incorporates all art movement in our dataset. A subset of this network revealed the clustering inherent in the art world (Fig. 1 and figs. S3 and S4). The network core was a dense community of major European and North American institutions, underlying their access to a common pool of artistic talents. Movement between the hubs in the core was exceptionally high: The link weight between Museum of Modern Art (MoMA) and Guggenheim was 33 times higher than expected if artists would move randomly between institutions (supplementary text S2.1), reflecting a highly concentrated movement of selected artists between a few prominent institutions. Multiple dense regional communities of institutions in Europe, Asia, South America, and Australia were relatively isolated from the core, indicating that members of these communities share artists mainly among themselves.

A network-based ranking using each institution's eigenvector centrality (*14*) was strongly correlated with known prestige measures (supplementary text S2.4 and fig. S5): (i) $N = 9392$ institutions were independently assigned grades from A to D by a team of experts at Magnus based on criteria including longevity, the artists exhibited, size and quality of exhibition space, and art fair participation. A-rated institutions had high network-based ranking, whereas those rated D were at the bottom half (Fig. 2A). (ii) For each institution, we computed the maximum relative price taken across all the artworks exhibited, observing a high correlation between network-based ranks and economic value of the exhibited artists artworks (Fig. 2B). The top 10–ranked institutions had the highest cumulative sales values (Fig. 2C and fig. S6), indicating that the coexhibition network, though its construction is agnostic to price, identified institutions that have access to highly valued artists. In general, an institution's geographic distance to one of the 10 largest hubs showed no relationship with prestige (fig. S7, a and b). By contrast, the network-based distance of an institution to one of the top 10 institutions was closely linked to its prestige (fig. S7, c and d). Thus, network effects play a defining role in influencing the evolution of an artist's reputation and valuation.

To show that artistic careers can be interpreted within the context of the institutions to which they have access, we grouped artists by the average prestige of their first five exhibits. We assigned an artist a high initial reputation if her work was on average exhibited in the top 20% of institutions as defined by network ranking; an artist had low initial reputation if his work was shown on average in the bottom 40% (supplementary text S3.1). A decade after their fifth exhibit, 39% of the high–initial reputation artists continued to exhibit (Fig. 2D). For low–initial reputation artists, only 14% remained active 10 years later. Next, we selected 31,794 artists, born between 1950 and 1990 with at least 10 exhibitions (Fig. 2E). As a group, high–initial reputation artists had continuous access to high-prestige institutions during their entire career (Fig. 3A). Of the 4058 high–initial reputation artists, 58.6% remain in high-prestige territory until the end of their recorded career, and only 0.2% had the average prestige of their five most recent exhibits in the bottom 40% (Fig. 2F). This lock-in effect was largely absent for low–initial reputation artists: Their reception improved with time, advancing slowly to institutions of increasing prestige (Fig. 3A). Only 10.2% of low–initial reputation artists had the average prestige of their five most recent exhibits in the top 20% (Fig. 2F). Overall, initial reputation (first five exhibits) predicted success across a variety of

[1]Network Science Institute, Northeastern University, Boston, MA, USA. [2]Harvard Institute for Quantitative Social Sciences, Cambridge, MA, USA. [3]Department of Mathematics and its Applications and Center for Network Science, Central European University, Budapest, Hungary. [4]Complexity Science Hub, Vienna, Austria. [5]ISI Foundation, Turin, Italy. [6]University of St Gallen, St. Gallen, Switzerland. [7]Zagreb School of Economics and Management, Zagreb, Croatia. [8]Division of Network Medicine, Department of Medicine, Harvard Medical School, Boston, MA, USA. [9]Department of Network and Data Science, Central European University, Budapest, Hungary.
*Corresponding author. Email: alb@neu.edu (A.-L.B.); c.riedl@neu.edu (C.R.)

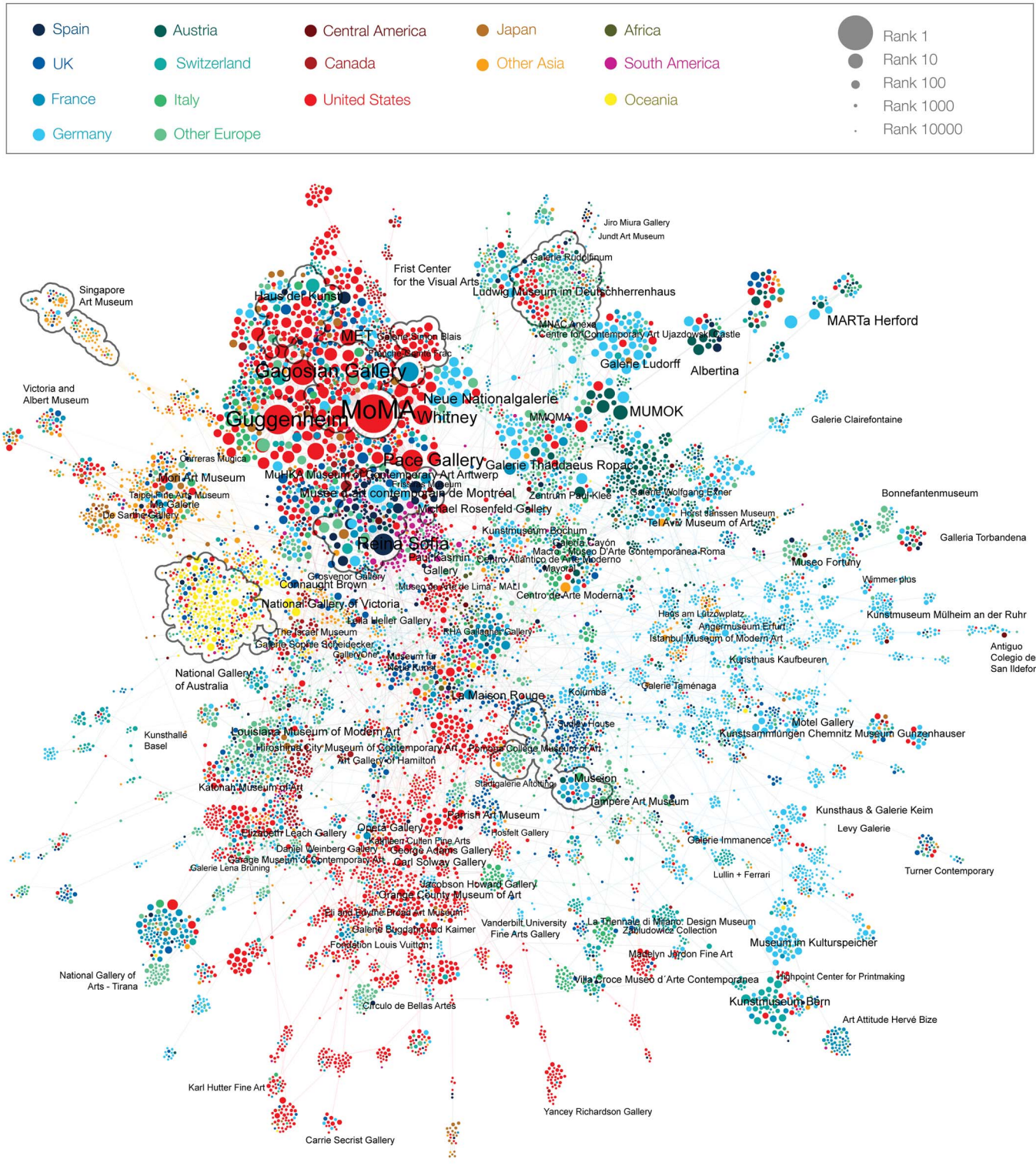

Fig. 1. Coexhibition network. Force-directed layout of the order $\tau = \infty$ coexhibition network, whose nodes are institutions (galleries, museums). Node size is proportional to each institution's eigenvector centrality. Nodes are connected if they both exhibited the same artist, with link weights being equal to the number of artists' coexhibitions. Node colors encode the region in which institutions are located. Links are of the same colors as their end nodes, or gray when end nodes have different colors. For visualization purposes, we only show the 12,238 nodes corresponding to institutions with more than 10 exhibits; we pruned the links by keeping the most statistically significant links (*20*) (supplementary text S2.2). We implemented community detection on the pruned network (*21*), identifying 122 communities (supplementary text S2.3). We highlighted five of them, the full community breakdown being shown in fig. S3. We also show the names of the most prestigious institution for each community.

measures: High–initial reputation artists had twice as many exhibitions as low–initial reputation artists (Fig. 2G); 49% of the exhibitions of high–initial reputation artists occurred outside of their home country, compared to 37% for low–initial reputation artists (Fig. 2G), and high–initial reputation artists showed more stability in institutional prestige (Fig. 2H). The work of a high–initial reputation artist was traded 4.7 times more often at auctions than that of a low–initial reputation artist (Fig. 2I), at a maximum price that was 5.2 times higher (Fig. 2I). We also collected 442,314 prices of artworks displayed in galleries, finding that the average maximum price of high–initial reputation artists was $193,064, compared to $40,476 for low–initial reputation artists (Fig. 2H). Thus, art careers were characterized by strong path dependence; artists starting in high-prestige institutions located at the center of the network showed a lower dropout rate and tended to maintain their status. By contrast, those starting at the periphery of the network showed a high dropout rate, but if they persisted, their access to top institutions gradually improved.

To model how reputation emerges in the art world, let $p[i_{\tau+1}|i_\tau]$ be the probability that an artist, currently exhibited at institution i_τ, next exhibits at institution $i_{\tau+1}$. We assume that the only institutions $i_{\tau+1}$ reachable for the artist are those that have exhibited an artist from institution i_τ before. We can therefore model an artistic career as a random walk on the order $\tau = 1$ network (*15*, *16*), the probability of moving to $i_{\tau+1}$ being proportional to the number of previous artists who transitioned from i_τ to $i_{\tau+1}$ (fig. S2). We assume that the network captures the connections between curators and institutions, guiding access to specific institutions. Independently of where artists started their career, this model directs them toward institutions of median prestige (Fig. 3B), failing to capture the lock-in effect observed in real careers. This suggests that access to institutions also depends on the artist's previous exhibition history, not only on current exhibition venue. To consider an artist's previous exhibition history $i_1, i_2, \ldots, i_\tau$ (*17*), we write the probability of the $i_\tau \to i_{\tau+1}$ transition as

$$p[i_{\tau+1}|i_\tau, \ldots, i_1] = K \times \mu[\pi_{i_{\tau+1}}; m_\tau] \times p[i_{\tau+1}|i_\tau] \quad (1)$$

where K is a normalization factor and the second term on the right-hand side captures the memory of the system about artists' reputations, written as

$$\mu[\pi_{i_{\tau+1}}; m_\tau] = \frac{p[\pi_{i_{\tau+1}}|m_\tau]}{p[\pi_{i_{\tau+1}}]} \quad (2)$$

where

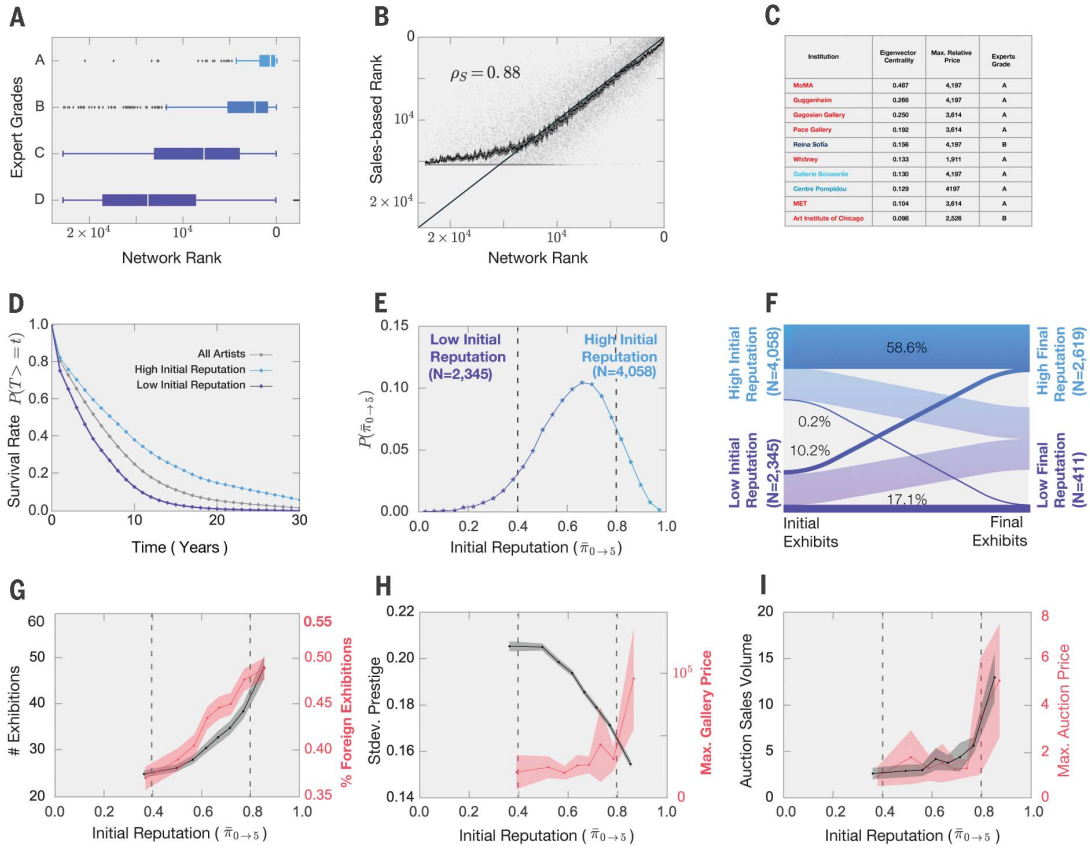

Fig. 2. Quantifying artistic careers. (**A**) Network-based prestige ranks, captured by eigenvector centrality, for institutions that were independently assigned different grades. (**B**) The relationship between sales-based ranks and eigenvector centrality-based network ranks, binned in 100 intervals, showing a high Spearman's correlation (ρ_S = 0.88). We report mean (black line) and standard error (gray shading) within each bin. (**C**) Data on top 10 institutions as predicted by the network-based ranking. Colors capture geographical location, as shown in Fig. 1. (**D**) Survival curves, showing the fraction of artists that continue to exhibit in the years following their first five exhibits based on the career of 99,265 artists with more than five exhibits. (**E**) Probability density function of average prestige during the first five exhibits for the 31,794 artists with more than 10 exhibits born between 1950 and 1990. (**F**) Diagram illustrating how the career high– and low–initial reputation artists evolves, showing the fraction of those artists whose final reputation (last five recorded exhibits) is either low or high. To show how the early career determines various success measures across a career, we consider as control variable the average prestige of the first five exhibits of an artist, and report (**G**) the total number of exhibits (left), the percentage of these exhibits outside of their home country (right), (**H**) the standard deviation of their exhibition prestige (left), the maximum price at which they are currently quoted in a gallery (in $, right), (**I**) the total number of their works that were sold in the auction market (left), and the maximum price (relative to the average market price) at which their work sold in the auction market (right). Each panel demonstrates the important role that initial reputation plays in shaping later access to institutions and financial reward.

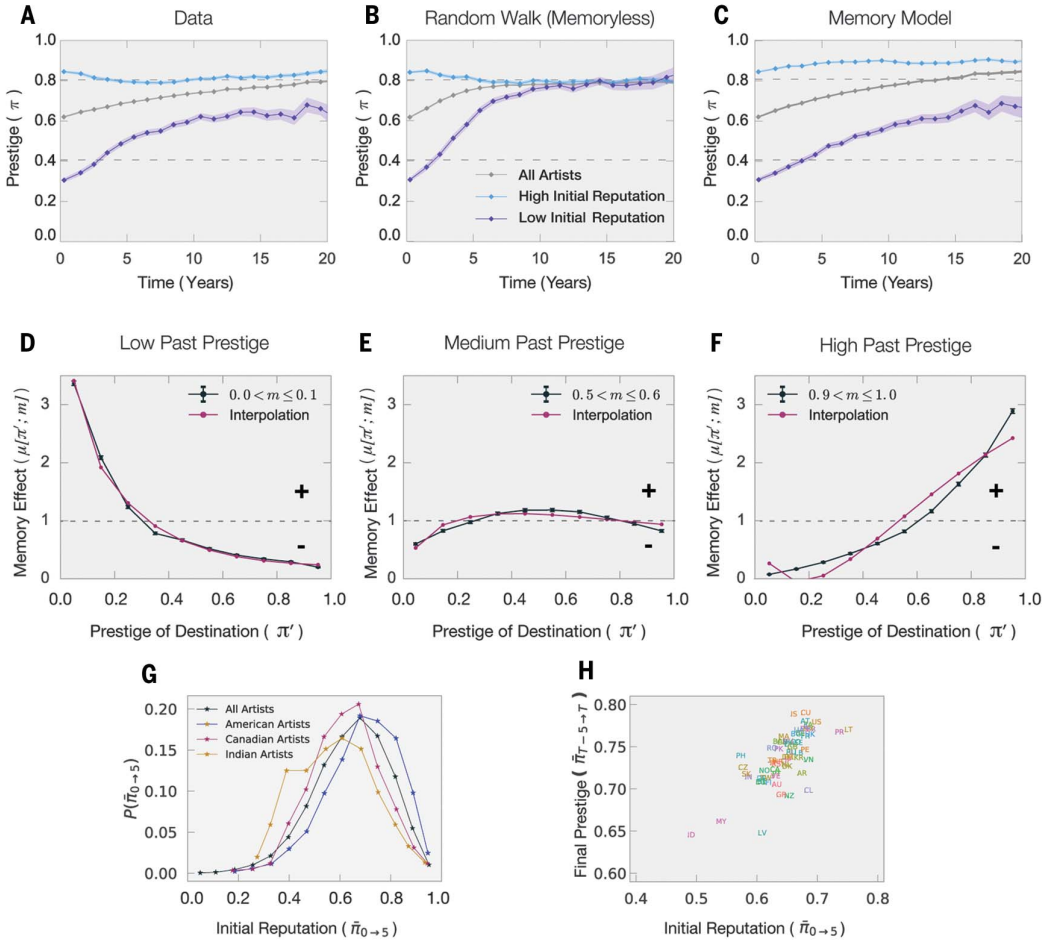

Fig. 3. Modeling the emergence of reputation. (**A**) For a random sample including 30% of the 31,794 artists with more than 10 exhibits born between 1950 and 1990, we show the evolving exhibition prestige over time. (**B**) Evolving exhibition prestige predicted by the random walk model (memoryless), documenting its failure to capture real careers. (**C**) The memory model predicts the evolution of prestige. We use the first five exhibits to initialize the models. The sequence of dates at which an artist's exhibitions occur was matched to the one we observe in the data. (**D** to **F**) Variation of the memory component with the prestige of the next exhibit π, for different ranges of values for past reputation m. π and m are reported in decile. (**G**) Probability density function of average prestige during the first five exhibits for the 31,794 artists, and the subset of those artists who were born in the United States, Canada, and India. (**H**) Final reputation versus initial reputation for artists of different country of origin.

$$m_\tau = \frac{1}{\tau}\sum_{k=1}^{n_\tau} \pi_{i_{\tau-k+1}} \qquad (3)$$

is the average reputation, representing the average prestige of the artist's past n_τ exhibitions. In other words, memory acts as a multiplicative weight that depends on the average past reputation of the artist and the prestige of the target institution. This allows us to measure the memory term $\mu[\pi_{i_{\tau+1}}; m_\tau]$ directly from the data, helping us document strong reputation effect for all artists (supplementary text S3.2 and Fig. 3, D to F). Consider an artist whose previous exhibitions conferred an average reputation in the bottom decile, e.g., m = 0.1 (Fig. 3D). His chances of exhibiting next at an institution whose prestige π is in the bottom decile was 3.4 times higher than expected by chance, and his probability of moving to a top-decile institution was only one-fifth of that expected by chance. The monotonically decreasing $\mu[\pi_{i_{\tau+1}}; m_\tau]$ with prestige π indicates that an artist with low previous reputation had a 17 times higher chance of moving next to a low-prestige institution than to a high-prestige one. We observe the opposite trend for an artist whose previous reputation was in the top decile, e.g., m = 0.9 (Fig. 3F): Her relative chances of exhibiting once again at a high-prestige institution were 42 times higher than moving to a low-prestige institution.

To test the role of reputation, we simulated the career of each artist in our sample, using as input only their first five exhibits and the universal (artist-independent) $\mu[\pi_{i_{\tau+1}}; m_\tau]$ functions to decide where they would exhibit next. The model accurately captured the lock-in effect observed in real careers (Fig. 3C). The forecast error saturated beyond n_τ = 12 (supplementary text 3.3 and fig. S8a), indicating that the past 12 exhibitions offered an optimal memory to capture the role of reputation in artistic careers. The modeling framework did not predict the specific institutions that exhibit an artist, but only their level of prestige (figs. S8, b to h, and S9). This is partly because there are many institutions within each community, with comparable prestige.

As Fig. 2F illustrates, 240 artists who began their career in low-prestige institutions did break through, having the average prestige of their last five recorded exhibits in high-prestige institutions. We find that those who do break through do so within the first 10 years of their careers (fig. S10a). We also find that among their first five exhibits, breakout artists exhibit in institutions with a wider range of rankings, their initial prestige standard deviation being 18.6%, compared to 10.3% for those who did not break through ($p = 10^{-22}$, fig. S10b); they exhibit in more distinct institutions, their initial fraction of exhibitions in distinct institutions being 70.3%, compared to 49.3% ($p = 10^{-21}$, fig. S10c); have higher maximum exhibition prestige (0.60 compared to 0.41, $p = 10^{-25}$, fig. S10d); and their network distance to MoMA is equal to 0.48, compared to 0.60 ($p = 10^{-26}$, fig. S10e). In other words, later access to high-prestige institutions is improved by an intensive early "shopping around."

Although talent is difficult to measure, we expect an artist's talent to be uncorrelated with their country of origin, implying that the distribution of initial reputation should not vary across artists of different origin. However, initial reputation was not equally distributed across artists of different country of origin (Fig. 3G). In many

countries, artists start and end their career in low-prestige institutions (Fig. 3H); those, however, born in countries with better access to the art network have a higher chance of starting and ending their career at the top.

Our analysis focused on art surveyed by galleries, museums, or auction houses, so non-object–based art, like performance art, was underrepresented. We also focused on success measures tied to institutional access, ignoring multiple dimensions through which art and artists enrich our society (*18*). Yet, even with this limited focus, our results codify the stratification of the art world, which limits access of artists to institutions that would be beneficial to their career. Quantifying these barriers and the mechanism of access could help establish policies to level the playing field. For example, the art world could benefit from the implementation of lottery systems that offer some underrepresented artists access to high-prestige venues, or blind selection procedures, successfully implemented in classical music (*19*), enhancing the inclusion of neglected works and artists.

REFERENCES AND NOTES

1. H. Bonus D. Ronte, *J. Cult. Econ.* **21**, 103 (1997).
2. P. Bourdieu, *The Field of Cultural Production* (Columbia Univ. Press, 1993).
3. O. Velthuis, *Rev. Austrian Econ.* **17**, 371–386 (2004).
4. V. A. Ginsburgh, J. C. van Ours, *Am. Econ. Rev.* **93**, 289–296 (2003).
5. M. Schich *et al*., *Science* **345**, 558–562 (2014).
6. M. Schich, I. Meirelles, *Leonardo* **49**, 445 (2016).
7. N. F. Campos, R. L. Barbosa, *Oxf. Econ. Pap.* **61**, 28–51 (2009).
8. N. Marinelli, G. Palomba, *Q. Rev. Econ. Finance* **51**, 212–224 (2011).
9. F. Etro, L. Pagani, *J. Cult. Econ.* **37**, 391–415 (2013).
10. R. Sinatra, D. Wang, P. Deville, C. Song, A.-L. Barabási, *Science* **354**, aaf5239 (2016).
11. L. Liu *et al*., *Nature* **559**, 396–399 (2018).
12. C. Castellano, S. Fortunato, V. Loreto, *Rev. Mod. Phys.* **81**, 591–646 (2009).
13. V. Sekara, A. Stopczynski, S. Lehmann, *Proc. Natl. Acad. Sci. U.S.A.* **113**, 9977–9982 (2016).
14. P. Bonacich, *Am. J. Sociol.* **92**, 1170–1182 (1987).
15. N. Masuda, M. A. Porter, R. Lambiotte, *Phys. Rep.* **716-717**, 1–58 (2017).
16. R. Sinatra, J. Gómez-Gardeñes, R. Lambiotte, V. Nicosia, V. Latora, *Phys. Rev. E Stat. Nonlin. Soft Matter Phys.* **83**, 030103 (2011).
17. M. Szell, R. Sinatra, G. Petri, S. Thurner, V. Latora, *Sci. Rep.* **2**, 457 (2012).
18. D. W. Galenson, *Old Masters and Young Geniuses: The Two Life Cycles of Artistic Creativity* (Princeton Univ. Press, 2011).
19. C. Goldin, C. Rouse, *Am. Econ. Rev.* **90**, 715–741 (2000).
20. M. A. Serrano, M. Boguñá, A. Vespignani, *Proc. Natl. Acad. Sci. U.S.A.* **106**, 6483–6488 (2009).
21. V. D. Blondel, J.-L. Guillaume, R. Lambiotte, R. Lefebvre, *J. Stat. Mech.* **2008**, P10008 (2008).
22. S. Fraiberger, Replication Data for: Quantifying Reputation and Success in Art. Harvard Dataverse, V5 (2018).

ACKNOWLEDGMENTS

We thank S. Balietti, J.A. Evans, M. Santolini, and M. Szell for their discussion and feedback and A. Grishchenko and K. Albercht for their help with visual design. **Funding:** This work was supported by NSF grant IIS-1514283 (C.R.), Air Force Office of Scientific Research grants FA9550-15-1-0077 and FA9550-15-1-0364 (A.-L.B. and R.S.), European Commission, H2020 Framework program, grant 641191 CIMPLEX (R.S., A.-L.B.), Templeton Foundation grant no. 61066 (R.S., A.-L.B.), and the ITI project "Just Data" funded by Central European University (R.S.). **Author contributions:** All authors discussed the results and commented on the manuscript. S.P.F. analyzed the data, developed the models and methods, and wrote the manuscript. R.S. analyzed the data and developed the methods. M.R. provided that data. A-L.B. and C.R. directed the research and wrote the manuscript. **Competing interests:** M.R. is CEO and Founder of magnus.net. **Data and materials availability:** The data necessary to replicate the research are available at Harvard Dataverse (*22*). Access to this dataset is only for noncommercial use or for replicating the results of the manuscript.

SUPPLEMENTARY MATERIALS

www.sciencemag.org/content/362/6416/825/suppl/DC1
Materials and Methods
Supplementary Text
Figs. S1 to S10
Reference (*23*)

13 February 2018; resubmitted 9 July 2018
Accepted 27 September 2018
Published online 8 November 2018
10.1126/science.aau7224

MASS SPECTROMETRY

Protein assemblies ejected directly from native membranes yield complexes for mass spectrometry

Dror S. Chorev[1], Lindsay A. Baker[2], Di Wu[1], Victoria Beilsten-Edmands[1], Sarah L. Rouse[3], Tzviya Zeev-Ben-Mordehai[2]*, Chimari Jiko[4], Firdaus Samsudin[5], Christoph Gerle[6,7], Syma Khalid[5], Alastair G. Stewart[8,9], Stephen J. Matthews[3], Kay Grünewald[2,10], Carol V. Robinson[1]†

Membrane proteins reside in lipid bilayers and are typically extracted from this environment for study, which often compromises their integrity. In this work, we ejected intact assemblies from membranes, without chemical disruption, and used mass spectrometry to define their composition. From *Escherichia coli* outer membranes, we identified a chaperone-porin association and lipid interactions in the β-barrel assembly machinery. We observed efflux pumps bridging inner and outer membranes, and from inner membranes we identified a pentameric pore of TonB, as well as the protein-conducting channel SecYEG in association with F_1F_O adenosine triphosphate (ATP) synthase. Intact mitochondrial membranes from *Bos taurus* yielded respiratory complexes and fatty acid–bound dimers of the ADP (adenosine diphosphate)/ATP translocase (ANT-1). These results highlight the importance of native membrane environments for retaining small-molecule binding, subunit interactions, and associated chaperones of the membrane proteome.

Genes encoding membrane proteins constitute 20 to 30% of the genome of all living cells and perform critical processes ranging from mediating drug resistance in bacteria to facilitating the complex mitochondrial respiratory chain in humans. Recent developments in structural biology, including high-resolution cryo–electron microscopy (cryo-EM), are uncovering new structures and roles of membrane proteins (*1*). Often, subunit stoichiometry and lipid binding properties of complexes extracted in detergent micelles have been controversial, prompting development of native mass spectrometry (nMS) methods. Now broadly accepted for retaining the stoichiometry of soluble complexes (*2*), recent developments in nMS of membrane protein assemblies have not only uncovered subunit stoichiometries but have also found roles for lipids in modulating structures (*3*, *4*). To reveal stoichiometry and lipid binding in the absence of detergents, alternative nMS approaches have been developed to analyze bicelles (*5*), amphipols (*6*), nanodiscs (*7*), and styrene maleic acid copolymer lipid particles (*8*). All of these approaches require some chemical intervention and high levels of protein expression, thereby restricting their use primarily to proteins overexpressed in bacteria. In this study, we aimed to overcome these limitations and show that we can obtain mass spectra for protein assemblies ejected directly from native membranes of prokaryotic and eukaryotic organisms and uncover many previously uncharacterized interactions in the process.

To develop this approach, we first used membrane protein–enriched extracellular vesicles (MPEEVs) overexpressing the epithelial fusion failure protein 1 (EFF-1), reported to be monomeric, or the anchor cell fusion failure protein 1 (AFF-1) with unknown stoichiometry (*9*, *10*). MPEEVs of both proteins from Syrian hamster BHK21 cultured cells were prepared and characterized as described previously (*9*). The presence of either EFF-1 or AFF-1 increased the diversity of cardiolipins (CDLs), as was confirmed by standard approaches (fig. S1, A and C). By subjecting these vesicles to sonication to destabilize their integrity (materials and methods and fig. S2) and to high energy across a modified Orbitrap MS (*11*), we released monomeric EFF-1 and intact dimeric AFF-1 directly from vesicles (fig. S1B).

Having established the feasibility of our approach, we investigated its application to additional native membranes. We separated outer and inner membranes of *Escherichia coli* via a sucrose gradient, prepared vesicles, and used proteomics to identify membrane proteins (*12*) (fig. S3). To interpret the mass spectra, we developed and applied a protocol that accounts for peak width, collision-induced dissociation (CID), and accurate mass, only accepting solutions within ±~0.3% of calculated masses (fig. S2 and tables S1 to S3). Starting from the low–mass/charge ratio (m/z) range of the spectrum recorded for *E. coli* outer membranes, we assigned BamC with a lipid anchor, a component of the β-barrel assembly machinery (BAM) (Fig. 1A) (*13*). Moving to higher m/z, we assigned DnaK, implicated previously in the assembly of outer membrane porins (*14*) and confirmed via CID of a 143-kDa complex together with OmpA (fig. S4). Previous reports that DnaK coimmunoprecipitates with full-length pro-OmpA but not with pro-OmpA(Δ3) (*14*) implied that sequences outside the β barrel are required to maintain accessibility of DnaK binding sites. Our measured mass (within 0.10%) is consistent with adenosine diphosphate (ADP)–bound DnaK binding to proOmpA and associating with a second OmpA, likely through the C-terminal dimerization domain (*15*), to form OmpA:proOmpA:DnaK:ADP (Fig. 1B).

Turning to the high-m/z region of the mass spectrum recorded for outer membranes, a predominant series of peaks was assigned to BAM (*13*). After detergent extraction and overexpression of all five subunits on a single plasmid, structural studies yielded primarily a 1:1:1:1:1 stoichiometry for Bam subunits (A to E) (*13*, *16*, *17*). From native membranes, however, a hexamer was ejected with a subunit composition of $ABCD(E)_2$ (Fig. 1, A and D). A small population of this complex had been observed previously from recombinant preparations (*17*). Because a domain swapped dimer was observed by x-ray analysis of BamE alone (*18*) and nuclear magnetic resonance (NMR) solution studies were consistent with a population of BamE dimers (*19*), we docked a BamE dimer into the BamABCD complex and used molecular dynamics (MD) simulation to test its stability (*20*). The complex remained stable for 5 μs, after heating to 323 K, consistent with its viability in the *E. coli* outer membrane lipid environment. A second series was assigned to the pentameric BamABCDE complex, its diffuse peaks consistent with binding of up to three CDL molecules (Fig. 1C and fig. S5). Preferential binding of phosphatidylglycerol over CDL had been reported previously (*19*), which prompted us to explore lipid binding preferences of BamE by means of MD simulations (three 5-μs trials) (Fig. 1E and fig. S6). As many as three CDL lipids made contact, indicating CDL attachment through BamE, which likely anchors the complex to a region of the membrane high in CDLs and may contribute to a membrane targeting mechanism.

Inner membrane vesicles prepared from *E. coli* represent a substantial challenge, as together

[1]Physical and Theoretical Chemistry Laboratory, University of Oxford, South Parks Road, Oxford OX1 3QZ, UK. [2]Division of Structural Biology, University of Oxford, Roosevelt Drive, Oxford OX3 7BN, UK. [3]Department of Life Sciences, Imperial College, London, South Kensington Campus, London SW7 2AZ, UK. [4]Institute for Integrated Radiation and Nuclear Science, Kyoto University, Kumatori, Japan. [5]School of Chemistry, University of Southampton, University Road, Southampton SO17 1BJ, UK. [6]Institute for Protein Research, Osaka University, Suita, Osaka, Japan. [7]Core Research for Evolutional Science and Technology, Japan and Science and Technology Agency, Kawaguchi, Japan. [8]Molecular, Structural and Computational Biology Division, Victor Chang Cardiac Research Institute, Darlinghurst, NSW, Australia. [9]Faculty of Medicine, The University of New South Wales, Sydney, NSW, Australia. [10]Centre of Structural Systems Biology (CSSB), Notkestr. 85, D-22607, Heinrich-Pette Institute/University of Hamburg, Hamburg, Germany.
*Present address: Cryo–Electron Microscopy, Bijvoet Center for Biomolecular Research, Utrecht University, Utrecht 3584 CH, Netherlands.
†Corresponding author. Email: carol.robinson@chem.ox.ac.uk

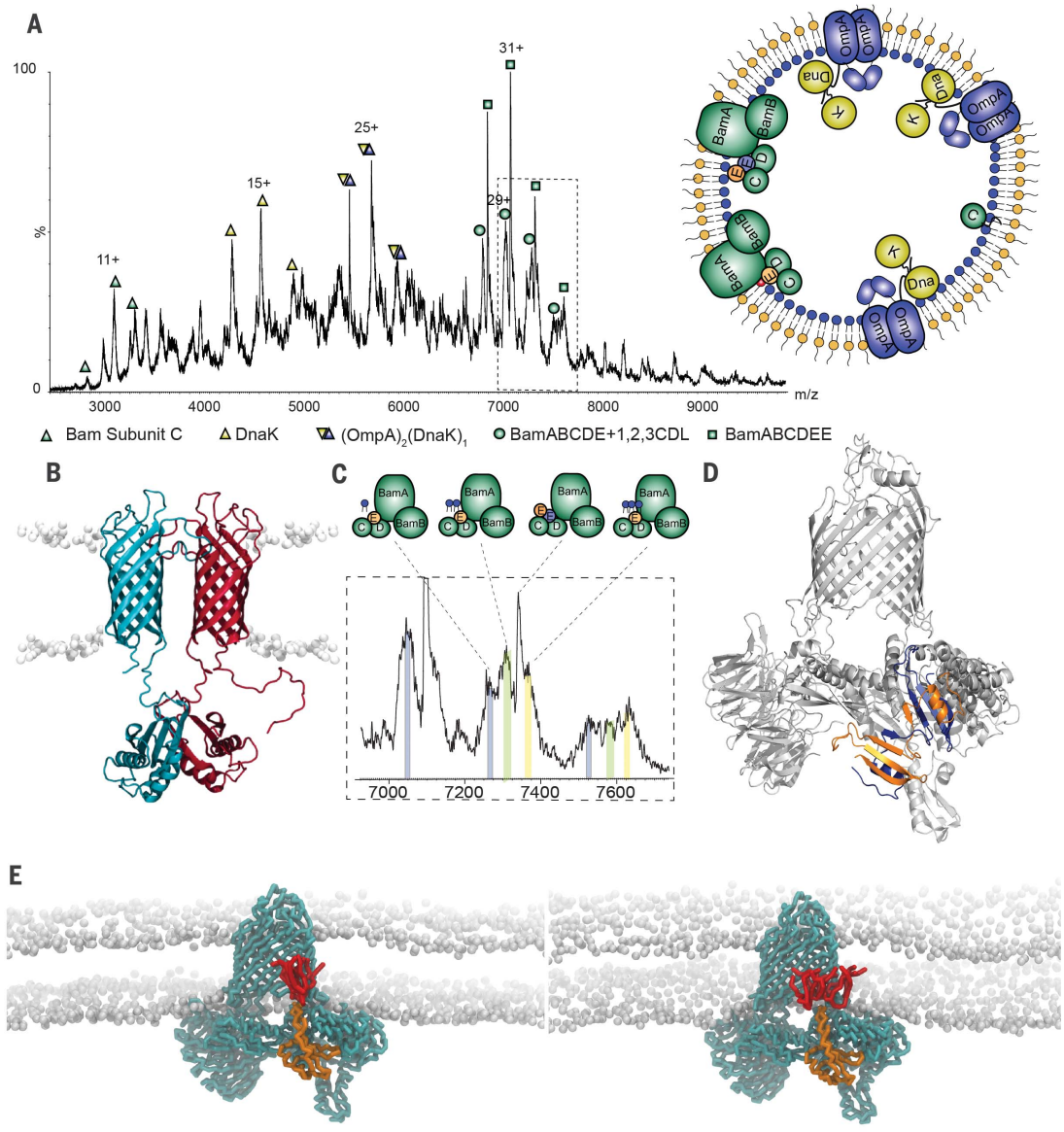

Fig. 1. Protein complexes ejected directly from *E. coli* outer membranes. (**A**) Peaks in the mass spectrum recorded at 400 V are assigned to BamC, DnaK, DnaK:OmpA:pro-OmpA, and two states of the Bam complex. The inset denotes observed complexes of an outer membrane vesicle. (**B**) Model of the OmpA dimer (*15*). The hydrophobic pro-sequence (red) is a potential binding site for DnaK. (**C**) Expansion of the mass spectrum assigned to the Bam complex [boxed region in (A)], with monomeric BamE (BamABCDE) binding to one, two, and three cardiolipins (gray, green, and yellow, respectively). (**D**) Atomic structure of the BamE dimer (PDB: 2YH9) (orange and blue) docked into the Bam complex (PDB: 5D0O) with the BamE monomer removed. (**E**) MD simulations of the BamABCDE complex (cyan) with monomeric BamE (orange) and two (left) and three (right) CDL molecules (red).

they contain a minimum of 42 different proteins (*12*) and yield complex spectra for assignment (fig. S7). We used the heterogeneity of cofactor binding to first identify cytochrome bo_3 and the CydAB cytochrome bd oxidase complex. Peaks corresponding to $(CyoB)_2(CyoC)_1(CyoD)_1$, with one or two $HemeO_3$ and HemeB factors and additional CDL binding (diffuse peaks), imply that lipid binding stabilizes structures with the full-heme complement, supported by reduced charge state (Fig. 2A) and in line with the proposed dimer association for cytochrome bo_3 from native membranes (*21*). Extensive peak splitting attributed to different heme groups (B558 and B595) and ubiquinol helped to identify the CydAB cytochrome bd oxidase complex (Fig. 2B and fig. S8). Both CydX and the paralogous small transmembrane protein AppX have the potential to interact with the CydAB complex and have overlapping cellular functions (*22*). From the native membrane, we found that CydX and AppX were able to interact simultaneously with CydAB to form a heterotetramer.

We next assigned, on the basis of mass, parts of the energy-transducing Ton complex located within the inner membrane. In the inner membrane, three integral membrane proteins reside: ExbB, ExbD, and TonB. From x-ray crystallography, a second copy of ExbD was located within the pentameric ExbB pore (*23*), whereas from EM, both hexameric and pentameric assemblies were defined (*24*). Our results confirm the existence of only the pentameric pore within the native membrane, with measured charge states implying trapping of one ExbD protomer within the compact globular complex (Fig. 2B).

At the higher-m/z region, subassemblies of multidrug efflux pumps, including AcrAB-TolC and the less well characterized but related pump MdtABTolC (*25*), spanning both membranes were uncovered (Fig. 2C). For AcrAB-TolC, all three inner membrane subunits (in AcrB) are preserved and bound to the recently discovered small subunit (AcrZ), as evidenced by mass spectra; thought to modulate substrate preference (*26*); and modeled into cryo-EM structures (*27*). One copy of the outer membrane protein TolC is bridged by a single copy of the periplasmic subunit AcrA to the inner membrane complex, yielding $AcrB_3$:$AcrZ_2$:AcrA:TolC. In the case of MdtABTolC, dimeric MdtB remains assembled with $(MdtA)_3$ and $(TolC)_2$ in the outer membrane ($MdtB_2MdtA_3$:$TolC_2$). Because all three MdtA subunits remain attached, they are likely supported by dimeric MdtB in the inner membrane, consistent with the role of MdtC in substrate binding (*28*) and not in supporting periplasmic subunits. During the sonication process and MS analysis, AcrABZ-TolC undergoes more extensive disassembly than MdtABTolC, which remains largely intact with charge states (fig. S9) indicative of highly charged subunits from AcrABZ-TolC undergoing CID (*29*).

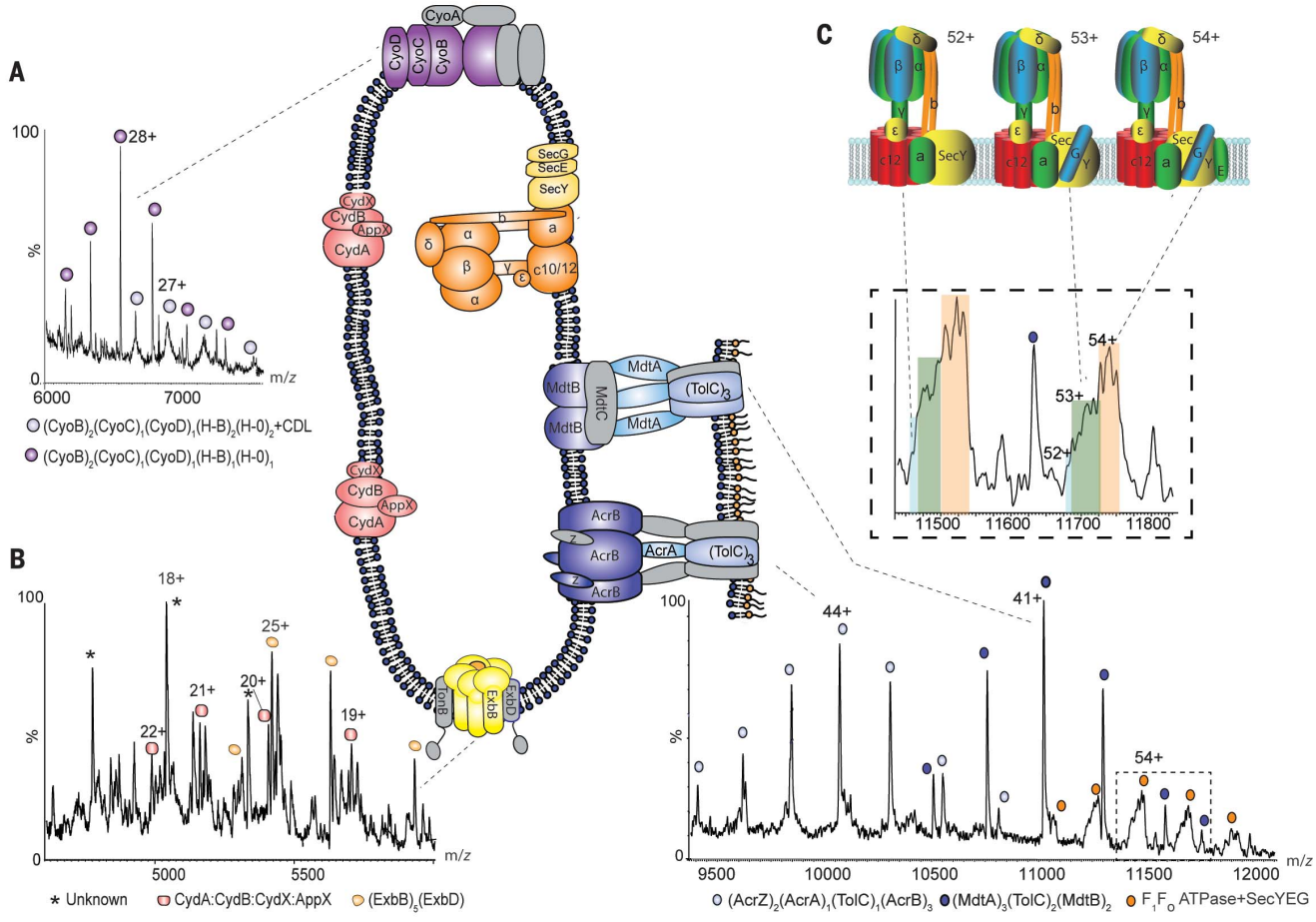

Fig. 2. Regions of the mass spectrum recorded for inner membranes from *E. coli* yield cytochromes, the Ton complex multidrug transporters, and the intact ATP synthase in complex with the SecYEG translocon. (**A** and **B**) Expanded regions of the spectrum assigned to cytochrome bo_3 and cytochrome bd oxidase, showing peak splitting due to binding of quinol and heme groups (fig. S8). The pentameric ExbB complex (with one copy of ExbD in the center of the pore) that forms part of the TonB complex is also observed (yellow). (**C**) High-*m/z* region of the mass spectrum assigned to multidrug efflux pumps AcrAB and MdtAB and the intact ATP synthase. Expansion of peaks assigned to the ATPase reveals binding of the SecY (blue), SecYG (green), and SecYEG (orange) charge states 52+, 53+, and 54+. Complexes observed in mass spectra are shown schematically, with subunits that have dissociated shown in gray.

The fact that both complexes survive at least in part, however, points to new ways of studying the effects of antibiotics on the assembly and conformational change of these multidrug resistance pumps.

At the highest *m/z* values, we also observed peak splitting due to ADP/ATP binding, which, together with dissociation of subunits with the mass of the c subunit, is indicative of ATP synthase (Fig. 2C and figs. S10 and S11). Mass differences between populations were assigned to binding of SecE, SecY, and SecG, consistent with SecYEG remaining in contact with the F_1F_O ATP synthase, as reported previously for insertion of subunit a (*30*). We next considered the stoichiometry of the F_O ring. Early reports had suggested a variable stoichiometry depending upon metabolic conditions (*31*), and our data are consistent with 12 c subunits in the F_O ring. We therefore conclude that, in the native membrane, interactions between F_1F_O ATPase and SecYEG are maintained after insertion in the membrane, together with c subunits in F_O, which are either lost during detergent extraction (*32*) or filtered out via other methods.

Observation of *E. coli* ATPase prompted us to consider inner mitochondrial membranes, densely populated with protein complexes responsible for control of the proton gradient and oxidative phosphorylation between the intermembrane space and the inner mitochondrial matrix (*33*). Surprisingly, inner mitochondrial membranes from *Bos taurus* yielded no substantial subassemblies of complex I or complex V (Fig. 3A). Other complexes in the respiratory chain that were observed include monomeric complex III; monomeric complex IV, with lipid and cofactor occupancy (*34*); and dimeric complex III, with seven core subunits confirmed by dissociation of cytochrome b and UQCRB (Fig. 3A and fig. S12).

Notably, the most abundant protein in the mass spectrum of the inner mitochondrial membrane was adenine nucleotide translocase 1 (ANT-1) (Fig. 3A). The stoichiometry of ANT-1 has remained controversial, with monomeric structures of ANT-1 and UCP2 solved by x-ray crystallography and NMR and proposed to be functional (*35*–*37*). However, in vivo and biochemical experiments were consistent with the functional unit of ANTs and uncoupling proteins (UCPs) being dimeric (*38*), a proposal supported by MD simulations on a short time scale (*39*). MS of ANT-1 revealed that it is predominantly dimeric with low-occupancy binding of a number of saturated fatty acids (palmitate anions), indicative of a transport mechanism rather than a specific binding interaction (Fig. 3A and fig. S13). MD simulations in lipid bilayers showed that, within 10 μs, tightly bound dimers formed predominantly if CDL was present in the inner leaflet of the membrane (fig. S14). Fatty acid binding was also observed with the palmitate head group buried between two helices in each subunit (Tyr^{132} and Phe^{177}) (Fig. 3B, fig. S14D, and movie S1). In situ binding of multiple palmitate

anions within the dimer ejected from the native mitochondrial membrane provides direct evidence to support the role of this fatty acid in the control of uncoupling through ANT-1–mediated, transport (*40*).

Because complexes I and V were largely absent from the spectra of inner mitochondrial membranes, we applied our protocol to intact mitochondria, without prior separation of inner and outer membranes, reasoning that the outer membrane and noninverted protein orientation may protect complexes exposed during sonication. The resulting mass spectra again revealed ANT-1 dimers bound to palmitate (fig. S13), as well as lipid-bound subassemblies of complex I bound to its flavin mononucleotide (FMN) cofactor and lipids, a complex IV dimer (Fig. 3D and fig. S15), as well as intact complex V bound to nucleotides.

The release of complexes I and V, only when protected by the outer membrane, prompts consideration of the mechanism of direct ejection from native membranes. The three steps to consider are (i) formation of vesicles, (ii) sonication in ammonium acetate to disrupt vesicles, and (iii) mass spectrometry under high electric fields from −400 to −700 V. During the first step, vesicles are formed from membrane preparations with protein complexes in both orientations. For purified inner mitochondrial membranes, we observe primarily inside-out vesicles with ATPase F_1 heads visible in cryo-EM images (fig. S16). We anticipate that sonication may

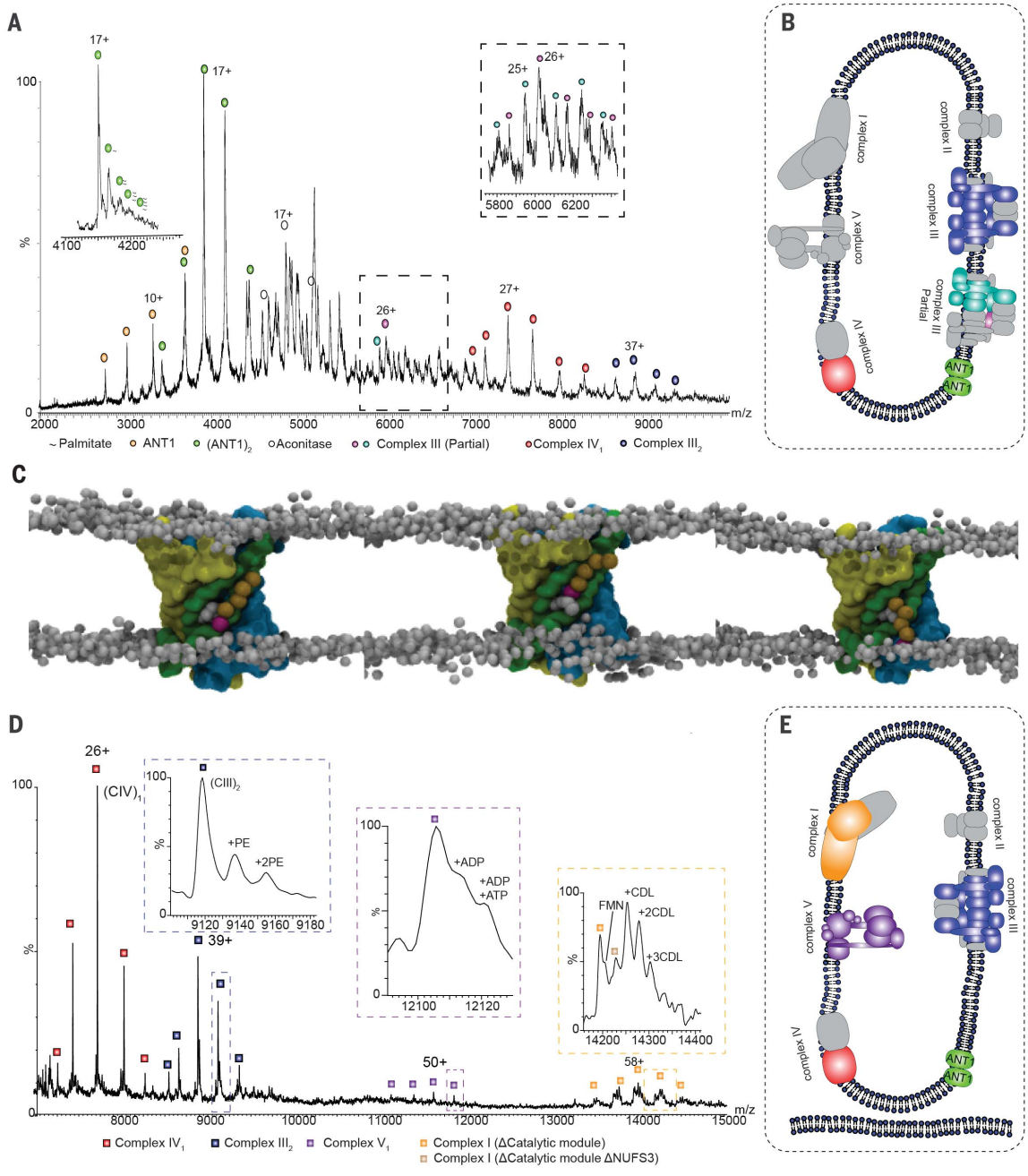

Fig. 3. Intact mitochondria and inner membranes yield complexes I, III, IV, and V, as well as ANT-1 (adenine nucleotide translocase 1) with palmitate transport through the dimer interface. (**A**) Mass spectrum of bovine mitochondrial inner membranes recorded at 600 V reveals the ANT-1 dimer, complexes III and IV, as well as aconitase. The left inset, recorded at 400 V, shows an expanded view of the spectrum at 4100 to 4300 *m/z* revealing multiple palmitate anions bounds to the dimer of ANT-1. The right inset shows an expansion of the boxed area in the main panel. (**B**) Depiction of the protein assemblies ejected from sonicated mitochondrial inner membranes. Subunits shown in gray have dissociated. (**C**) MD simulation of ANT-1 after 2.1, 2.5, and 2.6 μs (left to right) in an asymmetric membrane containing phosphatidylcholine (PC), phosphatidylethanolamine (PE), and CDL (only in the matrix leaflet). The protein surface is colored according to the three pseudo-repeats (R1, yellow; R2, green; R3, cyan), and the charged palmitate headgroup (magenta) is buried between helices three and four. (**D**) Complexes I, III, IV, and V are expelled from intact mitochondria. Intact complex V is observed with associated nucleotides, together with a dimer of complex IV (fig. S15) and partial assemblies of complex I (the charge state of the subassembly lacking NUFS3 is z = 56+), in the absence of the catalytic core, bound to FMN. Inset schematics represent assigned membrane complexes, color coded according to labels on the peaks. (**E**) Depiction of the protein assemblies ejected from sonicated intact mitochondrial membranes color coded according to the labels on the peaks. Gray subunits were not observed.

form defects in vesicles, thus allowing ingress of the ammonium acetate buffer used for electrospray. The third stage, in which high voltage is applied, favors expulsion of complexes charged by the electrospray process and attracted by the high electric field. Pronounced differences are observed between the two preparations from mitochondria. For inner membranes, we attribute the virtual absence of intact mitochondrial ATP synthase to exposure to shearing forces during sonication. Similar arguments could be made for the absence of complex I from inner membranes; its exposed hydrophilic peripheral arm may have sheared during sonication, leaving the hydrophobic membrane–embedded complex less susceptible to charge. By contrast, for intact mitochondria, complexes I and V are ejected largely intact, supporting the hypothesis that exposure to shearing forces during sonication is a key determinant in survival of complexes ejected from native membranes.

Although full details of the mechanism of ejection from native membranes into vacuum are the subject of ongoing research, the data presented here establish a detergent- and chemical-free MS approach that overcomes potential artifacts introduced by the use of these reagents. The number of new interactions of membrane proteins uncovered, with lipids, chaperones, and cofactors in association, is a testament to the stability endowed by the native membrane. Notably, access to the protein ensemble of different membrane compartments, at unparalleled mass resolution, will enable a new perspective on the effects of drugs and disease-associated mutations on target complexes within the context of their native membrane environments.

REFERENCES AND NOTES

1. K. R. Vinothkumar, R. Henderson, *Q. Rev. Biophys.* **49**, e13 (2016).
2. A. J. Heck, *Nat. Methods* **5**, 927–933 (2008).
3. K. Gupta *et al*., *Nature* **541**, 421–424 (2017).
4. A. Laganowsky *et al*., *Nature* **510**, 172–175 (2014).
5. J. T. Hopper *et al*., *Nat. Methods* **10**, 1206–1208 (2013).
6. C. Bechara *et al*., *Anal. Chem.* **84**, 6128–6135 (2012).
7. M. T. Marty, K. K. Hoi, J. Gault, C. V. Robinson, *Angew. Chem. Int. Ed. Engl.* **55**, 550–554 (2016).
8. V. Postis *et al*., *Biochim. Biophys. Acta* **1848**, 496–501 (2015).
9. T. Zeev-Ben-Mordehai, D. Vasishtan, C. A. Siebert, C. Whittle, K. Grünewald, *Structure* **22**, 1687–1692 (2014).
10. T. Zeev-Ben-Mordehai, D. Vasishtan, C. A. Siebert, K. Grünewald, *Nat. Commun.* **5**, 3912 (2014).
11. M. van de Waterbeemd *et al*., *Nat. Methods* **14**, 283–286 (2017).
12. F. Stenberg *et al*., *J. Biol. Chem.* **280**, 34409–34419 (2005).
13. J. Bakelar, S. K. Buchanan, N. Noinaj, *Science* **351**, 180–186 (2016).
14. H. Y. Qi, J. B. Hyndman, H. D. Bernstein, *J. Biol. Chem.* **277**, 51077–51083 (2002).
15. J. Marcoux *et al*., *Structure* **22**, 781–790 (2014).
16. Y. Gu *et al*., *Nature* **531**, 64–69 (2016).
17. M. G. Iadanza *et al*., *Nat. Commun.* **7**, 12865 (2016).
18. R. Albrecht, K. Zeth, *J. Biol. Chem.* **286**, 27792–27803 (2011).
19. T. J. Knowles *et al*., *EMBO Rep.* **12**, 123–128 (2011).
20. P. C. Hsu, F. Samsudin, J. Shearer, S. Khalid, *J. Phys. Chem. Lett.* **8**, 5513–5518 (2017).
21. F. Stenberg, G. von Heijne, D. O. Daley, *J. Mol. Biol.* **371**, 765–773 (2007).
22. C. E. VanOrsdel *et al*., *J. Bacteriol.* **195**, 3640–3650 (2013).
23. H. Celia *et al*., *Nature* **538**, 60–65 (2016).
24. S. Maki-Yonekura *et al*., *eLife* **7**, e35419 (2018).
25. J. Anes, M. P. McCusker, S. Fanning, M. Martins, *Front. Microbiol.* **6**, 587 (2015).
26. E. C. Hobbs, X. Yin, B. J. Paul, J. L. Astarita, G. Storz, *Proc. Natl. Acad. Sci. U.S.A.* **109**, 16696–16701 (2012).
27. Z. Wang *et al*., *eLife* **6**, e24905 (2017).
28. H. S. Kim, H. Nikaido, *Biochemistry* **51**, 4188–4197 (2012).
29. Z. Hall, H. Hernández, J. A. Marsh, S. A. Teichmann, C. V. Robinson, *Structure* **21**, 1325–1337 (2013).
30. S. Kol *et al*., *J. Mol. Biol.* **390**, 893–901 (2009).
31. R. A. Schemidt, J. Qu, J. R. Williams, W. S. Brusilow, *J. Bacteriol.* **180**, 3205–3208 (1998).
32. M. Sobti *et al*., *eLife* **5**, e21598 (2016).
33. W. Kühlbrandt, *BMC Biol.* **13**, 89 (2015).
34. I. Liko *et al*., *Proc. Natl. Acad. Sci. U.S.A.* **113**, 8230–8235 (2016).
35. E. Pebay-Peyroula *et al*., *Nature* **426**, 39–44 (2003).
36. M. J. Berardi, W. M. Shih, S. C. Harrison, J. J. Chou, *Nature* **476**, 109–113 (2011).
37. E. R. Kunji, P. G. Crichton, *Biochim. Biophys. Acta* **1797**, 817–831 (2010).
38. M. Klingenberg, *Biochim. Biophys. Acta* **1778**, 1978–2021 (2008).
39. G. Hedger *et al*., *Biochemistry* **55**, 6238–6249 (2016).
40. L. M. Sparks *et al*., *Diabetologia* **59**, 1030–1039 (2016).

ACKNOWLEDGMENTS

The authors thank C. J. Schofield for access to a probe sonicator and the Robinson group for helpful discussions. **Funding:** D.S.C. and C.V.R. are supported by the European Research Council grant no. 69551-ENABLE and a Wellcome Trust Investigator Award (104633/Z/14/Z). L.A.B. was supported by a Human Frontier Science Program Long Term Fellowship and a Canadian Institutes for Health Research Postdoctoral Fellowship. K.G. was supported by a Wellcome Trust Senior Research Fellowship (107806/Z/15/Z) and Core award (203141/Z/16/Z), the Human Frontiers Science Programme (RGP0055/2015), and MRC (MR/M019292/1). C.G. is supported by the JST (JPMJCR13M4), BINDS, and MEXT (Kiban B: 17H03647). F.S. and S.K. are supported by the BBSRC (BB/M029573/1). A.G.S. was supported by the NHMRC fellowship (1090408). **Author contributions:** D.S.C. produced the MPEEVs and performed MS experiments. L.A.B. and K.G. purified *E. coli* membranes and visualized vesicles by EM. D.W. established and executed the lipidomics. V.B.-E. provided critical advice for proteomics. S.L.R., S.J.M., S.K., and F.S. performed MD simulations. T.Z.-B.-M. provided critical support in establishing the MPEEV system. C.J. and C.G. purified intact mitochondria and inner membrane samples. A.G.S. provided critical review of the manuscript. D.S.C. and C.V.R. designed experiments, performed data analysis, and wrote the manuscript with contributions from all authors. **Competing interests:** D.S.C. and C.V.R. are inventors on a patent application (15820) filed through Oxford University Innovation that covers the use of sonicated lipid vesicles in combination with mass spectrometry. C.V.R. is a cofounding director of OMass Technologies, a company that uses mass spectrometry platforms for drug discovery. **Data and materials availability:** All data are available in the main text or the supplementary materials.

SUPPLEMENTARY MATERIALS

www.sciencemag.org/content/362/6416/829/suppl/DC1
Materials and Methods
Figs. S1 to S16
Tables S1 to S3
References (*41*–*59*)
Movie S1

6 May 2018; accepted 8 October 2018
10.1126/science.aau0976

INFLAMMATION

Small-molecule inhibitor of OGG1 suppresses proinflammatory gene expression and inflammation

Torkild Visnes[1,2]*, Armando Cázares-Körner[1]*†, Wenjing Hao[3]*, Olov Wallner[1]*, Geoffrey Masuyer[4], Olga Loseva[1], Oliver Mortusewicz[1], Elisée Wiita[1], Antonio Sarno[5,6], Aleksandr Manoilov[7,8], Juan Astorga-Wells[7,8], Ann-Sofie Jemth[1], Lang Pan[3]‡, Kumar Sanjiv[1], Stella Karsten[1], Camilla Gokturk[1], Maurice Grube[1], Evert J. Homan[1], Bishoy M. F. Hanna[1], Cynthia B. J. Paulin[1], Therese Pham[1], Azita Rasti[1], Ulrika Warpman Berglund[1], Catharina von Nicolai[1], Carlos Benitez-Buelga[1], Tobias Koolmeister[1], Dag Ivanic[1], Petar Iliev[1], Martin Scobie[1], Hans E. Krokan[5,6], Pawel Baranczewski[7,9,10], Per Artursson[9,10], Mikael Altun[1], Annika Jenmalm Jensen[11], Christina Kalderén[1], Xueqing Ba[3]§, Roman A. Zubarev[7,8,12], Pål Stenmark[4,13], Istvan Boldogh[3]¶, Thomas Helleday[1,14]¶

The onset of inflammation is associated with reactive oxygen species and oxidative damage to macromolecules like 7,8-dihydro-8-oxoguanine (8-oxoG) in DNA. Because 8-oxoguanine DNA glycosylase 1 (OGG1) binds 8-oxoG and because *Ogg1*-deficient mice are resistant to acute and systemic inflammation, we hypothesized that OGG1 inhibition may represent a strategy for the prevention and treatment of inflammation. We developed TH5487, a selective active-site inhibitor of OGG1, which hampers OGG1 binding to and repair of 8-oxoG and which is well tolerated by mice. TH5487 prevents tumor necrosis factor–α–induced OGG1-DNA interactions at guanine-rich promoters of proinflammatory genes. This, in turn, decreases DNA occupancy of nuclear factor κB and proinflammatory gene expression, resulting in decreased immune cell recruitment to mouse lungs. Thus, we present a proof of concept that targeting oxidative DNA repair can alleviate inflammatory conditions in vivo.

Upon exposure to proinflammatory agents, cells produce increased levels of reactive oxygen species (ROS), which induce oxidative DNA damage. Guanine is particularly vulnerable because it has the lowest oxidation potential among canonical DNA bases (*1*, *2*), resulting primarily in 7,8-dihydro-8-oxoguanine (8-oxoG), particularly at guanine-rich promoter regions (*3*, *4*). 8-Oxoguanine DNA glycosylase 1 (OGG1) binds with high affinity to 8-oxoG in double-stranded DNA to initiate DNA base excision repair. In addition to this role, OGG1 has distinct signal transduction functions (*5*–*7*), interacts with 8-oxoG in gene regulatory regions, and facilitates gene expression (*3*, *7*–*12*). These observations provide a potential explanation for the decreased inflammatory responses in *Ogg1*-deficient ($Ogg1^{-/-}$) mice (*13*–*16*), which are otherwise viable and largely healthy (*17*). Thus, we hypothesized that small-molecule OGG1 inhibitors may be clinically useful for the alleviation of inflammatory processes while still being well tolerated.

To screen for OGG1 inhibitors, we used a duplex oligonucleotide with the OGG1 substrate 8-oxo-7,8-dihydro-2′-deoxyadenosine and an excess of apurinic or apyrimidinic (AP) endonuclease 1 (APE1), which acts downstream of OGG1 and increases its turnover on damaged DNA (*18*) (Fig. 1, A and B). We screened a library containing 17,940 (table S1) and identified a hit molecule with a median inhibitory concentration (IC_{50}) of 8.6 μM. During hit expansion, we developed TH5487 as a potent OGG1 inhibitor with an IC_{50} of 342 nM, whereas structurally similar analogs TH2840 and TH5411 were inactive, with IC_{50} values exceeding 100 μM (Fig. 1, C and D, and figs. S1 to S3). This compound series was selective for OGG1; did not affect the activity of other DNA glycosylases (fig. S5A and table S2) or various Nudix hydrolases and diphosphatases (table S3); and did not intercalate DNA (fig. S5B). Previously, a hydrazide-based small molecule (O8) was reported to inhibit OGG1 with similar potency as TH5487 (*19*). O8 was found to inhibit catalytic imine formation in OGG1 (*19*), and we observed an increase in the potency of O8 by omitting APE1 from the reaction, in contrast to TH5487 (table S4). APE1 readily released fluorescence from a natural AP site but only partially from an AP-site substrate preincubated with O8 (fig. S5C). Thus, TH5487 primarily inhibited the DNA glycosylase activity of OGG1, whereas O8 appeared to interfere with downstream β-lyase activity. To further validate OGG1 inhibition by TH5487, we performed electrophoretic mobility shift assays, where OGG1 bound to 8-oxoG:C-containing duplex oligonucleotide in a concentration-dependent manner (fig. S4C). The amount of OGG1-DNA complexes decreased in a dose-dependent manner upon addition of TH5487 (Fig. 1E), demonstrating that TH5487 precludes OGG1 from binding oxidized DNA in vitro.

TH5487, but not the inactive analogs TH2840 and TH5411, increased the melting temperature for OGG1 in a concentration-dependent manner (Fig. 1F). Thus, TH5487-mediated protein destabilization did not account for the observed decrease in enzyme activity, suggesting that TH5487 binds OGG1 similarly to 8-oxoG extruded from DNA. Supporting this, treatment with TH5487 resulted in a lower deuteration for all peptides forming the active site cavity (Fig. 1G and table S5). Thus, TH5487 is a potent and selective active site inhibitor that prevents OGG1 from binding to its DNA substrate.

To identify the precise binding site for this class of inhibitors, we determined the x-ray crystal structure of mouse OGG1 in complex with the more soluble analog TH5675 (Fig. 1H; figs. S4 and S6, A to C; and table S6). TH5675 bound the active site (fig. S6D), albeit differently from the natural substrate (fig. S6E). Notably, the iodophenyl tail of TH5675 occupied the deeper hydrophobic pocket flanked by Phe^{319}, Cys^{253}, and Met^{257} and took the place of the 8-oxoguanine base. The central piperidyl linker was stabilized by hydrogen bonds with the catalytic Lys^{249} and the backbone of Gly^{42}, the residue that distinguishes 8-oxoguanine from guanine. The benzimidazolone core interacted with a lipophilic exosite, stabilized by Ile^{152} and Leu^{323} in addition to a π-stacking interaction with His^{270} (*20*). Notably, the Asp^{322} side chain was within hydrogen-bond distance of the solvent accessible amine, which corresponds to the bromine atom in TH5487 (fig. S6F). These

[1]Science for Life Laboratory, Department of Oncology-Pathology, Karolinska Institutet, S-171 76 Stockholm, Sweden. [2]Department of Biotechnology and Nanomedicine, SINTEF Industry, N-7465 Trondheim, Norway. [3]Department of Microbiology and Immunology, Sealy Center for Molecular Medicine, University of Texas Medical Branch at Galveston, Galveston, TX 77555, USA. [4]Department of Biochemistry and Biophysics, Stockholm University, S-106 91 Stockholm, Sweden. [5]Department of Clinical and Molecular Medicine, Norwegian University of Science and Technology, Trondheim, Norway. [6]The Liaison Committee for Education, Research, and Innovation in Central Norway, Trondheim, Norway. [7]Department of Medical Biochemistry and Biophysics, Karolinska Institutet, SE-17177 Stockholm, Sweden. [8]SciLifeLab, SE-17121 Solna, Sweden. [9]Science for Life Laboratory Drug Discovery and Development Platform, ADME of Therapeutics Facility, Department of Pharmacy, Uppsala University, Uppsala, Sweden. [10]Uppsala Drug Optimisation and Pharmaceutical Profiling Platform (UDOPP), Department of Pharmacy, Uppsala University, Uppsala, Sweden. [11]Chemical Biology Consortium Sweden, Science for Life Laboratory, Division of Translational Medicine and Chemical Biology, Department of Medical Biochemistry and Biophysics, Karolinska Institutet, S-171 21 Stockholm, Sweden. [12]Department of Pharmacological and Technological Chemistry, I.M. Sechenov First Moscow State Medical University, Moscow, Russia. [13]Department of Experimental Medical Science, Lund University, Lund, Sweden.

*These authors contributed equally to this work. †Present address: Department of Clinical Pharmacology, Karolinska University Hospital, SE-141 86 Stockholm, Sweden. ‡Present address: Department of Physiology, Xiangya Medical School in Central South University, Changsha, Hunan 410078, China. §Present address: Key Laboratory of Molecular Epigenetics of Ministry of Education, School of Life Science, Northeast Normal University, Changchun, Jilin 130024, China.

¶Corresponding author. Email: sboldogh@utmb.edu (I.B.); t.helleday@sheffield.ac.uk (T.H.)

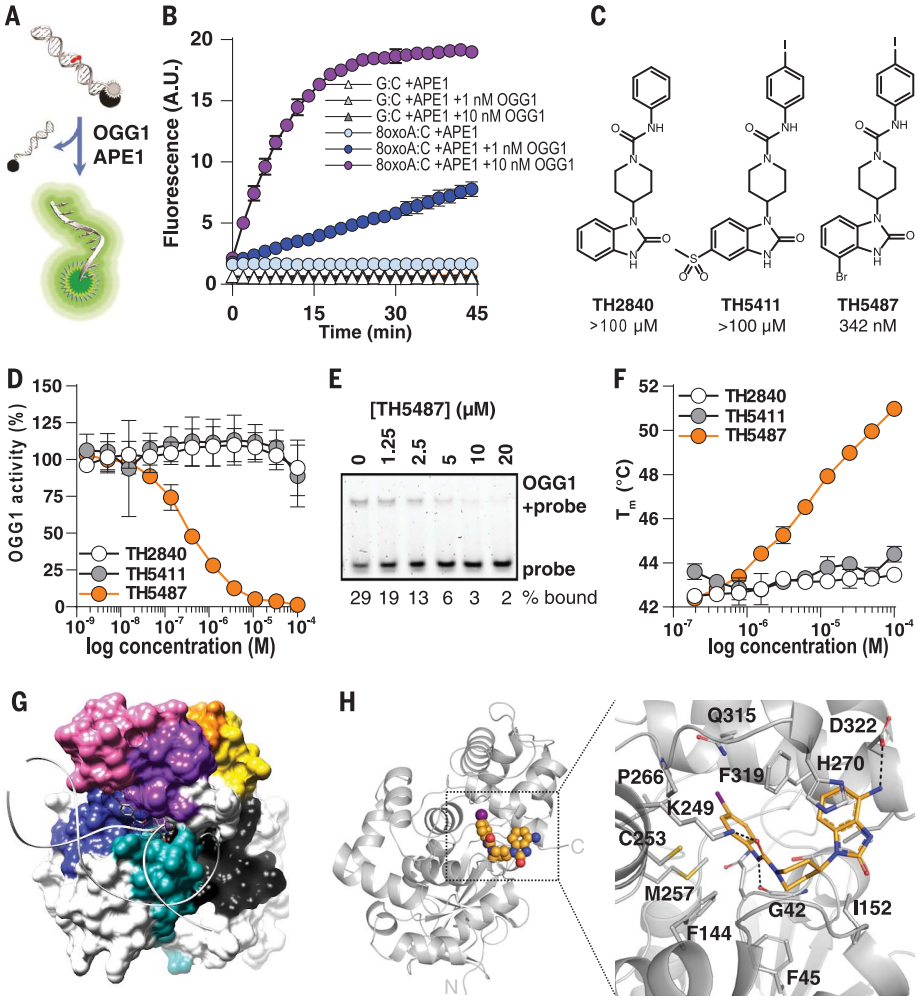

Fig. 1. Development and validation of OGG1 inhibitors. (**A**) A fluorophore and a quencher on opposite strands are separated upon OGG1-mediated excision of 8-oxoA and APE1 incision at the resulting apurinic site, causing a local melting of the DNA helix. (**B**) Excision of 8-oxoA:C, but not undamaged substrates, by OGG1 in the presence of APE1. Data are presented as averages ± SD of three technical replicates from four independent experiments. A.U., arbitrary units. (**C**) Chemical structures of the OGG1 inhibitors described herein. (**D**) Inhibition curves. 0.8 nM OGG1 and 2 nM APE1 were incubated with 10 nM OGG1 substrate and different concentrations of the indicated compounds. Data are presented as averages of four technical replicates from at least two independent experiments (n = 2 for TH2840 and TH5411, n = 33 for TH5487). (**E**) TH5487 precludes binding of OGG1 to damaged DNA. Ten nM of an OGG1-substrate duplex oligonucleotide was incubated with 100 nM OGG1 and the indicated concentrations of TH5487. This prevented the formation of OGG1-DNA complexes in a dose-dependent manner. The figure is representative of three independent experiments. (**F**) Differential scanning fluorimetry. OGG1 was incubated with SYPRO Orange and a dilution series of OGG1 inhibitors. TH5487, but not inactive analogs TH2840 and TH5411, confers the thermal stabilization of OGG1. Data are presented as averages ± SD of three technical replicates from three independent experiments. T_m, melting temperature. (**G**) Differences in deuterium uptake superimposed on an OGG1 model upon TH5487 binding (Protein Data Bank 1EBM). Colored regions show peptides protected from deuterium exchange. The molecular surface of TH5487 is shown as a semi-transparent surface, and DNA is displayed as a ribbon. (**H**) X-ray crystal structure of mouse OGG1 (gray) in complex with ligand (yellow). N and C termini are labeled. On the right is a close-up view of ligand binding. Important amino acid residues are marked; hydrogen-bond interactions are shown with black dashed lines. The view in (H) differs from the one in (G). Single-letter abbreviations for the amino acid residues are as follows: C, Cys; D, Asp; F, Phe; G, Gly; H, His; I, Ile; K, Lys; M, Met; P, Pro; and Q, Gln.

interactions were the result of a local conformational change in which the active site closed around the ligand (fig. S6G and movie S1).

For OGG1 inhibitors to be pharmacologically useful, they need to engage and inhibit OGG1 in cells. TH5487 increased the melting temperature of OGG1 in human cells (Fig. 2A), demonstrating that TH5487 engaged its intended target in living cells and protected it from thermal denaturation. Furthermore, TH5487 impaired repair of genomic 8-oxoG induced by $KBrO_3$. TH5487 caused a significant increase in genomic 8-oxoG after 2.5 hours (Fig. 2, B and C), and at 24 hours, 50 ± 8% of the 8-oxoG remained in the TH5487-treated cells (Fig. 2C), without disrupting proliferation (fig. S7A). Thus, genomic 8-oxoG and TH5487 were well tolerated by cells. Furthermore, the decrease in genomic 8-oxoG was a result of repair processes and not cellular replication. To further validate target engagement, we assessed the chromatin dynamics of OGG1–GFP (green fluorescent protein) fusion proteins. Cells were treated with $KBrO_3$ and released into medium containing TH5487 or dimethyl sulfoxide (DMSO). Consistent with previous reports (*21*), OGG1-GFP fusion proteins were immobilized at genomic DNA lesions introduced by $KBrO_3$. Treatment with TH5487 increased the nuclear mobility of OGG1-GFP both 3 and 5 hours after $KBrO_3$ exposure (Fig. 2, D and E, and fig. S7, B and C), suggesting that TH5487 prevented OGG1 binding to its genomic substrate in living cells.

OGG1 binds 8-oxoG at gene regulatory regions to mediate transcriptional activation in response to inflammatory stimuli (*3*, *7*–*11*). In the absence of functional OGG1, a decreased inflammatory response is observed (*3*, *12*–*16*, *22*). Because TH5487 prevents OGG1 from binding 8-oxoG in DNA, we examined if TH5487 could suppress proinflammatory gene expression. In line with previous observations (*12*), human embryonic kidney (HEK) 293T cells lacking OGG1 displayed a reduced induction of *CXCL1* [chemokine (C-X-C motif) ligand 1] mRNA after tumor necrosis factor–α (TNFα) stimulation (Fig. 2F and fig. S7, D and E). Treatment with 5 μM TH5487 decreased *CXCL1* expression by >50% in wild-type but not in *OGG1*-knockout cells (Fig. 2F). Thus, the compound may be used to specifically inhibit OGG1-dependent proinflammatory gene expression. Because respiratory epithelium is a key orchestrator of pulmonary innate immune responses (*23*), we stimulated a murine airway epithelial cell line (MLE 12) with TNFα (*24*), which increased the

expression of an array of proinflammatory cytokines as well as C-C and C-X-C chemokines (Fig. 3, A to C, and fig. S8). Importantly, TH5487 decreased the expression of the same genes to near pretreatment levels (Fig. 3, C and E, and figs. S8 to S12). Inhibition was dose-dependent (Fig. 3D and fig. S10) and also observed with the potent inflammatory agent lipopolysaccharide (LPS) (*25*) (Fig. 3F and figs. S11 and S12). Crucially, TH5487 decreased TNFα- and LPS-induced gene expression in diploid human small-airway epithelial cells (hSAECs) as well (Fig. 3, G to I, and figs. S9, S10, and S12).

ROS generate a localized increase in OGG1 substrates in guanine-rich promoter regions (*4*, *6*, *9*, *10*), including proinflammatory genes (*3*, *4*, *12*). Emerging evidence suggests that OGG1 binding to gene regulatory regions exerts an epigenetic role for 8-oxoG, causing OGG1 to act as a modulator of gene expression (*3*, *4*, *6*–*11*). Guanine oxidation leads to sequential recruitment of OGG1 and downstream transcriptional effectors (*3*, *8*–*11*), such as nuclear factor κB (NF-κB), which is the main driver of both TNFα- and LPS-induced proinflammatory gene expression (*26*). Consistent with the observation that TH5487 prevents OGG1 from engaging damaged DNA in vitro and in cells (Figs. 1E and 2, D and E), we observed that TH5487 decreased the recruitment of OGG1 to regulatory regions of proinflammatory cytokines in TNFα-challenged cells (Fig. 3J). Consequently, binding of NF-κB to the same regulatory regions was significantly decreased by TH5487 in the chromatin of TNFα-exposed cells (Fig. 3K) and to its recognition sequence in nuclear extracts from mouse and human cells by TH5487 (Fig. 3L and fig. S13, A to C). In the presence of OGG1, TH5487 decreased NF-κB occupancy on 8-oxoG–containing DNA, whereas TH5487 alone was unable to inhibit NF-κB (fig. S13, D and E). Thus, TH5487 decreases proinflammatory gene expression by perturbing DNA occupancy of NF-κB and potentially other OGG1-dependent transacting factors (*3*, *8*–*11*). TH5487 had no effect on the release of NF-κB from its inhibitory complex (fig. S14, A to C) but inhibited inflammatory gene expression similar to BMS-345541, an IκB kinase inhibitor (*27*) (fig. S15A). Thus, both TH5847 and BMS-345541 inhibit NF-κB function: TH5487 by preventing NF-κB binding to promoters (Fig. 3K) and BMS-345541 by inhibiting NF-κB activation (fig. S14, A to C). This results in the same readout in the form of diminished induction of proinflammatory genes. The previously developed OGG1 inhibitor O8 (*19*) did not affect gene expression (fig. S15A), possibly because, in contrast to TH5487, it allows OGG1 binding to damaged DNA (*19*) (fig. S15, B and C).

In addition, TH5487 is metabolically relatively stable and well tolerated in mice (fig. S16A and tables S7 to S10). To assess whether TH5487 could down-regulate chemotactic (C-C and C-X-C) mediators (*28*) in vivo, we challenged mouse lungs with TNFα and profiled the gene expression of proinflammatory mediators. TNFα robustly induced the expression of pulmonary proinflammatory genes, but a prophylactic injection of TH5487 decreased the expression levels (Fig. 4, A and B). Challenge with TNFα or LPS induced the robust recruitment of neutrophils to the airways, which was decreased by up to 85 ± 5% by the prophylactic intraperitoneal administration of TH5487 (Fig. 4C and fig. S16, B to G). We then administered TH5487 at different time points before or after challenge with TNFα and found that TH5487 reduced the pulmonary neutrophil count even when administered up to 9 hours after TNFα challenge (Fig. 4D and fig. S17). Thus, TH5487 is efficacious in vivo, suggesting that the compound could be used for the treatment of inflammatory conditions. Finally, another potent and structurally

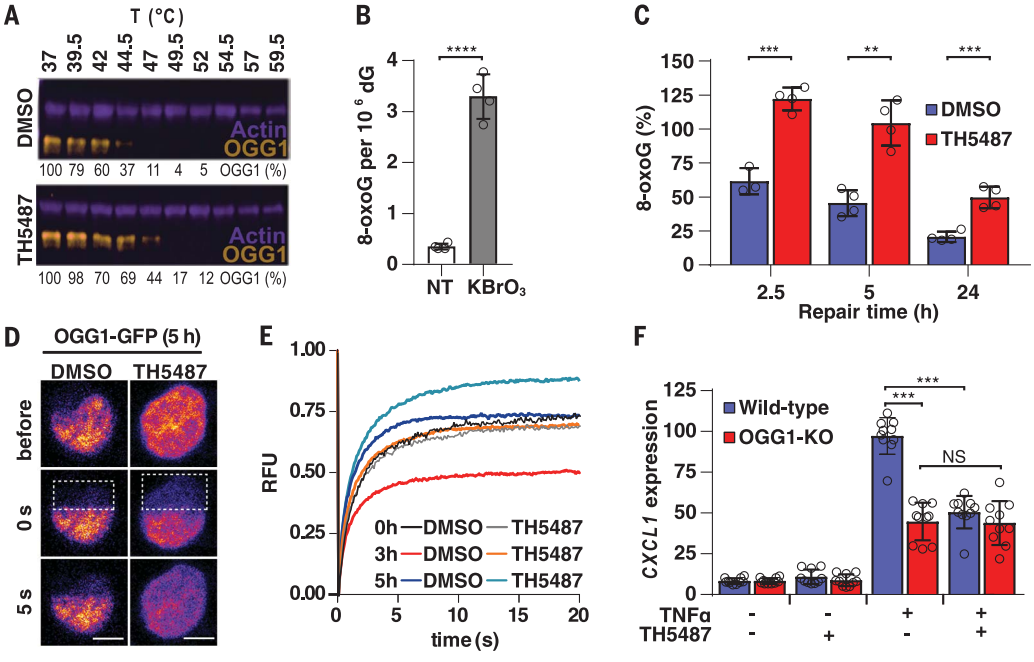

Fig. 2. TH5487 engages OGG1 in cells, inhibits DNA repair, and alters OGG1 chromatin dynamics. (**A**) Cellular thermal shift assay. Jurkat A3 cells were treated with 10 μM TH5487, and OGG1 thermal stability was analyzed by immunoblotting. Addition of 10 μM TH5487 to cultured cells increased the melting point of OGG1 by 3°C (n = 2 independent experiments). Actin was used as a loading control. (**B**) Induction of genomic 8-oxoG by $KBrO_3$. Duplicate cultures of Jurkat A3 cells were treated for 1 hour with 20 mM $KBrO_3$, and the amount of 8-oxoG in genomic DNA was determined by liquid chromatography–tandem mass spectrometry (LC-MS/MS). $KBrO_3$ induced a >10-fold increase in genomic 8-oxoG. Data are presented as averages ± SD of four replicates from two independent experiments. dG, deoxyguanosine. (**C**) Repair kinetics of genomic 8-oxoG. Cells treated with 20 mM $KBrO_3$ for 1 hour were washed and released into medium containing 10 μM TH5487 or 0.1% DMSO. Duplicate samples were taken at the indicated time points, and the genomic content of 8-oxoG was determined as in (B). TH5487 induced a notable delay in repair kinetics at 2.5-, 5- and 24-hour time points. Data are presented as averages ± SD of four replicates from two independent experiments. (**D**) Fluorescence recovery after photobleaching (FRAP). Jurkat A3 cells expressing OGG1-GFP were treated with 16 mM $KBrO_3$, washed, and released into medium with 10 μM TH5487 or 0.1% DMSO. A nuclear region was bleached, and recovery of fluorescence after photobleaching was recorded. Representative false-color images of DMSO- and TH5487-treated cells are shown. Dashed outlines indicate bleached areas. Scale bar, 5 μm. (**E**) Quantification of FRAP experiments. Ten μM TH5487 increased the nuclear mobility of OGG1-GFP at 3 and 5 hours after $KBrO_3$ treatment. Quantifications of two (0-hour) or three (3- and 5-hour) independent experiments are shown. RFU, relative fluorescence units. (**F**) TH5487 inhibits TNFα-induced *CXCL1* gene expression in wild-type, but not in *OGG1*-knockout (KO), HEK293T cells. Cells were treated with 0.05% DMSO or 5 μM TH5487 for 1 hour and TNFα (20 ng/ml) for 30 min. *CXCL1* mRNA levels were determined with quantitative polymerase chain reaction (qPCR). Data are presented as averages ± SD from three independent experiments. For (B), (C), and (F), $^{**}P < 0.01$, $^{***}P < 0.001$, $^{****}P < 0.0001$, and NS is not significant, using unpaired two-sided Student's t test.

distinct OGG1 inhibitor was recently published (*29*). When tested, this compound had comparable anti-inflammatory effects (fig. S18).

Thus, we have developed a pharmacologically useful OGG1 inhibitor that is a potent and selective active site binder that prevents OGG1 from engaging damaged DNA in vitro and in cells, resulting in decreased proinflammatory gene expression by a mechanism that is distinct from other established therapeutic agents (fig. S19). This is translated into a reduced neutrophil infiltration in mouse lungs challenged with TNFα or LPS, demonstrating that OGG1 inhibition may be a potentially useful strategy for the treatment of inflammation.

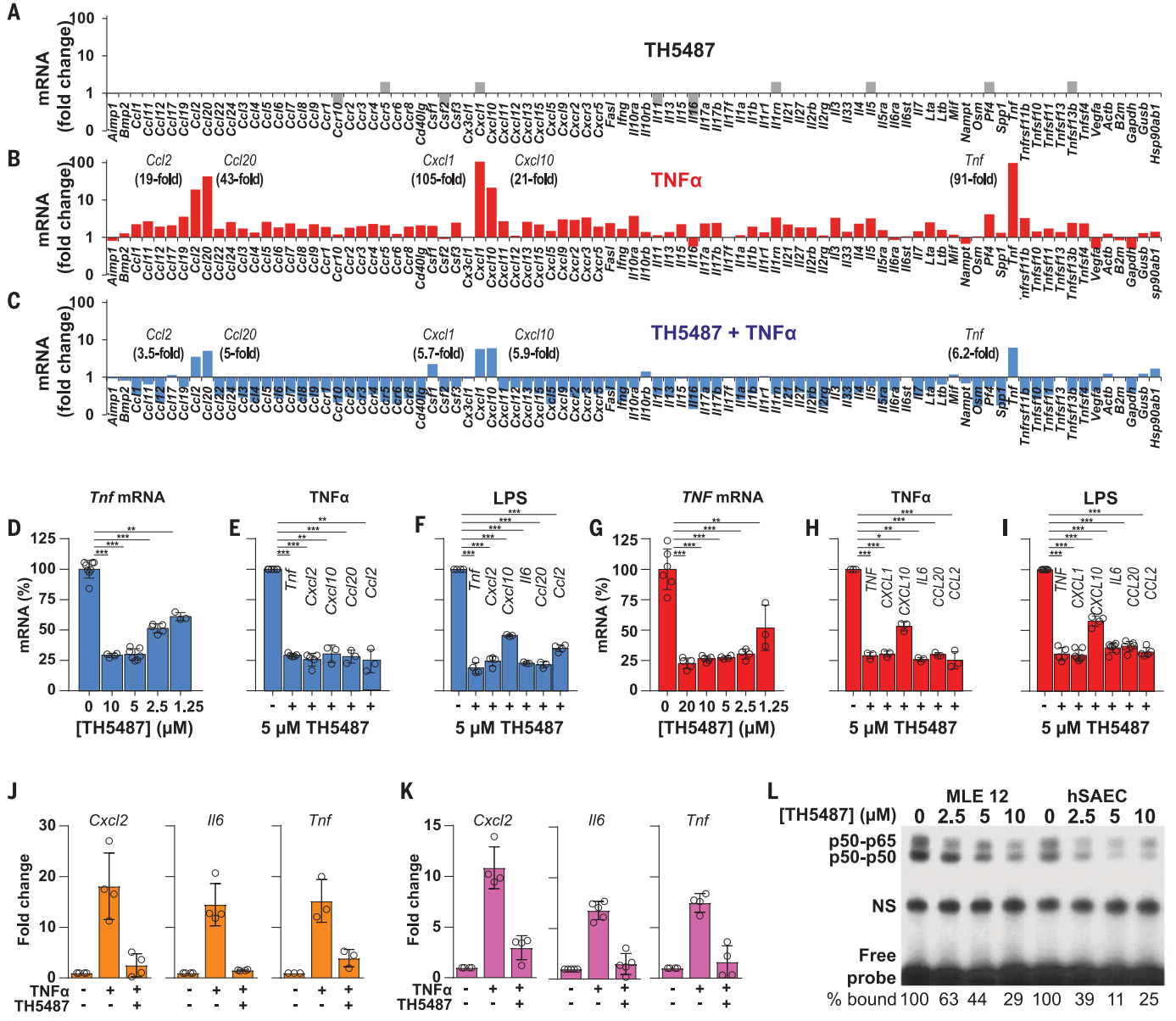

Fig. 3. Inhibition of proinflammatory gene expression and inflammation by TH5487, an active site binder of OGG1. (**A** to **C**) The effect of TH5487 on basal (A) and TNFα-induced expression of an array of proinflammatory cytokines, chemokines, and receptors [(B) and (C)] in mouse airway epithelial cells (MLE 12). Data analyses were performed according to the manufacturer's instructions using their web-based software package (www.qiagen.com/us/shop/genes-and-pathways/data-analysis-center-overview-page/). (**D**) The dose-dependent inhibition of TNFα-induced *Tnf* mRNA levels by TH5487 in MLE 12. (**E** and **F**) TH5487 inhibits the TNFα- (E) and LPS-induced (F) expression of proinflammatory genes in MLE 12. (**G**) Dose-dependent inhibition by TH5487 of TNFα-induced expression of *TNF* in hSAECs. (**H** and **I**) TH5487 inhibits TNFα- (H) or LPS-induced (I) expression of proinflammatory genes in hSAECs. In (A), (B), (C), (E), (F), (H), and (I), parallel cultures of cells were treated with solvent or TH5487 (5 μM) for 1 hour and TNFα (20 ng/ml for 30 min) or LPS (100 ng/ml for 1 hour) was added. In (D) and (G), decreasing concentrations of TH5487 were added before TNFα (20 ng/ml for 30 min). Changes in mRNA levels were determined by quantitative real-time PCR. Data are presented as averages ± SD from at least three independent experiments. (**J**) TH5487 decreases binding of OGG1 to promoters in chromatin. (**K**) TH5487 perturbs DNA occupancy of NF-κB in chromatin. In (J) and (K), data are presented as averages ± SD from four independent experiments, and MLE 12 cells were treated with solvent or 5 μM TH5487 for 1 hour and exposed to TNFα (20 ng/ml) for 30 min. Chromatin was immunoprecipitated using antibody to epitope-tagged OGG1, or the p65 subunit of NF-κB. Fold changes in OGG1 and NF-κB binding to the indicated proximal promoter regions were determined by qPCR. (**L**) TH5487 perturbs binding of NF-κB to 8-oxoG–containing synthetic DNA in nuclear extracts from MLE 12 or hSAEC cells. p50-p65, heterodimer of NF-κB; p50-p50, homodimer of NF-κB. Images are representative of three independent experiments. In (D) to (I), $*P < 0.05$, $**P < 0.01$, $***P < 0.001$, and NS is not significant, using unpaired two-sided Student's *t* test.

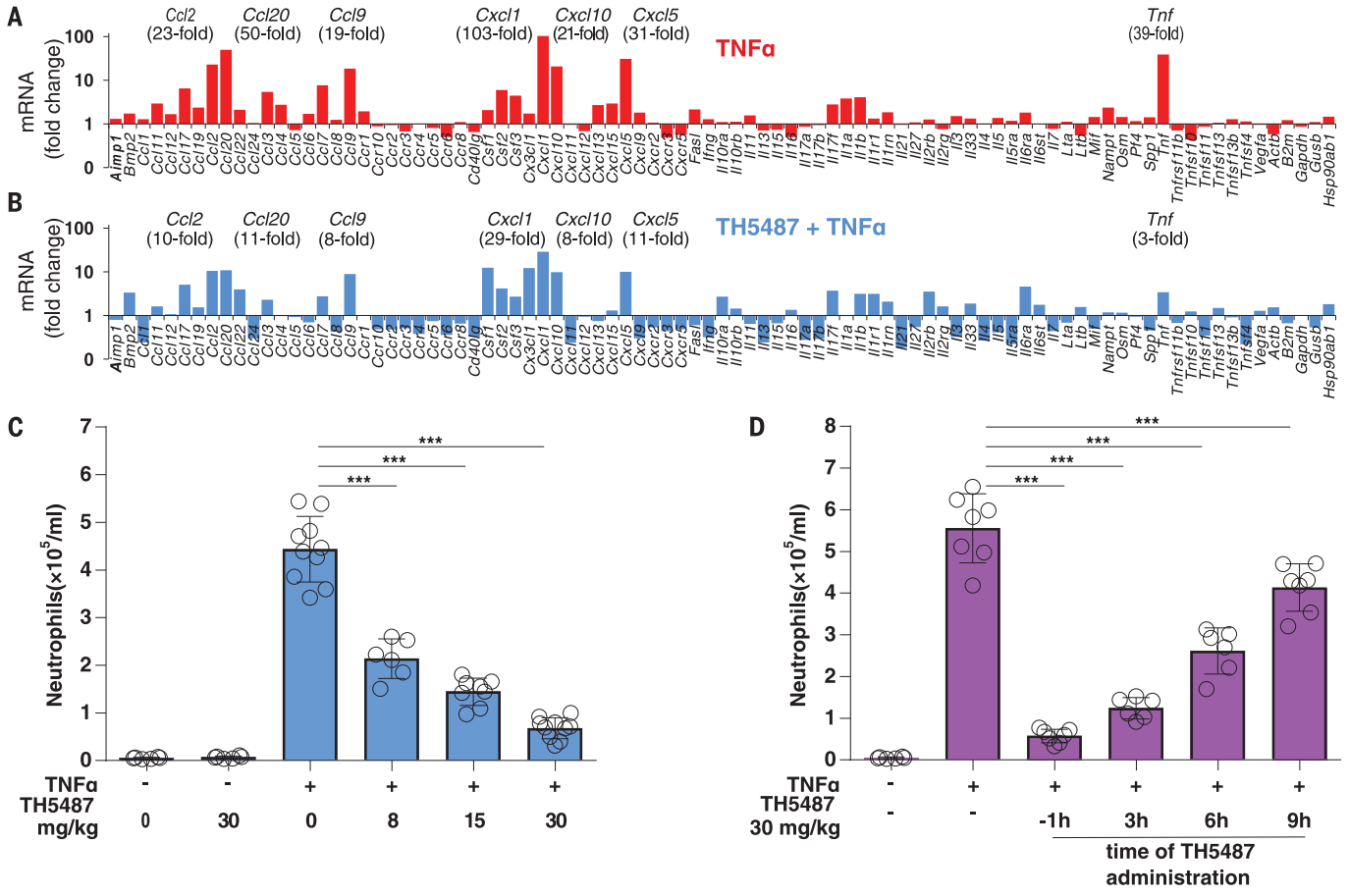

Fig. 4. TH5487 suppresses proinflammatory gene expression and lung inflammation in mice. (**A** and **B**) Groups of mice were treated intraperitoneally with TH5487 (30 mg/kg) or vehicle, and lungs were TNFα-challenged intranasally (20 ng/ml). The bars represent expression levels of mRNAs pooled from lungs of six individual mice. Target gene signals were normalized to housekeeping genes, and all data analyses were performed according to the manufacturer's instructions using their web-based software package (www.qiagen.com/us/shop/genes-and-pathways/data-analysis-center-overview-page/) ($n = 1$ experiment). (**C**) Dose dependent inhibition of TNFα-induced neutrophil infiltration by TH5487. Mice (50% female and 50% male) were treated intraperitoneally with increasing doses of TH5487 and challenged intranasally with TNFα. Sixteen hours after challenge, mice were euthanized and lavaged. Neutrophil numbers in bronchoalveolar lavage fluid were determined in a blinded fashion. (**D**) TH5487 interrupts TNFα-induced ongoing inflammatory processes. Randomly selected groups of mice (50% female and 50% male) were challenged intranasally with vehicle or 20 ng TNFα per lung, with TH5487 administered intraperitoneally 1 hour before or 3, 6, or 9 hours thereafter. Sixteen hours after TNFα stimulation, mice were euthanized and lavaged. The levels of neutrophil infiltration were assessed as described for (C). In (C) and (D), ***$P < 0.001$, using unpaired two-sided Student's t test.

REFERENCES AND NOTES

1. J. Cadet, T. Douki, J.-L. Ravanat, *Nat. Chem. Biol.* **2**, 348–349 (2006).
2. Y. Margolin, J.-F. Cloutier, V. Shafirovich, N. E. Geacintov, P. C. Dedon, *Nat. Chem. Biol.* **2**, 365–366 (2006).
3. L. Pan *et al.*, *J. Biol. Chem.* **291**, 25553–25566 (2016).
4. Y. Ding, A. M. Fleming, C. J. Burrows, *J. Am. Chem. Soc.* **139**, 2569–2572 (2017).
5. I. Boldogh *et al.*, *J. Biol. Chem.* **287**, 20769–20773 (2012).
6. M. Seifermann, B. Epe, *Free Radic. Biol. Med.* **107**, 258–265 (2017).
7. A. M. Fleming, Y. Ding, C. J. Burrows, *Proc. Natl. Acad. Sci. U.S.A.* **114**, 2604–2609 (2017).
8. S. Amente *et al.*, *Oncogene* **29**, 3691–3702 (2010).
9. V. Pastukh *et al.*, *Am. J. Physiol. Lung Cell. Mol. Physiol.* **309**, L1367–L1375 (2015).
10. V. Pastukh, M. Ruchko, O. Gorodnya, G. L. Wilson, M. N. Gillespie, *Free Radic. Biol. Med.* **43**, 1616–1626 (2007).
11. B. Perillo *et al.*, *Science* **319**, 202–206 (2008).
12. X. Ba *et al.*, *J. Immunol.* **192**, 2384–2394 (2014).
13. E. Touati *et al.*, *Helicobacter* **11**, 494–505 (2006).
14. J. G. Mabley *et al.*, *FASEB J.* **19**, 290–292 (2005).
15. G. Li *et al.*, *Free Radic. Biol. Med.* **52**, 392–401 (2012).
16. A. Bacsi *et al.*, *DNA Repair (Amst.)* **12**, 18–26 (2013).
17. A. Klungland *et al.*, *Proc. Natl. Acad. Sci. U.S.A.* **96**, 13300–13305 (1999).
18. A. E. Vidal, I. D. Hickson, S. Boiteux, J. P. Radicella, *Nucleic Acids Res.* **29**, 1285–1292 (2001).
19. N. Donley *et al.*, *ACS Chem. Biol.* **10**, 2334–2343 (2015).
20. A. Banerjee, W. Yang, M. Karplus, G. L. Verdine, *Nature* **434**, 612–618 (2005).
21. R. Amouroux, A. Campalans, B. Epe, J. P. Radicella, *Nucleic Acids Res.* **38**, 2878–2890 (2010).
22. L. Aguilera-Aguirre *et al.*, *J. Immunol.* **193**, 4643–4653 (2014).
23. J. A. Whitsett, T. Alenghat, *Nat. Immunol.* **16**, 27–35 (2015).
24. G. D. Kalliolias, L. B. Ivashkiv, *Nat. Rev. Rheumatol.* **12**, 49–62 (2016).
25. C. E. Bryant, D. R. Spring, M. Gangloff, N. J. Gay, *Nat. Rev. Microbiol.* **8**, 8–14 (2010).
26. Q. Li, I. M. Verma, *Nat. Rev. Immunol.* **2**, 725–734 (2002).
27. J. R. Burke *et al.*, *J. Biol. Chem.* **278**, 1450–1456 (2003).
28. A. Mantovani, R. Bonecchi, M. Locati, *Nat. Rev. Immunol.* **6**, 907–918 (2006).
29. Y. K. Tahara *et al.*, *J. Am. Chem. Soc.* **140**, 2105–2114 (2018).

ACKNOWLEDGMENTS

We are grateful to T. Lundbäck and the Chemical Biology Consortium Sweden for invaluable assistance in the establishment, performance, and analysis of the high-throughput screen. We are grateful to G. Dianov, S. Wallace, J. Parsons, and P. Herr for sharing expression vectors. We thank the Protein Science Facility at Karolinska Institute for the purification of DNA glycosylases for selectivity assays and K. Edfeldt, C. Sjögren, F. Pineiro, and S. Eriksson for administrative and technical support. We thank B. Dalhus, A. Klungland, and M. Bjørås for helpful discussions. The mass spectrometry analyses were performed at the Proteomics and Metabolomics Core Facility (PROMEC) at The Norwegian University of Science and Technology (NTNU) and the Central Norway Regional Health Authority. We thank the scientists at stations I04, and I24 of Diamond Light Source (UK) for their support during data collection (allocation MX15806). **Funding:** This work was funded by the National Institute of Allergic and Infectious Diseases NIAID/AI062885 (I.B.), The Faculty of Medicine at the Norwegian University of Science and Technology and the Central Norway Regional Health Authority (A.S. and H.E.K., project no. 46056921), Svanhild and Arne Must's Fund for Medical Research (A.S. and H.E.K.), Vinnova (A.C.-K and T.H.), the European Union's Horizon 2020 research and innovation program under the Marie Sklodowska-Curie grant agreement no. 722729 (B.M.F.H. and T.H.), the European Research Council (T.H. TAROX Programme), The Knut and Alice Wallenberg Foundation and the Swedish Foundation for Strategic Research (T.H. and P.S.), Swedish Research Council (T.H. and P.S.), Swedish Cancer Society (T.H. and P.S.), the

Swedish Children's Cancer Foundation (T.H.), the Swedish Pain Relief Foundation (T.H.), and the Torsten and Ragnar Söderberg Foundation (T.H.). **Author contributions:** T.V., A.C.-K., W.H., and O.W. contributed equally to this work. A.C.-K., O.W., T.K., D.I., P.I., and M.S. contributed to medicinal chemistry experiments. W.H., X.B., L.P., and I.B. designed, analyzed, and performed animal and cell culture experiments. T.V., A.C.-K., W.H., O.M., B.M.F.H., S.K., C.v.N., C.B.-B., C.K., M.A., I.B., and T.H. designed, performed, and analyzed cell biology experiments. T.V., A.C.-K., L.P., X.B., O.L., A.-S.J., A.J.J., E.W., E.J.H., C.B.J.P., M.G., and T.H. designed, performed, and analyzed biochemical and high-throughput experiments. G.M. and P.S. designed, performed, and analyzed the structural biology experiment. T.V., A.S., and H.E.K. designed, performed, and analyzed LC-MS/MS experiments. A.C.-K., A.M., J.A.-W., and R.A.Z. designed, performed, and analyzed hydrogen-deuterium exchange experiments. P.B., P.A., A.C.-K., C.G., K.S., T.P., U.W.B., and A.R. designed, performed, and analyzed ADME, pharmacology, and toxicology experiments. T.V., A.C.-K., I.B., and T.H. wrote the manuscript. All authors discussed results and approved the manuscript. **Competing interests:** T.V., A.C.-K., O.W., T.K., and T.H. are listed as inventors on a provisional U.S. patent application no. 62/636983, covering OGG1 inhibitors. The patent is fully owned by a nonprofit public foundation, the Helleday Foundation, and T.H. and U.W.B. are members of the foundation board developing OGG1 inhibitors toward the clinic. An inventor reward scheme is under discussion. The remaining authors declare no competing financial interests. **Data and materials availability:** Mouse inflammatory cytokines and receptors PCR array data have been deposited in the Gene Expression Omnibus (GEO), NCBI, and is accessible through GEO series accession nos. GSE106785 and GSE116809. The atomic coordinates and structure factors (codes 6G3X and 6G3Y) have been deposited in the Protein Data Bank (www.wwpdb.org/). The supplementary materials section contains additional data. All other data needed to evaluate the conclusions in this paper are present in either the main text or the supplementary materials.

SUPPLEMENTARY MATERIALS

www.sciencemag.org/content/362/6416/834/suppl/DC1
Materials and Methods
Figs. S1 to S20
Tables S1 to S13
References (*30*–*58*)
Movie S1

20 December 2017; resubmitted 30 April 2018
Accepted 24 September 2018
10.1126/science.aar8048

BIOTECHNOLOGY

Programmed DNA destruction by miniature CRISPR-Cas14 enzymes

Lucas B. Harrington[1*†], David Burstein[2*‡], Janice S. Chen[1†], David Paez-Espino[3], Enbo Ma[1], Isaac P. Witte[1], Joshua C. Cofsky[1], Nikos C. Kyrpides[3], Jillian F. Banfield[2,4,5], Jennifer A. Doudna[1,5,6,7,8§]

CRISPR-Cas systems provide microbes with adaptive immunity to infectious nucleic acids and are widely employed as genome editing tools. These tools use RNA-guided Cas proteins whose large size (950 to 1400 amino acids) has been considered essential to their specific DNA- or RNA-targeting activities. Here we present a set of CRISPR-Cas systems from uncultivated archaea that contain Cas14, a family of exceptionally compact RNA-guided nucleases (400 to 700 amino acids). Despite their small size, Cas14 proteins are capable of targeted single-stranded DNA (ssDNA) cleavage without restrictive sequence requirements. Moreover, target recognition by Cas14 triggers nonspecific cutting of ssDNA molecules, an activity that enables high-fidelity single-nucleotide polymorphism genotyping (Cas14-DETECTR). Metagenomic data show that multiple CRISPR-Cas14 systems evolved independently and suggest a potential evolutionary origin of single-effector CRISPR-based adaptive immunity.

Competition between microbes and viruses stimulated the evolution of CRISPR-based adaptive immunity to provide protection against infectious agents (*1*, *2*). In class 2 CRISPR-Cas systems, a single 100- to 200-kDa CRISPR-associated (Cas) protein with multiple functional domains carries out RNA-guided binding and cutting of DNA or RNA substrates (*3*, *4*). To determine whether simpler, smaller RNA-guided proteins occur in nature, we queried terabase-scale metagenomic datasets (*5*–*9*) for uncharacterized genes proximal to both a CRISPR array and *cas1*, the gene that encodes the universal CRISPR integrase (*10*, *11*). This analysis identified a diverse family of CRISPR-Cas systems that contain *cas1*, *cas2*, *cas4*, and a previously unrecognized gene, *cas14*, encoding a 40- to 70-kDa polypeptide (Fig. 1A). We initially identified 24 different *cas14* gene variants that cluster into three subgroups (Cas14a, Cas14b, and Cas 14c) on the basis of comparative sequence analysis (Fig. 1, A and B, and figs. S1 and S2). Cas14 proteins are ~400 to 700 amino acids (aa), about half the size of previously known class 2 CRISPR RNA-guided enzymes (950 to 1400 aa) (Fig. 1, C and D). Though the identified Cas14 proteins exhibit considerable sequence diversity, all are united by the presence of a predicted RuvC nuclease domain, whose organization is characteristic of type V CRISPR-Cas DNA-targeting enzymes (Fig. 1D) (*3*, *12*, *13*).

The Cas14 proteins we identified occur almost exclusively within DPANN, a superphylum of symbiotic archaea characterized by small cell and genome sizes (*14*, *15*). Phylogenetic comparisons showed that Cas14 proteins are widely diverse with similarities to C2c10 and C2c9, families of bacterial RuvC domain–containing proteins that are sometimes found near a CRISPR array but not together with other *cas* genes (Fig. 1B and fig. S1) (*3*). This observation and the small size of the *c2c10*, *c2c9*, and *cas14* genes made it improbable that these systems could function as stand-alone CRISPR effectors (*3*).

On the basis of their proximity to conserved genes responsible for creating genetic memory of infection (*cas1*, *cas2*, *cas4*) (fig. S3A), we explored whether CRISPR-Cas14 systems can actively acquire DNA sequences into their CRISPR arrays. Assembled metagenomic contiguous DNA sequences (contigs) for multiple CRISPR-Cas14 loci revealed that otherwise identical CRISPR systems showed diversity in their CRISPR arrays. These results are consistent with active adaptation to new infections, although without longitudinal sampling these data could also be explained by alternative biological mechanisms (Fig. 2A and fig. S3B) (*13*). The evidence suggesting acquisition of new DNA sequences led us to hypothesize that these CRISPR-Cas14 loci encode functional enzymes with nucleic acid targeting activity despite their small size. To test this possibility, we first investigated whether RNA components are produced from CRISPR-Cas14 loci. Environmental metatranscriptomic sequencing data were analyzed for the presence of RNA from the native archaeal host that contains CRISPR-Cas14a (Fig. 2B and fig. S4A). In addition to CRISPR RNAs (crRNAs), a highly abundant noncoding RNA was mapped to a ~130–base pair sequence located between *cas14a* and the adjacent CRISPR array. Notably, the 3′ end of this transcript was mostly complementary to the repeat segment of the crRNA (Fig. 2C and fig. S4B), as observed for trans-activating CRISPR RNAs (tracrRNAs) found in association with Cas9, Cas12b, and Cas12e CRISPR systems (*12*, *13*, *16*). In these previously studied systems, the double-stranded RNA–cutting enzyme ribonuclease III (RNase III) generates mature tracrRNAs and crRNAs, but no genes encoding RNase III were present in *cas14*-containing reconstructed genomes (fig. S5A), nor did Cas14a cleave its own pre-crRNA when tested biochemically (fig. S5B). These observations imply that an alternative mechanism for CRISPR-associated RNA processing exists in these hosts.

To test whether the Cas14a proteins and associated RNA components can assemble together in a heterologous organism, we introduced a plasmid into *Escherichia coli* containing a minimal CRISPR-Cas14a locus that includes the *cas14* gene, the CRISPR array, and intergenic regions

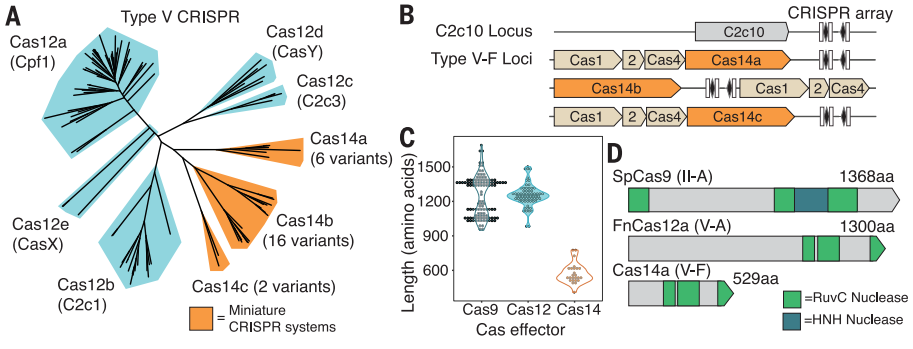

Fig. 1. Architecture and phylogeny of CRISPR-Cas14 genomic loci. (**A**) Phylogenetic tree of type V CRISPR systems. Newly identified miniature CRISPR systems are highlighted in orange. (**B**) Representative loci architectures for C2c10 and CRISPR-Cas14 systems. (**C**) Length distribution of Cas14a to Cas14c systems compared with Cas12a to Cas12e and Cas9. (**D**) Domain organization of Cas14a compared with Cas9 and Cas12a. Nuclease domains (RuvC and HNH) are indicated. Protein lengths are drawn to scale.

[1]Department of Molecular and Cell Biology, University of California, Berkeley, CA 94720, USA. [2]Department of Earth and Planetary Sciences, University of California, Berkeley, CA 94720, USA. [3]Department of Energy, Joint Genome Institute, Walnut Creek, CA 94598, USA. [4]Department of Environmental Science, Policy, and Management, University of California, Berkeley, CA 94720, USA. [5]Innovative Genomics Institute, University of California, Berkeley, CA 94720, USA. [6]MBIB Division, Lawrence Berkeley National Laboratory, Berkeley, CA 94720, USA. [7]Department of Chemistry, University of California, Berkeley, CA 94720, USA. [8]Howard Hughes Medical Institute, University of California, Berkeley, CA 94720, USA.
*These authors contributed equally to this work.
†Present address: Mammoth Biosciences, San Francisco, CA 94107, USA.
‡Present address: School of Molecular Cell Biology and Biotechnology, Tel Aviv University, Tel Aviv 69978, Israel.
§Corresponding author. Email: doudna@berkeley.edu

Corrected 14 November 2018. See full text.

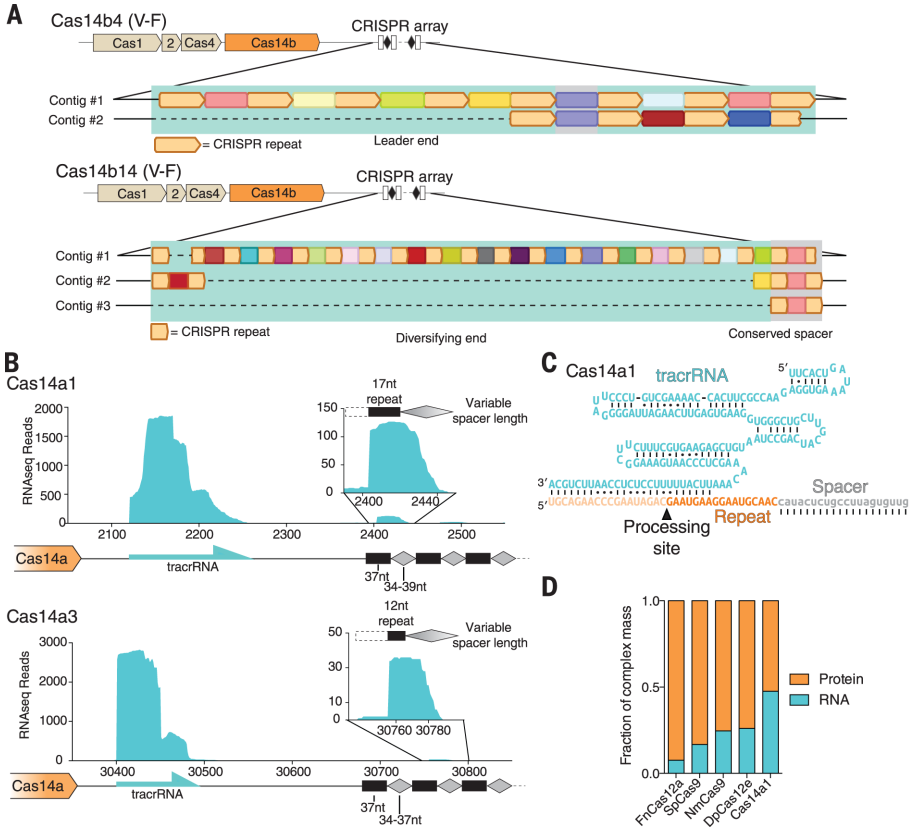

Fig. 2. CRISPR-Cas14a actively adapts and encodes a tracrRNA. (**A**) Spacer diversity for Cas14b4 and Cas14b14 with CRISPR repeats diagramed in tan and distinct spacers shown in different colors. (**B**) Metatranscriptomic reads mapped to Cas14a1 and Cas14a3 loci. The insets show an expanded view of the most abundant repeat and spacer sequence. nt, nucleotides. (**C**) In silico predicted structure of Cas14a1 crRNA and tracrRNA. Notably, RNase III orthologs were not identified in host genomes (fig. S5A). (**D**) Fraction of various CRISPR complex masses made up of RNA and protein.

containing the putative tracrRNA. Affinity purification of the Cas14a protein from cell lysate and sequencing of copurifying RNA revealed a highly abundant mature crRNA as well as the putative tracrRNA, albeit in lower relative abundance than what was shown by environmental metatranscriptomics, suggesting that Cas14 associates with both crRNA and tracrRNA (fig. S5C). The calculated mass of the assembled Cas14a protein–tracrRNA–crRNA particle is 48% RNA by weight compared with just 17% for *Streptococcus pyogenes* Cas9 (SpCas9) and 8% for *Francisella novicida* Cas12a (FnCas12a) (Fig. 2D), hinting at a central role of the RNA in the architecture of the Cas14a complex. Known class 2 CRISPR systems require a short sequence called a protospacer adjacent motif (PAM) to target double-stranded DNA (dsDNA) (*17*). To test whether Cas14a requires a PAM and can conduct dsDNA interference, we transformed *E. coli* expressing a minimal Cas14a locus with a dsDNA plasmid containing a randomized PAM region next to a sequence matching the target-encoding sequence (spacer) in the Cas14 array. Notably, no depletion of a PAM sequence was detected among *E. coli* transformants, suggesting that the CRISPR-Cas14a system is unable to target dsDNA, can do so without requiring a PAM, or is inactive in this heterologous host (fig. S6, A and B).

We next tested whether purified Cas14a-tracrRNA-crRNA complexes are capable of RNA-guided nucleic acid cleavage in vitro. All currently reconstituted DNA-targeting class 2 interference complexes are able to recognize both dsDNA and single-stranded DNA (ssDNA) substrates (*18*–*20*). We incubated purified Cas14a-tracrRNA-crRNA complexes with radiolabeled target oligonucleotides (ssDNA, dsDNA, and ssRNA) bearing a 20-nucleotide sequence complementary to the crRNA guide sequence or a noncomplementary ssDNA, and we analyzed these substrates for Cas14a-mediated cleavage. Only in the presence of a complementary ssDNA substrate was any cleavage product detected (Fig. 3A and fig. S7, A to C), and cleavage was dependent on the presence of both tracrRNA and crRNA, which could also be combined into a single-guide RNA (sgRNA) (Fig. 3B and fig. S8). The lack of detectable dsDNA cleavage suggests that Cas14a targets ssDNA selectively, although it is possible that some other host factor or sequence requirement could enable dsDNA recognition in the native host. Mutation of the conserved active site residues in the Cas14a RuvC domain eliminated cleavage activity (fig. S7, D and E), implicating RuvC as the domain responsible for DNA cutting. Moreover, Cas14a DNA cleavage was sensitive to truncation of the RNA components to lengths shorter than the naturally produced sequences (fig. S9, A to D). These results establish Cas14a as the smallest class 2 CRISPR effector demonstrated to conduct programmable RNA-guided DNA cleavage thus far.

Although we were unable to identify a dsDNA PAM in vivo, we tested whether Cas14a requires a PAM for ssDNA cleavage in vitro by tiling Cas14a guides across a ssDNA substrate (Fig. 3C). Despite sequence variation adjacent to the targets of these different guides, we observed cleavage for all four sequences. Notably, the cleavage sites occur beyond the guide-complementary region of the ssDNA and shift in response to guide binding position (Fig. 3C). These data demonstrate Cas14a is a ssDNA-targeting CRISPR endonuclease that does not require a PAM for activation.

On the basis of the observation that Cas14a cuts outside of the crRNA/DNA targeting heteroduplex, we hypothesized that Cas14a might possess target-activated nonspecific ssDNA cleavage activity, similar to the RuvC-containing enzyme Cas12a (*20*, *21*). To test this possibility, we incubated Cas14a-tracrRNA-crRNA with a complementary activator DNA and an aliquot of M13 bacteriophage ssDNA bearing no sequence complementarity to the Cas14a crRNA or activator (Fig. 3D). The M13 ssDNA was rapidly degraded to small fragments, an activity that was eliminated by mutation of the conserved Cas14a RuvC active site, suggesting that activation of Cas14a results in nonspecific ssDNA degradation. However, we were unable to observe Cas14a-mediated interference against the ssDNA bacteriophage ΦX174 when we expressed Cas14a heterologously in *E. coli* (fig. S10, A to C), possibly due to the dissimilarity between *E. coli* and Cas14a's native archaeal host. To investigate the specificity of target-dependent nonspecific DNA cutting activity by Cas14a, we adapted a fluorophore-quencher (FQ) assay in which cleavage of dye-labeled ssDNA generates a fluorescent signal (Fig. 4A) (*22*). When Cas14a was incubated with various guide RNA–target ssDNA pairs, a fluorescent signal was observed only in the presence of the cognate target and showed strong preference for longer FQ-containing substrates (fig. S10D and Fig. 4A). We next tested Cas14a mismatch tolerance by tiling 2-nucleotide mismatches across the targeted region in various ssDNA substrates. Surprisingly, mismatches near the middle of the ssDNA target strongly inhibited Cas14a activity, revealing an internal seed sequence that is distinct from the PAM-proximal seed region observed for dsDNA-targeting CRISPR-Cas systems (Fig. 4B and fig. S11, A to D). Moreover, DNA substrates containing strong secondary structure resulted in reduced activation of Cas14a (fig. S11E). Truncation of ssDNA substrates also resulted in reduced or undetectable trans cleavage (fig. S11F). Together, these results suggest a mechanism of fidelity distinct from dsDNA-targeting class 2 CRISPR systems, possibly using a mechanism similar to the ssRNA-targeting Cas13a enzymes (*23*–*25*).

Corrected 14 November 2018. See full text.

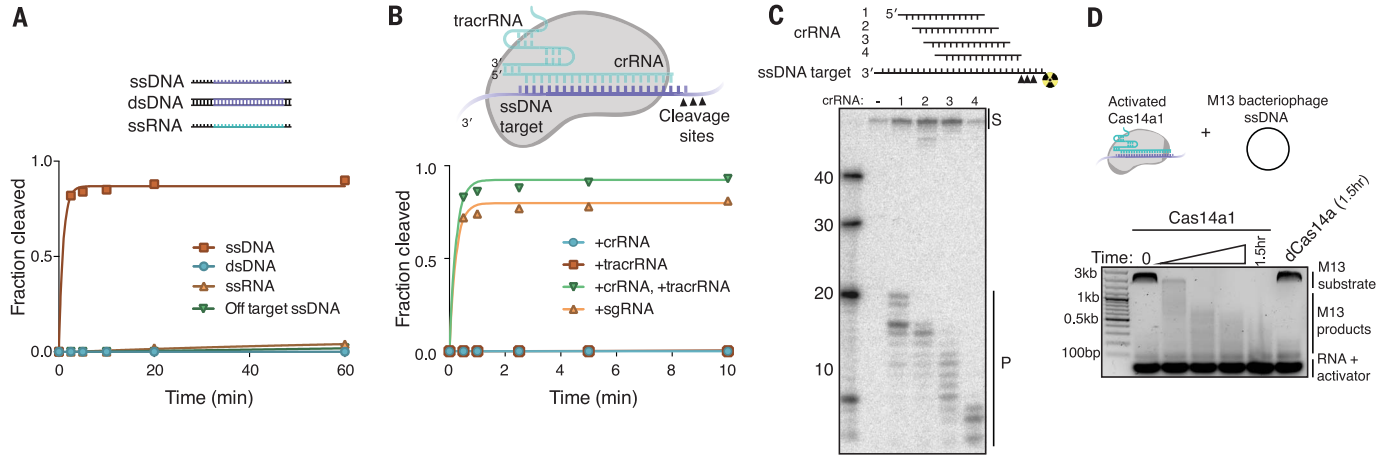

Fig. 3. CRISPR-Cas14a is an RNA-guided DNA endonuclease. (**A**) Cleavage kinetics of Cas14a1 targeting ssDNA, dsDNA, ssRNA, and off-target ssDNA. (**B**) Diagram of Cas14a RNP bound to target ssDNA and Cas14a1 cleavage kinetics of radiolabeled ssDNA in the presence of various RNA components. (**C**) Tiling of a ssDNA substrate by Cas14a1 guide sequences. (**D**) Cleavage of the ssDNA viral M13 genome with activated Cas14a1.

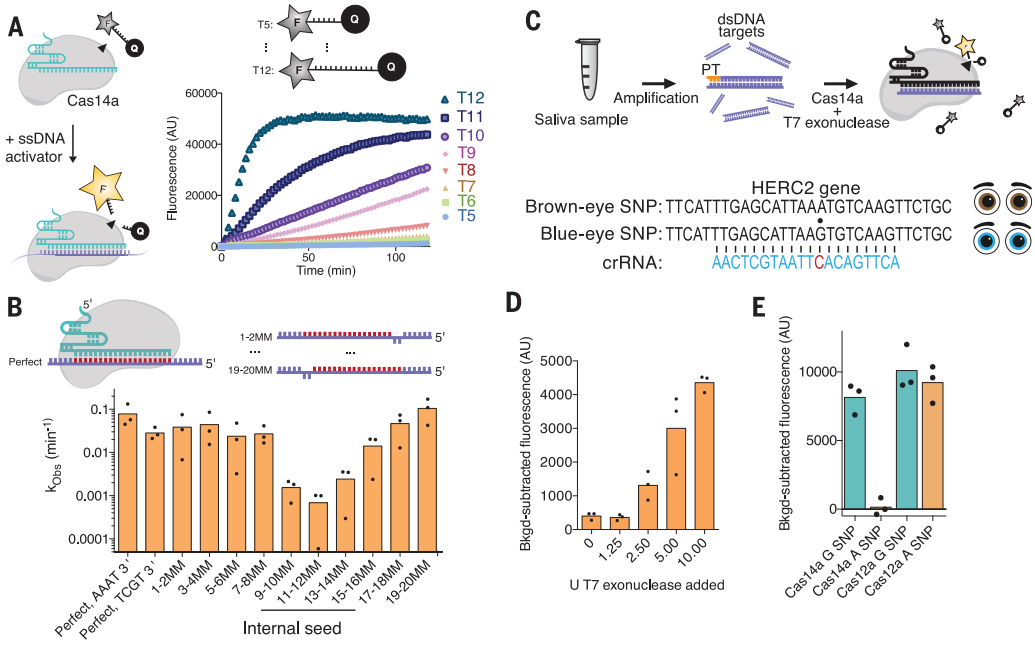

Fig. 4. High-fidelity ssDNA SNP detection by CRISPR-Cas14a. (**A**) FQ assay for detection of ssDNA by Cas14a1 and the cleavage kinetics for FQ substrates of various lengths. AU, arbitrary units. (**B**) Cleavage kinetics for Cas14a1 with mismatches tiled across the substrate (individual points represent replicate measurements). k_{Obs}, observed rate constant. (**C**) Diagram of Cas14-DETECTR strategy and *HERC2* eye color SNP. (**D**) Titration of T7 exonuclease and effect on Cas14a-DETECTR. Bkgd, background. (**E**) SNP detection using Cas14a-DETECTR with a blue-eye targeting guide for saliva samples from blue-eyed and brown-eyed individuals compared with ssDNA detection using Cas12a.

The target-dependent, nonspecific DNase activity of Cas12a serves as a DNA detection platform (DNA endonuclease-targeted CRISPR trans reporter, or DETECTR) for diagnostic uses (*20*, *26*). Although Cas12a exhibits low fidelity in discriminating against ssDNA substrates (*20*), Cas14a requires complementarity in the seed region for ssDNA substrate recognition. This improved specificity raised the possibility of using Cas14a for high-fidelity detection of DNA single-nucleotide polymorphisms (SNPs) without the constraint of a PAM sequence. To test this idea, DNA substrates were amplified using a phosphorothioate (PT)–containing primer to protect one strand from degradation by exonucleases. Upon addition of T7 exonuclease, the unmodified strand was degraded, leaving ssDNA substrates that can be detected by Cas14a (Fig. 4, C and D). As a proof of principle, we aimed to detect the human *HERC2* gene, which contains a SNP responsible for eye color (*27*). We amplified the *HERC2* gene from DNA in human saliva from both blue-eyed and brown-eyed individuals, using the PT amplification approach described above. When programmed with a guide RNA targeting the blue-eyed SNP, Cas12a failed to discriminate between the two ssDNA targets, exhibiting robust trans activity in both cases, whereas Cas14a exhibited strong activation in recognition of the blue-eyed SNP with near-background signal for the brown-eyed sample (Fig. 4E). The development of Cas14-DETECTR now allows for CRISPR-based detection of medically and ecologically important ssDNA pathogens as well as high-fidelity detection of SNPs without the constraint of a PAM sequence.

Further investigation of compact type V systems in metagenomic data revealed a large diversity of systems that, like Cas14a to Cas14c, include a gene encoding a short RuvC-containing protein adjacent to acquisition-associated *cas* genes and a CRISPR array. We found 20 additional such systems in various uncultivated microbes that cluster into five main families (Cas14d to Cas14h). Excluding *cas14g*, which is related to *cas12*b, the *cas14*-like genes form separate clades on the type V effector phylogeny (fig. S12, A and B), suggesting that these families evolved from independent domestication events of TnpB, the transposase-associated protein implicated as the evolutionary ancestor of type V CRISPR effectors (*3*). Phylogenetic reconstruction of their associated *cas1* genes indicated that they too have different origins for the *cas14* subtypes (fig. S2). Altogether, we identified 38 CRISPR-Cas14 systems belonging to eight families (Cas14a to Cas14h) and eight additional systems that could not be clustered with our analysis (termed Cas14u) (data S3).

The small size of the Cas14 proteins described here and their resemblance to type V effector proteins suggest that RNA-guided ssDNA cleavage may have existed as an ancestral class 2 CRISPR system (*28*, *29*). In this scenario, a small, domesticated TnpB-like ssDNA interference complex may have gained additional domains over time, gradually improving dsDNA recognition and cleavage. Related to this hypothesis, smaller Cas9 orthologs exhibit weaker dsDNA-targeting activity than their larger counterparts but retain the ability to robustly cleave ssDNA (*19*). Aside from the evolutionary implications, the ability of Cas14 to specifically target ssDNA suggests a role in defense against ssDNA viruses or mobile genetic elements that propagate through ssDNA intermediates (*30*). A ssDNA-targeting CRISPR system would be particularly advantageous in certain ecosystems where ssDNA viruses constitute the vast majority of viral abundance (*31*). The unexpected finding that these miniature CRISPR proteins can conduct targeted DNA cleavage highlights the diversity of CRISPR systems hidden in uncultivated organisms. Ongoing exploration of these underrepresented microbial lineages will likely continue to reveal new, unexpected insights into this microscopic arms race and lead to continued development of valuable CRISPR-based technologies.

REFERENCES AND NOTES

1. R. Barrangou *et al.*, *Science* **315**, 1709–1712 (2007).
2. S. A. Jackson *et al.*, *Science* **356**, eaal5056 (2017).
3. S. Shmakov *et al.*, *Nat. Rev. Microbiol.* **15**, 169–182 (2017).
4. J. S. Chen, J. A. Doudna, *Nat. Rev. Chem.* **1**, 0078 (2017).
5. C. T. Brown *et al.*, *Nature* **523**, 208–211 (2015).
6. K. Anantharaman *et al.*, *Nat. Commun.* **7**, 13219 (2016).
7. V. M. Markowitz *et al.*, *Nucleic Acids Res.* **42**, D568–D573 (2014).
8. A. J. Probst *et al.*, *Environ. Microbiol.* **19**, 459–474 (2017).
9. I. A. Chen *et al.*, *Nucleic Acids Res.* **45**, D507–D516 (2017).
10. I. Yosef, M. G. Goren, U. Qimron, *Nucleic Acids Res.* **40**, 5569–5576 (2012).
11. J. K. Nuñez, A. S. Y. Lee, A. Engelman, J. A. Doudna, *Nature* **519**, 193–198 (2015).
12. S. Shmakov *et al.*, *Mol. Cell* **60**, 385–397 (2015).
13. D. Burstein *et al.*, *Nature* **542**, 237–241 (2017).
14. C. Rinke *et al.*, *Nature* **499**, 431–437 (2013).
15. C. J. Castelle *et al.*, *Curr. Biol.* **25**, 690–701 (2015).
16. E. Deltcheva *et al.*, *Nature* **471**, 602–607 (2011).
17. F. J. M. Mojica, C. Díez-Villaseñor, J. García-Martínez, C. Almendros, *Microbiology* **155**, 733–740 (2009).
18. Y. Zhang, R. Rajan, H. S. Seifert, A. Mondragón, E. J. Sontheimer, *Mol. Cell* **60**, 242–255 (2015).
19. E. Ma, L. B. Harrington, M. R. O'Connell, K. Zhou, J. A. Doudna, *Mol. Cell* **60**, 398–407 (2015).
20. J. S. Chen *et al.*, *Science* **360**, 436–439 (2018).
21. B. Zetsche *et al.*, *Cell* **163**, 759–771 (2015).
22. A. East-Seletsky *et al.*, *Nature* **538**, 270–273 (2016).
23. L. Liu *et al.*, *Cell* **170**, 714–726.e10 (2017).
24. O. O. Abudayyeh *et al.*, *Science* **353**, aaf5573 (2016).
25. G. J. Knott *et al.*, *Nat. Struct. Mol. Biol.* **24**, 825–833 (2017).
26. S. Y. Li *et al.*, *Cell Res.* **28**, 491–493 (2018).
27. H. Eiberg *et al.*, *Hum. Genet.* **123**, 177–187 (2008).
28. E. V. Koonin, K. S. Makarova, F. Zhang, *Curr. Opin. Microbiol.* **37**, 67–78 (2017).
29. K. S. Makarova *et al.*, *Nat. Rev. Microbiol.* **13**, 722–736 (2015).
30. O. Barabas *et al.*, *Cell* **132**, 208–220 (2008).
31. M. Yoshida *et al.*, *Front. Microbiol.* **9**, 75 (2018).

ACKNOWLEDGMENTS

We thank N. Ma and K. Zhou for technical assistance and P. Harrington for graphic design assistance. **Funding:** D.B. was supported by a grant from the Paul Allen Frontiers Group. L.B.H., J.C.C., and J.S.C. were supported by U.S. National Science Foundation Graduate Research Fellowships. J.A.D. is an investigator of the Howard Hughes Medical Institute. This work was supported in part by a Frontiers Science award from the Paul Allen Institute to J.A.D. and J.F.B., a grant from the National Science Foundation (MCB-1244557 to J.A.D.), the Lawrence Berkeley National Laboratory's Sustainable Systems Scientific Focus Area funded by the U.S. Department of Energy (DE-AC02-05CH11231 to J.F.B.), and the Office of Science of the U.S. Department of Energy under contract no. DE-AC02–05CH11231. **Author contributions:** D.B. and D.P.-E. conducted the computational analysis. L.B.H., J.S.C., I.P.W., E.M., and J.C.C. designed and executed biochemical investigation of Cas14. L.B.H. designed and conducted experiments investigating Cas14 activity and assembly in *E. coli*. L.B.H. and D.B. conceived of the study. N.C.K., J.F.B., and J.A.D. supervised the research and experimental design. J.A.D., L.B.H., and D.B. wrote and revised the manuscript. All authors read, edited, and approved the manuscript. **Competing interests:** UC Regents have filed patents related to this work on which D.B., J.F.B., L.B.H., D.P.-E., J.S.C., and J.A.D. are inventors. L.B.H. and J.S.C. are cofounders of Mammoth Biosciences. I.P.W. is a consultant for Mammoth Biosciences. J.F.B. is a founder of Metagenomi. J.A.D. is a cofounder of Caribou Biosciences, Editas Medicine, Intellia Therapeutics, Scribe Therapeutics, and Mammoth Biosciences. J.A.D. is a scientific advisory board member of Caribou Biosciences, Intellia Therapeutics, eFFECTOR Therapeutics, Scribe Therapeutics, Synthego, Metagenomi, Mammoth Biosciences, and Inari. J.A.D. is a member of the board of directors at Driver and Johnson & Johnson and has sponsored research projects by Roche Biopharma and Biogen. **Data and materials availability:** Data S1 specifies the accession numbers, coordinates, and samples of origin for all CRISPR-Cas14 systems described in this study.

SUPPLEMENTARY MATERIALS

www.sciencemag.org/content/362/6416/839/suppl/DC1
Materials and Methods
Figs. S1 to S12
References (*32*–*42*)
Data S1 to S5

17 September 2018; accepted 6 October 2018
Published online 18 October 2018
10.1126/science.aav4294

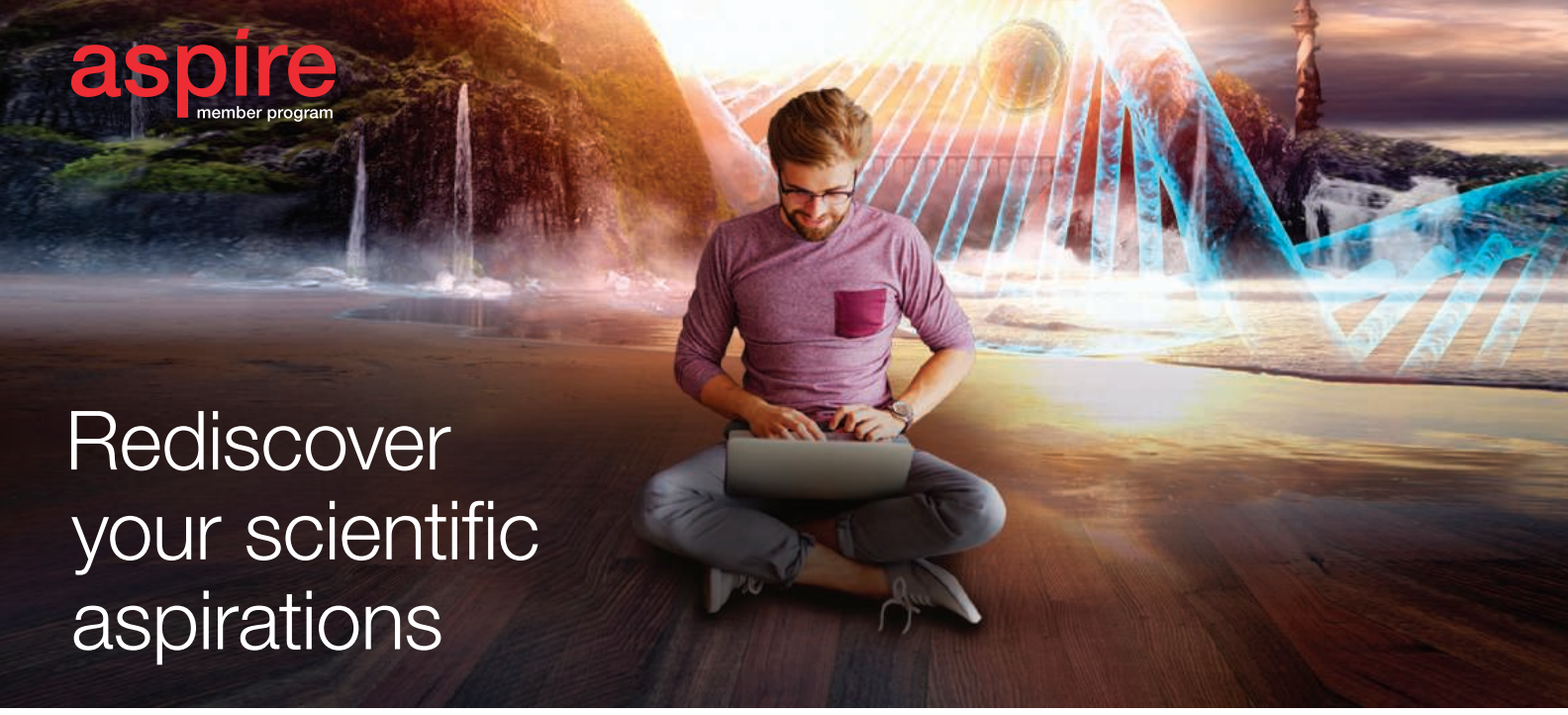

Get a free, full-size product, rewards, and more*

The Thermo Fisher Scientific Aspire™ member program* supports your lifelong love of science, empowering you with:

- A free, full-size product
- Rewards and discounts
- Career accelerators

Join now at **thermofisher.com/aspire**

Attending the ASCB | EMBO 2018 meeting? Visit us at booth #504

Limited-time offer—enroll now and receive 500 points**
Sign up today and get 500 points toward rewards catalog merchandise and discounts on products. Then collect more points for products you use in the lab—even if you didn't order or buy them.

If you need assistance, email **aspire@thermofisher.com**
or call **1 (800) 955-6288, ext. 46115**

Find out more at **thermofisher.com/aspire**

ThermoFisher SCIENTIFIC

Prix
Pour les sciences du vivant
Liliane Bettencourt

A TALENT DEDICATED TO LIFE SCIENCES

Pr. Veit Hornung

At the Ludwig Maximilian University in Munich, Veit Hornung and his team decipher the molecular mechanisms of inflammation and reveal the amazing complexity of the innate immune system. The project rewarded by the Liliane Bettencourt Prize for Life Sciences investigates the NLRP3 inflammasome, a protein complex at the crossroads of inflammatory responses. Understanding how the inflammasome is involved in response to endogenous alarm signals could lead to the development of new therapeutic molecules against type II diabetes or Alzheimer's disease.

Veit Hornung is the 2018 laureate of the Liliane Bettencourt Prize for Life Sciences. Since 1997, the prize has been awarded every year to talented life scientists, for the excellence of their work and the quality of their international publications. The Fondation Bettencourt Schueller was created by a family which trusts in people and their capabilities. Its aim is to promote initiative, creativity, and excellence. The Fondation Bettencourt Schueller wants to take talent to the top.

Fondation Bettencourt Schueller

Reconnue d'utilité publique depuis 1987

fondationbs.org

NEW ENGLAND BioLabs® Inc.

be INSPIRED
drive DISCOVERY
stay GENUINE

How low can you go?

NEBNext® Single Cell/ Low Input Library Prep Kit

With this unique streamlined method, high-quality, full-length transcript sequencing libraries are made directly from single cells, or from as little as 2 pg – 200 ng of total RNA.

- Detect more transcripts, including low-abundance transcripts
- Obtain uniform, full-length transcript coverage, regardless of input amount or sample type
- Save time with a streamlined workflow, minimal handling steps and hands-on time

Visit **NEBNext.com** to request your sample today.

Superior transcript detection with the NEBNext Single Cell/Low Input RNA Library Prep Kit

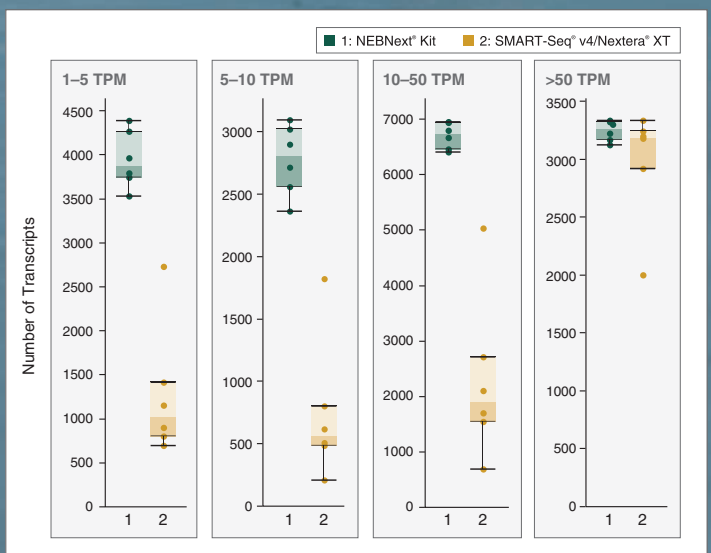

Sequencing libraries were generated from Jurkat single cells (6 replicates) using the NEBNext Single Cell/Low Input RNA Library Prep Kit, or the SMART-Seq® v4 Ultra® Low Input RNA Kit for Sequencing plus the Nextera® XT DNA Library Prep Kit. Libraries were sequenced on an Illumina® NextSeq® 500. Each dot represents the number of transcripts identified at the given Transcripts Per Kilobase Million (TPM) range, and each box represents the median, first and third quartiles per replicate and method. Salmon 0.6 was used for read mapping and quantification of all GENCODE v25 transcripts. Increased identification of low abundance transcripts is observed with the NEBNext libraries.

LOOK DEEPER

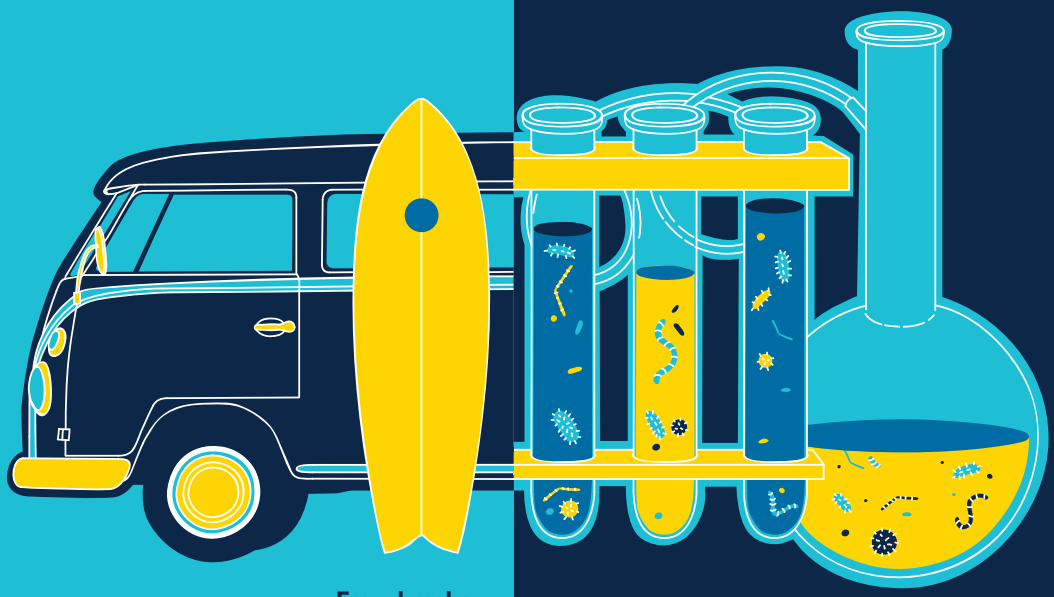

From breaks to breakthroughs. Not only is UC San Diego ***a top school for chemistry***, it's also No. 1 in surfing. (Naturally.) Where these worlds meet, you'll find surfer-scientist Cliff Kapono. He's hitting the planet's most amazing breaks to discover something even more inspiring: the surfer microbiome – and how the ocean shapes us.

UC San Diego

lookdeeper.ucsd.edu

Surfer, 2018
U.S. News & World Report, 2019

FUJITSU Human Centric AI

Zinrai

Fujitsu's Artificial Intelligence Framework

FUJITSU

"Zinrai" is Fujitsu's approach to human-centric Artificial Intelligence (AI). Based on many years of research and development, Zinrai incorporates the latest AI technologies across both products and services to transform business and create new value for all.

Fujitsu's Zinrai has many applications, including:

City Surveillance

Real time observation using image recognition systems

Retail

Analysis of shopper preferences by gaze tracking

Healthcare

Helping doctors make faster medical diagnosis

Digital Business Platform – MetaArc

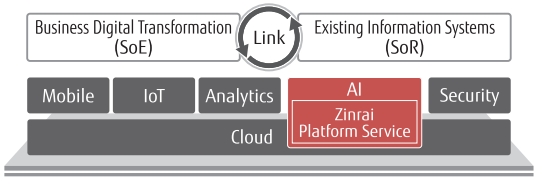

Services developed on Zinrai technology are available through MetaArc, accelerating innovation to creat new value.

*SoE: Systems of Engagement, SoR: Systems of Record

shaping tomorrow with you

sartorius

arium® mini:
The Only Ultrapure Water System with Integrated Bagtank Technology

Easy to operate with touch screen activated color display, the compact arium® mini delivers reliable and reproducible results.

Its unique bagtank technology can save valuable time in cleaning and prevent permanent biofilm, ensuring the highest water quality for your applications.

To find out more, visit:
www.sartorius.com/arium-mini

Call for Nominations
2018 Cozzarelli Prize

The PNAS Editorial Board is now accepting nominations through January 7, 2019, for the 2018 Cozzarelli Prize. This award recognizes scientific excellence and will be presented to the authors of six articles published in PNAS during 2018.

Nominations may be sent to pnas@nas.edu and should include a citation and brief explanation of the merits of the work. Award recipients will be recognized during the PNAS Editorial Board Meeting and the NAS Annual Meeting Awards Ceremony on April 28, 2019, in Washington, DC.

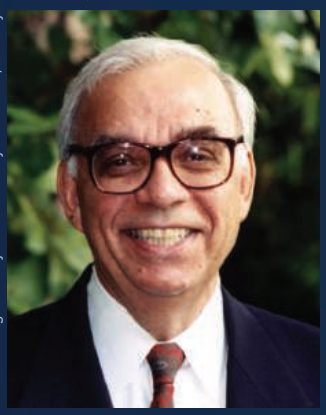

Image courtesy of the University of California, Berkeley.

Nicholas R. Cozzarelli,
former PNAS Editor-in-Chief

PNAS
www.pnas.org

For a list of previous winners and podcasts with the authors, visit http://www.pnas.org/page/about/cozzarelli-prize.

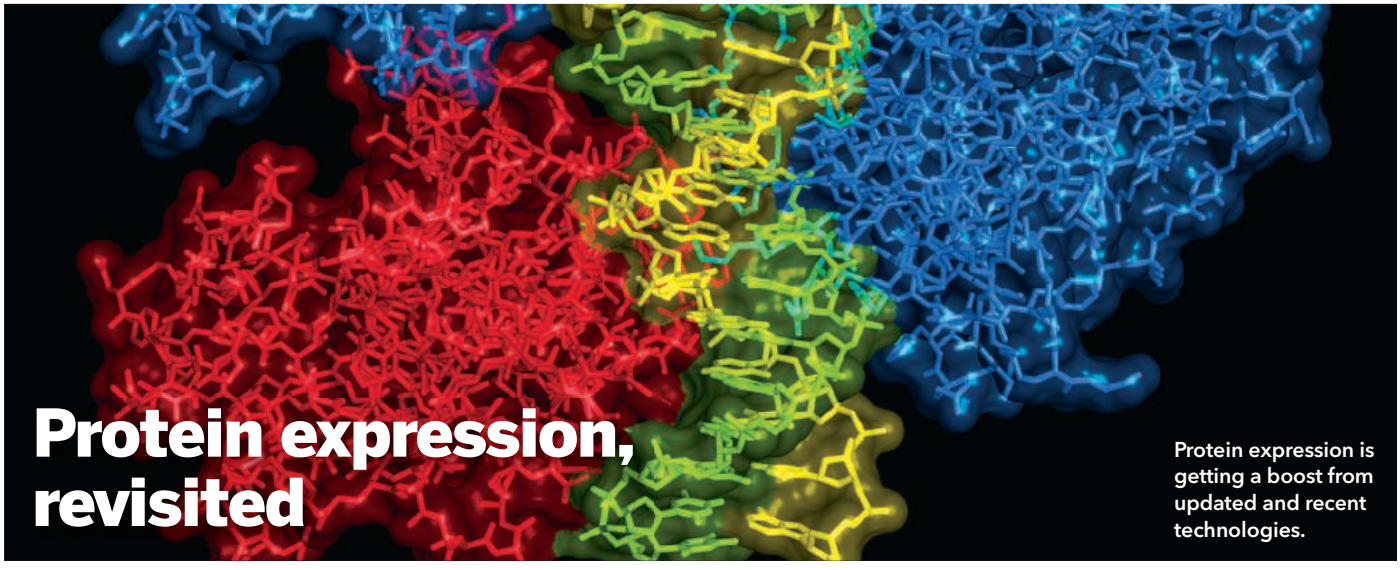

Protein expression, revisited

Protein expression is getting a boost from updated and recent technologies.

An integral tool in biological research, protein expression is increasingly important as a pharmaceutical production mechanism for biological therapeutics. The ability to direct the ultimate nature of proteins depends largely on the degree of control researchers have over the final product. The combination of old technologies—such as artificial enzymes—and new next-generation expression systems is revitalizing protein expression protocols. **By Caitlin Smith**

The advent of genome editing tools such as the CRISPR/Cas9 system has given scientists an affordable, accessible, and relatively simple method to alter genes. Yet precisely controlling protein expression through structural and posttranslational modifications takes on immense importance in the context of expressed therapeutic proteins, such as prescription medications. Controlling protein expression in other species, such as mosquitoes, may even aid researchers in eradicating malaria, the Zika and West Nile viruses, dengue fever, and other mosquito-borne illnesses.

Our quickly evolving molecular tools have far-reaching effects, as evidenced by the wide range of CRISPR applications already being used. "CRISPR systems are amazing resources for finding new tools to manipulate RNA and DNA," says Jamie Cate, professor in the departments of molecular and cell biology and biochemistry at the **University of California, Berkeley.** "I see the present as the biological equivalent of the transistor revolution for computers."

Other molecular tools are evolving alongside—and sometimes interacting with—CRISPR systems to broaden the scope and increase the potency and versatility of controls on protein expression. Artificial enzymes, for example, are shedding their limitations and gaining programmability. Molecular switches are becoming multifaceted, enabling greater fine-tuning. Next-generation expression systems can churn out greater yields of complex biological therapeutics than ever before. One thing is certain—as molecular controls become increasingly sophisticated, their myriad uses continue to expand.

Artificial enzymes for targeting DNA and RNA

Although it's a powerful tool, even the CRISPR/Cas9 system has occasional drawbacks. One is the requirement for a protospacer adjacent motif (PAM) sequence just upstream of the intended editing site. The PAM sequence is a binding signal for the Cas9 enzyme, so its presence is necessary, but also limiting (if a PAM sequence doesn't exist upstream of a desired editing site, one needs to be created). Huimin Zhao, theme leader for biosystems design at the **Carl R. Woese Institute for Genomic Biology, University of Illinois at Urbana-Champaign,** attempted to develop a CRISPR-like genome editing tool that would remove this constraint, and offer more versatility by permitting editing without a PAM sequence.

Zhao's lab developed an artificial restriction enzyme (ARE) system based on PfAgo, an Argonaute protein from the archaeon *Pyrococcus furiosus*, a prokaryote (single-celled) microbe. This platform surpasses traditional type II restriction enzymes—molecular scissors that cleave DNA at predefined sites (*1*).

"We can readily create an unlimited number of artificial restriction enzymes, with desired sequence specificity and defined sticky ends of varying lengths, using a simple system consisting of a single protein, PfAgo, and two DNA guides for targeting a specific dsDNA [double-stranded DNA] sequence," says Zhao. "This system can be multiplexed, in that the same protein can be loaded with multiple DNA guides for targeting several sites simultaneously."

Because the DNA guides show PfAgo where to cut, the system can be programmed to cut virtually anywhere. Another advantage is that PfAgo has longer recognition sequences (typically 16 base pairs) than do traditional restriction enzymes (which typically recognize 4 to 8 base pairs); a longer recognition sequence makes it more likely to find a unique cleavage site. Unlike previous artificial restriction enzymes, PfAgo can generate defined and longer sticky ends when cutting DNA, which aid in subsequently attaching DNA fragments together.

Zhao's lab is eager to apply its new technology. "We also developed a PfAgo/ARE-based direct cloning method to clone large, natural-product biosynthetic gene clusters for discovery of novel natural products that can potentially be used cont.>

as antibiotics and anticancer drugs," says Zhao. His newly formed company, **Modular Bioscience,** will explore PfAgo's use in medical diagnostics, such as liquid biopsies, and single-nucleotide polymorphism and pathogen detection.

Another CRISPR-associated Argonaute protein from the bacterium *Marinitoga piezophila* (MpAgo) is in the crosshairs of Cate's lab, which focuses on protein-translation mechanisms and regulation (*2*). "Our goal was to make an RNA-targeting technology that we could use to explore RNA biology in human cells," says Cate. They wanted to target RNA using an RNA-guided protein, as an alternative to labeling RNAs with covalent tags.

Postdoctoral researcher Audrey Lapinaite, a member of Cate's team, found the main challenge was "how to load the guide RNA into MpAgo inside cells," says Cate. She solved this problem by assembling guide RNA–protein complexes (RNPs) in vitro, then using the RNPs in cell-based experiments. Lapinaite found that a modification of the 5'-nucleotide of the guide RNA resulted in easily programmable RNPs with high affinity to their fully complementary RNA targets. Furthermore, the modified RNPs show high specificity, and can discriminate between RNA substrates differing by only one nucleotide.

Cate is excited to explore the prospects for manipulating RNAs using MpAgo RNPs. "We are most eager to use MpAgo for RNA targeting in human cells to explore human RNA biology, such as in imaging and proteomics experiments," he says. Because MpAgo is derived from bacteria, its use for therapeutic purposes is unlikely—but Cate hopes to apply this system to gain insight into how endogenous human Argonautes work.

Molecular switches

Given the enormous capabilities of CRISPR/Cas9 genome editing, the search is on for ways to make the system inducible, so that editing can be turned on or off at specific times. A United Kingdom–based collaboration between Yu-Hsuan Tsai from **Cardiff University** and Anthony Perry from the **University of Bath** reveals a new type of inducible CRISPR switch (*3*). Previous switches had drawbacks, such as leakiness of editing activity in the absence of signal, or a reliance on antibiotic use, which can increase the risk of antibiotic resistance. "We envisaged the use of an artificial, nonphysiological amino acid [that] would address these problems," says Tsai.

Tsai and Perry's groups used genetic code expansion to make a genome sensitive to an artificial signal. In cell lines and mouse embryos, researchers "expanded" the genetic code by inserting a toolkit that makes the expression of Cas9 (the enzyme required for genome editing) dependent on the presence of lysine derivative Lys (Boc). This non-natural amino acid is ideal for this purpose because it is cheap, safe, readily obtainable, and easy to administer to cells or whole animals.

The researchers showed that the presence of Lys (Boc) resulted in genomic editing, while in its absence no genomic editing occurred. The success of Tsai and Perry's switch may be due in part to the difference in strategies: "Our approach controls the translation of the functional Cas9 protein, whereas previous methods [use] posttranslational control, such as modulating the activity of translated protein by different stimuli," says Tsai.

Future applications of their work include gene drives, which virtually ensure that all progeny will inherit genetic changes that rapidly spread throughout a population of animals (in herds of livestock, for instance). Because the effect is inducible, its power can be more safely controlled. This new, inducible CRISPR switch may be more suitable "in clinical therapeutic genome editing in situ, or gene drives in which environmentally compatible control is paramount," says Tsai.

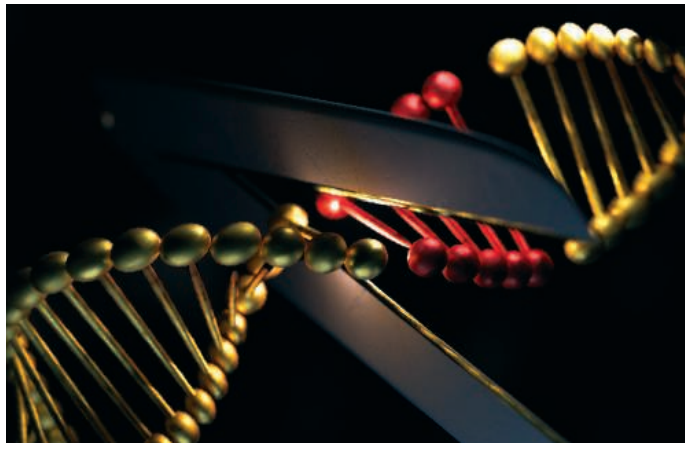

Next-gen expression systems may see further record expression levels with the incorporation of genome editing tools like CRISPR/Cas9.

Another type of molecular switch features an artificial enzyme, and was developed by a Swiss collaboration headed by Tom Ward, director of **NCCR (National Centre of Competence in Research) Molecular Systems Engineering,** a multidisciplinary initiative comprising researchers at the **University of Basel** and **ETH Zurich** (Swiss Federal Institute of Technology). Ward's lab took a modular design approach, combining their knowledge of artificial metalloenzymes with expertise in cell-penetrating modules from Stefan Matile's lab in the Department of Organic Chemistry at the University of Geneva, and a synthetic gene-switch module produced by Martin Fussenegger's lab in the Department of Biosystems Science and Engineering at ETH Zurich.

This new cell-penetrating disulfide module lets an artificial metalloenzyme enter a cell without harming it, "reminiscent of a Trojan horse," says Ward. Upon entry, the enzyme catalyzes a reaction that uncages a hormone. The synthetic gene-switch module detects the newly uncaged hormone and responds by turning on expression of the fluorescent indicator luciferase. "The gene switch is thus turned on by an abiotic reaction operated by an artificial enzyme," says Ward.

Now that the collaboration has established proof-of-concept for their system (*4*), they are actively pursuing biomedical applications that include interacting with a host protein—for example, a protein expressed by cancer cells that enables precise targeting. "Carbonic anhydrase is overexpressed on the surface of many cancer cell lines," says Ward. "We could use this protein to accumulate the artificial metalloenzyme either on the surface or inside of cancer cells; the system is turned on only when the artificial metalloenzyme binds to carbonic anhydrase."

Next-generation expression systems

Advances in molecular control of gene expression are also expanding the opportunities for protein expression systems. As drug manufacturers look for cheaper ways to express new biologic drugs, next-gen expression systems are gaining traction. Currently, the standard expression system is mammalian Chinese

Featured participants

AbSci
www.absci.com

Cardiff University
www.cardiff.ac.uk

Carl R. Woese Institute for Genomic Biology, University of Illinois at Urbana-Champaign
www.igb.illinois.edu

Dyadic
www.dyadic.com

ETH Zurich
www.ethz.ch/en.html

Modular Bioscience
modbiosci.com

NCCR Molecular Systems Engineering
www.nccr-mse.ch/en/home

University of Basel
www.unibas.ch/en.html

University of Bath
www.bath.ac.uk

University of California, Berkeley
www.berkeley.edu

hamster ovary (CHO) cell lines. However, the limitations of CHO cells—such as high cost and comparatively slow doubling times—make the next-gen systems worth considering for expressing new biopharmaceuticals, especially to help reduce the costs of important medicines.

For example, the SoluPro protein expression platform from **AbSci** can generate soluble, properly folded proteins at extremely high titers, currently 4g/L of full-length antibody and >20g/L of other complex products, using *Escherichia coli* expression. Typically, some human proteins can't be expressed in *E. coli*, and require mammalian cell lines for proper folding. AbSci's technology includes two innovations that make it possible to produce such proteins in *E. coli*, while taking advantage of the simplicity and lower costs of this expression system.

One creation is a semioxidized cytoplasm that produces soluble, disulfide-linked proteins. "Cytoplasmic production, which traditionally is limited by inclusion body formation, is desirable because it has significantly higher capacity than the periplasm, places no restrictions on protein size, and achieves dramatically shorter production cycles of one to two days, compared to secretion-based expression systems," says Sean McClain, AbSci's founder and CEO. The second innovation is SoluPro's dual inducible promoters, which can be independently controlled. This enables "tuning" of protein production rates by optimizing for the best protein-folding and titer.

"The SoluPro system's ability to properly fold proteins overcomes a large majority of the limitations found with traditional *E. coli* expression," says McClain. "We have successfully produced novel antibody scaffolds as well as IgG1 and IgG4 molecules where effector function is not desirable." Many of these novel antibody scaffolds, which are gaining increasing traction in development pipelines, are challenging to produce in CHO cells. "AbSci is keenly focused on these hard-to-produce next-generation antibody scaffolds, including bispecifics, Fc [fragment crystallizable]-fusion proteins, and other multispecific products, which SoluPro is ideally suited to manufacture efficiently," he says.

Dyadic offers another next-gen expression platform, the fungal-based C1 gene expression system. Dyadic's scientists took advantage of a serendipitous mutation that resulted in a several 100-fold increase in protein productivity of the filamentous *Myceliophthora thermophila* fungus (which the company nicknamed "C1," then created a molecular toolset to turn the fungus into a recombinant expression host). They are currently focused on biomedical efforts, applying the C1 expression platform to making biologic vaccines and drugs more affordable and accessible. Though filamentous fungus may sound exotic, in nature they are natural secreters (C1 has a 2-hour doubling time, compared to about 20 hours for CHO cells). They also use defined synthetic media, which is cheaper and avoids the need for viral inactivation required for CHO cells.

Today, biosimilars are being produced ineffectively by cell lines such as CHO cells, according to Dyadic's CEO Mark Emalfarb. However, says Emalfarb, "We can produce up to 2 to 5 times more, in a third of the time, and at a fraction of CHO media costs [as compared to] the reported average industry CHO productivity." And because C1 secretes its product into the media, the downstream protein harvesting steps are also simpler than those in other systems—for example, *E. coli* requires lysing of cells and purifying product from cell fractions, adding more complexity and cost.

Dyadic's C1 platform efficiently produces full-length monoclonal antibodies, antibody heavy and light chains, Fc-fusion proteins, Fabs (antigen-binding fragments), bispecific antibodies, and vaccines. "We can also make VLPs [virus-like particles], which are theoretically more potent types of vaccines, and are more difficult to express in general," says Emalfarb. "We even have a secreted VLP now, so less is lost in downstream processing."

Dyadic is also engineering C1 to produce human-like glycosylation in different forms, to allow pharmaceutical companies to evaluate them. "Unlike CHO cells, C1 cells are monoclonal cells," explains Matthew Jones, Dyadic's chief commercial officer. "C1 has the potential to produce more consistent, more homogeneous glycostructures for companies to evaluate, to test which ones may work better." A recently announced collaboration with the biopharmaceutical company Sanofi-Aventis Deutschland GmbH will study the use of the C1 technology to express different types of therapeutic compounds, such as vaccines and protein-based biologics.

Both *E. coli*- and yeast-based expression systems share other advantages, such as not requiring the expensive viral clearance steps needed in CHO cells. In addition, the lower costs of next-gen expression systems can in turn lower drug prices, while allowing drug manufacturers to maintain a profit margin—which incentivizes manufacturers to produce drugs with lower prices and make them available to the public. Both McClain and Emalfarb hope their companies' technologies will encourage manufacturers to market drugs that are good for society but not otherwise profitable, such as new influenza vaccines that cost less but work better.

None of this would be possible without the genetic tools that harness expression systems. As scientists achieve finer controls over genomes, the number of expression products will soar. For example, next-gen expression systems may see further record expression levels with the incorporation of genome editing tools like CRISPR/Cas9. As these tools continue to grow in sophistication, the benefits to patients will continue to increase—and may transform biomedicine in the process.

References

1. B. Enghiad, H. Zhao, *ACS Synth. Biol.* **6**, 752–757 (2017).
2. A. Lapinaite, J. A. Doudna, J. H. D. Cate, *Proc. Natl. Acad. Sci. U.S.A.* **115**, 3368–3373 (2018).
3. T. Suzuki *et al.*, *Sci. Rep.* **8**, 10051 (2018).
4. Y. Okamoto *et al.*, *Nature Comm.* **9**, 1943 (2018).

Caitlin Smith is a freelance science writer in Portland, Oregon.

Cloning Kit

Gibson Assembly Cloning allows for the insertion of one or more DNA fragments into virtually any location of any vector without the need for compatible restriction sites. In a single round of cloning, join multiple DNA fragments (1–15) to create seamless constructs without subcloning. With easy reaction setup and less than 5 min of hands-on time, go from DNA fragments to transformation-ready constructs in an hour or less. Gibson Assembly Cloning achieves cloning efficiencies of up to 95%. Three kits are available: Gibson Assembly HiFi 1-Step Kit, Gibson Assembly Ultra Kit, and Gibson Assembly Site-Directed Mutagenesis Kit.

SGI-DNA
For info: 855-474-4362
www.sgidna.com/reagents.html

Minicircle Services

When you want sustained transgene expression without the risks of introducing exogenous DNA—such as for developing animal models or pioneering new gene-therapy approaches—minicircle technology is a great option. But many labs don't have either the time or the in-house expertise to spend constructing and producing minicircles—which is why we offer Minicircle Cloning & Production Services. Delivered by our experienced scientific team, who routinely produce minicircles for large pharma partners, our services are very customizable. We can provide a complete end-to-end experience—we clone your complementary DNA (cDNA), microRNA (miRNA), or small hairpin RNA (shRNA) into one of our highly regarded minicircle parental vectors and assemble large quantities of minicircles—or only parts of the cloning and production process. We can even customize the parental vector for you.

System Biosciences
For info: 888-266-5066
www.systembio.com

cDNA Clones

TrueORF Gold is OriGene's collection of premium complementary DNA (cDNA) clones that have passed the ultimate tests: sequence verification and protein expression validation. Each TrueORF Gold clone has been used to transfect human cell lines for protein expression. In fact, OriGene has produced over 12,000 overexpression lysates from TrueORF-transfected human embryonic kidney 293 (HEK293) cells and subsequently purified over 5,000 human proteins from those cells. Each clone is fully sequenced with downloadable chromatogram files posted online. View and analyze the sequences before purchasing, and you will never worry about mutations when using TrueORF Gold. All clones are available for next-day shipment. Why spend weeks constructing a cDNA clone or having it synthesized? TrueORF Gold accelerates your research, experiment, degree, publication, or grant application, and gets you there faster. There is no need for subcloning or plasmid preparation. Order a TrueORF Gold clone today, and start your experiment tomorrow.

OriGene Technologies
For info: 888-267-4436
www.origene.com

HDR Plasmid Donor Kits

The Edit-R HDR Plasmid Donor Kits enable you to easily create a plasmid donor for insertion of either the mKate2 or enhanced green fluorescent protein (EGFP) fluorescence reporters, or a custom gene sequence of your choice, into almost any genomic location. Gene engineering using CRISPR/Cas9 relies on two pathways for repair of double-strand breaks in DNA: nonhomologous end joining (NHEJ) and homology-directed repair (HDR). Precise repair of DNA in order to generate a specific mutation or insert or remove a desired sequence requires the HDR pathway, and depends on the availability of a DNA donor template that can be used to repair the DNA break. The kits enable fast, efficient assembly of a DNA donor plasmid, and contain validated protocols for design, assembly, and confirmation of the plasmid.

Dharmacon
For info: 800-235-9880
dharmacon.horizondiscovery.com

Cell-Free Linear DNA Expression Kit

Arbor Biosciences' myTXTL Linear DNA Expression Kit allows for the use of linear DNA, including PCR products, gene fragments, and synthesized DNA, as input for transcription (TX) and translation (TL) in an *Escherichia coli*–based cell-free platform. Removing the requirements for cloning genes into plasmids, transforming cells, and further selecting for clones will greatly accelerate the design–build–test cycle for synthetic biology research and sampling in protein-screening applications. Created for use in pilot-scale studies as well as high-throughput analysis on automated liquid-handling platforms, myTXTL Linear DNA Expression Kit delivers a complete solution for protein research and analysis. The *E. coli*–based system is a ready-to-use master mix containing all the critical components required for cell-free protein production. End-users simply need to add their linear DNA to the master mix and incubate for as little as 30 min before analyzing the expressed product.

Arbor Biosciences
For info: 734-998-0751
www.arborbiosci.com

Human Exosomes

ZenBio offers fully characterized exosomes from placental mesenchymal stem cells, cord serum, and custom isolation. Exosomes are membrane vesicles stored intracellularly in endosomal compartments, and are secreted when these structures fuse with a cell's plasma membrane. They contain protein, DNA, and RNA, making them an attractive vector for paracrine signals delivered by stem cells. They may also be "loaded" with predetermined proteins and nucleic acid to achieve a desired effect, and can be stored as an off-the-shelf product with the potential to circumvent many of the limitations of viable cells for therapeutic applications in regenerative medicine. In vitro, exosomes from preadipocytes stimulate cell proliferation in a wound-healing model. In vivo, adipose-graft–derived exosomes have been shown to be a promising tool for skin repair and remodeling.

ZenBio
For info: 919-547-0692
www.zen-bio.com/products/cells/human-exosomes.php

Electronically submit your new product description or product literature information! Go to www.sciencemag.org/about/new-products-section for more information.

Newly offered instrumentation, apparatus, and laboratory materials of interest to researchers in all disciplines in academic, industrial, and governmental organizations are featured in this space. Emphasis is given to purpose, chief characteristics, and availability of products and materials. Endorsement by *Science* or AAAS of any products or materials mentioned is not implied. Additional information may be obtained from the manufacturer or supplier.

BIOLOGY ■ EARTH ■ ENVIRONMENT ■ LIFE ■ INTERDISCIPLINARY ■ PHYSICAL ■ MATERIAL ■ SOCIAL SCIENCES

Science Advances | AAAS

OPEN ACCESS, DIGITAL, AND FREE TO ALL READERS

OPEN ACCESS

Pushing the Boundaries of Knowledge

As AAAS's first multidisciplinary, open access journal, *Science Advances* publishes research that reflects the selectivity of high impact, innovative research you expect from the *Science* family of journals, published in an open access format to serve a vast and growing global audience. Check out the latest findings or learn how to submit your research: **ScienceAdvances.org**

Everything in one place for your gene-based research?

Brilliant!

cDNA Clones · Lentivirus · CRISPR · Antibodies · Proteins · RNAi · Tissues

OriGene Technologies.

Supporting your path to discovery

We are committed to providing you with high quality products and services. With over 2 million off-the-shelf products, we are here to support your gene-based research and scientific discoveries.

Shop now at www.origene.com

ORIGENE

Cloning Kit

Gibson Assembly Cloning allows for the insertion of one or more DNA fragments into virtually any location of any vector without the need for compatible restriction sites. In a single round of cloning, join multiple DNA fragments (1–15) to create seamless constructs without subcloning. With easy reaction setup and less than 5 min of hands-on time, go from DNA fragments to transformation-ready constructs in an hour or less. Gibson Assembly Cloning achieves cloning efficiencies of up to 95%. Three kits are available: Gibson Assembly HiFi 1-Step Kit, Gibson Assembly Ultra Kit, and Gibson Assembly Site-Directed Mutagenesis Kit.

SGI-DNA
For info: 855-474-4362
www.sgidna.com/reagents.html

Minicircle Services

When you want sustained transgene expression without the risks of introducing exogenous DNA—such as for developing animal models or pioneering new gene-therapy approaches—minicircle technology is a great option. But many labs don't have either the time or the in-house expertise to spend constructing and producing minicircles—which is why we offer Minicircle Cloning & Production Services. Delivered by our experienced scientific team, who routinely produce minicircles for large pharma partners, our services are very customizable. We can provide a complete end-to-end experience—we clone your complementary DNA (cDNA), microRNA (miRNA), or small hairpin RNA (shRNA) into one of our highly regarded minicircle parental vectors and assemble large quantities of minicircles—or only parts of the cloning and production process. We can even customize the parental vector for you.

System Biosciences
For info: 888-266-5066
www.systembio.com

cDNA Clones

TrueORF Gold is OriGene's collection of premium complementary DNA (cDNA) clones that have passed the ultimate tests: sequence verification and protein expression validation. Each TrueORF Gold clone has been used to transfect human cell lines for protein expression. In fact, OriGene has produced over 12,000 overexpression lysates from TrueORF-transfected human embryonic kidney 293 (HEK293) cells and subsequently purified over 5,000 human proteins from those cells. Each clone is fully sequenced with downloadable chromatogram files posted online. View and analyze the sequences before purchasing, and you will never worry about mutations when using TrueORF Gold. All clones are available for next-day shipment. Why spend weeks constructing a cDNA clone or having it synthesized? TrueORF Gold accelerates your research, experiment, degree, publication, or grant application, and gets you there faster. There is no need for subcloning or plasmid preparation. Order a TrueORF Gold clone today, and start your experiment tomorrow.

OriGene Technologies
For info: 888-267-4436
www.origene.com

HDR Plasmid Donor Kits

The Edit-R HDR Plasmid Donor Kits enable you to easily create a plasmid donor for insertion of either the mKate2 or enhanced green fluorescent protein (EGFP) fluorescence reporters, or a custom gene sequence of your choice, into almost any genomic location. Gene engineering using CRISPR/Cas9 relies on two pathways for repair of double-strand breaks in DNA: nonhomologous end joining (NHEJ) and homology-directed repair (HDR). Precise repair of DNA in order to generate a specific mutation or insert or remove a desired sequence requires the HDR pathway, and depends on the availability of a DNA donor template that can be used to repair the DNA break. The kits enable fast, efficient assembly of a DNA donor plasmid, and contain validated protocols for design, assembly, and confirmation of the plasmid.

Dharmacon
For info: 800-235-9880
dharmacon.horizondiscovery.com

Cell-Free Linear DNA Expression Kit

Arbor Biosciences' myTXTL Linear DNA Expression Kit allows for the use of linear DNA, including PCR products, gene fragments, and synthesized DNA, as input for transcription (TX) and translation (TL) in an *Escherichia coli*–based cell-free platform. Removing the requirements for cloning genes into plasmids, transforming cells, and further selecting for clones will greatly accelerate the design–build–test cycle for synthetic biology research and sampling in protein-screening applications. Created for use in pilot-scale studies as well as high-throughput analysis on automated liquid-handling platforms, myTXTL Linear DNA Expression Kit delivers a complete solution for protein research and analysis. The *E. coli*–based system is a ready-to-use master mix containing all the critical components required for cell-free protein production. End-users simply need to add their linear DNA to the master mix and incubate for as little as 30 min before analyzing the expressed product.

Arbor Biosciences
For info: 734-998-0751
www.arborbiosci.com

Human Exosomes

ZenBio offers fully characterized exosomes from placental mesenchymal stem cells, cord serum, and custom isolation. Exosomes are membrane vesicles stored intracellularly in endosomal compartments, and are secreted when these structures fuse with a cell's plasma membrane. They contain protein, DNA, and RNA, making them an attractive vector for paracrine signals delivered by stem cells. They may also be "loaded" with predetermined proteins and nucleic acid to achieve a desired effect, and can be stored as an off-the-shelf product with the potential to circumvent many of the limitations of viable cells for therapeutic applications in regenerative medicine. In vitro, exosomes from preadipocytes stimulate cell proliferation in a wound-healing model. In vivo, adipose-graft–derived exosomes have been shown to be a promising tool for skin repair and remodeling.

ZenBio
For info: 919-547-0692
www.zen-bio.com/products/cells/human-exosomes.php

Electronically submit your new product description or product literature information! Go to www.sciencemag.org/about/new-products-section for more information.

Newly offered instrumentation, apparatus, and laboratory materials of interest to researchers in all disciplines in academic, industrial, and governmental organizations are featured in this space. Emphasis is given to purpose, chief characteristics, and availability of products and materials. Endorsement by *Science* or AAAS of any products or materials mentioned is not implied. Additional information may be obtained from the manufacturer or supplier.

SCIENCE CAREERS ADVERTISING

For full advertising details, go to ScienceCareers.org and click For Employers, or call one of our representatives.

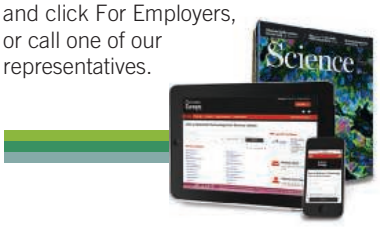

AMERICAS

+1 202 326-6577
+1 202 326-6578
advertise@sciencecareers.org

EUROPE, INDIA, AUSTRALIA, NEW ZEALAND, REST OF WORLD

+44 (0) 1223 326527
advertise@sciencecareers.org

CHINA, KOREA, SINGAPORE, TAIWAN, THAILAND

+86 131 4114 0012
advertise@sciencecareers.org

JAPAN

+81 3-6459-4174
advertise@sciencecareers.org

CUSTOMER SERVICE

AMERICAS

+1 202 326-6577

REST OF WORLD

+44 (0) 1223 326528

advertise@sciencecareers.org

All ads submitted for publication must comply with applicable U.S. and non-U.S. laws. *Science* reserves the right to refuse any advertisement at its sole discretion for any reason, including without limitation for offensive language or inappropriate content, and all advertising is subject to publisher approval. *Science* encourages our readers to alert us to any ads that they feel may be discriminatory or offensive.

ScienceCareers
FROM THE JOURNAL SCIENCE AAAS

ScienceCareers.org

Advance your career with expert advice from *Science* Careers.

Download Free Career Advice Booklets!

ScienceCareers.org/booklets

Featured Topics:

- Networking
- Industry or Academia
- Job Searching
- Non-Bench Careers
- And More

ScienceCareers
FROM THE JOURNAL SCIENCE AAAS

POSITIONS OPEN

Faculty Position in Medicinal Chemistry at The University of Kansas

We seek to fill a tenure track faculty position at the Assistant Professor level to commence by August 2019. Consideration will be given to applicants experienced in medicinal chemistry, chemical biology, natural products chemistry, organic chemistry, biochemistry or a closely related field. See detailed position description and application instructions at website: **https://employment.ku.edu/faculty/13139BR**. Application review begins December 5, 2018 and will continue as needed to fill the position. *KU is an Equal Opportunity/Affirmative Action Employer, full policy http://policy.ku.edu/IOA/nondiscrimination.*

ScienceCareers
FROM THE JOURNAL SCIENCE AAAS

Follow us for jobs, career advice and more!

@ScienceCareers

/ScienceCareers

Science Careers

ScienceCareers.org

Post Your Jobs

- **1,877,103** unique job seekers
- **250,657** job applications in 2016

ScienceCareers

Laureates of the 2017 Scientific Prizes

SCIENCE@WORK

The Fondation Bettencourt Schueller:
Helping scientists spread their wings

The Fondation Bettencourt Schueller is a French philanthropic organization founded in 1987 by Liliane Bettencourt, her husband, André Bettencourt, and her daughter, Françoise Bettencourt Meyers. The mission of the foundation is to support excellence and innovation in biomedical research and the arts, and to promote an inclusive society, all encapsulated in their motto, "Give talent wings."

Hugues de Thé

"You have to understand that this is a family foundation," says Hugues de Thé, president of the foundation's scientific advisory board and professor of oncology at the Collège de France in Paris. "And for the past 30 years the family has infused the foundation with its values." The foundation esteems "passion and a vision of disruptive and risky projects, creativity, liberty and innovation through hard work, and internationally competitive excellence," says de Thé.

To achieve its mission, the foundation awards prizes and grants to individuals who embody these values. Applications and nominations for life sciences prizes and other funding requests are stringently evaluated by an advisory board of 13 accomplished scientists, and by external review. A team of 20 foundation members works closely with the advisory board to identify important fields of endeavor in need of funding, and supports awardees and project developers, providing resources such as advice on business models, governance choices and best practices, networking opportunities, and technical support.

Funding the future

The foundation is best known in the scientific community for the annual Liliane Bettencourt Prize for Life Sciences, a prestigious award whose recipients include May-Britt Moser and Edvard I. Moser in 2006, winners of the 2014 Nobel Prize in Physiology or Medicine, and Benjamin Lehner in 2016, winner of the 2016 European Molecular Biology Organization (EMBO) Gold Medal. This € 300,000 (USD 350,000) prize is awarded to a researcher aged 45 years or younger; in odd-numbered years, the winner is chosen from researchers who are based in France, and in even-numbered years from those in Europe outside France.

The foundation awards three other life sciences prizes: (1) The Bettencourt Prize Coups d'élan pour la recherche française, which aims to improve infrastructure and working conditions for biomedical researchers by funding renovation, reorganization, acquisition of equipment and materials, and operational assistance. This € 250,000 (USD 290,000) prize is awarded annually to four research teams at the French National Institute of Health and Medical Research (Inserm) or at the Institute of Biological Sciences (INSB) of the National Center for Scientific Research (CNRS) in France; (2) The Young Researchers Bettencourt Prize, a € 25,000 (USD 29,000) prize awarded annually to 14 top early-career French Ph.D.s or M.D./Ph.D.s to enable them to do a postdoctoral internship abroad; and (3) The ATIP-Avenir grant, a € 300,000 (USD 350,000) award in partnership with Inserm and CNRS, given to researchers with outstanding projects who wish to create their own team and return or move to France.

PHOTOS: (TOP) © S. LOUBATON/CAPA PICTURES POUR LA FONDATION BETTENCOURT SCHUELLER; (BOTTOM) © G. BASSIGNAC/CAPA PICTURES POUR LA FONDATION BETTENCOURT SCHUELLER

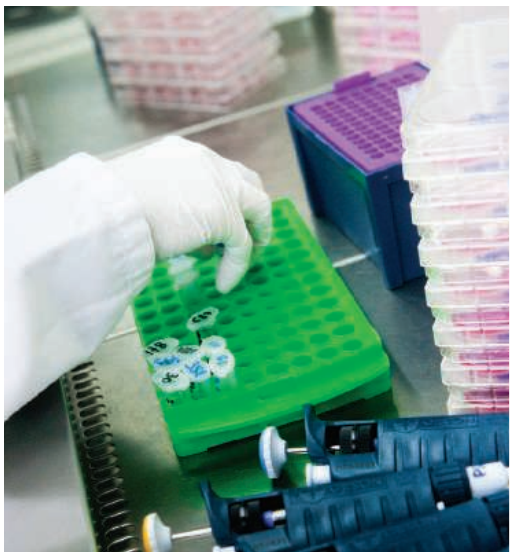

Edith Heard

Cédric Blanpain

In addition to these prizes, the foundation evaluates a continuous stream of requests and makes numerous grants in support of life sciences research. One example is an M.D./Ph.D. program established in France 15 years ago by the foundation in partnership with Inserm; this year, the program will include funding to allow assistant professors in medicine with a Ph.D. to have some protected time for research, away from hospital duties. Other examples include helping establish the Imagine Institute, the Brain and Spine Institute (ICM), and the Center for Interdisciplinary Research (CRI) in France; funding a system to digitize lectures at the Collège de France and make the videos publicly available; and promoting science education for high school students and the general public.

"The foundation listens to what are the emerging themes and areas that should be better explored, and that is very special—to have a foundation that is right there with the scientists, putting their finger on the pulse of what's important to do," says Edith Heard, professor at the Collège de France and unit director at the Institut Curie, in Paris; future director general of the European Molecular Biology Laboratory (EMBL) starting in January 2019; and member of the foundation's scientific advisory board. "They are unique because they have flexibility in terms of funding that one doesn't find elsewhere. The foundation is extremely professional in the way they do this and yet you feel part of a family, that you can connect with them."

As part of its humanitarian mission to promote an inclusive society, the foundation funds innovators who are working to create opportunities for people with disabilities, such as autism and hearing loss, or who are homeless or mentally ill. In 2016, the foundation established the Fondation Pour l'Audition, which supports research, treatment, and prevention of hearing loss with the goal of giving people with hearing issues equal access to educational, professional, and social opportunities. "They really care about helping society," says Heard. "That is something that comes across quite strongly in all of the actions I see coming out of the foundation."

Making a difference one researcher at a time

An awardee who represents the creativity and leadership valued by the foundation is Cédric Blanpain, professor at the Université Libre de Bruxelles, Belgium, and WELBIO (Walloon Excellence in Lifesciences and Biotechnology) investigator. Blanpain was the 2012 recipient of the Liliane Bettencourt Prize for Life Sciences for his discoveries in stem cell and cancer cell biology, which were made using novel methods developed by his lab. On the impact of winning the prize on his research, Blanpain says, "Of course I was very happy to get this award. It increases your visibility and helps you recruit better employees."

Blanpain's group discovered that killing a minor population of cancer stem cells via lineage ablation can lead to tumor regression. Describing this technique, he says, "The way we use lineage ablation—there are many different ways—is to express the receptor of an important toxin in the cancer stem cell population. If you don't express its receptor, the toxin is inert. But when the receptor is present and we inject the toxin, we wipe out the population of cancer stem cells carrying the receptor, and the tumor shrinks." His group also identified a population of tumor stem cells, with characteristics of both mesenchymal and epithelial cells, that can give rise to metastasis.

In describing his research approach, Blanpain says, "My scientific background has been influenced by my medical background, so much of my research has some kind of health-related objective. What I try to do in my lab is to use model systems to observe new paradigms in cancer cell and stem cell biology. We then use all the possible technologies offered to us—transcriptome assays, chromatin epigenetic characterization, and others—to understand the underlying molecular mechanisms. Finally, we attempt to apply what we have learned from this basic model to improving human health and adding to medical knowledge."

Awards are long-term investments for the foundation. "I know that former awardees may ask for additional support if they have new original and breakthrough projects" says Blanpain.

Heard echoes this sentiment. "They take great care of the people they connect with," she says. "Overall, it is a very interesting model for how to keep investing in the most promising research, and to get a feeling of what is needed in specific areas. It's also an example of how a foundation can really help science work, and hopefully it will lead to others adopting the model."

The Yangtze River Delta:

Growing and Prospering by Relying on Integration and Talent

The Yangtze River Delta has boasted the densest population, the most developed economy, the most thriving culture, and the highest living standard in China since ancient times. Because of its exceptionally advantageous location and abundant natural resources, the area has formed two strategic hubs that link it to oceans and connect it with inland areas.

The total economic aggregate of the delta's three provinces (Jiangsu, Zhejiang, and Anhui) and one municipality (Shanghai) reached RMB 1.95 billion (equivalent to USD 295 million as per the exchange rate at the end of 2017) for 2017, accounting for 23.6% of China's aggregate. The economic aggregate of the Yangtze River Delta Urban Agglomeration (YRDUA), which includes 26 cities, reached RMB 1.65 billion (USD 257 million) for 2017, ranking it as the fifth of the top six urban agglomerations worldwide. The per capita gross domestic product (GDP) of the area for 2017 reached RMB 87,400 (USD 13,600), equaling the primary level of developed countries. The per capita GDP of Shanghai, Jiangsu, and Zhejiang for 2017 reached RMB 124,600, RMB 107,200 and RMB 92,100 (USD 19,390, USD 16,680, and USD 14,330) respectively, nearly reaching the median level of developed countries as per the USD averages.

From the perspective of both economic aggregate and per-capita GDP, the YRDUA has ranked as an urban agglomeration with one of the largest economic aggregates and the highest economic vitality worldwide—and it is expected that these conditions will continue to improve.

Yangtze's Plan to Integrate and Develop

The three-year action plan for the integrative development of the Yangtze River Delta was published in 2018, further focusing on key areas such as traffic interconnection, mutual aid and protection for energy development, collaborative innovation in industries, the building of high-speed information highways, joint disaster prevention and environmental control, extensive and convenient public services, and the orderly opening of commercial markets. The plan's objectives are to establish the framework for a world-class urban agglomeration; build a primary facility system with relevant hubs, functions, and networks; and lay the foundation for innovation-driven systems for regional industry and collaborative development by 2020. When these goals are fully realized, the area will become a major conduit for bringing global resources to the Asia-Pacific region as well as a world-class urban center with global influence.

The high-quality integration of the Yangtze River Delta will no doubt reshape the layout of China's economic geography—and possibly that of the world.

The delta has already seen unprecedented changes even in the early stages of integration. First of all, in terms of adjusting administrative structures, the YRDUA has been guiding each city involved in forming its own unique functions by directing them to eliminate existing bureaucratic configurations. Secondly, the area has implemented

Shixin Wang
Deputy Chief Editor of China Education Online, Chief Executive Editor of AcaBridge

flexible coordination mechanisms at higher levels, established cost-sharing initiatives in specific project operations, and driven cooperation between different regions via "win-win" measures instead of administrative directives. More importantly, when high-speed growth was pursued, the delta used to focus on energy issues and traditional production factors such as labor force allocation; but it is now focused on stimulating innovation, fostering cooperation between science and technology industries and talent, and creating new industry highlands in order to play a more important role in reshaping the global economy.

In addition, the YRDUA is ensuring that required resources are in place to increase connectivity within the delta and to build coordinated development demonstration areas. The establishment of regional intercity railway network planning for co-construction of infrastructures; the creation of a world-class urban agglomeration with the fastest network connection speed through the installation of 5G networks; and the co-construction of the G60 Science & Technology Innovation Valley will be important approaches to securing high-quality integration in the region.

Seeking Talent to Finish the Picture

This "grand scroll" painting of Yangtze River Delta construction is being completed gradually, waiting for more skilled painters to add their master strokes.

Numerous high-level experts will act as these painters—and they will have a rich and varied "canvas" on which to work. Due to historic reasons and their differing levels of development, the delta's administrative divisions have diverse features: Shanghai boasts a highly advanced and innovative science and technology market and a strong educational system; Jiangsu has a solid economic foundation and a powerful manufacturing base; Zhejiang is famous for its wonderful market vitality and creative business models; and Anhui is eager to embrace new technology. However, all these areas have something in common: They are all in urgent need of high-level talent. Even though the Yangtze River Delta holds one of the largest concentrations of intellectual capital in China, the concerns of its administrative divisions about bringing in more talent are still quite obvious.

In regards to talent acquisition, the methods of Hangzhou and Ningbo, two Zhejiang-based cities famous for commerce, are a good example of the intense level of activity that is taking place.

As two subprovincial cities in Zhejiang, Hangzhou and Ningbo are recognized for their rapid and steady economic growth. In 2017, the GDP of these two cities reached RMB 1.13 trillion (USD 175.83 billion) and RMB 984.69 billion (USD 153.23 billion), respectively, ranking first and second in the province.

Hangzhou: Becoming a Talent Paradise

Even though it is a city rich in history and culture, and once named by Marco Polo as "a paradise on earth," Hangzhou hasn't been constrained by its traditions. On the contrary, like other Chinese cities, it has experienced its fastest economic growth in a decade. Its GDP has been No. 1 in all of Zhejiang for several years. As a city with an economic aggregate exceeding RMB 1.13 trillion, Hangzhou is one of the few Chinese cities maintaining an annual economic growth of more than 8%. As a result, the city has instituted more stringent requirements for acquiring talent and is now bringing in specialists from overseas. In recent years, it has introduced 29,000 high-level experts studying abroad and 15,000 foreign experts; foreigners have registered more than 4,980 new enterprises (acting as legal persons); and in 2017 the city's net inflow of both domestic and international talent ranked first place nationwide.

In February 2018, Hangzhou issued opinions on how to accelerate the internationalization of local talent as well as policies for acquiring overseas talent, such as providing a maximum of RMB 100 million (USD 143,500) as subsidies for foreign talent who start their business in the city, further intensifying the process. It's worth noting that Hangzhou has realized the importance of universities and research institutes for attracting top talent. Besides universities like Zhejiang University, which consolidated its strength after merging with other institutions in 1998 and became one of China's top schools, and Westlake University, which aroused fierce debates after its establishment and hopes to become a pioneer in China's higher education system, Hangzhou plans to set up more influential universities and scientific research institutes at home and abroad.

Ningbo: On the Fast Track for Talent

In terms of introducing universities, Ningbo shares Hangzhou's enthusiasm. It is expected that at least five universities will settle in Ningbo, including distinguished schools such as Zhejiang University, Beihang University, and the University of the Chinese Academy of Sciences (UCAS). The introduction of prestigious universities will not only bring concrete economic benefits to Ningbo but also expand its channels for introducing talent.

As Zhejiang's second-largest city, Ningbo is facing increasingly fierce regional competitions for talent. In the hope of being one of the top talent reservoirs among China's first-tier large cities, Ningbo issued four comprehensive talent policies within 10 months in 2017. In December 2017, it issued an announcement on using private capital to introduce high-end entrepreneurship teams, which it rated as the "most significant and striking" talent policy implemented by the city. It later announced the introduction of urgently needed high-level talent on the first work day of 2018, and subsequently issued the details about requirements for residence migration in order to attract talent and entrepreneurship teams, which included lowering the threshold for settling in Ningbo and providing grants for projects, allowances for purchasing houses, and subsidies for settling down. In September 2018, the city published what it calls the "1+X" measures for developing a "talent ecosystem," which would involve gathering top talent from expanding industries and forming a structure for "introducing, training, utilizing and retaining" them, while providing them with more support and more thorough guidance.

With an improved integration process, the Yangtze River Delta's economic dreams will definitely become a reality, as long the acquisition of talent keeps pace with urban development.

We welcome domestic and foreign scholars to contact us. We will provide you with free, one-on-one personal service, inform you about Yangtze River Delta region colleges and universities, and help you to learn about and apply for talent recruitment projects in this region. For assistance, please contact the personnel consultant at consultant@acabridge.edu.cn. For more details, please visit our website at www.edu.cn/jjcsj.

SEU, Shaping China's Research and Innovation Landscape

"What the Great Learning teaches, is to illustrate illustrious virtue, to renovate the people, and to rest in the highest excellence."

Located in the historically and culturally significant city of Nanjing, Southeast University (SEU) is one of the oldest institutions of higher learning in China. Its constant pursuit of the highest excellence has won it the accolades of "a sacred place of learning". Liuchao Juniper, the sacred and iconic tree on the flagship campus, weathered for over 1500 years, is a witness to its unremitting effort for perfection in the past 116 years.

The history of Southeast University can be traced back to 1902, when it was founded as Sanjiang Normal School. After that, it evolved successively into Liangjiang Normal School, Nanjing Higher Normal School, National Southeast University and National Central University, until it was renamed Southeast University in 1988. The motto -- striving for perfection--is interpreted as "self-perfection, care, perfection, preeminence". Upholding the motto, Southeast University has made substantial progress over the years, which fully embodies its pursuit of the highest excellence.

SEU is the place where the Science Society of China was established, thus the "birthplace of China's natural sciences". And it is at Mei'an-- the northwest corner of the campus-- that Xueheng Intellectual Group was founded, which was a milestone in the continuation of the Chinese traditional culture. SEU was the first co-educational university in China and the earliest adopter of the credit-based education system. It attracted a galaxy of elite returned scholars from overseas. Its tradition of excellence and pioneering work continue to echo down the decades.

As China's leading research-oriented university, SEU has developed China's first robot and is the first Chinese university that has set up robotics undergraduate program and molecular bioelectronics laboratory. She is the cradle of China's modern architecture, and the most important information science and industrial innovation powerhouse. She started China's art education, and has since occupied a dominant position in the research of art theory.

SEU is one of the only three universities in China that have persisted on undertaking Special Class for the Gifted Young, and one of the pilot universities with a series of reforms in the training mode aimed at developing top and innovative talents. It has fostered over 200 academicians of the Chinese Academy of Sciences and Chinese Academy of Engineering and nurtured over 330,000 outstanding graduates.

SEU was one of the few key universities that have been supported by the Chinese government's "211 Project", "985 Project" and now is one of the "Double First-class Initiative" universities, with 11 disciplines selected, ranking 8th among all Chinese universities. SEU offers 76 undergraduate programs and 33 first-level Ph.D. programs. Five disciplines, namely architecture, civil engineering, and transportation engineering, biomedical engineering, art theory rank No.1 in China; 11 disciplines including engineering, computer science, material science, mathematics, physics, chemistry, clinical medicine, biology and biochemistry, pharmacology and toxicology, neuroscience, behavioral sciences, social sciences are among ESI world top 1%, where engineering and computer science are among the top one thousandth.

SEU values the coordinated, integrated development of engineering, science, liberal arts and medical science. Powered by its 3 key state laboratories, 3 national engineering research centers, 2 national engineering technology research centers and other leading research platforms, SEU pushes for the world's scientific and technological frontiers and sticks to major national demands, committed to major strategic high-tech research, fundamental and applied basic research and cross-disciplinary integration. SEU continues to make the breakthroughs in the emerging, cutting-edge and interdisciplinary fields such as quantum information, artificial intelligence, cyber security, intelligent manufacturing, smart city, intelligent transportation, brain science and biomedical big data. SEU has been involved in and made major contributions to the projects such as Three Gorges Project of Yangtze River, Five-hundred-meter Aperture Spherical Radio Telescope construction, 5G mobile communication technology development, Antarctic scientific investigation, Manned Space Project, High-speed Railway network, Hong Kong-Zhuhai-Macao Bridge in China.

Boasting internationalization, SEU is a university of significant global impact. Scholars from all over the world come here to engage in teaching, research and exchange programs. Top students from all countries are attracted to the university in pursuit of their dreams.

Passing on the century-old tradition, integrating into the world development, SEU established AMS (Alpha Magnetic Spectrometer) Experimental Center jointly with Nobel laureate Prof. Samul Ting and SEU Shing-Tung Yau Center with Prof. Shing-Tung Yau, and set up Architecture Internationalization Demonstration School. SEU also initiated and established the UK-China University Consortium on Engineering Education and Research (UKCCEER), aiming to promote and facilitate strategic engagement and bilateral cooperation in transnational joint programs on postgraduate higher education and engineering research between the UK Partners and the China Partners, in the areas of energy and intelligent manufacturing in support of both countries' manufacturing ambitions. SEU has also engaged in cooperation and exchange programs with more than 150 overseas universities and research institutions.

"Strive for Perfection" is our century-old motto and value. "Becoming a world-renowned university for the sciences and dedicating itself to the country with talents" is our school-running philosophy. Attracting and gathering the best teachers, cultivating the leading talents with a strong sense of national pride and global vision for the future and the benefit of mankind, innovating the best scientific and technological achievements, contributing wisdom and strength to the social development and human progress are not only SEU's spirit and soul, but also our timeless creed and pursuit.

Opportunities to shine at ShanghaiTech University

ShanghaiTech University is a young and dynamic higher education institution aiming for high-quality research and global influence. To address challenges faced by China and the world, it seeks innovative solutions in energy, materials, environment, human health, data science, artificial intelligence (AI), and electrical engineering. An integral part of the Zhangjiang Comprehensive National Science Center, the university is now leading several frontier research projects at large-scale facilities. For more information, please visit: www.shanghaitech.edu.cn.

We are now seeking talented researchers for multiple faculty positions at all ranks in the following fields:

School of Physical Science and Technology: energy, system materials, photon and condensed state, material biology, environmental science and engineering

School of Life Science and Technology: molecular and cell biology, structural biology, neuroscience, immunology, stem cells and regenerative medicine, system biology and biological data, molecular imaging, biomedical engineering

School of Information Science and Technology: computer science, electrical engineering, information engineering, artificial intelligence, network and communication, virtual reality, statistics, big data and data mining

School of Entrepreneurship and Management: economics, finance, accounting, management, marketing, strategy and entrepreneurship

School of Creativity and Art: film production, life drawing, photography, VR and game coding, illustration & visualization, performing arts

Shanghai Institute for Advanced Immunochemical Studies: antibody therapy, Immunotherapy, cell therapy, regeneration medicine

iHuman Institute: bio-imaging, biology, chemistry, computational biology, AI/ML

Institute of Mathematical Sciences: pure mathematics, theory of computing, applied mathematics

Successful applicants will have a doctoral degree, and are expected to establish a record for independent, internationally recognized research, supervise students and teach high-quality courses.

ShanghaiTech University will offer attractive compensation packages, including:

Initial research support package: reasonable start-up funds, research associates and post-doctoral fellows, laboratory space to meet research needs

Compensation and benefits: highly competitive salary commensurate with experience and academic accomplishments, a comprehensive benefit package Subsidized housing: on-campus, 80/100/120 m^2 faculty apartments available at low rent for tenure and tenure-track faculty

Relocation & travel allowance: reimbursement of expenses for household relocation and family's one-way travel

Family assistance: support with children's education; affiliated kindergarten, primary and middle schools are under construction

To apply: using this format, please submit a cover letter (Firstname_Lastname_Cover_Letter.pdf), a research plan (Firstname_Lastname_Research_Plan.pdf), and a CV (Firstname_Lastname_CV.pdf) to shanghaitechuniversity@gmail.com.

Shanghai University of Engineering Science Talents Recruitment 2018

I. About the University

Shanghai University of Engineering Science (SUES) is a full-time regular institution of higher education with cross-disciplinary and coordinated study in Engineering Science, Economic Administration, and Art & Design. Located in the college town of Songjiang, Shanghai, the 250-acre university offers undergraduate programs in 75 academic and professional majors, postgraduate programs in 4 first-tier and 22 second-tier disciplines, as well as 3 professional degree programs, meanwhile, an international cultivation base is authorized to confer doctoral diplomas. Some 20,000 students take fulltime courses at the university (nearly 2,500 of them postgraduates), and 1,200 staff contribute to the teaching profession.

As one of the pilot programs of the training of outstanding engineers, which are directed by the Ministry Of Education of People's Republic of China, disciplines and majors in Shanghai University of Engineering Science keep close to the modern industries in Shanghai, and have exhibited highly characteristic features.

With its continuing expansion in cooperation and exchange with international institutions, SUES has so far conducted cooperation and exchange on an extensive scale with several dozen universities in countries such as America, Britain, and France.

SUES now sincerely welcomes overseas talents who are interested in higher education to join us.

II. Job Profile:

1) Crew members for talents programs in Shanghai University of Engineering Science: Zhihong Scholars, Tengfei Program, Zhanchi Program.
2) Teaching and researching faculty
3) Outstanding fresh graduates with a doctorate.

III. Application Channels

(Either works)

1) You can submit your application online through our Talents Recruitment System (http://zhaopin.sues.edu.cn).
2) Send your application materials and job objectives to us at jsk@sues.edu.cn.

IV. Contact Information

Address: 333 Longteng Road, Songjiang District, Shanghai
Contact Person: Ms. Miao, Ms. Zhu
Numbers: (+86) 021-67791252

V. Disciplines **(Including but not limited to)**

Science, Economics (Economics and Trade, Finance, etc.), Management Science (Business Administration, Management Science and Engineering, Logistics Management and Engineering, Industry Engineering, Tourism Administration, Public Administration, etc.), Literature (Journalism and Communication, Foreign Languages and Literatures, etc.), Art (Art, Design, etc.), Engineering (Mechanical Engineering, Power and Energy, Control Science and Engineering, Mechanical Engineering, Computer Sciences, Automation, Electrical/Electronic Engineering, Materials Science, Chemical and Pharmaceutical Engineering, Environmental Science and Engineering, Traffic and Transportation, Vehicle Engineering, Textile Engineering, Fashion Design and Engineering, Aeronautical Engineering, etc.)

Disciplines related to Mechanical Engineering are mainly recruited for the School of Automotive Engineering. The school now has 6 undergraduate departments, 1 first-tier postgraduate program in Mechanical Engineering, and 5 second-tier postgraduate programs. The teaching staff is rationally coordinated in age, knowledge, and disciplines. All members prove academic competence, 20 of them professors, 50 associate professors, 3 doctoral students' supervisors, and 99 lecturers with doctoral diplomas.

Over the past 3 years, the school has undertaken 163 scientific research projects, 30 of which are at the national level, 10 at the provincial level, 114 are industry-based. At present, 17 laboratories such as the Associate Center of Modern Equipment and Its Control Technologies have been established, covering an area of 3 acres, and many internship programs have been developed with more than 100 institutions. The school also lays emphasis on its openness to the outside world. A close relationship with 7 scientific research institutes such as University of Pennsylvania has been built, and in 2017, the school and University of Pennsylvania have reached an agreement on a "2+2" joint education program.

For actively promoting the construction plan of its first-class discipline of Mechanical Engineering, School of Automotive Engineering is now recruiting talents from all over the world.

JXUST First International Young Scholars' Forum 2018

Jiangxi University of Science and Technology (JXUST) Ganzhou, China

I. Profile of JXUST

Founded in 1958, Jiangxi University of Science and Technology (hereinafter shorted as JXUST) is jointly-sponsored by the Ministry of Education, the Ministry of Industry and Information Technology and Jiangxi Provincial Government. As one of the top-ranking universities in Jiangxi Province, JXUST offers a full range of undergraduate majors, plus master's and Ph.D. programs. It serves as an important base for the education and research of non-ferrous metallurgy industry in China. With an outstanding faculty trained globally, it is making great strides toward its goal of building a nationally first-class institution of higher education and cutting-edge research with broad societal impacts.

II. A quick introduction of the forum

For the first time in its history, JXUST will host a program for younger scholars, defined as those scholars with no more than ten years of tenure-track faculty experience. This includes graduate students as well as post-doctoral fellows, lecturers and visiting affiliates who have yet to secure a continuing faculty appointment.

In addition to serving as a platform for discussion and thought, the forum is designed to promote collaborative intellectual and research activity among researchers from different institutions and from a range of disciplines in science and engineering. This forum will offer young scholars the opportunity to present their work to their peers and to distinguished scholars from around the world.

III. Academic Disciplines

Academic disciplines involved in this Forum are as follows: Mining Engineering, Metallurgical Engineering, Material Science and Engineering, Chemical Engineering, Environmental Engineering, Civil Engineering, Mechanical Engineering, Electrical Engineering, Control Engineering, Information Technology, Computer Science and Engineering, Intelligent Manufacturing. New Material, New Energy, Economics, Management, Finance, Mathematics, Physic, Chemistry etc.

IV. Qualifications for applicants

Applicants for this forum, who shall be under the age of 40, are expected to have the wish of joining the faculty of JXUST.

In addition to having 2 years or more of post-doctoral research or work experience, applicants, who are expected to have a PhD degree in a relevant science and engineering field, must obey Chinese laws and have a proven track record of high-quality peer-reviewed academic publications. They are also encouraged to apply for the four national talents programs ("1000 Talents Program for Young Professionals", "Young Top Talents of the National High-Level Talents Support Plan", "Young Chang Jiang Scholars Program" and "The National Science Fund for Distinguished Young Scholars"), sponsored by the Central Government of China through JXUST.

V.Expenses Refund

The board and lodging expenses of the participants during the forum will be covered by the host. In addition, JXUST will finance participants' travel subsidies, including round-trip international airfare (Economy class seat), and transportation expenses within Chinese territory.

The travel subsidy shall be no higher than RMB 15,000 per person for scholars from European and American area, no higher than RMB 7,000 per person for scholars from Asian-Pacific region and no higher than RMB 5,000 per person for scholars from China (including Hongkong, Macaw and Taiwan). In addition, JXUST will arrange free pick-up services in Ganzhou airport and railway station during the forum.

VI. Schedule Timeline

1. Application Deadline: Dec. 10th, 2018.
2. Invitation Period: Sep. 25th – Dec. 10th, 2018.
3. Registration Date: Dec. 26th, 2018.
4. Forum duration: Dec. 27th- 28th, 2018.

Forum venue and airport (railway station) pick-up arrangement will be specified in the invitation letter.

VII. Salaries & Benefits

JXUST invites applications for tenure-track or tenured faculty positions at all ranks in all major science and engineering disciplines. Candidates with research interests in all related areas are encouraged to apply. There are extraordinary opportunities to develop major research and education programs with collaborations with other academic/industrial organizations nationwide and worldwide.

JXUST, in line with nationally first-class research universities, provides globally competitive compensation and benefit packages to the elite professionals.

1.Successful applicants of the four above-mentioned national talents programs

Candidates will be appointed to the faculty of JXUST at a level commensurate with each applicant's background and experience. JXUST offers a generous salary and startup package, including:

(1) Position & Salary: the successful candidate will be appointed as Chair Professor, with an annual salary of RMB 600,000 to 800,000 Yuan.

(2) Research Funding: a start-up fund of no less than RMB 3 million for science and engineering disciplines, and RMB 0.5 million for disciplines of humanities and social sciences (national and provincial level research funding excluded); platform construction funding will be considered by evaluation on actual conditions and needs.

(3) Housing Subsidy: an on-campus transitional housing with an area of approximate 100m2 and a housing subsidy of RMB 1.5 million (governmental award or subsidy excluded) provided in the period of employment.

(4) Living subsidy for accompanying spouse: a job offer to the candidate's spouse based on his/her qualifications, or a monthly allowance of RMB 2,000 for a duration of 6 years.

(5) Children's school admittance: the children of successful applicants are entitled to choose quality primary and secondary schools in line with local policies.

(6) Other supporting benefits: In addition to sound scientific research conditions, JXUST will provide research assistants on the basis of the actual needs.

2. Overseas-educated PhD degree holders

For excellent PhDs with at least two-year overseas education background or with doctorate degree of prestigious overseas universities, the benefit packages include:

1)Successful candidate will be appointed as associate professor and is entitled to corresponding salary and benefits, or appointed in accordance with tenure track system (no less than RMB 250,000 per year);

2)a living allowance no less than RMB 250,000, and an on-campus transitional housing or a housing subsidy of no less than RMB 150,000 provided;

3)a start-up research funding of RMB 200,000 for scholars of science and engineering disciplines and RMB 100,000 for scholars of humanities and social sciences;

4)a Spouse's allowance of RMB 100,000 or a job offer based on a spouse's qualifications;

5)assistance in children's school enrolment; above benefits are negotiable for very outstanding applicants.

Above benefits are negotiable based on the qualifications of applicants. JXUST is committed to offer selected applicants with competitive salaries and benefits no lower than the standard of its kind in Jiangxi Province.

VIII. Application Procedures

Fill in the Application Form online (Website: http://zpjob.acabridge.cn/frm/forum/join?f_id=17), or download the Application Form, fill in and send it to below E-mail address.

IX. Contact Information

Contacts: Li Bing, Zha Yuxin
Tel: 0086-797-8312591
Mobile: 0086-15297767555, 0086-19979706787
Email: jxlgrczp@163.com, justrsc@vip.163.com

THE UNIVERSITY OF TEXAS
MD Anderson Cancer Center
Making Cancer History®

OPEN RANK, TERM TENURE-TRACK / TERM TENURE

DEPARTMENT OF ENDOCRINE NEOPLASIA AND HORMONAL DISORDERS

The Department of Endocrine Neoplasia and Hormonal Disorders at The University of Texas MD Anderson Cancer Center seeks an individual of outstanding research capability in basic or translational sciences related to malignancies of the endocrine system, or more general endocrine disorders in the context of cancer. He/she will coordinate with existing departmental faculty research programs, with particular emphasis on endocrine malignancies (particularly thyroid and adrenal) and bone, reproductive, and metabolic abnormalities in cancer. The successful applicant will be expected to establish a competitively funded research program. Graduate teaching opportunities are available, a strong commitment to mentoring is encouraged, and performance of departmental and institutional service is expected. Applicants must be committed to working in a highly collaborative, multidisciplinary environment. Generous start-up packages are available for up to five years.

MD Anderson, ranked the #1 cancer center by *U.S. News & World Report,* is the world's largest treatment facility for oncologic diseases. Located within the Texas Medical Center campus in Houston, our location provides access to a world-renowned medical community and the splendid cultural and recreational diversity of a sophisticated, metropolitan area that is the country's fourth largest city.

Qualifications include a Ph.D. or equivalent degree in a relevant basic science field. Post-doctoral experience is a must, and evidence of research excellence and extramural funding is expected appropriate to rank.

Interested applicants should send letter of intent, curriculum vitae, contact information for three letters of reference, and research plan to:

Marie-Claude Hofmann, Ph.D. Professor
The University of Texas MD Anderson Cancer Center
Unit 1461, PO Box 301402, Houston, Texas 77230-3722
Email: mhofmann@mdanderson.org

MD Anderson Cancer Center is an equal opportunity employer and does not discriminate on the basis of race, color, religion, age, national origin, sex, sexual orientation, gender identity/expression, disability, veteran status, genetic information, or any other basis protected by federal, state, or local laws, unless such distinction is required by law. All positions at The University of Texas MD Anderson Cancer Center are security sensitive and subject to examination of criminal history record information. Smoke-free and drug-free environment.

UCONN HEALTH

DEPARTMENT OF IMMUNOLOGY
UNIVERSITY OF CONNECTICUT SCHOOL OF MEDICINE

The Department of Immunology at the University of Connecticut, School of Medicine, seeks an outstanding investigator for a tenure-track position at the Assistant or Associate Professor rank to establish an extramurally funded laboratory. We are searching for faculty candidates in all areas of Immunology including cellular and molecular immunology in various fields of infectious and inflammatory diseases, cancer, autoimmunity, vaccines, metabolism and others. Prospective candidates should bring innovative ideas and cutting edge technology to an already vibrant immunology community consisting of expertise in both adaptive and innate immunity. The ideal candidate will participate in graduate student training, and have access to a growing translational research community and an expanding scientific environment in the capital region. Salary and start-up funds are highly competitive and outstanding core facilities are available. Applicants must have a Ph.D. and/or M.D. with several years of postdoctoral training and a high impact publication record. For Associate Professor level, a history of extramural funding is expected. In addition to the beauty of the picturesque New England countryside, the Hartford area offers a lively art and cultural scene and an exceptional outdoor sports environment.

In a single PDF file please submit a curriculum vitae, maximum two-page summary of research accomplishments and interests, and the names and contact information of three references through the UConn Health Employment Services website, **https://jobs.uchc.edu**. Search no. 2019-260. Please address questions to the search committee chair, c/o Ms. Kimberly Young (Email: **immunology@uchc.edu**). For further information on UCH, please visit **https://health.uconn.edu/immunology**. The deadline to submit applications is January 31, 2019.

UConn Health is an Affirmative Action and Equal Employment Opportunity employer, who encourages Males, Females, Veterans, Minorities and Persons with Disabilities to apply.

University of New Mexico Comprehensive Cancer Center

Join Our Leadership, Clinical, and Research Faculty Teams

The University of New Mexico Comprehensive Cancer Center (UNMCCC) is the Official Cancer Center of New Mexico and the only National Cancer Institute (NCI) designated comprehensive cancer center in a 500-mile radius. Our 134 oncology physicians, 122 cancer research scientists, and staff focus on discovering the causes and cures for cancers disproportionately affecting the people of the American Southwest — primarily Hispanic, American Indian, and Non-Hispanic White — with strikingly different patterns of cancer incidence, mortality and disparity. In the past year, our center cared for 12,000 patients; 12 percent participated in therapeutic interventional studies and 35 percent in interventional studies. UNMCCC has outstanding programs in Cancer Control and Cancer Health Disparities; Cancer Genetics, Epigenetics, and Genomics; Cancer Cell and Systems Biology; and Cancer Therapeutics. Our research houses national centers: The Molecular Discovery and High Throughput Target Screening Center (nmmlsc.health.unm.edu), one of six Chemical Biology Consortium Centers of Excellence in The NCI NExT Program; Spatiotemporal Modeling of Cell Signaling (stmc.unm.edu), one of 13 NIH National Centers for Systems Biology; and a NIH Clinical and Translational Sciences Center. We enrich our endeavors by collaborating with Sandia and Los Alamos National Labs and Lovelace Respiratory Research Institute. Benefit from our Shared Resources including biospecimen collection and tissue analysis, genomics, biostatistics, bioinformatics, population science and behavioral interventions, and the conduct of clinical interventions. UNMCCC is the center of our statewide cancer clinical trials and health delivery research network — partly funded by a NCI NCORP Grant — and is an Oncology Research Information Exchange Network (ORIENcancer.org) member. Our center has conducted 60+ statewide community-based cancer education, prevention, screening, and behavioral intervention studies involving more than 10,000 New Mexicans. Visit cancer.unm.edu.

Cancer Cell Signaling & Systems Biology
(Tumor Microenvironment)

Seeking cancer cell biology, signaling, and systems biology experts with interests in dissecting mechanisms of perturbed signaling in cancer cells, analysis and modeling of pathways mediating therapeutic response or resistance, and analysis of cellular and signaling interactions and the immune response in the tumor microenvironment. *Search chairs: Diane Lidke and Eric Prossnitz*

Target & Drug Discovery

Seeking scientists and physician scientists focused on discovery and development of cancer diagnostic, therapeutic, and imaging agents in a therapeutics pipeline using innovative flow cytometric and other high throughput functional screening methods and chemo-informatics platforms for drug discovery. *Search chairs: Larry Sklar and Alan Tomkinson*

Epigenetics & Functional Genomics

Seeking experts in fundamental mechanisms of chromatin regulation and epigenetics in cancer model systems and human tissues, with interests in defining epigenetic signatures in model systems and population cohorts in response to environmental carcinogens prevalent in the American Southwest. *Search chairs: Alan Tomkinson and Scott Ness*

Biostatisticians
Two Positions: Associate/Full Professor • Assistant Professor

Seeking PhD biostatisticians to join an outstanding team engaged in statistical methodology relevant to cancer and in biostatistical applications integrated with basic, translational, clinical, and population science research. *Search chairs: Linda Cook and Shane Pankratz*

Health Services & Behavioral Intervention
Two Positions: Associate, Full Professor • Assistant Professor

Seeking faculty with scholarly achievements in health services, cancer care delivery, or behavioral intervention research, with interest in the minority populations of the American Southwest. *Search chairs: Linda Cook and Larissa Myaskovsky*

Cancer Molecular & Genetic Epidemiology
Two Positions: Associate/Full Professor • Assistant Professor

Seeking scientists in cancer population and molecular genetic and/or epigenetic epidemiology, particularly as it is used to assess/impact cancer health disparities, gene-environment interactions, and genetic ancestry and genetic risk assessment in multi-ethnic populations. *Search chairs: Marianne Berwick and Linda Cook*

Cancer Autophagy

Seeking funded scientists studying the regulation and roles of autophagy related to cancer biology with an interest in basic and translational research. Looking for applicants researching the intersection of autophagy and cancer, in areas including microenvironmental and oxidative stress, tumor cell growth and aggressiveness, and mitochondrial function. *Search chairs: Eric Prossnitz and Vojo Deretic*

Cancer Immunology

Seeking established mid-career or senior scientists and physician-scientists studying cancer immunology and/or the tumor microenvironment. Looking for scientific accomplishments exemplified by peer-reviewed funding and collaborative research in cancer immunology, immunotherapy, and/or the tumor microenvironment. *Search chairs: Eric Prossnitz and Sarah Adams*

For details and to apply, visit cancer.unm.edu/JoinTheBest

Questions? Contact Search Coordinator Amanda Leigh at ALeigh@salud.unm.edu, (505) 272-2201.

UNM is an Equal Opportunity/Affirmative Action Employer and Educator

Endowed Chairs and Professorships, significant resources, leadership roles, and comprehensive start-up packages available.

Photo: Bill Tondreau, "River Edge", panoramic photographic, courtesy of sumnerdene.com

Smithsonian Institution

Research Zoologist
Department of Invertebrate Zoology
National Museum of Natural History
Smithsonian Institution

The Smithsonian's National Museum of Natural History seeks a zoologist to conduct an integrative, specimen- or collection-based research program in invertebrate evolution and biodiversity (exclusive of hexapods, myriapods, and arachnids). The successful candidate is expected to develop an internationally recognized research program that makes important contributions to understanding invertebrate evolution and biodiversity through synthetic research involving phylogenetics, genetics, anatomy, development, genomics, biogeography, conservation, informatics, or related fields. Frequent publication of highly regarded papers in competitive, peer-reviewed journals, curation of collections in specialty area, service to the scientific community in leadership capacities, acquisition of external funding, engagement in outreach activities, and mentorship of students are expected.

Full-time, permanent appointment with full Government benefits to be filled at the GS-12 level; US citizenship and a one-year probationary period are required. The museum's authorized salary range for this position at this time is $81,548 - $86,984 per year. College transcripts and proof of U.S. accreditation for foreign study must be submitted online by the closing date of announcement. **For complete requirements and application procedures go to www.sihr.si.edu or www.usajobs.gov and refer to Announcement 19A-JW-304220-DEU-NMNH.** The announcement opens November 7, 2018. **Applications and all supporting documentation must be received on-line by January 7, 2019 and must reference the announcement number.** All applicants will be notified by email when their application is received.

The Smithsonian Institution is an Equal Opportunity Employer.

Smithsonian Institution

Research Zoologist
Department of Vertebrate Zoology
National Museum of Natural History
Smithsonian Institution

The Smithsonian's National Museum of Natural History seeks a zoologist to conduct an integrative specimen- or other collection-based research program in vertebrate evolution and biodiversity, in the disciplines of herpetology, ichthyology, mammalogy, and/or ornithology, especially mammalogy. The successful candidate is expected to develop an internationally recognized research program that makes important contributions to understanding vertebrate evolution and biodiversity through integrative research involving phylogenetics, anatomy, development, genomics, biogeography, conservation, informatics, or related fields. Frequent publication of highly regarded papers in competitive, peer-reviewed journals, curation of collections in specialty area, service to the scientific community in leadership capacities, acquisition of external funding, engagement in outreach activities, and mentorship of students are expected.

Full-time, permanent appointment with full Government benefits to be filled at the GS-12 level; US citizenship and a one-year probationary period are required. The museum's authorized salary range for this position at this time is $81,548 - $86,984 per year. College transcripts and proof of U.S. accreditation for foreign study must be submitted online by the closing date of announcement or your application will be disqualified. **For complete requirements and application procedures go to www.sihr.si.edu or www.usajobs.gov and refer to Announcement 19A-JW-304235-DEU-NMNH.** The announcement opens November 1, 2018. **Applications and all supporting documentation must be received on-line by December 13, 2018 and must reference the announcement number.** All applicants will be notified by email when their application is received.

The Smithsonian Institution is an Equal Opportunity Employer.

IOWA STATE UNIVERSITY

Assistant Professor in Systems Biology

Department of Genetics, Development & Cell Biology

The Department of Genetics, Development and Cell Biology (GDCB) at Iowa State University (ISU) (**https://www.gdcb.iastate.edu**) invites applications for a **tenure-track assistant professor** position in **Systems Biology**.

GDCB seeks to hire a systems biologist who addresses fundamental questions at a cellular or molecular level, using a combination of experimental (e.g., genomics, transcriptomics, proteomics, metabolomics, high-content microscopy) and computational (network analysis, modeling) approaches to address fundamental aspects of complex cellular or organismal functions. Scientists working in any model organism or across diverse species are encouraged to apply. Areas of interest include but are not limited to: cellular and developmental processes integral to plant or animal health or disease, phenomics, genetic and metabolic regulatory networks, and responses to environmental signals and stresses. Interdisciplinary or collaborative research that complements existing strengths of the department and ISU is encouraged.

Responsibilities include building a nationally recognized research program that competes successfully for extramural funding, advancing the discipline through high-quality publications, mentoring students, and effective teaching of undergraduate and graduate courses. The successful candidate will demonstrate excellent communication and leadership skills and will share the university's commitment to an inclusive environment that supports diversity.

Required qualifications include a Ph.D. in life sciences or relevant discipline and published record of high-quality research.

To view the full job description and to apply, please visit **https://www.iastatejobs.com/postings/36729** to view the entire vacancy and apply electronically. For full consideration, submit the application by **December 7, 2018**.

Iowa State University is an EO/AA Employer. All qualified applicants will receive consideration for employment without regard to race, color, religion, sex, national origin, disability, or protected Vets status.

PRINCETON UNIVERSITY

Princeton Environmental Institute

Senior Faculty Search in Carbon Mitigation

Princeton Environmental Institute – the interdisciplinary center of environmental research, education and outreach at Princeton University -- seeks distinguished candidates for a **senior appointment (tenured level) in any field relating to climate change and carbon mitigation**. We seek an individual with a demonstrated record of excellence in disciplinary scholarship and teaching, with complementary interests in interdisciplinary research and an ability to communicate to, and work with, entities outside the academy, including governments, nongovernmental organizations, industry partners, and the broader public. We are particularly interested in candidates who can take an active leadership role in Princeton's Carbon Mitigation Initiative (https://cmi.princeton.edu). The successful candidate will be jointly appointed in the department best suited to her or his research areas and in the Princeton Environmental Institute.

Applicants should apply online at **https://www.princeton.edu/acad-positions/position/9661** and should submit a letter of interest along with a vitae, research statement, teaching statement, and the names and contact information of three potential referees. The letter of interest should include the candidate's vision of the field and identify major unanswered questions of interest to them. Evaluation of applicants will begin on January 8, 2019 and continue until the position is filled.

We seek faculty members who will create a climate that embraces excellence and diversity, with a strong commitment to teaching and mentoring that will enhance the work of the institute and attract and retain a diverse student body.

Wake Forest™ School of Medicine

Wake Forest School of Medicine
Department of Neurobiology and Anatomy

NEUROSCIENCE POSITION

The Department of Neurobiology and Anatomy is initiating a search for a tenure-track faculty member working in SENSORY/MOTOR NEUROSCIENCE. The selected candidate will interact with a large and collaborative group of sensory, cognitive and motor systems neuroscientists with funded research programs spanning the visual, auditory, somatosensory, and motor systems, as well as training grants emphasizing integrative function and development. In addition to maintaining a robust internationally recognized research program, successful candidates will be expected to support institutional and departmental teaching and mentoring for graduate students, medical students, and junior faculty. Start-up package, laboratory space, salary and rank will be commensurate with experience. Information on the department may be viewed at:
https://school.wakehealth.edu/departments/Neurobiology-and-Anatomy

Wake Forest School of Medicine offers a dynamic environment for cutting edge multidisciplinary research. Collaborative opportunities with other research entities include the WFU Primate Facility; Alzheimer's Disease Center; NCI-funded Comprehensive Cancer Center; Wake Forest Institute for Regenerative Medicine (WFIRM); Sticht Center on Aging; and others. Wake Forest is an Affirmative Action/Equal Opportunity Employer.

Winston-Salem is a vibrant community with an exciting cultural environment that is perennially ranked among the best places to live in the U.S. Situated within close proximity to both the Blue Ridge Mountains and the coast, Winston-Salem allows residents opportunity for a wide array of recreational activities. Applicants should submit an application package as a single PDF consisting of their curriculum vitae, a brief description of current and future research interests, and contact information for three references to:
Lindsay Teague, Talent Acquisition, Wake Forest Baptist Medical Center at: Lindsay.Teague@wakehealth.edu or (336) 716-8393.

SANOFI – INSTITUT PASTEUR 2018 AWARDS 7TH EDITION

For this new edition, the Sanofi – Institut Pasteur Awards foster scientific excellence for Global Health.

SANOFI - INSTITUT PASTEUR 2018 AWARDS FOR BIOMEDICAL RESEARCH

INTERNATIONAL SENIOR AWARD

Dr. Claude-Agnès REYNAUD and Dr. Jean-Claude WEILL

Institut Necker-Enfants Malades, Paris, France

Claude-Agnès Reynaud and Jean-Claude Weill were awarded for discovering novel mechanisms by which B-cell antibody repertories are generated. They are amongst the world's leading experts on adaptive immunology.

INTERNATIONAL MID-CAREER AWARD

Dr. Maria MOTA

Instituto de Medicina Molecular João Lobo Antunes, Lisbon

Maria Mota was awarded for her contributions to elucidate how Plasmodium regulates iron levels in order to survive. Her scientific research is widely recognized and respected by the malaria community.

SANOFI

Institut Pasteur

By **Elizabeth Marchio**

Climbing out of the bottle

I opened my swollen, bleary eyes to see a young police officer crouched close to my face, pen hovering over a clipboard. It was the same officer who had taken my mugshot. I had woken from an uncomfortable sleep, my body draped across three chairs in the police station holding room, my arms pulled inside my shirt in a futile attempt to keep warm. I peeked at the clock: 3:13 a.m. My body ached so much that I couldn't focus on his words. Methodically, he ran through the intake form. "Are you feeling hopeless or have nothing to look forward to?" I blinked back a new round of tears, slowly understanding that he was asking me whether I intended to commit suicide while I was held in jail. This was rock bottom. It was also the wake-up call I needed.

Five years into a Ph.D. program and separated from my husband—a decision I had made—I was unable to right myself from a deep depression and had just been arrested for driving while intoxicated. My husband and I had started our Ph.D. programs at the same time. We were older than our classmates, which increased the pressure to succeed, and managing the workload put a major strain on our relationship. If we allowed anything other than work to be our top priority, even temporarily, we were overcome by guilt. We stopped making time to go camping or take regular vacations. I felt neglected and seemed to want more from him than he could provide. Although we both wanted to start a family at some point, it was not the "right time." We would always have time for our relationship later, we thought.

We were wrong. The tiny crack of disconnect widened. After 4 years as Ph.D. students, we went our own ways.

I struggled to continue on my Ph.D. journey alone. My isolation increased as friends graduated and left the area. Social media reminded me of the things I hadn't yet accomplished and sometimes felt I was too old to ever realize: a permanent job, a home, a family of my own—the American dream. Healthy coping mechanisms—such as going to the gym, joining a sports team, or simply sitting with my intense disappointment and fear about the future—felt like luxuries that I could not afford. Instead, my new normal became drinking after a hard day—which was just about every day. I knew my family had a history of alcoholism that had blighted my mother's childhood, but I did not think my mode of dealing with stress was self-destructive.

No, that's not true. I knew I was unhappy. I knew that waking up hungover with little recollection of the night before meant a day of work lost. Nevertheless, I did not care, as long as drinking brought momentary relief. I told myself that I was drinking as a way to cope with feeling left behind in life, but really, I was self-medicating to stop feeling anything at all.

"Healthy coping mechanisms ... felt like luxuries that I could not afford."

It ended with a wrecked car and an arrest. Fortunately, no one was physically harmed, but they could have been. After a year of court proceedings, I am now 4 months into a year of probation, which includes thrice-daily breathalyzer tests, bimonthly urinalyses, courses at Mothers Against Drunk Driving, fines, fees, and more shame than I ever thought possible. At first, it all seemed unfair. I did not think I had a problem, and I fought tooth and nail against the punishments.

But after hearing from a mother who lost her daughter because of a drunk driver, I finally faced up to my part in everything that happened. I had made the decision to pursue a Ph.D. I had made the decision to leave my husband. And I had made the decision to drink and drive. Now, I needed to make the decision to get my life back on track. I got my drinking under control. Somewhat miraculously, I just successfully defended my Ph.D. thesis, which brings a mixture of pride, relief, and regret that it cost me so much.

For others who are precariously close to the edge of their own self-destructive whirlpool, perhaps my story can serve as a cautionary tale. Life does not stop while you are in graduate school. Graduate school is a part of life. You have to take care of yourself and find healthy ways to cope. You have to pay attention. ■

Elizabeth Marchio is finishing her Ph.D. at Texas A&M University in College Station.

ILLUSTRATION: ROBERT NEUBECKER